

Lecture Notes in Mechanical Engineering

Amar Patnaik  
Ernst Kozeschnik  
Vikas Kukshal *Editors*

# Advances in Materials Processing and Manufacturing Applications

Proceedings of iCADMA 2020

 Springer

# **Lecture Notes in Mechanical Engineering**

## **Series Editors**

Francisco Cavas-Martínez, Departamento de Estructuras, Universidad Politécnica de Cartagena, Cartagena, Murcia, Spain

Fakher Chaari, National School of Engineers, University of Sfax, Sfax, Tunisia

Francesco Gherardini, Dipartimento di Ingegneria, Università di Modena e Reggio Emilia, Modena, Italy

Mohamed Haddar, National School of Engineers of Sfax (ENIS), Sfax, Tunisia

Vitalii Ivanov, Department of Manufacturing Engineering Machine and Tools, Sumy State University, Sumy, Ukraine

Young W. Kwon, Department of Manufacturing Engineering and Aerospace Engineering, Graduate School of Engineering and Applied Science, Monterey, CA, USA

Justyna Trojanowska, Poznan University of Technology, Poznan, Poland

Francesca di Mare, Institute of Energy Technology, Ruhr-Universität Bochum, Bochum, Nordrhein-Westfalen, Germany

**Lecture Notes in Mechanical Engineering (LNME)** publishes the latest developments in Mechanical Engineering—quickly, informally and with high quality. Original research reported in proceedings and post-proceedings represents the core of LNME. Volumes published in LNME embrace all aspects, subfields and new challenges of mechanical engineering. Topics in the series include:

- Engineering Design
- Machinery and Machine Elements
- Mechanical Structures and Stress Analysis
- Automotive Engineering
- Engine Technology
- Aerospace Technology and Astronautics
- Nanotechnology and Microengineering
- Control, Robotics, Mechatronics
- MEMS
- Theoretical and Applied Mechanics
- Dynamical Systems, Control
- Fluid Mechanics
- Engineering Thermodynamics, Heat and Mass Transfer
- Manufacturing
- Precision Engineering, Instrumentation, Measurement
- Materials Engineering
- Tribology and Surface Technology

To submit a proposal or request further information, please contact the Springer Editor of your location:

**China:** Ms. Ella Zhang at [ella.zhang@springer.com](mailto:ella.zhang@springer.com)

**India:** Priya Vyas at [priya.vyas@springer.com](mailto:priya.vyas@springer.com)

**Rest of Asia, Australia, New Zealand:** Swati Meherishi at [swati.meherishi@springer.com](mailto:swati.meherishi@springer.com)

**All other countries:** Dr. Leontina Di Cecco at [Leontina.dicecco@springer.com](mailto:Leontina.dicecco@springer.com)

To submit a proposal for a monograph, please check our Springer Tracts in Mechanical Engineering at <http://www.springer.com/series/11693> or contact [Leontina.dicecco@springer.com](mailto:Leontina.dicecco@springer.com)

**Indexed by SCOPUS. All books published in the series are submitted for consideration in Web of Science.**

More information about this series at <http://www.springer.com/series/11236>

Amar Patnaik · Ernst Kozeschnik ·  
Vikas Kukshal  
Editors

# Advances in Materials Processing and Manufacturing Applications

Proceedings of iCADMA 2020

 Springer



*Editors*

Amar Patnaik  
Department of Mechanical Engineering  
Malaviya National Institute  
of Technology Jaipur  
Jaipur, Rajasthan, India

Ernst Kozeschnik  
Institute of Materials Science  
and Technology  
TU Wien, Austria

Vikas Kukshal  
Department of Mechanical Engineering  
National Institute of Technology  
Uttarakhand  
Srinagar (Garhwal), Uttarakhand, India

ISSN 2195-4356

ISSN 2195-4364 (electronic)

Lecture Notes in Mechanical Engineering

ISBN 978-981-16-0908-4

ISBN 978-981-16-0909-1 (eBook)

<https://doi.org/10.1007/978-981-16-0909-1>

© The Editor(s) (if applicable) and The Author(s), under exclusive license to Springer Nature Singapore Pte Ltd. 2021

This work is subject to copyright. All rights are solely and exclusively licensed by the Publisher, whether the whole or part of the material is concerned, specifically the rights of translation, reprinting, reuse of illustrations, recitation, broadcasting, reproduction on microfilms or in any other physical way, and transmission or information storage and retrieval, electronic adaptation, computer software, or by similar or dissimilar methodology now known or hereafter developed.

The use of general descriptive names, registered names, trademarks, service marks, etc. in this publication does not imply, even in the absence of a specific statement, that such names are exempt from the relevant protective laws and regulations and therefore free for general use.

The publisher, the authors and the editors are safe to assume that the advice and information in this book are believed to be true and accurate at the date of publication. Neither the publisher nor the authors or the editors give a warranty, expressed or implied, with respect to the material contained herein or for any errors or omissions that may have been made. The publisher remains neutral with regard to jurisdictional claims in published maps and institutional affiliations.

This Springer imprint is published by the registered company Springer Nature Singapore Pte Ltd. The registered company address is: 152 Beach Road, #21-01/04 Gateway East, Singapore 189721, Singapore

# Foreword

I am greatly honored to write this foreword for the proceedings of the International Conference on Advances in Materials Processing and Manufacturing Applications 2020 (iCADMA-2020) held at MNIT Jaipur, Rajasthan, during November 5–6, 2020. The advanced materials and manufacturing processes are revolutionizing all the specialized areas in different fields such as electrical, electronics, mechanical, and civil. A high degree of novelty is needed in both structural and functional materials for achieving the goal of sustainability.

The conference has provided an excellent opportunity for academicians, researchers, technocrats, and students to present their research work in the emerging field of advanced material and manufacturing processes. The theme of the conference is immensely suitable for all the researchers exploring advanced material and manufacturing processes. The published chapter will certainly provide a future direction to the researchers working in the field of advanced materials and manufacturing.

The research articles published in the proceedings of iCADMA-2020 titled *Advances in Materials Processing and Manufacturing Applications* cover a wide range of very interesting topics. I appreciate the authors for their technical input and fruitful discussions and scientific interaction during the conference.

I would like to acknowledge the organizers from MNIT Jaipur and NIT Uttarakhand for organizing such an appropriate international conference.

I wish the authors good luck for their future endeavors.



Prof. Alok Satapathy

[alok@nitrkl.ac.in](mailto:alok@nitrkl.ac.in)

Professor

Department of Mechanical Engineering

National Institute of Technology

Rourkela, India

# Preface

It is with great pleasure to introduce the proceedings of the *International Conference on Advances in Materials Processing and Manufacturing Applications (iCADMA-2020)* which was held online at Malaviya National Institute of Technology Jaipur, India, during November 5–6, 2020.

This book comprises selected papers from the presentations conducted during iCADMA-2020 endorsed by the Scheme for Promotion of Academic and Research Collaboration (SPARC). The conference was sponsored by SPARC and TEQIP-III National Institute of Technology, Uttarakhand. The conference drew the attention of various distinguished researchers and delegates from all over the world including Montenegro, Australia, Bangladesh, USA, Ecuador, Oman, Belgium, Estonia, and India. The conference consisted of eight keynote lectures and 23 technical sessions given by renowned researchers and scholars working in the areas of materials, manufacturing, optimization, industrial engineering, and tribological studies from all over the world. To grace the quality of the program, some peer-reviewed papers were invited for the presentation. Distinguished researchers from India, Austria, New Guinea, and Hungary were invited to deliver eight keynote lectures sharing the latest research discoveries in their respective areas of expertise. In the technical sessions, authors made oral presentations, and each presentation was confined to 10 minutes, followed by question and answer. One excellent presenter from each technical session was chosen for the best paper award depending on the technical merit, presentation, and application.

iCADMA-2020 focused on all broader aspects concerning advanced materials, materials manufacturing and processing, engineering optimization and sustainable development, and tribology for industrial application. iCADMA-2020 brought together scientists, engineers, researchers, and scientists from an engineering background as well as research scholars and faculties from IITs, NITs, IIITs, and other academic institutions. The conference was organized through Zoom. Authors shared the screen, and attendees could discuss their work via online platform. Overall, the conference was held successfully through the platform. The conference committee was dedicated to the success of the conference.

Foreign institute presenters were from University of Donja Gorica, Military Institute of Science and Technology, University of Technology Sydney, Chittagong University of Engineering and Technology, University of California Los Angeles, Tallinn University of Technology, Campus De Nayer, Sint-Katelijne Waver, and Technical University of Ambato, Huachi Campus. Presenting authors from government research institutes were from Metallurgy Corp. R&D BHEL, CSIR-Central Mechanical Engineering Research Institute, CSIR-Institute of Minerals and Materials Technology, Bhubaneswar, Odisha, India. Industrialists were from IEA Consultants, Bangalore, and Belimo Actuators India Pvt. Ltd., Mumbai.

All accepted papers were subject to peer review by the conference committee and invited international reviewers. The papers were selected based on their quality and their relevance to the conference.

I would like to express special gratitude to the members of the conference committee and organizers of the conference. I would also like to thank the reviewers for their valuable time and advice which helped in improving the quality of the papers selected for presentation at the conference and for publication in the proceedings. Finally, I want to thank the authors, the chairpersons, sponsors, and all the participants for their support for iCADMA-2020.

Jaipur, India

Dr. Amar Patnaik  
Convener and Organizing Secretary  
iCADMA-2020

# Acknowledgements

The editorial team sincerely acknowledge all the contributors of the book chapters. We are grateful to all the authors for their encouragement and support and for contributing the foreword to this book. Our special thanks to Scheme for Promotion of Academic and Research Collaboration (SPARC) for providing us the platform to organize the two-day International Conference on Advances in Materials Processing and Manufacturing Applications (iCADMA-2020). This conference was sponsored by the SPARC, the backbone of this conference, and supported by TEQIP-III, NIT Uttarakhand. We gratefully acknowledge all the participating authors and delegates from distinguished countries for transforming their work in the form of a book.

We extend our sincere thanks to Prof. Ernst Kozeschnik, TU Wien, Austria, for showering his abundant grace to knowledge the authors. We are grateful to Prof. Udaykumar R. Yaragatti, Director, MNIT, and Prof. S. L. Soni, Director, NIT Uttarakhand, for their constant motivation and support throughout the conference. We are also thankful to Prof. M. L. Mittal for his suggestions from time to time. We owe gratitude to Prof. Jyotirmay Mathur for his continuous mentorship from planning to execution of iCADMA-2020. We would also like to convey our sincere thanks to the respected Registrar, MNIT Jaipur, for providing all the necessary administrative support. A heartfelt thanks to the technical program committee and review board members for their valuable suggestion in making the conference a grand success. We also extend our sincere thanks to our eminent keynote speakers and technical session chairs from the scientific research community, academia, and industries for providing their valuable inputs for the success of the conference. We would like to take this opportunity to place on record our hearty thanks to organizing committee, administration, accounts, and dear students for their massive and sincere efforts.

Amar Patnaik  
Ernst Kozeschnik  
Vikas Kukshal

# Contents

<b>Optimization of Wire EDM Process Parameters for Machining of INVAR 36 Alloy</b> . . . . .	1
Ankita Mohanty, Rupam Mohapatra, and Supriya Priyadarshini Das	
<b>Engineering Comportment of Clays Motleyed with Rice Pericarp Slag (RPS)</b> . . . . .	13
Shravankumar Shivappa Masalvad, Anamika Yadav, Suresh Hubballi, and Praveen Kumar Sakare	
<b>Mathematical Modeling of Thin-Layer Drying of Hygroscopic Material (<i>Solanum tuberosum</i>) in Fabricated Tunnel</b> . . . . .	21
Dinesh Kumar, L. P. Singh, and Anil Kumar Singh	
<b>Partial Replacement of Cement with Coconut Husk Ash: A Review</b> . . . . .	29
Reshma B. Philip, V. S. Ajay, Amal K. Reji, S. Athulya, and Asween Santhosh	
<b>Employability Improvisation of Students of Technical Courses Through a Novel Method of Course Development and Performance Assessment</b> . . . . .	37
Deepshikha Aggarwal, Deepti Sharma, and Archana B. Saxena	
<b>Monitoring of Resources in Building Projects Using Internet of Things: A Literature Review</b> . . . . .	49
Sameer Jain, Kavita Choudhary, and D. K. Sharma	
<b>A Review of Recent Technology Development in Multilevel Inverter and Their Application in PV Systems</b> . . . . .	57
Aditi Gupta and Deepak Verma	
<b>Image Analytics on Damage Assessment to Draw Inferences on Pre and Pat Incident Assessment</b> . . . . .	69
Harshit Sharma and M. Monica Subashini	

<b>Modification in Harness and Electrical System for Performance Optimization of Formula Student Car</b> . . . . .	79
Sushant Satputaley, Ankita Nagnath, Vikalp Shendekar, Mahesh Mohan, and Prateek Pargaonkar	
<b>Valorization and Promotion of Montenegrin Bridges Through Implementation of ICT Technologies</b> . . . . .	87
Anđela Jakšić Stojanović and Neven Šerić	
<b>Assessing the Research Status on Occupational Safety for Adopting Zero Accident Vision: A Bibliometric Analysis</b> . . . . .	95
Jai Narain, M. L. Meena, G. S. Dangayach, and Gaurav Gaurav	
<b>Review of Recent Studies on Mechanical and Tribological Characteristics of AMMCs</b> . . . . .	113
T. Akilan and M. Mahendiran	
<b>Effects of Process Parameters on Build Time of PolyJet Printed Parts Using Taguchi Method</b> . . . . .	125
Arivazhagan Pugalendhi, Rajesh Ranganathan, and Balamurugan Gopalakrishnan	
<b>Synthesis and Testing of Epoxy-Based Alumina–Silicon Carbide Particular Reinforced Composite</b> . . . . .	135
Rahul Sharma and Rahul Sen	
<b>Failure Investigation of Induction Motor Bearing of Electric Vehicle Due to Manufacturing Defect</b> . . . . .	145
Deepak Borse, V. B. Tungikar, and D. R. Patil	
<b>Studies on Oxidation Behaviour of Cobalt-Based Superalloy 605</b> . . . . .	155
K. Jithesh, M. Arivarasu, and M. Nageswara Rao	
<b>Advancements in Energy Storage Through Graphene</b> . . . . .	165
Rasmeet Singh	
<b>Nano-Minimum Quality Lubrication (NMQL) and Machining Characteristics of Surface Using Various Nanofluids in Different Machining Processes: A Computational Analysis</b> . . . . .	175
Anamika Tiwari, Deepak Agarwal, and Anurag Singh	
<b>Framework and Case Study for Optimizing Target Value of a Process Using Taguchi’s Asymmetric Loss Function</b> . . . . .	189
Anoop Pandey and Manish Chaturvedi	
<b>Analysis of Load Capacity of Functionally Graded Material Structures</b> . . . . .	197
Shubhatma Sharma and Manish Bhandari	



**Mechanical Property and Microstructure Analysis of Laser Beam Welded Aluminium (A6061)-Titanium (Ti6Al4V) Dissimilar Sheet Metals** . . . . . 207  
 Sudhin Chandran, R. Rajesh, and M. Dev Anand

**Parametric Optimization and Evaluation of RMD™ Welding Performance for ASTM A387 Grade 11 Steel Plates Using TOPSIS-Taguchi Approach** . . . . . 215  
 Dinbandhu and Kumar Abhishek

**The Magnetically Assisted Abrasive Flow Machining Process: Review** . . . . . 229  
 Anil Jindal, Sushil Mittal, and Parlad Kumar

**Comparison of Static and Harmonic Response of Structural Steel and Aluminium Alloy Automotive Shock Absorbers** . . . . . 241  
 Abhishek Sharma, Surendra Kumar Yadav, Anshul Yadav, Virendra Kumar, and Anil Kumar

**A Review Paper on Metal 3D Printing Technology** . . . . . 251  
 T. Nancharaiah

**Dimensional Tolerance Analysis of Mechanical Assemblies with Symmetric and Asymmetric Tolerances** . . . . . 261  
 Ravikant Mordia, A. K. Verma, and Deepak Verma

**Investigation of Dielectric Dependency on CNTFET Characteristics in Ballistic Regime** . . . . . 275  
 Argha Sarkar, Raja Suresh, N. Padmavathy, and Chinna Aswini

**Comparative Study on Heat Transfer of Plastic Injection Molding Process for Quality Enhancement** . . . . . 283  
 Rupesh Kumar Khutey and Chhabi Ram Matawale

**Corrosion Behaviour of Aluminium 6061/MWCNT Composite Prepared by Double Stir Casting Method** . . . . . 293  
 T. Arunkumar, K Aditya Sreevatsa, Dinesh R. Krishnan, and Ram Subbiah

**A Review on Recent Developments in Kenaf, Sisal, Pineapple, Bamboo and Banana Fiber-Reinforced Composites** . . . . . 301  
 Rittin Abraham Kurien, Ashwin Santhosh, Daniel Paul, Gowrisankar B. Kurup, and Greshma Susan Reji

**Studies on Erosion and Oxidation Behaviour of Cobalt-Based Coatings** . . . . . 311  
 Prashant Kumar Singh and Pallvita Yadav

**Free Vibration Analysis of Laminated Curved Beams Using Fifth-Order Shear and Normal Deformation Theory** . . . . . 319  
 P. V. Avhad and A. S. Sayyad

<b>Luminous Concrete as Green Building Material</b> . . . . .	327
Manisha Sharma, Tanpreet Singh, and Sahibdeep Singh Setia	
<b>Removal of Lead Using Isolated Microorganisms from Contaminated Soil</b> . . . . .	335
Neethu Jayan and M. Laxmi Deepak Bhatlu	
<b>Overview of Physical Properties and Applications: Ferroelectric Lithium Niobate (LiNbO<sub>3</sub>)</b> . . . . .	345
Madhu, Muskaan Jain, and Prashant Povel Dwivedi	
<b>A Study on Austenitic Stainless-Steel Machining by Wire EDM</b> . . . . .	353
Shatarupa Biswas, Yogesh Singh, and Manidipto Mukherjee	
<b>Design Optimization and Analytical Study of a Modified Hydrous Aluminium Phyllosilicate Pantile</b> . . . . .	367
Anantha Krishna Somayaji, Narasimha Marakala, K. Raghavendra Pai, and Ajit M. Hebbale	
<b>A Study on Recent Developments in Jute, Cotton, Coir, Silk and Abaca Fiber-reinforced Composites</b> . . . . .	375
Rittin Abraham Kurien, Ashwin Santhosh, Daniel Paul, Gowrisankar B. Kurup, Greshma Susan Reji, and D. Philip Selvaraj	
<b>A Computational Methodology for the Synthesis of Assur Groups</b> . . . . .	385
H. Manikandan, Vijayananda Kaup, and Harish Babu	
<b>A Methodology for Derivation of Isomorphism Index for Epicyclic Gear Transmission Systems</b> . . . . .	391
H. Manikandan, Vijayananda Kaup, and Harish Babu	
<b>Study and Review of Quality 4.0 in the Industry</b> . . . . .	399
Gaurav Gohane, Atul Bulkunde, Anish Parate, Prabhat Nagdeve, Vikas Mendhe, Shivam Pandey, and Hrithik Yadav	
<b>Experimental Investigation of Tool Wear Rate (TWR) During the EDM of Hybrid Aluminum Metal Matrix Composite Reinforced with SiCp and Grp</b> . . . . .	409
Mandeep Singh, Pardeep Kumar Mishra, Pragyan Parimita Mohaty, and Rasmeet Singh	
<b>Effect of Process Parameter on Plastic Parts Using ANOVA with Moldflow Simulation</b> . . . . .	421
Kalpit Jain, Devendra Somwanshi, and Akshay Jain	
<b>Study of Tool Wear in Friction Stir Processing of Metal Matrix Composites—A Review</b> . . . . .	431
Pratap Singh and K. Hans Raj	

**Graphene–Alumina Composite: The Advanced Coating Material for Developing Harder Surface of Steel Strip Substrate** . . . . . 441  
 Tapan Dash, Gaurab Kumar Sahoo, Binod Bihari Palei, and Tapan Kumar Rout

**Recent Advances of Reinforced Natural Polymers: A Review** . . . . . 449  
 Sartaj Singh, Saurabh Kango, Nitin Sharma, and Sumit Sharma

**Analysis on Different Types of Viscometers, Design, Materials, and Technology: A Review** . . . . . 459  
 Priyanka S. Bankar and M. B. S. Sreekara Reddy

**Approach Toward Design for Manufacturing Assembly of Fiber Reinforced Plastics Fan Blade for Cooling Tower** . . . . . 469  
 Ankush Sharma, Vikas Kukshal, Pankaj Agarwal, and Aniruddha V. Kapre

**Synthesis, Structural and Magnetic Properties of Gadolinium-Doped Ni–Zn Ferrites Synthesized by Sol–Gel Auto-Combustion Route** . . . . . 479  
 D. L. Chaudhari, A. M. Shahare, A. K. Nandanwar, D. S. Choudhary, and K. G. Rewatkar

**Numerical Investigation on the Friction Factor Estimation for Laminar and Turbulent Flow in Smooth Pipe** . . . . . 489  
 S. A. Mashalkar and S. P. Nagdewe

**Performance of SoilTech MK III Polymer and Fly Ash on Problematic Soil** . . . . . 497  
 Taranpreet Kaur, Pardeep Singh, and Heena Malhotra

**Equal Channel Angular Pressing (ECAP) with Al Alloy—A Review** . . . . . 505  
 Nani Gopal Roy, Debayan Mondal, Partha Pratim Dey, and Manojit Ghosh

**Comparative Analysis of the Payback Period for Different Types of Solar Energy Systems Used in India** . . . . . 515  
 Abhishek Dhiman and Gulshan Sachdeva

**Three-Wheeler (Loading Auto-Rickshaw) Suspension by FEA** . . . . . 523  
 Rajat Yadav and Kamal Sharma

**3D-Printed Orthosis: A Review on Design Process and Material Selection for Fused Deposition Modeling Process** . . . . . 531  
 Ravi Kumar and Saroj Kumar Sarangi

**Experimental Investigation During Machining of P20 Tool Steel Using EDM** . . . . . 539  
 Manoj Kumar, Ankit D. Oza, Mehul Prajapati, and Gaurang Joshi

**Techno Economic and Life Cycle Assessment of 1 MW Solar  
Parabolic Trough System for Udaipur Zone** ..... 549  
Neelam Rathore and Vijayendra Singh Sankhla

**Micromechanical Modeling and Simulation of Natural Fiber  
Polymer Composite** ..... 563  
Love Kerni, Sarbjeet Singh, and Narinder Kumar

**Author Index** ..... 575

# Editors and Contributors

## About the Editors

**Dr. Amar Patnaik** is Associate Professor of Mechanical Engineering at Malaviya National Institute of Technology Jaipur, India. Dr. Patnaik has more than 10 years of teaching experience and has taught a broad spectrum of courses at both the undergraduate and graduate levels. He also served in various administrative functions, including Dean of International Affairs and Coordinator of various projects. He has guided 20 Ph.D.s and several M.Tech. theses. He has published more than 180 research articles in reputed journals, contributed five book chapters, edited one book and filed seven patents. He is also the guest editor of various reputed international and national journals. Dr. Patnaik has delivered more than 30 lectures as a guest invite in different institutions and organizations. He is a life member of Tribology Society of India, Electron Microscope Society of India and ISTE.

**Prof. Ernst Kozeschnik** is Head of the Institute of Materials Science and Technology at TU Wien since 2009. He has supervised numerous master and Ph.D. thesis, teaches basic and advanced University courses and has authored and co-authored more than 140 scientific papers. He is the author of the textbook “Modeling precipitation kinetics.” Prof. Dr. Kozeschnik is Lead Developer of the MatCalc software package, which is used in many different universities and research centers worldwide. He is Head of the Scientific Advisory Board of MatCalc Engineering GmbH. Prof. Kozeschnik was rewarded a “Christian Doppler Laboratory” in 2007, which is one of the most renowned mid-term scientific funds in Austria.

**Dr. Vikas Kukshal** is Assistant Professor at the Department of Mechanical Engineering of the National Institute of Technology Uttarakhand, India. He has more than 10 years of teaching experience and has taught a broad spectrum of courses at both the undergraduate and graduate levels. He has authored and co-authored more than 26 articles in journals and conferences and contributed

seven book chapters. Presently, he acts as a reviewer of various national and international journals. He is a life member of Tribology Society of India, The Indian Institute of Metals and The Institution of Engineers.

## Contributors

**Kumar Abhishek** Department of Mechanical & Aero-Space Engineering, Institute of Infrastructure, Technology, Research and Management, (IITRAM), Ahmedabad, Gujarat, India

**Deepak Agarwal** IET, Dr. Rammanohar, Lohia Avadh University, Ayodhya, U.P., India

**Pankaj Agarwal** Department of Mechanical Engineering, Amity University, Jaipur, Rajasthan, India

**Deepshikha Aggarwal** Department of Information, Jagan Institute of Management Studies, Delhi, India

**V. S. Ajay** Department of Civil Engineering, Providence College of Engineering, Chengannur, Kerala, India

**T. Akilan** Department of Mechanical Engineering, Karpagam College of Engineering, Coimbatore, Tamil Nadu, India

**M. Arivarasu** Center for Innovative Manufacturing Research, Vellore Institute of Technology, Vellore, India

**T. Arunkumar** Department of Mechanical Engineering, CMR Institute of Technology, Bengaluru, India

**Chinna Aswini** Nanoelectronics Lab, Sree Vidyanikethan Engineering College, Tirupati, Andhra Pradesh, India

**S. Athulya** Department of Civil Engineering, Providence College of Engineering, Chengannur, Kerala, India

**P. V. Avhad** Department of Civil Engineering, SRES's Sanjivani College of Engineering, Savitribai Phule Pune University, Kopergaon, Maharashtra, India

**Harish Babu** Department of Mechanical Engineering (VTU-RC), CMR Institute of Technology, Bengaluru, Karnataka, India

**Priyanka S. Bankar** Mechanical Engineering Department, Koneru Lakshmaiah Educational Foundation, Vaddeswaram, Guntur, India

**M. Laxmi Deepak Bhatlu** Department of Chemical Engineering, Faculty of Engineering, Karpagam Academy of Higher Education, Coimbatore, India

**Shatarupa Biswas** NIT Silchar, Silchar, Assam, India

**Deepak Borse** Shri Guru Gobind Singhji Institute of Engineering and Technology, Nanded, India

**Atul Bulkunde** JDCOEM, Nagpur, India

**Sudhin Chandran** Noorul Islam Centre for Higher Education, Kumaracoil, Tamil Nadu, India

**D. L. Chaudhari** Department of Physics, S. S. Jaiswal College, Gondia, India

**D. S. Choudhary** Department of Physics, D. B. Science College, Gondia, India

**Kavita Choudhary** JK Lakshmi Pat University, Jaipur, Rajasthan, India

**G. S. Dangayach** Department of Mechanical Engineering, Malaviya National Institute of Technology Jaipur, Jaipur, India

**Supriya Priyadarshini Das** Production Engineering, Indira Gandhi Institute of Technology Sarang, Dhenkanal, Odisha, India

**Tapan Dash** Centurion University of Technology and Management, Bhubaneswar, Odisha, India

**M. Dev Anand** Noorul Islam Centre for Higher Education, Kumaracoil, Tamil Nadu, India

**Partha Pratim Dey** Department of Mechanical Engineering, IEST, Howrah, India

**Abhishek Dhiman** National Institute of Technology Kurukshetra, Kurukshetra, India

**Dinbandhu** Department of Mechanical & Aero-Space Engineering, Institute of Infrastructure, Technology, Research and Management, (IITRAM), Ahmedabad, Gujarat, India

**Prashant Povel Dwivedi** Department of Electronics and Communication Engineering, Manipal University Jaipur, Jaipur, Rajasthan, India

**Gaurav Gaurav** Department of Mechanical Engineering, Malaviya National Institute of Technology Jaipur, Jaipur, India

**Manojit Ghosh** Department of Metallurgy and Materials Engineering, IEST, Howrah, India

**Gaurav Gohane** JDCOEM, Nagpur, India

**Balamurugan Gopalakrishnan** Department of Mechanical Engineering, Coimbatore Institute of Technology, Coimbatore, India

**Aditi Gupta** Birla Institute of Technology, Jaipur, Rajasthan, India

**K. Hans Raj** Faculty of Engineering, Dayalbagh Educational Institute (Deemed University), Dayalbagh, Agra, India

**Ajit M. Hebbale** Department of Mechanical Engineering, N.M.A.M. Institute of Technology, Nitte, Udupi District, Karnataka, India

**Suresh Hubballi** Department of Civil Engineering, SDM College of Engineering and Technology, Dharwad, India

**Akshay Jain** Poornima College of Engineering, Jaipur, India

**Kalpita Jain** Poornima College of Engineering, Jaipur, India

**Muskaan Jain** Department of Electronics and Communication Engineering, Manipal University Jaipur, Jaipur, Rajasthan, India

**Sameer Jain** JK Lakshmi Pat University, Jaipur, Rajasthan, India

**Neethu Jayan** Department of Chemical Engineering, Faculty of Engineering, Karpagam Academy of Higher Education, Coimbatore, India

**Anil Jindal** Department of Mechanical Engineering, Punjabi University, Patiala, Punjab, India

**K. Jithesh** School of Mechanical Engineering, Vellore Institute of Technology, Vellore, Tamil Nadu, India;  
Department of Mechanical Engineering, Thejus Engineering College, Thrissur, Kerala, India

**Gaurang Joshi** Department of Mechanical Engineering, Marwadi University, Rajkot, India

**Saurabh Kango** Department of Mechanical Engineering, Dr. B. R. Ambedkar National Institute of Technology, Jalandhar, Punjab, India

**Aniruddha V. Kapre** Customizing and Logistics, Belimo Actuators India Pvt. Ltd., Mumbai, India

**Vijayananda Kaup** Department of Mechanical Engineering (VTU-RC), CMR Institute of Technology, Bengaluru, Karnataka, India

**Taranpreet Kaur** Department of Civil Engineering, GNDEC, Ludhiana, Punjab, India

**Love Kerni** Mechanical Engineering Department, GCET Jammu, Jammu, India;  
Mechanical Engineering Department, CT University, Ludhiana, Punjab, India

**Rupesh Kumar Khutey** Department of Mechanical Engineering, Shri Rawatpura Sarkar University, Raipur, India

**Dinesh R. Krishnan** Department of Mechanical Engineering, CMR Institute of Technology, Bengaluru, India



**Vikas Kukshal** Department of Mechanical Engineering, National Institute of Technology Uttarakhand, Srinagar (Garhwal), Uttarakhand, India

**Anil Kumar** Kamla Nehru Institute of Technology, Sultanpur, India

**Dinesh Kumar** Sam Higginbottom University of Agriculture, Technology and Sciences, Naini, Prayagraj, India

**Manoj Kumar** Department of Production and Industrial Engineering, Punjab Engineering College (Deemed to be University), Chandigarh, India

**Narinder Kumar** Mechanical Engineering Department, CT University, Ludhiana, Punjab, India

**Parlad Kumar** Department of Mechanical Engineering, Punjabi University, Patiala, Punjab, India

**Ravi Kumar** Department of Mechanical Engineering, Motihari College of Engineering, Motihari, Bihar, India

**Virendra Kumar** Kamla Nehru Institute of Technology, Sultanpur, India

**Rittin Abraham Kurien** Department of Mechanical Engineering, Saintgits College of Engineering, Kottayam, Kerala, India;  
Department of Mechanical Engineering, Karunya Institute of Technology and Sciences, Coimbatore, India

**Gowrisankar B. Kurup** Department of Mechanical Engineering, Saintgits College of Engineering, Kottayam, Kerala, India

**Madhu** Department of Electronics and Communication Engineering, Manipal University Jaipur, Jaipur, Rajasthan, India

**M. Mahendiran** Metallurgy & QMS, Eppinger Tooling Asia Pvt. Ltd, Coimbatore, Tamil Nadu, India

**Heena Malhotra** Department of Civil Engineering, GNDEC, Ludhiana, Punjab, India

**H. Manikandan** Department of Mechanical Engineering (VTU-RC), CMR Institute of Technology, Bengaluru, Karnataka, India

**Narasimha Marakala** Department of Mechanical Engineering, N.M.A.M. Institute of Technology, Nitte, Udipi District, Karnataka, India

**Shravankumar Shivappa Masalvad** Department of Civil Engineering, Sreenidhi Institute of Science and Technology, Hyderabad, India

**S. A. Mashalkar** Marathwada Mitra Mandal's College of Engineering, Pune, India

**Chhabi Ram Matawale** Department of Mechanical Engineering, Shri Rawatpura Sarkar University, Raipur, India

**M. L. Meena** Department of Mechanical Engineering, Malaviya National Institute of Technology Jaipur, Jaipur, India

**Vikas Mendhe** JDCOEM, Nagpur, India

**Pardeep Kumar Mishra** Department of Mechanical Engineering, College of Engineering and Technology, Tiruchirappalli, India

**Sushil Mittal** Department of Mechanical Engineering, Chandigarh University, Gharuan, Punjab, India

**Mahesh Mohan** Department of Mechanical Engineering, St. Vincent Pallotti College of Engineering and Technology, Nagpur, Maharashtra, India

**Ankita Mohanty** Production Engineering, Indira Gandhi Institute of Technology Sarang, Dhenkanal, Odisha, India

**Rupam Mohapatra** Production Engineering, Indira Gandhi Institute of Technology Sarang, Dhenkanal, Odisha, India

**Pragyan Parimita Mohaty** Department of Mechanical Engineering, VSSUT, Burla, India

**Debayan Mondal** Technology Campus, University of Calcutta, Kolkata, India

**Ravikant Mordia** Department of Mechanical Engineering, Jai Narain Vyas University, Jodhpur, Rajasthan, India

**Manidipto Mukherjee** CAMM, CSIR-CMERI, Durgapur, West Bengal, India

**Prabhat Nagdeve** JDCOEM, Nagpur, India

**S. P. Nagdewe** 3DPLM Software Solutions Ltd, Pune, India

**Ankita Nagnath** Department of Electronics and Telecommunication Engineering, St. Vincent Pallotti College of Engineering and Technology, Nagpur, Maharashtra, India

**T. Nancharaiah** Mechanical Engineering, Bapatla Engineering College, Bapatla, AP, India

**A. K. Nandanwar** Department of Physics, Dr. Ambedkar College, Nagpur, India

**Jai Narain** Department of Mechanical Engineering, Malaviya National Institute of Technology Jaipur, Jaipur, India

**Ankit D. Oza** Department of Engineering and Physical Sciences, The University for Innovation, Gandhinagar, India

**Binod Bihari Palei** CSIR-Institute of Minerals and Materials Technology, Bhubaneswar, Odisha, India

**Anoop Pandey** ABES Engineering College, Ghaziabad, Uttar Pradesh, India

**Shivam Pandey** JDCOEM, Nagpur, India

**Anish Parate** JDCOEM, Nagpur, India

**Prateek Pargaonkar** Department of Mechanical Engineering, St. Vincent Pallotti College of Engineering and Technology, Nagpur, Maharashtra, India

**D. R. Patil** National Engineering Industries, Savli, India

**Daniel Paul** Department of Mechanical Engineering, Saintgits College of Engineering, Kottayam, Kerala, India

**Reshma B. Philip** Structural Engineering and Construction Management, Department of Civil Engineering, Providence College of Engineering, Chengannur, Kerala, India

**Mehul Prajapati** Department of Production Engineering, D. J. Sanghvi College of Engineering, Mumbai, India

**Arivazhagan Pugalendhi** Department of Mechanical Engineering, Coimbatore Institute of Technology, Coimbatore, India

**K. Raghavendra Pai** Department of Mechanical Engineering, N.M.A.M. Institute of Technology, Nitte, Udupi District, Karnataka, India

**R. Rajesh** Noorul Islam Centre for Higher Education, Kumaracoil, Tamil Nadu, India

**Rajesh Ranganathan** Department of Mechanical Engineering, Coimbatore Institute of Technology, Coimbatore, India

**M. Nageswara Rao** School of Mechanical Engineering, Vellore Institute of Technology, Vellore, India

**Neelam Rathore** DREE, CTAE, Udaipur, India

**M. B. S. Sreekara Reddy** Mechanical Engineering Department, Koneru Lakshmaiah Educational Foundation, Vaddeswaram, Guntur, India

**Amal K. Reji** Department of Civil Engineering, Providence College of Engineering, Chengannur, Kerala, India

**Greshma Susan Reji** Department of Mechanical Engineering, Saintgits College of Engineering, Kottayam, Kerala, India

**K. G. Rewatkar** Department of Physics, Dr. Ambedkar College, Nagpur, India

**Tapan Kumar Rout** Research and Development Department, Tata Steel Ltd, Jamshedpur, India

**Nani Gopal Roy** Department of Mechanical Engineering, IEST, Howrah, India

**Gulshan Sachdeva** National Institute of Technology Kurukshetra, Kurukshetra, India

**Gaurab Kumar Sahoo** Centurion University of Technology and Management, Bhubaneswar, Odisha, India

**Praveen Kumar Sakare** Department of Civil Engineering, SDM College of Engineering and Technology, Dharwad, India

**Vijayendra Singh Sankhla** DME, GITS, Udaipur, India

**Ashwin Santhosh** Department of Mechanical Engineering, Saintgits College of Engineering, Kottayam, Kerala, India

**Asween Santhosh** Department of Civil Engineering, Providence College of Engineering, Chengannur, Kerala, India

**Saroj Kumar Sarangi** Department of Mechanical Engineering, National Institute of Technology, Patna, India

**Argha Sarkar** Electronics and Communication Engineering, Vishnu Institute of Technology, Kovvada, Andhra Pradesh, India

**Sushant Satputaley** Department of Mechanical Engineering, St. Vincent Pallotti College of Engineering and Technology, Nagpur, Maharashtra, India

**Archana B. Saxena** Department of Information, Jagan Institute of Management Studies, Delhi, India

**A. S. Sayyad** Department of Civil Engineering, SRES's Sanjivani College of Engineering, Savitribai Phule Pune University, Kopargaon, Maharashtra, India

**Neven Šerić** Faculty of Economics, Business and Tourism, University of Split, Split, Croatia

**D. Philip Selvaraj** Department of Mechanical Engineering, Karunya Institute of Technology and Sciences, Coimbatore, India

**Rahul Sen** Mechanical Engineering Department, Poornima College of Engineering, Jaipur, India

**Sahibdeep Singh Setia** Civil Engineering Department, GNDEC, Ludhiana, Punjab, India

**A. M. Shahare** Department of Physics, D. B. Science College, Gondia, India

**Abhishek Sharma** K.R. Mangalam University, Gurugram, India

**Ankush Sharma** Department of Mechanical Engineering, Malaviya National Institute of Technology, Jaipur, Rajasthan, India

**D. K. Sharma** JK Lakshmi University, Jaipur, Rajasthan, India

**Deepti Sharma** Department of Information, Jagan Institute of Management Studies, Delhi, India

**Harshit Sharma** VIT, Vellore, India

**Kamal Sharma** Department of Mechanical Engineering, IET, GLA University, Mathura, India

**Manisha Sharma** Civil Engineering Department, GNDEC, Ludhiana, Punjab, India

**Nitin Sharma** Department of Mechanical Engineering, Dr. B. R. Ambedkar National Institute of Technology, Jalandhar, Punjab, India

**Rahul Sharma** Mechanical Engineering Department, Poornima College of Engineering, Jaipur, India

**Shubhatma Sharma** Department of Mechanical Engineering, MBM Engineering College, J.N.V University, Jodhpur, India

**Sumit Sharma** Department of Mechanical Engineering, Dr. B. R. Ambedkar National Institute of Technology, Jalandhar, Punjab, India

**Vikalp Shendekar** Department of Mechanical Engineering, St. Vincent Pallotti College of Engineering and Technology, Nagpur, Maharashtra, India

**Anil Kumar Singh** Government Polytechnic, Chapra, Bihar, India

**Anurag Singh** IET, Dr. Rammanohar, Lohia Avadh University, Ayodhya, U.P., India

**L. P. Singh** Sam Higginbottom University of Agriculture, Technology and Sciences, Naini, Prayagraj, India

**Mandeep Singh** School of Mechanical and Mechatronic Engineering, University of Technology Sydney, Ultimo, NSW, Australia

**Pardeep Singh** Department of Civil Engineering, GNDEC, Ludhiana, Punjab, India

**Prashant Kumar Singh** Department of Mechanical Engineering, G H Raisoni University Amravati, Amravati, India

**Pratap Singh** Faculty of Engineering, Dayalbagh Educational Institute (Deemed University), Dayalbagh, Agra, India

**Rasmeet Singh** Dr. S.S. Bhatnagar University Institute of Chemical Engineering & Technology, Panjab University, Chandigarh, India

**Sarbjeeet Singh** Mechanical Engineering Department, GCET Jammu, Jammu, India

**Sartaj Singh** Department of Mechanical Engineering, Dr. B. R. Ambedkar National Institute of Technology, Jalandhar, Punjab, India

**Tanpreet Singh** Civil Engineering Department, GNDEC, Ludhiana, Punjab, India

**Yogesh Singh** NIT Silchar, Silchar, Assam, India

**Anantha Krishna Somayaji** Department of Mechanical Engineering, N.M.A.M. Institute of Technology, Nitte, Udipi District, Karnataka, India

**Devendra Somwanshi** Poornima College of Engineering, Jaipur, India

**K Aditya Sreevatsa** Department of Mechanical Engineering, CMR Institute of Technology, Bengaluru, India

**Andela Jakšić Stojanović** Faculty of Culture and Tourism, University of Donja Gorica, Podgorica, Montenegro

**M. Monica Subashini** VIT, Vellore, India

**Ram Subbiah** Department of Mechanical Engineering, Gokaraju Rangaraju Institute of Engineering and Technology, Hyderabad, India

**Raja Suresh** Ekalavya Innovation Labs, Ekalavya Group of Technologies, Tirupati, Andhra Pradesh, India

**Anamika Tiwari** IET, Dr. Rammanohar, Lohia Avadh University, Ayodhya, U.P., India

**V. B. Tungikar** Shri Guru Gobind Singhji Institute of Engineering and Technology, Nanded, India

**A. K. Verma** Department of Production and Industrial Engineering, Jai Narain Vyas University, Jodhpur, Rajasthan, India

**Deepak Verma** Birla Institute of Technology, Jaipur, Rajasthan, India;  
Department of Mechanical Engineering, Graphic Era Hill University, Dehradun, Uttarakhand, India

**Anamika Yadav** Department of Agricultural Engineering, Assam University, Silchar, India

**Anshul Yadav** Kamla Nehru Institute of Technology, Sultanpur, India

**Hrithik Yadav** JDCEM, Nagpur, India

**Pallvita Yadav** Department of Mechanical Engineering, SVNIT Surat, Surat, India

**Rajat Yadav** Department of Mechanical Engineering, IET, GLA University, Mathura, India

**Surendra Kumar Yadav** K.R. Mangalam University, Gurugram, India

# Abbreviations

ABS	Acrylonitrile butadiene styrene
AFM	Abrasive flow machining
AM	Additive manufacturing
AMMC	Aluminum metal matrix composites
ANOVA	Analysis of variance
ASS	Austenitic stainless steel
BA	Bagasse ash
BCS	Black cotton soil
BSPD	Brake system plausibility device
CBR	California bearing ratio
CFD	Computational fluid dynamics
CHA	Coconut husk ash
CNN	Convolutional neural network
CNT	Carbon nanotube
DFA	Design for assembly
DMLS	Direct metal laser sintering
DOE	Design of experiments
DOP	Depth of penetration
ECU	Engine control unit
EDM	Electrical discharge machining
EGTS	Epicyclic gear transmission systems
EMV	Electro-micro fluidic viscometer
FGM	Functionally graded materials
FSI	Free swell index
FSP	Friction stir processing
GFR	Gas flow rate
HAZ	Heat-affected zone
IOT	Internet of Things
LCA	Life cycle assessment
LL	Liquid limit

MAFM	Magnetically assisted abrasive flow machining
MFA	Mold flow adviser
MLI	Multilevel inverter
MRR	Material removal rate
MWCNT	Multi-walled carbon nanotubes
NDT	Non-destructive testing
NRP	Natural reinforced polymers
PBP	Payback period
PGT	Planetary gear trains
PI	Plasticity index
PL	Plastic limit
PMC	Polymer matrix composite
PVC	Polyvinylchloride
RE	Renewable energy
RMD	Regulated metal deposition
RMES	Root mean square error
RPS	Rice pericarp slag
SEM	Scanning electron microscope
SLM	Selective laser melting
SPD	Severe plastic deformation
SPV	Solar photovoltaic
SV	Servo voltage
SWH	Solar water heater
TWA	Three-wheeled auto rickshaws
TWR	Tool wear rate
UFG	Ultra-fine-grained
ZAV	Zero accident vision



# Optimization of Wire EDM Process Parameters for Machining of INVAR 36 Alloy



Ankita Mohanty, Rupam Mohapatra, and Supriya Priyadarshini Das

**Abstract** Wire EDM is an eco-friendly, non-traditional machining process with no contact between the workpiece and the wire electrode and has a widespread usage in the field of medical industry, automobile industry, etc. The purpose of this present work is to optimize various wire EDM input parameters for machining of INVAR 36. The Taguchi technique was used to carry out the optimization. The control parameters like pulse-on-time ( $T_{on}$ ), pulse-off-time ( $T_{off}$ ), servo voltage (SV) and wire feed rate (Wf) were chosen to analyse the effect of various parameters on material removal rate (MRR) and surface roughness (SR) of INVAR 36 alloy. To optimize the material removal rate (MRR) and surface roughness (SR), a total of 9 ( $L_9$  orthogonal array) experiments were performed. The Taguchi method was applied by using MINITAB 17 software to maximize MRR and minimize SR. The optimum level of process parameters for MRR was found to be 25  $\mu$ s pulse-on-time, 46  $\mu$ s pulse-off-time, 5 mm/min wire feed rate, 30 V servo voltage and for surface roughness (SR) 25  $\mu$ s pulse-on-time, 19  $\mu$ s pulse-off-time, 3 mm/min wire feed rate, 20 V servo voltage.

**Keywords** Wire EDM · INVAR 36 · Taguchi technique · Surface roughness · Material removal rate

## 1 Introduction

Invar 36, Fe-(64–36 wt%) Ni is the most common iron–nickel alloy found in 1896 and is basically used in opto-mechanical engineering. Invar 36 alloy is ferromagnetic and is characterized by low coefficient of thermal expansion (CTE) below its Curie temperature (279 °C) and has excellent mechanical properties. Invar alloy is widely used where high-dimensional stability is the main requirement. Its modulus

---

A. Mohanty (✉) · R. Mohapatra · S. P. Das  
Production Engineering, Indra Gandhi Institute of Technology, Sarang, Odisha, India  
e-mail: [ankitasimun24@gmail.com](mailto:ankitasimun24@gmail.com)

© The Author(s), under exclusive license to Springer Nature Singapore Pte Ltd. 2021  
A. Patnaik et al. (eds.), *Advances in Materials Processing and Manufacturing Applications*, Lecture Notes in Mechanical Engineering,  
[https://doi.org/10.1007/978-981-16-0909-1\\_1](https://doi.org/10.1007/978-981-16-0909-1_1)

of elasticity remains almost constant for wider range of temperature. Owing to the high work hardening and high ductility, it is difficult to cut. Besides, in the cutting process of Invar 36, high ductile chips are easily generated and seriously affect the life of cutting tools and production efficiency [1–6]. Wire cut electric discharge machining (WEDM) is the best available option to overcome these problems. Wire cut EDM is an advanced thermal-assisted, non-conventional machining process which is widely used in the manufacturing, automotive and aerospace industry. The most prominent characteristic of this process is that the cutting tool never comes in contact with the workpiece. Also there is no force, mechanical stresses, and vibration during the machining process. The travelling wire has a very small diameter (0.02–0.3 mm), and this helps the machine to make small cuts. The wire acts as the electrode and the material wear out due to the high amount of heat that tends to melt material [7]. The material is flushed out with the dielectric medium (distilled water, kerosene, ethylene glycol, etc.). The dielectric medium works as spark conductor and for cooling the tool, workpiece and the spark area. Wire EDM is considered to be a significant development in the field of non-traditional machining. It has high accuracy rate which can produce intricate shapes, cuts, etc [8]. In spite of this, proper selection of process parameter remains a challenging job.

Debta et al. [9] found that in WEDM process, with the increase of pulse-on-time ( $T_{on}$ ), the cutting velocity increases; whereas, the kerf width and taperness of the machined profile reduce after an optimal value. However, wire tension has no significant effect on the machining performances. Sharma et al. [10] studied the effect of various input process parameters ( $T_{on}$ ,  $T_{off}$ ,  $I_p$ ,  $T_w$ ) on the response characteristics (MRR,  $I_g$ , MT) by using Taguchi L9 orthogonal array of AISI D2 die steel (13 mm diameter) using a 0.25 mm dia wire electrode and found  $T_{off}$  has been the leading significant factor for MRR. Maurya et al. [11] performed wire electric discharge machining on Nicrofer 5716. Experiments were performed utilizing Taguchi's L9 orthogonal array. Further, the responses are modelled with the response surface methodology approach for eliminating the residuals from the input as well as responses to create quadratic relationship among input and response variables with high adequacy and precision. Singh et al. [12] studied the dimensional deviation in wire EDM of M42 HSS using cryogenically treated brass wire and used ANOVA for significance and found variation of around 3.15% from the predicted value. Divya et al. [13] used Taguchi method for single objective optimization and grey relational analysis for multi-objective analysis to optimize the input process parameters: ( $T_{on}$ ), pulse-off-time ( $T_{off}$ ), peak current ( $I_p$ ), servo voltage, wire feed rate and wire tension of Inconel 825. Sivaprakasam et al. [14] enumerated the effect of graphite nanopowder suspended in dielectric medium of micro-wire EDM process of Inconel alloy. Kumar [15] developed a fuzzy model in MATLAB to predict fuzzy response parameters in WEDM process on stainless steel material (AISI 630) and compared the experimental result with the fuzzy predicted result and found that the system gives an overall 90% accuracy from the fuzzy model.

**Fig. 1** WEDM machine

## 2 Experimental Procedure

The experiment was performed using ELECTRONICA ECOCUT four axes CNC WEDM (Fig. 1 and Table 1). The brass wire used can be reused. The gap between brass wire and work piece is 0.02 mm, and the gap is maintained by a computer-controlled positioning system. The wire having a diameter of 0.25 mm was used as electrode. Deionized water was used as dielectric, and the base material was 5 mm. Four machining parameters were chosen. They were pulse-on-time (Ton), pulse-off-time (Toff), wire feed rate (Wf) and servo voltage (SV). The experiments were performed using Taguchi L9 orthogonal array. The chosen input parameters and their levels are shown in Table 2.

## 3 Calculation for Material Removal Rate and Surface Roughness

Material removal rate (MRR) is the measurement of how much amount material is removed from a part in a given period of time. The mechanism behind material removal rate of wire EDM process is based on the transfer of electrical energy to thermal energy that classifies it as electrothermal process [16]. At a given instant of time, when suitable voltage is developed, electrostatic field is produced which causes the cathode to generate electrons. These electrons get attracted towards the anode and start moving towards them at a high velocity. Upon collision with the dielectric medium molecules, these are broken into negative and positive ions.

**Table 1** WEDM machine specification

Maximum table size	590 × 370 mm
Maximum workpiece height	200 mm
Maximum workpiece weight	600 kg
Main table traverse (X, Y)	450, 350 mm
Auxiliary table traverse (u, v)	15, 15 mm
Maximum wire spool capacity	6 kg
Wire diameter	0.25 mm

**Table 2** Various level of process parameters

Process parameters	Level 1	Level 2	Level 3
Pulse-on-time	10	25	35
Pulse-off-time	46	25	19
Wire feed rate	3	5	7
Servo voltage	25	20	30

Because of this spark is generated with high temperature and causes melting and vapourization of material from the workpiece [17]. The MRR is calculated using the following formula:

$$\text{MRR} \left( \frac{\text{mm}^3}{\text{min}} \right) = \frac{\text{Weight loss of the specimen (gm)}}{\rho \times t} \quad (1)$$

where  $t$  = machining time (min),  $\rho$  = density of the work piece ( $\text{g/mm}^3$ ), calculated using water displacement test.

All the nine workpieces were machined according to the factors listed in Table 5. Each workpiece size was  $10 \times 10$  mm. For each machining, the time was noted down and the weight was weighed after machining. Figure 2 shows the workpieces after machining.

**Fig. 2** Workpieces after machining

Surface roughness is a measure of closely spaced micro-irregularities present on the surface texture [18]. The surface roughness was measured using a Mitutoyo (SJ 410) Talysurf (Fig. 3). Surface roughness was measured along the longitudinal axis of work piece, two measurements were made and average surface roughness Ra, and Rz was taken into account.

### 4 Optimization Using L9 Orthogonal Array

Orthogonal array (OA) design is a fractional factorial design. These designs are not only applicable to two-level factorial experiments but also can investigate main effects when factors have more than two levels [18]. Since, total four input parameters are taken and nine experiments are performed hence, L9 orthogonal array is selected. Layout of the L9 orthogonal array is shown in Table 3.

**Fig. 3** Mitutoyo (SJ 410) Talysurf



**Table 3** Layout of the L9 orthogonal array

Experiment No.	A	B	C	D
1	1	1	1	1
2	1	2	2	2
3	1	3	3	3
4	2	1	2	3
5	2	2	3	1
6	2	3	1	2
7	3	1	3	2
8	3	2	1	3
9	3	3	2	1

## 5 Results

Table 4 shows various input parameters and their levels and experimental results. The graphs and the response tables obtained from MINITAB 17 show the influence of various input parameters (Ton, Toff, Wf and SV) on the MRR and SR. Signal-to-noise (S/N) ratio for MRR was calculated by larger is better, and the ranking was given by Minitab 17. The ranks were Wf 1, Ton 2, Toff time 3 and SV 4. The response table for MRR is shown in Table 5. From the S/N ratio response table for SR, calculated by smaller is better, the rankings were given as Wf 1, Toff 2, SV 3 and Ton 4. The response table for SR is shown in Table 6.

Figure 4 shows the effect of control parameters on MRR (means), and Fig. 5 shows the effect of control parameters on MRR (S/N ratio). Figure 6 shows the effect of control parameters on SR (means), and Fig. 7 shows the effect of control parameters on SR (S/N ratio).

## 6 Analysis of Variance (ANOVA)

### 6.1 Material Removal Rate (MRR)

Table 7 constructed from experimental data using MINITAB 17 shows the ANOVA table for MRR. In this study of analysis of variance, pooling method was adopted; this is because pooling is a process of disregarding an individual's parameter's contribution and thereafter adjusting the contributions of other process parameters. Pooling is employed when there is indeterminate situation and the effect of parameter in a process is insignificant. Pooling process results in nonzero estimates of sum of square and DOF of variance [19]. In this, the pooling effect is on pulse-off-time, having the least influence on the MRR process. Wire feed rate has the highest influence on MRR which contributes 46.99%. Pulse-on-time and

**Table 4** Input parameters for MRR and SR experimental results

Exp No.	Ton ( $\mu$ s)	Toff ( $\mu$ s)	Wf (m/min)	SV (volts)	MRR ( $\text{mm}^3/\text{min}$ )	Ra (mm)
1	10	46	3	25	1.7841	1.500
2	10	25	5	20	2.8108	1.250
3	10	19	7	30	2.6612	1.431
4	25	46	5	30	15.2207	1.306
5	25	25	7	25	3.5078	1.708
6	25	19	3	20	2.0226	0.582
7	35	46	7	20	2.0249	1.662
8	35	25	3	30	1.2157	1.224
9	35	19	5	25	6.5204	1.257

**Table 5** Response table for S/N ratios (MRR)

Level	Ton	Toff	Wf	SV
1	7.502	10.302	4.281	7.074
2	13.556	7.191	16.304	10.738
3	8.037	11.602	8.510	11.282
Delta	6.054	4.410	12.023	4.208
Rank	2	3	1	4

**Table 6** Response table for S/N ratios (SR)

Level	Ton	Toff	Wf	SV
1	-2.8576	-0.1327	-0.1920	-0.5498
2	-0.7557	-2.7812	-2.0813	-3.3861
3	-2.7183	-3.4178	-4.0584	-2.3958
Delta	2.1019	3.2851	3.8664	2.8363
Rank	4	2	1	3

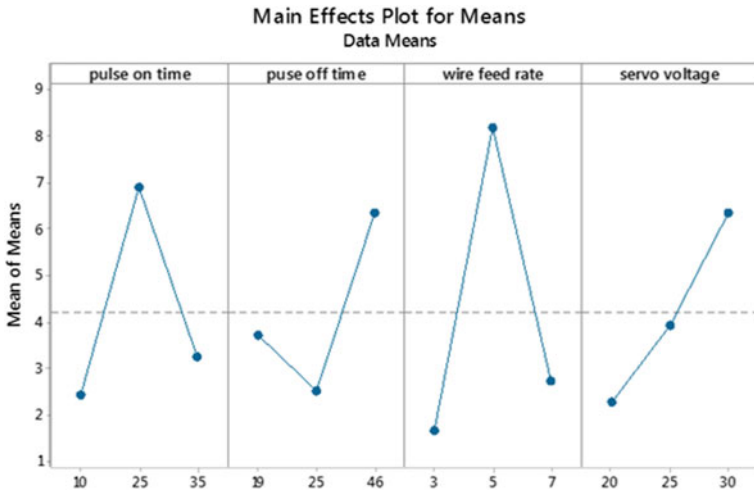


**Fig. 4** Effect of control parameters on MRR (means)

servo voltage have a contribution of 22.04% and 16.22%, respectively, with an error of 14.75%.

Regression Equation for MRR:

$$\begin{aligned}
 \text{MRR} = & 4.20 - 1.78 \text{ Ton}_{10} + 2.72 \text{ Ton}_{25} - 0.94 \text{ Ton}_{35} \\
 & - 2.52 \text{ Wf}_3 + 3.99 \text{ Wf}_5 - 1.47 \text{ Wf}_7 - 1.91 \text{ SV}_{20} \\
 & - 0.26 \text{ SV}_{25} + 2.17 \text{ SV}_{30}
 \end{aligned} \tag{2}$$

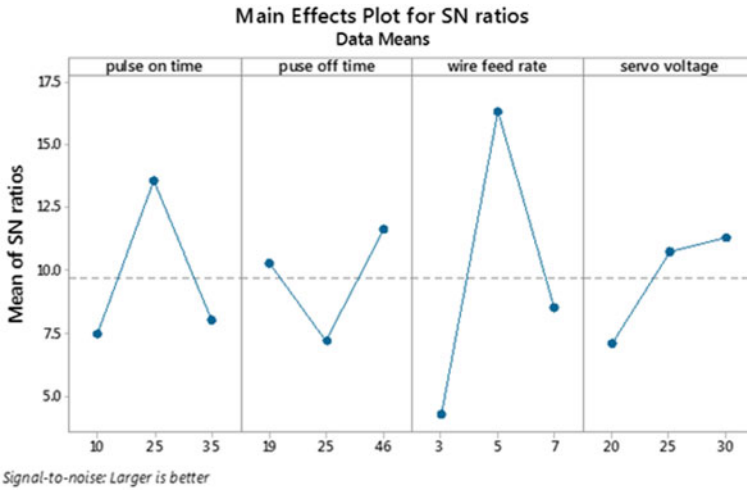


Fig. 5 Effect of control parameters on MRR (S/N ratio)

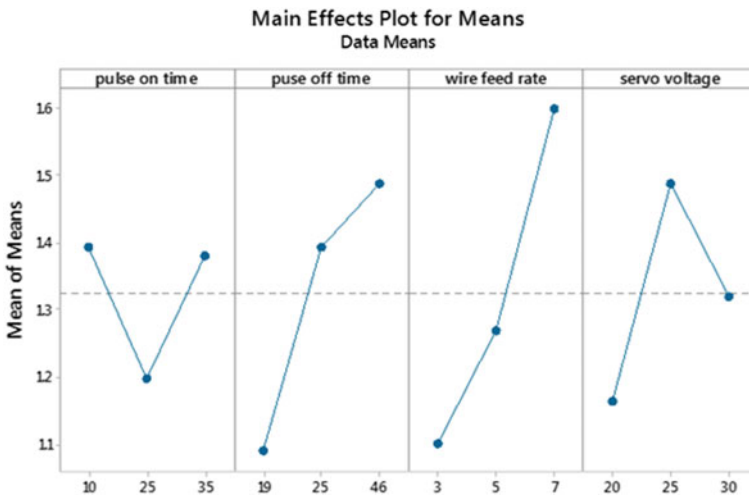


Fig. 6 Response table for S/N ratios (MRR)



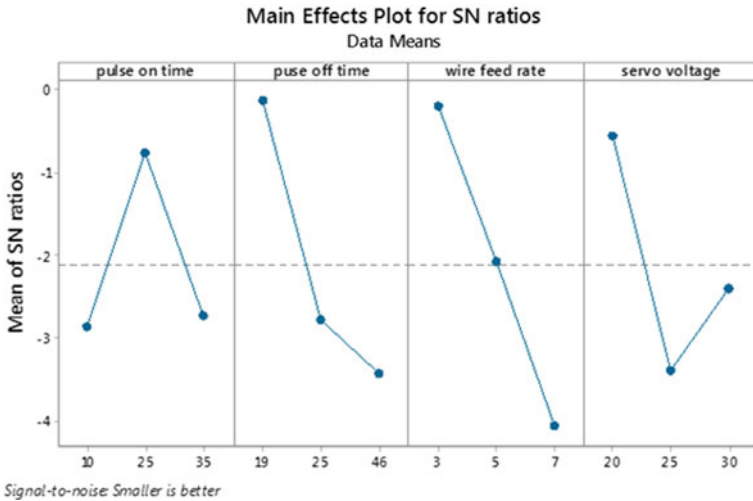


Fig. 7 Effect of control parameters on SR (S/N ratio)

Table 7 ANOVA table for MRR

Source	DF	Seq SS	Contribution in %	Adj SS	Adj MS	F value	P value
Ton	2	34.35	22.04	34.35	17.18	1.49	0.401
Wf	2	73.23	46.99	73.23	36.61	3.19	0.239
SV	2	25.27	16.22	25.27	12.63	1.10	0.476
<i>Toff Pooled</i>							
Error	2	22.98	14.75	22.98	11.49		
Total	8	155.83	100.00				

## 6.2 Surface Roughness (SR)

Regression equation for SR:

$$\begin{aligned}
 \text{SR} = & 1.3244 - 0.2224 \text{ Wf}_{3} - 0.0534 \text{ Wf}_{5} + 0.2759 \text{ Wf}_{79} \\
 & - 0.1598 \text{ SV}_{20} + 0.163 \text{ SV}_{25} - 0.0041 \text{ SV}_{30} \\
 & - 0.2344 \text{ Toff}_{19} + 0.0696 \text{ Toff}_{25} + 0.1649 \text{ Toff}_{46}
 \end{aligned}
 \tag{3}$$

Table 8 shows the ANOVA for SR. In this, the pooling effect is on pulse-on-time, having the least effect on the SR process. In this, the wire feed rate has also the highest influence which contributes 44.04%, and for pulse-off-time it is 29.83%. Servo voltage contributes 17.97% with an error of 8.16%.

**Table 8** ANOVA table for SR

Source	DF	Seq SS	Contribution in %	Adj SS	Adj MS	F value	P value
<i>Ton Pooled</i>							
Wf	2	0.38536	44.04	0.38536	0.19268	5.39	0.156
SV	2	0.15722	17.97	0.15722	0.07861	2.20	0.312
Toff	2	0.26097	29.83	0.26097	0.13049	3.65	0.215
Error	2	0.07143	8.16	0.07143	0.03572		
Total	8	0.87498	100.00				

## 7 Conclusion

Based on the results, the following conclusions were drawn from this experiment:

1. MRR increases with the increase in wire feed rate and pulse-on-time. Servo voltage has least effect on the material removal rate with a contribution of 16.22%.
2. The optimum level of process parameters for MRR is 25  $\mu$ s pulse-on-time, 46  $\mu$ s pulse-off-time, 5 mm/min wire feed rate and 30 V servo voltage.
3. Surface roughness increases with increase in wire feed rate and pulse-off-time. Servo voltage has least effect on the SR with a contribution of 17.97%.
4. The optimum level of process parameters for SR is 25  $\mu$ s pulse-on-time, 19  $\mu$ s pulse-off-time, 3 mm/min wire feed rate and 20 V servo voltage.
5. Wire feed rate is the highest influenced parameter on both MRR and SR and servo voltage being the least effective parameter.

It is important to note that the values of  $P$  in the ANOVA table are greater than the significance level (0.05). This states a conclusion that the parameters are less significant during the process. Proper selection of process parameters is very crucial in this context. The parameters vary from materials to materials. It is very necessary to select proper input parameter for determining their significance during the process. Therefore, this experiment presents an attempt to optimize the set of selected input parameters. However, more careful selection of parameters will yield better results and significance level.

## References

1. Gibb, S.: An introduction to invar. J. Inf. Knowl. Res. Mech. Eng. **2**(2), 434 (2013). 12 Nov to 13 Oct, ISSN 0975-668X
2. Li, H., Chen, B., Tan, C., Song, X., Feng, J.: Microstructure evolution and mechanical properties of laser metal deposition of Invar 36 alloy. **125**, Article-106037 (2020)
3. Yakout, M., Elbestawi, M.A., Veldhuis, S.C.: A study of thermal expansion coefficients and microstructure during selective laser melting of Invar 36 and stainless steel 316L. Addit. Manuf. **24**, 405–418 (2018)

4. Wei, K., Yang, Q., Ling, B., Yang, X., Xie, H., Qu, Z., Fang, D.: Mechanical properties of Invar 36 alloy additively manufactured by selective laser melting, *Mater. Sci. Eng. A* **772**, 138799. <https://doi.org/10.1016/j.msea.2019.138799>
5. Asgari, H., Salarian, M., Ma, H., Olubamiji, A., Vlasea, M.: On thermal expansion behavior of invar alloy fabricated by modulated laser powder bed fusion. *Mater. Des.* **160**, 895–905 (2018)
6. Khanna, N., Gandhia, A., Nakuma, B., Srivastava, A.: Optimization and analysis of surface roughness for INVAR-36 in end milling operations. *Mater. Today: Proc.* **5**(2), Part-1, 5281–5288 (2018)
7. Bhatt, D., Goyal, A.: Multi-objective optimization of machining parameters in wire EDM for AISI-304. *Mater. Today: Proc.* **18**, 4227–4242 (2019)
8. Fakir Mohamed, M., Lenin, K.: Optimization of wire EDM process parameters using Taguchi technique. *Mater. Today: Proc.* **21**, Part-1, 527–530 (2020)
9. Debta, M.K., Mishra, R., Masantaa, M.: Experimental investigation on the machining performance of AZ91D (90% Mg) alloy by wire-cut EDM. *Mater. Today: Proc.* <https://doi.org/10.1016/j.matpr.2020.802>
10. Sharma, S., Vates, U.K., Bansal, A.: Parametric optimization in wire EDM of D2 tool steel using Taguchi method. *Mater. Today: Proc.* (2020). <https://doi.org/10.1016/j.matpr.2020.802>
11. Maurya, R., Porwal, R.K., Kumar, V.: Parametric optimization in wire EDM of D2 tool steel using Taguchi method. *Mater. Today: Proc.* **26** (2020). <https://doi.org/10.1016/j.matpr.2020.802>
12. Singh, R., Singh, R.P., Tyagia, M., Kataria, R.: Investigation of dimensional deviation in wire EDM of M42 HSS using cryogenically treated brass wire. *Mater. Today: Proc.* **25**, Part-4, 679–685 (2020)
13. Divya, M., Sateesh, N., Subbiah, R.: Review on multi objective optimization of wire cut EDM process parameters using grey relational analysis. *Mater. Today: Proc.* <https://doi.org/10.1016/j.matpr.2020.02.645>
14. Sivaprakasama, P., Hariharan, P., Gowrib, S.: Experimental investigations on nano powder mixed micro-wire EDM process of inconel-718 alloy. *Measurement* **147**. <https://doi.org/10.1016/j.measurement.2019.07.072>
15. Kumar, J., Soota, T., Rajput, S.K.: Experimental evaluation and modelling of wire-EDM process parameter for stainless steel AISI 630. *Mater. Today: Proc.* **26**, Part-2, 1151–1158 (2020)
16. Kumar, R., Gandhi, V., Kant, K., Bector, M.: Performance study of wire cut electric discharge machining process by using Taguchi's parameter design approach. *Int. J. Eng. Inventions* **2** (2), 38–47, e-ISSN: 2278-7461, p-ISSN: 2319-6491
17. Singh, J., Singh, R., Kumar, R.: Review on effects of process parameters in wire cut EDM and wire electrode development. *Int. J. Innovative Res. Sci. Technol.* **2**(11), 701–705 (2016)
18. Subrahmanyam, M., Nancharaiah, T.: Optimization of process parameters in wire-cut EDM of Inconel 625 using Taguchi's approach. *Mater. Today: Proc.* **23** (2019). <https://doi.org/10.1016/j.matpr.2019.05.449>
19. Osayi, A.O., Egbe, E.A.P., Lawal, S.A.: Optimization of process parameters of manual arc welding of mild steel using Taguchi method. *Am. J. Mech. Eng.* **3**(3), 93–97 (2015)

# Engineering Comportment of Clays Motleyed with Rice Pericarp Slag (RPS)



Shravankumar Shivappa Masalvad , Anamika Yadav ,  
Suresh Hubballi , and Praveen Kumar Sakare 

**Abstract** The waste generated today is no more a waste according to many scientific community, and this waste has been put into many different of engineering application use. For example, the construction industry has plethora of such material which have been generated as waste, and further the progress and use of manufacturing and pastoral wastes, such as fly ash, blast furnace slag, metakaolin, rice pericarp slag (RPS), and bagasse ash (BA), are rapidly receiving attention as reviewed in many literatures [1–3]. The custom of ashes by the grinding process in cement concrete generally mends the properties of concrete, and the concretes encompassing ground fly ash or RPS are of good quality with condensed porosity and improved immunity to sulphate attack and chloride infiltration [4, 5] as well as great power [6–8]. Comparing to the fly ash which is the most common pozzolan being used worldwide in soil stabilization [9], the utilization of rice pericarp slag as pozzolanic material is still comparatively low. This tabloid benevolences the upshot of RPS on index and engineering properties of expansive clay. Liquid limit (LL), plastic limit (PL), plasticity index (PI) and free swell index (FSI) and unconfined compressive strength remained determined at capricious quantities of RPS. Unconfined compressive strength of the RPS clay amalgams was determined at their respective OMC and MDD, by piloting standard proctor compaction tests. LL, PI and FSI decreased significantly with increasing RPS content.

**Keywords** Expansive soil · FSI · RPS · Unconfined compressive strength

---

S. S. Masalvad (✉)

Department of Civil Engineering, Sreenidhi Institute of Science and Technology,  
Hyderabad 501301, India  
e-mail: [shravankumarsm@sreenidhi.edu.in](mailto:shravankumarsm@sreenidhi.edu.in)

A. Yadav

Department of Agricultural Engineering, Assam University, Silchar 788011, India

S. Hubballi · P. K. Sakare

Department of Civil Engineering, SDM College of Engineering and Technology,  
Dharwad 580002, India

## 1 Introduction

Expansive soils are susceptible to volumetric changes corresponding to changes in moisture content [5]. Heave and shrinkage occur in them alternatively in rainy and summer seasons [2]. Hence, civil engineering structures built on expansive clays experience detrimental cracking. Various innovative foundation practices have been devised for counteracting these problems. Some of these techniques include physical alteration and cushion techniques [10], drilled and belled piers [2], granular pile anchors and fly ash columns [8, 9].

Chemical stabilization is also quite effective in controlling swelling and shrinkage. In chemical stabilization, lime, cement,  $\text{CaCl}_2$  or fly ash is added to expansive clays to reduce swelling [1, 4, 7, 11]. Of the above chemicals, lime is considered the most efficacious in controlling heave. Plasticity, swelling and shrinkage decrease upon addition of lime to expansive soils. Strength of expansive clays treated with lime increased when compacted dry of optimum [12]. Rice pericarp slag (RPS), which can also be used as a pozzolanic additive to expansive soils, is obtained from the burning of rice husk. RPS contains  $\text{SiO}_2$  in amorphous form [3], which makes it pozzolanic. RPS can be used in lime–pozzolana mixes and Portland cement replacement [6].

This paper presents an experimental study on the effect of RPS on index and engineering properties of expansive soils. Liquid limit (LL), plastic limit (PL), plasticity index (PI) and free swell index (FSI) were the index properties studied at varying RPS content. And among the engineering properties, compaction characteristics and unconfined compressive strength (kPa) were determined at varying RPS content.

## 2 Experimental Investigation

### 2.1 Test Materials

The materials used in this investigation were expansive soil and rice pericarp slag, which were collected from Davangere, Karnataka, India. Geotechnical physiognomies of the capacious soil and the rice pericarp slag are shown in Table 1.

Table 2 shows the chemical analysis data of the soil and the RPS.

The expansive soil has a FSI of 122%. Based on the index properties and the grain size distribution, the soil is classified as CH (ASTM D2487). RPS particles exhibited a high angle of shearing resistance of  $\phi = 34.3^\circ$ .

**Table 1** Index and engineering properties of soil and rice pericarp slag (RPS)

Property	Soil	Rice pericarp slag
Gravel size (%)	0	0
Sand size (%)	11	84
Silt size (%)	27	16
Clay size (%)	56	0
Liquid limit, LL (%)	86	NP
Plastic limit, PL (%)	31	NP
Plasticity index, PI (%)	58	–
Free swell index, FSI (%)	123	Non-swelling
USCS classification	CH	Non-plastic
Optimum moisture content, OMC (%)	23	39
Maximum dry density, MDD (kN/m <sup>3</sup> )	13.5	8
California bearing ratio, CBR (%)	1	7

**Table 2** Chemical composition of soil and rice pericarp slag

Component	Quantity (%)	
	Soil	Rice pericarp slag (RPS)
Silica (SiO <sub>2</sub> )	51	96.53
Alumina (Al <sub>2</sub> O <sub>3</sub> )	17	0
Ferric oxide (Fe <sub>2</sub> O <sub>3</sub> )	7.5	0.21
Calcium (CaO)	3.38	0.25
Magnesium (MgO)	2.93	0
Sodium (Na <sub>2</sub> O)	5.8	0.40
Titanium (TiO <sub>2</sub> )	0.3	0
(V <sub>2</sub> O <sub>5</sub> )	0	0
(ZnO)	0	0
Loss of ignition	11.4	–

## 2.2 Tests Performed

### 1. Index properties

Index properties such as liquid limit (LL) and plastic limit (PL) were performed for the clay and clay–RPS blends.

### 2. Free swell index (FSI)

Free swell index (FSI) was also determined for the clay and clay–RPS blends. FSI is expressed [13] as

$$\text{FSI}\% = \frac{V_w - V_k}{V_k} \times 100 \quad (1)$$

where  $V_w$  and  $V_k$  are the volumes of the soil in water and kerosene, respectively.

It may be mentioned here that, for expansive clays, FSI is also an index property.

### 3. Compaction characteristics and unconfined compression strength

Compaction characteristics were also performed for clay, RPS and clay–RPS blends in the standard proctor test. Undrained shear strength (ASTM 2000, D2166) of the unblended soil and the soil blended with fly ash and RPS based on their dosages was determined at their respective OMC and MDD using cylindrical samples (38 mm in diameter and 76 mm in length) by conducting unconfined compression tests. The effect of curing period was also studied by curing the samples for 0 days, 7 days and 28 days.

### 4. Test variables

RPS was added in various percentages such as 6, 12, 18% and so on up to 30% to the dry clay for performing the tests.

## 3 Results and Discussion

Table 3 shows the entire test data obtained.

### 3.1 Index Properties

Figure 1 depicts the disparity of LL, PL and PI with RPS content. LL decreased from 84 to 28% when RPS content increased from 0 to 30%, indicating a reduction

**Table 3** Effect of rice pericarp slag (RPS) on index properties and engineering properties

Rice pericarp slag content (%)	Liquid limit, LL (%)	Plastic limit, PL (%)	Plasticity index, PI (%)	FSI (%)	OMC (%)	MDD (kN/m <sup>3</sup> )	Unconfined compressive strength (kPa) for curing periods of		
							0 days	7 days	28 days
0	84	29	55	125	25	15.5	120	200	200
6	80	30	50	108	25.6	15.1	117	215	235
12	73	31	42	92	26.2	14.7	114	230	270
18	66	32	34	75	27	14.35	111	240	285
24	52	34	18	60	27.8	14	108	250	300
30	28	NP	NP	20	29.4	13.2	102	280	340

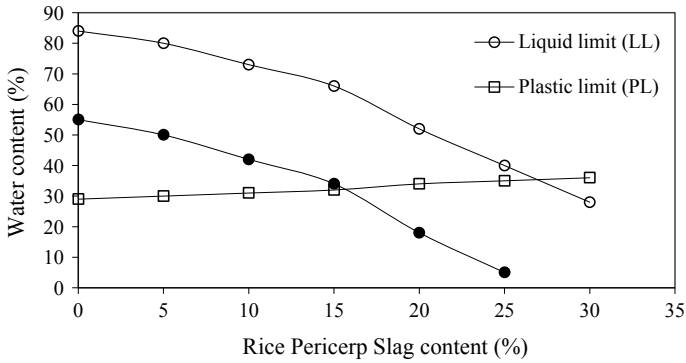


**Fig. 1** Effect of rice pericarp slag content on LL, PL and PI

of 64%. The decrease in LL by a huge amount can be attributed more to the auxiliary of expansive clay by an enormous extent of RPS particles than to RPS causing flocculation though it is pozzolanic. As RPS is of a very low specific gravity ( $G = 0.7$ ), a high number of RPS particles swap the original expansive soil for a given quantity. For the same purpose, at 30% preservative content, LL decreased more in the case of RPS than FA. Flocculation instigated by RPS increased PL by 21% when RPS increased from 0 to 30%. PI decreased from 55% to an extent that it was non-plastic (NP).

Free swell index (FSI) is an important parameter in the case of expansive soils. Figure 2 shows the variation of FSI with RPS content. FSI decreased from 125 to 20% when RPS content increased from 0 to 30% indicating a % reduction of 84%. The reduction in FSI with increase in RPS content can be attributed to both replacement of expansive clay particles by RPS and also to flocculation they caused.

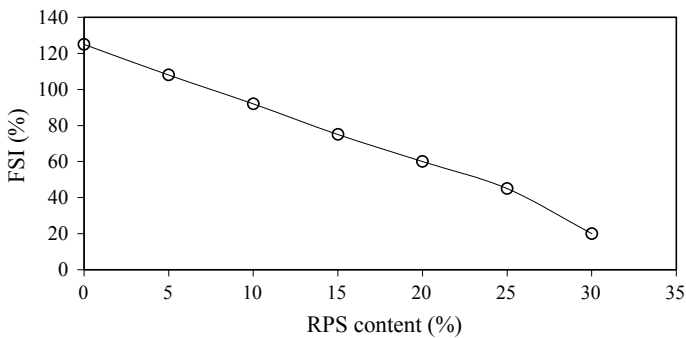


**Fig. 2** Effect of RPS on FSI



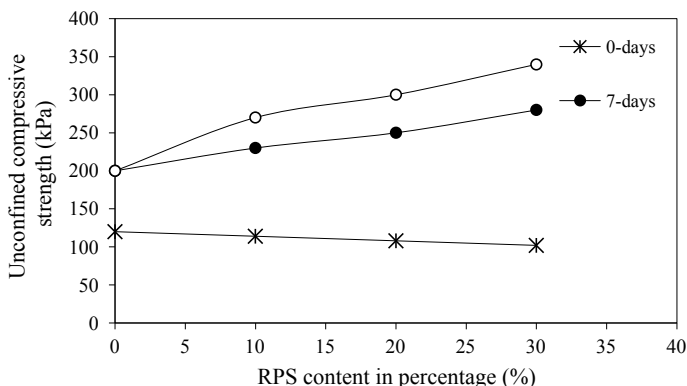


**Fig. 3** Effect of RPS content and curing period on unconfined compressive strength

### 3.2 Unconfined Compressive Strength

Figure 3 shows the distinction of UCS with RPS content for the curing periods of 0 days, 7 days and 28 days. At 0 days curing, UCS diminished slightly with increasing RPS content. This can be ascribed to the lessening in MDD with accumulative RPS content. However, UCS increased with increase in RPS content when the curing period increased to 7 days and 28 days. Further, for a given additive content, the UCS for 28 days was higher than that for 7 days. This can be attributed to increased pozzolanic reaction with increasing additive content and curing period.

## 4 Conclusion

LL and PI decreased significantly with increasing RPS content. At 30% RPS, the blend became non-plastic. FSI also decreased significantly with increasing RPS content. The FSI of the blends decreased by 81% at an RPS content of 32%. Unconfined compressive strength (kPa) of the RPS–clay blends decreased with increasing additive content when determined without curing. However, the unconfined strength of the RPS–clay blends increased with increase in additive content when the samples were cured for 7 days and 28 days. The experimental results indicate that the blends of expansive clays with 28% RPS, which have become non-plastic, non-swelling and compression-resistant at higher curing periods as the UCS results suggested that it could be used as cushion material for shallow footings or embankment material.

## References

1. Acosta, H., Edil, T., Benson, C.: Soil stabilization and drying using fly ash. Geo- Engineering Rep. No. 03-03, Department of Civil and Environmental Engineering, University of Wisconsin-Madison, Madison, Wisconsin (2003)
2. Chen, F.H.: Foundations on Expansive Soils. Elsevier Scientific Publishing Co., Amsterdam (1988)
3. Gambhir, M.L.: Concrete Technology, 2nd edn. McGraw Hill, New Delhi (1995)
4. Hoyos, L.R., Puppala, A.J., Chainuwat, P.: Dynamic properties of chemically stabilized sulfate rich clay. ASCE J. Geotech. Geoenviron. Eng. **130**(2), 153–162 (2004)
5. Lu, N., Lykos, W.: Unsaturated Soil Mechanics. Wiley, New York (2004)
6. Payá, J., Monzó, J., Borrachero, M.V., Mellado, A., Ordoñez, L.M.: Determination of amorphous silica in Rice Pericarp Slag by rapid analytical method. Cem. Concr. Res. **31**, 212–231 (2001)
7. Phanikumar, B.R., Sharma, R.S.: Effect of fly ash on engineering properties of expansive soils. ASCE J. Geotech. Geoenviron. Eng. **130**(7), 764–767 (2004)
8. Phanikumar, B.R., Sharma, R.S., Rao, A.S., Madhav, M.R.: Granular pile-anchor foundation (GPAF) system for improving the engineering behaviour of expansive clay beds. ASTM Geotech. Test. J. **27**(3), 279–287 (2004)
9. Phanikumar, B.R., Mani, A.J., Sathiyasheelan, S., Reddy, P.R.: Fly ash columns (FAC) as an innovative foundation technique for expansive clay beds. Geomech. Geoeng. Int. J. **4**(3), 183–188 (2009)
10. Phanikumar, B.R., Amshumalini, C., Karthika, R.: Swell consolidation characteristics of artificial sand-clay mixes. Geomech. Geoeng. Int. J. **7**(1), 69–74 (2012)
11. Phanikumar, B.R., Sreedharan, R., Aniruddh, C.: Swell-compressibility characteristics of lime-blended and cement-blended expansive clays—a comparative study. Geomech. Geoeng. Int. J. (2014). <https://doi.org/10.1080/17486025.2014.902120>
12. Ramesh, H.N.G., Sivapullaiah, P.V.: Role of moulding water content in lime stabilization of soil. Ground Improv. **64**(1), 15–19 (2010)
13. Holtz, W.G., Gibbs, H.J.: Engineering properties of expansive clays
14. Shrivankumar, S., Masalvad, et al.: Fluctuation of pressure due to bends in venturimeter. In: Recent Trends in Civil Engineering, pp. 833–846. Springer, Singapore (2021)

# Mathematical Modeling of Thin-Layer Drying of Hygroscopic Material (*Solanum tuberosum*) in Fabricated Tunnel



Dinesh Kumar, L. P. Singh, and Anil Kumar Singh

**Abstract** To investigate the characteristics of fresh potato in tunnel drying, an experimental setup of tunnel dryer was fabricated and installed in the laboratory. The samples of the potato for the drying were prepared in cubic shape of  $10 \times 10 \times 10 \text{ mm}^3$ . For the modeling of drying kinetics, drying data were observed at temperature of 50, 55, 60, 65, 70 and 75 °C, and data were fitted to different drying models. The selected models were tested based on model energy efficiency (EF), reduced chi square and root mean square error (RMSE) to select best fit of drying model. Results of the model nearly equal to modified page model with lower RMSE and reduced chi square value compared to page model. The observed data were fitted on Newton model, page model and modified page model. On the basis of experimental constant, modified page model was selected. In validation process, the model gave the maximum energy efficiency value **0.9823**, reduced value of chi square **0.0015** and minimum RMSE value **0.0323** at larger range of drying air temperature 45–60 °C.

**Keywords** Drying · Drying model · Air velocity · Moisture ratio tunnel dryer

## 1 Introduction

Potato is the fourth largest food crops in the world. Potato is member of Solanaceae family of the many plant stem solarium species, in which it is most widely cultivated. In 2014, worldwide production of potato (*S. tuberosum*) was more than 388 million tones which was consumed as food by people and used as animal feed and as potato starch in medicament industries [1]. The leading potato producers of the world are China, European Union, India, Russia, Ukraine, USA, Germany and

---

D. Kumar (✉) · L. P. Singh  
Sam Higginbottom University of Agriculture, Technology and Sciences,  
Naini, Prayagraj 211007, India

A. K. Singh  
Government Polytechnic, Chapra, Bihar 841418, India

Bangladesh, etc. India's potato production was estimated around 47 million tones in year 2014. In industry, the drying machinery has been widely used for processing of food products. During the drying of food materials, the food goes with undesirable changes that have negative effect on the food products.

Food drying is one of the oldest methods of processing and preserving food for later use. Food can be dried in the sun, in an oven or in a food dehydrator by using the right combination of warm temperature, low humidity and air current [2]. The common drying method is sun drying which has so many disadvantages. The traditional sun drying methods often yield poor quality, since the product is not protected against dust, rain, wind or even against birds, insects, rodents and domestic animals while drying. Soiling, contamination with microorganisms, formation of mycotoxins and infection with disease causing germs are the result [3].

Drying is one of the necessary processes for the preservation of agricultural products such as fruits and vegetables. This process enhances the life of agricultural products and their storage life and minimizes losses during storage life. Drying process reduces the shipping and transportation costs [4]. The thermal kinetics during drying the relationship between moisture ratios and drying instants was determined [5]. Based on the Lewis proposal, Newton's Law of Cooling

$$\frac{dM}{dt} = -k(M - M_0) \quad (1)$$

Thus, the main objective of this research is to develop an experimental drying setup cubical shape potatoes samples and to validate with existing drying models [6].

## 2 Materials and Methods

### 2.1 Materials

The fresh potatoes were collected from the near market in May–June. The full-size average dimension of potatoes was found 50–60 mm in length and 20–30 mm in width. The potatoes which were selected for the study were completely washed and peeled sliced into  $10 \times 10 \times 10 \text{ mm}^3$  using sharp knife [7].

### 2.2 Method

The experimental setup for carrying out the thin-layer drying is shown in Fig. 1. It consists of three main units: humidifier unit, air heating unit and drying unit. Humidifier is constructed by GI sheet in two cylindrical parts and is joined together by means of an air-tight flange joint. The lower part of the humidifier is of 0.3 m

diameter and 1 m height. A float valve is used in order to maintain a desired level of water in the lower portion of the humidifier. An overhead water tank is used to supply water to the humidifier unit. The air suction tunnel, 3 m long and 106 mm in diameter, is connected to the humidifier through an orifice meter just above the water level to measure the flow rate of drying air. The lower part of the humidifier is also provided with a water level indicator, a drain valve, two electric immersion heaters each of 2 kW capacity and a water pump and a 12 mm diameter perforated spray tube. It was intended that the atmospheric air be given a water bath by means of a fine spray produced in the humidification chamber using the perforated tube and the water pump to humidification to a desired dew point. At the top of the humidifier, two sets of louvers are provided to trap the water droplets from the moist air as shown in Fig. 1.

Humidifier unit is attached to the suction side of the blower. The drying air preparation unit was installed in three parts. The mid portion is a 1-m-long cylindrical shape with two diffusers at each end. Two heaters of 2-kW capacity each and three heaters of 1 kW capacity each are fitted into the cylindrical portion to raise the temperature of the air, coming out from the humidifier, to a desired value.

Thin-layer drying section consists of three sections: an air chamber, a base plate with five openings and an exposure chamber. The cylindrical air chamber is fitted with a 300 diffuser at 0.5 m height. The material drying unit is connected to the air preparation unit with the help of a 90°, 150 mm pipe bend to the diffuser. A 3-mm-thick mild steel base plate having five equi-spaced holes, each of 185 mm diameter, is fitted to the top of the plenum chamber. The openings are provided with rubber gaskets to prevent any leakage of air from the sides when drying pans are placed over them. To smooth functioning, placement of the drying pans, four small

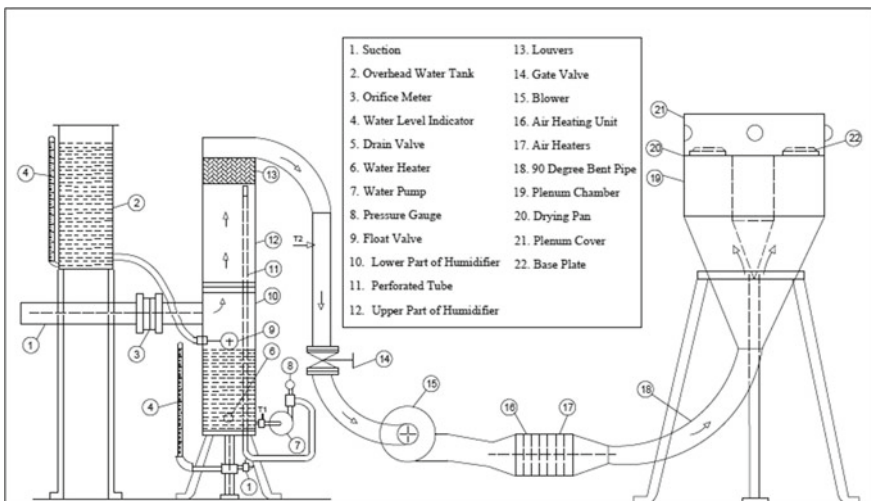


Fig. 1 Schematic diagram of thin-layer experimental setup

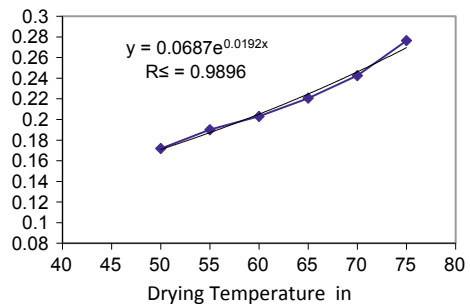
bearings are arranged to the plate toward each of the openings. During the experiments, temperature, velocity and relative humidity of drying air are recorded every 90 min. The temperature and relative humidity sensors are located at the inlet of the fan (T, RH), upstream (T1, RH1) and downstream of the tray (T2, RH2). The anemometer is located at the exit of the tunnel. The air was allowed to flow in the tunnel over the potato cubes with average velocity of 1 m/s, with 65% initial moisture content of potato on dry basis. With the time, the weight of the potato was observed to decrease gradually, and the humidity also decreased with the time. During the experiment, only drying temperatures are variable, and all other parameters are fixed.

### 3 Result and Discussion

The loss in weight during drying at different temperatures was converted into moisture contents (% d.b.). The relationship between moisture content and drying time for different temperatures is calculated. The moisture ratio was calculated from the moisture contents (% d.b.), the initial moisture content and the equilibrium moisture content at different temperature with time interval of 9 h. From the plot of moisture ratio versus drying time at different temperatures, it was observed that moisture ratio decreased rapidly during the first 8 h of drying as compared to the latter part of drying because of higher availability of free water during initial stages [8].

Variation in moisture ratio with time at different temperatures 50, 55, 60, 65, 70 and 75 °C was recorded. When a semilogarithmic plot of moisture ratio versus drying time was plotted at various temperatures, it results that drying time was reducing with increase in temperature. The value of drying coefficient was given by the slope of straight line, and the intercept gives the natural logarithmic value at different temperatures. Half-life method [9] was used in the calculation of drying coefficient  $K$  and plotted in Fig. 2.

**Fig. 2** Exponential graph of drying coefficient “K”



Hence the exponential model was fitted best with the following equation

$$K = 0.0687e^{0.0192T} \tag{2}$$

where “T” is the drying air temperature in °C.

Thus, the existing model Eq. (1) is modified for the experimental model using Eq. (2), and we get model drying equation for the experimental setup.

$$\frac{(M - M_e)}{(M_o - M_e)} = \exp^{-(0.0687e^{0.0192T})t} \tag{3}$$

where

- $t$  is the drying time in hours,
- $M_o$  initial moisture content,
- $M_e$  is equilibrium moisture content, and
- $M$  is moisture content after  $t$  time [10].

The value of drying coefficient is calculated from Eq. (2) (model parameter) for page model at 50 °C results that the energy efficiency is high at  $n = 1$ . Therefore, for  $n = 1$  page model also gives the maximum energy efficiency. Again, model was tested for the modified page model at varying value of  $n$ , and this model also results the maximum energy efficiency at  $n = 1$  at 50 °C as shown in Table 1.

Here in Table 2, all tested drying model values of chi square, RMSE and energy efficiency are shown [6].

From Table 2, it can be observed that lower value of RMSE is at 45–60 °C, and graph in Fig. 3 shows that energy efficiency is higher in the range of 45–60 °C for modified page model. These results show that the model was best fitted to the modified page model.

The comparative analysis of the experimental moisture ratio and the predicted moisture ratios based on modified page model  $MR = \exp^{(-Kt)^n}$  at drying air temperature 50 °C gave the value of experimental constant  $n = 1$  and drying coefficient  $K = 0.0687e^{0.0192T}$  (Fig. 4).

**Table 1** Modified page model at 50 value of  $n$

Temp	0.8	0.9	1	1.1	1.2	1.3
$\chi^2$	0.002499	0.001647	<b>0.001569</b>	0.002105	0.003114	0.004474
R.M.S.E.	0.034099	0.032153	<b>0.032316</b>	0.034438	0.038677	0.045654
EF	<b>0.971404</b>	<b>0.981305</b>	<b>0.982345</b>	<b>0.976507</b>	0.965537	0.950904

Source: At different value of  $n$ , optimum values are highlighted

**Table 2** Values of RMSE,  $\chi^2$  and EF for all model

Model	Temp	$\chi^2$	R.M.S.E.	EF
Newton model $MR = \exp(-Kr)$	45	0.002636	0.040902	0.967858
	50	0.001448	0.032316	0.982345
	55	0.001458	0.032696	0.982216
	60	0.002539	0.038809	0.969041
	65	0.004554	0.051156	0.944476
	70	0.007365	0.064292	0.910197
	75	0.010838	0.080846	0.867848
Page model $MR = \exp(-Kr)^n$	45	0.002856	0.040902	0.967858
	50	0.001569	0.032316	0.982345
	55	0.00158	0.032696	0.982216
	60	0.002751	0.038809	0.969041
	65	0.004933	0.051156	0.944476
	70	0.007979	0.064292	0.910197
	75	0.011741	0.080846	0.867848
Modified page $MR = \exp[-(Kr)^n]$	45	0.002856	0.040902	0.967858
	50	0.001569	0.032316	0.982345
	55	0.00158	0.032696	0.982216
	60	0.002751	0.038809	0.969041
	65	0.004933	0.051156	0.944476
	70	0.007979	0.064292	0.910197
	75	0.011741	0.080846	0.867848

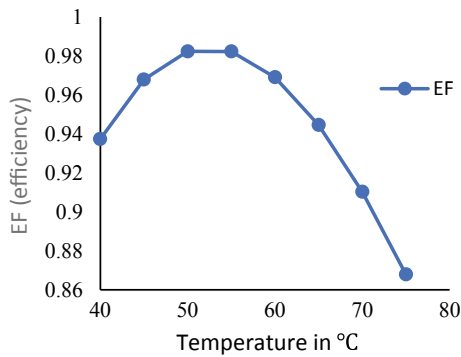


**Fig. 3** Value of EF versus temperature based on modified page model at experiment temperature 50 °C



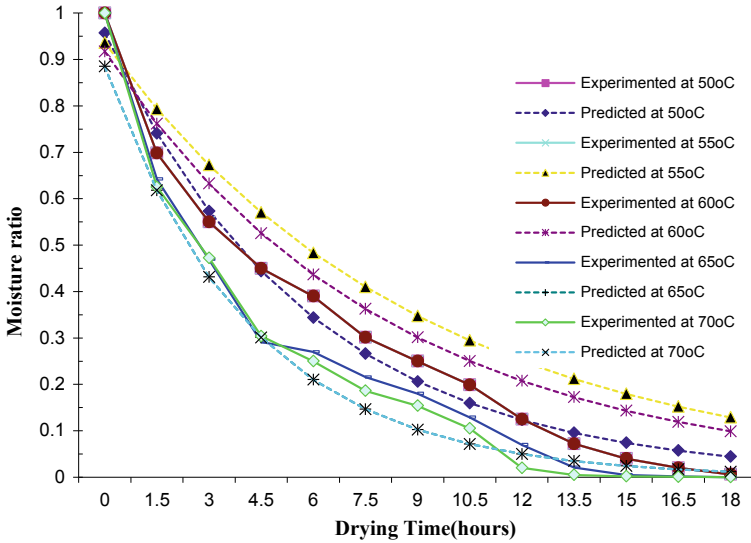


Fig. 4 Experimental and predicted moisture ratio versus time by modified page model

### 4 Conclusion

Thin-layer drying characteristics of *S. tuberosum* were investigated at various drying temperatures of air in tunnel dryer. The obtained data were fitted into drying models, namely Newton’s model, page model and modified page model and were compared on the basis of their statistical coefficients such as root mean square error (RMSE), chi square ( $\chi^2$ ) and efficiency (EF). The result showed that the predicted values were very close to experimental values. It was also found that out of all these models the values of RMSE and chi square were found lowest, and values of EF were found highest at particular temperature and in larger range value of constants  $n = 1$  on modified page model. The modified page model was found to be in good agreement with the experimental results  $\chi^2 = 0.0015$ , RMSE = 0.0323 and EF = 0.9823 for all drying temperatures taken up in the present study.

### References

1. Marcelo, S.B., Almeida, P.I.F.: Modeling of drying kinetic of potatoes taking into account shrinkage. *Procedia Food Sci.* **1**, 713–721 (2011)
2. Wankhade, P.K., Sapkal, R.S., Sapkal, V.S.: Drying characteristics of okra slices on drying in hot air dryer. *J. Procedia Eng.* **51**, 371–374 (2013)
3. Schirmer, P., Janjai, S., Esper, A., Smitabhindu, R., Muhlbauer, W.: Experimental investigation of the performance of the solar tunnel dryer for drying bananas. *Renew. Energy* **7**(2), 119–129 (1995)

4. Sacilik, K., Keskin, R., Elicin, A.K.: Mathematical modeling of solar tunnel drying of thin layer organic tomato. *J. Food Eng.* **73**, 231–238 (2006)
5. Gbaha, P., Andoh, H.Y., Saraka, J.K., Koua, B.K., Toure, S.: Experimental investigation of a solar dryer with natural convective heat flow. *Renew. Energy* **32**, 1817–1829 (2007)
6. Mohamadi, A., Rafiee, S., Keyhani, A., Djomeh, Z.E.: Estimation of thin layer drying characteristics of kiwifruit (cv. Hayward) with use of pages model. *American-Eurasian J. Agric. Environ. Sci.* **3**(5), 802–805 (2008)
7. Akpınar E., Midilli A., Bicer, Y.: Single layer drying behaviour of potato slice in a convective cyclone dryer and mathematical modeling. *Energy Convers. Manage.* **44**, 1689–1705 (2003)
8. Hossain, M.A., Bala, B.K.: Drying of hot chilli using solar tunnel drier. *J. Solar Energy* **81**, 85–92 (2007)
9. George, B.A., David, F.J., Donald, C.K., Priest, J.: Nuclear structure and nuclear technology. In: *International Edition University Physics*, pp. 842–869. Academic Press (1984)
10. Aregbesola, O.A., Ogunsina, B.S., Sofolahan, A.E., Chime, N.N.: Mathematical of thin layer drying characteristics of dika (*Irvingiagabonensis*) nuts and kernels. *Niger. Food J.* **33**, 83–89 (2015)

# Partial Replacement of Cement with Coconut Husk Ash: A Review



Reshma B. Philip, V. S. Ajay, Amal K. Reji, S. Athulya,  
and Asween Santhosh

**Abstract** Concrete is a strong building material holding fine aggregate and coarse aggregate bonded together with cement paste. Portland cement manufacturing can cause environmental impact at whole stages of the process including emission of huge amount of carbon dioxide. Use of agricultural waste as a coarse material for the production of concrete will reduce the expenditure of natural raw materials as resource and reduce the amount of solid waste in the environment. Due to the increasing cost of cement, it is now becoming unaffordable to use. Other binding materials are being used instead of cement, and one such agricultural waste is coconut husk ash (CHA). CHA is obtained by the burning of coconut husk at high temperatures. This paper covers the chemical properties and application of coconut husk ash. It deals with the effect of CHA on setting time, workability, compressive strength and porosity of concrete.

**Keywords** Concrete · Cement · Coconut husk ash · Setting time · Workability · Compressive strength · Porosity

## 1 Introduction

Among various materials used for building construction, concrete is the most frequently utilized medium. Concrete is best opted for its properties of strength, durability and aesthetics. Building construction using concrete is largely present in

---

R. B. Philip (✉)

Structural Engineering and Construction Management, Department of Civil Engineering,  
Providence College of Engineering, Chengannur, Kerala, India

V. S. Ajay · A. K. Reji · S. Athulya · A. Santhosh

Department of Civil Engineering, Providence College of Engineering, Chengannur, Kerala,  
India

spaces such as offices, mall, high-rise multi-purpose complexes and more. Foundations, beams, slabs, columns and other load-bearing elements are thus built using concrete. Cement is the binding element in concrete. The day-to-day demand for concrete is growing with the expansion in industrialization and urbanization. Critical environmental pollutions are caused with the increase in concrete utilization. Since its components of concrete are derived from nature, it results in the depletion of natural resources [1]. The use of natural and artificial pozzolans together with Portland cement not only results in a high strength concrete (HSC) by developing concrete microstructure but also finds an alternative preventive solution that promotes the environmental sustainability. Reduced heat of hydration and improved resistance against chemical agents are some of the properties obtained in concrete with the pozzolana activity [2]. There has been a growing interest in using supplementary cementitious materials that are derived from ashes of organic materials (mainly agricultural wastes) nowadays.

This paper reviews coconut husk ash as a replacement material in cement and deals with its effects on fresh and hardened properties of concrete. In 2010, the composition of World Cement Consumption was 3313 Million Metric Tons. Out of which 7% in India, 58% in China, 9% in developed countries and 26% in other countries. In 2009, the composition of coconut production in India was 10,894,000 tones. Kerala, Tamil Nadu, Karnataka and Andhra Pradesh were the leading coconut producing states in India [3]. Coconut is cultivated in over 86 countries in the world and India occupying the primary position within the world, yielding 13 billion nuts annually. But in the form of waste coconut, it also contribute to the nation's pollution problem as a solid waste [4].

## ***1.1 Applications***

- Coconut husk ash is a substitute method for producing silica from agricultural waste production with lower production cost.
- They can be used for the production of aluminium matrix composite using stir casting method.
- Coconut husk ash can be used as a stabilizing agent for upgrading soils with low plastic limit and California bearing ratio.
- Coconut husk ash can be adopted as an excellent mineral fertilizer.
- Coconut husk ash is currently used as a supplementary cementitious material in concrete.

## 2 Material

Worldwide production of coconut in 92 countries is about 10 million hectares. Around 75% of worldwide coconut productions are done by Indonesia, Philippines and India. Indonesia is world’s largest coconut producer. The coconut fruit contains 40% of coconut husk which includes 30% of fibre, with dust making up the rest. Lignin, cellulose, pyroligneous acid, gas, charcoal, tannin, tan and potassium are the major compositions. The coco casing contains materials that are immune to fungi and bacteria [5]. Coconut husk is a locally available agricultural waste material. The ash obtained after the burning of coconut husk is termed as coconut husk ash (CHA). The coconut husk is exposed outdoor for drying about 2–3 weeks to facilitate the burning process for ash collection, and then it is subjected to unrestrained combustion in open air for 3 h. Then it is subjected to cooling for about 12 h. The resulting ash is then collected and passed through IS sieve to obtain the required fineness, and this ash is used for further process [6]. Physically, the colour of coconut husk ash is dark grey.

## 3 Chemical Composition

The coconut husk ash composition is established using X-ray fluorescence (XRF) [7, 8]. The main aim of conducting an XRF is to ascertain the percentage of SiO<sub>2</sub>. The chemical composition of coconut husk ash shows the existence of silicon oxide in good load. Iron, magnesium and alkali oxides were also noticed in small amount, as depicted in Table 1. The presence of silicon oxide in coconut husk ash enhances its pozzolanic reactivity and cementitious properties, which makes it acceptable for the use in concrete [9, 10].

**Table 1** Composition of coconut husk ash (values are expressed in percentage %)

Oxides	Authors	
	Ikeagwuani et al. [9]	Kurniawan et al. [10]
SiO <sub>2</sub>	37	63.3
Al <sub>2</sub> O	7.74	0.25
CaO	2.14	0.77
MgO	0.21	0.29
Na <sub>2</sub> O	0.24	–
K <sub>2</sub> O	43.6	4.24
TiO <sub>2</sub>	0.04	0.04
Fe <sub>2</sub>	5.56	0.46
SO <sub>3</sub>	0.79	0.53
P <sub>2</sub> O <sub>5</sub>	2.62	0.63

## **4 Effect of Coconut Husk Ash on Setting Time of Cement**

Racaza and Cabahug [11] determined the initial and final setting time of cement with or without young coconut husk ash. They conducted tests to check whether blended cement satisfies the specification requirement which is detailed in ASTM C150 that setting time for cement must be between 45 and 375 min. It was observed that the cement blended with 60, 80 and 100% YCHA did not pass the requirements of time of setting. So, they focused on concrete with 20 and 40% YCHA replacement.

Arum et al. [12] observed the influence of coconut husk ash on initial and final setting time by replacing cement with 5, 10 and 15% of ash. Due to the addition of SCMs in cement, the amount of reaction was reduced causing a contraction in the hardening of the cement paste. The presence of alumina in the ash was the reason for the rate of reduction. They founded that the initial and final setting time of concrete with CHA were slightly higher than 100% of OPC mix but all were within the specified limits.

Obokparo and Arum [13] studied the effect of coconut husk ash on setting times of the concrete. Mixtures containing coconut husk ash up to 0, 5, 10, 15 and 20% of Portland cement by weight were replaced with CHA. It was observed that the setting time of ordinary Portland cement partially replaced by coconut husk ash rises with increase in percentage replacement.

## **5 Effect of Coconut Husk Ash on Workability of Concrete**

Arum et al. [12] determined the effect of CHA (5, 10 and 15% substitution) on compaction factor of the concrete. The test was conducted according to BSI standards. It was observed that compacting factor increases by increasing the coconut husk ash levels. It indicated that concrete with CHA mixes has an improved workability or compactability than concrete casted using 100% OPC.

Obokparo and Arum [13] conducted the workability by replacing cement with 5, 10, 15 and 20% of coconut husk ash. It was noted that the workability decreased at 5% addition of CHA in concrete mix and then started increasing gently making the concrete appropriately workable.

## **6 Effect of Coconut Husk Ash on Hardened Properties of Concrete**

### ***6.1 Compressive Strength***

Ettu et al. [14] studied the compressive strength by replacing cement with 5, 10, 15, 20 and 25% of coconut husk ash. From the results, it was detected that the

3–28 days compressive strength values of OPC replaced by CHA were much lesser than the normal values. While, 90 days compressive strength at 5–10% CHA replacements in OPC were greater than that of the control values. The 50 days strength was proportionate to the control values. He also stated that coconut husk ash (CHA) was courser than the OPC and could increase the compressive strength by making it into finer particles. There was a subsequent reduction in compressive strength by increasing the CHA content in OPC.

Racaza and Cabahug [11] replaced the cement by 0, 20, 40, 60, 80 and 100% of coconut husk ash and determined the compressive strength at 7, 14 and 28 days. It was found that compressive strength obtained at 20, 40 and 60% designed mixtures provided favourable applications for masonry purpose. Further increase in the percentage of CHA than 60% decreased the compressive strength.

Arum et al. [12] obtained the compressive strength of concrete specimens consisting of 5, 10 and 15% coconut husk ash at 7, 14, 21 and 28 days. It was detected that the compressive strength of concrete increased continuously as the CHA content increased from 0 to 15%. The 28 days strengths of concrete containing CHA were 103.1%, 106.2% and 109.8%, respectively for 5%, 10% and 15% replacements.

Obokparo and Arum [13] studied the effect of coconut husk ash on compressive strength of concrete with or without coconut husk ash at 7, 14, 28, 35, 42, 49 and 56 days. 5, 10 15 and 20% replacements of coconut husk ash were carried out. It was noted that compressive strength at 56 days of concrete with various percentage replacements had higher values as compared to 0% replacement. At 28 and 56 days, the compressive strength of concrete with 15% CHA had higher values than the strength of 100% OPC mixes at the same days.

Table 2 depicts the variation in compressive strength results from different studies.

**Table 2** Comparison of compressive strength results

Si. No.	Authors	CHA replacement (%)	Compressive strength			Unit
			7 days	14 days	28 days	
1	Ettu et al. [14]	0	14	21.5	23	N/mm <sup>2</sup>
		5	8	15.7	21.9	
		10	7.8	15.2	20	
		15	7	12.3	19	
		20	6.5	10.7	15.2	
		25	6.1	10	13	
2	Racaza et al. [11]	0	1317	1440	2043	psi
		20	1157	1493	1710	
		40	573	600	650	
		60	343	406	480	

## 6.2 Porosity

From the studies of Arum et al. [12], it was found that the addition of CHA in different percentages (5, 10 and 15%) caused reduction in porosity of concrete mixtures, due to the increased C–S–H gel formation.

## 7 Conclusions

Nowadays, the focus of industry is on sustainable development and concept of green economy which is important to environment and economy. The production of cement contributes to global warming, which leads to environmental changes. The utilization of agricultural waste makes the industry more eco-friendly and sustainable. The main aim of this review is to know the suitability of coconut husk ash as supplementary cementitious material. From the above research works, it could be concluded as follows:

- Coconut husk ash has great potential to earn a favourable output to be used as a supplementary cementitious material.
- From the chemical composition of CHA obtained mainly from X-ray fluorescence method, it shows the presence of good amount of silicon dioxide in it.
- The initial and final setting time of concrete with CHA are within values set by the standards.
- The workability of concrete with CHA replacements was better than that of control specimens.
- Up to a certain percentage replacement of coconut husk ash, it will give favourable compressive strength, after which the compressive strength decreases with rise in the coconut husk ash percentage.
- The addition of CHA in concrete also increases its density whereby reducing the porosity to a considerable extent.

## 8 Future Scope

These researches were mainly intended to inspect the influence of partial replacement of cement with coconut husk ash at different proportions in concrete. Works that may be conducted in future with CHA replacements are listed below:

- The influence of CHA additions in concrete using higher grades of concrete mixes with varying water–cement ratios.
- Further studies could be done by determining the tensile strength and deflections of concrete containing CHA.



- It checks on the durability parameters of CHA replaced concrete mixes including permeability, porosity, seepage characteristics and chemical attacks.
- CHA replaced concrete with plasticizer for higher grades of concrete.

## References

1. Aprianti, E., Shafigh, P., Bahri, S., Farahani, J.N.: Supplementary cementitious materials origin from agricultural wastes—a review. *Constr. Build. Mater.* **74**, 176–187 (2015)
2. Balagopal, V., Viswanathan, T.S.: A comprehensive exploration on sustainable supplementary cementitious materials derived from agro-wastes. *Int. J. Eng. Adv. Technol.* **9**(3), 2482–2489 (2020)
3. Van Dam, J.E.G., Van Den Oever, M.J.A., Keijsers, E.R.P.: Production process for high density high performance binderless boards from whole coconut husk. *Ind. Crops Prod.* **20**(1), 97–101 (2004)
4. Nagarajan, V.K., Aruna Devi, S., Manohari, S.P., Santha, M.M.: Experimental study on partial replacement of cement with coconut shell ash in concrete. *Int. J. Sci. Res.* **9**(5), 175–184 (2018)
5. Victor, E.: *Cocos nucifera* (coconut) fruit: a review of its medical properties. *Adv. Agric. Sci. Eng. Res.* **3**(3), 718–723 (2013)
6. Ikeagwuani, C.C., Nwoji, C.U., Okonkwo, C.: Compressibility characteristics of lateritic soil admixed with coconut husk ash and lime. *Int. J. Eng. Res. Technol.* **4**(11), 288–295 (2015)
7. Anuar, M.F., Fen, Y.W., Zaid, M.H.M., Matori, K.A., Khaidir, R.E.M.: Synthesis and structural properties of coconut husk as potential silica source. *Results Phys.* **11**, 1–4 (2018)
8. Anuar, M.F., Fen, Y.W., Zaid, M.H.M., Matori, K.A., Khaidir, R.E.M.: The physical and optical studies of crystalline silica derived from the green synthesis of coconut husk ash. *Appl. Sci.* **10**(6) (2020)
9. Ikeagwuani, C.C., Nwonu, D.C., Eze, C., Onuoha, I.: Investigation of shear strength parameters and effect of different compactive effort on lateritic soil stabilized with coconut husk ash and lime. *Niger. J. Technol.* **36**(4), 1016–1021 (2018)
10. Kurniawan, R.W., Hardiyanto, E., Faroqi, A.A.: Environmentally friendly material: coconut husk ash and fly ash as supplementary cementitious material. *Asian Acad. Soc. Int. Conf.* **2013**, 355–358 (2016)
11. Racaza, O.L., Cabahug, R.R.: Young coconut husk ash as partial cement replacement in masonry application. *Mindanao J. Sci. Technol.* **14**, 146–155 (2016)
12. Arum, C., Ikumapayi, C.M., Aralepo, G.O.: Ashes of biogenic wastes-pozzolanicity, prospects for use, and effects on some engineering properties of concrete. *Mater. Sci. Appl.* **4**(9), 521–527 (2013)
13. Obokparo, I.S., Arum, C.N.: Properties of ternary cementitious concrete matrix containing rice husk ash and coconut husk ash. *Int. J. Eng. Res.* **9**(2), 863–870 (2020)
14. Ettu, L.O., Ezeh, J.C., Ibearugbulem, O.M., Anya, U.C., Njoku, K.O.: Strength of binary blended cement composites containing plantain leaf ash. *IOSR J. Eng.* **3**(4), 54–59 (2013)

# Employability Improvisation of Students of Technical Courses Through a Novel Method of Course Development and Performance Assessment



Deepshikha Aggarwal, Deepti Sharma, and Archana B. Saxena

**Abstract** The education sector in India has seen a strong change in terms of professional courses. The public and private sectors have both been working toward making the students employable. The professional courses are designed at graduate and postgraduate levels to provide the skills to students that make them job ready. The colleges are teaching a predefined course curriculum in every course, and on the basis of this curriculum, exams are conducted and students are assessed. But this curriculum is not enough to make the students' job ready. The students need to be trained on the current trends in the industry, especially for the courses related to information technology. These extra efforts that the colleges provide for the students are termed as pre-placement activities. In this paper, we have conducted an analysis of the factors that impact the placement of students after the completion of Masters in Computer Application (MCA) course. This is higher education a post-graduate university course of 3 years. In this study, we have considered the marks obtained in university examination and other pre-placement activities including technical tests, technical interviews and personal interviews. The results of the analysis indicate how these different factors influence the placement of students after the course.

**Keywords** Placement · Pre-placement activities · Academic performance · Technical interviews · Non-technical interviews · Salary

---

D. Aggarwal · D. Sharma · A. B. Saxena (✉)  
Department of Information, Jagan Institute of Management Studies, Delhi, India  
e-mail: [archanab.saxena@jimsindia.org](mailto:archanab.saxena@jimsindia.org)

D. Aggarwal  
e-mail: [deepshikha.aggarwal@jimsindia.org](mailto:deepshikha.aggarwal@jimsindia.org)

D. Sharma  
e-mail: [deeptisharma@jimsindia.org](mailto:deeptisharma@jimsindia.org)

# 1 Introduction

The development in the field of education has been tremendous in the past few years. With the growth of professional colleges and courses, there has been a total change in the face of education in India [1]. The students in professional colleges are opting for these courses for the major goal of getting good jobs as soon as they complete their course. In today's scenario where most of the professional colleges are self-financed and not funded by the government, there is a tough competition to attract the maximum number of students [2]. The main reason that any student will take into consideration while selecting an institute for higher education is how good the placements of the institute are [3]. Therefore, all the colleges are working toward helping the students in attaining their goal of getting placed in a good company after their study. Education industry is also turning into a service industry where the students are the main focal point of any educational institute. The social and economic growth of a country is directly linked to the education and success of its youth [4].

The educational institutions imparting professional education play an important role in producing quality graduates and thus creating effective manpower for the country [5]. The academic performance of students has been a topic of research over the years. The academic institutions have been focusing more on various measures to improve the academic performance of the students. It has been also considered that the jobs that the students get after completing the courses are linked to their academic performance [6]. The main objective of the paper is to identify the factors that can impact curriculum-related subjects and pre-placement activities on the final placement of a postgraduate student. We have considered the academic performance as one of the factors and included various other factors as well. The academic performance of the students is measured in terms of the marks they score in the exams conducted by the university at the end of a semester [7]. The colleges assess the students on various other parameters such as personal interviews, technical tests and technical interviews as a part of pre-placement activities [8]. The projects conducted by the students are also evaluated. The analysis shows that the academic performance is not the only factor influencing the placement of students, and these considered factors also play an important role.

What are the important factors determining the placement of students after completing the Masters in Computer Application (MCA) course. MCA is a three-year full-time postgraduate course in information technology. Though, in this paper, authors have conducted the research and analysis on the data from an MCA college, but this analysis and results can be useful for any course in information technology. In order to attain the objective defined, the paper is organized as follows: Key and subordinate objectives are explained in Sect. 2. Further, "Research Methodology" is explained in Sect. 3 that consists of four steps: data collection, data analysis, dimension reduction and association analysis. At last, the paper is concluded with future scope and references considered during the study.

## 2 Research Objectives

The main objective of this research is to identify the impact of various factors on the final placement. The factors considered in the research are:

- Semester curriculum that a student has to study as per affiliating university guidelines for the award of respective degree.
- Pre-placement activities that the concern/respective college proposes.

Along with the attainment of the main objective, this research has also accomplished the following sub-aims:

1. Analysis of student's academic performance semester-wise.
2. Analysis of student's performance in distinct pre-placement activities.
3. Analysis of student's placement status [student-wise and year-wise].

## 3 Research Methodology

The methodology adopted by the authors during the execution of this research objective can be explained through the following steps;

### 3.1 Dataset Collection

Firstly, it is required to list the components that can impact the final placement of the student. All the academic activities that a student undergoes since admission till the placement are considered as an independent factor in the study. In order to generate authenticate results and consolidate solutions, dataset is collected from an affiliated college running MCA program as university affiliated program. The name of the college is purposefully kept secret by the authors. The actual scores/grades/marks of the last three year students are collected from the examination cell of college. It includes grades of internal as well as external examination. The pre-placement marks/scores are collected from the pre-placement cell of the respective college. The authenticity of the data is verified from the mark sheets issued by the university or the documents received by the college from the university. For the pre-placement-related grades, authors have to rely on what college has provided them as there is no means to verify that data. Students have studied multiple subjects each semester, so in order to reduce dimension, an average grade/score is allocated to all the subjects studied in one year and considered them as one factor. The final factors used in the study are mentioned below:

- Academic performance in the first year examination
- Academic performance in the second year examination

- Academic performance in the third year examination
- Technical test [individually conducted for each IT subject]
- Technical interview [individually conducted for each subject]
- Non-technical interviews.

### 3.2 Dataset Analysis

Datasets received from source are in Excel format. The authors are quite comfortable using SPSS, so all the analysis was completed in the SPSS version-20. Authors have executed all the analysis in the SPSS. In order to find the correlation between pre-placement activities and placement grade, Pearson correlation has been used by the authors because of the following reasons:

- Pearson correlation is most commonly used correlation in the normal distribution.
- It includes detailed description in its resulting table.
- It can offer positive as well as negative analysis.

All these factors were considered during analysis and chosen Pearson correlation to find association between concerned factors.

Although dataset consists of two types of details, demographic and academic details, the objective of the paper is to analyze the impact of academic performances on placement, so not much importance has been given to demographics, and authors have decided to exclude this part in the paper. The academic analyses of students are as follows:

- Analysis of marks of three batches of MCA course—2013–16, 2014–17 and 2015–2018.
- To analyze the impact of academic performance on placement, the results of three year marks are compiled and observed the performances in each year.
- Marks and analysis for the first year academic results.
- The frequency and percentages for different ranges of marks (Reference: Table 1; Fig. 1) scored by students in first year MCA. It can be observed that the maximum students' marks lie in between 70 and 80. It can be perceived that maximum students are scoring marks above the distinction marks, i.e., greater than 75.

Table 2 shows the marks and its analysis for the second year academic results [9]. It is observed from the Table 2 and Fig. 1 that a large number of students lie in the marks range of 70–80. In the third year also, the frequency of students is mostly in the range of 70 and 80 (Table 3).

**Table 1** Analysis of students’ performance in MCA first year

Marks	Frequency	Percent (%)	Valid percent (%)	Cumulative percent (%)
<60	2	1.1	1.1	1.1
>60 and <70	55	31.4	31.4	32.6
>70 and ≤80	80	45.7	45.7	78.3
>80 and ≤90	37	21.1	21.1	99.4
>90	1	0.6	0.6	100.0
Total	175	100.0	100.0	

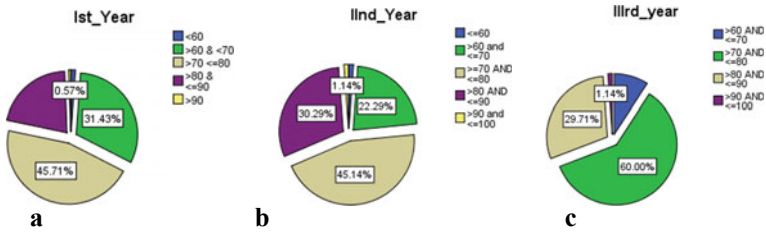


**Fig. 1** **a** Analysis of students’ performance in MCA first year, **b** analysis of students’ performance in MCA second year, **c** analysis of students’ performance in MCA third year

**Table 2** Analysis of students’ performance in MCA second year

Marks	Frequency	Percent	Valid percent	Cumulative percent
≤60	2	1.1	1.1	1.1
>60 and ≤70	39	22.3	22.3	23.4
≥70 and ≤80	79	45.1	45.1	68.6
>80 and ≤90	53	30.3	30.3	98.9
>90 and ≤100	2	1.1	1.1	100.0
Total	175	100.0	100.0	

**Table 3** Analysis of students’ performance in MCA third year

	Frequency	Percent	Valid percent	Cumulative percent
>60 and ≤70	16	9.1	9.1	9.1
>70 and ≤80	105	60.0	60.0	69.1
>80 and ≤90	52	29.7	29.7	98.9
>90 and ≤100	2	1.1	1.1	100.0
Total	175	100.0	100.0	

**Table 4** Analysis of students’ performance in pre-placement activities [technical test]

	Frequency	Percent	Valid percent	Cumulative percent
>60 and ≤70	1	0.6	0.6	0.6
>70 and ≤80	59	33.7	33.7	34.3
>80 and ≤90	91	52.0	52.0	86.3
>90 and <100	24	13.7	13.7	100.0
Total	175	100.0	100.0	

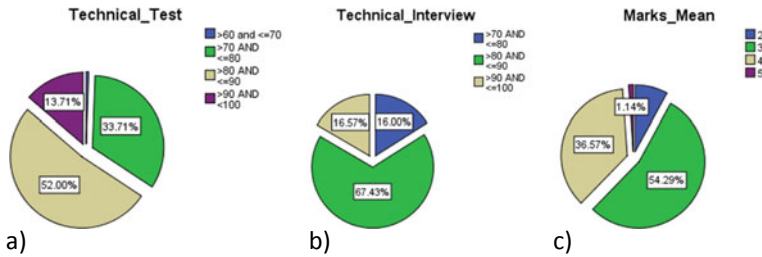


**Fig. 2** a Analysis of students’ performance in pre-placement activities [technical test], b analysis of students’ performance in pre-placement activities [technical interview], c analysis of students’ performance in three years

**Results for Technical Test:** In the second year of MCA, students undergo with various pre-placement activities like technical test, technical interviews and non-technical interviews. The maximum students are having marks in the range of 80–90 which is perceived as good marks (Table 4; Fig 2).

**Result for Technical Interviews:** Technical interviews are also a part of pre-placement activities that are conducted during the second year of MCA. In technical interviews, various topics like OOPs, databases, software engineering and programming concepts are being examined. The result analysis of these technical interviews is being shown below. In Table 5 and Fig. 2, it can be observed that if the students are scoring marks greater than 80, there are chances to get them placed in good company with respectable package [10].

**Table 5** Analysis of students’ performance in pre-placement activities [technical interview]

		Frequency	Percent	Valid percent	Cumulative percent
Valid	>70 and ≤80	28	16.0	16.0	16.0
	>80 and ≤90	118	67.4	67.4	83.4
	>90 and ≤100	29	16.6	16.6	100.0
	Total	175	100.0	100.0	

### 3.3 Dimension Reduction: Dimensions are Reduced by Calculating Mean

A dimension reduction process has been applied to all the above mentioned components [11]. Reduced factors are calculated as follows:

Mean Marks: Mean Marks = mean of 1st year marks + mean of 2nd year marks + mean of 3rd year marks.

The following table and figure show the mean marks of academic result of three years of MCA. The mean marks are calculated as the mean of marks of the students in all the three years of MCA course.

Through dimension reduction, authors have formed the following variables: Let individual semester results be treated as  $s_1, s_2, s_3, s_4, s_5$  and  $s_6$ .

$$\text{Total Marks} = \sum_5^{i=1} s_1 + s_2 + s_3 + s_4 + s_5 + s_6$$

Mean marks are then calculated for each student, and a score is then calculated as follows:

Score 1: Marks <60, Score 2: Marks >60 and ≤70, Score 3: Marks >70 and ≤80, Score 4: Marks >80 and ≤90, Score 5: Marks >90 (Table 6).

Technical Marks = mean of technical test marks + mean of technical interview marks.

Let technical test be  $t_1$  and technical interviews be  $t_2$ ,  
 Tech Marks =  $\sum_2^{i=1} t_1 + t_2$ .

Technical marks are a combination of mean marks of technical test and interviews. The analysis of students' performance is explained in Table 7 and Fig. 3. The tech marks mean is calculated as the mean of technical test marks and technical interview marks, and a score is given as follows:

Score 1: Marks <60, Score 2: Marks >60 and ≤70, Score 3: Marks >70 and ≤80, Score 4: Marks >80 and ≤90, Score 5: Marks >90 (Table 7; Fig. 3).

PI marks = non-technical interview marks. The PI marks are the personal interview marks, and a score is given as follows:

Score 1: Marks <60, Score 2: Marks >60 and ≤70, Score 3: Marks >70 and ≤80, Score 4: Marks >80 and ≤90, Score 5: Marks >90 (Table 8).

**Table 6** Analysis of students' performance in three years

Score	Frequency	Percent	Valid percent	Cumulative percent
2	14	8.0	8.0	8.0
3	95	54.3	54.3	62.3
4	64	36.6	36.6	98.9
5	2	1.1	1.1	100.0
Total	175	100.0	100.0	



**Table 7** Analysis of students’ performance in pre-placement activities [tech marks mean]

Score	Frequency	Percent	Valid percent	Cumulative percent
3	21	12.0	12.0	12.0
4	116	66.3	66.3	78.3
5	38	21.7	21.7	100.0
Total	175	100.0	100.0	

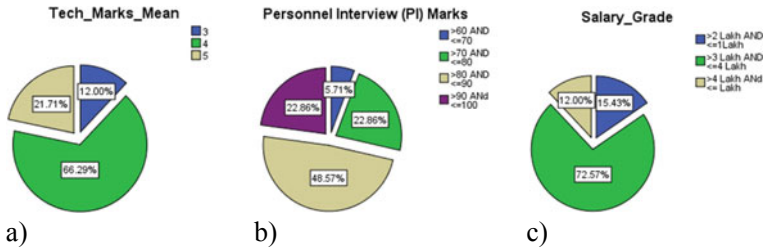


**Fig. 3** a Analysis of students’ performance in pre-placement activities [tech mean marks], b analysis of students’ performance in pre-placement activities [PI mean marks], c analysis of student’s performance on salary grade

**Table 8** Analysis of students’ performance in pre-placement activities [personal interview]

Score	Frequency	Percent	Valid percent	Cumulative percent
>60 and ≤70	10	5.7	5.7	5.7
>70 and ≤80	40	22.9	22.9	28.6
>80 and ≤90	85	48.6	48.6	77.1
>90 and ≤100	40	22.9	22.9	100.0
Total	175	100.0	100.0	

**Table 9** Salary grade

Salary grade	Frequency	Percent	Valid percent	Cumulative percent
>2 Lakh and ≤1Lakh	27	15.4	15.4	15.4
>3 Lakh and ≤4 Lakh	127	72.6	72.6	88.0
>4 Lakh and ≤Lakh	21	12.0	12.0	100.0
Total	175	100.0	100.0	

**Salary:** Salary is the measure of the goodness for placement of students [11]. During the next few steps, we will analyze the impact of various academic activities explained above (independent variables) on placement (dependent variable) which is measured on the scale of salary [12] (Table 9).

The salary is measured in INR (LPA—Lakhs Per Annum) which is given in different grades as follows: Grade 1: Salary <1 LPA, Grade 2: Salary >1 LPA and  $\leq 2$  LPA, Grade 3: Salary >2 LPA and  $\leq 3$  LPA, Grade 4: Salary >3 LPA and  $\leq 4.5$  LPA, Grade 5: Salary >4.5 LPA.

### 3.4 Association Analysis

There are two categories of variables considered during analysis purpose. The following variables are used to perform association analysis (Table 10):

The relationship between two variables can be studied through correlation coefficient [13]. The correlation coefficient creates a relationship between two variables [14]. The relationship must be linear, independent and normally distributed. In this study, the authors have tried to find the relationship between salary and marks of the subjects, technical test and technical interview and personal interviews [15]. As described above, mean marks are calculated from the average marks of the subjects of three years of MCA.

Tech score is a combination of technical test as well as technical interviews and is estimated from these two values. PI score is a resultant of average of personal interviews. There are few more fields also which are described in Table 11; marks + PI score which are a combination of exam marks and personal interview marks. Similarly, combination of tech score and exam marks is created as tech score + marks. In addition, marks + PI score + tech score is also formed by combining marks of these three fields. The Pearson correlation has been calculated to establish the relationship between salary and different assessments done for the students. The results are shown in Table 11 and Fig. 3.

This study clearly indicates that it is not only the academic marks that influence the placement of students in a company, but the marks in various pre-placement activities play a vital role. The above table and figure show that the correlation between salary grade and exam marks is 0.563, but when we combine marks + PI score + tech score, the correlation coefficient goes up to 0.684. It can thus be concluded that a student who performs well in university exams as well as other tests and interviews will be able to get a good placement.

**Table 10** Category of variables

Variable name	Variable type
Mean marks	Independent
Technical score	Independent
PI score	Independent
Salary grade	Dependent

**Table 11** Correlation analysis between dependent and independent variables

	Mean marks	Salary grade	Marks + PI score	Tech score + Marks	PI score	Marks + PI score + Tech score	Tech score
Mean marks	1.000000	0.5636688	0.4186760	0.4360457	0.4536794	0.5328785	0.4948876
Salary grade	0.5636688	1.000000	0.5376886	0.5702341	0.5915769	0.6146894	0.6675765
Marks + PI score	0.4186760	0.5376886	1.000000	0.9226242	0.8196417	0.8239066	0.7404787
Tech score + Marks	0.4360457	0.6002341	0.9226242	1.000000	0.7181608	0.7454613	0.7970884
PI score	0.4536794	0.5015769	0.8196417	0.7181608	1.000000	0.9337996	0.8559053
Marks +PI score + Tech score	0.5328785	0.6846894	0.8239066	0.7454613	0.9337996	1.000000	0.8664074
Tech score	0.4948876	0.5875765	0.7404787	0.7970884	0.8559053	0.8664074	1.000000

## 4 Conclusion and Future Scope

In this paper, we have analyzed various academic activities that a student has to go through during the three years of MCA technical course. The student is not only assessed on the basis of marks obtained in the end term examination, but a regular assessment is carried out in the form of technical tests, technical interviews and non-technical assessments. Domain of the paper is limited to the record of three batches of MCA students of a college in Delhi, India. This dataset is analyzed for the listed objectives, and association of dependent variable is identified with various independent variables. It has been noticed during the analysis that marks obtained by the students in combination with the pre-placement activities have more association with salary grade or placement package. The current results can be very helpful for academic institutions in planning their course structure and teaching pedagogy as the overall aim of all professional colleges is to make the students employable. The association depicted in this paper can define how variables are related. In the future, we plan to predict the behavior of the dependent variable (salary grade) by monitoring and manipulating the behavior of the independent variables (mean marks, technical score and PI marks).

## References

1. Aggarwal, D., Grover, D., Sharma, D.: Academic performance analysis of information technology students in higher education institutions. **8**(9s) (2019)
2. Deepshikha Aggarwal, D.S.: Application of clustering for student result. **7**(6C) (2019)
3. De Vos, A., De Hauw, S., Van der Heijden, B.I.: Competency development and career success: The mediating role of employability. **79**(2), October (2011)
4. Zuffo, R.G., Cortini, M., Maiolo, M.E.: Students' academic performance and employability: a study on Italian undergraduates. **19**(4) (2013)
5. Ana Azevedo, G.A.H.: Competency development in business graduates: An industry-driven approach for examining the alignment of undergraduate business education with industry requirements. **10**(1) (2012)
6. Alex Tymon, S.B.: Improved academic performance and enhanced employability? The potential double benefit of proactivity for business graduates. **10**(2) (2016)
7. Deepshikha Aggarwal, D.S.: Analysis of the factors influencing the choice of college for higher. **6**(9) (2018)
8. Cramer, D.: *Fundamental Statistics for Social Research*. Routledge, London (2016)
9. Sen, B., Ucar, E., Delen, D.: Predicting and analyzing secondary education placement-test scores: a data mining approach. *Expert Syst. Appl.*, 9468–9476, 10 Aug 2012
10. Barbara J.M.: Criteria for placement decisions in protective services. *Child Welfare*, 367–373 (1984)
11. Green, A.: *Placement Testing*. Heidelberg, Germany (2018)
12. Llinares-Insa, L.I., et al.: Employability appraisal scale (EAS): development and validation in a Spanish sample. **9** (2018)
13. Fairness and Test Use: The case of the SAT and Writing Placement for ESL students. Columbia (2006)

14. Chacón, S., Barbero, I., Vila, E.: Polychoric versus pearson correlations in exploratory and confirmatory factor analysis of ordinal variables. *Qual. Quant.*, 44–153 (2010)
15. Wall, D., Alderson, J.C., Clapham, C.: Evaluating a placement test. Sage Publication, p. 1 (1994)

# Monitoring of Resources in Building Projects Using Internet of Things: A Literature Review



Sameer Jain, Kavita Choudhary, and D. K. Sharma

**Abstract** In India, more than 90% construction projects end up getting delayed and, thus, resulting in the cost escalation of the project. Both the parties client and the contractors affect this condition. Hence, to avoid such delays after adopting different techniques and methods, the condition has never improved. The aim of this paper is to fulfill the objective of developing the discrete event-based system for labor, materials, and plant & equipment (LMP) on the construction site, for that the primary focus reviews the different ways to implement the Internet of Things (IoT) at the project site and improve the material handling, labor monitoring, and tracking the plant and equipment for better productivity and efficiency of the overall project.

**Keywords** Internet of things · Construction · Material · Labor · Equipment

## 1 Introduction

For any country, construction is the backbone of the development. According to Global Infrastructure Outlook Report, construction industry is poised to become the largest employer by 2022, employing more than 70 million people. “The industry is expected to grow at a compounded annual average rate of 6.5% to US \$691 billion in 2023. This is further to a registered output growth of 8–9% in 2017, up from 1.9%”.

The time and cost overruns lead to revenue loss to the owner of the company because delay happens in the projects. According to [1], Internet of Things which is abbreviated as ‘IoT’ can be defined as network comprising real-world devices or any physical objects, autonomous moving vehicles, and use objects incorporating

---

S. Jain (✉) · K. Choudhary · D. K. Sharma  
JK LakshmiPat University, Jaipur, Rajasthan, India  
e-mail: [kavitachoudhary@jklu.edu.in](mailto:kavitachoudhary@jklu.edu.in)

D. K. Sharma  
e-mail: [dinesh.sharma@jklu.edu.in](mailto:dinesh.sharma@jklu.edu.in)

sensors, embedded computing device with other interfaces like humans and machines, lined via wired or wireless networks, to capture contextual data from the environment. As per McKinsey Global Institute (2015), “The Internet of Things has a total potential economic impact of \$3.9–\$11.1 trillion per year in 2020.”

According to [2], IoT can help to track equipment, labor, and materials as it moves around the site, and means effective utilization of resources is a key to the project management. The key here is minimum wastage and optimal use of manpower, material, and equipment. Equipment is capital intensive and hence proper selection, utilization, and financing options, etc., are important to bring transparency in resource life cycle for measuring actual utilization, availability, cost, and norms, etc.

Many construction firms nowadays face a challenge of delivering complex projects on a schedule within a given timeline, budget, and maintaining a reasonable profit margin. Proper planning for managing resources using resource management in a project is necessary to meet the objectives of the project and the client’s requirement. Without resource management, the projects can delay or can become not profitable for the firm. The objective here is to maximize the utilization of the resources by reducing the wastage and increase the productivity. The productivity of different resources that are labor, material, and operation and maintenance are the key factors that result in an increased efficiency of a project.

## ***1.1 Material Handling***

For the construction industry, the term material handling refers to the delivery, movement, storage, and control of materials which are directly affecting the schedule of the project. In a project, hundreds of construction materials go through design, fabrication, and storage prior to the installation process. For this availability of material is to be checked by a store manager. Since not all the materials are cast on construction site, prefabricated materials are required to be ordered and stored. As the materials are used, a record in the store is to be kept regarding the material which has been used and the material which is still left in the inventory. This inspection is to be done on regular basis to keep a track of the material which at a later stage affects the procurement of material. If the material is not available at the site on time, it would cause an unnecessary delay which would cause an increase in the project cost.

According to [3], “the receipt and inspection of materials, to storage, assembly and usage, the material handling system should be organized and well-coordinated so that each individual working on site is aware of its working. Also, this is to be carried out keeping in mind that the cost of material in a project is 50–60% of the total cost of the project.”

According to [4], “material tracking is advancement of technology through any material kept on site can be tracked in terms of details and location. Tracking of

material and components in a project implies basic two sets that are positional accuracy and identification.”

According to [5], “Since recent advancement has open doors for automated data collection (ADC) technologies the tracking of material has become easier. One of the most used technology for tracking purpose is radio frequency identification (RFID) which gives the two-dimensional location when combined with global positioning system (GPS).”

## ***1.2 Labor Tracking***

According to [1, 6], “We can keep a track on time and attendance. This has a positive effect on the working culture of a labor. Tracking of labors help us in keeping a track on specific group of workers, whether they are performing the given work to them in proper manner, according to the allotted time or not”.

At a construction site, multiple subcontractors work on anything from HVAC systems to glassworks and plumbing works. If the final contractor gets a bill of 6000 men hours of plumbing work, they usually will not be ready to cross-check if that requirement is correct or inflated. And since multiple contracts with subcontractor are expensive, there is not sufficient incentive. Once the contractor applies labor trailing with a reduced trailing badge, he will then cross-check and verify all labor hours. Hence, with the use of IoT on construction site, accurate tracking of labor hours gets easier.

## ***1.3 Plant and Equipment Monitoring***

According to [1, 7, 8], “In relation to equipment monitoring and repair, sensors can enable machinery to detect and communicate maintenance requirements, send automated alerts for preventive maintenance, compile usage and maintenance data, and increase efficiency by remotely monitoring fuel consumption. In essence, it helps businesses ensure that their vehicles and machinery can be in use for the maximum possible time, which, in turn, boosts on-site productivity.”

## **2 Literature Review**

According to [3], “It states that the contribution of material and equipment cost varies 50–60% of the total cost of the project depend on size and scale, therefore to improve the efficiency and productivity the tracking of the equipment’s and materials is a necessary activity. Radio Frequency Identification (RFID) was used to



tracking of the materials which is combined with global positioning systems (GPS) which automatically detects the tags.”

According to [2], “It states that in order to complete a project within a given specific budget and time, the importance of knowing workforce productivity is necessary. In this thoracic posture data was captured by using a technique fusion spatiotemporal which automatically assess the data. Three zones at the site were identified for experimental set-up which was divided into material zone, work zone and the rest zone, then the experiment was performed by assigning a certain task to a pair of workers. The workers at site had to disassemble a deck and then reassemble it at a different place on site. The technology used for tracking their location and thoracic posture status are ultra-wideband technology (UWB) and physiological status monitoring (PSM).”

According to [9], “It states that the importance of tracking of resources such as equipment, labor in real time focused on sensing and visualization technology. In these different scenarios were created on construction site to investigate the procedure of increasing safety and task control management in a project. First scenario was non-availability of a worker working on site near the equipment. The data was published to a 3D online viewer and the safe and proximity threshold zone were computed. Second scenario is for to measure the productivity and safety performance of the site workers was computed in which the site workers was provided an ultra-wideband (UWB) tag on the helmet and the speed of monitored tag was calculated.”

According to [6], “It states that uses a method of converting the 2D coordinates into 3D coordinates by camera calibration, camera pose estimation, 2D tracking, and triangulation.”

According to [1], “It states it provides a model by using discrete event simulation (DES) for real-time monitoring construction operations with the help of actuators and sensors on construction site. This model codifies the plan of the operation by logic and resource flow as input data during the planning stage. During the execution phase the model is updated in real time to reflect the ongoing status of the site by the communication of different entities involved. Another model that is the finite state machine (FSM) model is also used and follows three steps: identifying all states of a machine, determining the input and creating a state transition diagram.”

According to [10], “On construction site there are challenges for the operation which are typically spread across large areas and require collaboration between several dissimilar resources. The uniqueness that creates logistical challenge for making automating decision on construction worksite. A framework for leveraging the ubiquity of devices that can be considered part of the Internet of Things (IoT) to inform real-time decision making and automation on construction worksite. The method for programmed based decision model are then made automatically on real time operation and relayed back to the entities on the worksite through the Internet of Things Infrastructure.”

According to [11], “outlined that how to unite both railways and highways in order to give a door-to-door service by tracking model system as people are more

interested in real-time tracking and are more concerned about the status of the parcel. IoT gives the potential to connect different modes of transportation in near future.”

According to [12], “It states that the present situation of construction industry has made to the development of smart construction objects (SCO’s). The SCOs is possible only when there is a smart mixing of skills of sensing, processing, networking, computing, and responding. Although SCOs in the construction sector is there at infant stage but it helps to take better decisions. A smart construction object must have three important properties-awareness, communicativeness and self-sufficiency. Each kind of the autonomy, awareness, and communicativeness are not fixed to a one-to-one correspondence. SCOs is capable of sensing, computing, communicating, and taking action without essentially involving human intervention.”

According to [13], “outlined that material coding, labeling, identifying, transmission, resolution, and application with the use of IoT for better inventory control. With the use of IoT we can automatically perceive, collect and intelligently analyze the information efficiently and manage them. The proper use of materials to reduce wastage, prevent illicit usage of materials, prevent theft, to achieve economy in construction.”

According to [14], “It states that causes of delay in construction industry are insufficient site management, Poor site coordination, Improper planning, No clarity in the scope of the construction project, Lack of coordination and Inefficient site management. IOT techniques—this captures real time behavior of the object enabled by IoT device so that optimal scheduling is achieved. The comparison of the proposed model and classic ant system presents the outperformance of average computational cost. There should be monitoring of day-to-day activity is required to minimize the delay of insufficient site management. So, the sensors to capture information are set and the real time monitoring of the sensor are done. Correlate sensor parameter and past failure or material needs into the actionable insights. Once the material needs or possibility of delay is identified then it is immediately connected to network and sent to the site manager. So, the site manager can take action regarding the issue even though the site manager is not present at the construction site.”

### 3 Proposed Methodology

This research is descriptive in nature. The descriptive method of research design helps researchers plan and carry out descriptive studies, designed to provide rich descriptive details about labor, material, and plant and equipment utilization, productivity, performance, equipment health, and maintenance requirements.

This type of research is often associated with cost optimization of ongoing projects. The outcomes of the same can also use for benchmarking P&E

performance. Also, the inputs can be factored suitably for any proposal stage projects bids.

This study is based on the data recorded by different IoT sensors by deploying a prototype model and monitoring the performance of LMP of any building project.

Initially, the testing of prototype model may take more time, and suitability of the physical environment at any construction project site will be the concern for implementation.

## 4 Conclusion

In this, the applications of Internet of Things (IoT) in the construction industry and certain prerequisites are prior to its implementation. Construction sector is going in verge of adopting new technology, and IoT is one of the emerging technologies. We have identified this gap, and actual implementation of IoT in material management includes tagging material with sensors and radio frequency identification (RFID); whereas, for labor monitoring accelerometer, motion sensors, global positioning system (GPS), global system for mobile (GSM), radio frequency, microcontrollers, etc., have been used. On-site labor tracking helps construction managers to manage difficult task of managing safety, productivity, and overall performance of the construction project and has created a IoT device to monitor the equipment. The real-time data collection technology integrated with the equipment with onboard sensors and microcontroller to provide real-time monitoring of equipment to enhance the productivity and the performance. Equipping assets with IoT device will help managers decide when to execute proactive maintenance to maximize performance and prevent any breakdowns. Human interference and human errors can be reduced to a greater extent through the use of this method. Plant and equipment tracking is done using finite state and discrete event-based method. In this way, the mobility and inventory could be effectively monitored completely independent of “human factor,” thus eliminating the chances of mismanagement, miscommunication, and theft.

## References

1. Ma, Z., Liu, Z., Zhang, D.: An integrated mobile material management system for construction sites. *AEI 2013: Building solutions for architectural engineering*. In: Proceedings of the 2013 Architectural Engineering National Conference, pp. 353–362 (2013). <https://doi.org/10.1061/9780784412909.034>
2. Cheng, T., Teizer, J., Migliaccio, G.C., Gatti, U.C.: Automated task-level activity analysis through fusion of real time location sensors and worker’s thoracic posture data. *Autom. Constr.* **29**, 24–39 (2013). <https://doi.org/10.1016/j.autcon.2012.08.003>

3. Song, J., Haas, C.T., Caldas, C.H.: Tracking the location of materials on construction job sites. *J. Constr. Eng. Manage.* **132**(9), 911–918 (2006). [https://doi.org/10.1061/\(asce\)0733-9364\(2006\)132:9\(911\)](https://doi.org/10.1061/(asce)0733-9364(2006)132:9(911))
4. Zanella, A., Bui, N., Castellani, A., Vangelista, L., Zorzi, M.: Internet of things for smart cities. *IEEE Internet of Things J.* **1**(1), 22–32 (2014). <https://doi.org/10.1109/JIOT.2014.2306328>
5. Jian-Mei, S., Li-Juan, W., Xi, Y., Jun-Shan, Y.: Design and implementation of intelligent kitchen system based on internet of things. In: *Proceedings—2018 International Conference on Smart Grid and Electrical Automation, ICSGEA 2018*, pp. 253–256 (2018). <https://doi.org/10.1109/ICSGEA.2018.00070>
6. Park, M.W., Koch, C., Brilakis, I.: Three-dimensional tracking of construction resources using an on-site camera system. *J. Comput. Civil Eng.* **26**(4), 541–549 (2012). [https://doi.org/10.1061/\(asce\)cp.1943-5487.0000168](https://doi.org/10.1061/(asce)cp.1943-5487.0000168)
7. Asensio, Á., Marco, Á., Blasco, R., Casas, R.: Protocol and architecture to bring things into internet of things. *Int. J. Distr. Sensor Netw.* **2014** (2014). <https://doi.org/10.1155/2014/158252>
8. Luo, X., Li, H., Huang, T., Skitmore, M.: Quantifying hazard exposure using real-time location data of construction workforce and equipment. *J. Constr. Eng. Manage.* **142**(8), 04016031 (2016). [https://doi.org/10.1061/\(asce\)co.1943-7862.0001139](https://doi.org/10.1061/(asce)co.1943-7862.0001139)
9. Cheng, T., et al.: Real-time data collection and visualization technology in construction. *Constr. Res. Congr.* **2010**, 339–348 (2010)
10. Louis, J., Dunston, P.S.: Integrating IoT into operational workflows for real-time and automated decision-making in repetitive construction operations. *Autom. Constr.*, 317–327 (2018). <https://doi.org/10.1016/j.autcon.2018.07.005>
11. Liu, X., Zhang, X., Xue, F., Liao, W.: United transportation of railways and highways omni distance tracking system model under the internet of things. In: *ICLEM 2010: Logistics for Sustained Economic Development—Infrastructure, Information, Integration—Proceedings of the 2010 International Conference of Logistics Engineering and Management*, 387, pp. 2210–2216 (2010). [https://doi.org/10.1061/41139\(387\)307](https://doi.org/10.1061/41139(387)307)
12. Niu, Y., Lu, W., Chen, K., Huang, G.G., Anumba, C.: Smart construction objects. *J. Comput. Civil Eng.* **30**(4), 04015070 (2016). [https://doi.org/10.1061/\(asce\)cp.1943-5487.0000550](https://doi.org/10.1061/(asce)cp.1943-5487.0000550)
13. Zhu, H., Hou, H., Hu, M., Geng, Y.: Things identification support system based on IoT. In: *ICLEM 2012: Logistics for Sustained Economic Development—Technology and Management for Efficiency—Proceedings of the 2012 International Conference of Logistics Engineering and Management*, pp. 397–403 (2012). <https://doi.org/10.1061/9780784412602.0063>
14. Jeevana, et al.: Internet of things (IOT) to prevent delays in construction industry. *Int. J. Pure Appl. Math.* **22**, 1037–1041 (2018)
15. Byun, J., Kim, S., Sa, J., Kim, S., Shin, Y.T., Kim, J.B.: Smart city implementation models based on IoT technology. *Adv. Sci. Technol. Lett.* **129**(41), 209–212 (2016)
16. Ghanem, A.G., Abdelrazig, Y.A.: A framework for real-time construction project progress tracking. In: *Earth and Space 2006—Proceedings of the 10th Biennial International Conference on Engineering, Construction, and Operations in Challenging Environments*, **2006**(850), 112 (2006). [https://doi.org/10.1061/40830\(188\)112](https://doi.org/10.1061/40830(188)112)
17. Das, R., Tuna, A., Demirel, S., Yurdakul, M.K.: A survey on the internet of things solutions for the elderly and disabled: applications, prospects, and challenges. *Int. J. Comput. Netw. Appl.* **4**(3) (2017). <https://doi.org/10.22247/ijcna/2017/49023>
18. How the internet of things will make freight shipping more efficient. [www.freightquote.com/blog/how-the-internet-of-things-will-make-freight-shipping-more-efficient](http://www.freightquote.com/blog/how-the-internet-of-things-will-make-freight-shipping-more-efficient). Accessed 18 Aug 2020
19. Kereri, et al.: Use of technology in material tracking in the construction industry business. *Afr. J. Bus. Manage.* **5**(1), 92–107 (2019)

20. Kanan, R., Elhassan, O., Bensalem, R.: An IoT-based autonomous system for workers' safety in construction sites with real-time alarming, monitoring, and positioning strategies. *Autom. Constr.*, 73–86 (2018). <https://doi.org/10.1016/j.autcon.2017.12.033>
21. Li, C.Z., Xue, F., Li, X., Hong, J., Shen, G.Q.: An internet of things-enabled BIM platform for on-site assembly services in prefabricated construction. *Autom. Constr.*, 146–161 (2018). <https://doi.org/10.1016/j.autcon.2018.01.001>
22. Louis, J., Dunston, P.S.: Methodology for real-time monitoring of construction operations using finite state machines and discrete-event operation models. *J. Constr. Eng. Manage.* **143**(3), 04016106 (2017). [https://doi.org/10.1061/\(asce\)co.1943-7862.0001243](https://doi.org/10.1061/(asce)co.1943-7862.0001243)
23. Madakam, et al.: Internet of things (IoT): a literature review. *J. Comput. Commun.* **3**, 164–173 (2015)
24. McCabe, B.Y., et al.: Roles, benefits, and challenges of using UAVs for indoor smart construction applications. *Comput. Civil Eng.*, 349–357 (2017)
25. Nunberg, G.: The advent of the internet. 12th April, Courses (2012)
26. Zhang, H., Yan, X., Li, H., Jin, R., Fu, H.: Real-time alarming, monitoring, and locating for non-hard-hat use in construction. *J. Constr. Eng. Manage.* **145**(3), 04019006 (2019). [https://doi.org/10.1061/\(asce\)co.1943-7862.0001629](https://doi.org/10.1061/(asce)co.1943-7862.0001629)
27. Zhang, M., Sun, F., Cheng, X.: Architecture of internet of things and its key technology integration based-on RFID. In: *Proceedings—2012 5th International Symposium on Computational Intelligence and Design, ISCID 2012*, 1, pp. 294–297 (2012). <https://doi.org/10.1109/ISCID.2012.81>
28. Zheng F., Chen S., Zhang J., Qiu F.: Internet of things technologies for urban public transport systems: a case application in Chengdu, China. *ICTE*, 335–351 (2015)
29. Zhou, C., Ding, L.Y.: Safety barrier warning system for underground construction sites using Internet-of-Things technologies. *Autom. Constr.*, 372–389 (2017). <https://doi.org/10.1016/j.autcon.2017.07.005>

# A Review of Recent Technology Development in Multilevel Inverter and Their Application in PV Systems



Aditi Gupta and Deepak Verma

**Abstract** The multilevel inverter (MLI) is gaining more popularity because of their wide applications in medium-voltage and high-power applications and their growing utility in renewable energy (RE), especially in PV systems. As the power generation using fossil fuel causes more pollution, and over a period of time, it will extinct. Hence, the world is seeking for new energy resources, and renewable energy has many advantages; they are sustainable, clean, pollution-free, and inexhaustible. The MLI has many uses in grid-connected PV systems. In this review article, the global status of renewable market, especially solar energy, classification of various inverter types, and their applications are reviewed and compared schematically, and the recent advancement has been discussed. It has been noticed that as the level of inverter increases, THD is reduced significantly with CHB having lowest THD and HM, and symmetric and asymmetric are the latest advancements in MLI.

**Keywords** Grid-connected PV systems · Multilevel inverter · Neutral point clamped · Flying capacitor · Cascaded H-bridge · Hybrid multi · Symmetric MLI · Asymmetric MLI

## 1 Introduction

Renewable energy (RE) sources, such as solar power, wind energy, biomass, and hydropower, are some of the major electricity generating resources today, and they make up to 28% of global electricity generation according to IEA for year 2020 [1]. The use of renewable resources is increasing because of their many advantages over fossil fuel like clean, pollution-free, and most importantly, they are inexhaustible. Their lower-carbon emission rapidly is considered the best solution as green energy. The solar energy systems are estimated to grow by 16% by the end of 2020 [1], and

---

A. Gupta (✉) · D. Verma  
Birla Institute of Technology, Mesra, Jaipur Campus, Jaipur, Rajasthan, India

© The Author(s), under exclusive license to Springer Nature Singapore Pte Ltd. 2021  
A. Patnaik et al. (eds.), *Advances in Materials Processing and Manufacturing Applications*, Lecture Notes in Mechanical Engineering,  
[https://doi.org/10.1007/978-981-16-0909-1\\_7](https://doi.org/10.1007/978-981-16-0909-1_7)

it is estimated that by 2050, our energy needs can be met by 85% and more by renewable energy [2].

Due to technological advancement in the PV system, the price of installation has decreased a lot, and it has become more affordable for everybody. The use of RE sources has increased extremely during the last 10 years because of the advancement in the grid integration technologies [3]. As discussed in [4], PV systems can be identified into two main groups, that are, (1st) the off-grid PV systems and (operated independently of the utility grid) (2nd) grid-connected (on-grid) PV systems. They have a combination of an inverter, energy source, utility grid, and PV systems. The inverter acts as an interfacing between the PV systems and the grid. An inverter is defined as a device that converts direct current (DC) into alternating current (AC). Inverters can be classified into two types: regular (two levels) inverter and multilevel inverter (MLI). As some loads require high power and some require medium power, so using high power for every load damage the medium and low load so a multilevel inverter is used as a substitute for high-power and medium-/high-voltage situation it gives output as high power from medium-voltage source. MLI is preferred more because of its multi-stepped output waveform. It has many applications in the industry like in dynamic voltage restorers (DVR), distribution static compensators (DSTATCOM), electric vehicles (EV), unified power flow controller (UPFC), grid integrated (PV) systems, and various other fields [5].

In 1975, Baker and Bannister coined the term MLI. In that topology, they made a series-connected full-bridge power cells with each cell having an isolated DC source and four switches [6]. This topology gives output as AC voltage staircase waveform. This staircase waveform has many advantages like low harmonic distortion and low switching stress and can be used for high-voltage applications. MLI is used in PV systems due to their advantages like reduced total harmonic distortion (THD) and lower power losses. The THD is reduced significantly as the number of levels is increased [7].

## 2 Global Status of Renewable Market

The world has installed 176 GW of RE power capacity; according to IRENA report 2019, it also states that 90% comes from wind and solar farms [8]. Many countries are shifting to RE power generation, and in that, specially, wind and solar powers because of their advantages like easily accessible to remote areas like villages and hilly areas and their technological advancement have also made it possible to be more affordable. According to IEA, RE power capacity aims to grow by 50% between 2019 and 2024, and the major growth will be seen in solar energy that is equivalent to 1200 GW. Solar PV alone accounts around 60% of the total gain expected [9].

India comes in the fifth position in solar power energy [10]; recently, a 750 MW solar power plant project has been set up in Rewa, Madhya Pradesh. It is expected

to be completed by 2022. It will help the country to reduce its carbon emission by 15 lakh ton per year. Solar power is the fastest growing RE source in the last decade.

This expansion is because of the growing demand for electricity, and PV system is best due to its increasing effectiveness, reducing carbon emission, and affordability in supporting the electricity grid. The affordability is increased in the grid integration of PV system which is due to the enhancement in the current grid connecting MLI technologies. The output AC staircase sinusoidal waveform is close to an actual sine waveform; as the levels increase, the THD will decrease [10].

### 3 Classification of MLI

MLI is used where a high-power output is needed for medium-voltage batteries, super capacitors, and solar panel; all are medium-voltage sources; hence, MLI is used in them. They are a cost-friendly solution due to their many benefits in industries. They consist of DC sources and semiconductor devices. MLI can be classified based on DC sources used. They are classified into two types, i.e., single DC source and multi-DC source which can be further classified as seen in Fig. 1.

#### 3.1 Single DC Source

Single DC source can further be divided into two major types: neutral point clamped MLI (NPC) and flying capacitor MLI (FC).

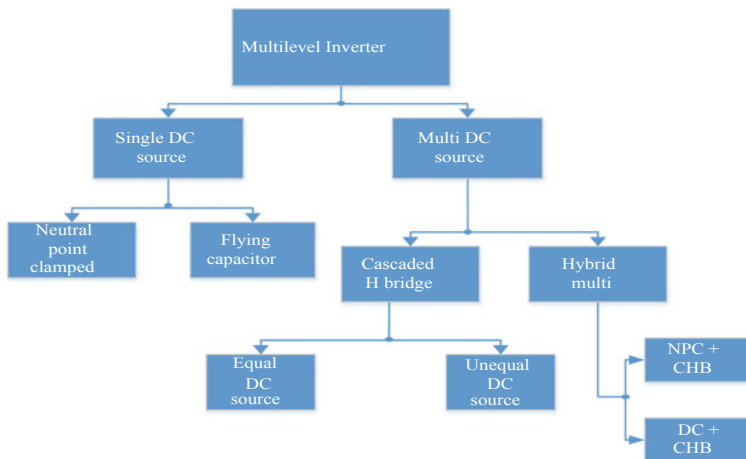


Fig. 1 Classification of MLI



### 3.1.1 Neutral Point Clamped MLI

This inverter was first introduced in 1980 by Baker and Banister [6]; they are also known as diode clamped MLI because they use a diode as their clamping device. In these inverters, capacitors are generally connected in series, and diodes are clamped to give a multiple voltage level [11–13]. A three-level NPC is shown in Fig. 2a. In this circuit, the voltage is divided into three levels of voltage by the help of two capacitors, where  $n$  denote the neutral point in the middle of the capacitors C1 and C2. The output voltage denoted as  $V_{np}$  has three levels. When switches S1 and S2 are turned on  $V_{dc}/2$ , voltage is generated, and for voltage  $-V_{dc}/2$ , switches S3 and S4 are to be turned on, and for having the 0-voltage level, switches S2 and S3 are to be turned on. The only difference between the traditional two-level inverter and three-level NPC is diodes D1 and D2. Where each diode blocks the voltage equal to the number of switches above it times the supplied DC voltage, hence diodes D1 and D2 switch voltage to half the level of input DC bus voltage [13]. A diode reduces the stress on other electrical devices connected to it by transferring the limited amount of voltage. The voltage across the point o and p has output  $V_{dc}$ , i.e.,  $V_{op} = V_{dc}$ , when both switches S1 and S2 are switched on or turned on. In this circuit, D2 balances the voltage sharing between the switches S3 and S4 where S1 blocks the voltage across capacitor C1, and S4 blocks the voltage across capacitor C2. The output  $V_{np}$  is AC in nature, while output  $V_{op}$  is DC in nature. A five-level NPC is shown in Fig. 2b; it generates five level output waveform by the combination of switches, diodes, and capacitors similarly like in case of three-level, but as it generates (five-level) a five-step voltage of input DC voltage. It has lower THD, and pulse generated is closer to a sine wave as compared to three-level. Its advantages are as follows: it has low cost and lesser number of components and has simple control logic for higher levels; its voltage harmonics is focused on double of the switching frequency, and it is more efficient for back-to-back power connections. Despite having many advantages, it has some disadvantages as follows: maintaining the charging and discharging is difficult, and as the levels increase having more clamping diodes increases the complexity and largeness, uneven power distribution among switches [14].

### 3.1.2 Flying Capacitor MLI

These were introduced in 1992; their structure is similar to NPC MLI. The only difference is that instead of clamped diodes, they use clamped capacitors, and they are called FC MLI because capacitors float with respect to earth potential. As shown in Fig. 2c, a three-level output is synthesized across the points p and n which is  $V_{dc}/2$ , 0, and  $-V_{dc}/2$ . Switches S1 and S2 are triggered for having voltage level,  $V_{dc}/2$ ; similarly for having voltage level  $-V_{dc}/2$ , switches S3 and S4 need to be switched on, and for having the 0-level, either pair of switches (S1, S3) or (S2, S4) needs to be turned on. When switches S1 and S3 are switched on, the clamped capacitor  $C_{p1}$  gets charged, and when S2 and S4 are triggered, it gets discharged [13]. By wisely

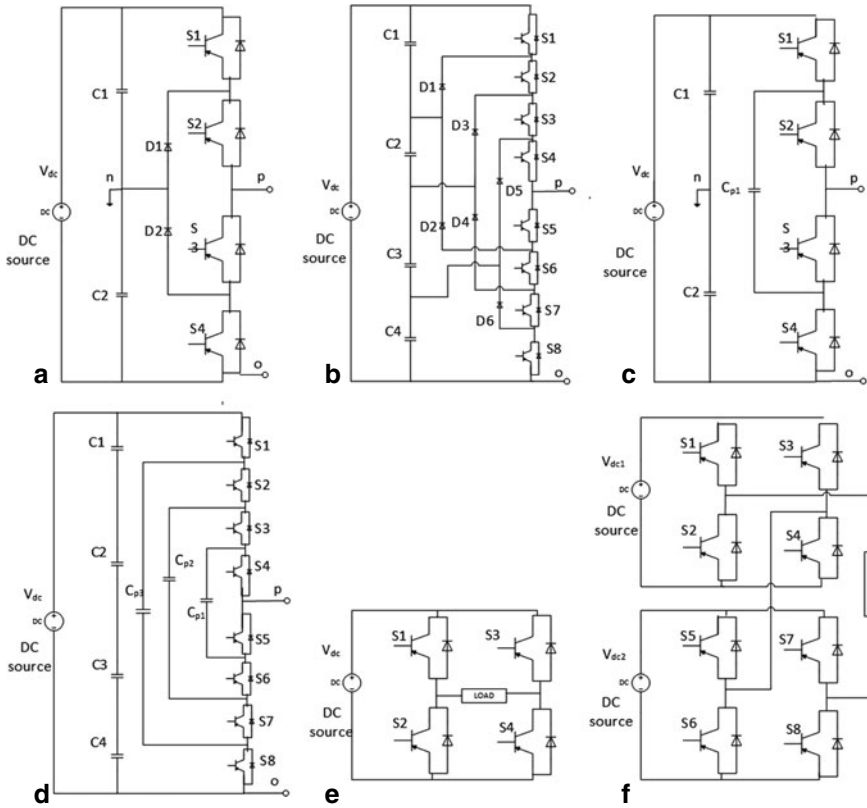


**Fig. 2** Circuit diagram of **a** three-level NPC MLI, **b** five-level NPC MLI, **c** three-level FC MLI, **d** five-level FC MLI, **e** three-level CHB MLI, **f** five-level CHB MLI [5, 13]

selecting the switch combination of the 0-level, charge across the clamped capacitor  $C_{p1}$  can be maintained. Similarly, a five-level FC MLI as shown in Fig. 2d produces five levels of voltage by same process as explained for three-level FC MLI; the only difference is that as the level of inverter increases, the THD is decreased significantly [7]. Its advantages are

- Each branch can be analyzed separately and individually.
- More modularity and easily extensible structure.
- Easy to balance capacitor voltage even for higher levels.

Its major disadvantage is pre-charging of capacitors, and tracing the voltage of floating capacitor is difficult, and it is expensive too [15–17].

## 3.2 Multi-DC Source

As the name suggests, they use multiple DC sources as input for the inverter. As seen in Fig. 1, multi-DC source MLI can also mainly further classified into two types: cascaded H-bridge (CHB) and hybrid multi (HM).

### 3.2.1 Cascaded H-bridge MLI

As the name suggests the CHB is a merger of two or more single-phase H-bridge inverters for having  $m$  level ( $m - 1$ )/2 H-bridge is needed and each H-bridge requires a separate DC source, where each H-bridge is merger of four switches and a DC source. As shown in Fig. 2e, each H-bridge generates a three-level waveform  $V_{dc}$ , 0, and  $-V_{dc}$ , where the  $V_{dc}$  is generated when switches S1 and S4 are on, similarly,  $-V_{dc}$  is obtained when switches S2 and S3 are on, and 0-level can be generated by using either pair (S1, S3) or (S2, S4), and the main output voltage is the summation of each H-bridge output voltage. The CHB MLI allows DC sources utilization with different levels of voltage magnitude that can be used to achieve a higher number of voltage levels as an output. As H-bridge is connected in series, each H-bridge should be supplied with isolated DC sources. A five-level CHB MLI is also shown in Fig. 2f. Its advantages are

- Less switching loss as it does not need any capacitors or diodes for clamping.
- Due to its flexible structure, it can be extended to any number of levels.
- Low distortions in the output waveform and THD are also very less.
- Can be operated at both fundamental and high switching frequencies.
- Easily used for high-power application.

It is most commonly used topology but it has few disadvantages like it needs separate DC sources or capacitor stand for each section and need the more complex controller and its asymmetric topology lacks in fault-tolerant capacity [5, 8, 9, 13].

CHB can be further identified into two types: equal DC source and unequal DC source. In equal DC source, all the DC source of H-bridge is equal to one another; however, quite often, DC sources are not equal to one another. As batteries might have different internal resistance, hence that topology is categorized under unequal DC sources CHB MLI the unequal DC source problem may even arise as each DC source will charge and discharge differently from another DC. Hence, the PWM technique is used to eliminate this problem [10].

### 3.2.2 Hybrid Multi

This is generally the combination of multi-DC source inverters and single DC source inverters. They become popular as they increase the quality of output waveform and enhance performance parameters; for example, NPC + CHB is a

combination of neutral point clamped and cascaded H-bridge MLI. This inverter will have higher efficiency and high-power quality due to low-frequency switching of power cells and large number of levels [18]. The other one is DC + CHB which consists of a half and full bridges of inverter cells. It uses floating DC links to lower voltage cells and to compensate the voltage distortion [15]. The topology is used for motor drive applications and low switching frequency; due to that the motor current, THD will increase [8]. Similarly, there are many possible combinations to increase the quality of output waveform.

### 4 Application and Comparison of Traditional Inverters

MLI is used in different applications such as NPC MLI are mainly used for static var compensation, variable speed motor drives, for interconnecting high-voltage system, DC or AC transmission line mainly for high voltage, and for high-power drives, whereas FC MLI is used in static var generation, for AC–DC and DC–AC conversion applications, sinusoidal currents rectifier and converters with high THD capability [7, 14]. CHB is the most commonly used MLI in industry, and it has many applications such as motor and EV drives, active filters, power factor compensators, and DC power source utilization and is mostly used for interfacing with renewable energy [5–14]. A comparison is shown in Table 1.

### 5 Recent Technology in MLI

Many new technologies are developed in MLI as NPC, FC, CHB as implementing them becomes costlier because of more switches, complex control and increase in the size of inverter. It can be overcome by using reduced switch count in MLI [16]. There are many reduced switch counts-based MLI, and they are classified as symmetric MLI, asymmetric MLI, transformer-based MLI.

**Table 1** Comparison of multilevel inverter topologies

Parameters	Multilevel inverter topology		
	NPC	FC	CHB
DC sources	1	1	$(m - 1)/2$
Switches	$2(m - 1)$	$2(m - 1)$	$4((m - 1)/2)$
DC bus capacitors	$m - 1$	$m - 1$	NIL
Clamping diodes	$(m - 1) (m - 2)$	NIL	NIL
Clamping capacitors	NIL	$(m - 1) (m - 2)/2$	NIL

$m$  is the level of inverter [5–8, 11–14, 19, 20]

## 5.1 Symmetric MLI

The reduced switch symmetric MLI can further be divided into two parts with H-bridge and without H-bridge as the word symmetric suggests that the DC sources used are symmetric or equal in magnitude. As compared to traditional CHB MLI, a basic symmetric requires one DC source and two switches. As switches are reduced significantly, as a result switch loss is also reduced. As shown in Fig. 3a, this inverter has two parts: one part is the level maker and the other is polarity maker. The level maker part consists of separate DC sources ( $n$ ) and main switches ( $n$ ), and the other part polarity maker part consists of H-bridge cell. It uses to produce 0 voltage level and also to change polarity in every half cycle, where S1 and S2 are switched on for positive half cycle and S3 and S4 is switched on for negative half cycle. An ( $m$ ) level inverter requires  $m + 4$  switching devices and  $2m + 1$  separate DC source and the DC source has voltage  $V_{dc}$ . The maximum output obtained will be  $mV_{dc}$  and the advantage of this topology is the lesser number of switches and lower conduction loss [17, 21].

## 5.2 Asymmetric MLI

The reduced switch asymmetric MLI uses the DC source, and switch number is the same as symmetric MLI, but it produces higher output voltage level. As the name suggests, they use asymmetric or unequal magnitude DC source. As shown in Fig. 3b, it is the fusion of a basic unit and an H-bridge. It also has two parts: the level maker which consists of switch, a DC source, and a diode; the diode is used to put a bound to the number of level generation and the second part is polarity maker. The basic unit produces a staircase voltage output and creates the level and the H-bridge for the polarity generation. This topology uses  $n$  number of diode, and power switches (PS) require  $n$  number of DC sources and a H-bridge. In this

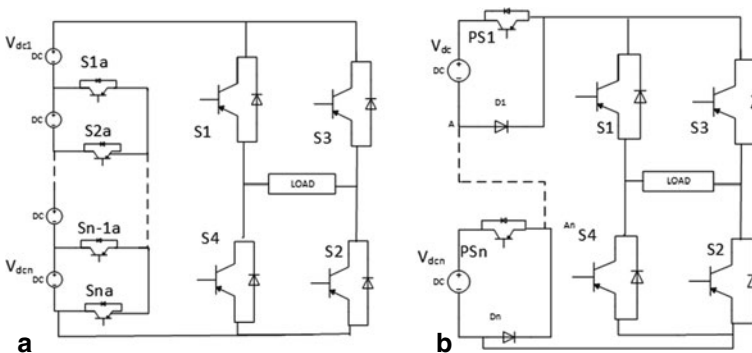


Fig. 3 a Symmetric MLI [17], b asymmetric MLI [21]

topology, the number of switches is reduced drastically; as compared to a traditional CHB MLI topology, it can generate a specific level of output voltage. For an  $3^m$  level inverter, it requires  $m + 4$  switches and  $m$  diodes [21].

### 5.3 Transformer-Based MLI

Transformer-based inverters can further be classified into line frequency transformer-based and high-frequency transformer-based inverter; they are safer to use as they have galvanic isolation and have reliability due to their compact and simple design, and any extra safety measure is not required; however, they are heavyweight and have low efficiency. The most generally used single-phase transformer-based grid-connected inverter is active NPC, Conergy NPC, half H-bridge, full H-bridge, HERIC, H5, H6, etc. [12].

## 6 Conclusion

RE sources are gaining high popularity due to their advantages, and the world is becoming more dependent on RE sources for power generation. In RE sources, solar energy is emerging as a more reliable and fastest growing due to advancement in technology and its advantage of being accessible even at remote locations. And for its integration in grid, MLI is widely used because it can be easily integrated with RE sources.

The MLI is generally used in medium/high-voltage and high-power output applications. The wide advantage of MLI like low harmonic distortion, operation on high and low switching frequency (in case of lower switching frequency, losses are less; hence, higher efficiency can be achieved), improvement of power quality has made MLI widely used in industries. Since their development, many new topologies and technology have been introduced which have improved efficiency a lot.

This review paper has discussed the current situation of RE sources and the global market status of solar energy and has classified commonly used MLI their advantages, disadvantages and their application have been discussed. For each MLI, the three-level topology has been explained and the diagram of three-level, as well as five-level, has been included for better understanding. As the number of levels in an inverter increases, the THD is reduced significantly; it has been noticed that CHB MLI has the lowest THD among all. The HM type is the latest advancement in MLI, and it is used for enhancing performance and waveform.

The traditional inverters require many components which increase the size and complexity of inverters; hence, recent technology in inverters is also discussed which is basically rectifications of some disadvantages in traditional inverters. Asymmetric inverter is most commonly used among them, and in transformer-based transformer, less inverters are more preferred as they are cost

effective, but leakage current problem still exists in them; hence, they require more safety measures. The objective of this review is to cover maximum of the topics in MLI and RE and solar and give a basic idea of MLI.

## References

1. IEA: Global energy review 2020. IEA, Paris (2020). <https://www.iea.org/reports/global-energy-review-2020>
2. Gielen, D., Boshell, F., Saygin, D., Bazilian, M., Wagner, N., Gorini, R.: The role of renewable energy in the global energy transformation. *Energy Strategy Rev.* **24**, 38–50 (2019). <https://doi.org/10.1016/j.esr.2019.01.006>
3. Tsengenes, G., Adamidis, G.: Investigation of the behavior of a three-phase grid connected photovoltaic system to control active and reactive power. *Lancet* **81**, 177–184 (2011). <https://doi.org/10.1016/j.epr.2010.08.008>
4. ElNozahy, M.S., Salama, M.M.A.: Technical impacts of grid-connected photovoltaic systems on electrical networks—a review. *J. Renew. Sustain. Energy* **5** (2013). <https://doi.org/10.1063/1.4808264>
5. Kala, P., Arora, S.: A comprehensive study of classical and hybrid multilevel inverter topologies for renewable energy applications. *Renew. Sustain. Energy Rev.* **76**, 905–931 (2017). <https://doi.org/10.1016/j.rser.2017.02.008>
6. Baker, R.H., Bannister, L.H.: Electric power converter. U.S. Patent 3,867,643 (1975)
7. Khadse, S., Mendole, R., Pandey, A.: A 5-level single phase flying capacitor multilevel inverter. *Int. Res. J. Eng. Technol. (IRJET)* **4**(2), Feb (2017), e-ISSN: 2395-0056
8. Natarajan, P., Kaliannan, P.: A comprehensive review on reduced switch multilevel inverter topologies, modulation, techniques and applications. *Renew. Sustain. Energy Rev.* **76C**, 1248–1282 (2017). <https://doi.org/10.1016/j.rser.2017.03.121>
9. Gaikwad, A., Arbune, P.A.: Study of cascaded H-bridge multilevel inverter. In: 2016 International Conference on Automatic Control and Dynamic Optimization Techniques (ICACDOT), Pune, 2016, pp. 179–182. <https://doi.org/10.1109/icacdot.2016.7877574>
10. Karthikeyan, R., Chenthur Pandian, S.: Generalized space vector modulation schemes for cascaded multilevel inverter to reduce harmonic distortion. <http://hdl.handle.net/10603/16448>
11. Latran, M.B., Teke, A.: Investigation of multilevel multifunctional grid connected inverter topologies and control strategies used in photovoltaic systems. *Renew. Sustain. Energy Rev.* **42** (2015). <https://doi.org/10.1016/j.rser.2014.10.030>
12. Khan, M., Ali, Z., Uddin, W.: A Comprehensive review on inverter topologies and control strategies for grid-connected photovoltaic system. *Renew. Sustain. Energy Rev.* **94** (2018). <https://doi.org/10.1016/j.eper.2018.06.053>
13. Subarnan, J.G.: Multilevel inverters an enabling technology
14. Multilevel Inverter—Types and Advantages. <https://www.elprocus.com/multilevel-inverter-types-advantages/>
15. Silva, C.A., Cordova, L.A., Lezana, P., Em-Pringham, L.: Implementation and control of a hybrid multilevel converter with floating DC links for current waveform improvement. *IEEE Trans. Ind. Electron.* **58**(6), 2304–2312, June (2011). <https://doi.org/10.1109/tie.2010.2064277>
16. Narendra, A., Naik, N.V., Panda, A.K., Tiwary, N.: A comprehensive review of PV driven electrical motors. *Solar Energy* (2020)
17. Menaka, S., Dr. Muralidharan, S.: Symmetric and asymmetric multilevel inverter topologies with device count: review. *Int. J. Pure Appl. Math* **120**(6), 10875–10904 (2018)

18. Chattopadhyay, S.K., Chakraborty, C., Pal, B.C.: Cascaded H-bridge and neutral point clamped hybrid asymmetric multilevel inverter topology for grid interactive transformer less photovoltaic power plant. In: IECON 2012—38th Annual Conference on IEEE Industrial Electronics Society, Montreal, QC, 2012, pp. 5074–5079. <https://doi.org/10.1109/iecon.2012.6389560>
19. Tsanova, T.: Renewables bring 72% of new global power capacity in 2019. Apr 06, 2020 13:25 CEST
20. IEA: Renewables 2019. IEA, Paris (2019). <https://www.iea.org/reports/renewables-2019>
21. Bana, P., Panda, K.P., Naayagi, R.T., Siano, P., Panda, G.: Recently developed reduced switch multilevel inverter for renewable energy integration and drives application topologies, comprehensive analysis and comparative evaluation. IEEE Acc., 1 (2019). <https://doi.org/10.1109/ac-CESS.2019.2913447>



# Image Analytics on Damage Assessment to Draw Inferences on Pre and Post Incident Assessment



Harshit Sharma  and M. Monica Subashini 

**Abstract** The image segmentation techniques have turned out to a mainstay in object detection and tracking techniques. The image recognition methodology can be of extrinsic use to the industrial sector, where it can be exploited for damage assessment to draw inferences on pre and post incident assessment. As far as image classification is concerned, the reason why researcher chose CNN technique is because it does not require feature engineering as is the case with other techniques like support vector machine. It also turns out to be independent of rectilinear motion and radiance of the object. Six Sigma has been discussed as a key factor for image analytics on damage assessment. The feature map is obtained by correlating input matrix and kernel in CNN technique. In the pre-post assessment done with the reference object, it can be inferred that the reference can be mapped onto the database, and the input image is compared for pixels to be mapped onto. If the pixels do not map on to the reference image, it is clear that the product synthesized is not meeting the threshold conditions and should therefore be classified as faulty. On the other hand, if there is a match, the product is fit for user consumption. If a faulty object undergoes a pre-incident damage assessment (via CNN classification technique) at the warehouse, it can be easily filtered out and prevent any third-party complaints. In this way, conglomerates to start-ups can ensure that the production process generates less than 3.44 defects per million.

**Keywords** Image analytics · Damage assessment · Computer vision · Six Sigma · Convolutional neural network · Object recognition

## 1 Introduction

The basic idea of image analytics revolves around the concept of computer vision. The researcher has utilized images and videos to detect, classify, and track objects and events to understand real-world scenarios. The first step is getting the image/

---

H. Sharma (✉) · M. M. Subashini  
VIT, Vellore 632014, India

video on which we have to work (most of the time, we take up real-time situations). The subsequent step is image processing, wherein we want to remove any sort of noise, adjust contrast, or perform some similar form of pre-processing. Then, we want to identify or more elaborately classify the objects involved in the scene. For instance, consider a busy street scenario, the user might be interested in keeping track of moving car (object of interest). After identification, we can go for interpretation where we can give traffic violation signals to the vehicle, which was being tracked in the hypothetical scenario discussed above [1]. Segmentation and blob analyses have turned out to be another mainstay in object detection and tracking [2]. Researcher has made use of MATLAB software as it has turned out to be a dominant software in exploring deep learning concepts [3].

In this research paper, researcher has made use of deep learning concepts for image recognition. Considering an in-depth learning approach to image recognition would irrefutably lead us to make use of convolutional neural networks (CNN) for feature extraction from dummy images [3]. Then, further training using this algorithm can help in extracting those features in contemporary images. The raw image can be obtained from the client, and then based on our segmentation process, we can go for finding the binary image, and further functions can be used for the feature extraction process [4]. This image recognition methodology can be of extrinsic use to the industrial sector, where it can be exploited for damage assessment to draw inferences on pre and post incident assessment.

## ***1.1 Methodology***

**Step 1**—Identification of an appropriate object for carrying out the object recognition process using CNN algorithm. Some of the parameters to be taken into account while selecting the prototype are surface area, volume, shape, size, radius, etc. A soft-drink can is selected as a prototype.

**Step 2**—Deciding the appropriate software to carry out the simulation process. MATLAB is selected because it has turned out to be a dominant software in exploring deep learning concepts.

**Step 3**—Capturing images of the soft drink can at different positions on a plane, varying illuminations. The database should contain the images of the can in both regular and deformed states for the damage assessment to be carried out.

**Step 4**—Formulating the MATLAB code for pre and post incident damage assessment which does the segmentation process [5]. The object is bounded in a two-dimensional frame.

**Step 5**—The feature map can be used to determine whether the can is defective or it is termed as a full connection if the pixels map with the reference image stored in the user's database. A full connection essentially indicates zero defect level of quality.

## 2 Six Sigma and Damage Assessment

Six Sigma has a pivotal role to play in the production sectors. Going back to the 80s, two gentlemen Bob Gavin and Bill Smith, both working at Motorola Inc, an America-based multinational telecommunications company, developed the Six Sigma quality improvement methodology in 1986. Six Sigma's basic idea was to improve the product quality so that the number of defects associated with the process becomes so few that they are statistically insignificant. For a device engineer, it is interpreted that the defects are materially insignificant. Industries can realize a continuous audit control environment as we look to remove/reduce the errors substantially.

The defective product may have either a design defect or a manufacturing defect associated with it. A defect can be classified as a manufacturing defect if an error occurs at the manufacturing time, causing deviation from the proposed design of the product. On the other hand, a defect is classified as a design defect if there is a flaw in the original blueprint.

If we have a process operating at 3 sigma, then we are allowing 66,802.7 errors per million opportunities [6]. Six Sigma is a set of tools and strategies for process improvement. A "process" can be anything from filling a can with coke in a production process or serving a Burger at a McDonald's restaurant. The term "Six Sigma" translates to having 3.4 defects per million products produced. Six Sigma is basically a management philosophy that intends to improve customer satisfaction to near perfection.

The selection of Six Sigma projects should be aligned with strategic business goals, including any of the following: cost reduction and profitability improvement, increase in customer satisfaction, improvement in product and service quality, reduction in the lead time of product or service, improvement in employee performance

Once Six Sigma is achieved in our processes, a little variation may still be acceptable, as we would always be within the customer's specification limits. Studies show that the general benefits will outweigh the costs within six to 12 months from the introduction of the Six Sigma software development program. Continuous returns will be much higher—usually, a 15–25% reduction in software development costs for the second year, with a further reduction thereafter. Some of the areas in testing where Six Sigma can be used are improving test effectiveness, increasing test coverage, etc. The ultimate goal of Six Sigma is to achieve a zero-defect level of quality. In Six Sigma, quality means taking care of customer expectations [7].

## ***2.1 Six Sigma: Variation and Impact on Organizational Performance***

The common objective in virtually all six sigma projects is the elimination of variance. Earlier variation was defined as an out of specification occurrence, but now, variation means to drift away from uniformity and consistency. Staying on target is what companies should strive for rather than meeting specifications. Most processes are generally distributed with a mean and standard deviation.

Regarding the impact on organization revenues with the use of Six Sigma, 84% of professionals believe that Six Sigma implementation has had an enormous impact on the revenues of their organization, 4% saw only a low impact on revenue, and 12% were undecided about the effects. Therefore, emphasizing damage assessment would be a critical factor for industries to comply with the Six Sigma rule and improve customer satisfaction.

## ***2.2 Correlation Between Six-Sigma and CNN***

Six Sigma concepts can be easily applied to the damage/defect index. Depending on the use case, the upper control limit (UCL) and lower control limit (LCL) can be fixed and then evaluate whether the damage assessment process carried out via CNN algorithm is within the permissible limits or not. Additionally, based on task performance, the researcher can see whether or not it will be pertinent for Six Sigma limits. It can also be noted that the image recognition process using CNN will only be relevant if carried out at Six Sigma level; else, the defect rate would be substantially high and cannot be considered for implementation at large-scale processes.

## **3 CNN and Image Recognition**

A significant contribution to the evolution of convolutional neural networks was given by Alex Krizhevsky, who used his skills to win the ImageNet competition in 2012. His noteworthy contribution was that he had brought down the classification error from 26 to 15%.

The convolutional neural network is better known as CNN which is basically a neural network model for dealing with 2-D image data, although it can also handle 1-D and 3-D data also. It is most popularly used for analyzing images and classification problems. In general, we can think CNN as an artificial neural network that has some type of specialization for being able to pick out or detect patterns and make sense out of them. This pattern analysis is what makes CNN useful for image recognition [8]. The differentiating feature of CNN as compared to the standard

multi-layer perceptron network is that a CNN has hidden layers called convolutional layers [9]. To elaborately understand the concept of the convolutional neural network, we must first understand the operation of convolution. This transformation is termed as a convolution operation. It is known that the technique was designed for 2-D input, and the multiplication is performed between an array of input data and a 2-D array of weights, called a kernel [10].

We are assuming a single input image with multiple edges, shapes, and textures. In this case, what the filter will seek in the input image are the edges and can, therefore, be classified as an edge detector [11]. The deeper our CNN network becomes, the more sophisticated these filters become. The output obtained after multiplying the filter with an input array once results in the 1-D output. Upon repeated multiplications, the output obtained is a two-dimensional array of output data. The 2-D data collected from the above operation is coined as ‘Feature Map’ [12].

Image classification is the task of taking an input image, and the result is a probability class that best narrates the image. The image recognition technique comes as an innate ability for humans. In contrast, in the case of machines, the expertise of recognizing an image is acquired by prior knowledge and training for varied image environments [13].

In the image analysis carried out in this paper, sigmoid activation function has been used. The researcher chose this model since in most use cases the output layer for CNN model is a multinomial logistic regression which requires normalization of the output layer units. The mathematical representation of sigmoid activation function is as follows:

$$y = \frac{1}{1 + e^{-x}} \quad (1)$$

There lies a significant difference between humans and computer vision. In computer vision, the can displayed above is interpreted as an array of pixels. This array of pixels is dictated by the resolution of the image. An image can be represented as  $200 \times 200 \times 3$ , where the first two numbers represent the pixel intensity at that point (range 0–255), while the third number represents the RGB value [14]. The convolution between the input image and the filter can be easily understood by the (Fig. 1).

While performing the above convolution, one of the key features which might be needed is zero paddings. Experts believe padding the input matrix with zeros on the periphery is beneficial as it allows the user to control the size of the output feature map. If zero padding is done to the input matrix, the convolution is termed as wide convolution. The resulting matrix obtained after wide convolution is a vector. If zero padding is not applied to the test matrix, the convolution can be termed as narrow convolution. So, the CNN procedure takes place in the following four substages:

0	1	0	1
1	1	1	0
0	0	1	1
1	0	0	1

**INPUT MATRIX**

1	0	0
0	0	1
1	1	0

**KERNEL**

0	1	0	1
1	1	1	0
0	0	1	1
1	0	0	1

**FEATURE MAP  
(OUTPUT)**

**Fig. 1** Convolution operation wherein input matrix is convolved with the kernel/filter resulting the feature map

- Wide or narrow convolution—This central layer performs a function called “convolution.” In context to CNN, convolution is a linear operation which involves multiplication of the user input matrix with the kernel/filter. As such, the 2-D output array obtained from convolution operation is called a “feature map” [11].
- Max pooling—The central idea is to assemble the sample at the bottom to reduce the complexity of the additional layers. In the context of image processing, it can be considered similar to reducing the correction [11].
- Flattening—Converting 2-D arrays into a single continuous vector. A fully connected layer awaits the vector as input. Convolution releases a series of filters, each of which is grid-shaped. Flattening specifies the performance map from these filters to the vector, so it enables backpropagation of the errors back through the convolutional layers.
- Full Connection—A perceptron model is termed full connection if and only if every neuron in the previous layer is connected to every neuron in the subsequent segment.

There are numerous methods available for image recognition, but the reason behind preferring this algorithm is to save time as it does not require feature engineering. Translation invariance and independence from illumination/radiance is another key factor for choosing this particular algorithm. The researcher is only interested in checking the concept of the image and translating, cropping, or grayscaling the image should not have any impact on the final results. These are some of the major factors which make CNNs better for image classification problems as compared to ANNs and RNNs which do not support the above functionalities. Also, algorithms like ANN have considerably high computational burden [2].

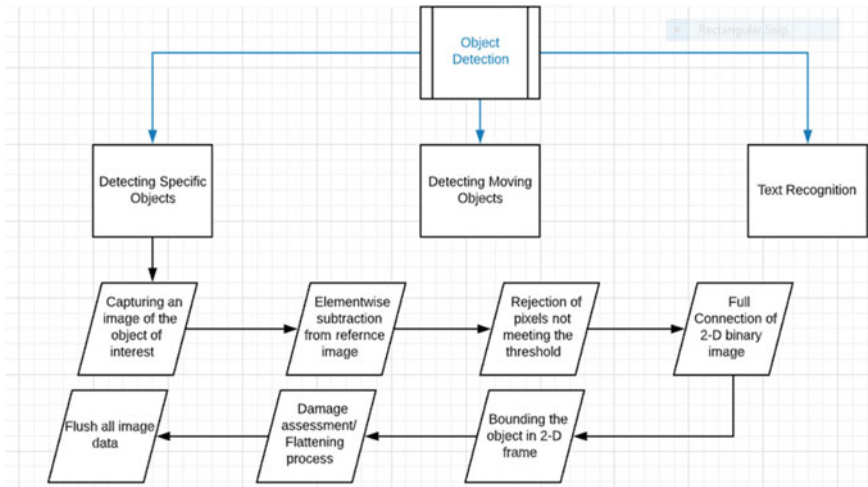


Fig. 2 Algorithm for the proposed methodology

### 3.1 Implementation

See Fig. 2.

### 3.2 Results (Damage Assessment)

There are a variety of parameters based on which the damaged product can be separated from products that meet the base criterion [15]. Based on the researcher's understanding of deep learning algorithms, image recognition is used for the above classification. We may go for a 2-D or 3-D damage assessment depending on the degree of accuracy the industry vies for. Some of the unique parameters of a product are as follows: volume, surface area, shape and size, color (iridescence), radius (for instance the radius of the base of the can), average/Euclidean distance in a cylindrical cartesian system

The coordinate plane projection contrast is figured by extruding the top of the mesh onto the three coordinates plane. We lead this projection by creating a picture of  $64 \times 64$  pixels for each plane [16].

## 4 Discussion

In the pre and pat assessment done with the reference can, it can be inferred that the reference can is mapped onto the database, and the input image is compared for pixels to mapped onto [17]. If the pixels do not map on to the reference image, it is



**Fig. 3** An ideal can prototype without any deformities (left) and a deformed can to be classified as defective via damage assessment (right)

clear that the product synthesized is not meeting the threshold conditions and should therefore be classified as faulty [18]. On the other hand, if there is a match, the product is fit for user consumption. With reference to computer vision, (Fig. 3) will act as the input matrix and would be comprehended in the following manner. Another key inference was that the can's position and illumination of the object's environment had no effect on the extracted feature map (output).

## 5 Conclusion

The world is growing autonomous day by day with an increased need for customer satisfaction. Therefore, it is essential for big industries to invest in areas like damage assessment and object recognition in order to keep with the customer needs and adhere to Six Sigma strategy. Those companies which neglected automation could not match the customer needs and faded away from the market sooner or later. Looking at the role of future engineers on a domain like AI and diversity is essential to avoid any biases. Therefore, damage assessment can be a source of employment to certain section of people with a technical background of AI or deep learning.

As discussed earlier, the perceptron model is termed as a full connection if and only if every neuron in the previous layer is connected to every neuron in the subsequent segment. In the scenario discussed in the above research paper, if a faulty object undergoes a pre-incident damage assessment at the warehouse, it can be easily filtered out and prevent any third-party complaints. In this way, conglomerates to start-ups can ensure that the production process generates less than 3.44 defects per million corresponding to a yield of 99.99966% [3]. The ultimate objective should be to achieve a zero-defect level of quality. The CNN technique has showed excellent performance in image recognition and deep learning methods. With recent accentuation on quality control concepts like Six Sigma and continuous improvement, techniques like CNN may find many useful applications in industrial sector.



## References

1. ICLG Homepage: <https://iclg.com/practice-areas/product-liability-laws-and-regulations/india>. Last accessed 10 May 2020
2. Tu, J.V.: Advantages and disadvantages of using artificial neural networks versus logistic regression for predicting medical outcomes. *J. Clin. Epidemiol.* **49**(11), 1225–1231 (1996)
3. Missinglink Homepage: <https://missinglink.ai/guides/computer-vision/neural-networks-image-recognition-methods-best-practices-applications/>. Last accessed 25 May 2020
4. Li, Y., Zhang, J., Gao, P., Jiang, L., Chen, M.: Grab cut image segmentation based on image region. In: 2018 IEEE 3rd International Conference on Image, Vision and Computing (ICIVC), pp. 311–315, Chongqing (2018)
5. Mathworks Homepage: <https://in.mathworks.com/matlabcentral/fileexchange/40079-january-2013-computer-vision-with-matlab-webinar-demo-files>. Last accessed 17 May 2020
6. Six Sigma Homepage: <https://www.whatissixsigma.net/six-sigma-calculator/>. Last accessed 5 June 2020
7. Wang, H.: A review of six sigma approach: methodology, implementation and future research. In: 4th International Conference on Wireless Communications, Networking and Mobile Computing, pp. 1–4. Dalian (2008)
8. Medium Homepage: <https://medium.com/machine-learning-researcher/convlutional-neural-network-cnn-2fc4faa7bb63>. Last accessed 24 May 2020
9. Bachtiar, Y.A., Adiono, T.: Convolutional neural network and maxpooling architecture on Zynq SoC FPGA. In: 2019 International Symposium on Electronics and Smart Devices (ISESD), pp. 1–5. Badung-Bali, Indonesia (2019)
10. Zhang, P., Bui, T.D., Suen, C.Y.: Recognition of similar objects using 2-D wavelet-fractal feature extraction. In: IEEE Xplore Object Recognition Supported by User Interaction for Service Robots 2002, vol. 2, pp. 316–319. Quebec City, Quebec, Canada (2002)
11. Albawi, S., Mohammed, T.A., Al-Zawi, S.: Understanding of a convolutional neural network. In: 2017 International Conference on Engineering and Technology (ICET), pp. 1–6. Antalya (2017)
12. Jiang, B., Li, X., Yin, L., Yue, W., Wang, S.: Object recognition in remote sensing images using combined deep features. In: IEEE 3rd Information Technology, Networking, Electronic and Automation Control Conference (ITNEC), pp. 606–610. Chengdu, China (2019)
13. WSCG Homepage: <http://wscg.zcu.cz/WSCG2018/Full/O47-full.PDF>. Last accessed 30 April 2020
14. Lucidchart Homepage: <https://www.lucidchart.com/pages>. Last accessed 29 May 2020
15. Nakajima, N., Tanaka, N., Yamada, K.: Document reconstruction and recognition from an image sequence. In: Proceedings Fourteenth International Conference on Pattern Recognition (Cat. No. 98EX170), vol. 1, pp. 922–925. Brisbane, Queensland, Australia (1998)
16. Todorovic, S., Ahuja, N.: Unsupervised category modeling, recognition, and segmentation in images. *IEEE Trans. Pattern Anal. Mach. Intell.* **30**(12), 2158–2174 (2008)
17. Imane, H., Abdelmajid, B., Aïcha, S., Yassine, R.: Large-scale image-to-video face retrieval with convolutional neural network features. *Int. J. Artif. Intell.* **9**(1), 40–45 (2020)
18. Keysers, D., Deselaers, T., Gollan, C., Ney, H.: Deformation models for image recognition. *IEEE Trans. Pattern Anal. Mach. Intell.* **29**(8), 1422–1435 (2007)

# Modification in Harness and Electrical System for Performance Optimization of Formula Student Car



Sushant Satputaley, Ankita Nagnath, Vikalp Shendekar,  
Mahesh Mohan, and Prateek Pargaonkar

**Abstract** Formula Bharat is an Indian Formula Student competition whose objective is to check the consciousness of viable building knowledge and under-study innovation through a focused stage. The challenge enables the teams to use an engine having a maximum displacement of 710 cc. Considering all the parameters, KTM RC390 engine was selected for the challenge on account of its unwavering quality, execution, and different components like engine control unit (ECU) to provide the most favorable execution and to obtain optimized performance. Being a formula student team, one must draw its whole attention toward weight reduction, and some of the components in the main harness of the KTM engine adds to the excessive weight; therefore, the trivial components are shortened from the formula race car. In order to achieve maximum efficiency, thorough study of the sensors, their respective connections, and ports were done. A PCB of BSPD and researched work on shutdown circuit which contains some safety components and switches for different hazardous situations has also been included. Taking all the concepts into consideration planning, designing and execution of all the methodologies for performance optimization of the formula race car have been achieved. The main objective of this research was to enhance the safety and achieve a performance boost in the car.

**Keywords** Engine control unit · Brake system plausibility device · Shutdown circuit

---

S. Satputaley (✉) · V. Shendekar · M. Mohan · P. Pargaonkar  
Department of Mechanical Engineering, St. Vincent Pallotti College of Engineering  
and Technology, Nagpur, Maharashtra, India

A. Nagnath  
Department of Electronics and Telecommunication Engineering, St. Vincent Pallotti College  
of Engineering and Technology, Nagpur, Maharashtra, India

© The Author(s), under exclusive license to Springer Nature Singapore Pte Ltd. 2021  
A. Patnaik et al. (eds.), *Advances in Materials Processing and Manufacturing  
Applications*, Lecture Notes in Mechanical Engineering,  
[https://doi.org/10.1007/978-981-16-0909-1\\_9](https://doi.org/10.1007/978-981-16-0909-1_9)

## 1 Introduction

These days, the researchers are moving their concentration toward the integration of mechanical and electronic gadgets as they are highly reliable such as ECU in automotive vehicles. ECU is essentially abbreviated as engine control unit, which controls a series of sensors and actuators in an internal combustion engine to increase the efficiency of engine. It is performed by reading values from the sensors situated within the engine bay. In view of data obtained from the information sensors (engine coolant temperature sensor, manifold absolute pressure sensor, air flow sensor and so on), the ECU decides optimum settings for the output actuators (injectors, idle speed control valve, and so on) [1]. Information sign is received by the sensors and output sign is given to the actuators. The input signals have been fed to processing unit by the sensors and corresponding output is given to actuators likewise. The actuators execute the decision taken by the control unit. The processing unit ensures the optimization of the fuel injection and ignition with the goal that it minimizes fuel utilization and emissions of pollutants and increases the torque and power accordingly. ECU increases the efficiency of vehicle thereby increasing the safety [2]. Shutdown circuit meant for different risky situations, which has been designed with high performance switches along with a BSPD.

## 2 Brake System Plausibility Device

BSPD is abbreviated as brake system plausibility device, a standalone non-programmable circuit, must open the shutdown circuit, when hard braking occurs and the throttle is more than 10% over idle position [3] which contains Two-input signal (0–5 V), brake failure detection, auto reset after 10 s and no heating problems. The BSPD is supplied from LVMS. BSPD works on the basis of data acquired from the two sensors, brake pressure sensor and throttle position sensor [3]. The components used in the circuit designing are closed and resettable conditions and a timing circuit is designed using same comparator blocks. The brake comparator checks that the pressure in the brake circuit is within an interval (0 = error). The throttle comparator checks that the throttle is open beyond a minimum threshold but less than 10% (0 = error). The output signals of the two comparators are in NOR (1 = error). The resistor  $R = 39 \text{ K}\Omega$  and the capacitor is MOSFET and it contains comparator IC LM393AD, potentiometer, Zener diode, NOR gate IC SN74AHC1G02DBVR, resistors, capacitors and battery. It contains two circuits—for managing the data from sensors and for timing circuit, each block has two comparators. The IC LM393AD has eight ports, pin number 8 is connected to VCC, 4 is ground, pin numbers 2, 3, 5 and 6 are the inputs of two comparators situated in one block. Pin numbers 2 and 5 are shorted and receive input signal from sensor. Pin number 3 is another input for comparator, and it compares the value under upper threshold, and pin number 6 compares under lower threshold. This

similar pattern is followed for both the comparator blocks, i.e., the brake comparator and the throttle comparator. The desired outputs from both the comparator blocks are fed as an input to the NOR gate IC. It checks whether both the conditions are satisfied for the engine to stop in order to avoid hazardous situations. For managing the timing of engine being opened  $C = 10 \mu\text{F}$  operate a time constant of 390 ms. The time 1 comparator determines a delay of about 500 ms (496 ms) in the activation of the system ( $0 = \text{error}$ ). The resistance  $R_{119} = 560 \text{ K}\Omega$  and the capacitor  $C = 10 \mu\text{F}$  operate a time constant of 5600 ms. The time 2 comparator determines a delay of about 9900 ms after which the BSPD is deactivated (reset condition) and the engine can be restarted ( $0 = \text{error}$ ). Both the brake signal and the accelerator signal are compared with two thresholds, one upper and one lower (Fig. 1).

Diodes operate a protection against peaks on all the signals. No heating problems, however, internal voltage regulator has protection against over-current and overheating. Brake failure shutdown: if signal from brake pressure sensor was under 0.45 V, the BSPD turns off the car. Auto reset is disabled when brake pressure sensor is about 5 V.

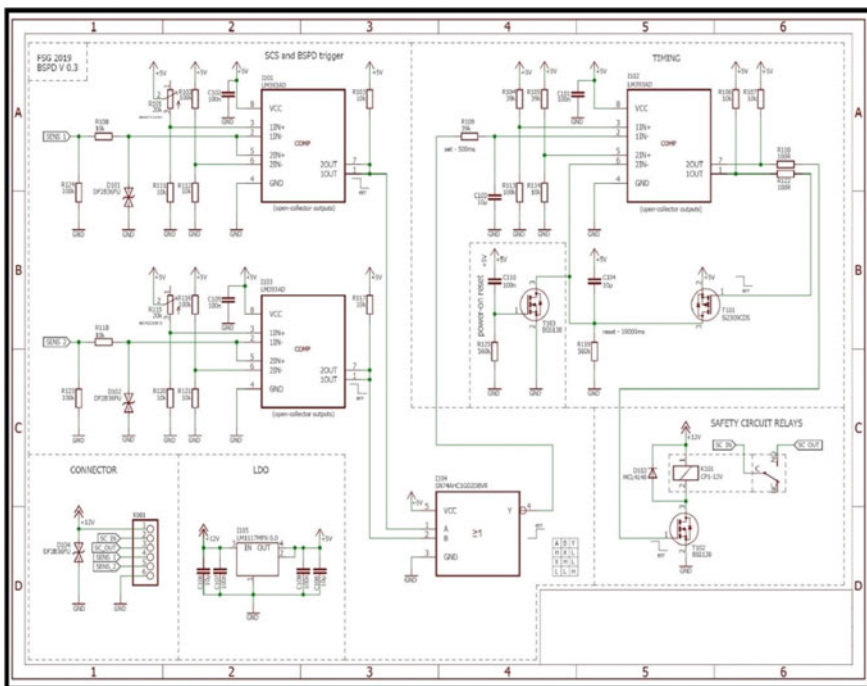


Fig. 1 Schematic layout of brake system plausibility device circuit [6]

### 3 Shutdown Circuit

The shutdown circuit is meant for safety purpose [4] as shown in Fig. 2.

#### 3.1 Low-Voltage Master Switch

LVMS is abbreviated as low-voltage master switch which completely disables power from low-voltage battery and alternator to low voltage system.

#### 3.2 Shutdown Buttons

In any hazardous situations, pushing the buttons results in opening the shutdown circuit. Generally, in a Formula car, there are three shutdown buttons. Two are on the either sides of main hoop, and one in the cockpit.

#### 3.3 Inertia Switch

An inertia switch must be part of shutdown circuit such that an impact will result in shutdown circuit being open.

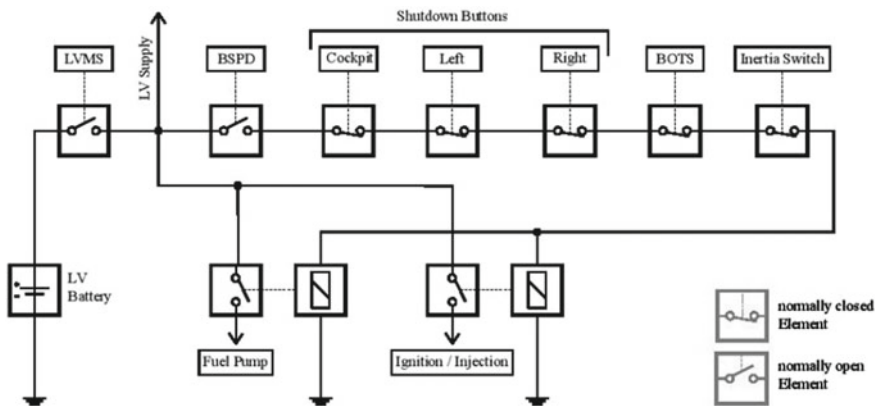


Fig. 2 Layout of the shutdown circuit [6]

### 3.4 BOTS

BOTS is abbreviated as brake over travel switch. In event of failure in one or both brake circuits, the brake pedal over travel will result in shutdown circuit being opened [3].

## 4 Harness

The harness of KTM RC 390 engine comprises of following sensors:

Throttle position sensor (TPS), temperature manifold absolute pressure sensor (TMAP), oxygen sensor, fuel-level sensor, crankshaft position sensor, rollover sensor, side stand sensor, engine oil pressure sensor, coolant sensor, speed sensor, idling, RPM sensor, gear position sensor, and clutch sensor.

As the diagram (Fig. 3a) shows the whole setup of sensors and switches that increases the weight of overall harness significantly as well as its complexity, hence for efficiency, the unnecessary sensors, switches, and some control unit have been scaled down. The ABS arrangement in KTM has two speed sensors associated with it that contributes to more weight; hence the whole arrangement has been reduced. Similarly, headlight, taillight, flashlight control units, and associated fuse connections are also removed. The sensors and switches that are not required for cranking are also removed and the wiring of main important sensors are extended (approximately 1.5 m each) as per the mounting and overall dimensions of the chassis. After optimization, in the formula, engine can be cranked in gear as the clutch sensor has been shortened. By studying the color codes of KTM RC390 engine, it can be cranked in gear as well in neutral [5].

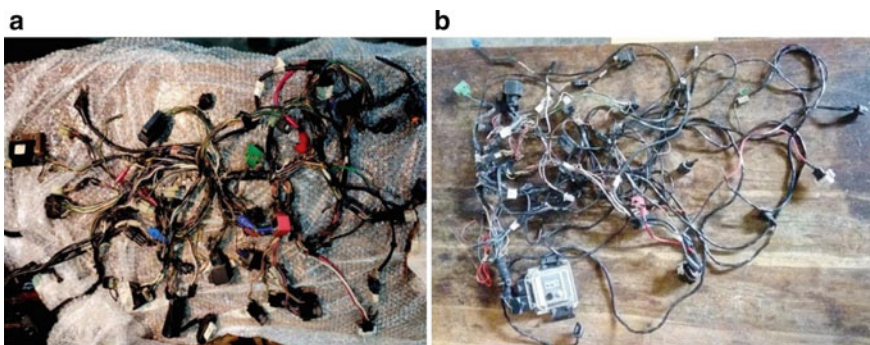


**Fig. 3** a Harness before optimization, b harness after optimization

## 5 Conclusion

In the process of designing a race car, an engineer has to consider various parameters which affect the overall performance of the car on the track like speed, acceleration, braking, aerodynamic effects, etc. These parameters are directly affected by the performance of different components under varying conditions. The engine—which is the powerhouse of a race car—is controlled by the ECU, and therefore, proper care has to be taken while working with the harness and its different connections to the ECU. In this research, proper color coding of the wiring in ECU connections were studied along with the sensors and different ports. In racing conditions, a few situations may occur where there is no control over the vehicle's performance. Hence, a shutdown circuit as a safety measure is utilized with the ECU which automatically turns the engine off instantly without wasting any time. But if an anomaly arises in hard braking conditions, a preventive measure is needed. Therefore, BSPD is used to shut down the engine to prevent any accidents. All the actuating conditions and the reset conditions have been taken care of. Before optimization, there was less efficiency in braking system, and after introducing BSPD, desired braking efficiency results have been achieved by maintaining time constant of 5600 ms and reset condition of 9900 ms. With all these components and their connections in the harness, the weight of the harness also increases. Increasing weight is always undesirable in a race car as it negatively affects the speed of the car. Hence, unwanted components of the harness are removed, and the harness is optimized to give desired performance. Due to the addition of shutdown buttons on the either side of the main hoop, the outside member can hustle and enable the actuation of the button thus increasing the safety as well as preventing the car from any damage. Before optimization and implementing this concept, there was only one kill button available with the driver for operation. With all these additions, a significant amount of performance boost has been achieved in the formula student car.

## References

1. Aithal, A., Donakonda, R.: Two wheeler engine control unit—development, challenges and solutions. SAE Technical Paper Series, 16th Asia Pacific Automotive Engineering Conference, 6 Oct, 2011, 2011-28-0003
2. Paolo, B., Stefano, M., Giovanbattista, V., Trifiletti, A.: ECU development and testing through numerical optimization and hardware in the loop simulations. SAE Technical Paper, 2001-12-01
3. [https://www.formulastudent.de/fileadmin/user\\_upload/all/2020/rules/FS-Rules\\_2020\\_V1.0.pdf](https://www.formulastudent.de/fileadmin/user_upload/all/2020/rules/FS-Rules_2020_V1.0.pdf)
4. Naga Sruthi, G.S., Vibhute, R., Karmarkar, U., Chandra, S., Iyengar, S.M.: Safety system of an electric vehicle for formula racing. In: 2014 IEEE International Conference on Vehicular Electronics and Safety, pp. 44–49, Hyderabad (2014)

5. Farrugia, M., Farrugia, M., Sangeorzan, B.: ECU development for a formula SAE engine. SAE Technical Paper Series, 2005 SAE World Congress, Detroit, Michigan, 11–14 April (2005)
6. Wiehen, C., Neuhaus, D.: Potential of electronically controlled brake systems. 1995 SAE Brazil, SAE Technical Paper 952278, 1995-10-01 (1995)



# Valorization and Promotion of Montenegrin Bridges Through Implementation of ICT Technologies



Andela Jakšić Stojanović  and Neven Šerić

**Abstract** Cultural heritage has important role for one nation and because of that it should be adequately preserved, protected, valorized, and promoted. This is extremely important in the era of the globalization in which global dominates over national/local. Important segment of cultural heritage are bridges which are extremely valuable from many different points of view such as historical, cultural, architectural, and artistic. Today, there are many bridges all around the world that attract people by fascinating works of arts and impressive feats of engineering, beautiful landscapes, unforgettable experiences, mysterious stories from the past, etc., and a lot of them became famous tourist attractions. In Montenegro, there are a lot of bridges built in different culture-historical periods of the past, with beautiful architecture, breath-taking scenery romantic legends and fairy tales connected to their past, but most of them are neither adequately preserved nor valorized. We strongly believe that they represent huge potential for tourist and cultural valorization and because of that we propose the innovative concept based on implementation of modern ICT technologies through creation of mobile applications, implementation of different digital tools, virtual and augmented reality, gamification, etc., which would make Montenegrin bridges particular destination icons. That concept would improve the process of preservation and protection of Montenegrin bridges and their promotion on international tourist market and contribute to creation of new tourist products and diversification and differentiation of tourist offer as well as to the sustainable development of destination itself.

**Keywords** Cultural heritage • Bridges • Valorization • Promotion • ICT technologies

---

A. J. Stojanović (✉)

Faculty of Culture and Tourism, University of Donja Gorica, Podgorica, Montenegro  
e-mail: [andjela.Jaksic@udg.edu.me](mailto:andjela.Jaksic@udg.edu.me)

N. Šerić

Faculty of Economics, Business and Tourism, University of Split, Split, Croatia

## 1 Introduction

Cultural heritage is more than just a collection of material and immaterial goods on certain place [1]. It is cultural identity of one nation, its past and its future, its culture, history, and tradition .... Because of that, adequate preservation, protection, valorization, and promotion of cultural heritage are extremely important especially in the era of globalization in which global dominates over national/local [2]. In that sense, bridges may and must be used as factors of differentiation and diversification of tourist offer on international tourist market and, if valorized and promoted adequately, as one of the destination's main competitive advantages on international tourist market.

In order to reach that, it is necessary to consider bridges not only as architectural or engineering objects made of stone, steel, etc., built in order to bridge two sides of river, but also as the objects which are extremely important from many different points of view—such as historical, architectural, cultural, and artistic. Only considering all these aspects, the cultural heritage may be adequately preserved, protected, valorized, and promoted.

Each bridge has its own story, but the fact is that the bridges were built not only to connect two sides of river, but to connect people as well. Some were constructed in order to bridge cultures and traditions, while some were designed and built in order to reach immortality. Although they were constructed from different reasons, the motivation for their construction was the same. It is the gap, not only in physical, but in emotional sense as well, the gap that should be filled and bridged by man's imaginations, dreams, hopes, efforts, courage ....

Today, there are many spectacular examples of bridges all around the world that attract people's attention from different reasons—because of fascinating works of art and impressive feats of engineering, beautiful landscapes and sceneries, mysterious and fairy-tale stories from past ... Many of them became tourist attractions which attract tourists from all over the world, and very often they are even the main reason for visiting particular destination.

## 2 Montenegrin Bridges—State of the Art

Officially, the first regulations regarding the cultural goods in Montenegro were adopted after Second World War. In 1949, Law on the Protection of Cultural Monuments and Natural Rarities in Montenegro was adopted, while first institution that dealt with protection of the cultural heritage, the Institute for the protection of Cultural Monuments and Natural Rarities, was established in 1948 [3].

According to the document "The state of cultural heritage in Montenegro" [4], only few bridges in Montenegro are recognized as cultural goods. But, despite of this fact, Montenegro is full of beautiful bridges that have a huge potential for tourist valorization. Some of the Montenegrin bridges are extremely valuable from

historical, cultural, or architectural point of view, and some are famous because of beautiful magic fairy tales and legends from the past, while there are also some bridges which were built in picturesque idyllic sceneries which give added value to their potential valorization.

Unfortunately, at the moment, there are not many available data about Montenegrin bridges, even about those which are recognized as cultural goods. There is not even a list that consists the exact number of bridges in Montenegro, although the Commission that was supposed to list all Montenegrin bridges and their condition was formed in 2013. Up to now, it is only known that only in the territory of the capital city, there are 108 bridges—29 of them are situated in town itself, while others are situated outside the town. Some information about their construction, architecture, cultural values as well as legends connected to their past may be found in stories and columns of bridge-lovers, mostly in newspapers or on some blogs on Internet. There are also some scarce information on promotional Web sites of local tourist organizations, as well as few stories written by journalist or writers fascinated by some of the bridges in Montenegro. Regarding photographs, for most of the bridges it is not possible to find high-quality professional photographs which could be used for their promotion on tourist market.

In order to have adequate inputs and measurement parameters for this paper, field research was conducted in order to identify the most interesting and valuable Montenegrin bridges that have the most potential for tourist valorization. Unfortunately, due do COVID-19 pandemic, the field research was carried out only in a part of central and north part of Montenegro, and the results of the research were published in scientific monograph *Montenegrin Bridges and Their Valorization* written by the authors of this paper, but it is still expected that realization of other part of the project regarding collection of data will be continued as soon as possible.

### **3 Valorization of Montenegrin Bridges Through Implementation of ICT Technologies**

Although there are some interesting examples of valorization of bridges in the world, we are strongly convinced that Montenegro should create completely new concept which will be based on the implementation of modern ICT technologies [5]. Such kind of valorization would fill the gap between past and future, traditional and modern, local and global, etc., which is widespread in modern society. In that sense, it is necessary to use all the advantages of information communications technologies (ICT) in order to protect and promote this extremely valuable segment of heritage [6]. The growing popularity of these technologies, innovations in this field, the access to online data, the use of remote sensing technologies and platforms, etc., open wide area of possibilities which should be used.

So, at the very beginning, it is necessary to create adequate digital base which would consist of all data about Montenegrin bridges—the list of the bridges, their main characteristics, data about their designers and sculptors, legends and stories connected with them, as well as professional photographs of the bridges and their surroundings. The investment in the process of digitalization of data not only regarding the bridges but also regarding other segments of cultural heritage would significantly contribute to the improvement of their protection and preservation, as well as their valorization and promotion on international tourist market. In later phases, this database may be connected with other similar bases in Europe in order to promote European cultural heritage [7]. Such base would allow creation of mobile applications for tourists which will enable them to get all data about Montenegrin bridges by one click, choosing the ones that should be visited, according to their own needs, interests, hopes, and desires. The application would include all relevant data for tourist's decision-making process, and in that way, it would significantly improve the quality of tourist offer.

ICT technologies may significantly contribute to the process of putting bridges in wider cultural, historical, and artist context, not as isolated objects. This means that, thanks to implementation of ICT technologies, it would be possible to mix real and reconstructed, present and past, reality and legends in order to impress tourists and create authentic experience.

It should also apply virtual reality and augmented reality [8] which represent the new ways of promoting destination content that may not only significantly improve the quality of tourist offer, but also ensure the sustainability of cultural heritage [9]. It is a quite new concept that creates a special experience for tourists and gives a new dimension to the destination itself. In that sense, it would be interesting to create and organize certain kind of virtual tours for tourists in which they would be able to identify that crucial wider context and recognize its importance from many different points of view. It would be great to offer tourists the virtual experience of enjoying in scenes of Battle in Mojkovac, which represents one of the most important battles in Montenegrin history, to find out more about courage of native people, about their costumes, weapon, etc. or to have the possibility to experience the rafting on beautiful Tara river and its canyon, the second deepest in the world, right behind America's Grand Canyon, to feel that virtual adrenaline challenge enjoying the excitement like never before. And if satisfied, to experience, but this time real rafting tour, enjoying in dreamy and beautiful natural scenery. Or to organize virtual zipline tour, the largest one in Europe, for those more even more passionate adrenaline lovers, with a spectacular view on canyon, river, forests, and cliffs.

In combination with virtual and augmented reality, some most modern methods of building information modeling (BIM) could be used as well, by integration of different types of information into a shared database constituting a source of 2D or 3D information that is shared and experienced by visitors [10, 11].

As already mentioned stories, legends, and anecdotes related to bridges may play a very significant role in promotion of this segment of tourist offer. It is necessary to prepare a quality online presentation of these contents and put special focus on

bridges which are located in the Central and Northern part of Montenegro, as well as on those that are still not yet promoted. In this way, the quality of Montenegro's tourist offer would be significantly improved, but at the same time, a more balanced distribution of tourist traffic would be enabled, which is one of the key problems that many tourist destinations face with. This kind of presentation may provoke an emotional reaction from potential visitors, give certain dose of mystery, and create new tourist attractions. These presentations would be promoted by different channels of digital marketing especially by social networks in order to reach as many target groups as possible.

Except presentation in digital media, it is also possible to reach more interactive approach by presentation of the content on interactive tables on the bridges that have the most potential for storytelling. Setting up interactive, instead of used static boards, may in the same time improve the degree of tourists' satisfaction and contribute to creation of authentic feelings and experiences. It is also possible to design and create digital city lights which would also be placed on bridges. Tourists would have the opportunity to enjoy in multimedia content about the bridge using special headphones. In that way, they would have the opportunity to learn more about particular bridge, its history, construction, legends connected with its past, etc., through interesting multimedia context. That multimedia context would include modeling, reconstruction, and visualization of the real environments from the past in order to create faithful virtual representation of certain objects or events from the past, which will significantly contribute to authenticity and uniqueness of tourists' feelings and experiences.

One interesting way of promotion of bridges is also the process of gamification which is extremely interesting for younger generations. In this way, it is possible to help the visitors to understand better how certain place might have looked like. As a part of a challenge, the gamers could also learn about history of Montenegro, its nature, cultural heritage, flora and fauna, etc. This technique has a great potential to improve the tourist's experiences, as well as to boosts the development of creative learning and educational tools.

Something that is extremely important is that the bridges should not be presented as separate segment, but in contrary as the integral part of tourist offer. That means, for example, that the visit of Bridge Đurđevića Tara would be integral part of visit of national park Durmitor, with its high peaks, abundant forests, and deep gorges. Visit to the bridge may be combined with visit of some of seventeen glacier lakes, rafting on River Tara or zipline activities, tracking, mountaineering, Alpine and Nordic skiing, fishing, camping, etc. Visit to bridges in little fishermen village Virpazar may be combined with overview of traditional village houses, buying local products on the square market, visit to the Besac Castle, and fortification built by the Turks in 1478. It is also possible to include visit to Skadar Lake because Virpazar is also the starting point for most boat excursions in the national park Skadar Lake which is famous for beautiful flora and fauna (around 270 kinds of birds inhabit this Lake), cultural monuments (more than 20 monasteries, churches, villages, fortresses, and sacred monuments,) and beautiful scenery. Bird watching, fishing, hunting, renting and ride in boat, swimming, and sunbathing are only some

of the activities that may be realized here. In addition, tourists have the opportunity to enjoy famous wine tasting and gastronomy tours. Overview of bridge on River of Crnojević may be one segment of visit to this old place which used to be the capital of Montenegrin state Zeta (1465–1490). Except this beautiful bridge, tourists may enjoy in this fairy-tale area, beautiful natural sceneries, visit to the house of St. Peter, the oldest building in this place, then visit to Monastery of St. Nicholas where the first Montenegrin book *Oktoih* was printed, etc. The same situation refers to bridges which are less famous among tourists, like those in Nikšić. Bridge tours would include the visit to some of the most interesting bridges which are mentioned in this paper, visit to beautiful lakes—Slano and Krupac Lake, visit to famous cave Crvena Stijena (Red Rock), which is the deepest in Europe after the El Castillo archeological site in Spain. By presentation of bridges as integral part of tourist offer of particular area, its quality may be significantly improved which would lead to the improvement of the level of tourists' satisfaction, better positioning on international tourist market as well as creation of recognizable image of the destination itself.

## 4 Conclusion

Montenegro is a country full of beautiful bridges. Some of them are famous because of their beautiful architecture, some of them because of breathtaking sceneries and landscapes that may be discovered, some are valuable because they represent masterpiece of certain cultural period from very rich and turbulent history, while some are authentic and special because of the beautiful legends and stories connected to their past. Having in mind the fact that tourism represents one of the main strategic pillars of economic development of the country, it is necessary to preserve, protect, valorize, and promote this important segment of Montenegrin cultural heritage and to make the bridges integral part of tourist offer. Although there are some spectacular examples of tourist valorization of bridges all around the world, we proposed completely new innovative concept based on implementation of modern ICT technologies through creation of mobile applications, implementation of different digital tools, virtual reality, gamification, etc.

This concept could be used not only in promotion and valorization of bridges, but also in the protection, preservation, valorization, and promotion of other segments of Montenegrin cultural heritage such as old towns and old urban settlements, archeological and sacral objects, castles, etc., which would contribute to diversification and differentiation of tourist offer, creation of new authentic image, sustainable development, and better positioning on global tourist market.

## References

1. Vecco, M.: A definition of cultural heritage: from the tangible to the intangible. *J. Cult. Heritage* **11**(3), 321–324 (2010)
2. Jakšić-Stojanović, A., Šerić, N.: *Montenegrin Lighthouses as Destination Icons*. Univerzitet Mediteran, Podgorica (2018)
3. Council of Europe: National Policy Report for Montenegro. <https://www.coe.int/en/web/herein-system/montenegro>, 2020/04/01
4. Malbaša, P., (ed.): *Stanje kulturne baštine u Crnoj Gori*. Ministarstvo kulture i medija, Podgorica (2006)
5. Jakšić-Stojanović, A., Gošović, A.: New aesthetic relations in architecture and cultural heritage through implementation of live sound effects on exterior of buildings. In: *Proceedings of 8th Mediterranean Conference on Embedded Computing (MECO)*, IEEE (2019)
6. Ott, M., Pozzi, F.: ICT and cultural heritage education: which added value? In: Lytras, M.D., Carroll, J.M., Damiani, E., Tennyson, R.D. (eds.) *Emerging Technologies and Information Systems for the Knowledge Society*. *Proceedings of First World Summit on the Knowledge Society*, pp. 131–138. Springer-Verlag, Berlin-Heidelberg (2008)
7. United Nations Educational, Scientific and Cultural Organization: Charter on the Preservation of the Digital Heritage. <https://unesdoc.unesco.org/ark:/48223/pf0000179529.page=2>. Last accessed 2020/04/05
8. Aziz, K.A., Siang, T.G.: Virtual reality and augmented reality combination as a holistic application for heritage preservation in the UNESCO world heritage site of Melaka. *Int. J. Soc. Sci. Humanity* **4**(5) (2014)
9. Ozdemir, E., Kilic, S.: Augmented reality: applications and implications for tourism. In: Rodrigues, M.F.J., et al. (eds.) *Handbook of Research on Technological Developments for Cultural Heritage and eTourism Applications*. IGI Global, USA (2017)
10. Figueiredo, M., Bernardes, P.J., Rodrigues, I.J.J., Goncalves, C.: A Framework supported by modeling and virtual/augmented reality for the preservation and dynamization of archeological-historical sites. In: Rodrigues, M.F.J., et al. (eds.) *Handbook of Research on Technological Developments for Cultural Heritage and eTourism Applications*. IGI Global, USA (2017)
11. Hurmuzlu, Y., Nwokaj, D.I.O.: *The Mechanical Systems Design Handbook: Modeling, Measurement and Control*. CRC Press, Taylor & Francis Group (2002)

# Assessing the Research Status on Occupational Safety for Adopting Zero Accident Vision: A Bibliometric Analysis



Jai Narain, M. L. Meena, G. S. Dangayach, and Gaurav Gaurav

**Abstract** Industrial accidents are severe mishaps that result in injuries and fatalities to people, and damage to property as well as environment. The effect of accident is so severe that a society has to pay for decades. The purpose of this article is to make readers to understand the research status on occupational safety in India for adopting zero accident vision (ZAV)-related literature through the data collected from the core collection of Web of Science and the Scopus database through bibliometric analysis. Different analyses have been carried out, such as research growth, author analysis, subject analysis, source analysis, author impact, country affiliation analysis, institution analysis, and scientific production. This study shows that since 2019, there has been an increase in the field of ZAV on occupational safety research, and it has a good range of applications in different fields. Co-citation analysis and Co-occurrence analysis also have been carried out to identify buzz word on ZAV and collaboration, contribution, and sharing of knowledge between the sources journals. The top 30 highly influential papers were also evaluated from two databases. The result analysis also reveals promising future research directions for researchers in the field of ZAV on occupational safety research.

**Keywords** Bibliometric analysis · Co-citation analysis · Zero accident vision (ZAV) · Safety management · Safety culture

## 1 Introduction

Accidents are unforeseen events, which not only causes harm to human, environment or property, unintentionally and unexpectedly but also reduced the productivity of the nation. Initially it was deemed that the accidents are inevitable during

---

J. Narain (✉) · M. L. Meena · G. S. Dangayach · G. Gaurav  
Department of Mechanical Engineering, Malaviya National Institute of Technology Jaipur,  
Jaipur 302017, India  
e-mail: [jainarain@mnit.ac.in](mailto:jainarain@mnit.ac.in)

© The Author(s), under exclusive license to Springer Nature Singapore Pte Ltd. 2021  
A. Patnaik et al. (eds.), *Advances in Materials Processing and Manufacturing Applications*, Lecture Notes in Mechanical Engineering,  
[https://doi.org/10.1007/978-981-16-0909-1\\_11](https://doi.org/10.1007/978-981-16-0909-1_11)



the works. But now various theories established that all accidents can be avoided by establishing proper safety management system. As per an estimate of the I.L.O [1], the estimated death per year is 2.34 million due to workplace accidents. The above includes 321,000 causing to accidents and remaining 2.02 million are caused by diseases due to working conditions, which results to a daily average death more than 5500. The I.L.O. states “The inadequate prevention of occupational diseases has profound negative effects not only on workers and their families but also on society at large due to the tremendous costs that it generates; particularly, in terms of loss of productivity and burdening of social security systems.” As per the International Social Security Association [2], the estimated non-fatal accidents are 270 million at workplace each year with an increase of 160 million cases of occupational illnesses; the burden of health care, rehabilitation, and invalidity is very big which estimate 4% of world GDP for only work injuries. Its cost can be as high as 10% of GDP in some developing countries.

The costs of occupational accidents may not be measured only in financial term but can be better judged by grouping into three categories: indirect costs, direct costs, and human costs. Direct costs consist of expenditure on medical. This data collection is easy to obtain and indirect costs include the costs related to missed opportunities for the deceased employee, the employer, and the society. The comparison of these costs is very difficult. The human costs are qualitative measure of workers life index at work place.

## ***1.1 Vision Zero Accidents***

Initially it was mindset that accidents happen due to human errors, and these can be prevented by a strong bureaucratic system. Almost all the nations have the government mechanism to prosecute the wrong doers. Unfortunately, the rate of accident cannot be reduced. One more aspect which is very critical in accident prevention is non-reporting and it is the outcome of this punishment-based government mechanism. The accidents and the reasons of accidents are being hidden and the actual cause of accident is neither known to the stack holder nor to the researchers. Due to this reason, the accidents are repeated for same cause. But improving safety of complex industrial systems is one of the most difficult tasks for company managements. There are so many methodologies developed in the field to help facing this challenge, but the ZAV is a promising approach developed in industry, but unfortunately it is not better addressed by the safety science research community. Actually, ZAV is based on the assumptions that all the serious accidents are preventable. There are some conflicts also on the basic of ZAV, as some researcher feels that taking goal as zero accident is impossible to achieve [3], they argue that achieving such perfection will increase bureaucratic methods in industrial management, to deal this challenge, various methods and concepts have been developed by researchers to check the role of safety climate and safety culture on human behavior [4]. Since last few decades, various industries have used the terms

“zero injury” and “zero accident” to express their commitment to safety. Zero accident vision (ZAV) proved to be one of the promising philosophies to improve safety. It is presumed that accidents can be avoided. According to Zwetsloot et al., ZAV is “an ambition and commitment to create and ensure safe work and prevent all (serious) accidents to achieve superior safety” [5]. In other words, “all work-related accidents, injuries and illnesses are preventable” [6]. The implementation of ZAV implies the need for a “generative” or at least “active” safety culture [7]. Igc et al. [8] measured the production workers perceptions in respect of ZAV success factor such as committed to safety, safe communication, safe climate, and learning from accidents by conducting a survey using a questionnaire given to four production plants in the Serbian military industrial complex.

To the best of our knowledge, only few studies conducted to access the ZAV on occupational safety. However, there is no study available on ZAV on occupational safety in India. This is the first of its kind study on ZAV based on bibliometric analysis. Therefore, there is an urgent need to critically review the research the field of ZAV on occupational safety and to suggest a way forward. To fill this gap, a detailed bibliometric analysis of the research field of ZAV on occupational safety was carried out. The main objective of this article is to explore the ideas and opportunities of the selected literature through bibliometric analysis for the period from 2009 to December 2019. The bibliometric analysis of data of Web of Science and Scopus presents the different aspect of research in the field of occupational safety and health in the world and its status in the India, the leading researcher working in the field, their research period and directions.

## 2 Data Collection and Methodology

For bibliometric analysis, data were extracted from Web of Science and Scopus databases in CSV and plain text file formats from 2009 to December 2019. Web of Science and Scopus are the most famous databases that provide unified and high-quality research publication statistics. Therefore, two databases were selected to extract information for bibliometric analysis. Use the “article title” search field in the Scopus and WoS databases to extract all the ZAV-related search word as shown in Search Criteria Table 1. Other visual analysis can be completed by integrating the extracted data with VoS Viewer software [9].

For the data collection, it was observed that the WoS has lesser number of documents related to ZAV than Scopus database. Also, the average citations per documents were more in WoS compared to the Scopus. As evident in Table 2, there are many parameters which were not constant in both the databases due to obvious reasons.

The documents is distributed according to their types of article, proceedings paper, editorial material, and review in WoS and Scopus data base. The numbers of

**Table 1** Search criteria

Date of search: 11/01/2020	Time: 11:00 IST	
	Database: WoS	Database: Scopus
Search string	“Zero accident vision” OR “Zero accident vision(ZAV)” OR (“Commitment strategy” OR “Occupational safety” OR “Accident Investigatio*” OR “Safety Management” OR “Accident analysis techniqu*” OR “Safety cultur*”) AND (“manufacturing Industr*” OR “compani*”) OR (“Safety research*” OR “Vision Zero” OR “Zero Vision” OR “Safety commitment*” OR “Safety communicatio*” OR “Safety cultur*” OR “Safety learning” OR “Safety leadershi*” OR “Road Accident*”) AND (“manufacturing Industr*” OR “compani*”)	“Zero accident vision” OR “Zero accident vision(ZAV)” OR (“Commitment strategy” OR “Occupational safety” OR “Accident Investigatio*” OR “Safety Management” OR “Accident analysis techniqu*” OR “Safety cultur*”) AND (“manufacturing Industr*” OR “compani*”) OR (“Safety research*” OR “Vision Zero” OR “Zero Vision” OR “Safety commitment*” OR “Safety communicatio*” OR “Safety cultur*” OR “Safety learning” OR “Safety leadershi*” OR “Road Accident*”) AND (“manufacturing Industr*” OR “compani*”)
Search in fields	Topic	Article title
Document type	All	All
Language	All	
Result	509 documents from all years till the search date	1983 documents from all years till the search date

**Table 2** Main information about data collection

Main information about collection			
WoS database		Scopus database	
Description	Results	Description	Results
Documents	509	Documents	1983
Sources (journals, books, etc.)	196	Sources (journals, books, etc.)	824
Keywords plus (ID)	977	Keywords plus (ID)	8688
Author’s keywords (DE)	1620	Author’s keywords (DE)	3966
Period	2009–2019	Period	2009–2019
Average citations per documents	11.9	Average citations per documents	6.179
Authors	1545	Authors	4784
Author appearances	1755	Author appearances	6102
Authors of single-authored documents	65	Authors of single-authored documents	341
Authors of multi-authored documents	1480	Authors of multi-authored documents	4443
Single-authored documents	73	Single-authored documents	435

(continued)

**Table 2** (continued)

Main information about collection			
WoS database		Scopus database	
Description	Results	Description	Results
Documents per author	0.329	Documents per author	0.415
Authors per document	3.04	Authors per document	2.41
Co-authors per documents	3.45	Co-authors per documents	3.08
Collaboration index	3.39	Collaboration index	2.87

**Table 3** Distribution of documents according to their types in WoS and Scopus

WoS database			Scopus database		
Document types	Records	Contribution (%)	Document types	Records	Contribution (%)
Article	124	73.81	Article	145	65.91
Review	12	0.96	Conference paper	49	22.27
Meeting abstract	10	0.8	Review	17	7.73
Editorial material	8	0.64	Book	3	1.36
Article, proceedings paper	7	0.56	Note	2	0.91
Book review	4	0.32	Abstract report	1	0.45
Correction	1	0.08	Article in press	1	0.45
Letter	1	0.08			
News item	1	0.08			
Short survey	1	0.08			

articles were maximum in Scopus database as well as book and book chapters. That clearly indicates that there is more demand of Scopus in the area of ZAV (Table 3).

### 3 Results and Discussion

#### 3.1 Research Growth

The status of annual growth of both the sources is given in Fig. 1, and it can be seen from the figure that annual growth rate in WoS database and Scopus database is 6.61% and 9.4%, respectively. This study shows that since 2019, there has been an increase in the field of ZAV on occupational safety research.

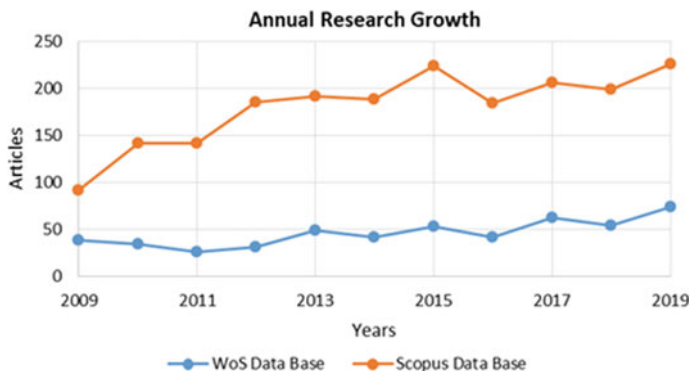


Fig. 1 Research growth in ZAV from WoS and Scopus database

### 3.2 Top Productive Authors

The top productive authors in the field with their productivity are given in Table 4. Figure 1 shows the research growth since 2009–2019 and top productive authors (Table 4).

There were more article published in Scopus than WoS. Also, Kines P was top author in WoS and Jacxsens L is top author in Scopus for publishing the articles.

### 3.3 Author Production and Author Productivity

Figures 2 and 3 depict the top author production over time in WoS and Scopus database which clearly states the importance of ZAV in current scenario at global

Table 4 Top 10 most relevant authors

Rank	WoS database			Scopus database		
	Author name	TP	TC	Author name	TP	TC
1	Kines P	6	123	Jacxsens L	23	576
2	Zhuang Zq	6	29	Luning Pa	17	341
3	Beck D	5	28	Uyttendaele M	16	486
4	Ghahramani A	5	20	Liu Y	11	7
5	Swuste P	5	31	Kirezieva K	9	167
6	Antonsson Ab	4	27	Mori K	9	15
7	Celik M	4	85	Wang Y	9	23
8	Lenhardt U	4	16	Arendt S	8	1
9	Moon I	4	14	Chen J	8	1
10	Nenonen S	4	46	Beck D	7	40

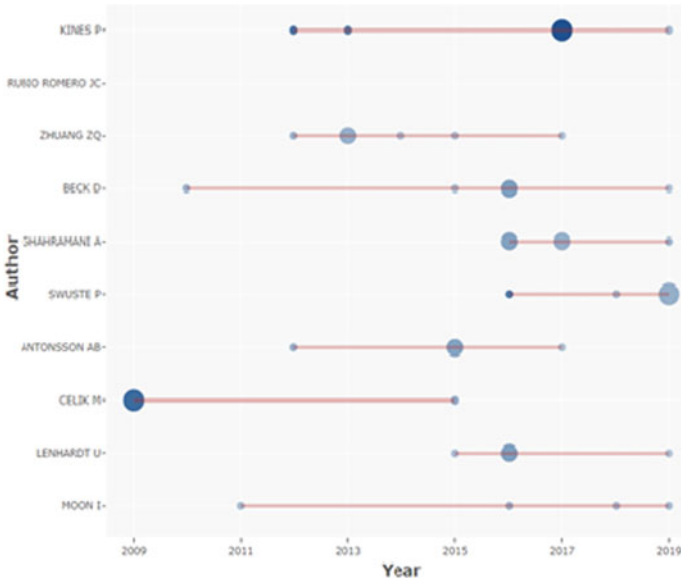


Fig. 2 Author production in WoS database

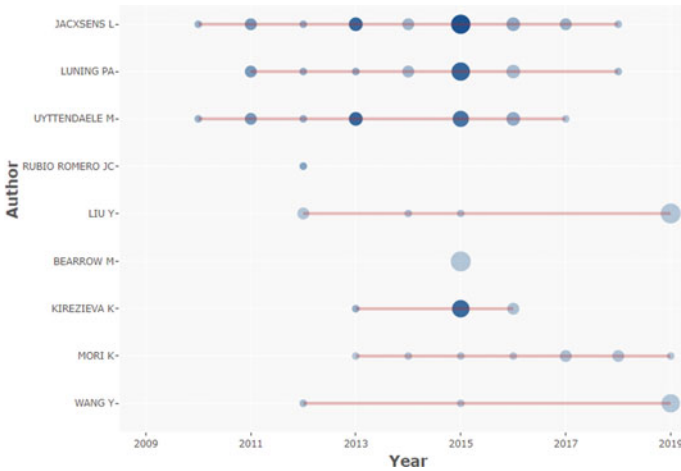


Fig. 3 Author production in Scopus database

level. The rank and values of the publications coming out of the area of ZAV have been increasing day by day due to its global implication and importance in the public domain as shown in Figs. 4 and 5.

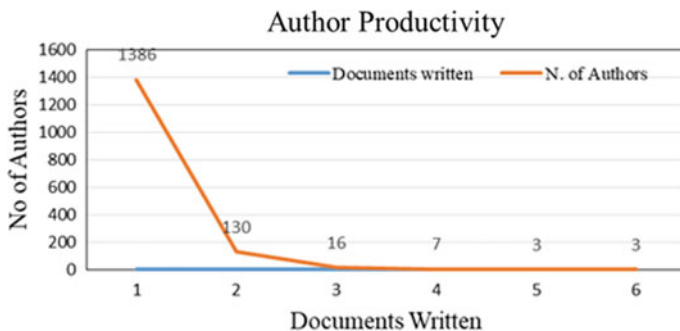


Fig. 4 Author productivity in WoS database

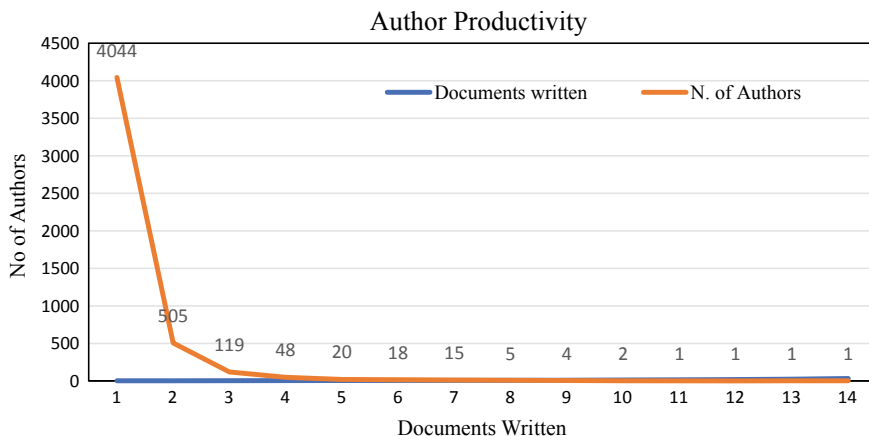


Fig. 5 Author productivity in WoS database

### 3.4 Most Relevant Affiliations and Country

The most relevant affiliations as well as top 10 countries publishing work on ZAV in WoS and Scopus were USA (Tables 5 and 6). It without any reservations states that USA preforms most of the ZAV research and all the corresponding authors are from USA as well as the USA is top most country which publishes the highest number of articles in the area of ZAV. It also states that the USA has more awareness and more control over accidents at work place and hence possesses healthy and responsible society.

**Table 5** Most relevant affiliations

R	WoS database		Scopus database	
	Affiliations	A	Affiliations	A
1	National Institute for Occupational Safety Health (NIOSH)	21	National Institute for Occupational Safety And Health	53
2	Delft University of Technology	14	University of Occupational And Environmental Health	27
3	University of Malaga	8	Wageningen University	25
4	Finnish Institute of Occupational Health	7	University of California	22
5	Istanbul Technical University	7	Finnish Institute of Occupational Health	19
6	National Research Centre for the Working Environment	7	Ghent University	19
7	Tampere University	7	University of Minho	19
8	University of Antwerp	7	Delft University of Technology	15
9	Netherlands Organization Applied Science Research	6	Universiti Teknologi Malaysia	13
10	Harvard University	6	Tampere University of Technology	12

**Table 6** Top 10 countries publishing

R	WoS database			Scopus database		
	Region	TP	%	Region	TP	%
1	USA	95	18.66	USA	360	18.15
2	Spain	34	6.68	China	80	4.03
3	China	33	6.48	Brazil	67	3.38
4	Germany	26	5.11	UK	58	2.92
5	Korea	26	5.11	Italy	54	2.72
6	Netherlands	21	4.13	Korea	52	2.62
7	Finland	20	3.93	Germany	48	2.42
8	Norway	19	3.73	Norway	48	2.42
9	Brazil	17	3.34	Spain	42	2.12
10	Italy	17	3.34	Malaysia	40	2.02

### 3.5 Global Scientific Production

Figures 6 and 7 show the global geographical distribution of scientific production of ZAV-related articles in WoS and Scopus database. USA is top most country in producing the scientifically relevant data and information in the ZAV research



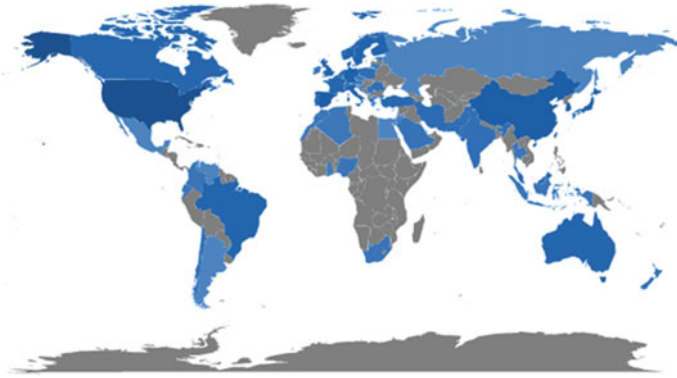


**Fig. 6** Global scientific production in WoS database

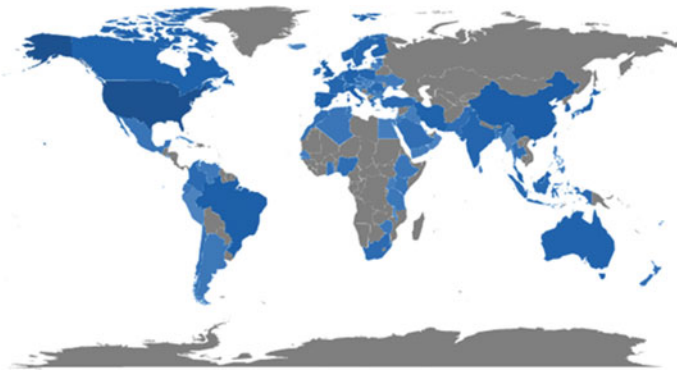


**Fig. 7** Global scientific production in Scopus database

domain. Since USA has all the protocols for ZAV and the people follow it strictly, the incident of accidents and work place is minimum.

### ***3.6 Trending Topic***

Safety culture, management and occupational safety are in much more trend in both the databases as observed in Table 7. These keywords signify the research work done in the areas of safety management, process, and occupational safety by the different research groups at the global and local levels leading to the production of high-quality research articles and then the protocols for the overall safety related to the ZAV.

**Table 7** Top 10 trending topic

	WoS database		Scopus database	
R	Authors keywords	F	Authors keywords	F
1	Safety management	41	Safety culture	96
2	Safety culture	34	Safety	93
3	Occupational safety	29	Safety management	89
4	Safety	23	Process safety management	69
5	Safety climate	21	Occupational safety	57
6	Occupational safety and health	19	Risk assessment	56
7	Risk assessment	15	Process safety	48
8	Occupational health	13	Safety climate	44
9	Accident analysis	8	Occupational safety and health	37
10	Safety management system	7	Occupational health and safety	32

### 3.7 Top Source Journal

Table 8 shows the top 10 journals and source impact of the same for publishing ZAV articles. Out of the top 10 journal, “Safety Science” is the top most journal for both the databases, i.e., WoS and Scopus having the maximum impact as source for the ZAV research articles. In table, “R” stands for rank and “F” stands for frequency.

### 3.8 Co-occurrence Analysis

Occupational health and safety are the buzz words coming again and again in the keywords network, that shows the importance of ZAV and it must be integrated with the daily life at work place to reduce the accidents (Figs. 8 and 9).

### 3.9 Co-citation Analysis

Figures 10 and 11 refer the co-citation network from WoS and Scopus for the analysis. It may be observed that the Safety Science is representing a big area that it says about the quality of research ZAV is having importance of. It is the ZAV which will be of much significance in the coming future to take down the number of accidents and work place.

**Table 8** Top 10 journals

R	WoS database			Scopus database		
	Journal	TP	TC	Journal	TP	TC
1	Safety Science	111	1952	Safety Science	176	3395
2	Process Safety Progress	23	48	Industrial Health	40	336
3	Work-A journal of prevention assessment and rehabilitation	20	74	AICHE annual meeting, conference proceedings	34	3
4	Journal of loss prevention in the process industries	18	345	Process Safety Progress	29	81
5	Journal of safety research	18	405	Institution of chemical engineers symposium series	28	1
6	Safety and health at work	17	54	Chemical engineering transactions	26	48
7	Journal of occupational and environmental hygiene	10	372	Safety and health at work	26	268
8	International journal of industrial ergonomics	7	228	Journal of safety research	23	570
9	Human factors and ergonomics in manufacturing and service industries	5	24	International journal of occupational safety and ergonomics	17	44
10	Journal of cleaner production	5	100	Journal of loss prevention in the process industries	16	208

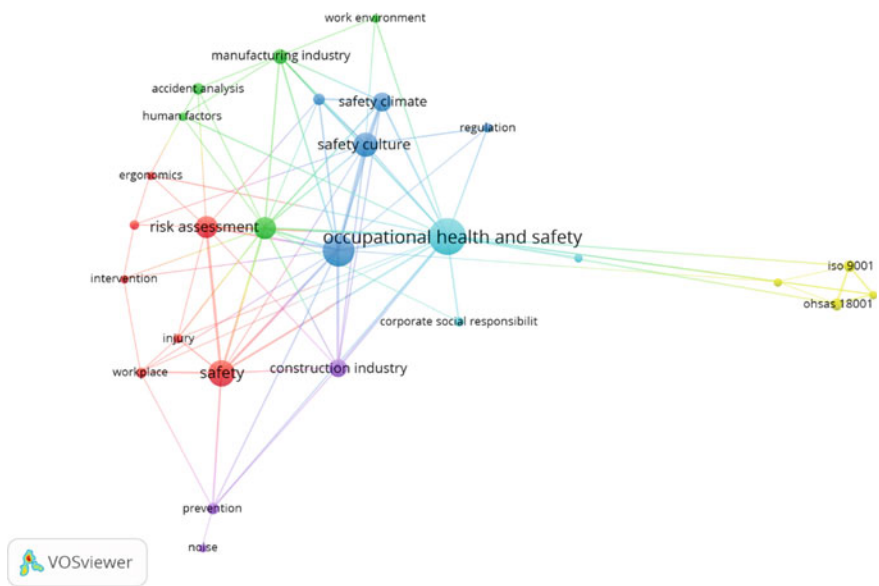


**Fig. 8** Author keywords network from WoS

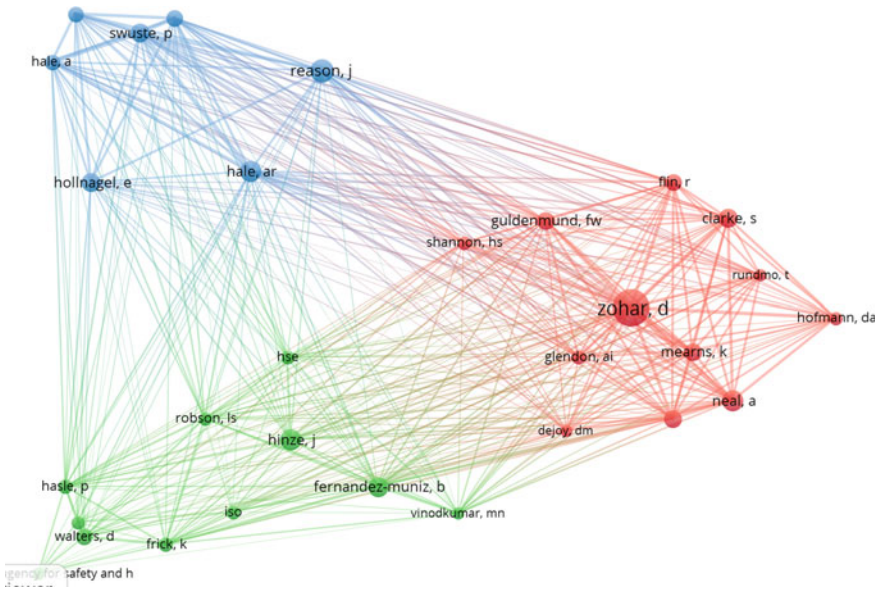


Fig. 9 Author keywords network from Scopus

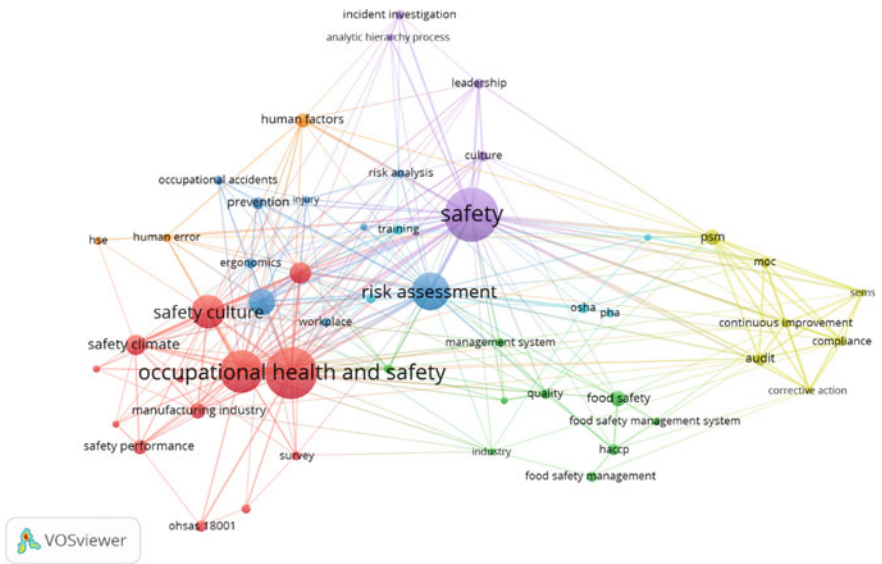
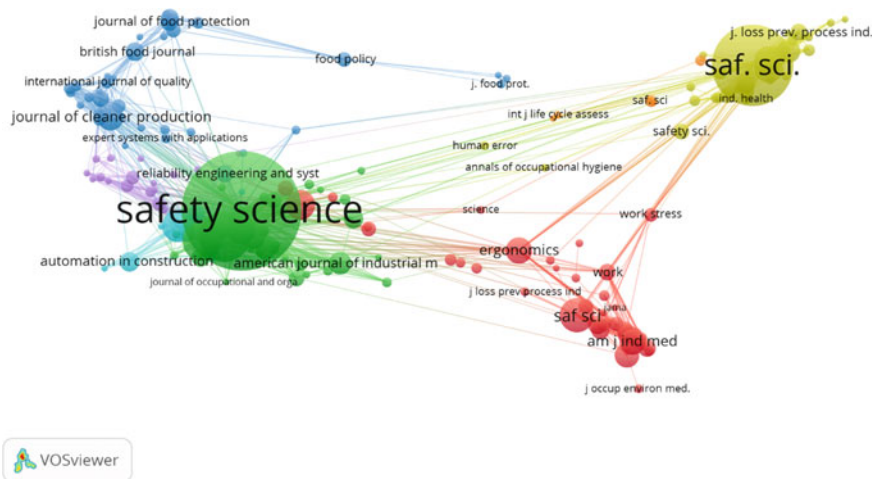


Fig. 10 Author-based co-citation network from WoS



**Fig. 11** Source-based co-citation network from Scopus

### 3.10 Top 20 Most Global Cited Documents from WoS and Scopus Database

See Table 9.

**Table 9** Top 20 most global cited documents from WoS and Scopus database

	Year of publication	Title	Source title	Total citation	Average citations per year
[10]	2009	Workplace safety: a meta-analysis of the roles of person and situation factors	Journal of applied psychology	534	44.50
[11]	2011	Risk analysis and assessment methodologies in the work sites: on a review, classification, and comparative study of the scientific literature of the period 2000–2009	Journal of loss prevention in the process industries	143	14.30
[12]	2014	Global estimates of the burden of injury and illness at work in 2012	Journal of occupational and environmental hygiene	117	16.71
[13]	2011	Nordic safety climate questionnaire (Nosacq-50): a new tool for diagnosing occupational safety climate	International journal of industrial ergonomics	99	9.90

(continued)

**Table 9** (continued)

	Year of publication	Title	Source title	Total citation	Average citations per year
[14]	2009	Global trend according to estimated number of occupational accidents and fatal work-related diseases at region and country level	Journal of safety research	98	8.17
[15]	2010	Evaluating safety management and culture interventions to improve safety: effective intervention strategies	Safety Science	92	8.36
[16]	2009	Safety climate factors and its relationship with accidents and personal attributes in the chemical industry	Safety Science	85	7.08
[17]	2012	Safety management in different high-risk domains—all the same?	Safety Science	75	8.33
[18]	2010	Safety leadership and safety behavior in container terminal operations	Safety Science	70	6.36
[19]	2009	A fuzzy multiattribute model for risk evaluation in work places	Safety Science	67	5.58
[20]	2009	Safety of the process industries in the twenty-first century: a changing need of process safety management for a changing industry	Journal of loss prevention in the process industries	61	5.08
[21]	2014	Risk-based management of occupational safety and health in the construction industry—part 1: background knowledge	Safety Science	59	8.43
[22]	2011	A study on the impact of management system certification on safety management	Safety Science	58	5.80
[23]	2010	Mitigating construction safety risks using prevention through design	Journal of safety research	58	5.27
[24]	2009	Safety management systems: performance differences between adopters and non-adopters	Safety Science	56	4.67
[25]	2012	Exploring the perceived influence of safety management practices on project performance in the construction industry	Safety Science	49	5.44

(continued)

**Table 9** (continued)

	Year of publication	Title	Source title	Total citation	Average citations per year
[26]	2014	QRAM a qualitative occupational safety risk assessment model for the construction industry that incorporate uncertainties by the use of fuzzy sets	Safety Science	46	6.57
[27]	2014	Improving safety culture through the health and safety organization: a case study	Journal of safety research	41	5.86
[28]	2011	Safety climate and safety behavior in the passenger ferry context	Accident analysis and prevention	41	4.10
[29]	2013	The case for research into the zero accident vision	Safety Science	39	4.88

## 4 Conclusion and Future Research Direction

An overview of the research on occupational safety in India for adopting zero accident vision (ZAV) was presented with the information related to research trends, sources, countries, institutions, keywords, authors, and top cited publications. Our analysis shows that research on ZAV on occupational safety has sharply increased over the past decade and most of the research on ZAV on occupational safety has been done in the safety field. From the top production of research article, USA is the leading country in both database. Consequently, from the keyword's analysis point of view, safety management, safety culture, and occupation safety are the buzz word for future research direction in the field of ZAV. From the source analysis, Safety Science, Process Safety Progress, and Industrial Health have good quality of published publications.

The ZAV is achievable with the help of many parameters which must not be omitted out while practicing the same. ZAV should not only be the research area instead its way of life at work place although there are still lots of room which provide opportunity for further research in this area, viz. human behavior and cognitive learning. But we believe that zero accident vision is a concept which if adopted by a company, motivates it to reduce its accidents from what its level is by following best practices of accident prevention. It never can be set as a goal, which not if achieved shall become a punishable offence, but it can be set as a target for perfection. In ZAV, the participation from workers to management is on self-esteemed and motivational basis, for betterment of society. During the accident investigation, focus should be on the reason for accident and not on who is responsible and what should be the punishment. Every reason of accident should be investigated and the efforts should be made to search the mechanism or method to

reduce the accident for same reason in future. All the accident report should be able to make public for awareness. Moreover, it is evident that the country like India is far behind to achieve the zero accident vision (ZAV). The planned and phasewise efforts are needed to reduce the accidents and finally to achieve the ZAV. The changes in national safety policy, relevant acts regulating the occupational health and safety are needed to be amended suitably to incorporate the core values of ZAV.

## References

1. International Labour Organization.: World Day for Safety and Health at Work (2013)
2. International Social Security Association.: Vision Zero: Social security and prevention go hand-in-hand
3. Dekker, S.: The Field Guide to Understanding 'Human Error'. Ashgate Publishing, Ltd. (2014)
4. Zwetsloot, G.I., Aaltonen, M., Wybo, J.L., Saari, J., Kines, P., De Beeck, R.O.: The case for research into the zero accident vision. *Saf. Sci.* **1**(58), 41–48 (2013)
5. Zwetsloot, G.I., Kines, P., Wybo, J.L., Ruotsala, R., Drupsteen, L., Bezemer, R.A.: Zero accident vision based strategies in organisations: innovative perspectives. *Saf. Sci.* **91**, 260–268 (2017)
6. Zwetsloot, G.I., Kines, P., Ruotsala, R., Drupsteen, L., Merivirta, M.L., Bezemer, R.A.: The importance of commitment, communication, culture and learning for the implementation of the zero accident vision in 27 companies in Europe. *Saf. Sci.* **15**(2), 22–32 (2017)
7. Zwetsloot, G., Leka, S., Kines, P.: Vision zero: from accident prevention to the promotion of health, safety and well-being at work. *Policy Pract. Health Saf.* **15**(2), 88–100 (2017)
8. Igić, D., Vuković, M., Urošević, S., Mladenović-Ranisavljević, I., Voza, D.: The relationship between ethical leadership, organizational commitment and zero accident vision implementation in the defense industry. *Int. J. Occup. Saf. Ergonomics* 1–1 (2020)
9. Van Eck, N.J., Waltman, L.: Software survey: VOS viewer, a computer program for bibliometric mapping. *Scientometrics* **84**(2), 523–538 (2010)
10. Christian, M.S., Bradley, J.C., Wallace, J.C., Burke, M.J.: Workplace safety: a meta-analysis of the roles of person and situation factors. *J. Appl. Psychol.* **94**(5), 1103 (2009)
11. Marhavilas, P.K., Koulouriotis, D., Gemeni, V.: Risk analysis and assessment methodologies in the work sites: on a review, classification and comparative study of the scientific literature of the period 2000–2009. *J. Loss Prev. Process. Ind.* **24**(5), 477–523 (2011)
12. Takala, J., Hämäläinen, P., Saarela, K.L., Yun, L.Y., Manickam, K., Jin, T.W., Heng, P., Tjong, C., Kheng, L.G., Lim, S., Lin, G.S.: Global estimates of the burden of injury and illness at work in 2012. *J. Occup. Environ. Hygiene* **11**(5), 326–337 (2014)
13. Kines, P., Lappalainen, J., Mikkelsen, K. L., Olsen, E., Pousette, A., Tharaldsen, J., Tömansson, K., Törner, M.: Nordic safety climate questionnaire (NOSACQ-50): a new tool for diagnosing occupational safety climate. *Int. J. Ind. Ergonomics* **41**(6), 634–46 (2011)
14. Hämäläinen, P., Saarela, K.L., Takala, J.: Global trend according to estimated number of occupational accidents and fatal work-related diseases at region and country level. *J. Saf. Res.* **40**(2), 125–139 (2009)
15. Hale, A.R., Guldenmund, F.W., Van Loenhout, P.L., Oh, J.I.: Evaluating safety management and culture interventions to improve safety: effective intervention strategies. *Saf. Sci.* **48**(8), 1026–1035 (2010)
16. Vinodkumar, M.N., Bhasi, M.J.: Safety climate factors and its relationship with accidents and personal attributes in the chemical industry. *Saf. Sci.* **47**(5), 659–667 (2009)



17. Grote, G.: Safety management in different high-risk domains—all the same? *Saf. Sci.* **50**(10), 1983–1992 (2012)
18. Lu, C.S., Yang, C.S.: Safety leadership and safety behavior in container terminal operations. *Saf. Sci.* **48**(2), 123–134 (2010)
19. Grassi, A., Gamberini, R., Mora, C., Rimini, B.: A fuzzy multi-attribute model for risk evaluation in workplaces. *Saf. Sci.* **47**(5), 707–716 (2009)
20. Knegeting, B., Pasman, H.J.: Safety of the process industries in the 21st century: a changing need of process safety management for a changing industry. *J. Loss Prev. Process Ind.* **22**(2), 162–168 (2009)
21. Sousa, V., Almeida, N.M., Dias, L.A.: Risk-based management of occupational safety and health in the construction industry—part 1: background knowledge. *Saf. Sci.* **66**, 75–86 (2014)
22. Vinodkumar, M.N., Bhasi, M.: A study on the impact of management system certification on safety management. *Saf. Sci.* **49**(3), 498–507 (2011)
23. Gangolells, M., Casals, M., Forcada, N., Roca, X., Fuertes, A.: Mitigating construction safety risks using prevention through design. *J. Saf. Res.* **41**(2), 107–122 (2010)
24. Bottani, E., Monica, L., Vignali, G.: Safety management systems: performance differences between adopters and non-adopters. *Saf. Sci.* **47**(2), 155–162 (2009)
25. Cheng, E.W., Ryan, N., Kelly, S.: Exploring the perceived influence of safety management practices on project performance in the construction industry. *Saf. Sci.* **50**(2), 363–369 (2012)
26. Pinto, A.: QRAM a qualitative occupational safety risk assessment model for the construction industry that incorporate uncertainties by the use of fuzzy sets. *Saf. Sci.* **63**, 57–76 (2014)
27. Nielsen, K.J.: Improving safety culture through the health and safety organization: a case study. *J. Saf. Res.* **48**, 7–17 (2014)
28. Lu, C.S., Yang, C.S.: Safety climate and safety behavior in the passenger ferry context. *Accid. Anal. Prev.* **43**(1), 329–341 (2011)
29. Zwetsloot, G.I., Aaltonen, M., Wybo, J.L., Saari, J., Kines, P., De Beeck, R.O.: The case for research into the zero accident vision. *Saf. Sci.* **58**, 41–48 (2013)

# Review of Recent Studies on Mechanical and Tribological Characteristics of AMMCs



T. Akilan and M. Mahendiran

**Abstract** Tribology-related research activities in metal matrix composites have seen great growth in recent times. Due to their higher stiffness, strength, wear resistance, lower weight and other advantages over monolithic metals, aluminium metal matrix composites (AMMCs) are preferred in many applications, nowadays. Aluminium composites are made by incorporating reinforcing materials into aluminium or its alloys. The reinforcing materials are mainly hard ceramic materials and they occur in the form of particulates, flakes, whiskers and fibres. The AMMCs are produced through various processes among which stir casting is the most commonly used method for particulate-reinforced composite. Some of the recent studies carried out on the mechanical and tribological behaviour of AMMCs made through stir-casting method are briefly summarized in this article. It has been established through research that AMMCs have better mechanical properties such as strength, stiffness, hardness, better tribological properties and lower ductility than their monolithic metals or their alloys. Also, the addition of solid lubricants like graphite and MoS<sub>2</sub> to the composites reduces coefficient of friction and improves the wear behaviour and machinability of the composites. It is observed that there is an inclination towards hybrid AMMCs and nanomaterial-reinforced AMMCs in the recent research works.

**Keywords** Tribology · Friction · Wear · AMMCs · Stir casting

---

T. Akilan (✉)

Department of Mechanical Engineering, Karpagam College of Engineering,  
Coimbatore, Tamil Nadu 641032, India

M. Mahendiran

Metallurgy & QMS, Eppinger Tooling Asia Pvt. Ltd, Coimbatore,  
Tamil Nadu 641202, India

## 1 Introduction

Aluminium-based composites are widely used in the transport industry because of their higher strength to density, superior tribological properties and better resistance to corrosion offered by the aluminium metal matrix composites (AMMCs) over the monolithic metals and alloys, which result in higher fuel efficiency and lower operating costs. Hence, AMMCs have replaced heavier metals and alloys in various applications in the aerospace, automobile and defence industries [1, 2]. During manufacturing of components, the materials encounter stringent conditions while cutting, drilling and grinding. Lot of research is being done on AMMCs for addressing above problems [3].

A composite consists of two or more phases with one or more discontinuous phase(s) called the reinforcing phase(s) distributed in the other continuous phase called the matrix. The composites have properties different from those of the matrix and the reinforcement [4]. Generally, the reinforcing material is hard and the matrix material is ductile. The reinforcing material increases the hardness, stiffness and strength of the composite. When a force acts on the composite, the matrix distributes the force to the reinforcement and the hard reinforcing material bears the applied force, thus giving superior properties. Depending on the reinforcing material used, composites can be called as particulate, flake, whisker and fibre composites, and depending on the matrix material, composites can be called as metal, polymer or ceramic composites. When carbon reinforcement is dispersed in carbon matrix, they are called as carbon-carbon composites [5].

In an AMMC, aluminium or its alloys can be used as the matrix material, and the reinforcement can be a ceramic particulate material such as  $\text{SiO}_2$ ,  $\text{Al}_2\text{O}_3$ ,  $\text{SiC}$ , fly ash,  $\text{B}_4\text{C}$ ,  $\text{TiC}$ ,  $\text{ZrB}_2$ ,  $\text{ZrO}_2$ ,  $\text{AlN}$  or a combination of these reinforcements (hybrid AMMCs). Nanoreinforcing materials like carbon nanotubes (single, double, multiwalled CNTs), graphenes, graphene nanoplatelets, etc., are used for applications in severe environments [2, 6]. Among the reinforcing ceramic particles,  $\text{SiC}$  and  $\text{B}_4\text{C}$  are the most important [7]. The properties of AMMCs can be changed by the choice of reinforcement material(s) and by changing the percentage of reinforcement(s). Aluminium and its alloys are good choice as matrix materials for composites, due to their low melting point (600–700 °C) and low specific gravity (2.7). AMMCs are fabricated by using various techniques such as stir casting, squeeze casting, powder metallurgy, diffusion bonding, spray co-deposition, liquid infiltration under pressure, rheocasting, and in situ processes. Stir-casting process is economical and easy to use, though non-uniform distribution of particulates is observed often [3, 5]. This review paper highlights the recent studies, in the last three to four years, carried out on the tribological aspects of friction, wear and the mechanical properties of AMMCs made through stir casting.

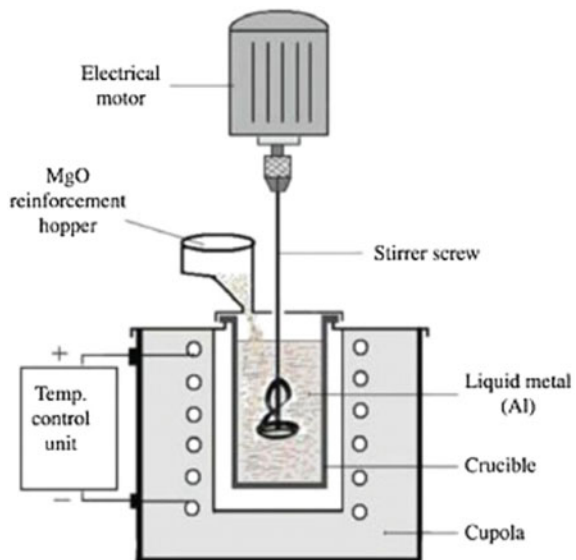
## 2 Stir-Casting Method

In this process, as shown in Fig. 1, aluminium or its alloy is heated in a furnace to a temperature above its melting point (700–800 °C). The particulates are dispersed into the melt by a motorized stirrer running at a fixed speed between 300 and 700 rpm. Addition of reinforcement particles is done after vortex formation, into the hot molten aluminium, and stirred for about 10–20 min. While heating and stirring, inert gas (argon) is passed over the melt to avoid oxidation of the metal. After the incorporation of the particles, the specimen is made by casting. Particulate reinforcement material can be added up to a maximum of 30% of the composite [3]. In this method, the distribution of the particulates is often non-uniform. Also, settling of particles occurs during solidification, resulting in non-uniform density and other properties. The distribution depends on the mixing time, temperature, solidification rate, wetting, specific gravity, size and shape of the reinforcing material, and the shape of the stirrer [8, 9].

In the two-step process, which gives better uniformity of dispersion than conventional method, aluminium is heated to 670 °C, initially. Then the melt is cooled down to 620 °C to a highly viscous state and the preheated particulates (to remove moisture) are added at the side of the vortex. Then, the viscous melt is reheated to a liquidus temperature of 655 °C and stirred again. The semi-solid state helps in better wetting of particulate [7, 8].

The AMMCs thus produced are tested for uniformity of distribution of the particulates in the matrix, using scanning electron microscopy (SEM) or any other suitable spectroscopic method. X-ray diffraction analysis (XRD) is used, commonly, to confirm the quantities of the various ingredients added to the composites.

**Fig. 1** Schematic diagram of stir casting [3]



### 3 Mechanical Properties

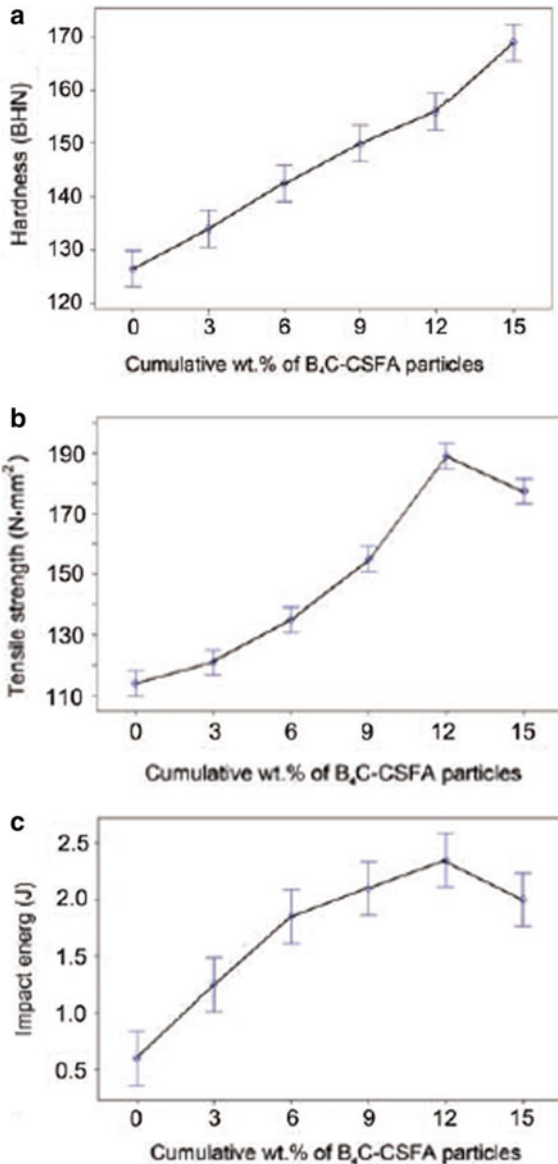
Properties of composites depend primarily on the type and amount of the reinforcement incorporated. Important properties tested in composites by many researchers include density, hardness, strength, and wear. Usually, density is determined using Archimedes method. Hardness is expressed as a number and measured using one of the methods such as Rockwell (ASTM E18), Brinell (ASTM E10), Knoop and Vicker's hardness (ASTM E92). Ultimate tensile strength (UTS), yield strength (YS), breaking strength, modulus and elongation (ductility) are measured in UTM using dumbbell-shaped specimens following standards like ASTM E8/E8M. Most researchers use pin-on-disc tribometer (ASTM G99) for testing wear.

The following research summaries state the work done on various composites and the findings. Subramaniam et al. [10] observed increasing hardness (Fig. 2a), tensile strength (Fig. 2b) and impact energy (Fig. 2c), with the increasing weight percentage of reinforcement in the composites made of Al7075 incorporated with  $B_4C$  and coconut shell fly ash (CSFA).

Jayaraj et al. [6] studied nano-AMMC of LM9 reinforced with multiwalled carbon nanotubes. The composites had improved hardness and thermal stability. A slight reduction in thermal conductivity was observed. Pitting corrosion resistance was reduced in the composite. James et al. [11] observed increased hardness in the hybrid AMMC made by reinforcing with SiC and  $TiB_2$ . Also, SiC added strength to the composite; addition of  $TiB_2$  to the composite reduced its strength, but increased the wear resistance. Subramani and Ganesh Murali [12] compared hybrid AMMCs made of A6061 matrix and particulates of  $Al_2O_3/SiCp/B_4C$  and reinforced with glass fibre and without glass fibre. Comparatively better mechanical properties were noted in the glass fibre-reinforced composites. But, minimal difference in the wear rates between the two composites is observed. Rebba and Ramanaiah [13] reported that hardness and tensile strength of composite made of Al 2024/ $MoS_2$  improved up to 4 wt% of  $MoS_2$ . Gopal Krishna et al. [14] studied 6061Al/ $B_4C$  composite and found that particle size and wt% of the reinforcement affected the tensile strength and hardness of the composite positively. Gopal Krishna et al. [15] observed increase in tensile strength and hardness of composite Al6061/ $B_4C$  with the increase in the wt% of  $B_4C$  particulates.

Sujith et al. [16] found that in situ composites of Al7079/TiC had homogenous microstructure and distribution of particulates. When wt% of TiC is increased, superior microhardness, UTS, YS, modulus and inferior ductility than unreinforced Al7079 were noted. Du et al. [17] showed homogeneous distribution of SiC particulates in Al-Si alloy using special stirrer with three equally spaced blades at a horizontal tilt angle of  $25^\circ$ , thereby enhancing tensile strength of the composite by more than 50%. Kumar et al. [18] compared the as-cast in situ composite of AA6061/TiC with hot forged in situ composite of AA6061/TiC, made by reaction of molten AA6061, potassium hexafluorotitanate salt and graphite. Due to homogeneous dispersion of TiC, hot forged composites had higher hardness and tensile

**Fig. 2** **a** Effect of wt% of B<sub>4</sub>C-CSFA particles on hardness of composite [10], **b** effect of wt% of B<sub>4</sub>C-CSFA particles on tensile strength of composite [10], **c** effect of wt% of B<sub>4</sub>C-CSFA particles on impact energy of composites [10]



strength than the as-cast composite. Selvaraj et al. [19] studied the hybrid AA2618/Si<sub>3</sub>N<sub>4</sub>/AlN/ZrB<sub>2</sub> composite with varying wt% of the reinforcements and observed superior microhardness, tensile strength and compressive strength, with increasing wt% of reinforcements. Afkham et al. [20] fabricated in situ nano-AMMC, reinforced with nano-Al<sub>2</sub>O<sub>3</sub> produced in situ, through chemical reaction of metal oxide powders (TiO<sub>2</sub>, ZnO, and recycled Pyrex) and hot aluminium melt, followed by hot

rolling of the composite. In comparison to unreinforced aluminium, the UTS, YS, and microhardness of composite were found to be superior and ductility inferior.

## 4 Tribological Properties

In the studies below, researchers have used the pin-on-disc tribometer (ASTM G99) for testing of wear resistance and coefficient of friction (COF). SEM analysis has been used to analyse mechanisms involved in wear of composites, on the worn surface and/or the debris, after the wear test. The wear mechanisms are found to be one or the combination of abrasion, adhesion, erosion, fatigue and corrosion. Most researchers have found that the wear rate, COF and mechanisms of wear depend on the test parameters like applied load, sliding speed, sliding distance, test time, and the weight % and type of reinforcement in the composite.

The following are summaries of some recent research papers that have been published by researchers on tribology of AMMCs produced through stir casting. Sardar et al. [21] found that applied load, abrasive size (SiC) and the interaction between abrasive size and load were the dominant factors affecting wear and COF of Al7075/Al<sub>2</sub>O<sub>3</sub> composite. Ramadoss et al. [22] compared the composites Al6063-T6/B<sub>4</sub>C and Al6063-T6/SiC and found that the SiC-reinforced composites had lower wear compared to B<sub>4</sub>C reinforced composites. Due to strong Al–Si bonding and interfacial interactions between SiC nanograin and the matrix, wear of the SiC-reinforced AMMCs (Fig. 3) was lower than that of B<sub>4</sub>C reinforced AMMCs for all the applied loads of 10, 20 and 30 N.

Subramanian et al. [23] investigated Al–Si10–Mg/SiC and sugarcane waste ash (bagasse ash) and observed that hardness, tensile, impact strength and wear resistance (Fig. 4a) improved with an increase in quantity of SiC in the composite, while COF (Fig. 4b) and the ductility decreased.

Pandiyarajan et al. [24] found that when aluminium AA6061 matrix is reinforced with various ratios of zirconium dioxide, the wear decreased with ZrO<sub>2</sub> % and that hardness improved with particulate percentage. The tensile strength, however, increased initially up to 6% of reinforcement and decreased, thereafter. When carbon in the form of graphite is added, the strength of the composite was reduced but its wear resistance and ductility were improved. Shanmugasundaram et al. [25] studied the effect of wt% of fly ash (FA), applied load and sliding speed on wear of AMMC and found that wt% of FA, applied load and sliding speed affected wear, in the given sequence. Harichandran and Selvakumar et al. [26] found that tensile, ductility, impact energy and wear behaviour of nano-B<sub>4</sub>C particulate AMMC by ultrasonic cavitation-assisted casting process were better than the micro-B<sub>4</sub>C composites. Alaneme et al. [27] reported improved corrosion and wear of hybrid composite of Al–Mg–Si/SiC/Rice Husk Ash; but, no change was observed when reinforced with only SiC.

Coyal et al. [28] found better tensile, hardness, COF and wear of AA6061/SiC composite than low-cost hybrid composite AA6061/SiC/jute ash. Rajesh et al. [29]

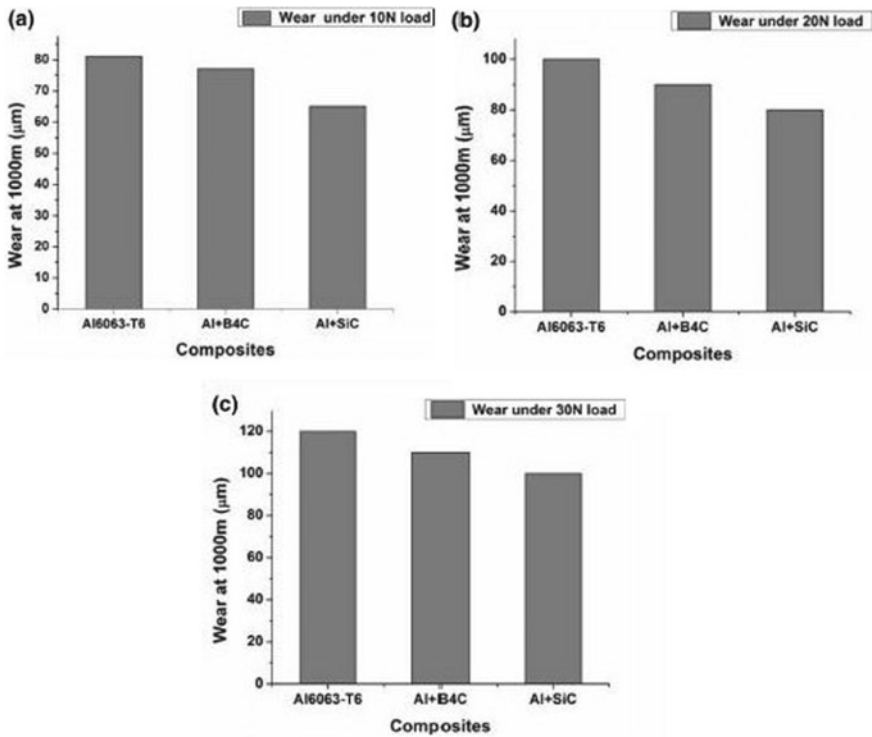


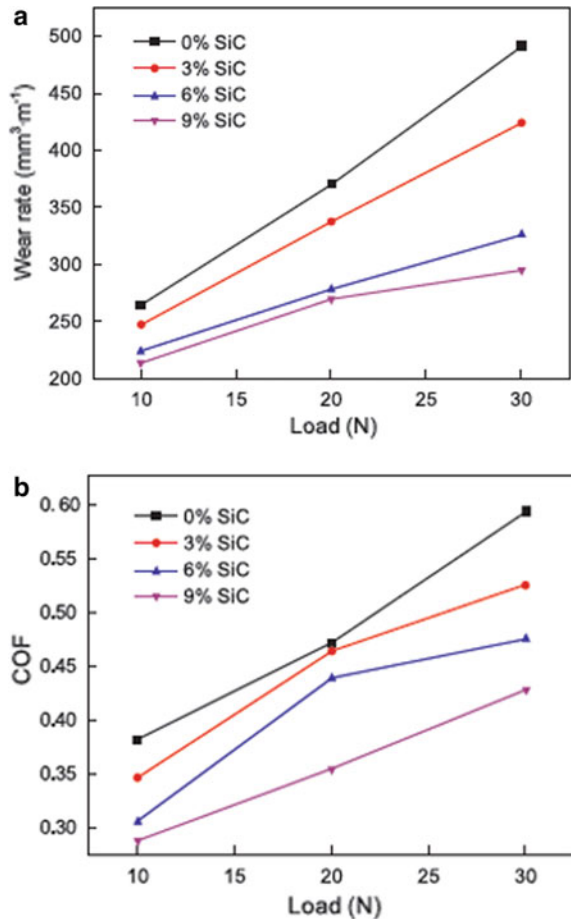
**Fig. 3** Wear ( $\mu\text{m}$ ) at different loads of unreinforced alloy, SiC and B<sub>4</sub>C reinforced composites [22]

proved that specific wear rate and COF can be reduced in the composite made of LM25/red mud compared to LM25, using multiobjective optimization based on ratio analysis method. Shuvho et al. [30] found that for the composite Al-6063/SiC/ $\text{Al}_2\text{O}_3/\text{TiO}_2$  wear resistance and COF were improved compared to the monolithic metal, and that applied load and sliding velocity affected the wear and COF. Bhasha and Balamurugan [31] reported that the hybrid composite AA6061/TiC/RHA (RHA-rice husk ash) showed improvement in microhardness, tensile strength and yield strength, with increase in wt% of the particulate up to 7%. Dwiwedi et al. [32] showed improvement in hardness and wear resistance of AMMC, by incorporating mussel shell (MS) as reinforcing particulate material in AA6061.

Rajesh et al. [33] compared the properties of as-cast and age-hardened (heat treated) hybrid Al7075/SiC/ $\text{Al}_2\text{O}_3$  composites and observed that samples with heat treatment had better mechanical and tribological properties over non-heat-treated samples. Ramkumar et al. [34] compared AA7075/TiC composites to the monolithic metal and noted superior hardness, bending strength, flexural strength, wear resistance and lower COF, with increase in wt% of TiC. Vinod et al. [35] focused on utilization of organic waste and inorganic waste particulates and prepared



**Fig. 4 a** Influence of applied load and SiC % on wear rate [23], **b** influence of applied load and SiC % on COF [23]



composite A356/RHA/FA (RHA-rice husk ash and FA-fly ash). They observed increased microhardness and compression strength in the composite. Also, they found that the hybrid composite possessed lower wear and COF than aluminium A356. Nallusamy et al. [36] studied the tribological behaviour of composite AA7075/B<sub>4</sub>C/Gr/fly ash and found that the composite showed better wear resistance, and also that larger reinforcement particle size offered higher hardness.

## 5 Conclusions

From the review, the following conclusions can be drawn:

- Stir casting is the most preferred and economical technique for fabricating AMMCs reinforced with particulates, though nanoparticulates are difficult to

disperse. The stirrer speed, stirring time and temperature of the melt, shape and geometry of the stirrer affect the dispersion of the particulates.

- Improvement in mechanical and tribological properties can be achieved by reinforcing aluminium and its alloys with particulate ceramic fillers, naturally available waste fillers and industrial waste like fly ash. Two or more reinforcing materials can be used to give the required mechanical and wear properties in hybrid composites.
- In general, higher the quantity of particulates, better are the mechanical and tribological properties of the composites. Also, particulate size and shape affect the strength and wear properties of the composites. However, in general, ductility is reduced when reinforcing material quantity is increased in the composites.
- Improvement in wear resistance of AMMCs can be achieved by reinforcing with different types and quantities of reinforcements, in the matrices. Coefficient of friction can be reduced by incorporating solid lubricants like graphite, molybdenum disulfide ( $\text{MoS}_2$ ) etc., in the composites.

## References

1. Surappa, M.K.: Aluminium matrix composites: challenges and Opportunities. *Sadhana* **28** (Parts 1 & 2), 319–334 (2003)
2. Moghadam, A.D., Omrani, E., Menezes, P.L., Rohatgi, P.K.: Mechanical and tribological properties of self-lubricating metal matrix nanocomposites reinforced by carbon nanotubes (CNTs) and graphene—a review. *Compos. B* (2015). <https://doi.org/10.1016/j.compositesb.2015.03.014>
3. Garg, P., Jamwal, A., Kumar, D., Sadasivuni, K.K., Hussain, C.M., Gupta, P.: Advance research progresses in aluminium matrix composites: manufacturing and applications. *J. Mater. Res. Technol.* **8**(5), 4924–4939 (2019)
4. Miracle, D.B.: Metal matrix composites—from science to technological significance. *Compos. Sci. Technol.* **65**, 2526–2540 (2005)
5. Kala, H., Mer, K.K.S., Kumar, S.: A review on mechanical and tribological behaviors of stir cast aluminum matrix composites. *Procedia Mater. Sci.* **6**, 1951–1960 (2014)
6. Jayaraj, A., Moorthy, C.V., Venkataramana, V.S.N., Jaikumar, S., Srinivas, V.: Corrosion, mechanical and thermal properties of aluminium alloy metal matrix nano composites (AA-MMNCs) with multi-walled carbon nanotubes. *SN Appl. Sci.* **2**, 1259 (2020)
7. Chellapandi, P., Senthil Kumar, A., Arungalai Vendan, S.: Experimental investigations on aluminum based metal matrix composites with  $\text{B}_4\text{C}$ ,  $\text{SiC}$  and  $\text{Mg}$ . *Carbon Sci. Tech.* **7**(1), 59–68 (2015)
8. Shanmughasundaram, P., Subramanian, R., Prabhu, G.: Synthesis of Al-Fly ash composites by modified two step stir casting method. *Adv. Mater. Res.* **488–489**, 775–781 (2012)
9. Pawar, P.B., Abhay, A.: Utpat development of aluminium based silicon carbide particulate metal matrix composite for spur gear. *Procedia Mater. Sci.* **6**, 1150–1156 (2014)
10. Subramaniam, B., Natarajan, B., Kaliyaperumal, B., Chelladurai, S.J.S.: Investigation on mechanical properties of aluminium 7075—boron carbide—coconut shell fly ash reinforced hybrid metal matrix composites. *China Foundry* **15**(6) 1672–6421(2018)
11. James, S.J., Venkatesan, K., Kuppan, P., Ramanujam, R.: Hybrid aluminium metal matrix composite reinforced with  $\text{SiC}$  and  $\text{TiB}_2$ . *Procedia Eng.* **97**, 1018–1026 (2014)

12. Nanjan, S., Janakiram, G.M.: Characteristics of A6061/(Glass Fibre +  $Al_2O_3$  + SiC + B<sub>4</sub>C) reinforced hybrid composite prepared through stir casting. *Adv. Mater. Sci. Eng.* Article ID 6104049, 12 (2019)
13. Rebba, B., Ramanaiah, N.: Evaluation of mechanical properties of aluminium alloy (Al-2024) reinforced with molybdenum disulphide (MOS<sub>2</sub>) metal matrix composites. *Procedia Mater. Sci.* **6**, 1161–1169 (2014)
14. Gopal Krishna, U.B., Sreenivas Rao, K.V., Vasudeva, B.: Effect of boron carbide reinforcement on aluminium matrix composites. *Int. J. Metall. Mater. Sci. Eng.* **3**(1), 41–48 (2013)
15. Gopal Krishna, U.B., Sreenivas Rao, K.V., Vasudeva, B.: Effect of percentage reinforcement of B<sub>4</sub>C on the tensile property of aluminium matrix composites. *Int. J. Mech. Eng. Robot. Res.* **1**(3), (2012)
16. Sujith, S.V., Mahapatra, M.M., Mulik, R.S.: An investigation into fabrication and characterization of direct reaction synthesized Al-7079-TiC in situ metal matrix composites. *Arch. Civil Mech. Eng.* **19**, 63–78 (2019)
17. Du, Y.-H., Zhang, P., Zhang, W.-Y., Wang, Y.-J.: Distribution of SiC particles in semisolid electromagnetic-mechanical stir-casting Al–SiC composite. *China Foundry* **15**(5) (2018). <https://doi.org/10.1007/s41230-018-8086-2>
18. Kumar, G.S.P., Koppad, P.G., Keshavamurthy, R., Alipour, M.: Microstructure and mechanical behaviour of in situ fabricated AA6061–TiC metal matrix composites. *Arch. Civil Mech. Eng.* **17**, 535–544 (2017)
19. Selvaraj, S.K., Nagarajan, M.K., Kumaraswamidhas, L.A.: An investigation of abrasive and erosion behavior of AA 2618 reinforced with Si<sub>3</sub>N<sub>4</sub>, AlN and ZrB<sub>2</sub> in situ composites by using optimization techniques. *Arch. Civil Mech. Eng.* **17**, 43–54 (2017)
20. Afkham, Y., Khosroshahi, R.A., Rahimpour, S., Aavani, C., Brabazon, D., Mousavian, R.T.: Enhanced mechanical properties of in situ aluminium matrix composites reinforced by alumina nanoparticles. *Arch. Civil Mech. Eng.* **18**, 215–226 (2018)
21. Sardar, S., Karmakar, S.K., Das, D.: Identification and modelling of applicable wear conditions for stir cast Al-composite. *Friction* **8**(5), 847–873 (2020)
22. Ramadoss, N., Pazhanivel, K., Ganesh Kumar, S., Arivanandhan, M., Anandan, P.: Effect of B<sub>4</sub>C and SiC nanoparticle reinforcement on the wear behavior and surface structure of aluminum (Al6063 T6) matrix composite. *SN Appl. Sci.* **2**, 903 (2020). <https://doi.org/10.1007/s42452-020-2712-5>
23. Subramanian, S., Arunachalam, B., Nallasivam, K., Pramanik, A.: Investigations on tribo-mechanical behaviour of Al-Si10-Mg/sugarcane bagasse ash/SiC hybrid composites. *China Foundry* **16**(4), 1672–6421(2019)
24. Pandiyarajan, R., Maran, P., Marimuthu, S., Ganesh, K.C.: Mechanical and tribological behavior of the metal matrix composite AA6061/ZrO<sub>2</sub>/C. *J. Mech. Sci. Technol.* **31**(10), 4711–4717 (2017)
25. Palanisamy, S., Ramanathan, S., Rangaraj, R.: Analysis of dry sliding wear behaviour of aluminium-fly ash composites: the Taguchi approach. *Adv. Mech. Eng.* **2013**, Article ID 658085, 10 (2013)
26. Harichandran, R., Selvakumar, N.: Effect of nano/micro B<sub>4</sub>C particles on the mechanical properties of aluminium metal matrix composites fabricated by ultrasonic cavitation-assisted solidification process. *Arch. Civil Mech. Eng.* **16**, 147–158 (2014)
27. Alaneme, K.K., Adewale, T.M., Olubambi, P.A.: Corrosion and wear behaviour of Al–Mg–Si alloy matrix hybrid composites reinforced with rice husk ash and silicon carbide. *J. Mater. Res. Technol.* **3**(1), 9–16 (2014)
28. Coyal, A., Yuvaraj, N., Butola, R., Tyagi, L.: An experimental analysis of tensile, hardness and wear properties of aluminium metal matrix composite through stir casting process. *SN Appl. Sci.* **2**, 892 (2020). <https://doi.org/10.1007/s42452-020-2657-8>
29. Rajesh, S., Rajakarunakaran, S., Suthakarapandian, R., Pitchipoo, P.: MOORA-based tribological studies on red mud reinforced aluminum metal matrix composites. *Adv. Tribol.* **2013**, Article ID 213914, 8 (2013)

30. Shuvho, M.B.A., Chowdhury, M.A., Hossain, N., Roy, B.K., Kowser, M.A., Islam, A.: Tribological study of Al-6063-based metal matrix embedded with SiC–Al<sub>2</sub>O<sub>3</sub>–TiO<sub>2</sub> particles. *SN Appl. Sci.* **2**, 287 (2020). <https://doi.org/10.1007/s42452-020-2064>
31. Bhasha, C., Balamurugan, K.: Fabrication and property evaluation of Al 6061+ x% (RHA + TiC) hybrid metal matrix composite. *SN Appl. Sci.* **1**, 977 (2019). <https://doi.org/10.1007/s42452-019-1016-0>
32. Dwiwedi, S.K., Srivastava, A.K., Chopkar, M.: Fabrication and dry sliding wear study of Al6061/mussel-shell particulate composites. *SN Appl. Sci.* **1**, 721 (2019). <https://doi.org/10.1007/s42452-019-0767-y>
33. Rajesh, M., Mohamed Kaleemulla, K., Saleemsab, D., Bharath, K.N.: Generation of mechanically mixed layer during wear in hybrid aluminum MMC under as-cast and age hardened conditions. *SN Appl. Sci.* **1**, 860 (2019). <https://doi.org/10.1007/s42452-019-0906-5>
34. Ramkumar, K.R., Sivasankaran, S., Al-Mufadi, F.A., Siddharth, S., Raghu, R.: Investigations on microstructure, mechanical, and tribological behaviour of AA 7075–x wt.% TiC composites for aerospace applications. *Arch. Civil Mech. Eng.* **19**, 428–438 (2019)
35. Vinod, B., Ramanathan, S., Anandajothi, M.: A novel approach for utilization of agro-industrial waste materials as reinforcement with Al–7Si–0.3 Mg matrix hybrid composite on tribological behavior. *SN Appl. Sci.* **1**, 62 (2019). <https://doi.org/10.1007/s42452-018-0066-z>
36. Nallusamy, S., Saravanan, S., Kannarasu, V., Rajaram Narayanan, M.: Experimental analysis on reinforced aluminium metal matrix with boron carbide, graphite and fly ash chemical composites. *Rasayan J. Chem.* **10**(4), 1368–1373 (2017)

# Effects of Process Parameters on Build Time of PolyJet Printed Parts Using Taguchi Method



Arivazhagan Pugalendhi , Rajesh Ranganathan ,  
and Balamurugan Gopalakrishnan

**Abstract** Every industry needs to minimize the design, manufacturing and product development cycle time to succeed viable benefit. Thereby, rapid manufacturing techniques play a major role over traditional manufacturing techniques. The PolyJet technology is one of the additive manufacturing (AM) technologies in which CAD data are directly used for producing the physical objects through layered manufacturing. Quality, lead time and cost of the 3D printed parts are significantly affected by various process parameters. So, optimization of process parameter is essential for reducing the lead time without sacrificing the quality of 3D printed parts. The aim of this work is to investigate the effects of process parameters on build time of the PolyJet printed parts by using Taguchi method. Signal-to-noise (S/N) ratio was used to analyze the scaling factors, find the optimum process parameters that reduce the build time and identify the importance of ranking for various factors which were investigated by analysis of variance (ANOVA). Finish type (A), material (B), thickness (C) and shape (D) as a selected four process parameters. The optimization results reveal that parameter C is the most significant influence followed by B, A, and D of the PolyJet printed parts and that the optimum combination of the parameters is A2B1C1D1. These results would be very useful for other researchers who working in the same era. This work offers a best recommendation that can be used to improve the quality of 3D printed parts in many sectors.

**Keywords** Additive manufacturing · Build time · Taguchi approach · Optimization · PolyJet

---

A. Pugalendhi (✉) · R. Ranganathan · B. Gopalakrishnan  
Department of Mechanical Engineering, Coimbatore Institute of Technology,  
Coimbatore Tamil Nadu, 641014, India

© The Author(s), under exclusive license to Springer Nature Singapore Pte Ltd. 2021  
A. Patnaik et al. (eds.), *Advances in Materials Processing and Manufacturing Applications*, Lecture Notes in Mechanical Engineering,  
[https://doi.org/10.1007/978-981-16-0909-1\\_13](https://doi.org/10.1007/978-981-16-0909-1_13)

## 1 Introduction

Industries mainly focus on improving the quality of products and their manufacturing processes in every stage of production; this is certainly due to the competitive environment. Optimization of quality, performance of designs, time and cost reduction is done by the one of the powerful scientific approach named as Taguchi method of experimental design (TMED) [1].

The main objective of the TMED is to study the influencing factors, predict the best level of factors and establish the contribution of each factor. Applications of TMED are used in the design and development of products and process for robust environmental conditions, manufacturing variations, product variations and minimizing the variation in processes [2]. The capability of TMED is to minimize the number of experiments and get a maximum amount of reliable data for analysis purpose [3]. The objective of this work is to investigate the effect of process parameters on build time for PolyJet printed parts by TMED.

## 2 Literature Review

Application of TMED is utilized for new product design and development process, and this is for a new ignition coil of an automotive vehicle. Increasing the customer satisfaction, reducing the defect rate and improving the profit are achieved by an optimal selection of parameters [4]. Soylak et al. investigated the parameters that are influencing the aircraft wing design at low speeds using TMED. Significant parameters are determined by less number of experiments in  $L_8$  orthogonal array (OA) which resulted in time and cost saving as well as faster in design [5].

In recent years, TMED plays a major role in additive manufacturing (AM) field to evaluate the effects of process parameters on quality characteristics of 3D printed parts [6–9]. The unique mechanism of the layer-by-layer manufacturing technique of AM is utilized in many fields for solving the numerous critical problems of the recent era. In AM, computer-aided design (CAD) file is directly converted into raw materials as per the slicing and rasterizing of the complex geometry of the product [10]. Capabilities of AM such as design flexibility, reduced lead time, reduction of material waste and higher level of customization lead to rapid growth in many fields [11, 12].

One of the recent developments in the AM is multi-material additive manufacturing (MMAM), which prints digital parts having the properties of two or more materials [13]. The PolyJet technology produces fully cured multi-material parts by utilizing simultaneous jets of ultraviolet (UV) curable photopolymers through multiple nozzles, and then, instantaneously curing is performed by UV rays [14]. Quality of the PolyJet printed part is defined by mechanical property, surface roughness and dimensional accuracy, which depends on the machine, material and its process parameters [15]. Cost of the product depends on build time, material and

energy consumption [16]. Total cost of the product can be predicted based on build time [17].

Haghighi and Li have studied the individual responses of machine operating cost, dimensional performances, energy and material consumption of 3D printed parts. From this study, manufacturing cost and dimensional performance are significantly affected by the orientation of the part. They also found that, above mentioned factors are better while reducing the fill density, but it is vice versa in terms of mechanical properties [18].

Kechagias et al. conducted experiments to determine the optimal process parameters of PolyJet printed parts for achieving the better dimensional accuracy by the Taguchi  $L_4$  array. The importance of each parameter was identified by Analysis of Variances (ANOVA). The results revealed that external and internal dimensional accuracy was affected by layer thickness and the scale factor, respectively [19].

The literature review stated the optimization of AM process parameters by means of TMED. There is no such work which was conducted for analyzing the process parameter that influence the build time of the part produced through the digital material (DM) printing mode in the recently developed technology. This paper investigates about the influence of PolyJet process parameters on build time of multi-material parts by using TMED. Three different model materials were printed in DM mode with varying thickness and finish types. The influence of each factor and optimum combination of input factors were identified by ANOVA and S/N ratio, respectively. These results are very useful to provide a unique way of meeting optimal selection of process parameters.

### 3 Experiment Details

Stratasys Objet260 Connex PolyJet machine is used for this study. PolyJet printed parts have two types of surface finish, namely (i) matte finish and (ii) glossy finish. This machine offers 16  $\mu\text{m}$  layer thickness for single material mode and 30  $\mu\text{m}$  layer thickness for DM mode. The three types of printing approaches are possible in DM mode, as follows;

- Mixed part—Build two materials in the same part without mixing.
- Mixed tray—Printing of different kinds of parts with different model materials.
- Mixed material—Composite model materials with appropriate proportions to make single part.

Initially, transparent rigid material of VeroClear (VC), opaque rigid material of VeroWhite (VW) and flexible material of TangoPlus (T+) are widely used, and the same has been chosen for investigation. Material properties of the selected materials are populated in Table 1. Among different material combinations, VeroClear-TangoPlus (VC-T+) and VeroWhite-TangoPlus (VW-T+) are printed in mixed material approach. Despite, VeroClear-VeroWhite (VC-VW) is printed in

**Table 1** Properties of selected PolyJet materials

Properties	VeroClear	VeroWhite	TangoPlus
Tensile strength	50–65 MPa	50–65 MPa	0.8–1.5 MPa
Elongation at break	10–25%	10–25%	170–220%
Shore hardness	83–86 D	83–86 D	26–28 A
Polymerized density	1.18–1.19 g/cm <sup>3</sup>	1.17–1.18 g/cm <sup>3</sup>	1.12–1.13 g/cm <sup>3</sup>

Source (Stratasys 2018)

mixed tray approach, due to impossible mixing of VC and VW. Three different shapes of test samples with three different thicknesses are selected for this study, and all the samples are printed in XY direction as shown in Fig. 1. Design of test samples and machine communication is performed by SolidWorks and Objet Studio software, respectively.

## 4 Methodology

The experiments were designed using Taguchi method for the process parameters of finish type, model material, thickness and shape of the samples. Table 2 displays the level of the process parameters of DOE ( $2^1, 3^3$ ). A number of experiments are acquired by the statistical method of Taguchi orthogonal array by using Minitab

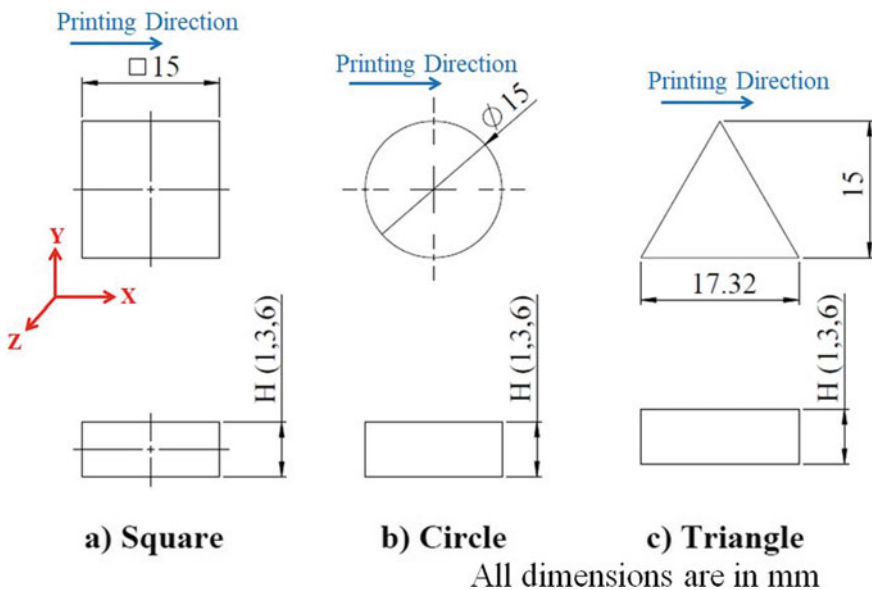


**Fig. 1** Dimensions of the test samples with its printing direction



**Table 2** Levels of process parameters for DOE

Control factor	Symbol	Unit	Level 1	Level 2	Level 3
Finish type	A	–	Matte	Glossy	–
Material	B	–	VC-T+	VW-T+	VC-VW
Thickness	C	mm	1	3	6
Shape	D	–	Square	Circle	Triangle

software. Each experiment from  $L_{18}$  OA was conducted three times randomly, and average response values are recorded. The effect of each parameter on build time was analyzed through ANOVA and S/N ratio, which determines the optimum combination of the process parameters. Build time, height of printed specimen and numbers of layers are referred as a response which saves the cost and quicker production while it is lesser. Thereby, characteristic of lower-the-better quality is assessed by using measured data at the  $i^{\text{th}}$  experiment ( $y_i$ ) and number of observations in an experiment ( $n$ ) as shown in the Eq. (1).

$$\eta = S/N = -10 \log \left[ \frac{1}{n} \sum_{i=1}^n y_i^2 \right] \quad (1)$$

## 5 Results and Discussion

Printing details of  $L_{18}$  OA for DOE are detailed in Table 3. Material consumption, build time, specimen height and number of layers of each experiment in Objet Studio are discussed. Specimen height includes height of bottom support, actual model and top support. In case of the glossy finish, top surface of the 3D printed part is free from support. Table 3 values infer that experiments of VC-T+ and VW-T+ show the same reading in all responses. This is since; both are printed in DM approach. Despite, mixed tray approach of matte-finished VC-VW is higher than VC-T+ and VW-T+, and glossy finished VC-VW values are matched with VC-T+ and VW-T+.

Matte-finished samples of VC-T+ and VW-T+ require additional build time of 1 min, 0.30 mm of support height and 10 layers when compared to glossy finished VC-T+ and VW-T+ samples. Similarly, matte-finished samples of VC-VW require additional 3 mm of support height. Further, in order to build the same amount of layers (here its 100 layers), it takes an extra 10 min to complete the print, rather than for glossy finished VC-VW. From these values, it infers that the build time can be varied for different material combination and finish type. Support height and number of layers required to complete the product can be calculated by using Eqs. (2) and (3).

**Table 3** Orthogonal array ( $L_{18}$ ) of DOE and its printing details

Experiment	Control factors				Build time (min)	Specimen height (mm)	Number of layers (nos)	Material consumption (g)		
	A	B	C	D				Model 1	Model 2	Support
a	1	1	1	1	11	2.35	79	1	2	3
b	1	1	2	2	18	4.36	146	1	2	3
c	1	1	3	3	28	7.36	246	1	3	3
d	1	2	1	1	11	2.35	79	1	2	3
e	1	2	2	2	18	4.36	146	1	2	3
f	1	2	3	3	28	7.36	246	2	2	3
g	1	3	1	2	20	5.05	169	2	2	4
h	1	3	2	3	27	7.06	236	2	2	5
i	1	3	3	1	37	10.06	336	4	4	6
j	2	1	1	3	10	2.05	69	1	1	3
k	2	1	2	1	17	4.06	136	1	2	3
l	2	1	3	2	27	7.06	236	1	3	3
m	2	2	1	2	10	2.05	69	1	2	3
n	2	2	2	3	17	4.06	136	1	2	3
o	2	2	3	1	27	7.06	236	2	3	3
p	2	3	1	3	10	2.05	69	1	2	3
q	2	3	2	1	17	4.06	136	2	3	3
r	2	3	3	2	27	7.06	236	3	3	3

$$\text{Specimen height} = \text{Bottom support} + \text{Actual part} + \text{Top Support} \quad (2)$$

$$\text{Number of layers} = \text{Specimen height} / \text{Layer thickness} \quad (3)$$

From Eqs. (2) and (3), for achieving 1.05 mm height of bottom support requires 35 layers to print. This is for achieving 0.30 mm height of top support, which requires 10 layers to print VC-T+ and VW-T+ samples. Correspondingly, for VC-VW samples, bottom support height and layers are the same as VC-T+ and VW-T+. However, 3 mm height of top support requires 100 layers to complete for VC-VW samples. Noticeably, during printing of matte-finished VC-VW printing, there is a significant height difference in top supports of VC and VW samples. The difference between the matte-finished VC and VW samples with support of experiment “g” is shown in Fig. 2a. At this juncture, VW sample is subjected to additional curing time until the VC sample has to be completed. In this regard, machine holding time of VW sample (i.e., time gap between part completion and part removal from build tray) depends on the VC samples. In the case of glossy finished VC-VW, VC-T+ and VW-T+ samples, there is no significant height difference in top supports. PolyJet printed samples after post-processing are shown in Fig. 2b.

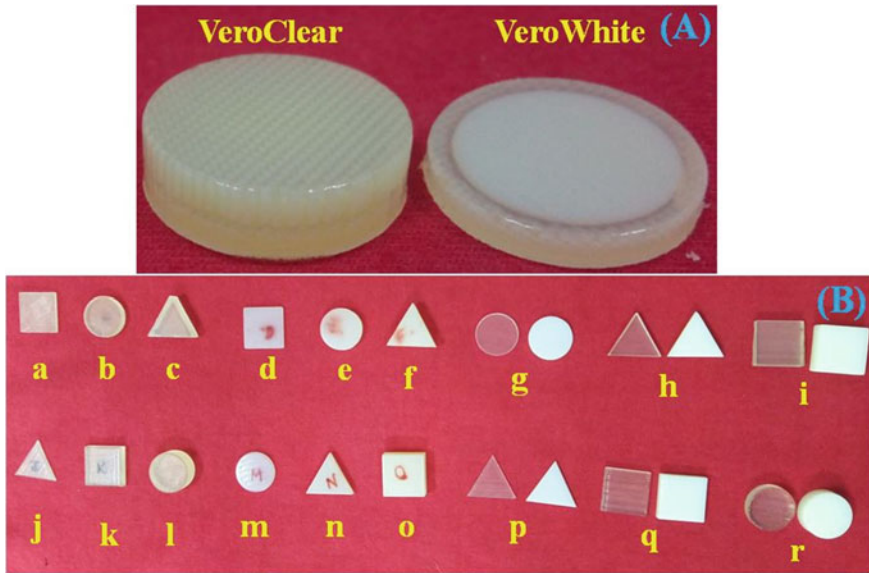


Fig. 2 PolyJet printed samples **a** experiment “g” with support, **b** all experiments without support

S/N response table for build time, height of a printed specimen and number of layers of the DOE are populated in Table 4. Importance of ranking of different factors and the optimum combinations of process parameters are identified by S/N ratio. The results from Table 4 conclude that build time is affected mostly by thickness of the test sample. It is followed by model material, finish type and shape of the test sample. Finish type (A2) of glossy, material (B1) as VC-T+ thickness (C1) of 1 mm and shape (D1) of square sample were identified as an optimum combination of process parameters for build time. A2B1C1D1 is the optimal combination for all the responses. This is based on the approaches that lower the better quality character.

Maximum thickness for VC-VW material and matte finish of the sample requires longer build time to complete the print. From the shapes considered, it was identified (square, circle and triangle) that circular shape has the highest build time, followed by a triangle and square shape with minimum effect. The obtained results inferred that increase in specimen height will substantially increase the number of layers and build time significantly. The results of ANOVA analysis of build time, specimen height and number of layers are listed in Table 5. In all, the results of analysis, selected process parameters of thickness, material and finish type are having a significant effect on responses, whereas *p* values are less than 0.05 [20]. However, shape of the sample did not significantly impact the responses.

From this study, it is observed that build time is significantly affected by the dimension of the sample in Z-axis, i.e., thickness of the sample. In PolyJet machine, print heads move in X and Y axes and build tray moves in Z-axis. Material

**Table 4** S/N response table for build time, specimen height and number of layers

Response	Control factors	Symbol	Level 1	Level 2	Level 3	Rank
Build time	Finish type	A	-26.20	-24.50	-	3
	Material	B	-24.69	-24.82	-26.54	2
	Thickness	C	-21.42	-25.44	-29.19	1
	Shape	D	-25.14	-25.72	-25.19	4
Specimen height	Finish type	A	-14.02	-11.79	-	3
	Material	B	-12.15	-12.15	-14.41	2
	Thickness	C	-7.93	-13.17	-17.60	1
	Shape	D	-12.70	-13.30	-12.715	4
Number of layers	Finish type	A	-44.52	-42.30	-	3
	Material	B	-42.66	-42.66	-44.91	2
	Thickness	C	-38.47	-43.67	-48.09	1
	Shape	D	-43.21	-43.80	-43.22	4

**Table 5** Results of ANOVA for build time, specimen height and number of layers

Response	Variation source	Degree of freedom	Sum of squares	Mean square	F-ratio	p value	% of contribution
Build time	Finish type	1	68.06	68.056	8.05	0.018	6.23
	Material	2	78.11	39.056	4.62	0.038	7.15
	Thickness	2	860.11	430.056	50.86	0.000	78.84
	Shape	2	0.11	0.056	0.01	0.993	0.01
	Error	10	84.56	8.4566			
	Total	17	1090.94				
Specimen height	Finish type	1	6.48	6.480	8.89	0.014	6.65
	Material	2	7.29	3.645	5.00	0.031	7.48
	Thickness	2	76.28	38.140	52.32	0.000	78.36
	Shape	2	0.00	0.000	0.00	1.000	0
	Error	10	7.29	0.729			
	Total	17	97.34				
Number of layers	Finish type	1	7200	7200	8.89	0.014	6.65
	Material	2	8100	4050	5.00	0.031	7.48
	Thickness	2	84756	42378	52.32	0.000	78.36
	Shape	2	0	0	0.00	1.000	0
	Error	10	8100	810			
	Total	17	108156				

deposition and solidification are performed on back and forth movement; then, build tray moves in downward direction for the operations of the next layers until the part is completed. Thereby, placing the part's smallest dimensions along the Z-axis is advisable [21]. Similarly, matte-finished samples have higher build time than glossy finished samples, due to additional supports in the top surface [22]. Due to material property, curing temperature of VC and mixed tray DM mode, VC-VW requires longer printing time than VC-T+ and VW-T+. This research paper provides a unique way of attaining optimal selection of process parameters. The obtained results are helpful for performing the optimization in build time with respect to orientation, finish type and combination of model material in DM mode.

## 6 Conclusion

The study was about evaluating the effects of selected PolyJet process parameters (finish, material, thickness and shape) on the build time, specimen height and number of layers of the test samples. To reduce the cost and time, Taguchi OA was defined for the required number of experiments to conduct the analysis. The optimal combination of process parameters was suggested using the DOE. From this methodology, it was found that thickness of the sample was the most dominating factor for build time, specimen height and number of layers. In addition, required number of layers and its height for both bottom and top support layer are calculated for selected material combination. Through this work, glossy finish, VC-T+ square sample used here is found to have the minimum thickness of 1 mm, which is identified as an optimal selection. All the results were provided for a clear understanding for guiding the optimization of process parameters. This optimal selection is also used for the prediction of the build time as well as cost of the 3D printed parts for various applications.

## References

1. Vlachogiannis, J.G., Roy, R.K.: Robust PID controllers by Taguchi's method. *TQM Mag.* **55** (4), 456–466 (2005)
2. Montgomery, D.C.: Experimental design for product and process design and development. *J. Roy. Stat. Soc. Ser. D (The Statistician)* **48**(2), 159–177 (1999)
3. Roy, R.K.: A primer on the Taguchi method. Society of Manufacturing Engineers (2010)
4. Morgan, J., Antony, J., Perry, D., Wang, C., Kumar, M.: An application of Taguchi method of experimental design for new product design and development process. *Assembly Autom.* **26** (1), 18–24 (2006)
5. Soylak, M., Gökçe, N.K., Topal, E.S.: Aircraft wing design at low speeds using Taguchi method. *Aircr. Eng. Aerosp. Technol.* **90**(1), 51–55 (2018)
6. Liu, X., Zhang, M., Li, S., Si, L., Peng, J., Hu, Y.: Mechanical property parametric appraisal of fused deposition modeling parts based on the gray Taguchi method. *Int. J. Adv. Manuf. Technol.* **89**(5), 2387–2397 (2017)

7. Wang, C.C., Lin, T.W., Hu, S.S.: Optimizing the rapid prototyping process by integrating the Taguchi method with the Gray relational analysis. *Rapid Prototyping J.* **13**(5), 304–315 (2007)
8. Lee, B.H., Abdullah, J., Khan, Z.A.: Optimization of rapid prototyping parameters for production of flexible ABS object. *J. Mater. Process. Technol.* **169**(1), 54–61 (2005)
9. Sood, A.K., Ohdar, R.K., Mahapatra, S.S.: Improving dimensional accuracy of fused deposition modelling processed part using grey Taguchi method. *Mater. Des.* **30**(10), 4243–4252 (2009)
10. Chen, L., He, Y., Yang, Y., Niu, S., Ren, H.: The research status and development trend of additive manufacturing technology. *Int. J. Adv. Manuf. Technol.* **89**(9–12), 3651–3660 (2017)
11. Gardan, J.: Smart materials in additive manufacturing: state of the art and trends. *Virtual Phys. Prototyping* **14**(1), 1–18 (2019)
12. Singamneni, S., Yifan, L.V., Hewitt, A., Chalk, R., Thomas, W.: Additive manufacturing for the aircraft industry: a review. *J. Aeronaut. Astronaut. Eng.* **8**(214), 2 (2019)
13. Espalin, D., Ramirez, J.A., Medina, F., Wicker, R.: Multi-material, multi-technology FDM: exploring build process variations. *Rapid Prototyping J.* **20**(3), 236–244 (2014)
14. Vaezi, M., Chianrabutra, S., Mellor, B., Yang, S.: Multiple material additive manufacturing—Part 1: a review. *Virtual Phys. Prototyping* **8**(1), 19–50 (2013)
15. Keşy, A., Kotliński, J.: Mechanical properties of parts produced by using polymer jetting technology. *Arch. Civil Mech. Eng.* **10**(3), 37–50 (2010)
16. Baumers, M., Tuck, C., Wildman, R., Ashcroft, I., Rosamond, E., Hague, R.: Transparency built-in: energy consumption and cost estimation for additive manufacturing. *J. Ind. Ecol.* **17**(3), 418–431 (2013)
17. Di Angelo, L., Di Stefano, P.: A neural network-based build time estimator for layer manufactured objects. *Int. J. Adv. Manuf. Technol.* **57**(1–4), 215–224 (2011)
18. Haghghi, A., Li, L.: Study of the relationship between dimensional performance and manufacturing cost in fused deposition modeling. *Rapid Prototyping J.* **24**(2), 395–408 (2018)
19. Kechagias, J.P.A.I., Stavropoulos, P., Koutsomichalis, A., Ntintakis, I., Vaxevanidis, N.: Dimensional accuracy optimization of prototypes produced by PolyJet direct 3D printing technology. *Adv. Eng. Mech. Mater.* 61–65 (2014)
20. uz Zaman, U.K., Boesch, E., Siadat, A., Rivette, M., Baqai, A.A.: Impact of fused deposition modeling (FDM) process parameters on strength of built parts using Taguchi's design of experiments. *Int. J. Adv. Manuf. Technol.* **101**(5–8), 1215–1226 (2019)
21. Bikas, H., Lianos, A.K., Stavropoulos, P.: A design framework for additive manufacturing. *Int. J. Adv. Manuf. Technol.* **103**(9–12), 3769–3783 (2019)
22. Moore, J.P., Williams, C.B.: Fatigue properties of parts printed by PolyJet material jetting. *Rapid Prototyping J.* **21**(6), 675–685 (2015)

# Synthesis and Testing of Epoxy-Based Alumina–Silicon Carbide Particular Reinforced Composite



Rahul Sharma and Rahul Sen

**Abstract** The research paper describes the development of a new set of polymer composites from epoxy. The polymer matrix composite (PMC) comprises epoxy resin (LY 556), E-glass fiber as a reinforced material, and alumina and silicon carbide as filler material. The epoxy resin (LY 556) and hardener (HY951) are mixed in 10:1 at room temperature. It is synthesized by different weight percentage of aluminum oxide/silicon carbide (1:1) (0, 2, 4, and 6 wt%). The testing includes the investigations of density, moisture content, and dimensional stability. It is observed from experiment work that 2 wt% aluminum oxide–silicon carbide-filled glass fiber-reinforced epoxy composite sample possesses optimum mechanical properties. It comprises (2.651 g/cm<sup>3</sup>) density, (0.672%) percentage of absorption, (0.646%) percentage of moisture content, and least linear swelling in all dimensions, which is required in all general application areas where the epoxy-based composites are prominently used like—automobile, aircrafts components, and sports goods.

**Keywords** Composite polymer · Epoxy · Alumina · Silicon carbide

## 1 Introduction

Combine properties of different material can be achieved by adding two or more material which is known as a composite material. They are combined in such a way that the resulting composite material or composite possesses superior properties which are not obtainable with single constituent materials [1, 2]. The polymer matrix composites (PMCs) with wove glass fiber have interesting applications in aerospace, structural, and automobile engineering. The mechanical properties of PMCs are completely dependent upon the particulate size, filler–matrix interface adhesion, and loading characteristics. Strengthening of polymers is generally achieved with the reinforcement of fibers. On the other hand, higher tensile strength

---

R. Sharma (✉) · R. Sen  
Mechanical Engineering Department, Poornima College of Engineering, Jaipur 302022, India

and higher impact strength are generally achieved by adding more layers of fiber in the polymer matrix. The glass fibers consist of such properties and that is why these are extensively used as reinforcement material in epoxy matrix-based composites. The mechanical strength of polymer composite can be made better by the addition of silicon-iron oxide particulates along with fibers [3]. Silicon carbide shows favorable chemical and mechanical characteristics at high temperatures in structural applications. Alumina has advantages that include dielectric properties, hard, alkali attack at elevated temperatures, high strength, wear resistant, stiffness, and resistance to strong acid [4]. Considering all such information, an attempt has been made to develop and synthesize the above-mentioned composites from the materials discussed and its properties investigated by general testing.

### ***1.1 Literature Review***

Various research works also been done on such matters. Nano-SiC particulate-filled RCF/epoxy composites decreased water uptake with an increase in the percentage of the weight n-SiC particles [5, 6]. Aluminum oxide and silicon carbide (1:1) particulates were reinforced into the epoxy resin-based composites, attributes the better mechanical characteristics as compared to polyester resin-based composites [7]. M. S. Sham Prasad et al. investigated the chopped stands E-glass fiber composites with filler aluminum oxide. It was observed by the author from the experiment that 4 wt%  $\text{Al}_2\text{O}_3$  composite possess maximum mechanical properties among other filler specimens. [8]. At the high percentage of the weight of wood dust reinforced epoxy composites, it is examined that tensile as well as flexural behaviors of epoxy-based composites dropped due to the agglomeration in between the filler molecules around the matrix which barriers the proper curing of the composite [9]. The addition nanoparticulates of SiC was improved not only thermal resistance but also mechanical characteristics [10]. Similar erosion wears testing conduction  $\text{Al}_2\text{O}_3$  filler glass fiber-reinforced polyester composite based is examined to lower wear rate as compared to SiC and CBPD modifiers polyester-based composites [11]. Ashik K P and Ramesh S Sharma et al. evaluated that the mechanical characteristic and water uptake resistance decreased with increase coconut coir fiber in coconut coir/glass fiber epoxy-based composites [12]. Micron size silica surface has less tends of the nature of hydrophilic as compared to nano-SiC particulate [13]. Nanoalumina particulate is well scattered in composites so absorb more water as compared to pure epoxy [14]. So it is clear from the works of literature that the silicon carbide and aluminum oxide are suitable filler materials, which can be used in developing new epoxy-based composite. Here in the research work, both of these are used as filler materials, as discussed in the materials and methodology section.



## 2 Materials and Methodology

Al<sub>2</sub>O<sub>3</sub> (200 mesh) and SiC (1200 mesh) (1:1) particulates were reinforced into the epoxy resin (chemical formula shown in Fig. 1a) at the varying amount of 0, 2, 4, and 6 wt%. The epoxy taken in beaker and the aluminum and silicon carbide were mixed into it in the required ratio, and the solution is stirred for 5–8 min. Also, curing agent HY951 (araldite hardener, the chemical formula shown in Fig. 1b) is mixed with epoxy composite in 1:10 (as per resin and hardener manufacturer’s recommendation). The release gel is spread on the inside surface of the bottom mold sheet. Epoxy resin is spread uniformly on the mold sheet using a brush after that E-glass fiber is placed on it. A roller is used to remove the air traps present on the mold surface and to remove the excess of polymer present on the surface. Mild pressure is applied on the roller while moving it on the surface. The same process is repeated until the eight layers of glass fiber (5 mm thickness) are stacked. The release gel is spread on the inside surface of the top mold sheet before placing it on the mold. The pressure is applied by placing the 3 kg sand lime brick (dimension 230 mm × 110 mm) on the stacked layers. After curing at room temperature in 24 h, the mold is opened and the composite part is taken out.

## 3 Result and Discussions

### 3.1 Density Analysis

Density can be calculated [17] by the followed formula (1).

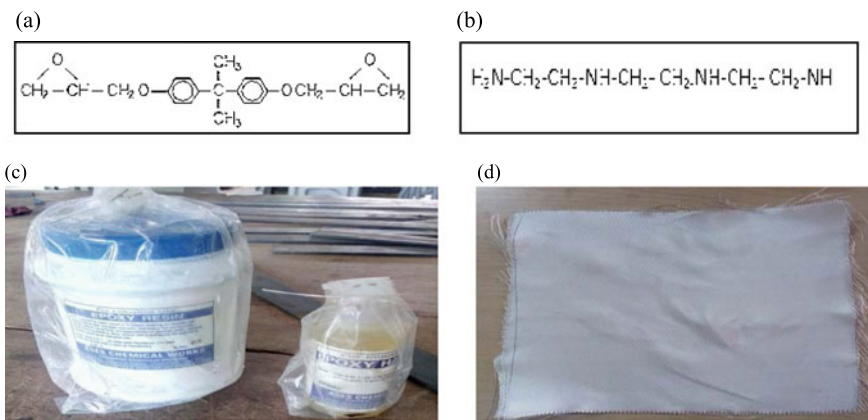


**Fig. 1** a Formula of epoxy (LY 556) [15], b formula of hardener resin (HY951) [16], c epoxy resin (LY 556) and hardener (HY951), d E-glass fiber

$$\text{Density} = \frac{W_a \times \sigma_w}{W_a - W_w} \quad (1)$$

where

$W_w$  = Mass of specimen weighed in distilled water.

$W_a$  = Mass of specimen weighed in air.

$\sigma_w$  = Density of distilled water at NTP (0.998 gm/cm<sup>3</sup>).

From the result of density measurement of specimens 40 mm in length, 20 mm in width with a 5 mm average thickness, the curve of density versus the percentage of the weight of Al<sub>2</sub>O<sub>3</sub>/SiC (1:1) particulate with woven E-glass fiber-reinforced epoxy composites was sketched, as shown in Fig. 2b. The composite without particulate filler has a maximum value of density 2.708 g/cm<sup>3</sup> due to better bonding between the epoxy resin and glass fiber as well as minimum voids formation. After that, it was observed from Fig. 2b that the value of density of Al<sub>2</sub>O<sub>3</sub>/SiC (1:1) particulates-filled epoxy-based composite with 2 wt% suddenly decreased due to the formation of voids. Void formation in a composite is accused due to air bubbles entrapped within the PMC, vapors arising during curing of epoxy and hardener and residual solvents. Voids are also accused due to resin difficult to wet fiber completely after mixing of Al<sub>2</sub>O<sub>3</sub>/SiC (1:1) particles [17]. It was observed from Fig. 2b that the value of the density is further increased from 2 to 6 wt% of Al<sub>2</sub>O<sub>3</sub>/SiC (1:1) content epoxy-based composites due to the increase of density of Al<sub>2</sub>O<sub>3</sub>/SiC (1:1) particulates in composites [18]. The 2 wt% composite is lighter than among others as it possesses the lowest density (2.651 g/cm<sup>3</sup>) which is required in all general application areas.

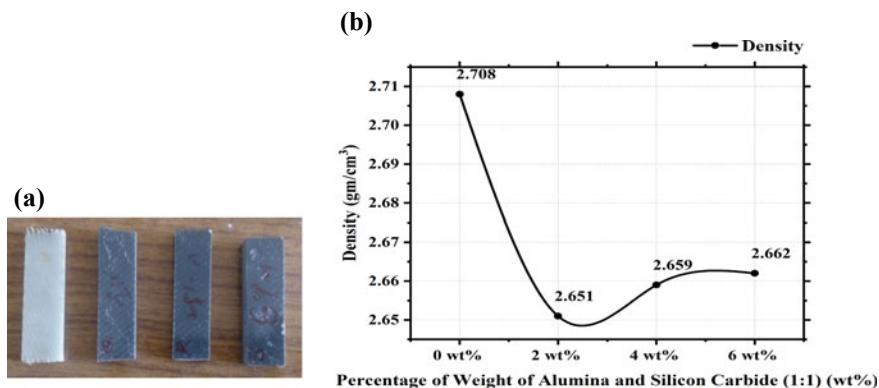


Fig. 2 a Specimens for density test, b comparison of density

### 3.2 Moisture Content (MC)

For this experiment’s first weight, the samples hereafter kept in the oven for dry until a constant weight is reached. In most cases, 16–24 h drying period is enough to gain constant mass. When constant mass reaches again weight the samples. The size of the specimen for moisture content test according to ASTM D 570 is 20 mm × 20 mm with a 5 mm average thickness. The moisture content can be calculated [19] by the followed formula (2).

$$\text{Moisture Content} = \frac{W_{mci} - W_{mcf}}{W_{mcf}} \times 100 \tag{2}$$

where

$W_{mci}$  = Initial weight of the specimen before drying in oven.

$W_{mcf}$  = weight of specimen after drying in oven.

The graph of the percentage of MC versus bakes time of Al<sub>2</sub>O<sub>3</sub>/SiC (1:1) particulate with woven E-glass fiber-reinforced epoxy composites shown in Fig. 3a. The composite without particulate filler has a maximum value of percentage of MC 0.901% due to the free hydroxyl group inside of the resin matrix as well as fiber [20]. It was observed from Fig. 3a that the value of percentage of MC is decreased from 2 to 6 wt% of Al<sub>2</sub>O<sub>3</sub>/SiC (1:1) content epoxy-based composites due to the decrement of free hydroxyl group inside composites with an increment of the percentage of the weight of Al<sub>2</sub>O<sub>3</sub>/SiC (1:1) particulate. The minimum moisture content (0.646%) found in a 6 wt% sample, but the 2 wt% is also having the just near value of 0.672%. So both specimens have almost equal moisture content, as visible from the graph.

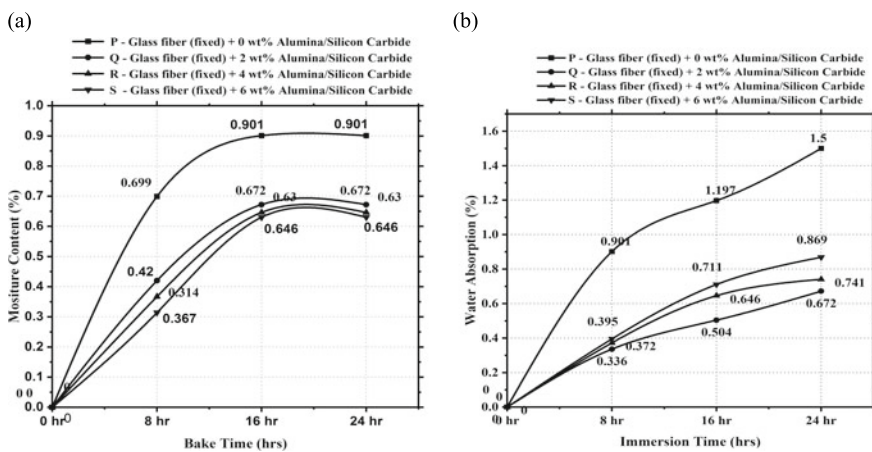


Fig. 3 a Comparison of moisture content and b comparison of water absorption

### 3.3 Water Absorption (WA)

The size of the specimen for water absorption test according to ASTM D570 is  $20 \times 20 \text{ mm}^2$  with 5 mm average thickness. All specimens are kept in an electric oven at  $80 \text{ }^\circ\text{C}$  for 24 h to remove the moisture. Dip the samples in water for 24 h and then take out and weight again. It can be calculated [17] by the followed formula (3).

$$\text{Water Absorption} = \frac{W_{\text{wabf}} - W_{\text{wabi}}}{W_{\text{wabi}}} \times 100 \quad (3)$$

where

$W_{\text{wabf}}$  = Final weight of the specimen after immersion in water.

$W_{\text{wabi}}$  = Initial weight of the specimen before immersion in water.

The composite without particulate filler form Fig. 3b has a maximum value of percentage of WA 1.5% due to poor compatibility between the epoxy resin and glass fiber. After that, it was observed from Fig. 3b that the value of the percentage of WA in  $\text{Al}_2\text{O}_3/\text{SiC}$  (1:1) particulates-filled epoxy-based composite with 2 wt% suddenly decreased due to the presence of SiC particulate [5, 21]. It was observed from Fig. 3b that its value increased from 2 to 6 wt% in  $\text{Al}_2\text{O}_3/\text{SiC}$  (1:1) samples due to increment of  $\text{Al}_2\text{O}_3$  wt% particulate. Less the water absorption capacity means low degradation and higher stability characteristics. The lowest percentage of absorption (0.672%) found with a 2 wt% sample for 24 h of water immersion [21].

### 3.4 Linear Swelling

Linear swelling gives an idea of change in thickness/width/length. The size of the specimen for linear swelling test according to ASTM D570 is  $20 \text{ mm} \times 20 \text{ mm}$  with 5 mm average thickness. All specimens are kept in an electric oven at  $80 \text{ }^\circ\text{C}$  for 24 h to remove the moisture. The length/thickness/width of each dried samples measured before the test and then dip them for 24 h in water and then measure them again after test. The linear swelling can be calculated [17] by the followed formula (4).

$$\text{Linear Swelling} = \frac{L_{\text{lsf}} - L_{\text{lsi}}}{L_{\text{lsi}}} \times 100 \quad (4)$$

where

$L_{\text{lsf}}$  = Final length/width/thickness of the sample after immersion in water.

$L_{\text{lsi}}$  = Initial length/width/thickness of sample before immersion in water.

Figure 4a represents the curve of the percentage of thickness swelling (TS) versus immersion time of different percentage of the weight of  $Al_2O_3/SiC$  (1:1) particulate with woven E-glass fiber-reinforced epoxy composites. The composite without particulate filler has a maximum value of percentage of TS 25.568% due to poor compatibility between the epoxy resin and glass fiber (correlation between WA and TS). After that, it was observed from Fig. 4a that the value of the percentage of TS in  $Al_2O_3/SiC$  (1:1) particulates-filled epoxy-based composite with 2 wt% suddenly decreased due to the presence of SiC particulate. It was observed from Fig. 4a that the value of percentage of TS is increased from 2 to 6 wt% of  $Al_2O_3/SiC$  (1:1) content epoxy-based composites due to increment of  $Al_2O_3$  wt% particulate [6]. Similarly, it was observed from Fig. 4b and c that the value of

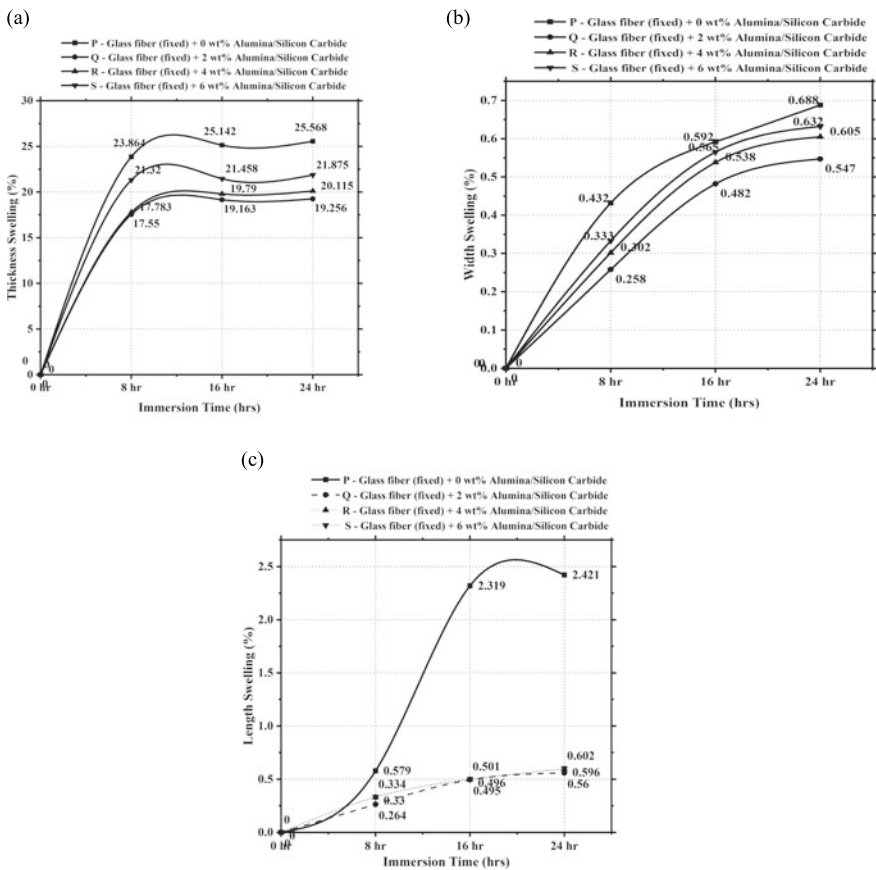


**Fig. 4** a Comparison of thickness swelling, b comparison of width swelling composites, c comparison of length swelling

percentage of width swelling and length swelling are increases from 2 to 6 wt% of  $\text{Al}_2\text{O}_3/\text{SiC}$  (1:1) content epoxy-based composites due to increment of  $\text{Al}_2\text{O}_3$  wt% particulate. The least swelling in overall volume is found in the 2 wt% sample [21].

## 4 Conclusion

Experimental and analytical evaluation of the optimum physical properties found in the epoxy composite sample with 2 wt% of  $\text{Al}_2\text{O}_3/\text{SiC}$  particulates, which comprises (2.651  $\text{g}/\text{cm}^3$ ) density, (0.672%) percentage of absorption, (0.646%) percentage of a percentage of moisture content, and least linear swelling in all dimensions. These qualities are required in all general application areas where the epoxy-based composites are prominently used like—automobile, aircrafts components, and sports goods. In future, characterization and mechanical testing's for developed composite will be checked for different combinations. The literature review papers show that the microparticles composite absorb less water and show better dimensional stability and the same thing is obtained in the results also. It justifies the correctness of the work.

## References

1. Patnaik, A., Satapathy, A., Mahapatra, S.S., Dash, R.R.: Tribo-performance of polyester hybrid composites: damage assessment and parameter optimization using Taguchi design. *Mater. Des.* **30**(1), 57–67 (2009). <https://doi.org/10.1016/j.matdes.2008.04.057>
2. Patnaik, A., Kumar, P., Biswas, S., Kumar, M.: Investigations on micro-mechanical and thermal characteristics of glass fiber reinforced epoxy based binary composite structure using finite element method. *Comput. Mater. Sci.* **62**, 142–151 (2012). <https://doi.org/10.1016/j.commatsci.2012.05.020>
3. Rajadurai, A.: Thermo-mechanical characterization of siliconized E-glass fiber/hematite particles reinforced epoxy resin hybrid composite. *Appl. Surf. Sci.* **384**, 99–106 (2016). <https://doi.org/10.1016/j.apsusc.2016.04.185>
4. Patnaik, A.: Development, characterization and solid particle erosion response of polyester based hybrid composites. PhD Dissertation (2008)
5. Alamri, H., Low, I.M.: Effect of water absorption on the mechanical properties of n-SiC filled recycled cellulose fibre reinforced epoxy eco-nanocomposites. *Polym. Testing* **31**(6), 810–818 (2012). <https://doi.org/10.1016/j.polymertesting.2012.06.001>
6. Alamri, H., Low, I.M.: Effect of water absorption on the mechanical properties of nano-filler reinforced epoxy nanocomposites. *Mater. Des.* **42**, 214–222 (2012). <https://doi.org/10.1016/j.matdes.2012.05.060>
7. Rajesh, S., VijayaRamnath, B., Elanchezian, C., Aravind, N., Rahul, V.V., Sathish, S.: Analysis of mechanical behavior of glass fibre/ $\text{Al}_2\text{O}_3$ -SiC reinforced polymer composites. *Procedia Eng.* **97**, 598–606 (2014). <https://doi.org/10.1016/j.proeng.2014.12.288>
8. Ravikumar, M., Prasad, M.S.: Fracture toughness and mechanical properties of aluminum oxide filled chopped strand mat e-glass fibre reinforced-epoxy composites. *Int. J. Sci. Res. Publ.* **4**(7), 1–7 (2014)

9. Kumar, R., Kumar, K., Sahoo, P., Bhowmik, S.: Study of mechanical properties of wood dust reinforced epoxy composite. *Procedia Mater. Sci.* **6**, 551–556 (2014). <https://doi.org/10.1016/j.mspro.2014.07.070>
10. Kwon, D.J., Shin, P.S., Kim, J.H., Baek, Y.M., Park, H.S., DeVries, K.L., Park, J.M.: Interfacial properties and thermal aging of glass fiber/epoxy composites reinforced with SiC and SiO<sub>2</sub> nanoparticles. *Compos. B Eng.* **130**, 46–53 (2017). <https://doi.org/10.1016/j.compositesb.2017.07.045>
11. Mahapatra, S.S., Patnaik, A.: Study on mechanical and erosion wear behavior of hybrid composites using Taguchi experimental design. *Mater. Des.* **30**(8), 2791–2801 (2009). <https://doi.org/10.1016/j.matdes.2009.01.037>
12. Ashik, K.P., Sharma, R.S., Guptha, V.J.: Investigation of moisture absorption and mechanical properties of natural/glass fiber reinforced polymer hybrid composites. *Mater. Today: Proc.* **5** (1), 3000–3007 (2018). <https://doi.org/10.1016/j.matpr.2018.01.099>
13. Sun, Y., Zhang, Z., Wong, C.P.: Influence of interphase and moisture on the dielectric spectroscopy of epoxy/silica composites. *Polymer* **46**(7), 2297–2305 (2005). <https://doi.org/10.1016/j.polymer.2005.01.041>
14. Yousri, O.M., Abdellatif, M.H., Bassioni, G.: Effect of Al<sub>2</sub>O<sub>3</sub> nanoparticles on the mechanical and physical properties of epoxy composite. *Arab. J. Sci. Eng.* **43**(3), 1511–1517 (2018). <https://doi.org/10.1007/s13369-017-2955-7>
15. Rao, S., Rao, R.M.V.G.K.: Cure studies on bifunctional epoxy matrices using a domestic microwave oven. *Polym. Testing* **27**(5), 645–652 (2008). <https://doi.org/10.1016/j.polymertesting.2008.04.005>
16. Ratna, D., Simon, G.P.: Mechanical characterization and morphology of carboxyl randomized poly (2-ethyl hexyl acrylate) liquid rubber toughened epoxy resins. *Polymer* **42**(18), 7739–7747 (2001). [https://doi.org/10.1016/S0032-3861\(01\)00278-6](https://doi.org/10.1016/S0032-3861(01)00278-6)
17. Atiqah, A., Jawaid, M., Ishak, M.R., Sapuan, S.M.: Moisture absorption and thickness swelling behaviour of sugar palm fibre reinforced thermoplastic polyurethane. *Procedia Eng.* **184**, 581–586 (2017). <https://doi.org/10.1016/j.proeng.2017.04.142>
18. Afzaluddin, A., Jawaid, M., Salit, M.S., Ishak, M.R.: Physical and mechanical properties of sugar palm/glass fiber reinforced thermoplastic polyurethane hybrid composites. *J. Mater. Res. Technol.* **8**(1), 950–959 (2019). <https://doi.org/10.1016/j.jmrt.2018.04.024>
19. Sánchez, M.L., Morales, L.Y., Caicedo, J.D.: Physical and mechanical properties of agglomerated panels made from bamboo fiber and vegetable resin. *Constr. Build. Mater.* **156**, 330–339 (2017). <https://doi.org/10.1016/j.conbuildmat.2017.09.003>
20. Sahari, J., Sapuan, S.M., Zainudin, E.S., Maleque, M.A.: Mechanical and thermal properties of environmentally friendly composites derived from sugar palm tree. *Mater. Des.* **49**, 285–289 (2013). <https://doi.org/10.1016/j.matdes.2013.01.048>
21. Candan, Z., Akbulut, T.: Physical and mechanical properties of nanoreinforced particleboard composites. *Maderas. Ciencia y tecnología* **17**(2), 319–334 (2015). <https://doi.org/10.4067/S0718-221X2015005000030>

# Failure Investigation of Induction Motor Bearing of Electric Vehicle Due to Manufacturing Defect



Deepak Borse, V. B. Tungikar, and D. R. Patil

**Abstract** The electric vehicle is the new domain of researcher because the replacement of Internal combustion engine. According to working principle, there are quite challenging aspects of electric vehicle. The high speed, low friction and controlled NVH are demanding factors from parts' manufacturers. In this paper, the acoustic failure of a ball bearing is studied for an application of high-speed induction motor. The root cause of bearing is identified from the batch of similar bearings. To validate the failure behavior, life durability testing of bearing is carried out. The testing incorporates the acoustic measurements, temperature monitoring and capturing the revolutions of bearing. Results are presented in the form of acoustic sound pressure plots with noise level as well as corresponding temperature. The study reveals that even the deep groove ball bearing is made from good quality of material, but grinding and super-finishing can be responsible for the unintentional cause of the defect. The author has recommended the threshold values of waviness as well as the intensity of stone marks to manufacture the premium class bearings for electric vehicles.

**Keywords** Bearing · Acoustic · Electric vehicle · Super-Finishing · Waviness

## 1 Introduction

The electric vehicles are mechanically driven by induction motors. These motors are very sensitively analyzed for a noise perspective due to government regulations. The acoustic techniques play a crucial role to capture the realistic behavior of deep groove ball bearing at high speed. The manufacturing of such a high-speed bearing needs special precautions and control parameters. Induction motors generate a

---

D. Borse (✉) · V. B. Tungikar  
Shri Guru Gobind Singhji Institute of Engineering and Technology, Nanded 431605, India

D. R. Patil  
National Engineering Industries, Savli 391775, India



different kind of acoustic behaviors when they are operated from medium speed to high speed. The small version of preoperational damages can lead to catastrophic failures of rolling bearings.

Catastrophic failures can be avoided by using predefined additional inspections at bearing level as well as electric motor assembly. At the level of bearing manufacturing, non-destructive testing of rings such as magnetic particle inspections, eddy current testing, nital etching and visual inspection at 10x scale can prevent the abnormality. Generally, these NDTs are cost-adding process which is not practiced in ordinary bearing manufacturing. At electric motor, many acoustic testing with the prognostic feature can be performed to avoid catastrophic failures of bearings. The sensitivity test of bearing and running torque of bearing are the best techniques to instant judge the quality of bearing.

There are few factors other than manufacturing defects which cause failure. They are an inadequate selection of radial internal clearance, grease, sealing solution. Also, the fitment process should be carefully selected. Induction heating of bearing ID before the assembly is the only way to fit the bearing for an electric vehicle; otherwise, the hammer press, push fitting will cause the damages.

In electric motor, improper ventilation of heat, current leakage from housing, electric pitting, frictions due to low air gap winding are the reason behind the failure of the bearing.

Vibrations are generated by deep groove ball bearing due to the multiple lobes on races and quantity of rolling elements. These vibrations exert the amplitude toward the housing through stationary outer ring. Many severe noise and vibration problems in bearing are due to cause of an adequate operation safety and waviness pattern beyond threshold limit.

Many researchers have studied the root cause of bearing degradation in filed failure. In heavy load applications, tapered roller bearings are widely used. Heavy loads make fatigue failure if bearings are manufactured with non-standard practices [1]. Xiao and Zhi [2] have analyzed the tapered roller bearing undergoes brittle hoop fracture during assembly of the gearbox. The tapered roller bearing application is intermediate shaft end bearings. The researcher has studied the micro-crack generated near to bearing marking surface. Marking is generally used for identification and marked on the cone's smaller head of tapered roller bearing. Grinding burn and the laser-marking surface have overlapped that cause a taper down in race hardness in the localized area. Walter et al. have researched on the premature failure of a full ceramic deep groove ball bearing. The failure has occurred in the mini mixture in the pharmaceutical industry. The material of rolling element and ring are silicon nitride and  $ZrO_2$  respectively. Researchers have demonstrated failure results in the form of Raman spectroscopy and fractography. The root cause was the phase transition to monoclinic from a tetragonal phase [3, 4]. Xu et al. investigated the dramatic changes in load distribution and contact angle of the angular contact ball bearing due to a localized defect. The researcher has developed a mathematical model by considering the high-speed gyroscopic effect and centrifugal force of an angular contact ball bearing. The effect of increased speed creates a significant impact on centrifugal force and load distribution toward the outer ring from the

inner ring [5, 6]. Liu [7] has studied the tribological aspects of bearing failure in variable frequency drive motors. A researcher has proposed the hypothesis of skin effect to uncover the nature of there common symptoms. The fluting on the outer raceway has identified in ball pass frequency of bearing in vibration analysis. Jing et al. [8] have investigated the surface level fatigue failure of ball bearing due to localized defect like a dent. A researcher has initiated a mathematical model which simulates the effect of a dent on rings of bearing. Borse and Tungikar [9] have systematically validated the acoustic behavior of deep groove ball bearing by considering the pre-operation damages on bearing during manufacturing. The durability of the screw drilling tool mainly depends on the rigidity of tungsten carbide bearing. This bearing transmits radial shock loads, corrosion and fatigue. The premature wear in tungsten carbide bearing has been investigated. The results are presented by using high-resolution scanning electron microscopy, optical microscope, X-ray diffractometer, electronic probe micro-analyzer, energy spectrometer, differential thermal and thermo-gravimetric analyzer [10, 11]. Acoustic characteristics are a very essential tool to extract the real-time behavior of rolling bearings [12–14].

Rolling bearing of an electric vehicle needs to fulfill the criterion of high-speed, low friction and optimized NVH. In this research, the authors have studied the failed bearing due to nonlinear acoustic behavior after complaint raised from the end-user. At first glance, scratch marks on the raceway and out of circularity are observed. The bearing is tested until failure to capture the acoustic behavior of bearing at three different duty cycles. Duty cycles of load and speed are considered as light, moderate and high. Results are presented in the form of acoustic sound pressure plot at different stages of testing.

## 2 Defect Analysis

Probable defects which are observed from the batch of failed bearings are scratch marks and waviness profile. The both non-conformities are elaborated below.

### 2.1 *Scratch Marks*

Bearing races undergo various operations starting from bar rolling, forging, annealing, machining, hardening, quenching, tempering, hard turning, face grinding, bore and track grinding, super-finishing till assembly. Any preoperational damages can cause the reason for failure. Figure 1 shows the scratch mark observed on bearing raceways due to worn out stone holder. The scratch mark is visualized at the scale of 50  $\mu\text{m}$ . The depth of this scratch is 0.9  $\mu\text{m}$ . Generally, this situation occurs at the end of tool life. The quantity of races is honed by this tool before replacing is considered for assembly.

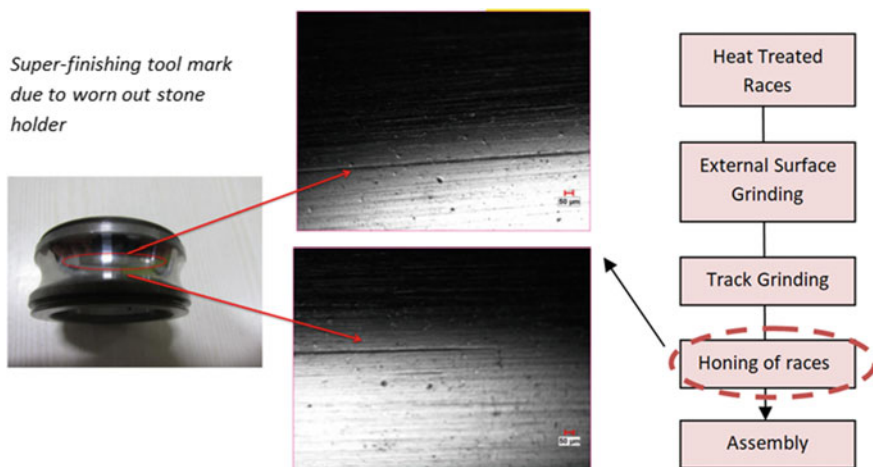


**Fig. 1** Tool marks on raceway

## 2.2 Waviness

Waviness is one of the essential parameters for high-speed application. Bearings should have the waviness value less than  $2.5 \mu\text{m}$  according to the size of the bearing. The profile of waviness exhibits the off-center grinding of the raceway due to inadequate dressing of the grinding wheel, offset position of the ring on the work head, or job stop. Waviness is measured on talysond measurement equipment which is  $5.5 \mu\text{m}$ .

## 3 Experimental Analysis

Validation of the identified defect is carried out with the help of an experimental setup as shown in Fig. 2. In the experimental setup, test bearings are mounted on a rotating shaft which is balanced by supported bearings. Supporter bearings are GMN6210 deep groove ball bearings. The test rig consists of radial- and axial-type hydraulic loading arrangements, acoustic sensors, a temperature sensor, and a bearing revolution recorder. The speed of the bearing can be verified with the help of a laser-based non-contact-type tachometer. The test bearing for an experiment is 6205 deep groove ball bearing with grease lubrication. The test rig is driven by a low-noise electric motor. The motor is connected via a rigid coupling system. Fits between the bore of the housing and the outer diameter of the bearing are conserved as loose. However, between the shaft diameter and the bearing bore is considered as a tight fit g1. The surface finish of the inner diameter of the housing is  $0.5 \mu\text{m}$ , and the surface finish of the shaft diameter is  $0.3 \mu\text{m}$ . The test has been carried out in a semi-anechoic room whose surrounding noise level when all machines are off is 18 dB(A).

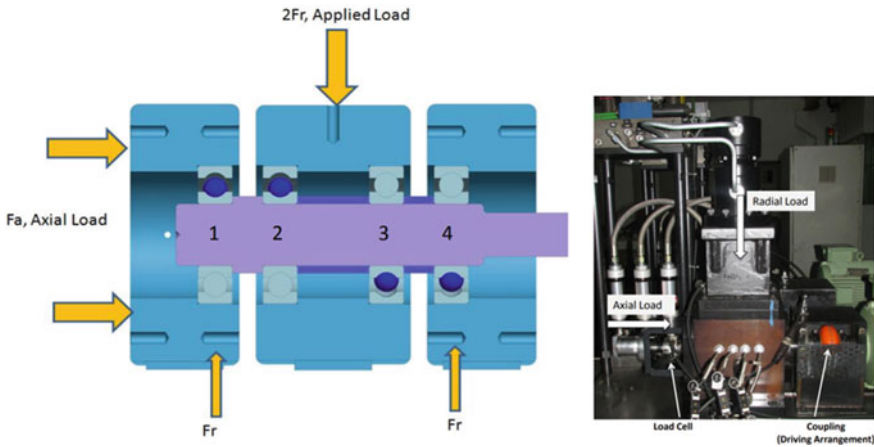


**Fig. 2** Experimental setup for life testing

The test bearing response having waviness pattern of  $5.5 \mu\text{m}$  has been experimentally evaluated. The test bearing duty cycle is enlisted in Table 1. Duty cycles are considered according to realistic field level testing of electric vehicles. The cycle consists of three modules light-, medium- and high speed-load limits.

The amplitude of vibration is recorded through the tri-axial type of accelerometer. FFT spectrum shows three directional appearances of peaks (horizontal, vertical and axial). The displacement of rotating elements of the test bearing at the time of interaction with picks and valley of waviness is illustrated in the FFT spectrum. The fundamental frequencies are captured from the outer race of test bearing. The corresponding waviness of failed bearing can be visualized at fault frequency of 281.8 Hz and harmonic 562.2 Hz.

The waviness pattern on the outer race component of the test bearing is approached by all rotating components with the time of equal interval. The speed of approach to the each and every peak-to-peak waviness pattern is the frequency of fundamental train frequency multiplied by number of rotating elements. The fundamental train frequency, sidebands and ball pass frequency of outer race are observed in experimental validations.

**Table 1** Testing cycle of bearing

Parameters	Duty cycle 1	Duty cycle 2	Duty cycle 3
Radial load $F_r$ , N	300	450	950
Axial load $F_a$ , N	300	600	1750
Speed, rpm	3000	6000	9000
Duration	Till failure	Till failure	Till failure

This supplementary frequency apart from ball pass frequency of outer ring is also captured in original FFT spectrum; the reason behind of these additional frequencies is due to supported bearings small variation in spring-based loading system and radial internal clearance. The supplementary frequencies are generated due to the one or more subsystems in electric motors. Subsystems consist of fins on the rotor, air gap, windings, exhaust fan, transmission bearing or support bearings. The ball pass frequency of inner race and its corresponding harmonics are observed in the experimentally simulated spectrum. In this experiment, the loaded zone of test bearing is circumferentially distributed at the angle of  $12^\circ$  angle from the central axis of bearing. This central axis is perpendicular to the bearing rotating axis. The loading zone of the outer race is opposite to axial force direction. However, in case of inner ring load zone is in the same side of the axial load direction.

The waviness pattern of the raceway is throughout the curvature of track raceway of bearings.

### 3.1 Metallurgical Property

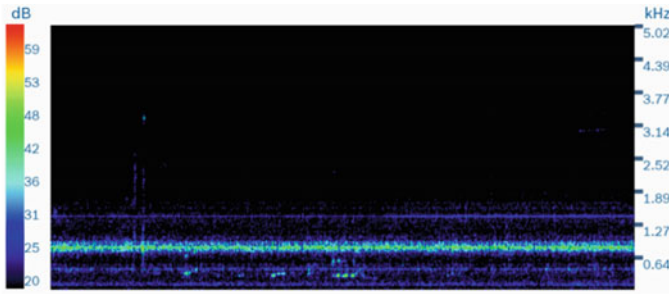
Table 2 represents the chemical composition of SUJ2/AISI52100 bearing material. To evaluate the surface hardness profile, Rockwell C hardness test was carried out. There is not much difference observed in microstructure between previous test bearing and after testing of 800 h. There is no such difference observed in the profile before and after in hardness and composition.

## 4 Results

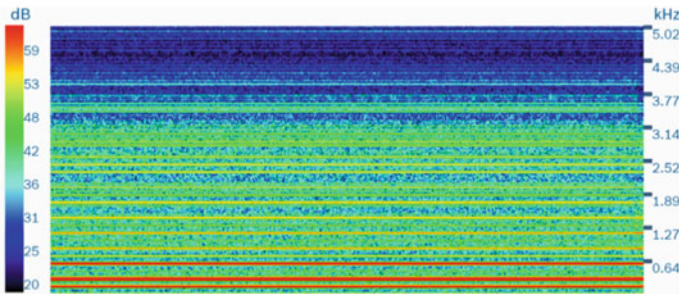
The experiments are carried out for all duty cycles. For low and moderated speed-load condition, failure pattern was not observed within 1000 h testing. In the case of high-speed and high-load duty cycle, failures with warnings are detected. The acoustic sound pressure plot after 100 h of life testing is shown in Fig. 3a. The pressure plot shows very ideal kind of bearing signature except for the small impression of peaks between 640 and 1270 Hz. It suggests that bearing cannot fail immediately if scratch marks or waviness patterns deviate from the process. After

**Table 2** Chemical composition, hardness and ra% (SUJ2/AISI52100)

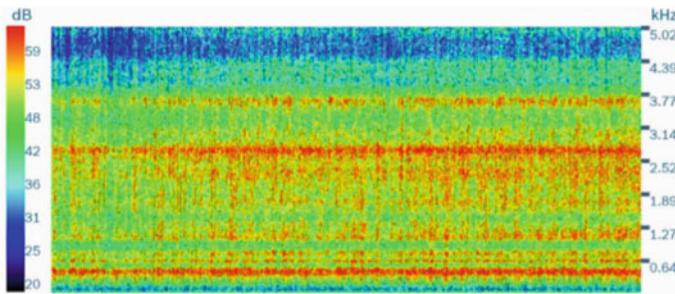
Bearing components	C (%)	Mn (%)	Si (%)	Cr (%)	S (%)	P (%)	Hardness (HRc)	Retained austenite (RA%)
Outer	1.03	0.31	0.30	1.51	0.002	0.009	62.6	13.4
Inner	1.02	0.34	0.28	1.52	0.002	0.015	63.0	11.7



(a)



(b)



(c)

**Fig. 3** a Sound pressure level after 100 h test (55 dB; 75 °C), b sound pressure level after 400 h test (61 dB; 87 °C), c sound pressure level after 805 h test (68 dB; 105 °C)

completion of the endurance life test of 400 h, another sound pressure is captured. Noise level of bearing is increased by 11%. The temperature of bearing is also increased by 12 °C in Fig. 3b. Generally, the internal combustion engines operate at speed up to 6000 rpm, where typical operating speed criterion in electric mobility starts from 8000 to 25,000 rpm. Hence, ordinary rolling bearings need to closely monitor at high speed. In Fig. 3c, sound pressure level is captured after completion

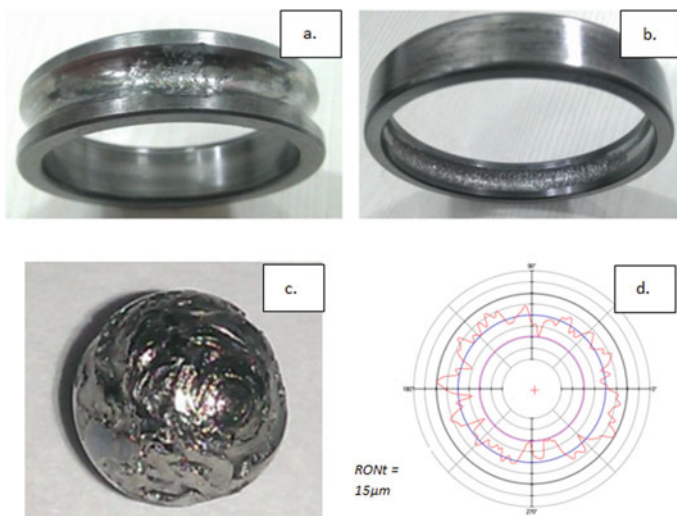


**Fig. 4** Bearing components after 800 h test **a** inner ring, **b** outer ring, **c** ball, **d** waviness profile

of 805 h test where noise level is further increased by 7 dB and temperature by 18 °C. The cutoff temperature was set at 105 °C, so bearing could not complete a 1000 h test. It has run 80.5% of target life. Damaged parts are shown in Fig. 4a–c. Photographs of failed bearing indicate the catastrophic degradation of balls and rings. Figure 4d shows the further distortion of waviness of track raceway, increased by 5.5 times than before testing.

## 5 Conclusion

In this paper, a failure study of bearing due to acoustic signals is carried out. The main cause of failure is observed as a scratch mark on raceway due to worn out of honing stone holder and waviness of track.

- Non-conformities of scratch marks and waviness do not allow to sudden failure. It shows a warning in acoustic behavior.
- When rotating element strikes at peaks of waviness, it creates further micro-level moments. It leads to higher-amplitude value in the low-band frequency spectrum.
- Acceptance limit of waviness, scratch limit should be less than 2 µm and 0.08 µm, respectively.
- Supplementary frequencies are observed due to internal radial clearance of support bearing.



- Acoustic measurement in the form of sound pressure plot is the best technique to get the warning of pre-operational damages of bearings.
- High-speed and high-load condition in electric vehicle application can create catastrophic failures if it is not manufactured with premium accuracy class.

**Acknowledgements** The author acknowledges the experimental support provided by a national bearing company, India. The author is thankful to machine operators of grinding line shop and metrological team.

## References

1. Ali, J., Borse, D.: Failure investigation of rear axle taper roller bearing by using the vibration spectrum. *J. Fail. Anal. Preven.* **20**, 1091–1096 (2020). <https://doi.org/10.1007/s11668-020-00935-5>
2. Xu, X.-L., Yu, Z.-W.: Failure analysis of tapered roller bearing inner rings used in heavy truck. *Eng. Fail. Anal.* **111**, 104474 (2020)
3. Bayer, R.G., Sirico, J.L.: Some observations concerning the friction and wear characteristics of sliding systems involving cast ceramic. *Wear* **16**, 421–430 (1970)
4. Harrer, W., Deluca, M., Morrell, R.: Failure analysis of a ceramic ball race bearing made of Y-TZP zirconia. *Eng. Fail. Anal.* **36**, 262–268 (2014)
5. Xu, L., et al.: Analysis of varying contact angles and load distributions in defective angular contact ball bearing. *Eng. Fail. Anal.* **91**, 449–464 (2018)
6. Upadhyay, S.H., Jain, S.C., Harsha, S.P.: Non-linear vibration signature analysis of a high-speed rotating shaft due to ball size variations and varying number of balls. *Proc. IMechE, Part K: J. Multi-body Dyn.* **223**, 83–105 (2009)
7. Liu, W.: The prevalent motor bearing premature failures due to the high frequency electric current passage. *Eng. Fail. Anal.* **45**, 118–127 (2014)
8. Liua, J., Wua, H., Shaoa, Y.: A theoretical study on vibrations of a ball bearing caused by a dent on the races. *Eng. Fail. Anal.* **83**, 220–229 (2018)
9. Borse, D., Tungikar, V.B.: Acoustic response of high-speed deep groove ball bearing by modifying the internal geometry. *Proc. IMechE, Part K: J. Multi-body Dyn.* **234** (2020). <https://doi.org/10.1177/1464419320955114>
10. Liu, Q.-C., et al.: Failure analysis of tungsten carbide bearing on screw drill. *Eng. Fail. Anal.* **89**, 37–45 (2018)
11. Lynagh, N., Rahnejat, H., Ebrahimi, M., Aini, R.: Bearing induced vibration in precision high speed routing spindles. *Int. J. Mach. Tools Manuf.* **40**(4), 561–577 (2000)
12. Crocker, M.J.: *Handbook of Noise and Vibration Control*. John Wiley & Sons (1998)
13. Crocker, M.J.: *Handbook of Acoustics*. John Wiley & Sons (2007)
14. Harris, T.A.: *Rolling Bearing Analysis*, 3rd edn. Wiley, New York (2001)



# Studies on Oxidation Behaviour of Cobalt-Based Superalloy 605



K. Jithesh, M. Arivarasu, and M. Nageswara Rao

**Abstract** Alloy L605 is a cobalt-based superalloy finding applications in the production of several critical components in gas turbine engines. Different parts made of this alloy are used in the aerospace industry. It is meant for use at temperatures up to 980 °C, and applications involve different types of oxidising environments. It hence becomes imperative to establish a thorough understanding of the oxidation behaviour of the alloy at high temperatures. The present study deals with oxidation behaviour of the alloy in the temperature range 650–850 °C in laboratory air environment under cyclic loading conditions. In addition to thermogravimetry, X-ray diffraction and EDAX analysis of the oxidised surfaces were carried out to study the oxidation reaction. The alloy showed considerable weight loss at 850 °C; there was no perceptible weight change at 650 °C. The reaction zone was found to be rich in O, Co, Cr and Mn. The activation energy for oxidation was calculated; it appears that outward diffusion of Mn and formation of Mn-containing compounds at the surface influence the activation energy.

**Keywords** Cobalt-base superalloy 605 · Oxidation · Weight loss · Parabolic rate constant · Activation energy · Manganese chromite

---

K. Jithesh · M. N. Rao (✉)

School of Mechanical Engineering, Vellore Institute of Technology,  
Vellore Tamil Nadu 632014, India  
e-mail: [m.nageswararao@vit.ac.in](mailto:m.nageswararao@vit.ac.in)

K. Jithesh

Department of Mechanical Engineering, Thejus Engineering College,  
Thrissur, Kerala 680584, India

M. Arivarasu

Center for Innovative Manufacturing Research, Vellore Institute of Technology,  
Vellore Tamil Nadu 632014, India

## 1 Introduction

Alloy 605 is a cobalt–nickel–chromium–tungsten alloy. It possesses a good combination of high-temperature strength and good resistance to high-temperature oxidation. It is used both in wrought form and cast form. Because of its attractive combination of properties, it has found applications in the aerospace industry. Several parts in military and commercial gas turbine engines are made of this alloy. An important application for the alloy is as a bearing material for balls and races. The material is generally considered adequate for applications at temperatures up to 980 °C. For applications involving higher temperatures, Alloy 230 or Alloy 188 are used.

Because several of its applications involve exposure to high temperatures in oxidising environments, the study of the oxidation behaviour of the alloy becomes important. Wolf and Sandrock [1] were among the early researchers to carry out experiments to study the oxidation of this alloy. Their studies focussed on optimising the levels of Si and Mn to maximise the resistance of the alloy to oxidation. Mudgal et al. [2] studied the high-temperature cyclic oxidation behaviour of the alloy at 900 °C in a laboratory air environment. They observed that the alloy has better oxidation resistance than Alloy 600. Jithesh and Arivarasu [3] studied the oxidation behaviour of Alloy 605 over the temperature range 750–950 °C. They concluded that the oxidation followed a parabolic law at all temperatures and the rate constant increased with increasing temperature.

There has been some work on the oxidation resistance of cobalt-base alloys but with a composition different from that of 605 Alloy. Yu et al. [4] studied the oxidation behaviour of a model cobalt-base superalloy and concluded that an inner continuous Al<sub>2</sub>O<sub>3</sub>-rich layer contributed to its high oxidation resistance. Kaarali et al. [5] studied the oxidation behaviour of Co–Cr alloys containing varying levels of W; they concluded that W blocks Co diffusion towards the alloy surface and improves the corrosion resistance.

There are still some unanswered questions relating to the oxidation behaviour of the alloy. There is very little information in the published literature on the role played by different elements in the alloy during oxidation. For example, such information is available in plenty in nickel-base alloys. There is no data available on the activation energy for the oxidation of the alloy. The present study attempts to throw some light on these aspects.

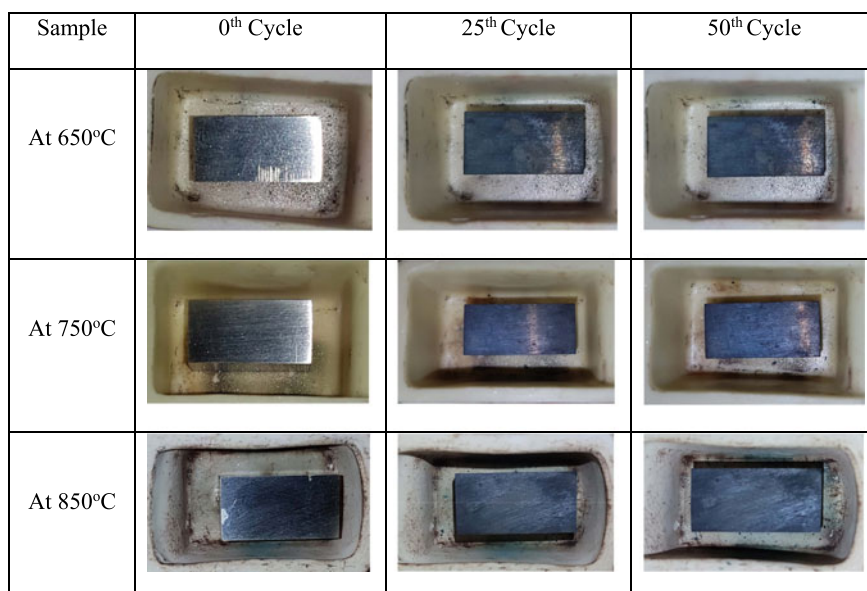
## 2 Materials and Experimental Methods

The air oxidation experiments were conducted using commercially available alloy L605. The chemical composition was determined by using optical emission spectroscopy. It was found to be Co-11.91Ni-18.39Cr-14.78 W-1.45Mn-0.35Fe-0.13 Si, the numbers being in wt%. Three samples of dimensions 20 × 10 × 7.2 mm

were prepared by wire EDM. The samples were polished using standard metallographic procedures and then acetone-cleaned. Oxidation study was carried out by using individual samples at temperatures of 650, 750 and 850 °C using distinct silicon carbide tubular furnaces. The experiment was carried out for 50 cycles, in which each cycle consists of 1-h of hold time in the furnace and 20 min of room temperature cooling. Weight changes for each sample were measured by means of an electronic balance and noted at the end of each cycle. Thermogravimetry, X-ray diffraction and EDAX analysis of the oxidised surfaces were carried out to study the oxidation reaction. Also, the activation energy for oxidation was calculated.

### 3 Results

A small amount of spallation was observed, the amount increasing with increasing temperature. There was a weight loss observed at all the three temperatures, the loss at 850 °C being substantially more than those at 650 and 750 °C. The macro-images of samples at 0th, 25th and 50th cycle are shown in Fig. 1. The weight change followed a parabolic law; the parabolic rate constant ( $K_p$ ) was calculated for the three temperatures, and the values are shown in Table 1. There was an increase of the constant with increasing temperature.

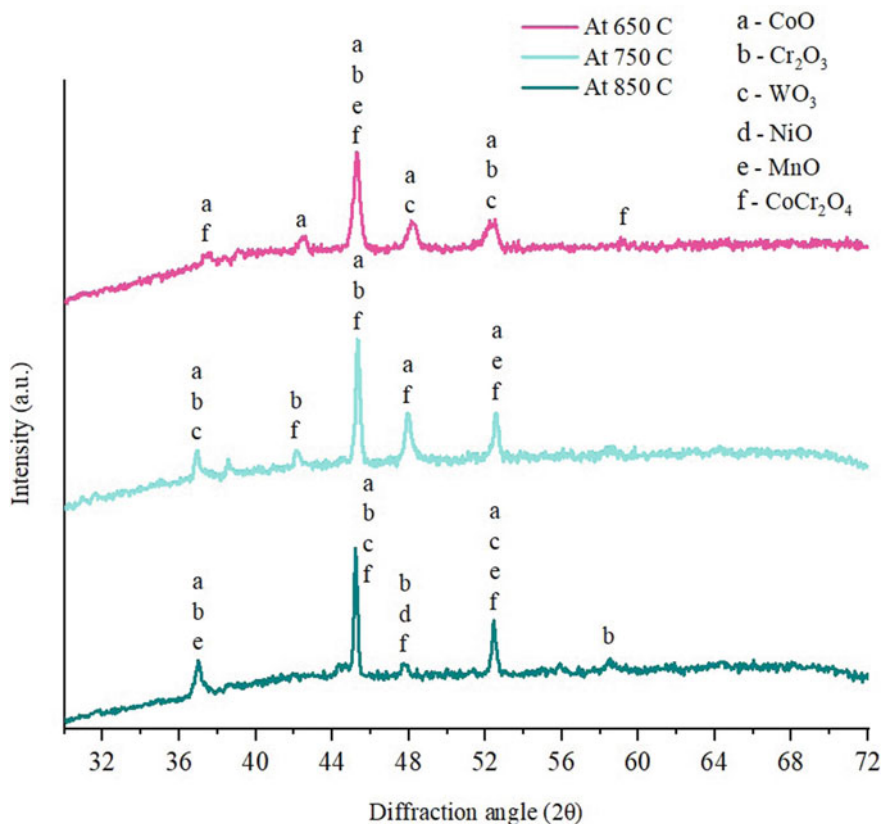


**Fig. 1** Macro-images of samples at 0th, 25th and 50th cycles during air oxidation study

**Table 1** Weight change and parabolic rate constant ( $K_p$ ) values at various temperatures

Serial number	Temperature °C	Weight loss ( $\text{mg}/\text{cm}^2$ )	Parabolic rate constant ( $K_p$ ) $10^{-10} \text{ g}^2 \text{ cm}^{-4} \text{ s}^{-1}$
1	650	0.131	0.96
2	750	0.214	2.56
3	850	0.596	19.70

XRD analysis of the corroded surfaces is given in Fig. 2. The presence of  $\text{CoO}$ ,  $\text{Cr}_2\text{O}_3$ ,  $\text{CoCr}_2\text{O}_4$ ,  $\text{NiO}$ ,  $\text{MnO}$  and  $\text{WO}_3$  phases are seen as products of oxidation. The EDS analysis of the surfaces exposed to 50 cycles of corrosion at the three temperatures is given in Table 2. The values are all in wt%.

**Fig. 2** XRD analysis of air oxidised samples after 50 cycles at three different temperatures

**Table 2** EDS analysis results at various temperatures

Element	650 °C	750 °C	850 °C
Co	44.34	33.51	32.45
Cr	15.79	21.73	22.34
O	27.19	29.29	28.15
W	1.56	1.99	1.70
Mn	9.04	12.34	11.51
Ni	–	–	2.91

## 4 Discussion

### 4.1 Values of the Parabolic Rate Constant

The values of the parabolic rate constant ( $K_p$ ) calculated from the present study for the oxidation of the alloy at the three temperatures are given in Table 1. Expectedly, the rate constant increases with increasing temperature. Mudgal et al. carried out oxidation studies on the same alloy. Their study was, however, carried out at 900 °C. They reported a weight gain at 900 °C, as opposed to the weight loss observed in the present study at 650, 750 and 850 °C. The value of the parabolic rate constant calculated by them was  $0.08 \times 10^{-10} \text{ g}^2 \cdot \text{cm}^{-4} \cdot \text{s}^{-1}$ . While the present study was not carried out at 900 °C, the increasing trend of the constant with increasing temperature suggests that the constant has to have a value higher than  $19.7091 \times 10^{-10} \text{ g}^2 \cdot \text{cm}^{-4} \cdot \text{s}^{-1}$ . There is thus a difference of more than two orders of magnitude. Both studies were carried out on the same alloy, and the starting material in both cases was in the form of a plate, similar in thickness. Thus, it is rather surprising that the results can be so very much different. The Fe content in the alloy studied by Mudgal et al. is 3.0%, in comparison to 0.35% in the present alloy. Higher iron content in nickel-base superalloys is expected to result in a higher rate constant value, due to the less protective nature of iron oxide. If Fe was to exert a similar influence in cobalt-base superalloys, the difference in Fe content would not be able to explain the difference in  $K_p$  value. Cr content is higher in the material studied by Mudgal et al. It was 20.0 versus 18.39 in the material studied by the present researchers. It has been reported in the context of nickel-base superalloys that Cr exerts little or no influence on weight gain in Ni–Cr alloys containing W [6]. There is lack of clarity as to why much lower parabolic rate constant was obtained by Mudgal et al. It is also not known, as to what is the effect of moisture in the air environment on the rate of oxidation. Further studies would be required in this direction.

## 4.2 *Factors Contributing to Weight Loss During Oxidation*

Oxidation of elements during exposure to air environment at high temperatures should contribute to a weight gain. There is evidence that Co, Cr, W, Ni get oxidised and this should result in the formation of their respective oxides. Some of these oxides may then combine with each other, forming spinel-type compounds. In any case, it should result in a weight gain. The temperatures at which the oxidation studies were carried out were such that the oxides and spinels formed are chemically stable; no decomposition or volatilisation entailing weight loss is expected. It is hence believed that the observed spalling is primarily responsible for the measured weight loss. It has been reported that manganese chromite forms during high-temperature exposure of Phynox, a cobalt-based superalloy [7] and under cyclic oxidation conditions it can spall off. It is believed that similar spalling of oxide scale is responsible for the weight loss observed in the present study. The presence of high levels of Mn and Cr at the surface, as revealed by EDS analysis, provides supporting evidence. Higher the oxidation temperature, higher is the severity of thermal cycling and higher is the intensity of spalling. The increasing weight loss observed with increasing test temperature can thus be explained.

## 4.3 *Surface Chemical Composition*

The Mn content in the alloy was only 1.45%. However, the surface oxide layer contained substantially higher levels of Mn—9.04, 12.34 and 11.51 wt% at 650, 750 and 850 °C, respectively. The results reported by Mudgal et al. were similar in that after oxidation at 900 °C, and the surface Mn levels were high—10.69 and 15.97. This indicates that Mn diffuses to the surface very fast. It has been documented that Mn diffuses faster than Ni, Cr and Fe in Cr<sub>2</sub>O<sub>3</sub> scale [9]. Hatab et al. reported the presence of Mn containing phases in the external oxide scale in alloy 617, even though the Mn content was as low as 0.03–0.3% in the base alloy. Mudgal et al. reported a significant presence of Mn in the external oxide scale in Alloy 600 (6.26 and 13.53), even though the base alloy had only 0.5% Mn. The starting Mn content in Alloy 605 is substantially higher (1.45 wt%); this is also a factor, it is believed, contributing to the high levels of Mn observed in the surface EDS analysis.

A substantial amount of Cr was present in the oxide scale at all temperatures, Cr content in the scale increasing with increasing temperature. It was 15.79, 21.73 and 22.34 at 650, 750 and 850 °C, respectively. This shows that after 50 heating and cooling cycles, the chromium oxide content in the scale was the highest at 850 °C. Whatever chromium oxide forms is expected to be present on the surface at the studied temperatures since evaporation of this oxide is expected to start only at higher temperatures (~1050 °C).

While the W was present in the alloy at a level of  $\sim 15$  wt%, it was present at the surface at a level of only 1.5–2 wt%. This observation matches with that made by Mudgal et al. in their oxidation studies carried out on the same alloy at 900 °C. The studies by Karaali et al. brought out that during oxidation of Co–Cr–W alloys, there was a topmost layer at the surface, which was essentially made of cobalt oxide. W was present in the form of its oxide in a layer beneath the cobalt oxide layer. The low percentage of W, obtained through EDAX analysis, may thus be a result of the topmost surface layer containing little or no W.

Substantial levels of Co were reported by EDS analysis of the corroded surfaces at all three temperatures. The Co level decreased with increasing exposure temperature. The levels in wt% were 44.34, 33.51 and 32.45, respectively, at 650, 750 and 850 °C. With an increase in exposure temperature, there is an increase in chromium oxide level, and this seems to be occurring at the expense of cobalt oxide.

#### 4.4 Activation Energy

The rate constant can be described by Arrhenius equation [8]

$$k = k_0 \exp(-Q/RT) \quad (1)$$

where  $k_0$  is the pre-exponential factor,  $Q$  is the activation energy,  $R$  is the gas constant, and  $T$  is temperature in Kelvin scale.

The activation energy  $Q$  can be obtained by rearranging Eq. (1):

$$\text{Log } k = \text{Log } k_0 - (Q/2.303 R)(1/T) \quad (2)$$

Figure 3 is a plot of  $\text{Log } k$  versus  $1/T$ . It was assumed that a single mechanism operates and that a single value of activation energy holds good. Best straight-line fit has been attempted. Based on the slope of the straight line, the activation energy value has been calculated. The value worked out to 129 kJ/mol. A similar value was obtained for second stage oxidation in nickel-base superalloy 617 [9]. It was interpreted by Hatab et al. that the activation energy value gets influenced by the formation of Mn-based compounds to meet the oxide scale boundary. There is a significant presence of Mn in Alloy 605, and the SEM-EDS analysis also confirmed active participation of Mn in surface oxide formation. It is thus possible that the formation of Mn-based compounds at the surface affects activation energy for the oxidation of Alloy 605.

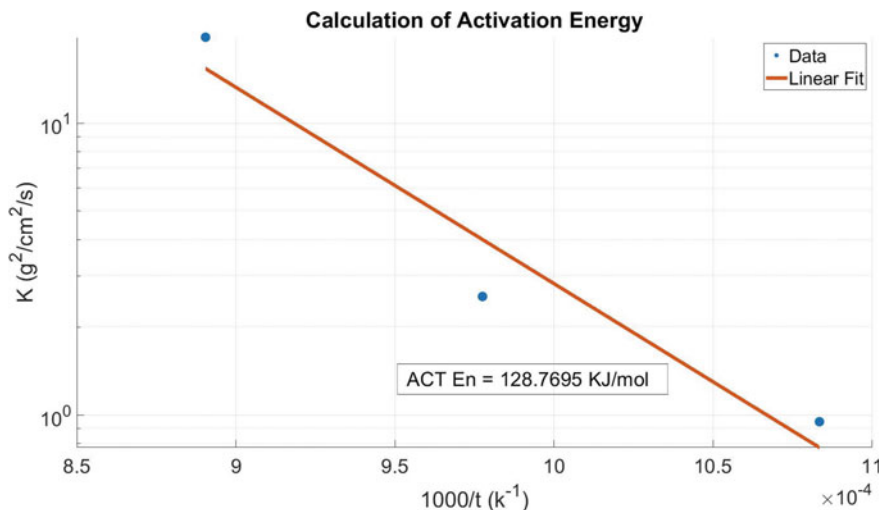


**Fig. 3** Arrhenius plot of the parabolic rate constants versus the inverse of absolute temperatures

## 5 Conclusions

Oxidation of the cobalt-base superalloy 605 in laboratory air environment was studied in the temperature range 650–850 °C, and the following were the major findings:

1. The present results show a weight loss during oxidation tests; this is in variance to the weight gain reported in the published literature. Further experimentation is required to get a comprehensive picture of the factors which can influence the oxidation rate.
2. The formation of manganese chromite-type compound at the surface and its spallation under cyclic thermal loading conditions is believed to be responsible for the observed weight loss.
3. Manganese is a surface-active element. With its high diffusivity through the scale, it travels to the surface and influences the corrosion process significantly.

## References

1. Wolf, J.S., Sandrock, G.D.: Some Observations Concerning the Oxidation of the Cobalt-Base Superalloy L-605 (HS-25). No. NASA-TN-D-4715. National Aeronautics and Space Administration, Cleveland, OH, Lewis Research Center (1968)
2. Mudgal, D., Kumar, S., Singh, S., Prakash, S.: Corrosion behavior of bare, Cr<sub>3</sub>C<sub>2</sub>-25%(NiCr), and Cr<sub>3</sub>C<sub>2</sub>-25%(NiCr)+ 0.4% CeO<sub>2</sub>-Coated Superni 600 under molten salt at 900 °C. *J. Mater. Eng. Perform.* **23**(11), 3805–3818 (2014)



3. Jithesh, K., Arivarasu, M.: An investigation on hot corrosion and oxidation behavior of cobalt-based superalloy L605 in the simulated aero-engine environment at various temperatures. *Mater. Res. Express* **6**(12), 126530 (2019)
4. Yu, B., et al.: High temperature oxidation behavior of a novel cobalt-nickel-base superalloy. *J. Alloys Compd.* **765**, 1148–1157 (2018)
5. Karaali, A., Mirouh, K., Hamamda, S., Guiraldenq, P.: Effect of tungsten 0–8 wt.% on the oxidation of Co–Cr alloys. *Comput. Mater. Sci.* **33**(1–3), 37–43 (2005)
6. Park, S.-J., Seo, S.-M., Yoo, Y.-S., Jeong, H.-W., Jang, H.J.: Statistical study of the effects of the composition on the oxidation resistance of Ni-based superalloys. *J. Nanomaterials* **2015** (2015)
7. Buscail, H., Riffard, F., Issartel, C., Perrier, S.: Oxidation mechanism of cobalt based alloy at high temperatures (800–1100 °C). *Corros. Eng. Sci. Technol.* **47**(6), 404–410 (2012)
8. Tung, H.-M., Stubbins, J.F.: Incipient oxidation kinetics of alloy 617 and residual stress of the oxide scale formed in air at temperatures between 850 and 1000 °C. *J. Nucl. Mater.* **424**(1–3), 23–28 (2012)
9. Al-Hatab, K.A., Al-Bukhaiti, M.A., Krupp, U.: Cyclic oxidation kinetics and oxide scale morphologies developed on alloy 617. *Appl. Surf. Sci.* **318**, 275–279 (2014)

# Advancements in Energy Storage Through Graphene



Rasmeet Singh 

**Abstract** Graphene-based systems have developed enormous attention for energy storage applications. This article highlights the advancement accomplished in developing electrochemical, chemical, and electrical frameworks that employ graphene to store energy. These systems have been covered through the development of lithium ion batteries, systems to store hydrogen, and supercapacitors. To boost the research, US Department of Energy (DOE) has initiated the energy program to set substantial targets to materialize the energy storage devices. Early experimental as well as theoretical studies have been summarized on employing systems for energy storage through graphene. The development of graphene-based systems is a young and recent topic and has shown an upward trend in very less time. This manuscript will be beneficial for early budding researchers who have interest in experimenting graphene-based technologies and are willing to work on energy storage devices.

**Keywords** Energy storage · Graphene · Li-ion batteries · Electrochemical · Hydrogen spillover

## 1 Introduction

In growing energy crises, storage of sustainable energy is the key feature to face the global challenges. In fact, the designing and production of such systems do not solely satisfy the targets, but the system should be energy efficient and should outshine the supply and demand for mobile applications. The three major energy storage techniques include (i) electrochemically, (ii) chemically, and (iii) electrically. Also, a large number of materials are available for energy storage. However, the list reduces to very few if we consider the factor of economy and energy to weight ratio of the system. Carbon is the lightest element which can be used for

---

R. Singh (✉)

Dr. S.S. Bhatnagar University Institute of Chemical Engineering and Technology,  
Panjab University, Chandigarh 160014, India

energy storage in various forms. It provides high specific surface area as well as high energy capacity. Initially, carbon nanotubes were widely used to store energy [1]. It is lightweight and has a surface area of  $1315 \text{ m}^2 \text{ g}^{-1}$  for single walled structures. Moreover, these can be mass produced [2]. The only drawback that does not make carbon nanotubes an ideal candidate is that it has a high production cost and it is complex to remove several residual metallic impurities from the pores.

Graphene has been a center of attraction for energy storage materials. It is lightweight, inert in nature, and has a low price. It is a monolayer sheet with  $\text{sp}^2$  hybridized carbon atoms and has unique mechanical, chemical, thermal, electrical, optical, and electrochemical properties [3]. It has a surface area larger than a simple carbon sheet, i.e.,  $2630 \text{ m}^2 \text{ g}^{-1}$ . The family of graphene materials includes chemically or structurally derived graphenes. This includes double-layer and multi-layer graphenes. The highly preferred chemically induced graphene is known as graphene oxide. There are several methods present for the synthesis of graphene. These includes thermal decomposition of graphite oxide followed by the reduction of graphene oxide to graphene, chemical vapor deposition (CVD) development of graphene on a metal catalyst, preparation through graphite mechanical cleavage (the Scotch-tape method), electrochemical exfoliation of graphite compound, and unzipping of carbon nanotubes [4, 5]. Apart from this, various other methods have been developed for graphene synthesis. Each application requires graphene with different properties, and hence, the synthesis techniques also vary depending upon the requirements. For instance, the reduction of graphene oxide forms a single atom graphene layer with multiple defects [6]. These defects further significantly affect the chemical and physical properties of the compound. The main aim of this review is to explore the main advances that occurred for utilizing graphene as an energy storage through electrochemical, chemical, and electrical paths.

## 2 Electrochemical Storage Through Batteries

From the portable electronic devices to automotive systems, electrochemical energy storage through rechargeable batteries is in daily use. The most common and popular rechargeable electrochemical energy storage device is lithium (Li)-based batteries. From the past few decades,  $\text{Li}^+$  ions compacted into graphite lattice have been the area of intensive research due to strong potential of electrochemical energy storage in graphene-based systems [7]. In terms of Li density, the graphite system with relatively lower Li-ions density shows less specific capacity of around  $372 \text{ mA h g}^{-1}$  [8]. Whereas in case of single graphene sheets, the capacity rises to  $744 \text{ mA h g}^{-1}$ , especially when Li is embedded on both the sides of the graphene sheet. Since graphitic carbon forms  $\text{LiC}_6$  structures, therefore embedding Li on multiple sides of graphene leads to  $\text{LiC}_3$  structures [9]. The graphite electrodes lack behind due to its lateral size and lengthy diffusion pathways of Li into the material. The only solution to this is to minimize the lateral dimensions, i.e., x-y axes, of the graphite compound to ease the process of  $\text{Li}^+$  diffusion into the interlayer spaces for

higher reversibility. The material with 10s or 100s nanometers of lateral dimensions and length in micrometers is known as stacked platelet graphene nanofibers. The basal planes in this type of system lie at the end of nanofibers and also have edge-like sides with interlayer spacing among graphite, hence making it an ideal candidate for exceptional electrochemical properties. Due to small lateral sizes, the capacity increases to  $461 \text{ mA h g}^{-1}$  [10]. Also, the storage capacity varies inversely with the stacked graphene platelet nanofiber. Further, to enhance the specific capacity of  $\text{Li}^+$  ions batteries, graphene sheets were introduced as electrodes to raise the capacity till  $540 \text{ mA h g}^{-1}$ . It was observed that when carbon nanotubes (CNTs) and fullerenes were placed as spacers between the graphene sheets, the energy storage capacity further increased to  $730 \text{ mA h g}^{-1}$  and  $784 \text{ mA h g}^{-1}$ , respectively. Wang et al. [11] used graphene paper as a cathode and Li as anode, giving a capacity of  $582 \text{ mA h g}^{-1}$ . Takamura et al. [12] explored that the high discharge capacity of Li-ion battery anodes is due to nano sized cavities in the graphene sheets. Hence, these nanopores and nanoholes can play an effective role in governing the selectivity of the system. This study was set as a basis for further growth of  $\text{Li}^+$  graphene-based batteries [13]. The important breakthrough from this research was that  $\text{C}_{60}$  segregated graphene nanosheets possess higher capacity than the theoretical value of the  $\text{LiC}_3$  model. Pan et al. [14] deeply investigated this statement by series of experiments. Further, it was claimed that since few  $\text{Li}^+$  ions may get stored in interfacial layers among (002), still the majority of  $\text{Li}^+$  were found in the graphene defects. The initial stages of reaction of Li and active defects happen at relatively low potential. The discharge of Li from strong bonds with defects demands high voltage during the charging process and creates a large voltage hysteresis. In disordered graphene, Pan et al. [14] identified the highest reversible capacity of  $794\text{--}1054 \text{ mA h g}^{-1}$ . These values were somehow comparable with  $\text{Li}_2$  covalent representation (i.e.,  $1116 \text{ mA h g}^{-1}$  in  $\text{LiC}_2$ ) developed by Sato et al. [15] for disordered carbon.

The graphene-based batteries did not perform well in the initial stages of development, but are exhibiting efficient cyclic operation with 90–95% efficiency in current devices. Metal/graphene combination nanocomposites were suggested as a pathway to enhance the capacity of Li batteries. Wang et al. [17] firstly illustrated the storage capacity of tin (Sn)/graphene composite systems through voltammetry and DFT-based experiments. Sn showed an overall storage capacity of  $994 \text{ mA h g}^{-1}$ . The  $\text{Li}^+$  ions in reaction with Sn create  $\text{Li}_{4.4}\text{Sn}$  without any aggregation. However, clustering of Sn atoms and nanoparticles may occur when reaction is done through pristine Sn. Hence, the continuous operation results in the loss of capacity effectiveness of the material. Here, graphene can play multiple roles of both supporting Sn and simultaneously absorbing Li atoms. For such a system, Wang et al. [17] reported the storage capacity of  $795 \text{ mA h g}^{-1}$ . Wu et al. [16] discussed another metal oxide composite for graphene-based batteries. Further, Wu installed  $\text{Co}_3\text{O}_4$  particles of size 10–30 nm as spacers homogeneously between the graphene sheets. System gave a cyclic efficiency of 98% with a capacity of  $935 \text{ mA h g}^{-1}$  after 30 days of working. On another hand,  $\text{TiO}_2$  nanoparticles/graphene framework gave cyclic efficiency of 98% [18]. Further, self-assembled

nanocomposites comprising ordered and alternative nanocrystalline layers of metal oxides (i.e.,  $\text{SnO}_2$ ,  $\text{NiO}$ , and  $\text{MnO}_2$ ) were synthesized with graphene stacks which showed a capacity of  $760 \text{ mA h g}^{-1}$ . Graphene also exhibits conducting support to olivine-based  $\text{LiFePO}_4$ -based batteries. This system exhibits almost negligible decrease in capacity even after hundreds of cycles [19].

### 3 Chemical Storage of Hydrogen

Hydrogen tops the list of most promising clean fuels due to water as its only by-product. Hydrogen fuel is free from any type of sulfurous oxides ( $\text{SO}_x$ ), nitrous oxides ( $\text{NO}_x$ ), and carbon dioxide ( $\text{CO}_2$ ) emissions [20]. The liquid storage technique of hydrogen was launched by NASA's Apollo program a long back. However, such a system is not safe for regular use in on-board applications. Hence, the substrate (or the sorbent) technique comes out to be the most promising. The US DOE gave 6.5 wt% as a target for storing hydrogen in sorbents at ambient conditions with a volumetric density of  $62 \text{ kg H}_2 \text{ m}^{-3}$  [21]. Such a target is highly challenging to achieve, especially when the stoichiometric ratio of carbon and hydrogen is 7.7 wt% of hydrogen. For hydrogen storage in sorbents, two highly preferred approaches include (i) atomic hydrogen storage through hydrogen spillover or (ii) molecular hydrogen storage. These two techniques are intensively discussed in the following sections.

#### 3.1 Hydrogen Spillover

Dissociation of hydrogen molecules on the surface of metal catalyst, where a part of molecule gets attached to the catalyst surface and rest of the molecule diffuses on the support is known as hydrogen spillover. For energy storage applications, the support is graphene, and transition elements act as catalysts. The most favorable transition elements are platinum (Pt), palladium (Pd), or nickel (Ni) [22]. Presently, most of the elements show the capacity of 1 wt% at 100 atm pressure and room temperature, which is far away from DOE targets. Researchers then suggested building a bridge between catalyst particle and graphene/graphite surface to enhance the spillover. For completely hydrogenated graphene, the theoretical capacity could be as high as 7.7 wt%, meeting DOE targets. Even after extreme development of spillover principles, findings are still made to fully understand the reason behind dissociation of hydrogen molecules into atomic form and to spill throughout the graphene sheets [23].

Lin et al. [24] gave theoretical findings that hydrogen spillover is kinetically and thermodynamically stable technique and does not essentially require complete saturation of metal clumps before spillover. The spillover technique is still conventional even if the metal clusters are completely saturated. It was also concluded

that the process involving pristine graphene is thermodynamically unstable, hence doped graphene is preferred for hydrogen spillover as it promotes hydrogen up to great extent. Moreover, stone-wales type of surface defects in graphene highly enhances the hydrogen binding capacity. These effects are majorly found on chemically reduced graphene/graphene interfaces synthesized from graphite through oxidative acid treatment, consequential exfoliation followed by chemical reduction [25].

### 3.2 *Molecular Storage of Hydrogen*

Hydrogen molecules are nonpolar in nature. The interactions of hydrogen molecules with graphene-based frameworks are totally governed on the basis of London dispersion forces, also known as dipole-dipole induced forces. It has been shown in various studies that graphite nanofibers (also known as stacked graphene platelet nanofibers) exhibit very high capacity to store hydrogen [26]. All around the globe, extensive research has been carried out to monitor the hydrogen adsorption capacity of graphene-based materials and further document various recommendations for future experiments. The spatial dispersal of molecular hydrogen adsorbs on the graphene surface and gets delocalized. This leads to the free lateral movement of hydrogen molecules. An attractive force of  $-1.2 \text{ kJ mol}^{-1}$  exists in the hydrogen/graphene system at ambient temperature [27]. Free energy physisorption of graphene gets activated at an equilibrium constant of 1.6, and hence, the single layer of graphene enhances the uptake of hydrogen at room temperature by an approximate value of 60%. Thus, there is no meaning of utilizing only graphite/graphene interface for hydrogen storage. Hence, to accelerate the binding capability, it was recommended to design a sandwich like model to uptake hydrogen in-between the neighboring layers. The theoretical studies show that interlayer distance between graphene sheets is 6 Å. Therefore, a single monolayer can harbor about 2–3 wt% hydrogen at 5 MPa. The obtained storage capacity came out to be a breakthrough but still was less than US DOE targets.

To meet the targets, researchers suggested to accompany two layers of molecular hydrogen in mono graphene-graphene interlayer. This suggestion would only be possible if the consecutive graphene layers are separated by 8 Å, rather than 6 Å. The new system would give a gravimetric storage capacity of 5.0–6.5% of hydrogen. This technique would only be successful if suitable nano-architectonic graphene sheets are separated from each other. For this, short carbon nano-tube pillars and fullerenes were used as spacers between the graphene layers. For a similar alternative, Yildirim and Ciraci [28] considered Kubas interactions among molecular hydrogen, and transition metals were considered a potential system to bind hydrogen molecules to provide significant capacity. Graphene oxide on the other hand is an ideal material to hold metals when it is attached with a suitable functional group. The oxygen groups present in graphene layers form strong bonds

with titanium (Ti) [29]. Ti forms a bond with oxygen from multiple sides, hence results in hydrogen storage capacity of 4.9 wt% with 64 g L<sup>-1</sup> mass concentration.

Several theoretical studies have demonstrated potential metal doping with graphene, especially boron (B) and aluminum (Al) with highly improved binding capacity for hydrogen. Various other theoretical studies have suggested C<sub>3</sub>N<sub>4</sub> sheets [30], planar graphene [31], and pristine B sheets [32] embedded with alkali metals as good hydrogen uptake materials with storage capacities ranging from 7.8 to 10.7 wt% of hydrogen. Calcium (Ca)-decorated graphene gives the storage capacity of approximately 5 wt% [33]. Ca prefers to absorb over the zig-zag edge of graphene, resulting in 10 Å distance of Ca–Ca. Every Ca atom absorbs six hydrogen molecules. Lee et al. [33] described the structure of hydrogen as an adsorbate on graphene through scanning tunneling microscopy (STM). It was observed that at low coverage areas, the hydrogen dimmers formed on protruding areas. While at higher coverage, a random adsorption into the large hydrogen bunch was noticed. It was further concluded that a methodology should be developed for measurement of space-size and hydrogen storage capacity for nanostructured carbon-based materials. Anderson et al. [34] used nuclear magnetic resonance spectroscopy (NMR) for the characterization of nanopores of size <2.4 nm in carbon nanospace. The results demonstrated that at 100 K and 0.2 MPa, such nanopores can uptake up to 2.3 wt% hydrogen. Further, it was shown that hydrogen can be stored nanoporous carbon and can be produced through carbon crystallization.

## 4 Electrical Storage Through Supercapacitors

Supercapacitors, also known as ultra-capacitors, are electronic devices that can store energy and liberate it in a short interval of time with high power potential and substantial current density [35]. They show high dynamic charge dissemination with extended cycle life (i.e., 100,000 cycles). Energy storage in supercapacitors follows two main principles: (i) by charge transfer to redox molecules layer on electrode surface or (ii) storing pure charge on electrode or electrolyte interface through EDLC (i.e., electrochemical double-layer capacitance). The mechanism of EDLC is directly proportional to the area in contact with solution. Graphene becomes an ideal supercapacitor compound for EDLC in its maximum surface area of 2630 m<sup>2</sup> g<sup>-1</sup>. Stoller et al. [36] firstly discovered that chemically altered graphene has higher capacitance of 99 F g<sup>-1</sup> and 135 F g<sup>-1</sup> for organic electrolytes and aqueous electrolytes, respectively. Further, Wang et al. [37] carried modifications into graphene-based mediums to increase its capacitance to 205 F g<sup>-1</sup>. Si et al. [38] recommended to insert Pt nanocrystals of diameter 4 nm between the graphene layers that will improve the capacitance up to 269 F g<sup>-1</sup>. Thus, it is a well-known fact from above observations that suitably doped graphene-based materials can act as good supercapacitors. In recent years, carbon nanotubes have also been used to separate graphene sheets, which gave a capacitance of 12 F g<sup>-1</sup> [39].

For large pseudo-capacitance devices, graphene sheets can be employed to support the system which will reduce the clustering to maximize the area exposed to electrochemical processes.  $\text{MnO}_2$  nanocrystals synthesized on a graphene sheets system provided the capacitance of  $197 \text{ F g}^{-1}$ . This value of capacitance is higher than  $10.9 \text{ F g}^{-1}$  and  $6.8 \text{ F g}^{-1}$  shown by graphene oxide and bulk  $\text{MnO}_2$ , respectively [40]. Further, highest capacitance of  $1335 \text{ F g}^{-1}$  was obtained by Wang et al. [41] through  $\text{Ni}(\text{OH})_2$  nano-plates synthesized on graphene sheets. Further it was observed that  $\text{Ni}(\text{OH})_2$  nano-plates on graphene sheets outperformed  $\text{Ni}(\text{OH})_2$  grown on highly oxidized graphene oxide sheets, which have the property of electrical insulation. This shows that the substrate plays a major role in designing and working of the system. Several other compounds like  $\text{SnO}_2$  and  $\text{ZnO}$  were also used to modify the graphene; however, their capacitance values are low, i.e.,  $62 \text{ F g}^{-1}$ .

Graphene and polymer system nanocomposites has proved to be an attractive option for supercapacitors. Graphene modified with polyaniline nanomaterials is easy to manufacture and also shows a capacitance in the range of  $233\text{--}1046 \text{ F g}^{-1}$ , varying with nanostructure of the composite. PSS or poly(sodium-4-styrenesulfonate)-graphene nanocomposite also showed good capacitance. Even after 14,860 cycles, the capacitance of  $190 \text{ F g}^{-1}$  decreased by only 12% [42]. For portable/wearable devices, graphene/polymer material came out to be the best due to its flexibility and mechanical strength.

## 5 Conclusion

In this paper, a review of graphene-based systems for energy storage has been presented. The innovation of most of the devices started to happen in the year 2008. Thus, this is a very recent topic of discussion which has a wide scope in future. From theoretical studies, it can be concluded that graphene is an ideal material which has all the potential to meet DOE's targets to store hydrogen. However, there is still a long path to cover for that. It can be noted that for energy storage devices, a suitable nano-architectonic pattern with proper separation between graphene layers is a critical parameter to obtain high-performing materials. Conventional spacing between graphene sheets not only avoids restacking, but also avails nanoengineered space to molecules or ions to interact. There is still a lot more to explore and research as graphene equipped energy storage devices not only pose challenging, but are also a promising research area.



## References

1. Sun, L., et al.: Roles of carbon nanotubes in novel energy storage devices. *Carbon* **122**, 462–474 (2017)
2. Yan, Q., et al.: Mass production of graphene materials from solid carbon sources using a molecular cracking and welding method. *J. Mater. Chem. A* **7**(23), 13978–13985 (2019)
3. Chae, S., et al.: Anomalous restoration of  $sp^2$  hybridization in graphene functionalization. *Nanoscale* **12**(25), 13351–13359 (2020)
4. Jakhar, R., Yap, J.E., Joshi, R.: Microwave reduction of graphene oxide. *Carbon* (2020)
5. Hussain, A., et al.: Synthesis of graphene from solid carbon sources: a focused review. *Mater. Chem. Phys.* **248**, 122924 (2020)
6. De Silva, K.K.H., et al.: Chemical reduction of graphene oxide using green reductants. *Carbon* **119**, 190–199 (2017)
7. Lucu, M., et al.: A critical review on self-adaptive Li-ion battery ageing models. *J. Power Sources* **401**, 85–101 (2018)
8. Bruce, P.G., Scrosati, Bruno, Tarascon, J.-M.: Nanomaterials for rechargeable lithium batteries. *Angew. Chem. Int. Ed.* **47**(16), 2930–2946 (2008)
9. Cai, X., et al.: Graphene and graphene-based composites as Li-ion battery electrode materials and their application in full cells. *J. Mater. Chem. A* **5**(30), 15423–15446 (2017)
10. Subramanian, V., Zhu, H., Wei, B.: High rate reversibility anode materials of lithium batteries from vapor-grown carbon nanofibers. *J. Phys. Chem. B* **110**(14), 7178–7183 (2006)
11. Wang, C., et al.: Electrochemical properties of graphene paper electrodes used in lithium batteries. *Chem. Mater.* **21**(13), 2604–2606 (2009)
12. Takamura, T., et al.: Identification of nano-sized holes by TEM in the graphene layer of graphite and the high rate discharge capability of Li-ion battery anodes. *Electrochimica Acta* **53**(3), 1055–1061 (2007)
13. Yoo, E.J., et al.: Large reversible Li storage of graphene nanosheet families for use in rechargeable lithium ion batteries. *Nano Lett.* **8**(8), 2277–2282 (2008)
14. Pan, D., et al.: Li storage properties of disordered graphene nanosheets. *Chem. Mater.* **21**(14), 3136–3142 (2009)
15. Sato, K., et al.: A mechanism of lithium storage in disordered carbons. *Science* **264**(5158), 556–558 (1994)
16. Wu, Z.-S., et al.: Graphene anchored with  $Co_3O_4$  nanoparticles as anode of lithium ion batteries with enhanced reversible capacity and cyclic performance. *ACS Nano* **4**(6), 3187–3194 (2010)
17. Wang, G., et al.: Sn/graphene nanocomposite with 3D architecture for enhanced reversible lithium storage in lithium ion batteries. *J. Mater. Chem.* **19**(44), 8378–8384 (2009)
18. Wang, D., et al.: Self-assembled  $TiO_2$ -graphene hybrid nanostructures for enhanced Li-ion insertion. *ACS Nano* **3**(4), 907–914 (2009)
19. Rong, J., et al.: Preparation of  $TiO_2/Co_3O_4$  nanostructured materials by a two-step hydrothermal method and their electrode performance in lithium ion batteries. *Int. J. Electrochem. Sci* **12**, 11987–11996 (2017)
20. Singh, R., Altaee, A., Gautam, S.: Nanomaterials in the advancement of hydrogen energy storage. *Heliyon* **6**(7), e04487 (2020)
21. Islam, E., et al.: Detailed Analysis of US Department of Energy Engine Targets Compared to Existing Engine Technologies. No. 2020-01-0835. SAE Technical Paper (2020)
22. Sun, Z., et al.: Enhancing hydrogen storage properties of  $MgH_2$  by transition metals and carbon materials: a brief review. *Front. Chem.* **8** (2020)
23. Wang, C.-Y., et al.: Observation and simulation of hydrogen storage via spillover. *Curr. Opin. Chem. Eng.* **21**, 116–121 (2018)
24. Lin, Y., Ding, F., Yakobson, B.I.: Hydrogen storage by spillover on graphene as a phase nucleation process. *Phys. Rev. B* **78**(4), 041402 (2008)

25. Skákalová, V., et al.: Chemical oxidation of graphite: evolution of the structure and properties. *J. Phys. Chem. C* **122**(1), 929–935 (2018)
26. Li, S., et al.: Hierarchically structured electrospinning nanofibers for catalysis and energy storage. *Compos. Commun.* **13**, 1–11 (2019)
27. Baburin, I.A., Seifert, G.: Hydrogen storage by physisorption in nanostructured graphene-based materials: simulations and experiments. *B07*, B11
28. Yildirim, T., Ciraci, S.: Titanium-decorated carbon nanotubes as a potential high-capacity hydrogen storage medium. *Phys. Rev. Lett.* **94**(17), 175501 (2005)
29. Yuan, L., et al.: Hydrogen storage capacity on Ti-decorated porous graphene: first-principles investigation. *Appl. Surf. Sci.* **434**, 843–849 (2018)
30. Fan, M., et al.: Recent progress in 2D or 3D N-doped graphene synthesis and the characterizations, properties, and modulations of N species. *J. Mater. Sci.* **51**(23), 10323–10349 (2016)
31. Bouša, D., et al.: Planar polyolefin nanostripes: perhydrogenated graphene. *Chem. A Eur. J.* **23**(49), 11961–11968 (2017)
32. Er, S., de Wijs, G.A., Brocks, G.: DFT study of planar boron sheets: a new template for hydrogen storage. *J. Phys. Chem. C* **113**(43), 18962–18967 (2009)
33. Lee, H., et al.: Calcium-decorated graphene-based nanostructures for hydrogen storage. *Nano Lett.* **10**(3), 793–798 (2010)
34. Anderson, R.J., et al.: NMR methods for characterizing the pore structures and hydrogen storage properties of microporous carbons. *J. Am. Chem. Soc.* **132**(25), 8618–8626 (2010)
35. Afif, A., et al.: Advanced materials and technologies for hybrid supercapacitors for energy storage—a review. *J. Energy Storage* **25**, 100852 (2019)
36. Stoller, M.D., et al.: Graphene-based ultracapacitors. *Nano Lett.* **8**(10), 3498–3502 (2008)
37. Wang, Y., et al.: Supercapacitor devices based on graphene materials. *J. Phys. Chem. C* **113**(30), 13103–13107 (2009)
38. Si, Y., Samulski, E.T.: Exfoliated graphene separated by platinum nanoparticles. *Chem. Mater.* **20**(21), 6792–6797 (2008)
39. Lu, Z., et al.: Superelastic hybrid CNT/graphene fibers for wearable energy storage. *Adv. Energy Mater.* **8**(8), 1702047 (2018)
40. Chen, S., et al.: Graphene oxide–MnO<sub>2</sub> nanocomposites for supercapacitors. *ACS Nano* **4**(5), 2822–2830 (2010)
41. Wang, H., et al.: Ni (OH)<sub>2</sub> nanoplates grown on graphene as advanced electrochemical pseudocapacitor materials. *J. Am. Chem. Soc.* **132**(21), 7472–7477 (2010)
42. Jeong, H.K., Jin, M., Ra, E.J., Sheem, K.Y., Han, G.H., Arepalli, S., Lee, Y.H.: *ACS Nano*. **4**, 1162 (2010). Crossref, ISI

# Nano-Minimum Quality Lubrication (NMQL) and Machining Characteristics of Surface Using Various Nanofluids in Different Machining Processes: A Computational Analysis



Anamika Tiwari, Deepak Agarwal, and Anurag Singh

**Abstract** The nanoparticles mixed at different concentration in basefluid are called nanofluid. By the addition of different nanoparticles with different concentration in different basefluid, we got the enhancement of various properties which we analyzed in this paper. In this article, we analyzed the nanoparticles ( $\text{Al}_2\text{O}_3$ , CuO and  $\text{TiO}_2$ ) at concentration (0%, 1%, 2%, 3%, 4%, 5% and 6 vol.%) into the basefluid (water) through MATLAB and obtained the different input parameters like thermal conductivity, specific heat, viscosity and density, and we got that during different parameter analysis different nanofluids show their property enhancement, hence we can use different nanoparticles during different machining process according to the properties we required for machining.

**Keywords** Thermal conductivity · Specific heat · Viscosity · Density · Concentration

## 1 Introduction

The utilization of conventional coolant happens in metal removal process so as to build efficiency, work quality and so on; however, we notice that traditional liquids just act oil yet decline in temperature did not happened and furthermore ordinary liquid produces poor impact on health of worker and environmental condition [1]. So for expanding the thermal conductivity rate, macro- or micro-sized particles are utilized in traditional liquid so these particles expansion in customary liquid diminished down the temperature yet some issue emerges with them which are as follows:

---

A. Tiwari (✉) · D. Agarwal · A. Singh  
IET, Dr. Rammanohar, Lohia Avadh University, Ayodhya, U.P., India  
e-mail: [lncs@springer.com](mailto:lncs@springer.com)

© The Author(s), under exclusive license to Springer Nature Singapore Pte Ltd. 2021  
A. Patnaik et al. (eds.), *Advances in Materials Processing and Manufacturing Applications*, Lecture Notes in Mechanical Engineering,  
[https://doi.org/10.1007/978-981-16-0909-1\\_18](https://doi.org/10.1007/978-981-16-0909-1_18)

- Clogging of particles among instrument and workpiece interface [2].
- Pressure drop and rough surface completion because of stopped up particles among device and workpiece [3].

So the need of nanometered size ( $<10^{-9}$ ) particles emerges as they are exceptionally little in size, consequently no clogging and better surface finish obtained [4]. The expansion in thermal conductivity relies upon nanoparticles materials, sizes and focuses. Nanoparticles have increasingly surface region-to-volume ratio; 1 nm round particles have surface zone-to-volume proportion 1000 times more prominent than that of 1  $\mu\text{m}$  particles [5]. Molecule size is the major physical boundary in nanofluids, since it tends to be utilized to adjust the nanofluid warm properties just as the suspension security of nanoparticles. Subsequently, nanofluids can ready to stream flow through small-scale channels with the spattering of nanoparticles [6]. The nano-suspensions show high thermal conductivity which is major because of upgraded convection between the nanoparticles and base fluid surfaces. Another high potential advantage is that the nanoparticles have lower measurements so that the scattered nanoparticles by all accounts are like a base liquid particle in suspension [7].

## 2 Analysis

### 2.1 Specific Parameters

We selected different parameters for the analysis of the nanofluid as follows (Table 1).

**Table 1** Specifications for analysis

Specification	Value
Temperature	20 °C or 293 K
n (empirical scaling factor)	3 (spherical)
d (average diameter of nanoparticles)	50–75 nm
Mean velocity (v)	1 m/s
Concentration	0, 1, 2, 3, 4, 5 and 6%
Machining process	Grinding, milling, drilling, turning, etc.
Nanoparticle	$\text{Al}_2\text{O}_3$ , CuO, $\text{TiO}_2$
Basefluid	Water

## 2.2 Input Parameters

There are various input parameters which we are using for the analysis of nanofluid with different concentration of nanoparticles on basefluid such as thermal conductivity, specific heat, viscosity and density which is described along with the formula [8] as below (Table 2).

### Thermal Conductivity Enhancement

NPs have large surface area to volume so heat transfer rate is very high by combination of Cu, Al<sub>2</sub>O<sub>3</sub>, TiO<sub>2</sub> in basefluid like oils/water, etc. Thermal conductivity of nanofluids differs with the size, shape and material sort of nanoparticles [9]. Besides, nanofluids with circular shape nanoparticles show a littler increment in thermal conductivity contrasted and the nanofluids having round and hollow (nano-pole or cylinder) nanoparticles [10].

The thermal conductivity of a nanofluid is given by [11]:

$$k_{nf} = k_f \left[ \frac{k_p + (n - 1)k_f - (n - 1)\phi(k_f - k_p)}{k_p + (n - 1)k_f + \phi(k_f - k_p)} \right] \tag{1}$$

where

$k_{nf}$  = nanofluid thermal conductivity,

$k_f$  = base fluid thermal conductivity,

$k_p$  = bulk solid particle thermal conductivity,

$\phi$  = particle volume fraction, and

$n$  = empirical scaling factor. Spherical nanoparticles are used in this study for which  $n = 3$  [12].

For our analysis,

$k_f = 0.613$  (W/m-K)

$n = 3$

$k_p = 40$  [Al<sub>2</sub>O<sub>3</sub>],  $k_p = 33$  [CuO],  $k_p = 8.4$  [TiO<sub>2</sub>] in (W/m-K)

$k_{nf}$  is calculated in the below table by the formula above (Table 3).

**Table 2** Thermophysical properties of basefluid and nanofluid at 20 °C or 293 K

Property	Basefluid	Nanoparticles		
	Water	Al <sub>2</sub> O <sub>3</sub>	CuO	TiO <sub>2</sub>
Thermal conductivity (W/m-K)	0.613	40	33	8.4
Density (kg/m <sup>3</sup> )	997.1	3960	6000	4230
Specific heat (J/kg-K)	4179	773	551	692
Viscosity (kg/ms)	$8.91 \times 10^{-4}$	–	–	–

**Table 3** Thermal conductivity properties of various nanofluids with varying concentrations

Nanofluid	Thermal conductivity (W/m-K)		
	Water + Al <sub>2</sub> O <sub>3</sub> ( $\varphi$ )	Water + CuO( $\varphi$ )	Water + TiO <sub>2</sub> ( $\varphi$ )
[Water + $\varphi$ (value)]			
Water + 0%	0.613	0.613	0.613
Water + 1%	0.630	0.630	0.628
Water + 2%	0.649	0.648	0.643
Water + 3%	0.667	0.667	0.659
Water + 4%	0.686	0.685	0.674
Water + 5%	0.705	0.704	0.690
Water + 6%	0.725	0.724	0.707

### Density

The effective density of nanofluids is given by [13]

$$\rho_{nf} = (1 - \varphi)\rho_f + \varphi\rho_s \quad (2)$$

where

$\rho_{nf}$  is the nanofluid density.

$\rho_s$  and  $\rho_f$  are the densities of the solid particles and base fluid, respectively.

For our analysis,

$$\rho_f = 997.1 \text{ kg/m}^3$$

$$\rho_s = 3960 \text{ [Al}_2\text{O}_3\text{]}, \rho_s = 6000 \text{ [CuO]}, \rho_s = 4230 \text{ [TiO}_2\text{]} \text{ in kg/m}^3$$

$\rho_{nf}$  is calculated in the below table by the formula above (Table 4).

**Table 4** Density properties of various nanofluids with varying concentrations

Nanofluid	Density (kg/m <sup>3</sup> )		
	Water + Al <sub>2</sub> O <sub>3</sub> ( $\varphi$ )	Water + CuO( $\varphi$ )	Water + TiO <sub>2</sub> ( $\varphi$ )
[Water + $\varphi$ (value)]			
Water + 0%	997.1	997.1	997.1
Water + 1%	1026.73	1047.13	1029.43
Water + 2%	1056.36	1097.16	1061.76
Water + 3%	1085.99	1147.19	1094.09
Water + 4%	1115.62	1197.22	1126.42
Water + 5%	1145.24	1247.24	1158.74
Water + 6%	1174.87	1297.28	1191.07

**Specific Heat**

Specific heat capacities of nanofluids are different from that of base fluid such as water and oil and vary with the size, shape, dimension and volume concentration of nanoparticles.

The specific heat of nanofluids,  $C_{pnf}$  [14], can be calculated using equation as

$$C_{pnf} = \phi C_{ps} + (1 - \phi)C_{pf} \tag{3}$$

where

$C_{ps}$  = specific heat of solid particles and

$C_{pf}$  = specific heat of base fluid.

For our analysis,

$C_{pf} = 4179$  (J/kg-K)

$C_{ps} = 773$  [ $Al_2O_3$ ],  $C_{ps} = 551$  [CuO],  $C_{ps} = 692$  [ $TiO_2$ ] in (J/kg-K)

$C_{pnf}$  is calculated in the below table by the formula above (Table 5).

**Viscosity**

The particle suspension viscosity is obtained by the formula given as [15]

$$\mu_r = \mu_{nf} / \mu_{bf} = (1 + 2.5 \phi) \tag{4}$$

where

$\phi$  = particle volume fraction and

$\mu$  = fluid dynamic viscosity;

the subscripts bf, nf and r refer, respectively, to the basefluid, the nanofluid and to the ‘nanofluid-to-base fluid’ ratio of viscosity.

**Table 5** Specific heat properties of various nanofluids with varying concentrations

Nanofluid	Specific heat (J/kg-K)		
	Water + $Al_2O_3(\phi)$	Water + $CuO(\phi)$	Water + $TiO_2(\phi)$
Water + 0%	4179.00	4179.00	4179.00
Water + 1%	4144.94	4142.72	4144.13
Water + 2%	4110.88	4106.44	4109.26
Water + 3%	4076.82	4070.16	4074.39
Water + 4%	4042.76	4033.88	4039.52
Water + 5%	4008.70	3997.60	4004.65
Water + 6%	3974.64	3961.32	3969.78

**Table 6** Viscosity properties of various nanofluids with varying concentrations

Nanofluid	Viscosity (kg/m-s)		
	Water + Al <sub>2</sub> O <sub>3</sub> ( $\varphi$ )	Water + CuO( $\varphi$ )	Water + TiO <sub>2</sub> ( $\varphi$ )
Water + 0%	$8.91 \times 10^{-4}$	$8.91 \times 10^{-4}$	$8.91 \times 10^{-4}$
Water + 1%	$9.13 \times 10^{-4}$	$9.13 \times 10^{-4}$	$9.13 \times 10^{-4}$
Water + 2%	$9.35 \times 10^{-4}$	$9.35 \times 10^{-4}$	$9.35 \times 10^{-4}$
Water + 3%	$9.58 \times 10^{-4}$	$9.58 \times 10^{-4}$	$9.58 \times 10^{-4}$
Water + 4%	$9.80 \times 10^{-4}$	$9.80 \times 10^{-4}$	$9.80 \times 10^{-4}$
Water + 5%	$1.00 \times 10^{-3}$	$1.00 \times 10^{-3}$	$1.00 \times 10^{-3}$
Water + 6%	$1.02 \times 10^{-3}$	$1.02 \times 10^{-3}$	$1.02 \times 10^{-3}$

For our analysis,

$$\mu_{bf} = 8.91 \times 10^{-4} \text{ (kg/m-s) [16]}$$

$\mu_{nf}$  is calculated in the below table by the formula above (Table 6).

The analysis of the nanofluid is done through MATLAB in order to obtain the graph of different concentration of nanoparticles in basefluid in order to get the nanofluid and their various parameters are measured such as

- Thermal conductivity,
- Specific heat,
- Viscosity and
- Density

### 3 MATLAB Program

```

fprintf('Enter Your Choice')
fprintf('\n 1 : for AL2O3')
fprintf('\n 2 : for CuO')
fprintf('\n 3 : for TiO2')
n = input('\nEnter a number: ');
switch n
case 1
    %Thermal Conductivity
    kp=40;
    kf = 0.613;
    P = input('\n Enter the value of Phi');
    knf = kf*[(kp + 2*kf - 2*P*(kf-kp))/(kp + 2*kf + P*(kf-kp))];

    %Specific Heat
    Cf = 4179;
    Cp = 773;
    Cnf = P*Cp + (1-P)*Cf;

```



```

%Viscosity
Uf= 0.000891;
Unf = Uf*(1 + 2.5*P);

%Density
Pf=997.1;
Pp=3960;
Den = (1-P)*Pf +P*Pp;

fprintf('Thermophysical Properties of Base fluids and Nano Particles at 293K or 20C for
AL2O3; Phi = %f\n', P)
fprintf('Thermal Conductivity = %f\n', knf)
fprintf('Specific Heat = %f\n', Cnf)
fprintf('Viscosity = %f\n', Unf)
fprintf('Density = %f\n', Den)
case 2
%Thermal Conductivity
kp=33
kf = 0.613
P = input('\n Enter the value of Phi')
knf = kf*[(kp + 2*kf - 2*P*(kf-kp))/(kp + 2*kf + P*(kf-kp))];

% Specific Heat
Cf = 4179
Cp = 551
Cnf = P*Cp + (1-P)*Cf

%Viscosity
Uf= 0.000891
Unf = Uf*(1 + 2.5*P)

%Density
Pf=997.1
Pp=6000
Den = (1-P)*Pf +P*Pp

fprintf('Thermophysical Properties of Base fluids and Nano Particles at 293K or 20C for CuO;
Phi = %f\n', P)
fprintf('Thermal Conductivity = %f\n', knf)
fprintf('Specific Heat = %f\n', Cnf)
fprintf('Viscosity = %f\n', Unf)
fprintf('Density = %f\n', Den)

case 3
%Thermal Conductivity
kp=8.4
kf = 0.613
P = input('\n Enter the value of Phi')
knf = kf*[(kp + 2*kf - 2*P*(kf-kp))/(kp + 2*kf + P*(kf-kp))];

% Specific Heat
Cf = 4179
Cp = 692
Cnf = P*Cp + (1-P)*Cf

```

```

%Viscosity
Uf= 0.000891
Unf= Uf*(1 + 2.5*P)

%Density
Pf=997.1
Pp=6000
Den = (1-P)*Pf +P*Pp

fprintf('Thermophysical Properties of Base fluids and Nano Particles at 293K or 20C for TiO2;
Phi = %f\n', P)
fprintf('Thermal Conductivity = %f\n', knf)
fprintf('Specific Heat = %f\n', Cnf)
fprintf('Viscosity = %f\n', Unf)
fprintf('Density = %f\n', Den)

otherwise
disp('Wrong Choice')
end

```

## 4 Result and Discussion

### 4.1 Thermal Conductivity Graph for $Al_2O_3$ , $CuO$ and $TiO_2$

Through the MATLAB analysis, we are getting following graph for three nano-fluids using the thermal conductivity formula and graph is shown as below.

At 0% nanoparticles in basefluid (water), the thermal conductivity is 0.613 (W/m-K), and as we are increasing the concentration of nanoparticles in basefluid we are getting that the thermal conductivity increases and at 6% we are getting the thermal conductivity of  $Al_2O_3$  nanofluid as 0.725 (W/m-K),  $CuO$  nanofluid as 0.724 (W/m-K) and  $TiO_2$  nanofluid as 0.707 (W/m-K).

From the above information and below graph of Fig. 1, we are getting that the highest thermal conductivity is obtained for  $Al_2O_3$ , hence it is the best among all three for dissipating heat from machine zone as coolant and lubricant.

### 4.2 Specific Heat Graph for $Al_2O_3$ , $CuO$ and $TiO_2$

Through the MATLAB analysis, we are getting following graph for three nano-fluids using the specific heat formula and graph is shown as below.

At 0% nanoparticles in basefluid (water), the specific heat is 4179 (J/kg-K), and as we are increasing the concentration of nanoparticles in basefluid we are getting that the specific heat decreases and at 6% we are getting the specific heat of  $Al_2O_3$

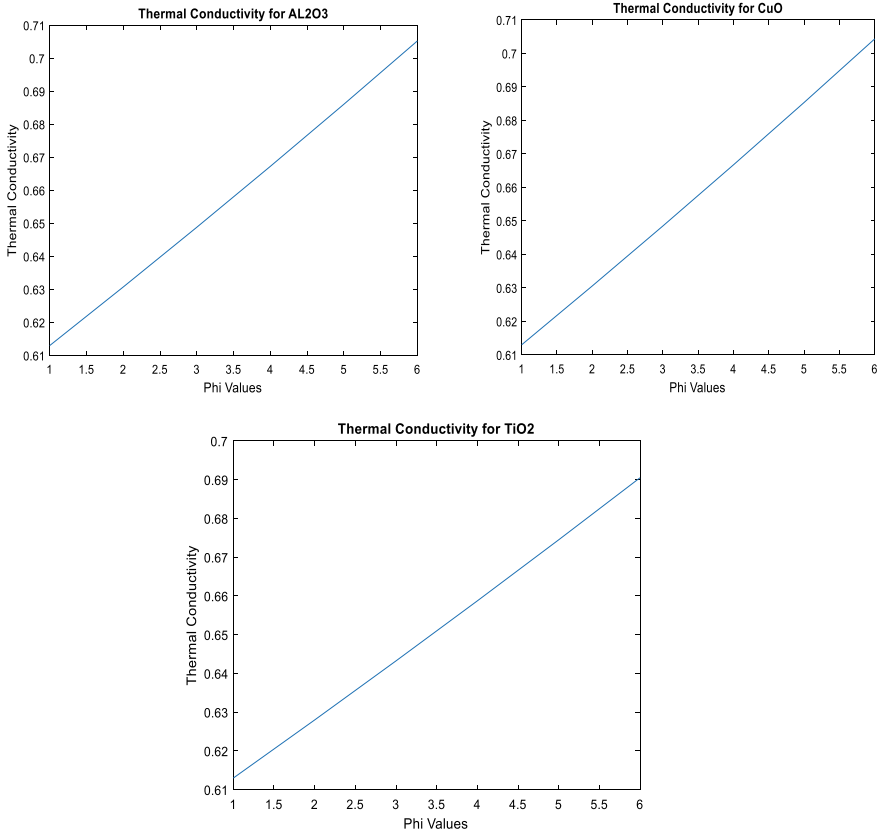


**Fig. 1** Thermal conductivity graph at different  $\phi$  values for AL<sub>2</sub>O<sub>3</sub>, CuO and TiO<sub>2</sub>, respectively

nanofluid as 3974.64 (J/kg-K), CuO nanofluid as 3961.32 (J/kg-K) and TiO<sub>2</sub> nanofluid as 3969.78 (J/kg-K). Measurements show that the specific heat value decreases as the volumetric concentration of nanoparticles increases. This decrease is compatible with the lower specific heat of particles being added to the base fluid. The specific heat increases with an increase in temperature [17].

From the above information and from below graph of Fig. 2, we are getting that the lowest specific heat is obtained for CuO, hence CuO is the best among all three for dissipating heat from machining zone as coolant and lubricant.

### 4.3 Density Graph for Al<sub>2</sub>O<sub>3</sub>, CuO and TiO<sub>2</sub>

Through the MATLAB analysis, we are getting following graph for three nano-fluids using the density formula and graph is shown as below.

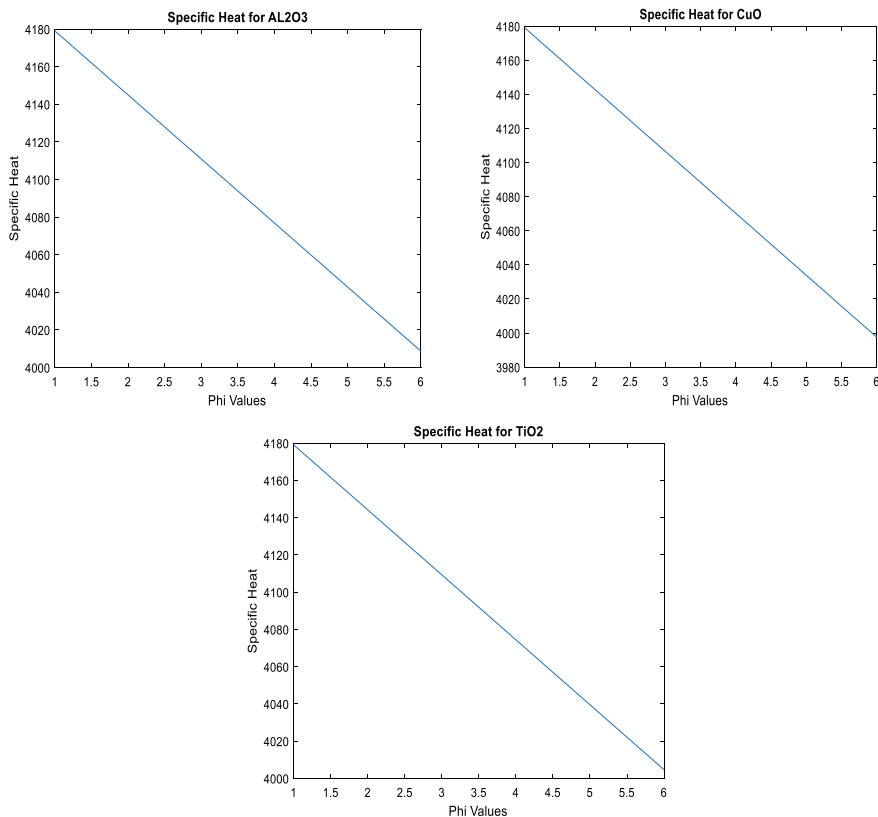


**Fig. 2** Specific heat graph at different  $\phi$  values for AL<sub>2</sub>O<sub>3</sub>, CuO and TiO<sub>2</sub>, respectively

At 0% nanoparticles in basefluid (water), the density is 997.1 kg/m<sup>3</sup>, and as we are increasing the concentration of nanoparticles in basefluid we are getting that the density increases and at 6% we are getting the density of AL<sub>2</sub>O<sub>3</sub> nanofluid as 1174.87 kg/m<sup>3</sup>, CuO nanofluid as 1297.28 kg/m<sup>3</sup> and TiO<sub>2</sub> nanofluid as 1191.07 kg/m<sup>3</sup>. The density of nanofluids, for example, is a thermophysical property that has received very limited research attention. The importance of density is that it is directly related to the Reynolds number, the Nusselt number, pressure loss and the Darcy friction factor. As a result, the heat transfer coefficient, which quantifies the effectiveness of heat transfer, depends on density (among other properties). In heat transfer analysis, the heat transfer coefficient generally increases with increasing density, and the stability of nanofluid suspensions is affected by density [18].

From the above information and from below graph of Fig. 3, we are getting that the highest density is obtained for CuO, hence CuO is the best among all three for dissipating heat from machining zone as coolant and lubricant.

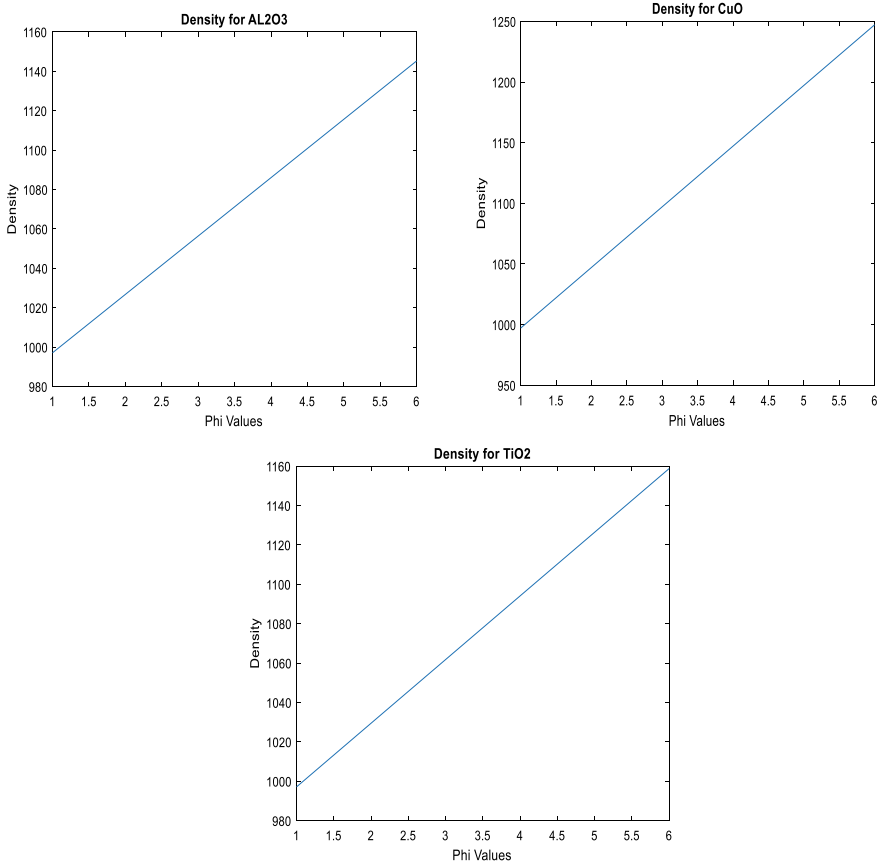


**Fig. 3** Density graph at different  $\phi$  values for  $Al_2O_3$ , CuO and  $TiO_2$ , respectively

#### 4.4 Viscosity Graph for $Al_2O_3$ , CuO and $TiO_2$

Through the MATLAB analysis, we are getting following graph for three nano-fluids using the Viscosity formula and graph is shown as below.

At 0% nanoparticles in basefluid (water), the thermal conductivity is  $8.91 \times 10^{-4}$  (kg/m-s), and as we are increasing the concentration of nanoparticles in basefluid we are getting that the thermal conductivity increases and at 6% we are getting the thermal conductivity of  $Al_2O_3$  nanofluid, CuO nanofluid and  $TiO_2$  nanofluid as  $1.02 \times 10^{-3}$  (kg/m-s). A higher concentration nanofluid has a larger relative viscosity because the 5 and 6 vol.% nanofluid has a higher possibility for forming agglomerates in comparison with the 1 vol.% nanofluid [19].

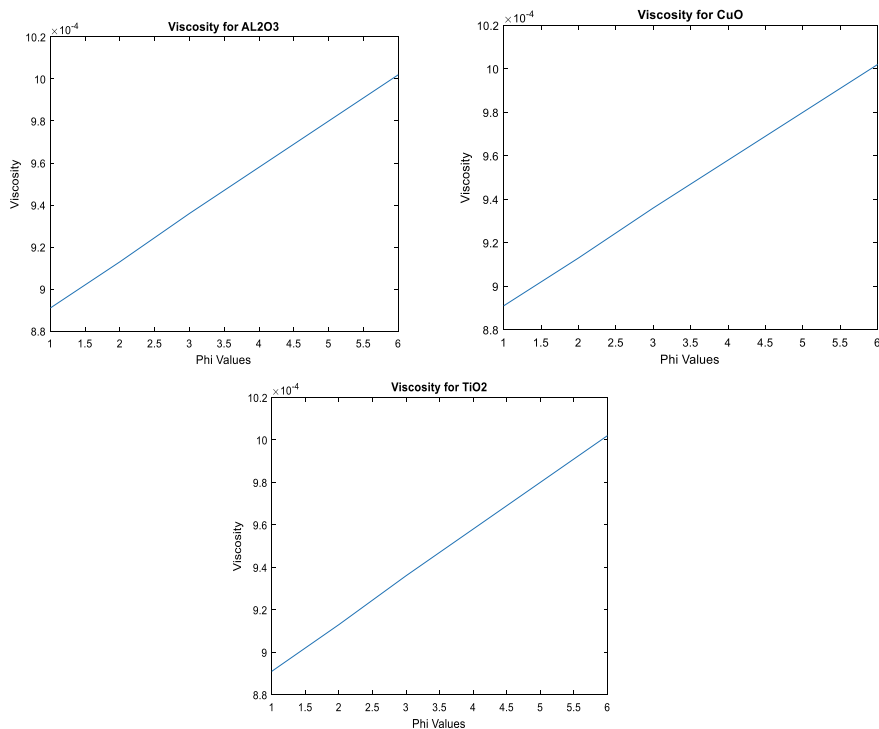


**Fig. 4** Viscosity graph at different  $\phi$  values for AL<sub>2</sub>O<sub>3</sub>, CuO and TiO<sub>2</sub>, respectively

From the above information and from below graph of Fig. 4, we are getting that the viscosity is the factor that only depends on basefluid viscosity and concentration of nanoparticles as we are increasing the concentration, viscosity increases. At 1–5 vol.% nanofluid, they are non-Newtonian fluid and after 5% they follow Newtonian fluid property.

## 5 Conclusion

From analysis of different nanofluid (AL<sub>2</sub>O<sub>3</sub>, CuO, TiO<sub>2</sub>) at different concentration through MATLAB, we concluded various parameters such as thermal conductivity, specific heat, viscosity and density as follows:

- The highest thermal conductivity is obtained for AL<sub>2</sub>O<sub>3</sub>, hence AL<sub>2</sub>O<sub>3</sub> is the best among all three (AL<sub>2</sub>O<sub>3</sub>, CuO, TiO<sub>2</sub>) for dissipating heat from machining zone as coolant and lubricant.

- The heat transfer coefficient generally increases with increasing density, and the stability of nanofluid suspensions is affected by density and through analysis highest value obtained for CuO.
- The viscosity is the factor that only depends on basefluid viscosity and concentration of nanoparticles as we are increasing the concentration, viscosity increases. At 1–5 vol.% nanofluid, they are non-Newtonian fluid and after 5% they follow Newtonian fluid property.
- 5–6 vol.% exhibits best performance while further increasing of nanoparticles concentration in basefluid worsened the performance.
- Since nanofluid lubrication decreases the consumption of cutting fluid as well as the cutting energy or cutting power while improving surface quality, so this technique leads to environmental-friendly green manufacturing or sustainable manufacturing.

## 6 Scope for Future Work

By the use of cooling fluid/nanofluid in machining, workpiece gets good surface finish due to various property enhancements like high thermal conductivity, good lubricating property and rheological properties of nanofluid.

- But for future purpose, the properties can be enhanced by changing various parameters like NP's size, shape, concentration, flow rate, spray nozzle angle and distance of spraying.
- The disadvantages of using nanofluids are that it gives negative impact to environment and worker's health and cost is also high. So, scope is there for researchers to develop new type/modified nanofluid which are eco-friendly and less costly.
- Another promising area is to make/test the combination of different types of nanoparticles (hybrid nanoparticles) in order to enhance the results regarding metal removal rate, surface finish, thermal conductivity and various other properties.

**Acknowledgements** We would like to thanks to Professor Raj Kumar Tiwari for his expert advice and Mrs. Shail Tiwari for her encouragement during preparation of the review paper.

## References

1. Alade, I.O., Oyehan, T.A., Popoola, I.K., Olatunji, S.O., Bagudu, A.: Modeling thermal conductivity enhancement of metal and metallic oxide nanofluids using support vector regression. *Adv. Powder Technol.* **29**(1), 157–167 (2018)
2. Kumar, M.P., Kanth, V.K., Ramki, A., Jagadish, K.E.: *Experimental Investigation of Active Flux Coatings on AA-6082 Using A-TIG Welding Process BT—Recent Advances in Material Sciences*. Springer, Singapore (2019)

3. Nazari, M.A., Ahmadi, M.H., Sadeghzadeh, M., Shafii, M.B., Goodarzi, M.: A review on application of nanofluid in various types of heat pipes. *J. Cent. South Univ.* **26**(5), 1021–1041 (2019)
4. Ali, M.A.M., Khalil, A.N.M., Azmi, A.I.: Effect of minimum quantity lubricant of  $Al_2O_3$  nanoparticle with SDBS on surface roughness during turning of mild steel. *Adv. Mater. Res.* **1119**, 75–79 (2015)
5. Sharma, A.K., Tiwari, A.K.: Rheological behavior of nanofluids: a review. *Renew. Sustainable Energy Rev.* (2016)
6. Sharma, B.S.K., Gupta, S.M.: Preparation and evaluation of stable nanofluids for heat transfer application: a review. *Exp. Therm. Fluid Sci.* **79**, 202–212 (2016)
7. Behera, B.C., Setti, C.D., Ghosh, S., Rao, P.V.: Spreadability studies of metal working fluids on tool surface and its impact on minimum amount cooling and lubrication turning. *J. Mater. Process. Technol.* **244**, 1–16 (2017)
8. Srikant, R.R., Rao, D.N., Subrahmanyam, M.S., Krishna, P.V.: Applicability of cutting fluids with nanoparticle inclusion as coolants in machining. *Proc. Inst. Mech. Eng. Part J J. Eng. Tribol.* **223**(2), 221–225 (2009)
9. Bag, R., Panda, A., Sahoo, A.K., Kumar, R.: A brief study on effects of nano cutting fluids in hard turning of AISI 4340 steel. *Mater. Today Proc.* (2020)
10. Pryazhnikov, M.I., Minakov, A.V., Rudyak, V.Y., Guzei, D.V.: Thermal conductivity measurements of nanofluids. *Int. J. Heat Mass Transf.* **104**, 1275–1282 (2017)
11. Sen, B., Mia, M., Gupta, M.K., Rahman, M.A., Mandal, U.K., Mondal, S.P.: Influence of  $Al_2O_3$  and palm oil–mixed nano–fluid on machining performances of Inconel-690: if-then rules–based FIS model in eco-benign milling. *Int. J. Adv. Manuf. Technol.* **103**(9–12), 3389–3403 (2019)
12. Najiha, M.S., Rahman, M.M., Kadirgama, K.: Performance of water-based  $TiO_2$  nanofluid during the minimum quantity lubrication machining of aluminium alloy, AA6061-T6, vol. 135. Elsevier Ltd (2016)
13. Dhinesh Kumar, D., Valan Arasu, A.: A comprehensive review of preparation, characterization, properties and stability of hybrid nanofluids. *Renew. Sustain. Energy Rev.* **81**(2017), 1669–1689 (2018)
14. Hegab, H., Kishawy, H.A., Umer, U., Mohany, A.: A model for machining with nano-additives based minimum quantity lubrication. *Int. J. Adv. Manuf. Technol.* **102**(5–8), 2013–2028 (2019)
15. Wang, Y., et al.: Experimental evaluation on tribological performance of the wheel/workpiece interface in minimum quantity lubrication grinding with different concentrations of  $Al_2O_3$  nanofluids. *J. Clean. Prod.* **142**, 3571–3583 (2017)
16. Zhang, Y., Li, C., Jia, D., Zhang, D., Zhang, X.: Experimental evaluation of  $MoS_2$  nanoparticles in jet MQL grinding with different types of vegetable oil as base oil. *J. Clean. Prod.* **87**(C), 930–940 (2015)
17. Sharma, A.K., Tiwari, A.K., Dixit, A.R.: Characterization of  $TiO_2$ ,  $Al_2O_3$  and  $SiO_2$  nanoparticle based cutting fluids. *Mater. Today Proc.* **3**(6), 1890–1898 (2016)
18. Chaudhari, S.S., Chakule, R.R., Talmale, P.S.: Experimental study of heat transfer characteristics of  $Al_2O_3$  and CuO nanofluids for machining application. *Mater. Today Proc.* **18**, 788–797 (2019)
19. Das, A., Pradhan, O., Patel, S.K., Das, S.R., Biswal, B.B.: Performance appraisal of various nanofluids during hard machining of AISI 4340 steel. *J. Manuf. Process.* **46**(September), 248–270 (2019)



# Framework and Case Study for Optimizing Target Value of a Process Using Taguchi's Asymmetric Loss Function



Anoop Pandey and Manish Chaturvedi

**Abstract** In manufacturing sector, process designing for meeting the target value, so as to have a trade-off between the scrap and rework, is generally carried out by hit and trial method. In the present study, a framework for implementing the process has been proposed. The framework proposed here is focused to obtain the optimized value of the process target designated by 'm' in Taguchi's loss function through a CAIV cycle of data collection, analysis, implementation, and validation. A case study of piston ring manufacturing company is also given in the study to explain the proposed framework in detail. It is observed that on systematically implementing of the framework using Taguchi's quadratic loss function, a balance between loss due to scrap and loss due to rework was established. Twenty batches of the rings were further inspected for the average loss incurred per batch which brought down the average loss value for manufacturing of pistons by almost 14% per batch.

**Keywords** Asymmetric loss function • Scrap and rework cost • Optimizing average loss value • Manufacturing industry

## 1 Introduction

Generally, 'Nominal the Best' loss function suits to the most of the manufacturing processes owing to the type of tolerances given by the designer. While using this function for process design, most of the designers ignore the asymmetric nature of the curve pertaining to the difference between rework and scrap cost. This results in high losses either because of scrap or of rework [1]. A trade-off between these can

---

A. Pandey (✉)  
ABES Engineering College, Ghaziabad, Uttar Pradesh 201009, India  
e-mail: [anoop.pandey@abes.ac.in](mailto:anoop.pandey@abes.ac.in)

M. Chaturvedi  
Department of Mechanical Engineering, University Engineering College,  
Rajasthan Technical University, Kota, Rajasthan 324010, India

be established by optimizing the total loss function suggested by Taguchi [2]. The function finds detailed application in vivid sectors of engineering right from design and development stage to manufacturing, operation, supplier evaluation, etc. An optimum mean value of the process can be determined considering quality loss and cost related to manufacturing [3] and a tolerance design which is unbalanced in nature [4, 5]. The Taguchi's loss function is also widely used for determining optimum process parameters and tolerances with suggestion related to inspection plans during the design stage of a product [6]. The function has also been used in conjunction with analytical hierarchy process and VIKOR for supplier selection [7] and airports evaluation [8], respectively. The function has also been effectively used in quality control and management by designing economic control charts [9].

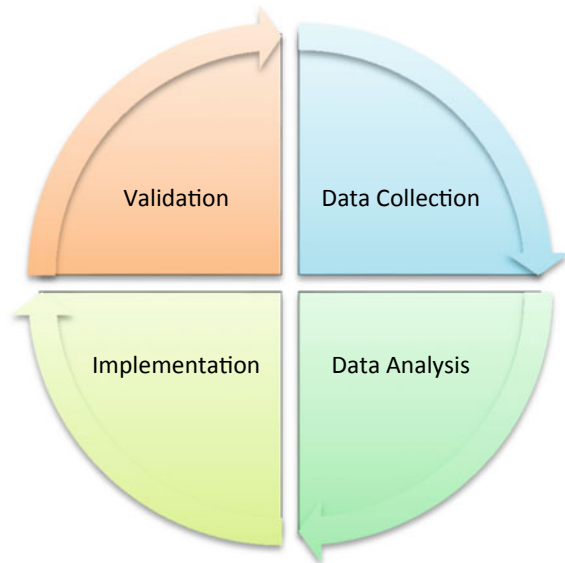
The present study is about proposing a generic framework which suits optimizing the Taguchi's loss function cost pertaining to asymmetric behaviour of the curve in manufacturing industry. A case related to manufacturing of piston rings in a leading autocomponent manufacturing unit located in UP, India, is presented with the approach mentioned in the suggested framework.

## 2 Methodology

The four-step framework cycle 'CAIV' for using Taguchi's loss function to optimize the total loss is shown in Fig. 1.

**The first step** of the cycle deals with collection of data related to the process using tools like process flowcharts, specification limits as the voice of customer,

Fig. 1 CAIV cycle



process capability, manufacturing and measuring capabilities, value stream mapping, etc. This data is used to estimate the rework (R) and scrap cost (S) yielded by the process through existing process values and parameters.

In the **second step**, analysis of the data is done by plotting different values of R corresponding to loss yielded on the right side of the target value ' $m$ '. Similarly, the value of S corresponding to the loss yielded is plotted on the left side of the target value ' $m$ ' and analysed. Subsequently, a trend line of required degree is fitted on the curve using MS EXCEL. Generally, a second-order polynomial is chosen as it relates with the quadratic loss function suggested by Taguchi. Finally, the equation of the trend line obtained is analysed for attaining the minimum value of loss function by obtaining its second-order derivative and checking for its positive value. This gives the revised value of the target ' $m$ ' as ' $m_{\text{revised}}$ '.

The **third step** deals with implementing the  $m_{\text{revised}}$  in the process by making due and necessary adjustments in the process and parameters affecting the target value. The effect of  $m_{\text{revised}}$  is also noted in the step.

The **fourth step** is for checking the certainty of the obtained results with the help of hypothesis testing.

Following are the sub-steps of the framework.

- Data collection:
  - Existing process values and parameters
  - Rework cost (R) estimation
  - Scrap cost (S) estimation
- Data analysis
  - Plotting 'R' and 'S' on Taguchi's Loss Function template
  - Trend line fitting using excel and checking accuracy of trend line and obtaining corresponding equation
  - Analysing trend line equation for condition of minima for loss function and obtaining revised value of the target ' $m$ '
- Implementation
  - Setting revised ' $m$ ' as the process target
- Validation
  - Through hypothesis testing.

### 3 Piston Ring Manufacturing Case

The piston rings used in IC engines are crucial components of an engine. The critical-to-quality (CTQ) characteristics of these rings are their thickness along with the diameters [10]. In a study conducted by Anoop Pandey and Harsh Vishwakarma

in 2020 for reducing the rejection rate of piston rings [11], QC tools were used to improve the existing process to overcome the problem of rejection of batches of piston rings. But the overall loss being yielded by the process was not optimized in the study.

**Data Collection:**

Following data was collected from the operations department of the company:

- Batch size of piston rings = 300 pieces
- Permissible piston ring thickness value (Specification limit as VOC): 2.9 + 0.1 mm
- The detailed manufacturing process of the piston rings
- Manufacturing cost for one ring—Rs 5/piece
- Average rework cost (R) for one ring per unit thickness = 40% of manufacturing cost/mm = Rs 2/piece/mm
- Process target value ‘m’ = 2.9 mm, USL = 3.0 mm, and LSL = 2.8 mm
- Scrap cost per ring (S) = manufacturing cost by the point of scrapping = Rs 5/ piece
- Total loss = loss due to rework + loss due to scrap
- Average number of rings reworked per batch = 12 pieces per batch
- Average number of rings scrapped per batch = 8 pieces per batch
- Total average loss per batch = 12 \* 2 + 8 \* 5 = 64 Rs per batch.

**Data Analysis:**

It can be understood from the Taguchi’s loss function graph that the point P corresponds to the target value on x-axis and zero loss on y-axis. Similarly, the coordinates for all the other points along with point P are shown in Table 1.

The points P, A, B, and C were plotted using MS EXCEL line graph and then a 2° polynomial trend line was imposed on the graph shown in Fig. 2. The equation of the 2° polynomial trend line was also obtained shown in Eq. 1.

$$y = 1.3x^2 - 7.86x + 11.3 = k(x - m)^2 \tag{1}$$

where

y: the average loss function (the dependent variable)

x: the CTQ characteristic dimension (here piston ring thickness).

**Table 1** Description and coordinate values of the points

Point	Description	Coordinates
P	(target value, loss yielded)	(2.9, 0)
A	(observed dimension, loss yielded)	(3, 2 * 0.1) = (3, 0.2)
B	(observed dimension, loss yielded)	(3.1, 2 * 0.2) = (3.1, 0.4)
C	(observed dimension, loss yielded)	(2.8, 5)

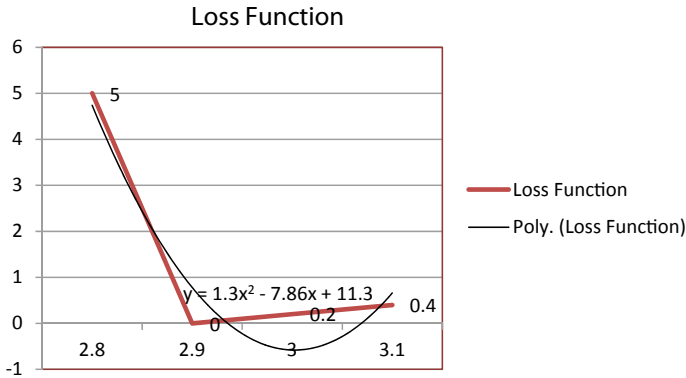


Fig. 2 Loss function

As is evident that the value of ‘ $x$ ’ for which the loss function ‘ $y$ ’ as obtained by the Eq. 1 gets minimized should be the target value for the process.

For this, the condition of minima for the Eq. 1 was checked by obtaining the positive value of the second derivative of the equation. This fact is also evident from the graph shown in Fig. 2.

Further the factors of Eq. 1 were obtained to get the two values of the process for which the loss function should be minimized. This is again evident from the graph that two real values of the factors can be obtained for the purpose as the curve is intersecting the  $y = 0$  line at two places for  $y > 0$ .

The two factors of the equation  $x_1$  and  $x_2$  obtained are 2.94 and 3.06, respectively. Since the second factor  $x_2$  is slightly above the USL thus is not considered for making it the target value of the process. While the first factor of 2.94 suits the design limitations for making the target of the process.

Thus,

$$m_{\text{revised}} = 2.94$$

## 4 Implementation

### 4.1 Result

Further the  $m_{\text{revised}}$  value was set as the target value for the process by making suitable adjustments in the process parameters and following data was collected from the operation department of the company to analyse the effect of changing the target value on the total loss function:

- Average number of rings reworked per batch = 15 pieces per batch
- Average number of rings scrapped per batch = 5 pieces per batch

- Total average loss per batch =  $15 * 2 + 8 * 5 = 55$  Rs per batch
- % reduction in average loss per batch =  $9/64 * 100 = 14.0625\%$ .

The above data was estimated with the help of 20 random samples of piston ring batches produced after revising the target value. Average loss per batch for all the 20 samples was obtained. The data shown in Table 2 obtained was analysed to observe that average loss per batch was Rs 55 with standard deviation of 2.1. **Sample Heading (Third Level)**. Only two levels of headings should be numbered. Lower-level headings remain unnumbered; they are formatted as run-in headings.

## 4.2 Validation

For validating the results through the modelling, t-student test was used.

**Null Hypothesis:** Total average loss due to scrap and rework before and after the adjustment of target value to  $m_{\text{revised}}$  is same.

$$H_0: \mu_y = \bar{x}$$

**Alternative Hypothesis:** Total average loss due to scrap and rework after the adjustment of target value to  $m_{\text{revised}}$  is lesser than that before the adjustment of target value to  $m_{\text{revised}}$ .

$$H_a: \bar{x} < \mu_y$$

**Table 2** Average loss per batch after adjusting the target value

Sample batch number	Average loss (Rs)	Sample batch number	Average loss (Rs)
1	58	2	54
3	58	4	54
5	54	6	55
7	58	8	52
9	53	10	52
11	54	12	57
13	58	14	54
15	54	16	54
17	53	18	54
19	58	20	56

Test statistics:

- $\mu_y = 64$  Rs
- $\bar{x} = 55$  Rs
- $\sigma_s = 2.1$
- $n = 20$
- degree of freedom = 19
- confidence level ( $\alpha$ ) = 95%.

Calculated  $t$  value is obtained using  $t$  test formula shown in Eq. 2

$$t = \frac{\bar{x} - \mu_0}{\frac{\sigma_s}{\sqrt{n}}} \tag{2}$$

This gives a value of  $-18.681$ .

Tabulated  $t$  value for a left-tailed test with confidence level of 95% and degree of freedom 19 is  $-1.729$ .

Since the calculated value falls in the critical region, null hypothesis was rejected and alternative hypothesis was accepted. Thus, it was validated that the total average loss due to scrap and rework after the adjustment of target value to  $m_{\text{revised}}$  is lesser than that before the adjustment of target value to  $m_{\text{revised}}$ .

## 5 Conclusion

Taguchi’s loss function equation is a proven and reliable method that can be used for optimizing the loss caused due to rework and scrap. The systematic framework of CAIV suggested in the paper with the help of a practical case study can help the users in implementing the same in manufacturing industries to reduce the overall loss. As observed the total average loss was brought down by more than 14% by implementing the technique systematically. Also the hypothesis testing validated the modality and credibility of the method.

## References

1. Zhang, J., Li, W., Wang, K., Jin, R.: Process adjustment with an asymmetric quality loss function. *J. Manuf. Syst.* **33**(1), 159–165 (2014). <https://doi.org/10.1016/j.jmsy.2013.10.001>
2. Pandey, A., Pandey, N.K., Ahmed, H.: Review of symmetricity in Taguchi’s loss function for performance measurement to monitor cost of rejection. *Trends Mech. Eng. Technol.* **9**(1), 59–68 (2019)
3. Chen, C.H., Lai, M.T.: Determining the optimum process mean based on quadratic quality loss function and rectifying inspection plan. *Eur. J. Oper. Res.* **182**(2), 755–763 (2007). <https://doi.org/10.1016/j.ejor.2006.09.035>

4. Li, M.H.C.: Unbalanced tolerance design and manufacturing setting with asymmetrical linear loss function. *Int. J. Adv. Manuf. Technol.* **20**(5), 334–340 (2002). <https://doi.org/10.1007/s001700200160>
5. Li, M.H.C.: Quality loss function based manufacturing process setting models for unbalanced tolerance design. *Int. J. Adv. Manuf. Technol.* **16**(1), 39–45 (2000). <https://doi.org/10.1007/PL00013130>
6. Jeang, A.: Optimal parameter and tolerance design with a complete inspection plan. *Int. J. Adv. Manuf. Technol.* **20**(2), 121–127 (2002). <https://doi.org/10.1007/s001700200133>
7. Liao, C.N., Kao, H.P.: Supplier selection model using Taguchi loss function, analytical hierarchy process and multi-choice goal programming. *Comput. Ind. Eng.* **58**(4), 571–577 (2010). <https://doi.org/10.1016/j.cie.2009.12.004>
8. Shojaei, P., Seyed Haeri, S.A., Mohammadi, S.: Airports evaluation and ranking model using Taguchi loss function, best-worst method and VIKOR technique. *J. Air Transp. Manag.* **68**, 4–13 (2018) <https://doi.org/10.1016/j.jairtraman.2017.05.006>
9. Alexander, S.M., Dillman, M.A., Usher, J.S., Damodaran, B.: Economic design of control charts using the Taguchi loss function. *Comput. Ind. Eng.* **28**(3), 671–679 (1995). [https://doi.org/10.1016/0360-8352\(94\)00219-D](https://doi.org/10.1016/0360-8352(94)00219-D)
10. Dunaevsky, V.V.: Analysis of distortions of cylinders and conformability of piston rings. *Tribol. Trans.* **33**(1), 33–40 (1990). <https://doi.org/10.1080/10402009008981927>
11. Anoop, P., Harsh, V.: Using qc tools to investigate the problem of rejection of piston rings—a case study of engine component manufacturing organization. *Int. J. Sci. Technol. Res.* **9**(4), 2410–2416 (2020)



# Analysis of Load Capacity of Functionally Graded Material Structures



Shubhatma Sharma and Manish Bhandari

**Abstract** Functionally graded materials are made up of predefined combination of ceramic and metals. The functionally graded materials (FGM) have been developed as high temperature-resistant and heat-resistant materials in space engineering and nuclear engineering. The FGM exhibits the resultant properties of ceramics and metal. The ceramics are involved for resistance in a high-temperature environment, while the metal contributes toward fracture toughness. The variation in strength and other properties may arise from geometry and other variable material properties like density. The studies related to energy-absorbing configurations in consideration with graded properties are of a great interest these days in research areas. These structural elements having graded properties have application in areas like vehicles, ships, safety devices and other load carrying members. The idea behind the functionally graded materials (FGM) is to have variable properties in a dimension following a particular law. The main objective of this paper is to understand the load capacity variations of such materials when graded in terms of different parameters such as diameter and thickness. In this research paper, a study is conducted on a FGM tapered frustum structure to identify the exact variation in the load capacities of such members when graded in terms of diameter, thickness, endurance strength, etc., in accordance with the empirical relations, the study on which has been previously conducted, to make it useful for designing of such members.

**Keywords** FGM · Load · Endurance strength

---

S. Sharma (✉) · M. Bhandari  
Department of Mechanical Engineering, MBM Engineering College, J.N.V University,  
Jodhpur 342003, India

© The Author(s), under exclusive license to Springer Nature Singapore Pte Ltd. 2021  
A. Patnaik et al. (eds.), *Advances in Materials Processing and Manufacturing Applications*, Lecture Notes in Mechanical Engineering,  
[https://doi.org/10.1007/978-981-16-0909-1\\_20](https://doi.org/10.1007/978-981-16-0909-1_20)

197

## 1 Introduction

Functionally graded materials are made up of predefined combination of ceramic and metals. The functionally graded materials (FGM) have been developed as high temperature-resistant and heat-resistant materials in space engineering and nuclear engineering. The FGM exhibits the resultant properties of ceramics and metal. The ceramics are involved for resistance in a high-temperature environment, while the metal contributes toward fracture toughness. The variation in strength and other properties may arise from geometry and other variable material properties like density. The fabrication of these materials might be a difficult task but can be accompanied with the advance of manufacturing science and process technology. With the advance of computer technology, numerical simulation and surrogate optimization methods have been widely applied in the crashworthiness analysis and design of tapered tubes. Mamalis and Johnson [1] considered thin-walled circular cylinders and frusta. Based on the compression tests of thin-walled cylinders and frusta, empirical expressions [2, 3] of the mean crushing load were firstly derived for frusta with various semi-apical angle by fitting the results of frusta with various crumpling modes. A theoretical model was proposed to analyze the extensional mode of the frusta, and the mean force was correlated with the yield stress of material, wall thickness, top diameter and semi-apical angle of the frusta. They applied axial compression and obtained results for the quasi-static crumpling of thin-walled circular cylinders and frusta. Mamalis et al. [4] studied extensible plastic collapse of thin-wall frusta as energy absorbers and obtained the energy-absorbing capacity results. Wierzbicki et al. [5] applied a two folding elements model to study the progressive crushing of tubes. The paper investigates the antiplane shear problem of a dissimilar interfacial circular crack in cylindrically anisotropic composites. Using the theory of analytical functions, a general solution based on a complex variable displacement function is obtained, which is similar to Lekhnitskii's stress potentials for rectilinearly anisotropic material. For some cases, the circular crack problems are reduced to Hilbert problems which are solved in a closed form. The first three-term asymptotic expansions of the near crack-tip stress field are given to identify the role of the curvature effect. The asymptotic solutions are further compared with exact solutions. These solutions show that the leading term exhibits an inverse square root stress singularity regardless of the material properties. In order to compare the stress field near the crack tip for a curved crack with that of a planar crack, a solution for a rectilinearly anisotropic body Nagel and Thambiratnam [6] investigated the energy absorption response of tapered thin-walled rectangular tubes numerically and compared with that of straight tubes. Influences of various factors including wall thickness, taper angle, impact mass and velocity were analyzed. Due to symmetry of the geometry, loading and deformation modes, only one quarter of each of the straight tubes, double-tapered tubes and frusta were modeled by applying suitable boundary conditions along each unloaded edge of the quarter model. Such modeling technique serves to reduce computation time and has been used in previous studies on the axial loading of thin-walled

square columns. In 2007, Avalle and Chiandussi [7] introduced a tapered initiator to a tubular component as the front structure or front longitudinal beam of a vehicle body. Liu [8] conducted optimization of tapered thin-walled square tubes. Besides improving load uniformity, another significant merit of tapered tubes is to resist oblique loads. In fact, the energy-absorbing structures are always subject to oblique or inclined loads in the real crashing events. The smaller end of tapered tubes is generally toward the striker since the relatively weak end is easier to deform and transfer less transverse force to bend the structure. Zhang et al. [9] applied dynamic crushing load based on the circle arc model and presented uniform and density graded cellular structures. Apart from the experimental analysis, a theoretical analysis was also performed to predict the mean crushing force of multi-cell tubes with graded thickness. Fan and Zou [10] found the effect of defects on dynamic crushing properties of functionally graded honeycomb structures. Lu et al. [11] considered axially graded tailor rolled square tubes and conducted axial crashing analysis for both wall thickness and material strength.

In the current paper, axial load capacity has been analyzed of a conical frusta made up of functionally graded material, and the results are presented in graphical form with the help of equations that are previously established. The main objective of this paper is to understand the load capacity variations of such materials when graded in terms of different parameters such as diameter and thickness.

## 2 Classification of FGM Structures

The functionally graded materials can be classified as [10].

### 2.1 *Thin-Walled Structures with Graded Diameter*

These are employed mainly to improve the load uniformity of absorber and to endure axial and oblique impact situations. This endurance strength is governed by various factors including wall thickness, taper angle, impact mass and velocity, etc., while in action, the smaller end of tapered tubes is generally toward the striker since it transfers less transverse force to the bend structure. The capacity of energy-absorbing component can be further increased by adopting multi-cell sections.

### 2.2 *Thin Wall Structure with Graded Thickness*

Unlike the former case, the materials with variable wall thickness are also employed for improving energy absorption capacity. The structures can be produced using

tailor rolled blank technology (TRB). The structures produced from TRB tend to have comparable performance with light mass. These structures can be of two types:

- (a) Wall thickness is linearly distributed along the cross section width called single surface gradient (SSG).
- (b) Wall thickness is linearly distributed along the height called double surface gradient (DSG). Apart from this, distribution of thickness can be linear as well as nonlinear, and even the distribution direction can be axial or transverse.

### ***2.3 Thin Wall Structures with Graded Properties***

In order to obtain energy-absorbing structure with graded properties like strength and hardness, tailor hot stamping (THS) is often used. By doing so, different mechanical properties would be shown by different regions of same part. The properties can be graded in accordance with the geometrical configuration and loading directions.

### ***2.4 Tailor Welded Wall Structure***

Above mentioned graded properties might not reach the maximum advantage and work only up to certain limit but if, metal sheets with different thickness, strength and material types joined, lead to a much more feasible and ideal design strategy. These can be joined by laser welding technique to have better stiffness, absorption and crash behavior by optimal combination of all above. In these structures, the deformation modes are more complex.

### ***2.5 Cellular Materials with Graded Properties***

The cellular materials having porous microstructure such as foams and honey combs, having light weight can also be considered for high performance parameters. The impact strength in such cases hugely depends on density. The performance of these graded foams can be further increased if the density difference between each layer is increased. Apart from foams, bamboo structure can also be employed as self-optimizing graded structure, which has its fibers non-uniformly distributed through the thickness. Metal hollow spheres (MHS), due to high uniformity of internal topologies, are also employed as special foam to improve low density metal materials. MHS foam can reduce plateau stress and is more advantageous in energy absorption. The other category of cellular materials with properties includes

honeycombs, showing different properties in different directions which results in more complex influence of density gradient and structure response. Sandwich structures with cross arranged graded honeycombs are best under blast loading when high density is applied in upper layer and also under high velocity impacts.

### 3 Methodology

The early studies on the axial crushing of tapered tubes were performed by Mamalis and Johnson [4] and Mamalis et al. [5] in the 1980s. Based on the compression tests of thin-walled cylinders and frusta, empirical expressions of the mean crushing load were firstly derived for frusta with various semi-apical angle by fitting the results of frusta with various crumpling modes. A theoretical model was then proposed to analyze the extensional mode of the frusta [10], and the mean force was correlated with the yield stress ‘Y’ of material, wall thickness ‘t’, top diameter ‘D’ and semi-apical angle ‘φ’ of the frusta. A schematic diagram for the dimensions of a thin-walled frustum is shown in Fig. 1. The FGM Frustram is made of zirconia (ceramic) and aluminum (metal) grading.

Considering a sample of tapered section having wall thickness ‘t’, top diameter ‘D’, semi-apical angle ‘φ’ and height ‘H’.

Load capacity [2, 3].

For FGM tapered section graded diameter:

$$P = 7.925 \times \sigma \times \sqrt{D} \times \sqrt[3]{t} \tag{1}$$

where

*P*—Load capacity (N)

*D*—Diameter of cross section (mm)

*T*—Thickness of sheet metal (mm)

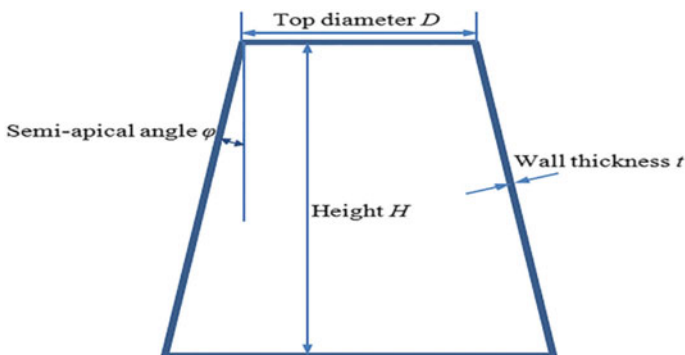


Fig. 1 Thin-walled frustum

$\sigma$ —Strength of material (N/mm<sup>2</sup>)

For a tapered section:

$$P = Se \times A \tag{2}$$

where  $Se = K_1 \times K_2 \times K_3 \times K_4 \times K_5 Se'$

$P$ —Load capacity (N)

$K_1$ —Surface finish factor (0.68)

$K_2$ —Size factor (0.85)

$K_3$ —Reliability factor (0.897)

$K_4$ —Stress concentration factor (0.45)

$K_5$ —Axial load factor (0.8)

$Se'$ —Endurance strength (N/mm<sup>2</sup>)

$Se$ —Corrected endurance strength (N/mm<sup>2</sup>)

### 3.1 FGM Constituents

FGM Frustram is made of zirconia (ceramic) and aluminum (metal) grading for microcomponents with properties of both aluminum and zirconia. This being a very popular FGM has been used in many studies [12–14]. Multi-layer FGMs are modeled using highly stable alumina/zirconia suspensions.

The properties of Zirconia and Aluminum are listed in Table 1.

## 4 Results

The following graphs show the variation and trend followed in the load capacity of the FGM structure when used under grading different parameters keeping others constant. This can be useful while designing the components under different loading conditions.

Figure 2 shows the variation of load capacity with increase in diameter using the empirical relationship (Eq. 1). The trend observed here shows that the axial load capacity of the structure increases linearly with increase in diameter when other parameters including thickness and compressive strength are kept constant and do

**Table 1** Properties of zirconia and aluminum [9, 14]

	Ceramic	Metal
Material	Zirconia	Aluminum
Elastic limit	635–690 MPa	150–180 MPa
Density	5.68 g/cm <sup>3</sup>	2.95 g/cm <sup>3</sup>
Poisson's ratio	0.28	0.34

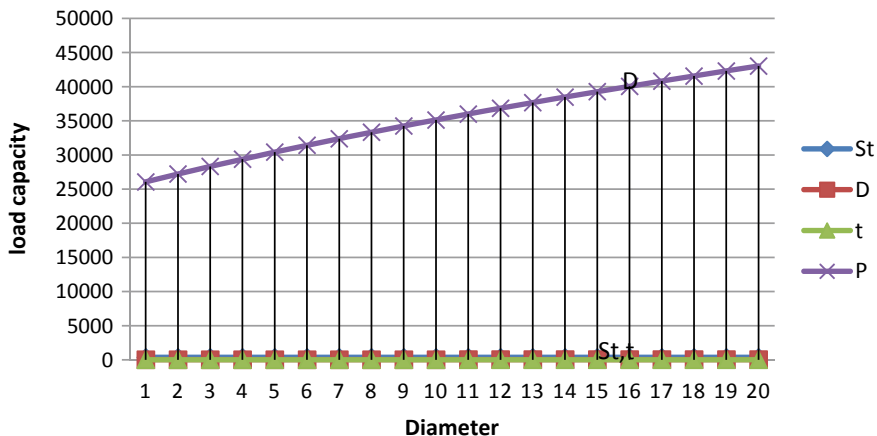


Fig. 2 FGM tapered section FGM graded diameter

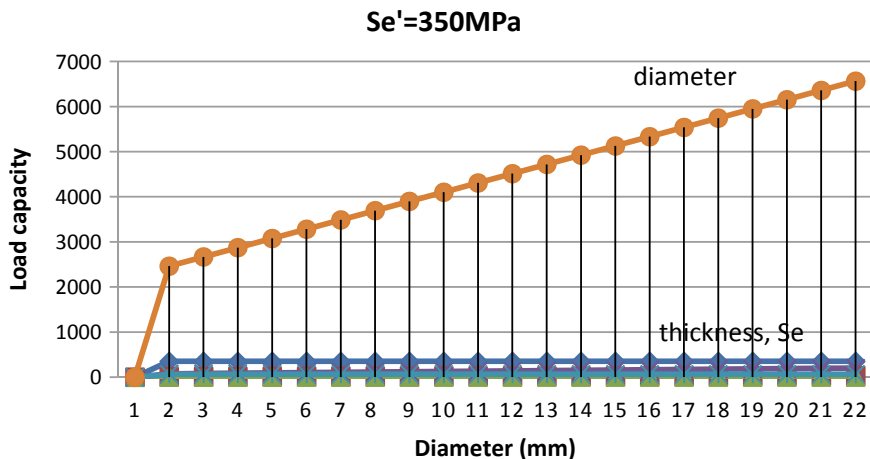


Fig. 3 FGM graded diameter

not exhibit significant change. Figure 3 shows the variation of load capacity with graded diameter when it is calculated with endurance strength equation considering impact loading (Eq. 2), and it is observed that load capacity increases linearly with a greater slope as compared to the previous case.

Figure 4 shows the variation of load capacity with graded thickness keeping the diameter constant using empirical relation (Eq. 1), and it is observed that the load capacity increases not linearly but with a greater slope which can be of great use in applications where intense loading condition is present. Figure 5 shows the variation of load capacity of FGM material which has higher endurance strength

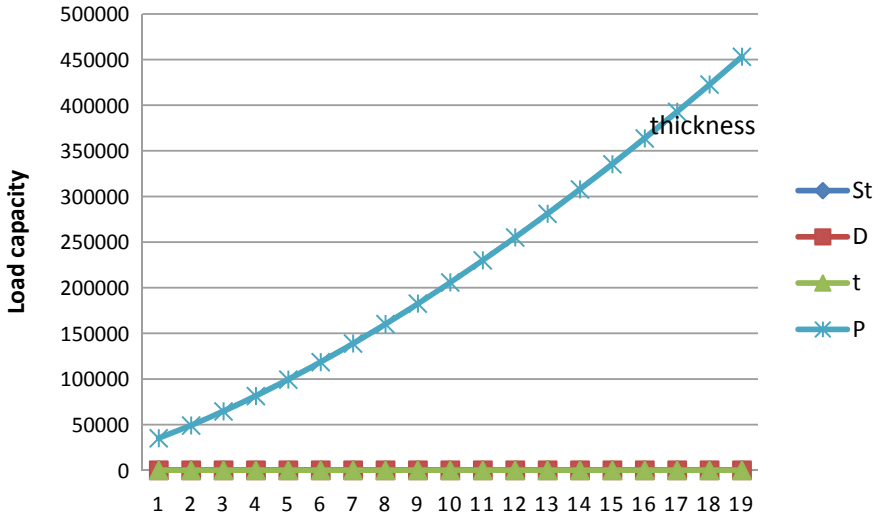


Fig. 4 Variation of load capacity with graded thickness

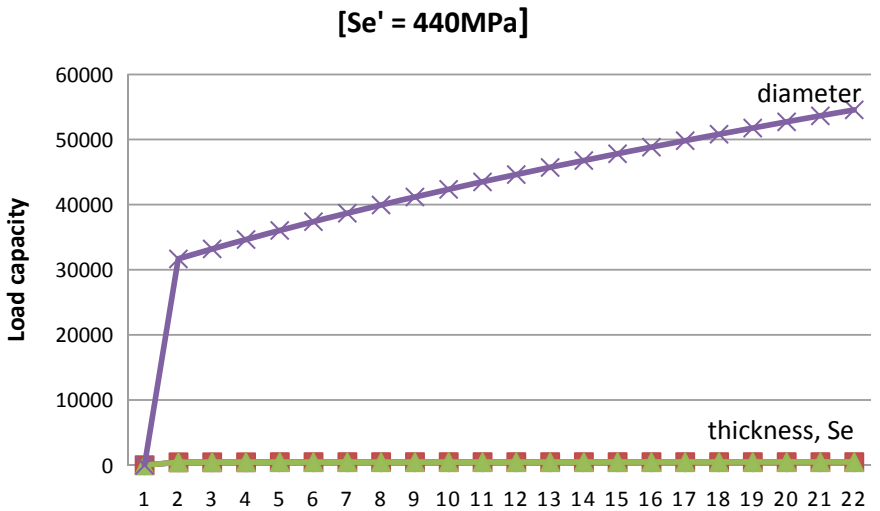


Fig. 5 Variation of load capacity of FGM material

(440 MPa) using Eq. (1), and it is observed that the initial value of load capacity has increased the entire range of load capacity, keeping the thickness constant and grading the diameter.



## 5 Conclusions

1. Through reviewing a great number of published works, gradient characteristics were found to provide more feasible and effective design for energy-absorbing structures and materials. The structures and materials with graded properties could absorb higher energy with less weight and in a more controlled manner for various load conditions, keeping different combinations of graded properties such as length, thickness, diameter and density.
2. It is evident from the above results that grading different parameters clearly improves the load bearing capacity of the member subjected to loading. It hence explains that the use of graded materials can actually be used in loading conditions where high energy-absorbing capacity is required.
3. Recently, crashworthiness of advanced structures and materials with graded properties raised enormous concerns. Introducing gradient to structures and materials could considerably reduce weight and at the same time improve performance by making reasonable designs of the gradient parameters.
4. In general, the introducing of gradients brings bigger flexibility and wider design domain in related energy-absorbing structures and materials. The crashworthiness performance of these structures and materials could definitely be further improved by appropriate design optimization.
5. Apart from the manufacturing technologies, some modeling and computational methodologies based on macro-micromechanics and topology optimization may also be introduced to analyze and design graded structures and materials.

## References

1. Mamalis, A., Johnson, W.: The quasi-static crumpling of thin-walled circular cylinders and frusta under axial compression. *Int. J. Mech. Sci.* **25**, 713–732 (1983)
2. Shigley, J.: *Mechanical Engineering Design*, 8th edn. Budynas-Nisbet (2000)
3. Shigley, J., Mischke, C., Brown, T.: *Standard Handbook of Machine Design*, 3rd edn. McGraw-Hill, New York (2004)
4. Mamalis, A., Manolakos, D., Saigal, S., Viegelaahn, G., Johnson, W.: Extensible plastic collapse of thin-wall frusta as energy absorbers. *Int. J. MechSci.* **28**, 219–229 (1986)
5. Wierzbicki, T., Bhat, S., Abramowicz, W., Brodtkin, D.: A two folding elements model of progressive crushing of tubes. *Int. J. Solids Struct.* **29**, 3269–3288 (1992)
6. Nagel, G., Thambiratnam, D.: A numerical study on the impact response and energy absorption of tapered thin-walled tubes. *Int. J. Mech. Sci.* **46**(2), 201–216 (2004)
7. Avalle, M., Chiandussi, G.: Optimisation of a vehicle energy absorbing steel component with experimental validation. *Int. J. Impact Eng* **34**, 843–858 (2007)
8. Liu, Y.: Design optimisation of tapered thin-walled square tubes. *Int. J. Crashworthiness* **13**, 543–550 (2008)
9. Zhang, J., Wei, H., Wang, Z., Zhao, L.: Dynamic crushing of uniform and density graded cellular structures based on the circle arc model. *Latin Am. J. Solids Struct.* **12**, 1102–1125 (2015)

10. Fan, T., Zou, G.: Influences of defects on dynamic crushing properties of functionally graded honeycomb structures. *J. Sandwich Struct. Mater.* **17**, 295–307 (2015)
11. Lu, R., Liu, X., Chen, S., Hu, X., Liu, L.: Axial crushing analysis for tailor rolled square tubes with axially graded both wall thickness and material strength. *Thin-walled Struct.* **117**, 10–24 (2017)
12. Hassanin, H., Jiang, K.: Fabricating functionally graded ceramic micro-components using soft lithography. In: *Advances in Ceramic Matrix Composites* (2014)
13. Feng, X., Xiong, Z., Zhange, H.: A review on functionally graded structures and materials for energy absorption. *Eng. Struct.* **171**, 309–325 (2018)
14. Bhandari, M.: Mechanical computations of FGM plate subjected to transverse load. *Int. J. Emer. Trends Eng. Res.* **8**, 1–7 (2020)

# Mechanical Property and Microstructure Analysis of Laser Beam Welded Aluminium (A6061)-Titanium (Ti6Al4V) Dissimilar Sheet Metals



Sudhin Chandran, R. Rajesh, and M. Dev Anand

**Abstract** Developing vogue in engineering, such as lightweighting, expanded execution, and usefulness builds the utilization of complex material, crossover fabric, and in this way, the requirement for fastening different metals. Al and Ti compounds are generally utilized in the aviation and automobile industry because of their appealing properties, like small density, intense conductivity, superior strength, and solidness. Nonetheless, the fastening of Al and Ti combinations by conventional welding techniques is troublesome because of the development of bulk intermetallic mixes. Laser beam welding is efficient for titanium–aluminium welding, a bigger pretence in aviation, automobile, electronics, and different sectors. In this research, distinct 2 mm thickness A6061 and Ti6Al4V butt seams were created by moving a laser supply on the Ti sheet’s top side. Titanium alloy Ti6Al4V and aluminium amalgam 6061 were effectively joined by laser beam welding. The mechanical and microstructural qualities of the welded joints were assessed. The weld piece displays a blend of fine recrystallized particles of the aluminium compound and titanium compound.

**Keywords** Laser beam welding · Titanium · Aluminium · Mechanical properties · Microstructure

## 1 Introduction

Developing production fields like aviation, automobile, and power generation calls for particular items by integrating lightweight and recyclability characteristics. As original material frequently flops to handle those necessities, a blend of at least two materials can fulfill a particular manufacturing sector requirement [1, 2]. Divergent joints can give application-oriented solutions. Specifically, Al–Ti lightweight

---

S. Chandran (✉) · R. Rajesh · M. Dev Anand  
Noorul Islam Centre for Higher Education, Kumaracoil 629 180, Tamil Nadu, India

© The Author(s), under exclusive license to Springer Nature Singapore Pte Ltd. 2021  
A. Patnaik et al. (eds.), *Advances in Materials Processing and Manufacturing Applications*, Lecture Notes in Mechanical Engineering,  
[https://doi.org/10.1007/978-981-16-0909-1\\_21](https://doi.org/10.1007/978-981-16-0909-1_21)

207

crossover fabric has a broad scope of utilizations and likely possibilities in aviation, automobile, and electronics businesses. A decrease in weight and fuel utilization speaks to a fundamental necessity. Weight decrease is unequivocally requested for vitality and typical asset savings [3]. However, Al propounds lesser density, diminished expenses, and sheet framing properties. Ti composites display exceptional corrosion properties, biosimilarity, more excellent elasticity, and excellent temperature conduct, which get them perfect contenders for usage in basically two territories of utilization: corrosion-resistant facility and explicit strength active assemblies [4, 5].

Al–Ti fabric is now utilized in few glides of planes, in which the Al honeycomb is joined to the Ti outside layer. Another model is the seat-track in the airplane: it is proposed to utilize Ti rather than Al for the creation of the jeopardized zone of the seat trail, to forestall corrosion, which necessarily follows up on the components in the cabin. The blend of an Al-compound with Ti6Al4V for airplane seat trail appeared in Fig. 1a [6].

Mechanical joining strategies like riveting, screwing and press-joining are now highly utilized because they do not demand metallurgical similarity among the materials fastened. Al to Ti's association develops troublesome while employing the conventional fastening techniques because of their enormous distinction in thermo-physical properties and development of expanded brittle intermetallic compound layers. Figure 1(b) reveals the Ti–Al binary phase diagram [4, 7].

Welding of tinny sheet presents various difficulties to the welding of thicker areas. Welding of tinny sheet necessitates superior positional precision and small warmth contribution since weld infiltration is certifiably not a significant matter for flimsy sheets; however, a lot of heat generation can prompt considerable contortion. Welding of distinct materials is difficult because of the variety in both materials' physical and substance properties [8, 9]. A few ways to deal with weld titanium to aluminium have been crafted earlier [10]. Laser beam welding is one of the most generally utilized welding strategies for a unique joint as of not long ago.

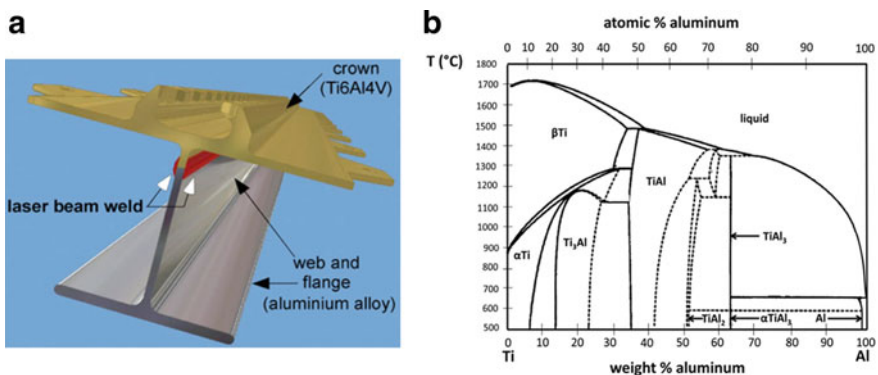


**Fig. 1** a Traveller seat trail. b Ti–Al binary phase diagram

Contrasted and ordinary weld techniques, laser beam welding have numerous favourable circumstances, such as rapid accuracy, smaller weld globule, smaller warmth influenced zone, and better controllability. The cementing time in a constant laser beam welding is quicker than other methods [11, 12]. Laser welding can give a considerable advantage to the welding of titanium (Ti6Al4V) and aluminium (A6061) thin sheets with exactness and quick handling capability [13]. The procedure of the arrangement of Ti/Al dissemination holding joint quality relies upon the metallurgical blend rate and the interface structure in the dispersion zone. It can reach or even surpass the quality of pure aluminium after TiAl<sub>3</sub> structures a layer [14].

This article unveils an investigation of the laser welding of 6061 aluminium sheet–titanium (Ti6Al4V) compound sheet, involving examining the mechanical properties and the microstructure perceptions. They were regarded as the two materials well on the way to be utilized in rocket construction [15].

## 2 Experimental Procedure

Distinct material joining of Ti4V6Al and A6061 sheets utilized in this investigation, and the dimension of the sheets was 100 × 60 × 2 mm. The chemical composition of the parent metal is recorded in Tables 1 and 2, separately. An imaginative and promising procedure created the welds, likewise, alluded to laser offset welding. The laser beam was moved on the Ti sheet top side with the expectation to produce the keyhole. Ti parent metal was dissolved by direct irradiation, while Al parent metal liquefied through warmth conduction through the interface. A drawing of the welding design has appeared in Fig. 2a, b publicized the laser beam welding equipment. Laser offset impacts the thickness of the interfacial IMC layer and the mechanical property of the joint. With expanding laser offset, the thickness of the interfacial IMC layer diminishes, and the joint's rigidity rises [16].

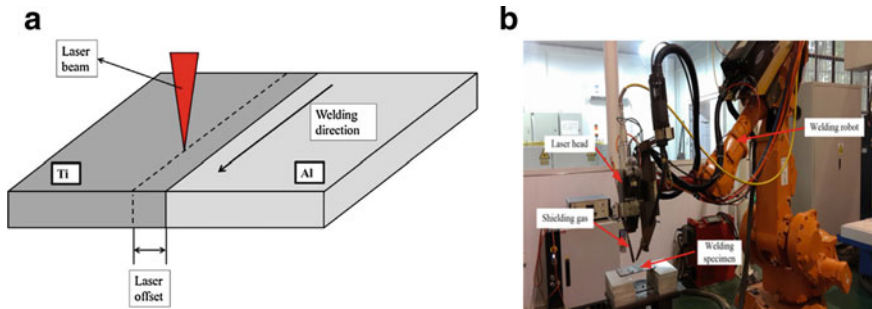
The trial was planned depending on a three factor three-level factorial statistical design. Laser power, welding speed and offset speak to the autonomous input factors. The optimized laser parameters are 1800 W power, 2.2 m/min speed and offset 0.3 mm. Metallographic samples were set up as indicated by standard methodology. The joints were cross-separated oppositely to the welding course for metallographic investigation. The joints' microstructures were analysed with a scanning electron microscope (SEM). SEM perception samples were cleaned with standard pounding strategies and synthetically carved by Keller's reagents solution. Backscattered electron pictures of SEM were utilized to dissect the interfacial IMC layer.

**Table 1** Chemical constitution of parent metal titanium alloy (Ti6Al4V)

Ti	C	Fe	N	Al	O	V	H	Y	Other
Balance	0.08	0.03	0.05	5.5–6.75	0.20	3.5–4.5	0.015	0.005	0.40

**Table 2** Chemical composition of base material aluminium 6061

Al	Si	Fe	Cu	Mn	Mg	Cr	Zn	Ti	Other
Balance	0.40–0.80	0.70	0.15–0.40	0.15	0.8–1.2	0.04–0.35	0.25	0.15	0.15

**Fig. 2** a Sketch of the welding configuration. b Laser beam welding equipment

The tensile test samples were set up as indicated by ASTM-E8 specification and are led by utilizing a Shimadzu 20 kN tensile test set up to decide the peculiarity of the materials and seam quality for the welded tests.

### 3 Results and Discussion

Figure 3 exhibits the cross-segment of the weld. The two regions reveal a welded zone and heat influenced area. The titanium's fusion was because of the exemplary penetration mode welding while the aluminium merged for the warmth that was led within the Al–Ti connection. The exchange of heat from Ti to Al delivered the coherence among the Ti and the Al fusion areas. The microstructural investigation showed a super-slim layer of intermetallic  $TiAl_3$  at the interface, which metallurgically connects Ti6Al4V and A6061 sheets. It is evident from the SEM micrographs demonstrated that there is no fastening imperfection in the boundary. The distortion groups close to the boundary region were essentially shaped in aluminium; this may be because of its temporary hardness. In any case, these groups may likewise be the aftereffect of cold deformation in the Al sheet creation. This outcome affirms that the interface is in a unique situation according to a metallurgical perspective.

Figure 4a shows that the crack sample and a section of the crack surface are shown. The tensile test strategy was chosen to decide weld strength, which was acknowledged by utilizing a tensile testing unit. It very well may be noticed that the fracture would, in general, spread in the vicinity of the welding joint. The tensile

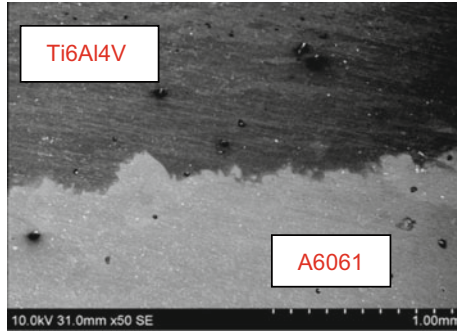


**Fig. 3** Microstructure of welded sample



**Fig. 4** **a** Tensile test break sample. **b** Hardness test specimen

strength of the laser beam welded titanium–aluminium seams arrived at 205 MPa, and it was near to the tensile strength of A6061 parent material.

Hardness is similar to the extent of the strength of the weld seam. The Vickers test is a broadly used procedure since it is essential and detached. In the Vickers hardness strategy indenting the sample test with a diamond indenter. It is a right pyramid with a square foot and a state of  $136^\circ$  between various forms. The constant load is exerted for a specific time and cleared while the tiny load is in position. It indicates that the hardness of weldment is 290 HV. Figure 4b displays the hardness trial samples.

## 4 Conclusions

The laser welding of tinny Al and Ti sheets was executed by concentrating the laser beam on the titanium amalgam area. The microstructure, mechanical properties and arrangement of the interfacial IMC layer of the distinct butt seam were reviewed.

- (1) Welding of Ti6Al4V/A6061 distinct composites with 2 mm thickness by the laser beam can deliver seams with great impression under welding states of 1800 W laser power, 2.2 m/min welding speed, and 0.3 mm laser offset at titanium compound section.

- (2) The fastening method of Ti6Al4V/A6061 distinct amalgams by laser welding is by developing intermetallic stage  $TiAl_3$  at the boundary.
- (3) The metallurgy impacted the mechanical conduct of the weld. The break takes place in the consolidated territory at an ultimate strength that was near to that of A6061.

## References

1. Casalino, G., et al.: Mechanical and microstructure analysis of AA6061 and Ti6Al4 V fiber laser butt weld. *Optik (Stuttg)* **148**, 151–156 (2017). <https://doi.org/10.1016/j.jjleo.2017.08.138>
2. Martinsen, K., Hu, S.J., Carlson, B.E.: Manufacturing technology joining of dissimilar materials. *CIRP Ann.* <https://doi.org/10.1016/j.cirp.2015.05.006> (2015)
3. Chen, S., Li, L., Chen, Y., Huang, J.: Joining mechanism of Ti/Al dissimilar alloys during laser welding-brazing process. *J. Alloys Compd.* **509**(3), 891–898 (2011). <https://doi.org/10.1016/j.jallcom.2010.09.125>
4. Casalino, G., Mortello, M.: Modeling and experimental analysis of fiber laser offset welding of Al-Ti butt joints. *Int. J. Adv. Manuf.* (2015). <https://doi.org/10.1007/s00170-015-7562-8>
5. Kahraman, N., Gulenc, B., Findik, F.: Corrosion and mechanical-microstructural aspects of dissimilar joints of Ti-6Al-4V and Al plates. *Int. J. Impact Eng* **34**(8), 1423–1432 (2007). <https://doi.org/10.1016/j.ijimpeng.2006.08.003>
6. Vaidya, W.V., et al.: Improving interfacial properties of a laser beam welded Dissimilar joint of aluminium AA6056 and titanium Ti6Al4V for aeronautical applications. *J. Mater. Sci.* **45** (22), 6242–6254 (2010). <https://doi.org/10.1007/s10853-010-4719-6>
7. Chen, S.H., Li, L.Q., Chen, Y.B.: Interfacial reaction mode and its influence on tensile strength in laser joining Al alloy to Ti alloy. *Mater. Sci. Technol.* **26**(2), 230–235 (2010). <https://doi.org/10.1179/174328409X399056>
8. Fan, Y., et al.: A comparison of microstructure and mechanical properties of welded thin Ti6Al4V with three different types of laser. A comparison of microstructure and mechanical properties of welded thin Ti6Al4V with three different types of laser, vol. 8917, Mar. (2016). <https://doi.org/10.1179/1432891715z.0000000001542>
9. Olabi, A.G., Alsinani, F.O., Alabdulkarim, A.A., Ruggiero, A., Tricarico, L., Benyounis, K. Y.: Optimizing the CO<sub>2</sub> laser welding process for dissimilar materials. *Opt. Lasers Eng.* **51**(7), 832–839 (2013). <https://doi.org/10.1016/j.optlaseng.2013.01.024>
10. Dressler, U., Biallas, G., Alfaro Mercado, U.: Friction stir welding of titanium alloy TiAl6V4 to aluminium alloy AA2024-T3. *Mater. Sci. Eng. A* **526**(1–2), 113–117 (2009). <https://doi.org/10.1016/j.msea.2009.07.006>
11. Zhao, X., Zhang, J., Song, X., Guo, W.: Investigation on mechanical properties of laser welded joints for Ti-6Al-4V titanium alloy. *Mater. Sci. Technol.* **29**(12), 1405–1413 (2013). <https://doi.org/10.1179/1743284713y.00000000314>
12. Tsukamoto, S.: Laser welding. *Weld. Int.* **17**(10), 767–774 (2003)
13. Chandran, S., Rajesh, R., Anand, M.D.: A review—studies on heat treatment of laser beam welded Ti/Al dissimilar sheet metals. *J. Adv. Res. Dyn. Control Syst.* **11**(8 Special Issue), 725–733 (2019)
14. Wei, Y., Aiping, W., Guisheng, Z., Jialie, R.: Formation process of the bonding joint in Ti/Al diffusion bonding. *Mater. Sci. Eng., A* **480**(1–2), 456–463 (2008). <https://doi.org/10.1016/j.msea.2007.07.027>



15. Zhu, Z., Lee, K.Y., Wang, X.: Ultrasonic welding of dissimilar metals, AA6061 and Ti6Al4V. *Int. J. Adv. Manuf. Technol.* **59**(5–8), 569–574 (2012). <https://doi.org/10.1007/s00170-011-3534-9>
16. Song, Z., Nakata, K., Wu, A., Liao, J.: Interfacial microstructure and mechanical property of Ti6Al4V/A6061 dissimilar joint by direct laser brazing without filler metal and groove. *Mater. Sci. Eng., A* **560**, 111–120 (2013). <https://doi.org/10.1016/j.msea.2012.09.044>

# Parametric Optimization and Evaluation of RMD<sup>TM</sup> Welding Performance for ASTM A387 Grade 11 Steel Plates Using TOPSIS-Taguchi Approach



Dinbandhu  and Kumar Abhishek 

**Abstract** Continually increasing demands in pipeline welding concerning quality, frequent usage of superior, heat-sensitive, and corrosion-resistant materials alongside high assembly costs encourage the assessment of a welding process in detail. The only way to conquer such problems was the adaptation of technologically innovative welding methods that integrate the goodness of sophisticated power supply units and advanced software configuration. One such method is regulated metal deposition (RMD<sup>TM</sup>) welding. This work explores the influence of RMD<sup>TM</sup> welding variables and optimizes them for the best output responses. For that, voltage (V), current (A), and gas flow rate (GFR) were selected as welding variables, and their responses have been measured in terms of bead height (BH), bead width (BW), heat-affected zone (HAZ), and depth of penetration (DOP) by taking bead-on-plate trails on chrome moly steel plates. A novel optimization route based on the integrated concept of the TOPSIS-Taguchi approach has also been proposed, which delivers the optimal parametric setting as current = 100 A, voltage = 13 V, and gas flow rate = 21 L/min.

**Keywords** RMD<sup>TM</sup> welding · Cr-Mo steels · TOPSIS · Optimization · DOP · HAZ

## 1 Introduction

Regulated metal deposition (RMD<sup>TM</sup>) welding is a novel welding method comprehensively used by several manufacturers and fabricators for performing root pass welding in oil and gas pipeline industries. As conventional methods of welding were not able to comply with the expectations of fabricators in terms of productivity and quality, Miller Electric Mfg. introduced this method and patented it in 2004.

---

Dinbandhu · K. Abhishek (✉)  
Department of Mechanical & Aero-Space Engineering, Institute of Infrastructure,  
Technology, Research and Management, (IITRAM), Ahmedabad, Gujarat 380026, India

This technique is an improvement over the conventional shortcircuiting mode of the GMAW process based on the manipulations of current and voltage waveforms that govern and adjust the movement of liquified droplets from the filler metal (wire electrode) to the weld pool. The manipulations in current and voltage waveforms are accomplished through a newly developed inverter-based power supply unit that houses computer-programmed innovative digital control devices. The RMD<sup>TM</sup> welding technique offers numerous advantages over conventional welding methods that can alleviate a welding firm's quality, efficiency, and productivity. It delivers a steady droplet deposition. Consequently, it becomes more convenient for the welder to handle the weld puddle. It eliminates the condition of high–low misalignment between pipe sections leading to effortlessly bridging the gap up to 4.8 mm. It eradicates the need for backing gas while welding, leading to a noteworthy enhancement in productivity and reduction in welding cost. The process works to keep a uniform arc length regardless of the filler wire stick out, making it easier for the new welders to master it with less training. It is impeccably suitable for the root pass welds, producing a 3.2–6.4 mm thick throat, thus removing the necessity of a GTAW hot pass. It has high travel speeds of 152.4–304.8 mm (6–12 in.) per minute as compared to the speeds of conventional welding (3–8 in./min) and GTAW (3–5 in./min). Therefore, the deposition rate increases. Due to the stable weld puddle and smooth metal transfer, spatter-free and slag-free welds are produced. The sidewall splashing also gets decreased. Hence, the process ends the possibilities of re-works like grinding, post-work cleaning on the finished weld leading to improved productivity and quality with time and cost savings [1–8].

Nascimento and Vilarinho [9] welded carbon steel pipes using an advanced GMAW welding method known as surface tension transfer (STT<sup>TM</sup>) welding. The pipes, having an 8 inch diameter and 8 mm thickness, were welded in downhill progression. For that, Ar + 25% CO<sub>2</sub> gas was utilized as the shielding gas, whereas ER70S-6, having 1.2 mm diameter, was employed as the filler wire. Mechanical tests were performed along with the visual inspection of the welded samples to check their feasibility in industrial applications. The obtained results were good, yielding better outcomes than the traditional welding techniques. Sharma and Dwivedi [10] used multipass-TIG and activated flux TIG welding processes for the coalescence of dissimilar 304H ASS-P92 steel joints. A comparative study of these two processes was done using mechanical properties, metallurgical features, angular distortion, and bead morphology. The economic aspects of both processes were also examined. Hilkes and Gross [11] discussed Cr-Mo steels' welding applications in the petrochemical and power generation sectors. Several experiments were performed using SMAW, SAW, GTAW, FCAW, and GMAW on Cr-Mo steels. The maximum service temperature of Cr-Mo steels was also discussed, along with an elaboration on their chemical composition. This paper also spreads some light on the applicability of different welding consumables and methods for Cr-Mo steels. A proper guideline on interpass temperatures and pre-heating of these steels is also communicated. Sumesh et al. [12] welded carbon steel plates through robotic GMAW integrated with Fronius power source and obtained defect-free welds, welds with burn through and porosity defects. A decision tree

algorithm has been incorporated to categorize the weld defects by establishing a correlation between voltage and current signatures. Terner et al. [13] performed welding operations on low-carbon steels and investigated the effects of input parameters, namely current, shielding gas, voltage, and welding speed on the bead geometry. Response surface methodology (RSM) was adopted for the experimental design. The development of mathematical models was also done to envisage the bead geometry, hardness, and heat input as a function of welding parameters and obtain the optimal weld settings. Prajapati et al. [14] conducted bead-on-plate trails for Cr-Mo grade 11 plates of steel using RMD<sup>TM</sup> welding and optimized the welding parameters, namely voltage, current, and gas flow rate for HAZ, DOP, and BW. L<sub>9</sub> arrangement, along with the combined approach of gray-fuzzy-Taguchi, was applied for obtaining optimal settings. The study reveals that RMD<sup>TM</sup> welding is highly influenced by voltage.

The existing literature details the effect of several welding parameters on low-carbon steels, stainless steels, and superalloys using some conventional processes like GMAW and GTAW and advanced processes such as RMD<sup>TM</sup>, STT, and CMT. But the literature is scarce on RMD<sup>TM</sup> welding of low alloy steels. Only a few researchers have examined the HAZ and DOP of Cr-Mo steels for the RMD<sup>TM</sup> welding. Hence, this work not only examines the outcomes of RMD<sup>TM</sup> welding variables on Cr-Mo steels by assessing the heat affected zone (HAZ), depth of penetration (DOP), bead width (BW), and bead height (BH) but also proposes a novel optimization route using Taguchi-utility approach and adds on some salient features of this advanced welding method in the existed literature database.

## 2 Materials and Methods

In this work, ASTM A387 grade 11 steel plates of 500 mm × 150 mm × 6 mm in size have been incorporated as the base material. Using Miller's 'Continuum 500' welding machine, bead-on-plate trails (Fig. 1) were performed on them. 'MEGAFIL 237 M', a metal-cored wire electrode, was used as the filler wire. To do so, three input variables viz. current, voltage, and GFR were selected. These control variables were assigned certain levels, as shown in Table 1. Then, the design of experiments was modeled based on Taguchi's L<sub>25</sub> setup. The measured output responses were HAZ, DOP, BW, and BH (Fig. 2). To measure these output responses, the bead-on-plate samples were cut, polished, etched (Fig. 1), and placed under a microscope individually. All the experimental trails with their respective output responses have been represented in Table 2.

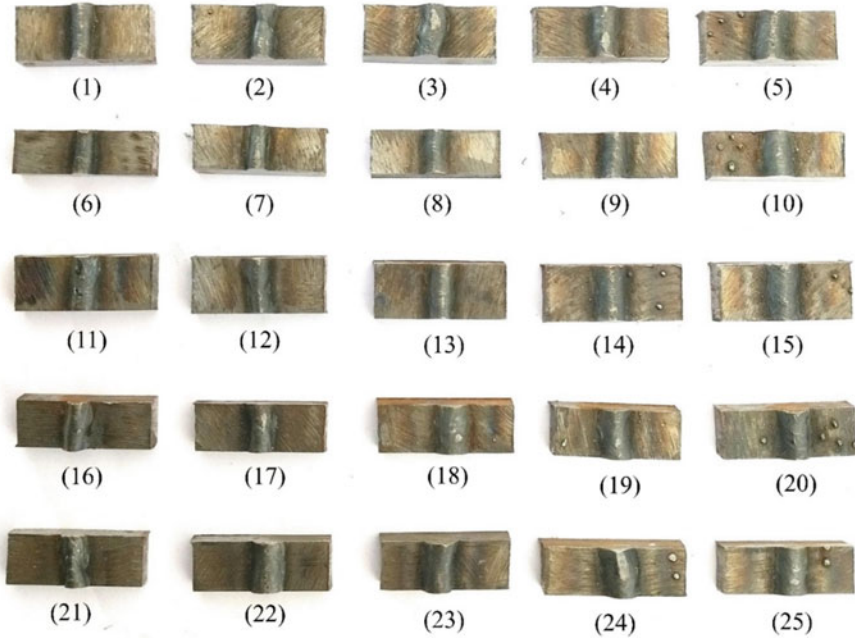


**Fig. 1** Cut and polished bead-on-plate welding samples

**Table 1** Allocation of levels to the welding variables

Welding variables	Levels (L)				
	1	2	3	4	5
A	90	100	110	120	130
V	13	14	15	16	17
GFR	13	15	17	19	21

### 2.1 TOPSIS Method

Technique for order preference by similarity to ideal solution, abbreviated as TOPSIS, is a MADM technique used to find the best substitutes in the solution space for a problem. Ching-Lai Hwang and Kwangsun Yoon proposed it in 1981 [15, 16]. The straightforward logic of the approach makes it easier for the user to understand and implement. It measures the degree of closeness to the ideal solution where the chosen/best substitutes should have the minimum separation distance from the positive ideal solution. Meanwhile, it must be too far from the negative ideal solution [17, 18]. The positive ideal solution consists of the best performance values shown by any substitute for respective attributes. At the same time, the negative ideal solution is a set of worst performance values [17, 19]. This method has substantial application areas such as design and engineering, logistics, supply

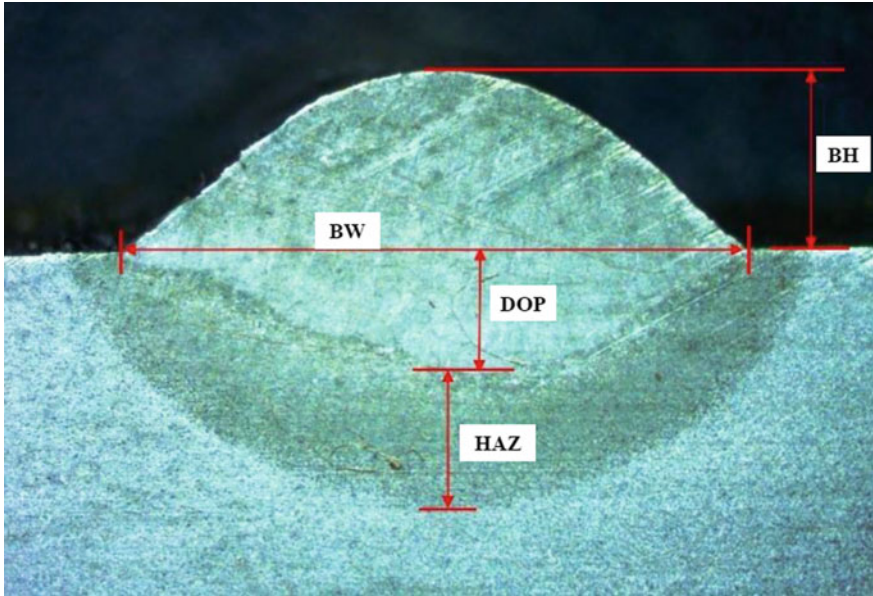


Fig. 2 Assessment of output responses

chain management, marketing, manufacturing, due to its several advantageous features. It is simple to understand, program, and use. It maintains the same number of steps, regardless of problem size [20, 21]. The approach involves the following steps for converting multiple attributes into a single response [17–19]:

**Step 1:** Formation of a decision matrix:

$$D = \begin{matrix} A_1 \\ A_2 \\ \cdot \\ A_i \\ \cdot \\ A_m \end{matrix} \begin{bmatrix} x_{11} & x_{12} & \cdot & x_{1j} & x_{1n} \\ x_{21} & x_{22} & \cdot & x_{2j} & x_{2n} \\ \cdot & \cdot & \cdot & \cdot & \cdot \\ x_{i1} & x_{i2} & \cdot & x_{ij} & \cdot \\ \cdot & \cdot & \cdot & \cdot & \cdot \\ x_{m1} & x_{m2} & \cdot & x_{mj} & x_{mn} \end{bmatrix} \tag{1}$$

where  $A_i (i = 1, 2, \dots, m)$  denotes the promising substitutes;  $x_j (j = 1, 2, \dots, n)$  signifies the attributes relating to the performance of the substitute;  $j = 1, 2, \dots, n$  and  $x_{ij}$  signify the performance of  $A_i$  for attribute  $X_j$

**Step 2:** Normalization of decision matrix:

$$r_{ij} = \frac{x_{ij}}{\sqrt{\sum_{i=1}^m x_{ij}^2}} \tag{2}$$

where  $r_{ij}$  depicts the normalized performance of  $A_i$  for attribute  $X_j$

**Table 2** Experimental runs and their respective output responses

Trails	Current (A)	Voltage (V)	GFR (L./min.)	HAZ (mm)	DOP (mm)	BW (mm)	BH (mm)
1	90	13	13	1.19	0.84	5.12	2.4
2	90	14	15	1.30	1.16	5.58	2.91
3	90	15	17	1.37	1.18	5.86	2.22
4	90	16	19	1.68	1.33	6.67	2.74
5	90	17	21	2.04	1.16	7.08	2.71
6	100	13	15	0.93	0.90	5.23	2.75
7	100	14	17	1.16	1.13	4.94	2.52
8	100	15	19	1.06	1.22	5.49	1.87
9	100	16	21	1.30	1.50	6.48	2.29
10	100	17	13	1.67	1.41	6.83	2.18
11	110	13	17	1.54	0.96	5.95	2.85
12	110	14	19	1.30	0.98	5.78	2.35
13	110	15	21	1.20	1.29	5.37	2.17
14	110	16	13	1.86	1.38	7.10	2.39
15	110	17	15	1.54	1.65	7.80	2.57
16	120	13	19	1.16	1.28	5.72	2.84
17	120	14	21	1.30	1.32	5.86	2.66
18	120	15	13	1.86	1.07	7.47	2.57
19	120	16	15	1.84	1.35	7.68	2.49
20	120	17	17	1.90	1.91	7.40	2.45
21	130	13	21	1.13	1.10	5.33	2.97
22	130	14	13	1.68	0.99	6.95	2.72
23	130	15	15	1.42	1.20	6.55	2.86
24	130	16	17	1.62	1.75	7.94	2.29
25	130	17	19	1.80	1.45	7.65	2.22

**Step 3:** Formation of a weighted normalized decision matrix:

$$V = [v_{ij}]V = w_j r_{ij}$$

$$D = \begin{bmatrix} y_{11} & y_{12} & \cdot & y_{1j} & y_{1n} \\ y_{21} & y_{22} & \cdot & y_{2j} & y_{2n} \\ \cdot & \cdot & \cdot & \cdot & \cdot \\ y_{i1} & y_{i2} & \cdot & y_{ij} & \cdot \\ \cdot & \cdot & \cdot & \cdot & \cdot \\ y_{m1} & y_{m2} & \cdot & y_{mj} & y_{mn} \end{bmatrix} \tag{3}$$

where  $\sum_{j=1}^n w_j = 1$

**Step 4:** Finding the positive ideal (best) and the negative ideal (worst) solutions:

(a) The positive ideal (best) solution:

$$\begin{aligned}
 A^+ &= \left\{ \left( \max_i y_{ij} | j \in J \right), \left( \min_i y_{ij} | j \in J' | i = 1, 2, \dots, m \right) \right\} \\
 &= \left\{ y_1^+, y_2^+, \dots, y_j^+, \dots, y_n^+ \right\}
 \end{aligned}
 \tag{4}$$

(b) The negative ideal (worst) solution:

$$\begin{aligned}
 A^- &= \left\{ \left( \min_i y_{ij} | j \in J \right), \left( \max_i y_{ij} | j \in J' | i = 1, 2, \dots, m \right) \right\} \\
 &= \left\{ y_1^-, y_2^-, \dots, y_j^-, \dots, y_n^- \right\}
 \end{aligned}
 \tag{5}$$

where

$J = \{j = 1, 2, \dots, n | j\}$ : allied with the advantageous attributes

$J' = \{j = 1, 2, \dots, n | j\}$ : allied with nonadvantageous attributes

**Step 5:** Distance measurement of substitutes from ideal solutions. The separation distance of each substitute from the ideal solutions is measured by n-dimensional Euclidean distance using the following equations:

$$S_i^+ = \sqrt{\sum_{j=1}^n (y_{ij} - y_j^+)^2} \quad i = 1, 2, \dots, m
 \tag{6}$$

$$S_i^- = \sqrt{\sum_{j=1}^n (y_{ij} - y_j^-)^2} \quad i = 1, 2, \dots, m
 \tag{7}$$

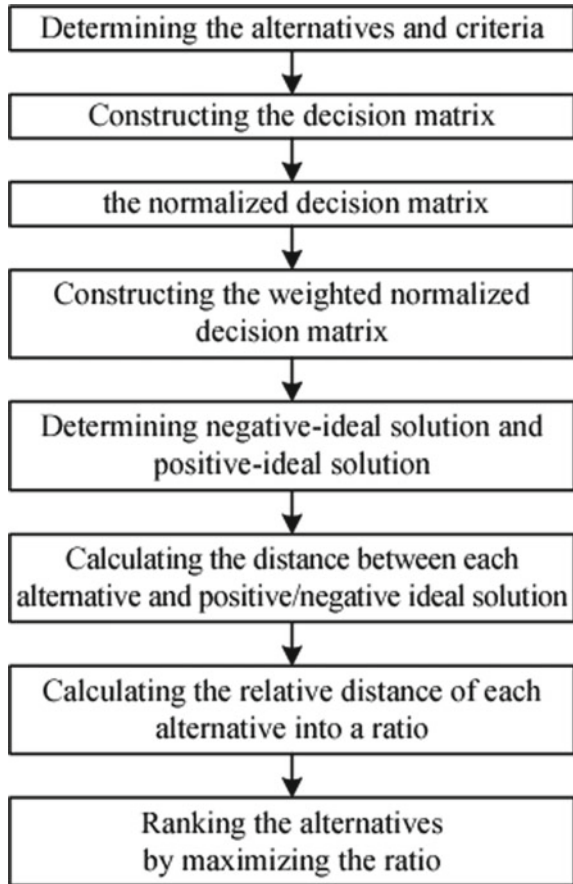
**Step 6:** Evaluation of overall performance coefficient nearest to the ideal solution:

$$C_i^+ = \frac{S_i^-}{S_i^+ + S_i^-}, \quad i = 1, 2, \dots, m; \quad 0 \leq C_i^+ \leq 1
 \tag{8}$$

Figure 3 depicts the proposed optimization route.



**Fig. 3** Flow diagram of TOPSIS for multi-response optimization



### 3 Result and Discussion

Experiments have been carried out as per  $L_{25}$  orthogonal array and experimental data for the welding performance evaluation characteristics viz. HAZ, DOP, BW, BH has been recorded and furnished in Table 2. Firstly, the aforementioned evaluation characteristics were normalized using Eq. 2. These normalized values are presented in Table 3. In the present work, all the responses are assumed of equal importance. Therefore, equal weight (0.25) has been assigned to each output characteristic, and weighted values were calculated using Eq. 3 (Table 3). As the aforementioned evaluation characteristics are conflicting, it is necessary to determine the positive ideal and negative ideal solutions (Table 4). In the present context, lower values are preferable for HAZ, BW, and BH, so the lowest value of these characteristics was considered a positive ideal solution and vice versa. Similarly, for DOP, higher values are preferable; hence, the highest value of DOP has been considered as a positive ideal solution and vice versa. Subsequently,

**Table 3** Normalized and weighted values for the experimental data

N-HAZ	N-DOP	N-BW	N-BH	W-HAZ	W-DOP	W-BW	W-BH
0.1883	0.109767	0.811502	0.45451	0.047064	0.027442	0.202875	0.113627
0.2247	0.207529	0.963869	0.6682	0.056167	0.051882	0.240967	0.16705
0.2495	0.215876	1.063028	0.38889	0.062379	0.053969	0.265757	0.097222
0.3752	0.276838	1.377213	0.592409	0.093802	0.06921	0.344303	0.148102
0.5532	0.207529	1.551729	0.579508	0.13831	0.051882	0.387932	0.144877
0.1150	0.124612	0.846745	0.596741	0.028745	0.031153	0.211686	0.149185
0.1789	0.199698	0.755446	0.501097	0.044721	0.049925	0.188861	0.125274
0.1494	0.233065	0.933027	0.275933	0.037343	0.058266	0.233257	0.068983
0.2247	0.347694	1.299869	0.413801	0.056167	0.086923	0.324967	0.10345
0.3708	0.307966	1.444079	0.375002	0.092689	0.076992	0.36102	0.09375
0.3153	0.142773	1.095932	0.64093	0.07882	0.035693	0.273983	0.160232
0.2247	0.150628	1.034201	0.435769	0.056167	0.037657	0.25855	0.108942
0.1914	0.260083	0.892685	0.371569	0.047858	0.065021	0.223171	0.092892
0.4599	0.29798	1.560509	0.45073	0.11498	0.074495	0.390127	0.112682
0.3153	0.42507	1.883383	0.521179	0.07882	0.106267	0.470846	0.130295
0.1789	0.255278	1.012842	0.63644	0.044721	0.063819	0.25321	0.15911
0.2247	0.269418	1.063028	0.558321	0.056167	0.067354	0.265757	0.13958
0.4599	0.176778	1.727391	0.521179	0.11498	0.044195	0.431848	0.130295
0.4501	0.283519	1.825879	0.489237	0.11252	0.07088	0.45647	0.122309
0.4799	0.568115	1.695169	0.473645	0.119978	0.142029	0.423792	0.118411
0.1698	0.18721	0.879435	0.696039	0.042438	0.046802	0.219859	0.17401
0.3752	0.153705	1.495268	0.583792	0.093802	0.038426	0.373817	0.145948
0.2681	0.222152	1.328104	0.645435	0.067015	0.055538	0.332026	0.161359
0.3489	0.476421	1.951599	0.413801	0.087222	0.119105	0.4879	0.10345
0.4307	0.328432	1.811642	0.38889	0.107681	0.082108	0.45291	0.097222

**Table 4** Positive ideal (best) and negative ideal (worst) solutions

	HAZ	DOP	BW	BH
A-	0.13831	0.027442	0.4879	0.17401
A+	0.028745	0.142029	0.188861	0.068983

separation distance from the positive ideal solution and the negative ideal solution has been assessed using Eqs. 6 and 7, respectively, and tabulated in Table 5. Then, the closeness coefficient value was determined using Eq. 8, whose highest value is preferable. To finish, Taguchi was implemented on the closeness coefficient to assess the optimal welding combination [17, 22, 23]. The optimal welding combination has been achieved as current = 100 A, voltage = 13 V, and gas flow rate = 21 L/min. The predicted S/N ratio has also been computed to validate the

**Table 5** Separation distance from positive ideal (best) and the negative ideal (worst) solutions along with the closeness coefficient and their respective S/N ratios

S+	S-	C+	S/N ratio	P-S/N ratio
0.125124	0.305305	0.709304	-2.98336	0.389632
0.145643	0.261475	0.642259	-3.84579	
0.124888	0.248421	0.665457	-3.5376	
0.199897	0.158167	0.441729	-7.09689	
0.255974	0.106956	0.294703	-10.6123	
0.138736	0.298209	0.682487	-3.31812	
0.109123	0.317905	0.744459	-2.56318	
0.095192	0.294989	0.756032	-2.4292	
0.153305	0.204479	0.571515	-4.85944	
0.196398	0.16455	0.455884	-6.82291	
0.17143	0.222615	0.564948	-4.95983	
0.134535	0.252363	0.652272	-3.71142	
0.089694	0.293692	0.766048	-2.31488	
0.233274	0.126803	0.352156	-9.0653	
0.295063	0.109338	0.270369	-11.3609	
0.136516	0.255702	0.651938	-3.71587	
0.131249	0.242639	0.648962	-3.75561	
0.282509	0.076667	0.213453	-13.4139	
0.294178	0.078822	0.21132	-13.5012	
0.256829	0.143763	0.358876	-8.90111	
0.145767	0.285329	0.661868	-3.58457	
0.234734	0.126111	0.349488	-9.13135	
0.194875	0.174153	0.471924	-6.52256	
0.307504	0.126456	0.291401	-10.7102	
0.283448	0.105106	0.270506	-11.3565	

**Table 6** Mean response table for the signal to noise ratios

Level	Current	Voltage	GFR
1	-5.615	-3.712	-8.283
2	-3.999	-4.601	-7.710
3	-6.282	-5.644	-6.134
4	-8.658	-9.047	-5.662
5	-8.261	-9.811	-5.025
Delta	4.659	6.098	3.258
Rank	2	3	1

optimal combination. From Table 5, it has been observed that the predicted S/N ratio is higher among the computed S/N ratios giving justification to the obtained optimal combination (Fig. 4). Table 6 represents the mean response table, which tells that the voltage is the most significant factor.

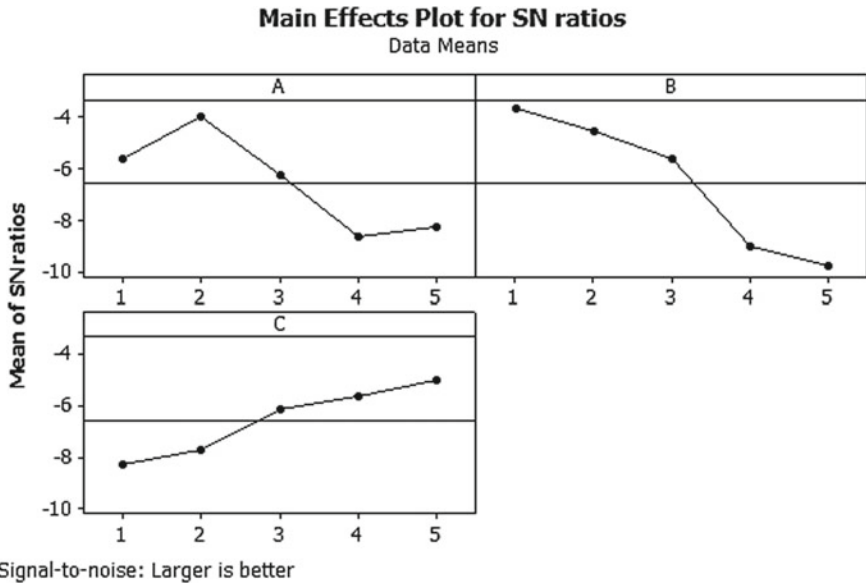


Fig. 4 Main effects plot for parametric settings

## 4 Conclusion

The study uncovers the following conclusive findings:

- i. This work proposes a multi-attribute optimization route utilizing the TOPSIS-Taguchi concept to access the optimal parameter settings for RMD<sup>TM</sup> welding of chrome moly grade 11 steel.
- ii. The weld arc current at 100 A with a 13 V weld arc voltage and 21 L/min. of the gas flow rate yield the optimal combination for the RMD<sup>TM</sup> welding of chrome moly grade 11 steel.
- iii. The proposed methodology may be incorporated into the welding industries to assess the favorable welding condition. Besides accessing the favorable welding condition, the proposed methodology may also be fruitful in offline quality production and control and continuous quality improvement for pipeline welding in the oil and gas sectors.

## References

1. Dinbandhu, Prajapati, V., Vora, J.J., Das, S., Abhishek, K.: Experimental studies of Regulated Metal Deposition (RMD<sup>TM</sup>) on ASTM A387 (11) steel: study of parametric influence and welding performance optimization. *J. Braz. Soc. Mech. Sci. Eng.* **42**, 78 (2020). <https://doi.org/10.1007/s40430-019-2155-3>

2. Bandhu, D., Kumar, R., Nishant, A., Thakur, A.: Characterization of friction stir welding for AA 2014-6061 and influence of aging on their mechanical behavior. In: 5th National Conference on Topical Transcend in Mechanical Technology SJBIT Bangalore (TTMT-17) International, pp. 98–102 (2017)
3. Das, S., Vora, J.J., Patel, V.: Regulated Metal Deposition (RMD<sup>TM</sup>) technique for welding applications: an advanced gas metal arc welding process. In: Advances in Welding Technologies for Process Development, pp. 23–32 (2019)
4. Bandhu, D., Jani, S., Thakur, A.: Characterization of frictional stir welding for two dissimilar materials and influence of ageing on their mechanical properties. *Int. J. Res. Eng., IT Social Sci.* **07**, 21–25 (2017)
5. Cuhel, J.: Modified GMAW for Root Passes. *TPJ-Tube Pipe J.-Fabricator*, 1–4 (2008)
6. Roth, M.: Shinn Mechanical Uses PipeWorx Welding System to Increase Pipe Fabrication Quality and Productivity (2018)
7. Roth, M.: Graham Corporation Meets Reduced Rework Objectives With Help from Miller's PipeWorx<sup>TM</sup> Welding Systems (2018)
8. Cuhel, J., Packard, K.: RMD ® Short-Circuit Metal Transfer, Pulsed MIG Processes with Metal-Cored Wires Improve Pipe Fabrication for Swarfager Welding, pp. 1–8 (2018)
9. Nascimento, L.A. do, Vilarinho, L.O.: Evaluation of GMAW Processes GMAW Controlled Short- Circuit Transfer (STT) applied To Mechanized Girth Welding. In: Congresso Nacional de Engenharia Mecânica Fortaleza/CE, pp. 1–16 (2016)
10. Sharma, P., Dwivedi, D.K.: Comparative study of activated flux-GTAW and multipass-GTAW dissimilar P92 steel-304H ASS joints. *Mater. Manuf. Processes* **34**, 1195–1204 (2019). <https://doi.org/10.1080/10426914.2019.1605175>
11. Hilkes, J., Gross, V.: Welding CrMo steels for power generation and petrochemical applications—past, present and future-. *Weld. World* **53**, 499–504 (2009)
12. Sumesh, A., Nair, B.B., Rameshkumar, K., Santhakumari, A., Raja, A., Mohandas, K.: Decision tree based weld defect classification using current and voltage signatures in GMAW process. In: *Materials Today: Proceedings*, pp. 8354–8363. Elsevier (2018). <https://doi.org/10.1016/j.matpr.2017.11.528>
13. Terner, M., Bayarsaikhan, T.-A., Hong, H.-U., Lee, J.-H.: Influence of gas metal arc welding parameters on the bead properties in automatic cladding. *J. Weld. Joining* **35**, 16–25 (2017). <https://doi.org/10.5781/jwj.2017.35.1.16>
14. Prajapati, V., Dinbandhu, Vora, J.J., Das, S., Abhishek, K.: Study of parametric influence and welding performance optimization during regulated metal deposition (RMD<sup>TM</sup>) using grey integrated with fuzzy taguchi approach. *J. Manuf. Processes* **54**, 286–300 (2020). <https://doi.org/10.1016/j.jmappro.2020.03.017>
15. Vommi, V.B.: Topsis with statistical distances: a new approach to MADM. *Decis. Sci. Lett.* **6**, 49–66 (2017). <https://doi.org/10.5267/j.dsl.2016.8.001>
16. Panda, S.N., Bagal, D.K., Pattanaik, A. Kumar, Patnaik, D., Barua, A., Jeet, S., Parida, B., Naik, B.: Comparative evaluation for studying the parametric influences on quality of electrode using taguchi method coupled with MOORA, DFA, and TOPSIS method for electrochemical machining. In: *Recent Advances in Mechanical Infrastructure*, pp. 115–129 (2020). [https://doi.org/10.1007/978-981-32-9971-9\\_13](https://doi.org/10.1007/978-981-32-9971-9_13)
17. Sonkar, V., Abhishek, K., Datta, S., Mahapatra, S.S.: Multi-objective optimization in drilling of GFRP composites: a degree of similarity approach. In: *3rd International Conference on Materials Processing and Characterisation (ICMPC 2014)*, pp. 538–543. Elsevier (2014). <https://doi.org/10.1016/j.mspro.2014.07.068>
18. Kamaraj, M., Santhanakrishnan, R., Muthu, E.: Investigation of surface roughness and MRR in drilling of Al<sub>2</sub>O<sub>3</sub> particle and sisal fibre reinforced epoxy composites using TOPSIS based Taguchi method. In: *IOP Conference Series: Materials Science and Engineering*. Institute of Physics Publishing (2018). <https://doi.org/10.1088/1757-899X/402/1/012095>
19. Abhishek, K.: Experimental Investigations on Machining of CFRP Composites: Study of Parametric Influence and Machining Performance Optimization (2015). <https://doi.org/10.1007/s11390-005-0552-9>

20. Sun, C.C., Lin, G.T.R.: Using fuzzy TOPSIS method for evaluating the competitive advantages of shopping websites. *Expert Syst. Appl.* **36**, 11764–11771 (2009). <https://doi.org/10.1016/j.eswa.2009.04.017>
21. Velasquez, M., Hester, P.T.: *An Analysis of Multi-Criteria Decision Making Methods* (2013)
22. Kumar Verma, R., Kumar, J., Kumar Kharwar, P., Abhishek, K.: TOPSIS based Taguchi approach for Multi-criteria optimization in quality and productivity characteristics
23. Vora, J.J., Abhishek, K., Ramkumar, P.: Different methodologies for the parametric optimization of welding processes. In: *Advances in Welding Technologies for Process Development*, pp. 55–75. CRC Press (2019). <https://doi.org/10.1201/9781351234825-4>

# The Magnetically Assisted Abrasive Flow Machining Process: Review



Anil Jindal, Sushil Mittal, and Parlad Kumar

**Abstract** This paper presents an extensive review for the magnetically assisted abrasive flow machining (MAFM) process. MAFM is used to superfinish advanced materials such as metal matrix composites (MMCs), super alloys, ceramics. In the MAFM process, the magnetic field can be generated using fixed or varied field magnets. The research work highlighted broad classification of the MAFM process. This study gives the detailed insight into experimental investigation involving important process parameters such as magnetic flux, extrusion pressure, no. of cycles, etc. and response parameters such as material removal rate (MRR), surface roughness associated with MAFM. The key roles of MAFM in machining of nanomaterials are discussed, and the advantages of MAFM are outlined. The importance of MAFM process in the present scenario is highlighted. This paper will provide extensive and better understanding of the MAFM process.

**Keywords** Magnetically assisted abrasive flow machining (MAFM) · Abrasive flow machining (AFM) · Material removal rate (MRR) · Surface roughness · Metal matrix composites (MMCs)

## 1 Introduction

MAFM is a process to finish the hard and complex geometry profiles with superior finishing and accuracy. High-quality and limited dimensional tolerance parts utilized in the aircraft, automobile, and shipbuilding industries require excellent surface finish. Common materials used for machining process include tool steel and cemented carbides. In case of MAFM process, the commonly used abrasive flow materials are sintered mixture of aluminium, silicon carbide and iron powder. Conventional methods like filing, lapping, honing, superfinishing, grinding, pol-

---

A. Jindal (✉) · P. Kumar  
Department of Mechanical Engineering, Punjabi University, Patiala, Punjab, India

S. Mittal  
Department of Mechanical Engineering, Chandigarh University, Gharuan, Punjab, India

ishing and buffing are used to modify the surface texture produced by manufacturing process [1, 2]. Abrasive flow machining (AFM) process came into existence in 1960. AFM process improved the surface roughness from 2 to 0.2  $\mu\text{m}$  are in inner finishing of turbo engines, aerospace [3]. To further optimize the finishing operation, unconventional machining process like MAFM is gaining attention due to their ability to supply better surface finish than the conventional processes. MAFM is a process in which a magnetic flux is used as a machining force. This force directs the abrasive particles towards the target surface. The efficiency of the method is controllable by the electrical current to stop the over-finishing of surface roughness with careful monitoring of the process [4]. Therefore, MAFM has been used for accuracy of surface finishing due to many advantages like self-adaptability, controllability and self-sharpening [5] (Fig. 1).

## 2 Process Parameters of MAFM

In MAFM process, the common process parameters are:

- extrusion pressure
- no. of cycles
- magnetic flux density
- work piece materials
- mesh size of abrasives
- concentration of abrasives

The common response parameters are:

- Surface roughness ( $R_a$ )
- Material removal rate (MRR) (Fig. 2).

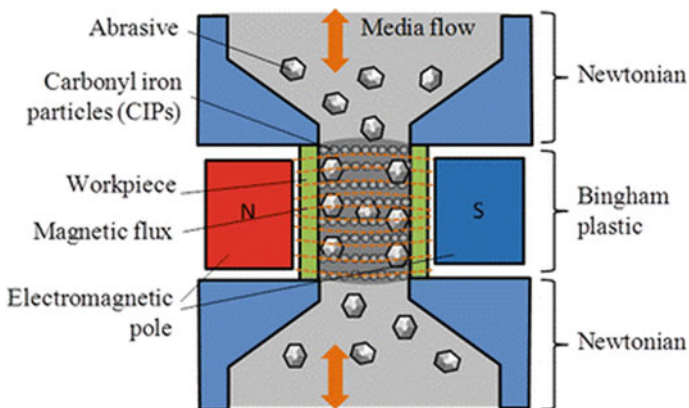


Fig. 1 Media flow in MAFM [6, 7]



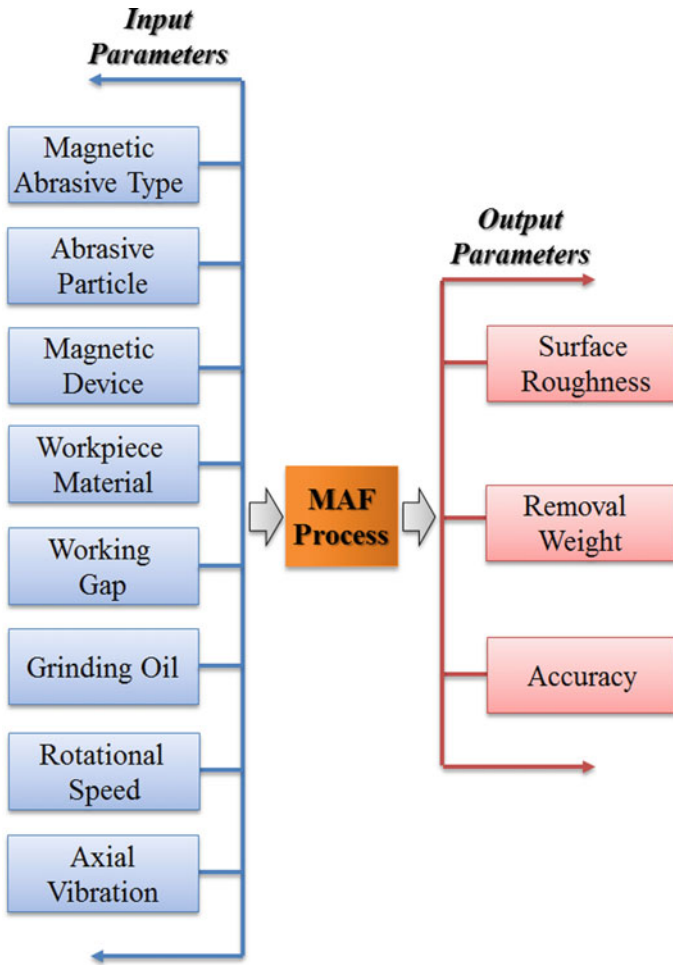


Fig. 2 Process parameters of MAFM [8, 9]

The work done by several researchers signify the feasibility, effectiveness and economic aspect of MAFM in various manufacturing domains. Ramesh Babu et al. (1998) investigated the effect of varied input parameters on the surface quality of chrome steel work piece. It was observed that roughness and hardness of the work piece influencing the surface finish significantly [10]. Yamaguchi and Shinmura proposed an indoor magnetic abrasive finishing process for quality finishing of inner surface of the tubes. It was observed that surface texture is filled with micro-scratches, and this feature exhibits that the MAFM process provides smoothing with high MRR [11]. It is studied that different researchers had done

experiment for understanding the results of different input parameters on surface finishing during MAFM process.

Studies of the main features of the MAFM process to form the model for kinematic process were performed and investigated for the outcome of input parameters like rotational speed of electromagnet, abrasive particles size and current intensity in output parameters, namely edge and surface finishing. The comparative study performed for the traditional grinding and superfinishing method to elucidate the nanomachining capabilities of MAFM process (Fig. 3).

The analysis of the principle and property of the unbounded MAPs on chrome steel (SUS 304) by cylindrical MAFM process was conducted. It was explained that how Ra and MRR affected by the process parameters as well as their mechanism. It was found that steel grit produces superior finishing than that of iron grit when mixed with SiC abrasive [12]. The study of the principle of electrolytic magnetic abrasive finishing (EMAF) was conducted in 2003. The analysis conducted for the impact of various process parameters with different range in Ra and MRR. The experimental result also shows that with a high electrolytic current, EMAF process produces excellent finishing characteristics [13].

In 2004, experiments conducted on stainless steel during MAFM process using Taguchi design experiment and located the optimum input parameters. It was explained that how Ra affected by input parameters, namely voltage, revolution speed of the electromagnet, abrasive particles size and dealing gap. The design

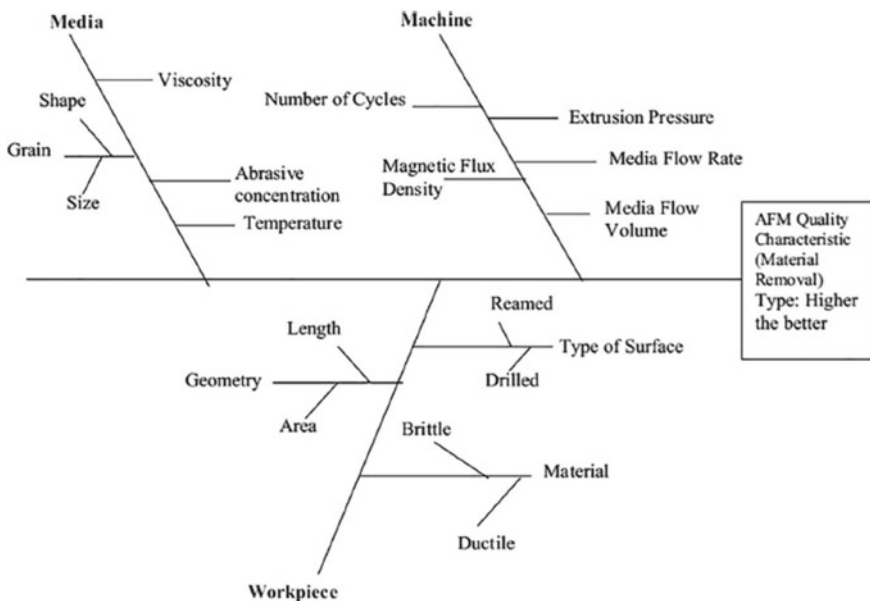
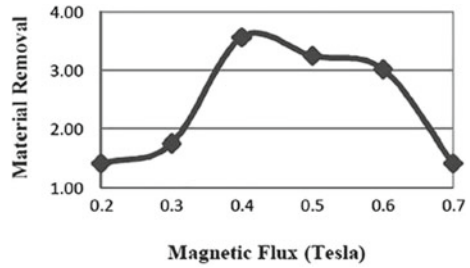


Fig. 3 Ishikawa cause-effect diagram for MAFM process [12]

**Fig. 4** Effect of magnetic flux in MAFM process [14]



made of the force transducer for inspection of the finishing process and fabricated to calculate the force during MAFM process [14] (Fig. 4).

In 2012, introduction of a hybrid machining as cylindrical electrochemical magnetic abrasive machining (C-EMAM) is employed in cylindrical surface for effective surface finishing which is hard by other machining processes. It was observed that for magnetic steel, how Ra and MRR are influenced with the electro-chemical dissolution and magnetic abrasion, respectively [15]. It was observed that to enhance the finishing quality, magnetic field should be used [16].

### 3 Advancements in MAFM Process

Singh et al. [17] investigated the abrasive flow machining assisted by the magnetic field for the parametric optimization using Taguchi method. It was found that aluminium and stainless steel work pieces showed poor surface finishing with magnetic-assisted abrasive flow machining, but brass work piece showed very good surface finishing with magnetic-assisted abrasive flow machining.

Chahal et al. [18] investigated the abrasive flow machining of Al-6061 alloy assisted with the electrochemical machining. It was also recommended to use hybrid abrasive flow machining to finish complex geometrical shapes for obtaining the superfinishing.

It was reported that the magnetic-assisted abrasive flow machining of H13 tool steel. The cutting tool used was SiC, Al<sub>2</sub>O<sub>3</sub> abrasive particles with hydraulic oil. It was found that the increase in the magnetic field intensity and number of abrasive particles increases MRR and surface finishing of the H13 tool steel. It was recommended that the magnetic-assisted abrasive flow machining should be used for finishing harder materials [19–21] (Fig. 5).

Mittal et al. [23] investigated the AFM process. The orthogonal array was used to examine the effect of different input parameters on the performance of the process, whereas the analysis of variance (ANOVA) was used to check the significance of the different input parameters. Based on the orthogonal array and ANOVA technique, the relation between input and output parameters was established. It was found that the extrusion pressure and no. of cycles are the two significant factors in case of AFM process (Fig. 6).

**Fig. 5** Ferromagnetic particle in MAFM process [22]

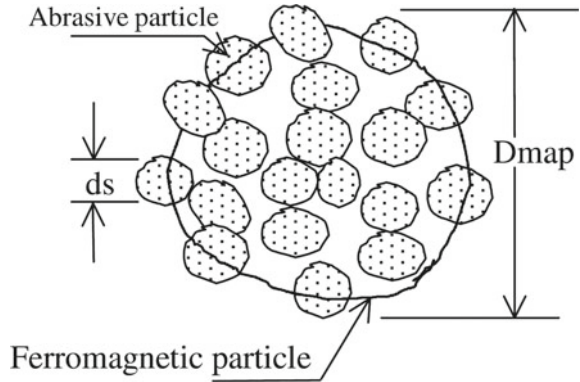
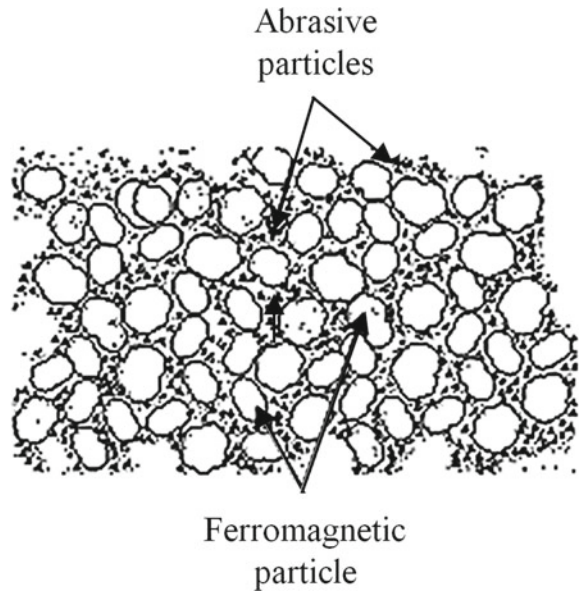


**Fig. 6** Structural model of the unbounded magnetic abrasive particles [24]



Mittal et al. [25] found that extrusion pressure helps in increasing the surface finishing and MRR of the AFM process.

Sankar et al. [26] reported the nanomachining of surgical stainless steel using abrasive flow machining. It was found that the AFM process successfully removed the hard recast layer of the work piece and significantly improved the surface finishing.

Ya et al. [27] reported that the AFM process is very useful in achieving good surface finishing and MRR of hollow steel work pieces. Zhang et al. [28] found that the MAFM process is an advanced non-conventional machining for achieving smooth surface finishing for hard materials which is practically not possible with

conventional machining. Tan et al. [29] reported that the AFM process helped in reducing the cutting time of the material.

Gao et al. [30] investigated the abrasive flow machining of blisk for obtaining surface uniformity. The blade surface of blisk used for aerospace was machined using abrasive flow machining. The work piece material was made up of steel. The SiC abrasive particles with hydraulic oil were used for machining. The testing was conducted using 3D surface profiler. The guide blocks were provided in addition to the fixture in abrasive flow machining. The surface uniformity of the blisk was improved after abrasive flow machining.

Gao and Wu [31] reported the abrasive flow machining of bearing ring raceways for obtaining precision polishing using 3D printing and CNC machining. It was found that the assistance of 3D printing and CNC machining to the abrasive flow machining improved the surface finishing of the bearing ring raceways and provided the precision polishing of the work piece.

Mihotovic et al. [32] investigated the AFM process for complex automotive parts. The AFM process significantly improved the surface finishing of the work pieces. It was proposed to use abrasive flow machining for machining complex geometrical work pieces.

Sankar et al. [33] reported the abrasive flow machining of Al alloy work pieces at microlevel/nanosurface level. The abrasive flow machining significantly improved the surface finishing of the work piece.

Subramanian et al. [34] investigated the AFM process for biomedical implants. It was found that the decrease in working pressure increases the surface finishing and MRR for the given work piece. It was recommended to adopt the abrasive flow machining for finishing the biomedical implants.

Kavithaa and Balashanmugam [35] investigated the abrasive flow finishing of pharmaceutical components such as prosthetic implants and extrusion die used for biomedical industries. It was found that the abrasive flow machining has significantly increased the surface finishing of the prosthetic implants and biomedical components.

Tan et al. [36] investigated the comparative study between soft abrasive flow and three-phase (solid–liquid–gas) abrasive flow machining using bubble collapsing. It was found that the bubble collapsing results into the increase of abrasive flow velocity resulting into superior efficiency of three-phase (solid–liquid–gas) abrasive flow machining as compared with soft abrasive flow machining. The surface finishing was greatly improved using three-phase (solid–liquid–gas) abrasive flow machining.

Sylvain et al. [37] reported the combined chemical—abrasive flow machining for work piece Inconel 625 for supersurface finishing. It was found that the combined chemical—abrasive flow machining process successfully removed the semi-welded particles and significantly improves the surface finishing of the work piece.

Venkatesh et al. [38] found that ultrasonic-assisted AFM process can be used for the finishing of long and non-straight internal and external holes.

Sankar et al. [39] investigated the modelling of viscoelastic medium and simulation of microholes superfinished by abrasive flow machining process for work piece surgical stainless steel (316L). The abrasive flow finishing process not only removes the hard recast layer from the inner wall of microhole but also finishes outer sharp edges.

Kursad and Omer [40] investigated the effect of abrasive types on the work piece DIN 1.2379 tool steel. It was found that abrasive media prepared using  $B_4C$  and  $SiC$  gave more surface finishing and improvement as compared with  $Al_2O_3$  and Garnet.

Ling et al. [41] investigated the numerical simulation of abrasive flow machined  $90^\circ$  elbow pipe made up of carbon steel using solid-liquid two-phase machining. It was found that increasing the inlet velocity of abrasive flow increases the dynamic pressure in the curved path of the work piece which improves the surface finishing of elbow pipe. The technology of finishing elbow pipe provides support and development for the AFM process. Qing et al. [42] found that more intense is the collision and friction of abrasive flow with the wall, finer will be the surface polishing of the nozzle.

Yeo and Nagalingam [43] reported the abrasive flow machining of additive manufactured work piece. It was found that abrasive flow machining of aluminium alloy work piece successfully removed surface irregularities and resulted into smoother surface.

## 4 Conclusions

Many engineering components such as aerospace panels, automobile nozzles, dies, I.C. engines part such as piston cylinder surface are manufactured by using  $Al/SiC/B_4C$  metal matrix composites. These components have wide range of applications in aerospace, automobile, defence and electronic industries due to their high hardness, wear resistance and reduced weight. The main problem in these components is their machining due to their high value of hardness. This problem further becomes more severe in case of machining of internal sides of a cylindrical hole or any other irregular shape. The literature suggests that over the years, different methods have been developed for such hard and difficult to machine components. Out of these methods, magnetic abrasive flow machining is considered as a best suitable finishing process for simple as well as complex geometries.

In the recent past, magnetic abrasive flow machining process has been used by researchers for machining of different metals such as stainless steel, brass, aluminium, etc. and metal matrix composites such as aluminium metal reinforced with ceramics such as  $SiC$ ,  $B_4C$ , etc. The existing research studies suggest that the use of magnetic abrasive flow machining has significant effect on the material removal rate and surface roughness of the work pieces. The various irregularities occurred on the surface of work piece after micro-EDM machining was successfully removed using

magnetic abrasive flow machining. The magnetic abrasive flow machining process is useful for machining of Al/SiC/B<sub>4</sub>C hybrid MMCs also. This technology is useful for superfinishing of complex geometries.

## 5 Future Scope of the Work

MAFM process may be suitable for superfinishing of the medical parts and biomedical parts. Various medical and biomedical devices such as pacemakers, hip joints, knee joints can be super finished using MAFM. The magnetic abrasive flow machining can also be used in combination with the advanced machining technology to obtain highly customized surface profiles and finishing. The MAFM can greatly reduce the time, effort and money in superfinishing the intricate profiles with maximum accuracy.

## References

1. Mellal, M.A., Williams, E.J.: Parameter optimization of advanced machining processes using optimization algorithm. *J. Int. Manuf.* **28**, 927–942 (2014)
2. Saraeian, P., Mehr, H.S., Moradi, B., Tavakoli, H., Alrahmani, O.K.: Parameter optimization of advanced machining processes using optimization algorithm. *Mater. Manuf. Process.* **31**, 2023–2029 (2016)
3. Groeger, F., Segel, E., Uhlmann, S., Robkamp: Definition of edges in correlation to abrasive flow machining as a finishing process. *Surf. Topography Metrol. Prop.* **6**(3), 1–11 (2018)
4. Jain, V.K.: *Advanced Machining Processes*. Allied Publishers, Mumbai (2002)
5. Shinmura, T., Takazawa, K., Hatano, E.: Study on magnetic abrasive process-application to plane finishing. *Bull. Jpn Soc. Precis. Eng.* **19**, 289–291 (1985)
6. Ahmad, S., Gangwar, S.: Optimization of process parameters affecting surface roughness in magnetic abrasive flow machining. *J. Mater. Manuf. Processes* **32**(15), 1723–1729 (2017)
7. Sato, T., Yeo, S., Zarepour, H.: *Handbook of Manufacturing Engineering and Technology*. Springer, pp. 1051–1088 (2015)
8. Sadiq, A., Shunmugam, M.S.: Investigation into magnetorheological abrasive honing (MRAH). *Int. J. Mach. Tools Manuf.* **49**, 554–560 (2009)
9. Heng, L., Kim, Y.J., Mun, S.D.: Review of superfinishing by the magnetic abrasive finishing process. *High Speed Mach.* **3**, 42–55 (2017)
10. Jayakumar, P., Babu, N.R., Radhakrishnan, V.: Experimental studies on the improvement of work surface finish by magnetic abrasive machining. *Proc. ISPE* **3903**, 9–19 (1998)
11. Yamaguchi, H., Shinmura, T.: Study of the surface modification resulting from an internal magnetic abrasive finishing process. *Wear* **225–229**, 246–255 (1999)
12. Khairy, A.B.: Aspects of surface and edge finish by the magneto abrasive particles. *J. Mater. Process. Technol.* **116**, 77–83 (2001)
13. Chang, G.W., Yan, B.H., Hsu, R.T.: Study on cylindrical magnetic abrasive finishing using unbounded magnetic abrasive. *Int. J. Mach. Tools Manuf.* **42**, 575–83 (2002)
14. Yan, B.H., Chang, G.W., Cheng, T.J., Hsu, R.T.: Electrolytic magnetic abrasive finishing process. *Int. J. Mach. Tools Manuf.* **43**, 1355–1366 (2003)
15. Singh, D.K., Jain, V.K., Raghuram, V.: The parametric study of the magnetic abrasive finishing process. *J. Mater. Process. Technol.* **149**, 22–29 (2004)

16. Judal, K.B., Yadava, V.: Experimental investigations into cylindrical electro-chemical magnetic abrasive machining of AISI-420. *Int. J. Abras. Technol.* **5**, 315–331 (2012)
17. Singh, S., Shan, H., Kumar, P.: Parametric optimization of magnetic field assisted abrasive flow machining by the Taguchi method. *Qual. Reliab. Eng. Int.* **18**(4), 273–283 (2002)
18. Chahal, B., Gupta, R., Vaishya, R.: Experimental Investigation to optimize process parameters in electrochemical assisted abrasive flow finishing of Al-6061 alloy using Taguchi method. *I-manager's J. Mater. Sci.* **3**(1), 14–22 (2015)
19. Jayswal, S.C., Jain, V.K.: Modeling and simulation of magnetic abrasive finishing process. *Int. J. Adv. Manuf. Technol.* **26**, 477–490 (2005)
20. Judal, Y.: Review of research work in magnetic abrasive finishing. In: *Proceedings of National Conference on Recent Advances in Manufacturing (RAM-2010) SVNIT Surat*, pp. 59–65 (2010)
21. Shabgard, M., Tabriz, F., Gholipour, A.: Experimental study of the effects of abrasive particle size and workpiece hardness in magnetic abrasive flow machining. *Modares Mech. Eng.* **16** (8), 131–138 (2016)
22. Singh, S., Shan, H.S.: Development of magneto abrasive flow machining process. *Int. J. Mach. Tools Manuf.* **42**, 953–959 (2002)
23. Mittal, S., Kumar, V., Kansal, H.: Multi objective optimization of process parameters involved in micro-finishing of Al/SiC MMCs by abrasive flow machining process. *J. Mater.: Des. Appl.* **232**(4), 1–14 (2016)
24. Sankar, M., Jain, V., Ramkumar, J., Sareen, S., Singh, S.: Medium rheological characterization and performance study during rotational abrasive flow finishing (R-AFF) of Al alloy and Al alloy/SiC MMCs. *Int. J. Adv. Manuf. Technol.* **96**(9–12), 1–15 (2018)
25. Mittal, S., Kumar, V., Kansal, H.: Study of machining characteristics of MMCs using abrasive flow machining. *Int. J. Surf. Eng. Mater. Technol.* **2**(2), 29–33 (2012)
26. Sankar, M., Singh, S., Kumar, D., Rajurkar, K.: Nano-finishing of microslots on surgical stainless steel by abrasive flow finishing process: experimentation and modeling. *J. Micro Nano Manuf.* **6**(2), 1–12 (2018)
27. Dong, Z., Ya, G., Liu, J.: Study on machining mechanism of high viscoelastic abrasive flow machining for surface finishing. *J. Eng. Manuf.* **231**(4), 1–10 (2015)
28. Zhang, X., Xu, Y., Li, J., Zhou, Z., Wei, L.: Quality influence and process parameter optimization of T-pipe in abrasive flow finishing. *J. Adv. Mech. Eng.* **9**(8), 1–13 (2017)
29. Tan, D., Ji, S., Fu, Y.: An improved soft abrasive flow finishing method based on fluid collision theory. *Int. J. Adv. Manuf. Technol.* **85**(5–8), 1261–1274 (2016)
30. Gao, H., Fu, Y., Wang, X., Wei, H., Li, S.: Blade surface uniformity of blisk finished by abrasive flow machining. *Int. J. Adv. Manuf. Technol.* **84**(5–8), 1725–1735 (2016)
31. Gao, H., Wu, M.: Experimental study on large size bearing ring raceways precision polishing with abrasive flowing machine (AFM) method. *Int. J. Adv. Manuf. Technol.* **83**(9–12), 1927–1935 (2016)
32. Mihotovic, V., Uhlmann, E., Robkamp, S., Dethlefs, A.: A pragmatic modeling approach in abrasive flow machining for complex-shaped automotive components. *CIRP Conf. High Performance Cutting* **46**, 51–54 (2016)
33. Sankar, M., Singh, S., Raj, A., Jain, V.: Finishing of force analysis and simulation of nano surface roughness in abrasive flow finishing process using medium rheological properties. *Int. J. Adv. Manuf. Technol.* **85**(9–12), 2163–2178 (2016)
34. Subramanian, K., Balashanmugam, N., Kumar, P.: Nanometric finishing on biomedical implants by abrasive flow finishing. *J. Inst. Eng.* **97**(1), 55–61 (2016)
35. Kavithaa, T., Balashanmugam, N.: Nanometric finishing of typical industrial components by abrasive flow finishing. *Int. J. Adv. Manuf. Technol.* **85**(9–12), 2189–2196 (2016)
36. Ge, J., Ji, S., Tan, D.: A gas-liquid-solid three phase abrasive flow processing method based on bubble collapsing. *Int. J. Adv. Manuf. Technol.* **95**(1–4), 1069–1085 (2018)
37. Mohammadian, N., Turenne, S., Brailovski, V.: Surface finish control of additively-manufactured Inconel 625 components using combined chemical-abrasive flow polishing. *J. Mater. Process. Technol.* **252**, 728–738 (2018)



38. Venkatesh, G., Sood, D., Sharma, A.: On surface integrity of Al2014 alloy finished by Ultrasonic assisted abrasive flow machining. *Mater. Sci. Eng.* **346**, 1–8 (2018)
39. Sankar, M., Singh, S., Kumar, D., Jain, V.: Viscoelastic medium modeling and surface roughness simulation of micro holes finished by abrasive flow finishing process. *Int. J. Adv. Manuf. Technol.* **95**(1–4), 1–18 (2018)
40. Kursad, O.E.: Effects of abrasive types on the surface integrity of abrasive-flow-machined surfaces. *J. Eng. Manuf.* **232**(6), 1–10 (2016)
41. Ling, G., Li, J., Wang, B., Hu, J.: Numerical simulation analysis of polished elbow in solid-liquid two phase abrasive flow machining. *Mater. Sci. Eng.* **382**, 1–6 (2018)
42. Qing, W., Su, N., Ling, G., Li, J.: Numerical simulation analysis of polished elbow in solid-liquid two phase abrasive flow machining. *Mater. Sci. Eng.* **382**, 7–12 (2018)
43. Yeo, S., Nagalingam, A.: Controlled hydrodynamic cavitation erosion with abrasive particles for internal surface modification of additive manufactured components. *Int. J. Sci. Technol. Friction, Lubr. Wear* **414–415**, 89–100 (2018)

# Comparison of Static and Harmonic Response of Structural Steel and Aluminium Alloy Automotive Shock Absorbers



Abhishek Sharma, Surendra Kumar Yadav, Anshul Yadav, Virendra Kumar, and Anil Kumar

**Abstract** In this study, two different materials, i.e. structural steel and aluminium alloy 6061, are used as potential shock absorber materials, and their performance is calculated using FEA analysis. The stresses, deformations, fatigue life and vibrational analysis of both the shock absorbers are compared. It is concluded from this study that the shock absorber made of structural steel shows excellent stress resistance even at heavy loads and the fatigue life of steel is higher than that of shock absorber made of aluminium. However, both the materials show approximately equal vibrations when the loading is applied. The study suggests that both these materials can be used in the shock absorber. However, because of high strength and high fatigue life characteristics, shock absorber made of structural steel should be preferred over shock absorber made of aluminium.

**Keywords** Finite element method · Shock absorber · Fatigue life · Vibrational analysis

## 1 Introduction

A shock absorber reduces vibration by dissipating energy, smooths vehicle motion and ensures that vehicle's tires remain in contact with the road. The basic working principle of the shock absorber is energy conversion and dissipation. The energy that causes vibration (kinetic energy) is converted into heat energy, and then this heat is released in atmosphere through heat exchanging mechanism. Both hydraulic and pneumatic shock absorbers are available. Hydraulic shock absorbers use oil as fluid while pneumatic shock absorbers carry air that is heated and exhausted to the outer atmosphere [1]. In the absence of this heat dissipation mechanism, if only spring is used to absorb energy that is induced by bumps or uneven road, the

---

A. Sharma · S. K. Yadav  
K.R. Mangalam University, Gurugram, India

A. Yadav · V. Kumar (✉) · A. Kumar (✉)  
Kamla Nehru Institute of Technology, Sultanpur, India

vehicle will continue to bounce and will have continuous vibration until all the potential energy that was stored by spring is released. This will cause a very bumpy and unsmooth drive. To ensure controlled and smooth drive, a dampening system in the form of the shock absorber is used. The fluid present in this system is forced into small restricted openings known as orifices. This pushing of the fluid increases hydraulic resistance that converts kinetic energy into heat energy [2].

In actual sense, the shock absorber is an oil pump. It has two mounts, upper and lower mounts. Upper mounts connect with vehicle's frame, while lower mounts connect with the axle. The upper mount is connected with piston rod which is connected with the piston. When the wheel of a vehicle comes in contact with a bump or anything that induce vertical vibration in it, the spring starts to coil and uncoil. This transfers energy to shock absorber. The moving piston pushes fluid into the orifices that are present on the piston, and because of the relatively small size of orifices, a small amount of fluid passes through and that too under very high pressure. This causes the piston to slow down as a result of which spring motion is slowed down [3]. A complete cycle is comprised of two parts, i.e. compression cycle and extension cycle. Compression cycle is also known as bump cycle, while the extension cycle is known as the rebound cycle. Compression cycle starts when the piston moves downwards and compresses fluid that is below the piston. During the extension cycle, the piston moves upwards towards the pressure tube and compress fluid that is above the piston [4]. Modern shock absorbers adjust according to the velocity of the vehicle. The faster it moves, the more resistance the shock absorber will provide [5–12].

## 2 Computational Details

ANSYS has a built-in material library where there are a vast number of materials that are categorized based on its physical properties and general behaviour. We selected two materials for our analysis and compared its effects. The two materials selected in our analysis were structural steel and aluminium alloy. The simplified geometry is shown in Fig. 1a. In this study, relatively midsized mesh elements were used with quadratic elements type to reduce the computational power requirement. This reduces the overall simulation run time. Image of the mesh and its details are shown in Fig. 1b.

Since shock absorbers are usually connected to the chassis on one side and tire on the other side, one can assume that one side of the shock absorber is fixed and there is a force acting on the other side of the shock absorber. The horizontal/lateral movement is restricted by applying remote displacement and making the motion in  $x$ - and  $z$ -direction as well as rotation in all the axes.

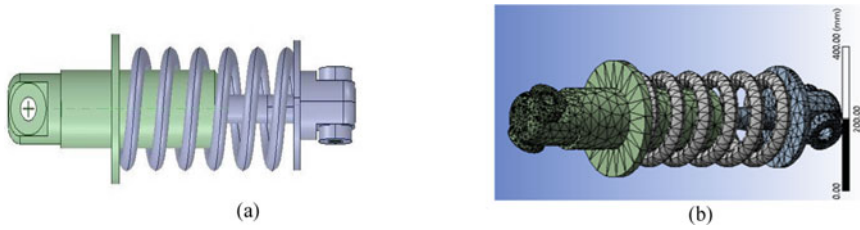


**Fig. 1** **a** 3D view of shock absorber, **b** image of generated mesh in ANSYS

## 2.1 Static, Fatigue and Vibration Analysis

In static analysis, results were analyzed for the following parameters: total deformation, von Mises stresses, equivalent strain, the factor of safety (based on tensile yield stress and shear yield stress). Total deformation shows the magnitude of displacement/deformation of the resultant vector. This includes the combined effect of all three axes. Von Mises stresses were evaluated because it is industry standard. Both shear and tensile factor of safety were analyzed to see if the model is safe in both tensile and shear stress conditions. Because shear yield strength is 57% of the total tensile yield strength, it's a good idea to check if the model could withstand such stresses. Fatigue analysis was analysed using Goodman criteria. Fully reversed force method was used, which means that the force will oscillate between  $-100\%$  and  $+100\%$ . Five parameters were checked to see the behaviour of the model, namely life, damage, the factor of safety, biaxiality indication and fatigue sensitivity analysis. All the other analyses settings are the same as static analysis except that in vibration analysis. We used three different damping ratios: 0.2, 0.25 and 0.3. Analyses were performed to predict the harmonic response of the model under these damping ratios. Three parameters were analysed, which are amplitude/phase angle versus frequency, vibration-induced deformation and vibration-induced stresses.

## 3 Results and Discussion

### 3.1 Static Analysis

Based on the boundary conditions and material as structural steel, the solver predicted that the maximum total deformation obtained was 9.72 mm. Based on the boundary conditions and material as aluminium alloy, the solver predicted that the maximum total deformation obtained was 25.8 mm. The contour of the deformation is shown in Fig. 2.

Based on the material properties of structural steel and the boundary conditions, the predicted maximum von Mises strain was  $0.6 \times 10^{-4}$ . Based on the material properties of aluminium alloy, and the boundary conditions, the predicted

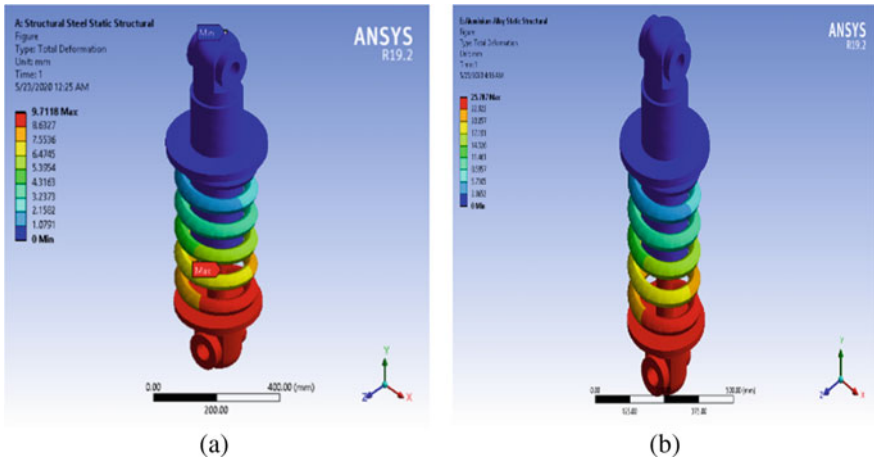


Fig. 2 Contour of total deformation produced in a structural steel, b aluminium alloy

maximum von Mises strain was  $1.55 \times 10^{-3}$ . The contour of von Mises strain is shown in Fig. 3.

Based on the material properties of structural steel and the boundary conditions, the predicted minimum factor of safety is 2.21. This factor of safety is based on tensile yield stress criteria. Based on the material properties of aluminium alloy, and the boundary conditions, the predicted minimum factor of safety is 4.5. This factor of safety is also based on tensile yield stress criteria. The contour of the factor of safety is shown in Fig. 4.

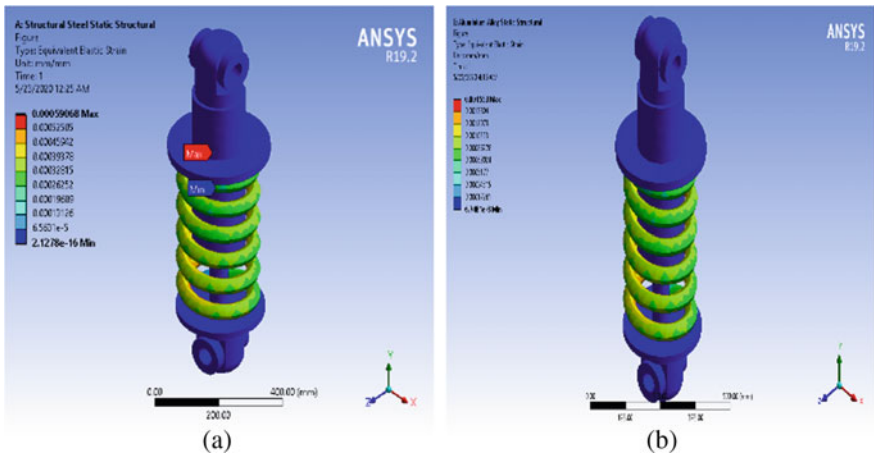
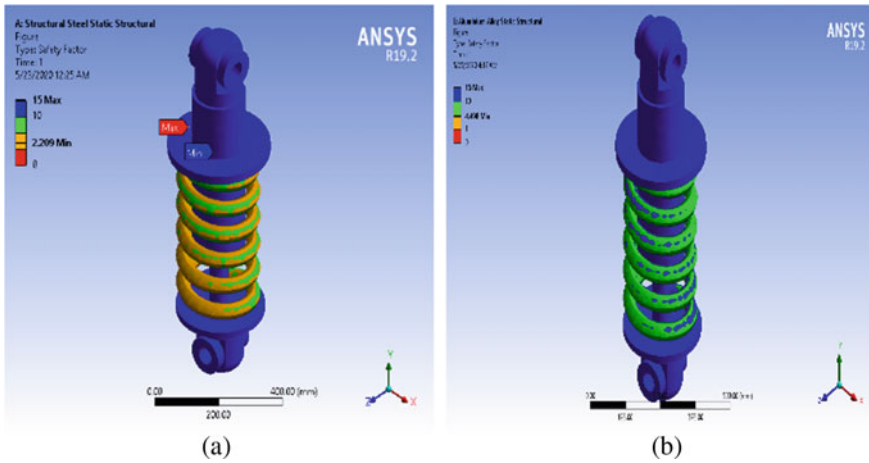
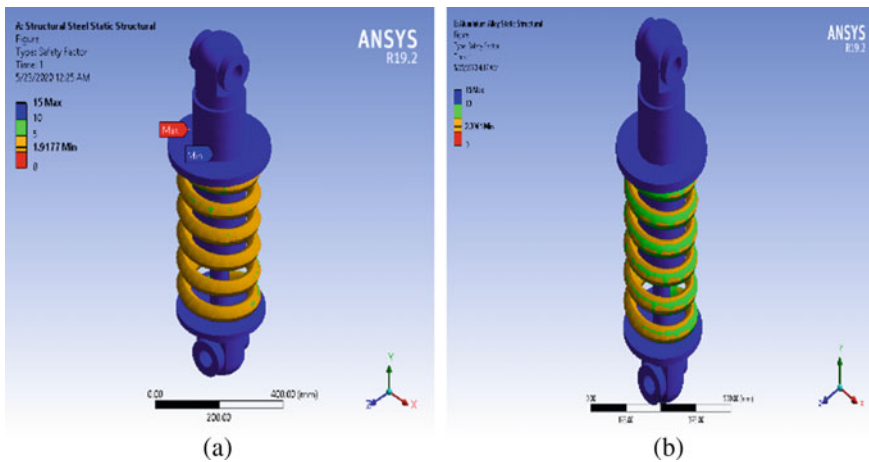


Fig. 3 Contour of equivalent elastic strain produced in a structural steel, b aluminium alloy



**Fig. 4** Contour of the factor of safety based on tensile stress in **a** structural steel, **b** aluminium alloy

Based on the material properties of structural steel and the boundary conditions, the predicted minimum factor of safety is 1.92. This factor of safety is based on shear yield stress criteria. Based on the material properties of aluminium alloy, and the boundary conditions, the predicted minimum factor of safety is 2.3. This factor of safety is also based on shear yield stress criteria. The contour of the factor of safety is shown in Fig. 5.



**Fig. 5** Contour of factor of safety based on shear stress of **a** structural steel, **b** aluminium alloy

### 3.2 Fatigue Analysis

Fatigue analysis was performed to predict the performance of a shock absorber under cyclic loading condition. Because shock absorbers are always subjected to cyclic loadings, fatigue analysis is one of the key criteria to scrutinize the mechanical design of a shock absorber. The minimum strain-life cycles are  $2 \times 10^5$  cycles. The least value lies on the inside of the spring (internal diameter). This is due to the maximum stress concentration levels in the same region. Repeated higher stresses in the region cause strain hardening, thus making the model prone to failure. The minimum strain-life cycles are  $5.33 \times 10^5$  cycles. The least value lies on the inside of the spring (internal diameter). This is due to the maximum stress concentration levels in the same region. Repeated higher stresses in the region cause strain hardening, thus making the model prone to failure. Life based on properties of the material and the specified boundary conditions are shown in Fig. 6.

The minimum fatigue factor of safety is depicted in Fig. 7. The minimum factor of safety is 0.76. This lies in the region of higher stress concentration. The minimum factor of safety is 0.95. This lies in the region of higher stress concentration.

### 3.3 Harmonic Analysis

Harmonic analysis is done to find out the response behaviour, total deformation and total vibration-induced stresses. The amplitude versus frequency response of the design is depicted in Fig. 8 for structure steel and specified boundary conditions. The results indicate that at lower frequencies, the amplitude of vibration is higher,

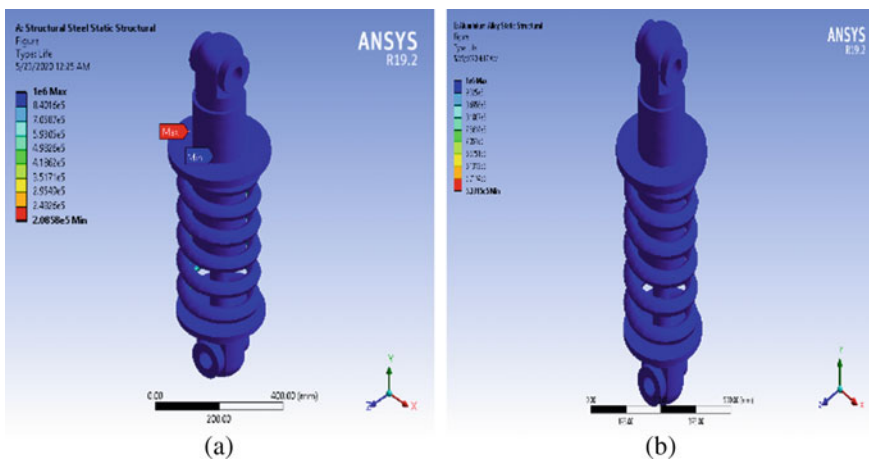
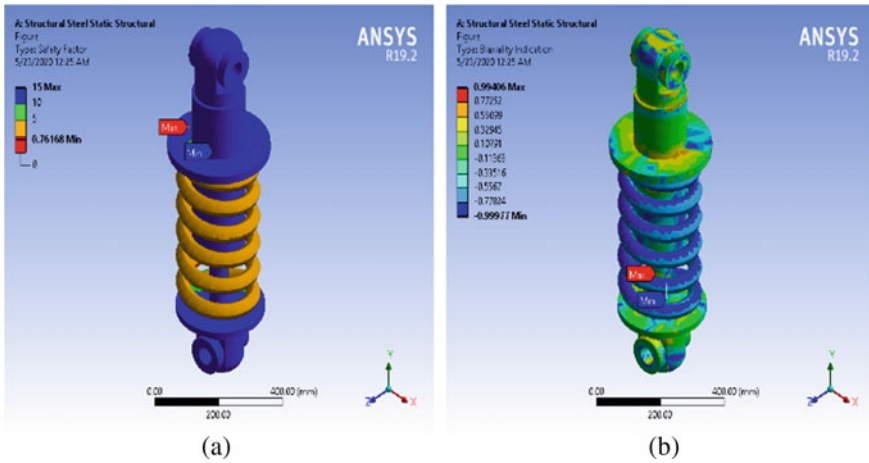
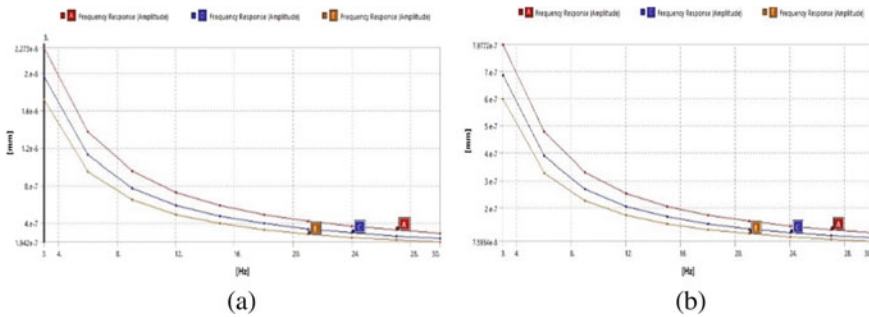


Fig. 6 Contour of life based on fatigue analysis of a structural steel, b aluminium alloy



**Fig. 7** Contour of factor of safety based on fatigue analysis of **a** structural steel, **b** aluminium alloy



**Fig. 8** Amplitude versus frequency response **a** structural steel, **b** aluminium alloy

for higher frequencies, the amplitude is low. This is represented by an asymptotic curve. One can also understand that for higher damping ratio, the amplitude of vibration is lower and vice versa. The amplitude versus frequency response of the design is depicted in Fig. 8 for aluminium alloy and specified boundary conditions. The results indicate that at lower frequencies, the amplitude of vibration is higher, for higher frequencies the amplitude is low. This is represented by an asymptotic curve. One can also understand that for higher damping ratio, the amplitude of vibration is lower and vice versa.

The phase angle versus frequency response of the design is shown in Fig. 8 for structural steel and specified boundary conditions. The results indicate that at lower frequencies, the phase angle of vibration is higher, for higher frequencies, the amplitude is low. This is represented by an asymptotic curve. One can also understand that for higher damping ratio, the phase angle of vibration is lower and



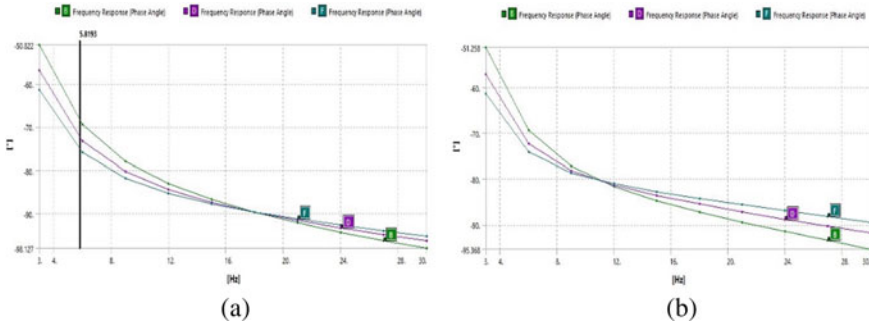


**Fig. 9** Plot of phase angle versus frequency response of **a** structural steel, **b** aluminium alloy

**Table 1** Results of the analysis on structural steel and aluminium alloy

Parameter	Aluminium alloy	Structural steel
Von Mises stress (MPa)	10.5.5	71
Equivalent strain (mm/mm)	0.00153	0.0006
Total deformation (mm)	25.787	9.71
Tensile factor of safety	4.5	2.21
Shear factor of safety	2.3	1.92
Stress life (cycles)	$5.33 \times 10^5$	$2.086 \times 10^5$
Damage	1875.6	4794.5
Biaxiality	-0.999 to 0.99	-0.999 to 0.994
Fatigue sensitivity at 50%	$10^6$	$10^6$
Fatigue sensitivity at 150%	8525	46,776
Fatigue factor of safety	0.948	0.762

vice versa. However, after around 18 Hz, this trend is the opposite. The phase angle versus frequency response of the design is given in Fig. 9 for aluminium alloy and specified boundary conditions. The results indicate that at lower frequencies, the phase angle of vibration is higher, for higher frequencies the amplitude is low. This is represented by an asymptotic curve. One can also understand that for higher damping ratio, the phase angle of vibration is lower and vice versa. However, after around 11 Hz, this trend is the opposite.

The complete results of the analysis done in the study are given in Table 1.

## 4 Conclusions

Two different materials were analysed for the spring shock absorber under different criteria to find the best material among the two. Under static criteria, aluminium shows higher von Mises, higher strain and higher deformation than structural steel,

but the factor of safety for aluminium is higher for this shock absorber than the structural steel. The total deformation is higher (25 mm) but is still within a reasonable range. Fatigue criteria suggest that aluminium alloy shows a higher strain life (0.5 million cycles compared to 0.2 million cycles) and higher fatigue factor of safety (0.95 compared to 0.76), but the sensitivity analysis suggests that even an increase in 50% loading will result in a huge reduction in life. The simulations suggest that at 150% loading condition, the structural steel gives 5.5 times more available life than aluminium alloy. Since an automotive vehicle is always subjected to variable loading conditions, structural steel will give a higher life cycle, in other words, run more miles than aluminium alloy shock absorbers. Vibration analysis suggests that aluminium alloy will present higher vibration-induced deformations and less vibration-induced stresses than structural steel. This suggests that the aluminium alloy will have smoother but bumpy (vertically) ride. Structural steel, however, presents lower deformation (stiffer ride) but relatively higher vibrational induced stresses which are detrimental to the structural integrity of shock absorber.

## References

1. Singh, W.S., Srilatha, N.: Design and analysis of shock absorber: a review. *Mater. Today Proc.* **5**(2), 4832–4837 (2018)
2. Guntur, H.L., Hendrowati, W., Lubis, R.R.: Development and analysis of a regenerative shock absorber for vehicle suspension. *J. Syst. Des. Dyn.* **7**(3), 304–315 (2013)
3. Duym, S., Stiens, R., Reybrouck, K.: Evaluation of shock absorber models. *Veh. Syst. Dyn.* **27**(2), 109–127 (1997)
4. Jerrelind, J., Stensson, A.: Nonlinear dynamics of parts in engineering systems. *Chaos, Solitons Fractals* **11**(15), 2413–2428 (2000)
5. Johnson, D.J., Tony, A.: Design and analysis of a shock absorber. *Int. J. Res. Eng. Technol.* **01**(04), 578–592 (2012)
6. Prusova, O.L., Khamitov, R.N.: Thermodynamic basics of the pneumatic shock-absorber working. In: *Dynamics of Systems, Mechanisms and Machines, Dynamics 2014—Proceedings*, pp. 1–4 (2014)
7. Alonso, M., Comas, Á.: Modelling a twin tube cavitating shock absorber. *Proc. Inst. Mech. Eng. Part D J. Automob. Eng.* **220**(8), 1031–1040 (2006)
8. Moura, G.C.R., Aguilar, M.T.P., Pertence, A.E.M., Cetlin, P.R.: The failure analysis of a deep drawing die in the manufacturing of an automotive shock absorber cap. *Eng. Fail. Anal.* **11**(6), 943–950 (2004)
9. Gallardo, J.M., Soria, L., Herrera, E.J.: Investigation of service failures in automobile shock absorbers. *Eng. Fail. Anal.* **14**(2), 355–363 (2007)
10. Chatterjee, S., Nandy, S.: Optimization of a shock absorber using Finite Element Analysis. *Int. J. Sci. Eng. Technol. Res.* **7**(8), 564–568 (2018)
11. Salunkhe, K.B., Kumbhojkar, P.A.A., Shrotri, P.A.P.: Design and analysis of the helical spring for mono shock rear suspension in unicorn bike by using fea software. *Int. J. Sci. Res. Rev.* **07**(07), 258–271 (2019)
12. Prawoto, Y., Ikeda, M., Manville, S.K., Nishikawa, A.: Design and failure modes of automotive suspension springs. *Eng. Fail. Anal.* **15**(8), 1155–1174 (2008)

# A Review Paper on Metal 3D Printing Technology



T. Nancharaiah

**Abstract** Metal additive manufacturing (AM) is also referred to as 3D printing and rapid prototyping. It is a revolutionary technology that produces 99.99% dense parts directly from 3D CAD data using the powder bed fusion process known as direct metal laser sintering (DMLS). Metal 3D printing is an ideal process for complex oil and gas components, custom medical guides, part-consolidated aerospace parts and tough functional prototypes. This paper reviews about the introduction to metal 3D printing. It covers the basic principles of SLM and DMLS, the key benefits and limitations of the technology.

**Keywords** Additive manufacturing · 3D printing · SLM · DMLS

## 1 Introduction

Additive manufacturing (AM), also known as 3D printing, is a process of joining materials to make objects from 3D model data, usually layer upon layer, as opposed to subtractive manufacturing methodologies. Metal AM processes can be broadly classified into two major groups—powder bed fusion-based technologies (PBF) and directed energy deposition (DED)-based technologies. Both of these technologies can be further classified based on the type of energy source used. In PBF-based technologies, thermal energy selectively fuses regions of powder bed. Selective laser sintering/melting (SLS/SLM), direct metal laser sintering (DMLS) laser cusing and electron beam melting (EBM) are main representative processes of PBF-based technologies. Under PBF process, DMLS is an additive manufacturing (AM) or rapid prototyping (RP) process that uses metal powder and a high power laser to sinter together a useable part. This method is capable of producing very dense parts but in order to achieve gas or pressure tightness, post-treatment is often required. Most trade names such as laser sintering, cusing, etc. are describing the same process but not different technologies. The process is very similar to an existing AM

---

T. Nancharaiah (✉)

Mechanical Engineering, Bapatla Engineering College, Bapatla 522102, AP, India

process called selective laser sintering (SLS), both SLS and DMLS are conceptually the same process, but instead of using polymers or coated metal powders in the case of SLS, DMLS uses uncoated pre-alloyed metal powders as the sintering material. The electron beam melting (EBM) technology uses a heated powder bed of metal in a vacuum that is then melted and formed layer by layer using an electron beam energy source similar to that of an electron beam welding/electron microscope. In DED-based technologies focused thermal energy is used to fuse materials (powder or wire form) by melting as they are being deposited. Laser engineered net shaping (LENS), direct metal deposition (DMD), electron beam free form fabrication (EBFFF) and arc-based AM are some of the popular DED-based technologies. Many researchers are working on DMLS process to develop the new materials and process parameters in laser powder bed fusion.

Marattukalam et al. developed the parameters for selective laser melting of  $Zr_{59.3}Cu_{28.8}Al_{10.4}Nb_{1.5}$  (trade name AMZ4), allowing crack-free bulk metallic glass with low porosity. The phase formation was found to be strongly influenced by the heating power of the laser. X-ray amorphous samples were obtained with laser power at and below 75 W. The hardness and Young's modulus in the as-processed samples were found to increase marginally with increased fraction of the crystalline phase [1]. N. P. Calta et al. worked on the effect of pulsed laser used during the powder bed fusion (L-PBF); additive manufacturing (AM) process on Inconel 718 (IN718) material properties has been investigated. Argon gas atomized (AGA) IN718 powder is characterized in terms of flow, density, particle size distribution, morphology and ultimate tensile strength [2]. Konstantinos Georgila et al. studied about the geometry of an auxetic, re-entrant honeycomb structure made from Inconel 718 (IN718) and was optimized with respect to the process parameters of laser melting process using a Renishaw AM250 after which the quasi-static behaviour was analysed under tensile loading. Two different PBF process parameters were used with two different laser energy densities to manufacture the auxetic structures with three different strut thicknesses (0.3, 0.6 and 0.9 mm) in 2 building orientations (XY and ZX plane). Finite element analysis was also done in order to compare the stress-strain curves and the deformation mode obtained from numerical modelling and experiment, and a good agreement was observed [3]. L. Delcuse et al. reviewed the effects of major process parameters on build quality (porosity, residual stress and composition changes) and materials properties (microstructure and micro segregation), and to serve as a guide on how these parameters may be modified to achieve specific design goals for a given part on laser powder bed fusion [4]. J. P. Oliveira et al. studied the influence of process parameters during laser powder bed fusion on the microstructure, tensile strength, and build time of 316L parts is studied. By increasing both, scan speed and hatch distance, an improved productivity while maintaining acceptable properties was achieved. The samples produced with the lowest energy density had 32% elongation compared to 45% for the samples produced with standard process parameters. This study clearly indicates that the build time can be improved while maintaining good mechanical properties by adjusting the process parameters [5].

## 2 Working of Metal 3D Printing

The basic fabrication process for SLM and DMLS is very similar. It works as:

- i. The build chamber is first filled with inert gas (e.g. argon) to minimize the oxidation of the metal powder, and then, it is heated to the optimal build temperature.
- ii. A thin layer of metal powder is spread over the build platform and a high power laser scans the cross section of the component, melting (or fusing) the metal particles together and creating the next layer. The entire area of the model is scanned, so the part is built fully solid.
- iii. When the scanning process is complete, the build platform moves downwards by one layer thickness and the recoater spreads another thin layer of metal powder. The process is repeated until the whole part is complete.
- iv. When the build process is finished, the parts are fully encapsulated in the metal powder. Unlike polymer powder bed fusion process (such as SLS), the parts are attached to the build platform through support structures. Support in metal 3D printing is built using the same material as the part and is always required to mitigate the warping and distortion that may occur due to the high processing temperatures.

When the bin cools to room temperature, the excess powder is manually removed and the parts are typically heat treated while still attached to the build platform to relieve any residual stresses. Then the components are detached from the build plate via cutting, machining or wire EDM and are ready for use or further post-processing (Figs. 1 and 2).

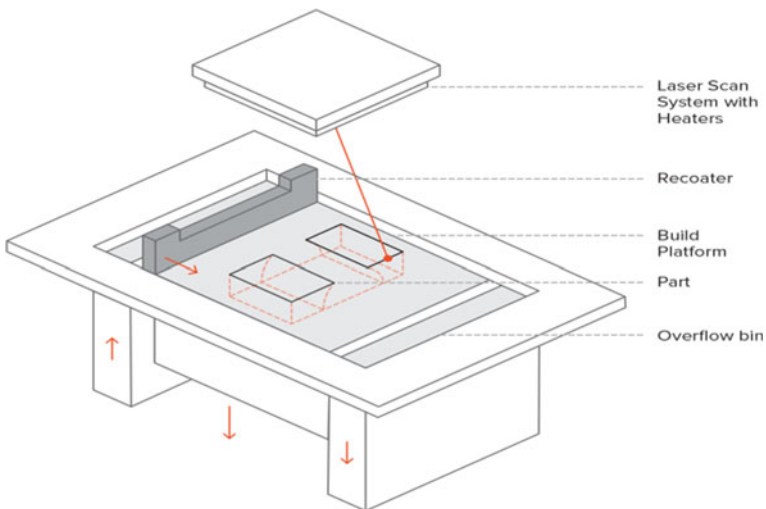


**Fig. 1** Schematic of an SLM/DMLS printer

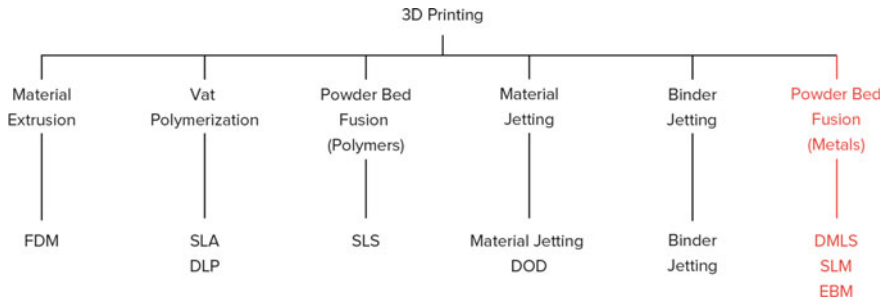


Fig. 2 Classification of 3D printing

### 3 Difference Between SLM and DMLS

Selective laser melting (SLM) and direct metal laser sintering (DMLS) are two metal additive manufacturing processes that belong to the powder bed fusion 3D printing family. The two technologies have a lot of similarities: both use a laser to scan and selectively fuse (or melt) the metal powder particles, bonding them together and building a part layer by layer. Also, the materials used in both processes are metals that come in a granular form.

The differences between SLM and DMLS come down to the fundamentals of the particle bonding process (and also patents). SLM uses metal powders with a single melting temperature and fully melts the particles, while in DMLS the powder is composed of materials with variable melting points that fuse on a molecular level at elevated temperatures. SLM produces parts from a single metal, while DMLS produces parts from metal alloys. Both SLM and DMLS are used in industrial applications to create end-use engineering products. There are other additive manufacturing processes that can be used to produce dense metal parts, such as electron beam melting (EBM) and ultrasonic additive manufacturing (UAM). Their availability and applications are limited (Fig. 3).

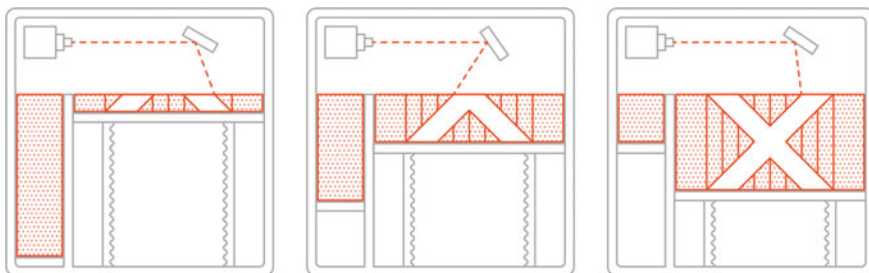


Fig. 3 SLM/DMLS printing process

## 4 Characteristics of SLM and DMLS

In SLM and DMLS, almost all process parameters are set by the machine manufacturer. The layer height used in metal 3D printing varies between 20 and 50 microns and depends on the properties of the metal powder (flowability, particle size distribution, shape, etc.).

The typical build size of a metal 3D printing system is  $250 \times 150 \times 150$  mm, but larger machines are also available (up to  $500 \times 280 \times 360$  mm). The dimensionally accuracy that a metal 3D printer can achieve is approximately  $\pm 0.1$  mm.

Metal printers can be used of small batch manufacturing, but the capabilities of metal 3D printing systems resemble more the batch manufacturing capabilities of FDM or SLA machines than that of SLS printers: they are restricted by the available print area (XY-direction), as the parts have to be attached to the build platform.

The metal powder in SLM and DMLS is highly recyclable; typically less than 5% is wasted. After each print, the unused powder is collected, sieved and then topped up with fresh material to the level required for the next built. Waste in metal printing though comes in the form of support structures, which are crucial for the successful completion of a build but can increase the amount of the required material (and the cost) drastically.

## 5 Benefits and Limitations of Metal 3D Printing

It is important to understand that metal 3D printing is a powerful tool that comes with many unique benefits. Yet, its current limitations do not always make it the best option when it comes to manufacturing of metal parts. Here it summarized the most important advantages and disadvantages of metal 3D printing. Use them to understand where metal 3D printing stands today and where it is headed in the near future.

### 5.1 *Benefits of Metal 3D Printing*

- (a) Geometric complexity at no extra cost.
- (b) Optimized lightweight structures.
- (c) Increased part functionality.
- (d) Merging assemblies into a single part.
- (e) Simpler manufacturing supply chains.
- (f) Excellent material properties.

## 5.2 *Limitations of Metal 3D Printing*

- (a) Higher cost than traditional manufacturing.
- (b) Limited economies of scale.
- (c) A unique set of design rules.
- (d) Post-processing is almost always required.

## 5.3 *Applications of Metal 3D Printing*

The key industrial applications of metal 3D printing are space industry, health care, automotive, industrial tooling and product development.

### (i) *Space*

Creating lightweight structures is of paramount importance for the space industry. The current cost of launching a kilogram of payload into space is approximately \$10,000–\$20,000. So, metal 3D printing of topology optimized parts has great potential here. For example, to provide micro-antenna products, Optisys used DMLS/SLM to reduce the number of discrete pieces of their tracking antenna arrays from 100 to only 1. With this simplification, Optisys managed to reduce the lead time from eleven months to two, while achieving a 95% weight reduction (Fig. 4).

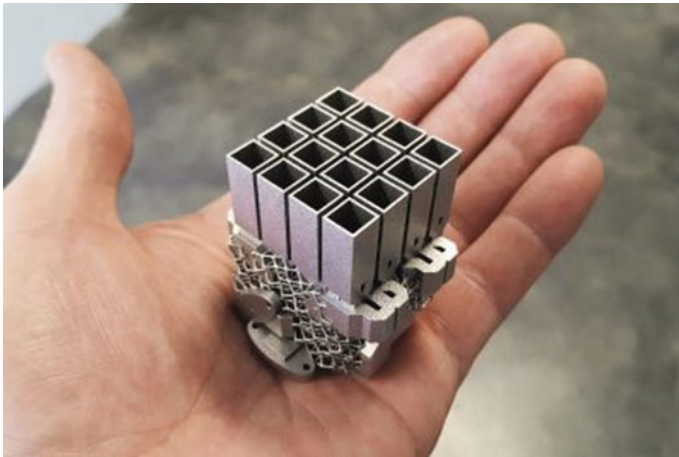


**Fig. 4** Antenna arrays



(ii) *Health care*

The ability to create organic structures, personalized to the anatomy of every individual, makes metal 3D printing a very appealing solution for the medical industry. Today, medical implants from biocompatible materials (such as titanium) are one of the major uses of metal 3D printing.

Back in 2007, Dr. Guido Grappiolo was the first surgeon to implant a 3D-printed hip cup implant. With the help of Lima Corporate and Arcam, he designed the Delta-TT Cup, a titanium implant with a lattice structure that accelerates patient rehabilitation and bone growth. A decade later, more than 100,000 of these hip cups have been implanted successfully to patients.

(iii) *Automotive*

The adoption of metal 3D printing as a manufacturing option for end parts in the automotive industry is increasing rapidly. For the time being, high performance and racing are the main applications of metal 3D printing.

The TU Delft Formula Student team used DMLS to manufacture their topology-optimized bracket for their formula car. This bracket is the main connection point between the wheel and the chassis, and it is designed to withstand forces up to 400 kg. The re-designed titanium bracket has half the weight and twice the strength of an equivalent part machined out of steel (Fig. 5).

(iv) *Industrial tooling*

Metal 3D printing is used today to create industrial tools with added functionality. These advanced tools can greatly increase the productivity of other processes.

For example, metal moulds with internal conformal cooling channels can be manufactured using DMLS/SLM 3D printing. These cooling channels can be



**Fig. 5** Titanium bracket



**Fig. 6** Metal moulds

printed to any shape and closer to the part than subtractive methods can accomplish. A printed metal mould can cost about \$10,000, which is considerable compared to the \$4,000 that the same mould would cost if it was CNC machined. The increased cost brings significant performance improvements. Users reported injection cycles that are shorter by 60–70% with almost no scrap (Fig. 6).

(v) *Product development*

The main applications of metal extrusion today are the manufacture of metal prototypes. When compared to other in-house solutions, the time savings offered by metal extrusion can greatly reduce the time-to-market of new engineering products. Lumenium is a start-up that develops innovative internal combustion engines. They were seeking a faster and more cost-effective approach to prototyping their engine parts. Traditionally, their development cycle is approximately 3.5 years. By incorporating metal extrusion in their workflow, they estimated that they reduced their development time by 25% to 2 years and 9 months (Fig. 7).

## 6 Conclusions

Metal additive manufacturing is an ‘additive’ technology that works by fusing together very fine layers of metal powder using a focused laser beam. This powder bed fusion process can produce complex geometries which might not have been possible using traditional manufacturing techniques. The fundamental mechanics of the two metal additive manufacturing processes, SLM and DMLS are discussed and highlighted the main advantages and limitations of the metal 3D printing technology. There is a scope to study the effect of various processes parameters,



**Fig. 7** Metal prototype

properties of metal powders and various post-processing techniques on the characteristics of the 3D printing parts. Also new metal powders can be developed for various applications. Finally, it can conclude that metal 3D printing technologies' importance and social impact increase gradually day to day on human life, economy and modern society.

## References

1. Marattukalam, J.J., Pacheco, V., Karlsson, D., Riekehr, L., Lindwall, J., Forsberg, F., Jansson, U., Sahlberg, M., Hjärvarsson, B.: Development of process parameters for selective laser melting of a Zr-based bulk metallic glass. *Addit. Manuf.* **33**, Article ID 101124 (2020)
2. Calta, N.P., Martin, A.A., Hammons, J.A., Nielsen, M.H., Roehling, T.T., Fezzaa, K., Matthews, M.J., Jeffries, J.R., Willey, T.M., Lee, J.R.I.: Pressure dependence of the laser-metal interaction under laser powder bed fusion conditions probed by in situ X-ray imaging. *Addit. Manuf.* **32**, 101084 (2020)
3. Georgila, K., Khan, R.H.U., Kartal, M.E.: The influence of pulsed laser powder bed fusion process parameters on Inconel 718 material properties. *Mater. Sci. Eng.: A* **769**, 2 Jan. (2020)
4. Delcuse, L., Bahi, S., Gunpath, U., Rusinek, A., Wood, P., Miguelez, M.H.: Effect of powder bed fusion laser melting process parameters, build orientation and strut thickness on porosity, accuracy and tensile properties of an auxetic structure in IN718 alloy. *Addit. Manuf.* **36**, Dec. (2020)
5. Oliveira, J.P., LaLonde, A.D., Ma, J.: Processing parameters in laser powder bed fusion metal additive manufacturing. *Mater. Des.* **193** (2020)

# Dimensional Tolerance Analysis of Mechanical Assemblies with Symmetric and Asymmetric Tolerances



Ravikant Mordia, A. K. Verma, and Deepak Verma

**Abstract** Geometric and dimensional tolerances are the key factors for the proper assembly of the parts, their manufacturability, and design functions. Hence, these need proper evaluation. This paper presents automatic tolerance analysis of the dimensional tolerances by using modified worst-case and root sum square (statistical) methods. This helps in reducing production and assembly time, error and human interaction, leading to lower manufacturing cost. In contrast to the original worst-case and root sum square methods which consider only symmetric tolerances without sensitivity, the modified methods can handle the asymmetric tolerances and also consider sensitivity. The influences of the lower and upper tolerance bounds of the manufactured dimensions on the assembly lower and upper bounds are shown in the form of percentage contributions on graphs in the modified models. In the modified models, linear and nonlinear problems are defined by using the Taylor series expansion which is implemented in the MATLAB. Finally, a perspective overview for future research of automatic tolerance analysis for the other problems is presented.

**Keywords** Dimensional tolerance analysis • Worst-case and statistical methods • Linear and nonlinear variables • Symmetric and asymmetric tolerances • Upper tolerance limit and lower tolerance limit • Percentage contribution

---

R. Mordia (✉)

Department of Mechanical Engineering, Jai Narain Vyas University, Jodhpur, Rajasthan 342011, India

e-mail: [ramordia.mech@jnvu.edu.in](mailto:ramordia.mech@jnvu.edu.in)

A. K. Verma

Department of Production and Industrial Engineering, Jai Narain Vyas University, Jodhpur, Rajasthan 342011, India

e-mail: [akverma.pi@jnvu.edu.in](mailto:akverma.pi@jnvu.edu.in)

D. Verma

Department of Mechanical Engineering, Graphic Era Hill University, Dehradun, Uttarakhand 248002, India

© The Author(s), under exclusive license to Springer Nature Singapore Pte Ltd. 2021

261

A. Patnaik et al. (eds.), *Advances in Materials Processing and Manufacturing*

*Applications*, Lecture Notes in Mechanical Engineering,

[https://doi.org/10.1007/978-981-16-0909-1\\_26](https://doi.org/10.1007/978-981-16-0909-1_26)

## 1 Introduction

Tolerance is the quantity of dimensional variation of an element in a mechanical assembly, which reduces the manufacturing cost without adversely affecting the performance. Tolerance is essential as by nature, material behaviour and producing processes are not precise; therefore, the two factory-made elements cannot be identical to each other. Hence, there will always be some variation within the factory-made elements. Drawings with properly applied tolerances are very effective tool to have uniform interpretation of an assembly and effective pricing. Therefore, tolerance analysis is vital not solely to verify the flexibility of elements to assemble but the quality of assembled elements. Manual tolerance identifications can increase the variability in elements or assembly tolerance build-up that successively affects the standard of the elements or the assembly. Therefore, the automatic tolerance analysis of the assemblies is very important to decrease the design complexities and the prices of the products/assembly and to minimize the human interaction also. Numerous researchers have given the different ways for tolerance analysis. Various computer-aided tolerance (CAT) packages are developed for automatic tolerance specification and accumulation of assembly variables. D. E. Whitney [1] classified the mechanical assemblies made of different components into three categories, which are mechanisms, structures, and distributive systems. Zhang et al. [2] presented a concise study to the statistical tolerance and clearance analyses of mechanical assemblies. They proposed an approach for tolerance analysis by using an effective CAT analysis software VisVSA. The presented approach is based on the Monte Carlo simulation which gives the assurance of the preciseness of the assembly specifications and generation of optimal tolerance distribution. Chen et al. [3] described four methods of 3D tolerance analyses and also presented a comparison among them. The proposed methods by them are the tolerance map (T-Map), direct linearization method (DLM), unified Jacobian–Torsor model, and matrix model. Mohan et al. [4] represented a procedure for automatic generation of the direction of controls of the mechanical assemblies or parts using a CAD model. The input to the set-up is a STEP file containing the information about the geometry of parts or assemblies. The directions of controls (DoCs) loops are correlated with each other based on their orientations. Hence, the junction nodes are used to include the orientations with the DoC chains so that they can be joined into a constraint feature graph. Khodagyan and Movahhedy [5] introduced a mathematical methodology for automatic tolerance accumulation in mechanical assemblies on the basis of fuzzy logic. They developed this approach for asymmetric tolerance analysis for assembly models with variability in the part tolerances by using the WC and the RSS models. Qin et al. [6] described an approach based on description logic SROIQ (D) for automatically designing the tolerance types and generation of geometric tolerance zones (GTZs) in the CAD system. Zhong et al. [7] proposed an approach based on ontology for automatic assembly tolerance types generation to decrease the variability of parts in an assembly and also to support the semantic conformity in

designing the assembly tolerance specifications. Cheng and Tsai [8] developed a Lagrange multiplier method for optimum statistical tolerances accumulation to minimize the manufacturing costs subject to the constraint on dimensional chains and the machining efficiency. Greenwood and Chase [9] presented the worst-case and the root sum square models to solve nonlinear problems for dimensional tolerance analysis of the assemblies with symmetric and bilateral limits. Haghghi et al. [10] developed an automatic GDT generation method in which identification of critical tolerance loops is required. According to their approach, the global constraints (relationships of the assembly features), the local constraints (relationships of the component features), and the direction of controls are required to develop the tolerance chains. Movahhedy and Khodaygan [11] implemented the worst-case and the statistical approaches for asymmetric tolerance analysis of mechanical assemblies. They also analysed the effect of the individual component dimensions on the upper bounds and the lower bounds of the critical dimension of the assembly. Mullins and Anderson [12] proposed that the geometric constraints recognition in a mechanical assembly is required to illustrate the effects of the variations in the dimensions of that assembly. They presented a method based on a search algorithm along with a graphical representation for the recognition of such assembly constraints in a 3D CAD model of the assembly. Shen et al. [13] addressed some methodologies to generate minimum or maximum tolerance charts automatically. But this approach is limited to only one-dimensional (1D) worst-case tolerance analysis in mechanical assemblies. Sambhoos et al. [14] presented a methodology on the basis of a relationship model of parts for assembly design variation. It takes assembly mating relationships at the feature level referred as an assembly mating graph. They classified the mating relationships as observed relationships, unobserved relationships, and interference relationships.

This paper presents a mathematical model for dimensional tolerance analysis by using the worst-case and also the statistical procedure. The basic purpose of dimensional tolerance analysis is to get a robust design. Any process is considered good when it can be employed at an early design/development stage, because it is possible to change the nominal geometry of a mechanical assembly at an early stage. The worst-case (WC) methodology needs complete interchangeability (100% acceptance rate). It means that the accuracy of the result obtained from the WC methodology is required to be within the functional requirements of the assembly, and the success probability of the assembly is to be 100 per cent. In contrast, the statistical or root sum square (RSS) methodology needs less than 100% acceptance rate. In this methodology, it is assumed that errors within the components are independent and normally distributed. Variance is often used to calculate the assembly preciseness as the deviations/variations from the geometry are identical for every statistically independent direction. The calculation method in the RSS methodology is less strict to confirm that the most of the products are inside the scope of the functional requirements of the assembly. The results provided by the WC methodology are too pessimistic, whereas the results provided by the RSS methodology are highly optimistic. In the above two methods, the precise assembly function (dependent variable or dimension) can be defined as a linear function in

terms of the part dimensions (independent variables). As in a journal bearing, the clearance is decided by the independent variables: the shaft and bearing diameters. The spring stiffness of a helical spring could be an assembly function, whereas the coil diameter, wire diameters, and the number of turns are independent variables. If we tend to use these methods for tolerance analysis, some consideration should be given to the limits or bounds of the tolerance of the manufactured dimensions. These two methods are very popular for tolerance analysis in mechanical assemblies due to their simplicity, but they are limited to (i) linear assembly functions and (ii) symmetrical tolerances. Unfortunately, many assemblies have unilateral and asymmetrical tolerances, which they fail to handle.

In this work, the WC and RSS methods are modified to accommodate nonlinear assembly functions and asymmetrical and unilateral tolerances. The modified methods are implemented in MATLAB and illustrated with two examples. For each example, a bar graph of influence of individual part dimensions on the assembly variable in terms of the percentage contribution has been shown. This shows the potential influence of every part variations on the assembly variation.

## 2 Methodology

### 2.1 *Calculating the Assembly Variation Using Linearized Method*

In this section, the worst-case (WC) and the statistical (RSS) models for tolerance analysis for the linear and nonlinear problems have been reviewed briefly to provide a background for developing the modified methods.

**Worst-Case Analysis Model.** Generally, this method is used for tolerance analysis when various parts are combined to make an assembly. In the WC analysis, we add or subtract maximum or minimum tolerances related to the nominal dimensions of the component/part to illustrate the possible worst conditions. Thus, said tolerance accumulation makes an assembly at its minimum or maximum acceptable dimensions. The WC analysis is used when the assembly has a critical interface with another part feature that is not allowed to obstruct significantly. By critical, it means that it is a consumer requirement or a safety issue. The standard WC model is given in Eq. (1) in the form of the sum of all part dimensions at min/max values (called as the assembly/design function) by Khodagyan and Movahhedy [5].

$$X = \pm X_1 \pm X_2 \pm X_3 \dots \pm X_n \quad (1)$$

where  $X$  is the assembly or design variable,  $X_1, X_2, X_3, \dots, X_n$  are the manufactured (independent) variables.

The design function is sometimes represented in the form given in Eq. (2):

$$X = g(X_1, X_2, X_3 \dots X_n) \tag{2}$$

For nonlinear problems, it can be challenging to define the design or assembly function. However, for a small change in the dependent or assembly dimension, the nonlinear problems can be defined by using the Taylor series in the WC tolerance analysis, as proposed by W. H. Greenwood and K. W. Chase [9] and is given in Eq. (3).

$$\Delta X = \sum_{i=1}^n \frac{\partial g}{\partial X_i} \Delta X_i + \frac{1}{2} \sum_{i=1}^n \frac{\partial g}{\partial X_i} \sum_{j=1}^n \frac{\partial g}{\partial X_j} \Delta X_i \Delta X_j + \dots \tag{3}$$

In the WC tolerance analysis, only first-order terms and absolute terms are used. The general WC tolerance analysis equation can be expressed as given in Eqs. (4) and (5):

$$T_X = \left| \frac{\partial g}{\partial X_1} \right| T_1 + \left| \frac{\partial g}{\partial X_2} \right| T_2 + \left| \frac{\partial g}{\partial X_3} \right| T_3 + \dots + \left| \frac{\partial g}{\partial X_n} \right| T_n \tag{4}$$

$$X_{\text{nominal}} \approx \left| \frac{\partial g}{\partial X_1} \right| X_1 + \left| \frac{\partial g}{\partial X_2} \right| X_2 + \left| \frac{\partial g}{\partial X_3} \right| X_3 + \dots + \left| \frac{\partial g}{\partial X_n} \right| X_n \tag{5}$$

where  $T_i$  is the tolerance of  $i$ th manufactured/independent variable or dimension and  $\frac{\partial g}{\partial X_i}$  is the sensitivity. For a nonlinear problem, we have to assign some fixed values to each partial derivative as these derivatives define some specific sensitivities. Each part dimension and its tolerance limits will induce these sensitivities on the assembly or critical dimensions and their tolerance limits. If components/parts are manufactured within specifications, then it is guaranteed that assemblies will be within the specifications by using the WC analysis.

**Statistical Analysis Model.** The statistical tolerance analysis method, also known as root sum square (RSS) method, is based on the approximation of population parameters. By assuming that all the component dimensions are independent and normally distributed, an approximation of the assembly function using Taylor series expansion results in Eq. (6), as given by W. H. Greenwood and K. W. Chase [9]:

$$T_X = \sqrt{\left[ \left( \frac{\partial g}{\partial X_1} \right)^2 T_1^2 + \left( \frac{\partial g}{\partial X_2} \right)^2 T_2^2 + \left( \frac{\partial g}{\partial X_3} \right)^2 T_3^2 + \dots + \left( \frac{\partial g}{\partial X_n} \right)^2 T_n^2 \right]} \tag{6}$$

Currently, the statistical tolerance analysis model is very popular method. However, in this method, even if all the components/parts of an assembly are within the specifications, the defective assembly may result. That is why it is conceptually



unattractive to many designers. However, the probability of occurring this is very less. Further, the assumptions that the manufactured variables are independent and normally distributed are generally not obvious in actuality. The main capabilities of the RSS method for tolerance analysis are the ease of automation and the ability to simplify even the most complex design functions.

## 2.2 Modified Tolerance Analysis Models

The tolerance analysis methods which are discussed above are relevant to symmetric tolerances only. The modified methods (WC and statistical methods) for tolerance analysis are presented in this section which can handle unilateral tolerances and asymmetric tolerances as well.

The modified relations (given in Eqs. (7 and 8)) to estimate the tolerance limits for the worst-case and statistical methods can be expressed on the basis of Eq. (4) as follows:

$$UTL_j, LTL_j = \frac{1}{2} \sum_{i=1}^n \left[ \left| \frac{\partial g_j}{\partial X_i} \right| (UL_i + LL_i) + k \left( \frac{\partial g_j}{\partial X_i} \right) (UL_i - LL_i) \right] \quad (7)$$

$$\text{where } k = \begin{cases} +1 \text{ for UL} \\ -1 \text{ for LL} \end{cases}$$

$$UTL_j, LTL_j = \sqrt{\frac{1}{2} \sum_{i=1}^n \left[ \left| \frac{\partial g_j}{\partial X_i} \right| (UL_i + LL_i) + k \left( \frac{\partial g_j}{\partial X_i} \right) (UL_i - LL_i) \right]^2} \quad (8)$$

$$\text{where } k = \begin{cases} +1 \text{ for UL} \\ -1 \text{ for LL} \end{cases}$$

where the index  $i$  is for manufactured dimensions or independent variables, the index  $j$  is for assembly or dependent variables,  $\left( \frac{\partial g_j}{\partial X_i} \right)$  is the sensitivity coefficient, UTL, and LTL are the upper and the lower tolerance limits of the specified design or assembly variable, respectively.

## 2.3 Percentage Contributions of Each of the Individual Component Tolerance on a Specific Assembly Variable

Tolerance analysis of an assembly presents two graphical representations: the sensitivity and the percentage contribution, which shows how the part tolerances influence the assembly variations. The sensitivity representation shows the

sensitivity of the assembly function to component dimensional variations. This sensitivity is a percentage of the potential impact of dimensional variations of all the parts on a particular assembly function. On aggregation of all the percentage contributions, Eq. (9) results

$$P_1 + P_2 + P_3 + \dots + P_n = 100\% \tag{9}$$

Percentage contribution ( $P_i$ ) is the proportion value of each of the individual part dimensions. This percentage contribution is the measure of existing effects of each of the part tolerance on the variations of an assembly variable.

Percentage contribution (%WC) of each of the component tolerances on the upper tolerance limit (UTL<sub>*j*</sub>) and lower tolerance limit (LTL<sub>*j*</sub>) of assembly function are given in Eqs. (10) and (11), respectively.

$$\%WC \text{ on } UTL_j = \frac{\left[ \left| \frac{\partial g_j}{\partial X_i} \right| (UL_i + LL_i) + \left( \frac{\partial g_j}{\partial X_i} \right) (UL_i - LL_i) \right]}{\sum_{i=1}^n \left[ \left| \frac{\partial g_j}{\partial X_i} \right| (UL_i + LL_i) + \left( \frac{\partial g_j}{\partial X_i} \right) (UL_i - LL_i) \right]} \times 100 \tag{10}$$

$$\%WC \text{ on } LTL_j = \frac{\left[ \left| \frac{\partial g_j}{\partial X_i} \right| (UL_i + LL_i) - \left( \frac{\partial g_j}{\partial X_i} \right) (UL_i - LL_i) \right]}{\sum_{i=1}^n \left[ \left| \frac{\partial g_j}{\partial X_i} \right| (UL_i + LL_i) - \left( \frac{\partial g_j}{\partial X_i} \right) (UL_i - LL_i) \right]} \times 100 \tag{11}$$

Percentage contribution (%RSS) of each of the component tolerances on the upper tolerance limit (UTL<sub>*j*</sub>) and lower tolerance limit (LTL<sub>*j*</sub>) of assembly variable are given in Eqs. (12) and (13), respectively.

$$\%RSS \text{ on } UTL_j = \frac{\left[ \left| \frac{\partial g_j}{\partial X_i} \right| (UL_i + LL_i) + \left( \frac{\partial g_j}{\partial X_i} \right) (UL_i - LL_i) \right]^2}{\sum_{i=1}^n \left[ \left| \frac{\partial g_j}{\partial X_i} \right| (UL_i + LL_i) + \left( \frac{\partial g_j}{\partial X_i} \right) (UL_i - LL_i) \right]^2} \times 100 \tag{12}$$

$$\%RSS \text{ on } LTL_j = \frac{\left[ \left| \frac{\partial g_j}{\partial X_i} \right| (UL_i + LL_i) - \left( \frac{\partial g_j}{\partial X_i} \right) (UL_i - LL_i) \right]^2}{\sum_{i=1}^n \left[ \left| \frac{\partial g_j}{\partial X_i} \right| (UL_i + LL_i) - \left( \frac{\partial g_j}{\partial X_i} \right) (UL_i - LL_i) \right]^2} \times 100 \tag{13}$$

### 3 Case Study

To illustrate effectiveness of the modified WC and RSS methods, the following examples are given.

### 3.1 Example 1: Thermos Flask

As shown in Fig. 1, it is an insulating storage vessel that keeps the contents to remain cooler or hotter than its surroundings. It is made up of two different flasks that are placed one within another and are attached at the neck. The space between these two flasks is partially vacated to create partial vacuum. Because of this vacuum, the heat conduction or convection is reduced.

Our aim is to maintain the gap  $X$  within some limits so that there can be a proper insulation between the two flasks to reduce heat conduction or convection. This  $X$  is called the critical dimension or the assembly variable. The other dimensions are  $X_1$ ,  $X_2$ , and  $X_3$ , where  $X_1$  is the overall thickness of the flask wall,  $X_2$  is the inner flask wall thickness, and  $X_3$  which is the outer flask wall thickness. These are the manufactured dimensions (Table 1).

The assembly function can be written as follows:

$$X = X_1 - X_2 - X_3 \quad (14)$$

**Fig. 1** Thermos flask

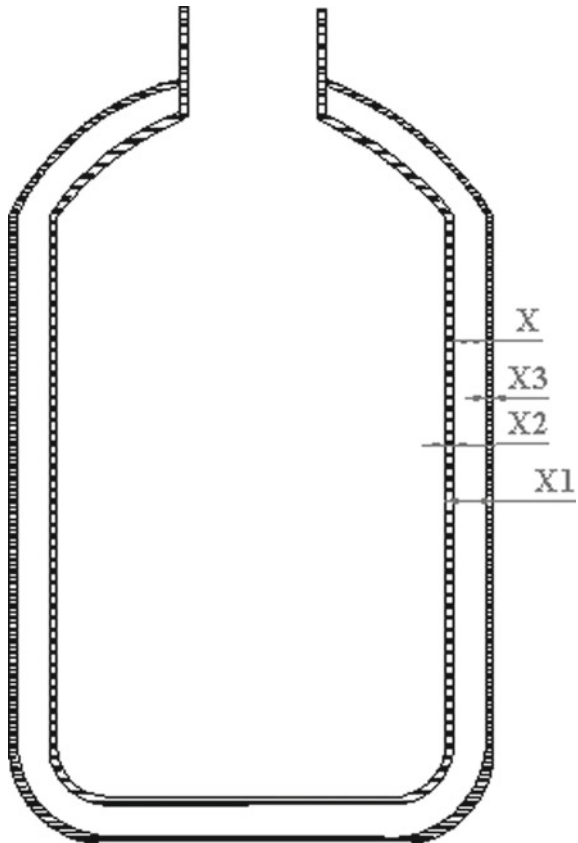


**Table 1** Manufactured variables with tolerances and sensitivities for thermos flask model

Variables	Values (mm)	Sensitivities	UL (mm)	LL (mm)
$X_1$	10	+1	0.042	0.039
$X_2$	2	-1	0.037	0.036
$X_3$	1.5	-1	0.037	0.036

### 4 Result and Conclusion

It is clear from Table 2 that the results of tolerance accumulation of an assembly with asymmetric tolerances of the manufactured variables can cause the asymmetric tolerance limits for an assembly function.

The influence of each of the manufactured variable made on the UTL and LTL of the assembly or design function ( $X$ ) is shown in terms of the percentage contributions using the modified worst-case method in Fig. 2a, b, respectively. Figure 3a, b shows the same using the modified RSS method. It is clear from these graphs that  $X_1$  is most influential on  $X$  for proper vacuum.

**Table 2** UTL and LTL of assembly variable ( $X$ ) by using the modified WC and RSS methods

Tolerance analysis method	UTL (mm)	LTL (mm)
Modified WC	0.114	0.113
Modified RSS	0.0933	0.0922

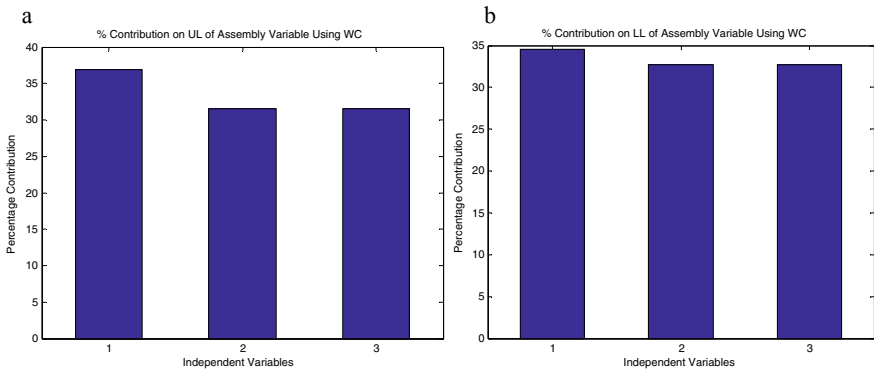


**Fig. 2** a Influence of  $X_i$  on UTL and; b on LTL of  $X$  using the modified WC method

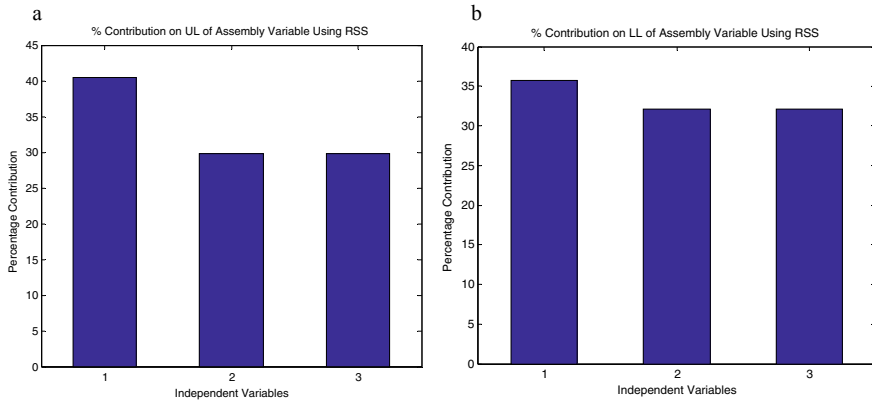


**Fig. 3** **a** Influence of  $X_i$  on UTL and; **b** on LTL of X using the modified RSS method

### 4.1 Example 2: One-Way Clutch Assembly

This is a two-dimensional assembly made up of four parts: rollers, springs, a hub, and a cage as shown in Fig. 4. In this example, the design or assembly variable is the contact angle ( $\theta$ ) between the roller and the cage, which is nonlinear.

We can define this assembly variable ( $\theta$ ) as a nonlinear function of the independent variables  $X_1, X_2, X_3,$  and  $X_4$  by the trigonometry as follows:

$$\text{Adjacent, } AB = \left(X_2 + \frac{X_3 + X_4}{2}\right) \text{ and hypotenuse } AC = \left(X_1 - \frac{X_3 + X_4}{2}\right) \quad (15)$$

$$\theta = \text{Cos}^{-1} \left( \frac{X_2 + \frac{X_3 + X_4}{2}}{X_1 - \frac{X_3 + X_4}{2}} \right) \quad (16)$$

where  $X_1$  is the diameter of the cage,  $X_2$  is the height of the hub,  $X_3$  is the diameter of the upper roller, and  $X_4$  is the diameter of the lower roller. The nominal values of these variables with their tolerance limits are given in Table 3.

The sensitivities for the cage, hub, and rollers are calculated automatically by putting the values of the independent variables and by doing partial derivation of the assembly function w.r.t. each independent variable, respectively, as given in Eq. (17).

$$\frac{\partial \theta}{\partial X_1} = 0.1032, \frac{\partial \theta}{\partial X_2} = -0.1039, \frac{\partial \theta}{\partial X_3} = -0.1035, \frac{\partial \theta}{\partial X_4} = -0.1035 \quad (17)$$

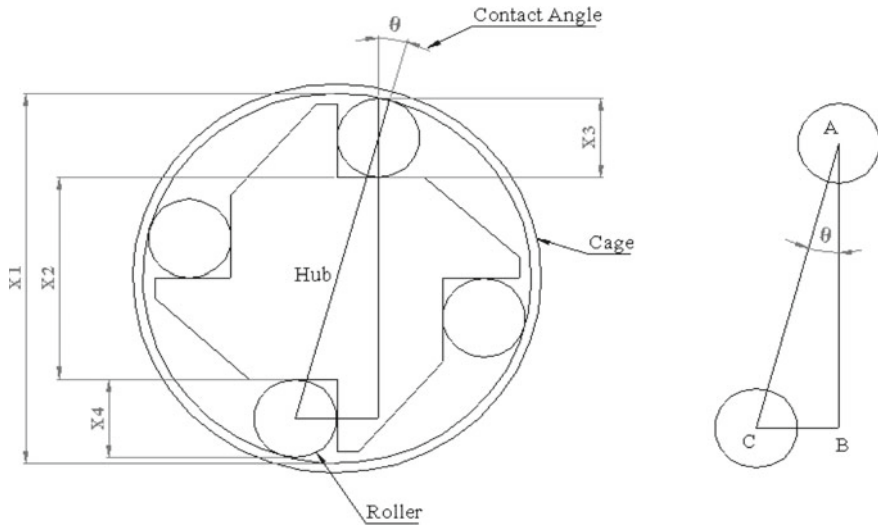


**Fig. 4** One-way clutch assembly

**Table 3** Nominal dimensions, sensitivities, and tolerance limits of independent variables for one-way clutch model

Variables	Values (mm)	Sensitivities	UL (mm)	LL (mm)
$X_1$	101.60	0.1032	0.155	0.135
$X_2$	55.29	-0.1039	0.16	0.14
$X_3$	22.86	-0.1035	0.01	0.015
$X_4$	22.86	-0.1035	0.01	0.015

## 5 Result and Conclusion

The results obtained for the upper and lower tolerance limits of contact angle ( $\theta$ ) by using the modified WC and statistical methods are given in Table 4. The influence of each of the manufactured variable made on the UTL and LTL of the design variable ( $X$ ) is shown in terms of the percentage contributions using the modified worst-case method in Fig. 5a, b, respectively. Figure 6 a, b shows the same using the modified RSS method.

**Table 4** UTL and LTL of the design variable ( $\theta$ ) using modified WC and RSS methods

Tolerance analysis method	UTL (rad)	LTL (rad)
Modified WC	0.0336	0.0326
Modified RSS	0.0307	0.0307

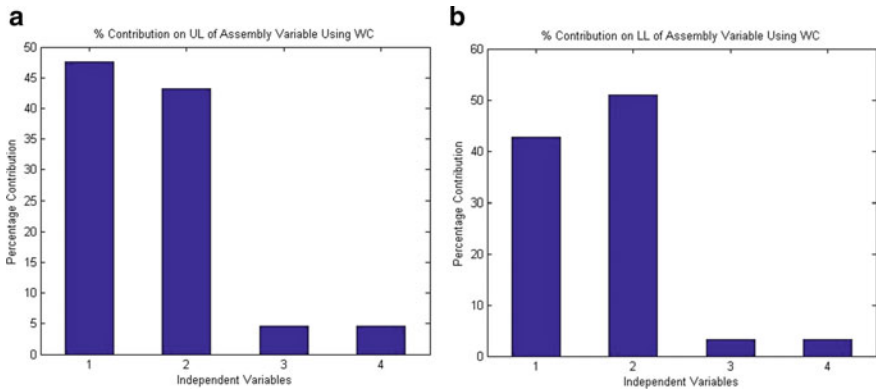


Fig. 5 a Influence of  $X_i$  on UTL and; b on LTL of  $\theta$  using the WC method

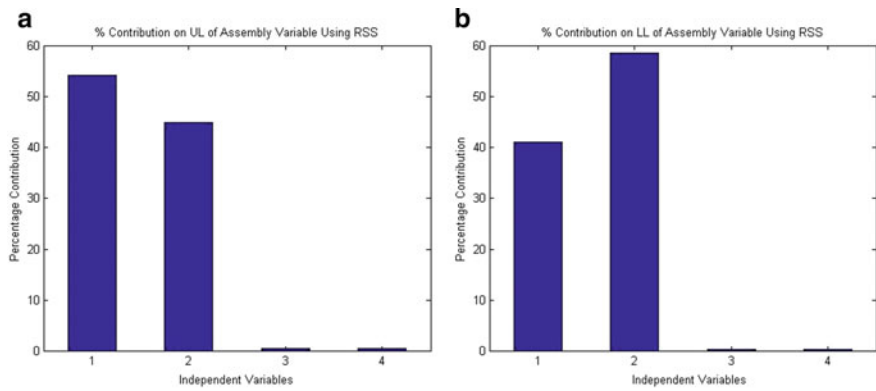


Fig. 6 a Influence of  $X_i$  on UTL and; b on LTL of  $\theta$  using Statistical (RSS) method

From Figs. 5a and 6a, we can say that the variables  $X_1$  and  $X_2$  are the critical dimensions to the contact angle ( $\theta$ ) for calculating the upper tolerance limit of that variable, while  $X_3$  and  $X_4$  have the lower contribution in influencing the assembly variable (contact angle). Figures 5b and 6b are showing the same results for calculating the lower tolerance limit of the contact angle ( $\theta$ ).

## 6 Conclusions and Future Scope

In the present work, modifications in the worst-case and root sum square methods have been reported, which makes these methods to perform the tolerance analysis of assembly variables with nonlinear assembly function and asymmetric/unilateral

tolerances. The effectiveness of the modified methods has been illustrated with simple examples. In this work, the modified worst-case and root sum square methods are presented for the automatic tolerance analysis for the UTL and the LTL of the assembly variable w.r.t. the manufactured variables with asymmetric tolerances. In these new methods, sign of the sensitivities is also considered showing that how sensitive is the critical dimension w.r.t. the variations in each part dimensions. The influence of the manufactured dimensions on the critical dimension has been also presented in terms of percentage contributions in the form of bar charts for the tolerance limits. These contributions show that how an assembly variable is affected by each part tolerances. A linear problem of the thermos flask is presented in which the critical dimension is the gap between two coaxial flasks. The tolerance limits of the design variable or assembly function and the percentage contribution of each individual dimension which are given with the linear and asymmetric tolerances are also presented in this work. Another tolerance analysis for a nonlinear example of a one-way clutch model has also been done in this work in which the assembly variable is the contact angle between the roller and the cage. Here, the magnitude of the sensitivities of the individual-independent variable may differ from 1 because of nonlinearity that affects the assembly variable. It is also shown how the individual dimension affects the assembly variable by the percentage contribution of those dimensions in the form of bar charts.

Thus, the benefits of the presented approach are that it is easy to automate and also it can model both the symmetric and the asymmetric tolerance limits.

In future work, this can be further extended in the field of automatic tolerance analysis for the other problems as follows:

- Tolerance analysis of free-form surfaces.
- Geometric tolerance analysis for the assemblability based on geometric conditions, for design functions and for minimum manufacturing cost using an effective tolerance cost model.

## References

1. Whitney, D.E.: Mechanical assemblies—their design, manufacture, and role in product development. *Oxford Ser. Adv. Manuf.* **1**, 112–140 (2004)
2. Zhang, H., Zhan, G., Li, W., Wei, Q., Li, M., Tian, Y.: The method of tolerance analysis based on the Monte Carlo. *Adv. Mater. Res.* **1039**, 140–145 (2014)
3. Chen, H., Jin, S., Li, Z., Lai, X.: A comprehensive study of three dimensional tolerance analysis methods. *Comput. Aided Des.* **53**, 1–13 (2014)
4. Mohan, P., Haghighi, P., Shah, J.J., Davidson, J.K.: Automatic detection of directions of control in mechanical parts. In: *Proceedings of ASME 2014 International Manufacturing Science and Engineering Conference*, vol. 1, pp. 1–10 (2014)
5. Khodaygan, S., Movahhedy, M.R.: Tolerance analysis of assemblies with asymmetric tolerances by unified uncertainty accumulation model based on fuzzy logic. *Int. J. Adv. Manuf. Technol.* **53**, 777–788 (2010)



6. Qin, Y., Lu, W., Liu, X., Huang, M., Zhou, L., Jiang, X.: Description logic based automatic generation of geometric tolerance zones. *Int. J. Adv. Manuf. Technol.* **79**, 1221–1237 (2015)
7. Zhong, Y., Qin, Y., Huang, M., Lu, W., Gao, W., Du, Y.: Automatically generating assembly tolerance types with an ontology based approach. *Comput. Aided Des.* **45**, 1253–1275 (2013)
8. Cheng, K.M., Tsai, J.C.: Optimal statistical tolerance allocation of assemblies for minimum manufacturing cost. *Appl. Mech. Mater.* **52–54**, 1818–1823 (2011)
9. Greenwood, W.H., Chase, K.W.: Worst case tolerance analysis with nonlinear problems. *ASME J. Eng. Ind.* **110**, 232–235 (1988 and 1990)
10. Haghghi, P., Mohan, P., Shah, J.J., Davidson, J.K.: Automatic detection and extraction of tolerance stacks in mechanical assemblies. In: *Proceedings of the ASME 2014 International Design Engineering Technical Conferences and Computers and Information in Engineering Conference*, vol. 2, pp. 4143–4152 (2014)
11. Movahhedy, M.R., Khodaygan, S.: Tolerance analysis of mechanical assemblies with asymmetric tolerances. *SAE Trans. J. Mater. Manuf.* **1**, 407–418 (2007)
12. Mullins, S.H., Anderson, D.C.: Automatic identification of geometric constraints in mechanical assemblies. *Comput. Aided Des.* **30**(9), 715–726 (1998)
13. Shen, Z., Shah, J., Davidson, J.: Automatic generation of min/max tolerance charts for tolerance analysis from CAD models. *Int. J. Comput. Integr. Manuf.* **21**(8), 869–884 (2008)
14. Sambhoos, K., Koc, B., Nagi, R.: Extracting assembly mating graphs for assembly variant design. *ASME J. Comput. Inf. Sci. Eng.* **9**(3), 1–9 (2009)

# Investigation of Dielectric Dependency on CNTFET Characteristics in Ballistic Regime



Argha Sarkar, Raja Suresh, N. Padmavathy, and Chinna Aswini

**Abstract** Carbon nanotube (CNT)-based field effect transistor is replacing the bulk metal oxide field effect transistor. Herein, the cylindrical carbon nanotube field effect transistor is considered to study the effect of different dielectrics on the characteristics of carbon nanotube field effect transistor. Different dielectric materials like Teflon, silicon nitride, zirconium dioxide, hafnium dioxide and titanium dioxide are analyzed, and the comparative analysis is done with respect to several parameters like carrier injection velocity, conductance, drain-induced barrier lowering, transconductance, subthreshold swing and voltage gain. The overall investigation is made considering the parameters such as nanotube diameter (0.6 nm), gate insulator thickness (1.5 nm) for all the dielectrics,  $V_{th}$  (0.32 V), gate and drain control parameters (1 and 0), series resistance (0), at temperature 300 K, with final gate and drain voltages as 2 and 1 V. The impacts of dielectric materials on such parameters are investigated in FETToy and the relationship is understood.

**Keywords** Cylindrical CNTFET · Dielectric · Carrier injection velocity · Transconductance · FETToy

---

A. Sarkar (✉) · N. Padmavathy  
Electronics and Communication Engineering, Vishnu Institute of Technology,  
Kovvada, Andhra Pradesh 534202, India

R. Suresh  
Ekalavya Innovation Labs, Ekalavya Group of Technologies,  
Tirupati, Andhra Pradesh 517501, India

C. Aswini  
Nanoelectronics Lab, Sree Vidyanikethan Engineering College,  
Tirupati, Andhra Pradesh 517102, India

## 1 Introduction

Last few decades, silicon technology has achieved substantial growth. Scaling of devices may lead to the rise of short channel effects, power leakage. The silicon made transistors undergo low reliability, performance degradation and will consume more power [1].

The authentication of the circuit operation will depend on the ON and OFF states of the device in the digital logic integrated circuits. In MOSFET's scaling will rise to short channel effects like higher leakage current, more subthreshold swing (SS) and drain-induced barrier lowering (DIBL). The device temperature and leakage current are directly proportional to each other in nanodevices. The leakage current should always be low for a device as the leakage current increases the OFF current of the circuit which will lead to an increase in the device temperature.

To overcome the scaling limitation and to reduce leakage, current dielectric materials instead of silicon dioxide ( $\text{SiO}_2$ ) should be used [2]. Instead of silicon dioxide the high-K dielectrics is preferable as an insulator in nanotechnology due to the reason of direct tunneling of electrons from insulator to substrate leading to more power dissipation [3].

For the channel materials of FET's carbon nanotube is one of the potential materials. CNT's [4] are made up of graphene, which are allotropes of carbon. The basic properties of the carbon nanotube are resulted by the way the graphene sheet is folded [5]. It has strong  $\text{sp}^2$  bonding. There are single wall CNT, double wall CNT and multi-wall CNT's [6]. It has good tensile strength and excellent electrical and mechanical properties [7].

CNT's can show both metallic and semiconducting properties based on their chirality value.

$$C = na_1 + ma_2 \quad (1)$$

where  $n, m$  = chirality parameter and  $a_1, a_2$  are the chirality vectors.

If  $(n = m)$  or  $(n - m = 3i)$ , where  $i$  is an integer shows metallic properties else semiconductor [8]. The characterization of CNT is divided into two types zigzag and armchair.

- Zigzag:  $n \neq 0, m = 0$  or  $n = 0, m \neq 0$
- Armchair:  $n = m$ .

## 2 Cylindrical CNTFET

Importantly, two types of CNTFET structures are there (i) planar structure and (ii) vertical structure. Here, Fig. 1 depicts the cylindrical or coaxial CNTFET, which is a single wall vertical CNTFET structure [9].

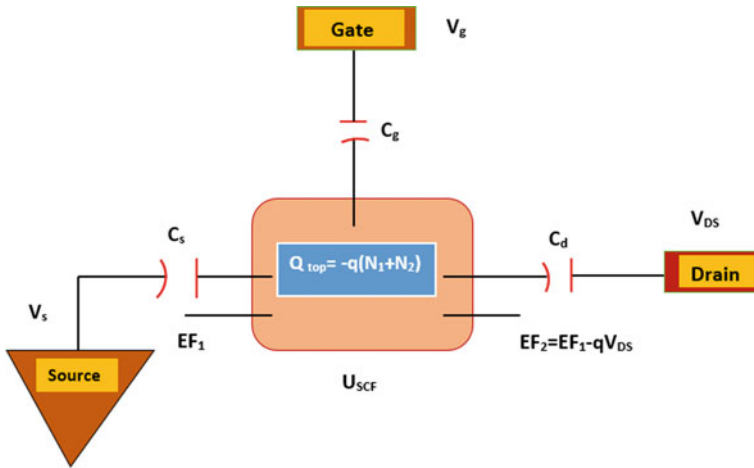


Fig. 1 2D capacitive model of transistors in ballistic regime

Cylindrical CNTFET with constant thickness 1.5 nm and (at temperature 300 k) the distinct dielectric materials like Teflon (2.1), silicon nitride (7), hafnium dioxide (15), zirconium dioxide (25) and titanium dioxide (35) are considered, and the brunt of these changes are studied for various specifications like drain-induced barrier lowering (DIBL), ( $g_m$ ) transconductance, ( $g_d$ ) output conductance, ( $A_v$ ) voltage gain and subthreshold swing (SS).

### 3 Mathematical Analysis in Ballistic Regime

Though silicon dioxide has low subthreshold swing it cannot be used as a dielectric material because carbon nanotube field effect transistor is having high DIBL and lower  $g_m$ ,  $g_d$ ,  $A_v$ . The proposed solution is the usage of high dielectric material to the gate insulator [10, 11]. These dielectric materials are considered for the simulation and analyzed in the FETToy. Different dielectric materials with dielectric values are shown in Table 1.

**Table 1** Proposed dielectric materials and their relative dielectric values

Oxide name	Chemical formula	Dielectric constant
Teflon	$(C_2F_4)_n$	2.1
Silicon nitride	$Si_3N_4$	7
Zirconium dioxide	$ZrO_2$	15
Hafnium dioxide	$HfO_2$	25
Titanium dioxide	$TiO_2$	35

### 3.1 Transconductance ( $g_m$ )

The mathematical formula of transconductance is given by [11, 12].

$$g_m = \frac{\mu \left( \frac{C_{ox}}{L} \right)}{\left( \frac{V_{ds}}{L} \right)} \quad (2)$$

where  $C_{ox}$  = oxide capacitance

$L$  = channel length,

$\mu$  = carrier mobility.

From Table 3 it is clear that as the dielectric value increases the  $g_m$  also increases, as it is directly proportional to each other.

It is clear that transconductance ( $g_m$ ) is proportionate to the dielectric constant. Transconductance determines the dominance of  $V_{gs}$  over  $I_d$ . It is the ratio of output and input of device. It decides the carbon nanotube FET signal amplification.

### 3.2 Voltage Gain ( $A_v$ )

From Table 1, it is observed the dielectric increases. The ratio of  $g_m$  to  $g_d$  is the voltage gain of CNTFETs. It is directly proportional to the dielectric constant. It implies that if the dielectric increases the voltage gain will also increase. For amplification of signal, high voltage gain is desirable.

### 3.3 Carrier Injection Velocity ( $V_{inj}$ )

As the dielectric value increases, the carrier injection velocity also increases. From Tables 2 and 3, it is found that  $V_{inj}$  increases with inflation in dielectric values. When  $V_{inj}$  is high the transistor will regulate high on current.

### 3.4 Output Conductance ( $g_d$ )

It is the ratio of change in drain current to the change in the drain source voltage at constant  $V_{gs}$ .

Output conductance ( $g_d$ ) is the reciprocal of the output resistance ( $r_o$ ) and is basically the ratio of change in drain current to change in drain source voltage  $V_{ds}$  at constant  $V_{gs}$  and is represented as

**Table 2** Parameters and their effects on the different dielectrics

Dielectric	Parameters	
Increases	Carrier injection velocity $V_{inj}$ (m/S)	▲
Increases	Drain-induced barrier lowering DIBL (mV/V)	▼
Increases	Subthreshold swing SS (mV/dec)	▼
Increases	Transconductance $g_m$ (S/m)	▲
Increases	Output conductance $g_d$ (S/m)	▲
Increases	Voltage gain ( $A_v$ )	▲

**Table 3** Considered parameters and their dielectric values

Parameters	Dielectric				
	Teflon 2.1	Silicon nitride 7	Hafnium dioxide 15	Zirconium dioxide 25	Titanium dioxide 35
$V_{inj}$ (m/S)	3.576e + 05	5.713e + 05	5.245e + 05	4.163e + 05	3.751e + 05
DIBL (mV/ V)	3.98	-728.81	-794.66	-251.01	117.97
SS (mV/ dec)	179.54	136.81	110.92	61.99	-1056.16
$g_m$ (S/m)	3.119e-05	8.388	2.848e-05	5.710e-07	2.404e-08
$g_d$ (S/m)	3.99e-16	2.345e-07	1.490e-04	1.552e-04	1.552e-04
$A_v$	779.61	357.66	0.19	0.00	0.00

$$g_d = \frac{\int I_d}{\int V_{ds}} \quad (3)$$

It is observed in Table 3 that if the dielectric increases, the  $g_d$  will also increase which will, in turn, increase the drain current [12].

### 3.5 Subthreshold Swing (SS)

The SS in CNTFET is given by the above formula [12].

$$SS = \left| \frac{d \log_{10} G}{dV_g} \right|^{-1} \quad (4)$$

For SS, 60 mV/decade at room temperature is the lowest theoretical limit [13]. The transistor shrinking depends upon SS. The behavior of subthreshold swing is observed in Table 3.

### 3.6 Drain-Induced Barrier Lowering (DIBL)

The formula for DIBL is given as [14],

$$\text{DIBL} = \frac{V_{\text{TH}}(\text{Low } V_{\text{DS}}) - V_{\text{TH}}(\text{High } V_{\text{DS}})}{\text{High } V_{\text{DS}} - \text{Low } V_{\text{DS}}} \quad (5)$$

At higher  $V_{\text{DS}}$ , DIBL creates short channel effect because of the reduction in  $V_{\text{TH}}$  of the transistor. The parameters effect and their corresponding dielectric changes have been mentioned briefly in Table 2.

## 4 Results and Analysis

By using the nanoHUB platform [15], the overall simulation is done. By considering different types of dielectric material, the device parameters like drain-induced barrier lowering, carrier injection velocity, transconductance, subthreshold swing and voltage gain output conductance have been analyzed and their corresponding values are shown in Table 3.

The drain current and  $g_m/I_d$  versus gate voltage plots are depicted in Figs. 2, 3 and 4. The considered parameters are: nanotube diameter 0.6, gate insulator thickness as 1.5 nm for all the dielectrics,  $V_{\text{th}}$  is 0.32 V, gate and drain control parameters as 1 and 0, series resistance is 0, at temperature 300 K, with final gate and drain voltages as 2 and 1 V.

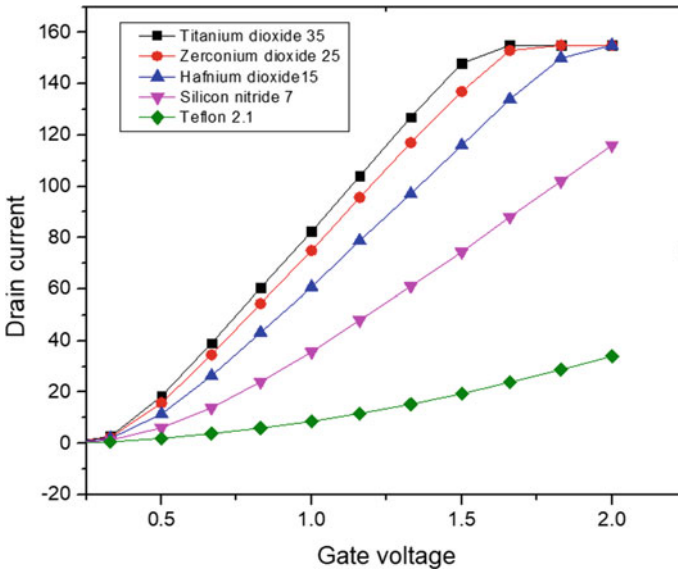


Fig. 2 Graph of OFF current for drain current versus gate voltage for different dielectrics

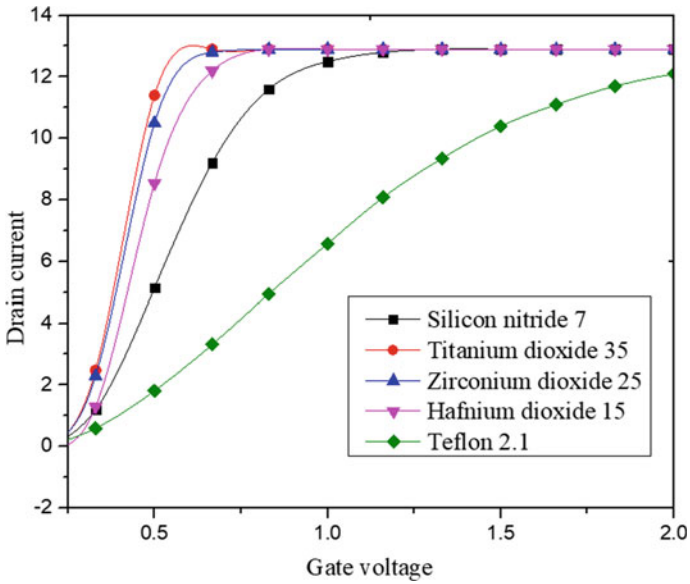


Fig. 3 Graph of ON current for drain current versus gate voltage for different dielectrics

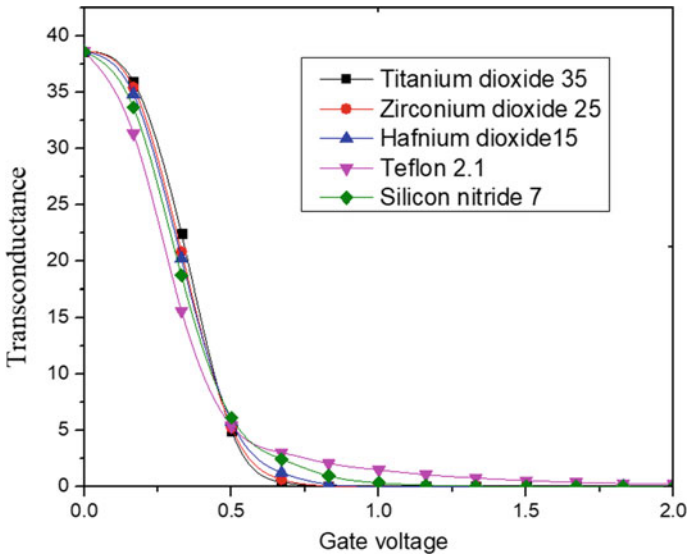


Fig. 4 Graph for  $g_m/I_d$  versus gate voltage for different dielectrics



## 5 Conclusion

In this investigation, different dielectrics are considered for the comparative analysis. It is clear that drain current increases for higher dielectric material. The ON current must be higher for higher dielectric materials. Increased transconductance implies a higher gain in the case of higher dielectric materials. Different CNTFET parameters are analyzed with respect to different dielectric materials. Finally, it is found that higher dielectric materials are the most suitable for fabricating CNTFETs in the ballistic regimes.

## References

1. Wilson, L.: International technology roadmap for semiconductors (ITRS). *Semicond. Ind. Assoc.* **1** (2013)
2. Suehle, J.S., Vogel, E.M., Edelstein, M.D., Richter, C.A., Nguyen, N.V., Levin, I., Kaiser, D. L., Wu, H., Bernstein, J.B.: Challenges of high-k gate dielectrics for future MOS devices. In: 6th International Symposium on Plasma-and Process-Induced Damage, IEEE, pp. 90–93. IEEE Cat. No. 01TH8538 (2001)
3. Zorian, Y.: Testing the monster chip. *IEEE Spect.* **36**(7), 54–60 (1999)
4. Iijima, S., Ajayan, P.M., Ichihashi, T.: Growth model for carbon nanotubes. *Phys. Rev. Lett.* **69**(21), 3100 (1992)
5. de Heer, W.A., Berger, C., Conrad, E., First, P., Murali, R., Meindl, J.: Pionics: the emerging science and technology of graphene-based nanoelectronics. In: IEEE International Electron Devices Meeting, pp. 199–202 (2007)
6. Mousa, Marwan S.: Comparison between single-walled CNT, multi-walled CNT, and carbon nanotube-fiber Pyrograf III. *Conf. Ser.: Mater. Sci. Eng.* **305**(1), 12–25 (2018)
7. Mahar, B., Laslau, C., Yip, R., Sun, Y.: Development of carbon nanotube-based sensors—a review. *IEEE Sens. J.* **7**(2), 266–284 (2007)
8. Saito, R., Fujita, M., Dresselhaus, G., Dresselhaus, M.S.: Electronic structure of graphene tubules based on C 60. *Phys. Rev. B* **46**(3), 1804 (1992)
9. Pavan Kalyan, G.V., Sarkar, A., Aswini, C., Chakraborty, P.: Characterization of CNT and its carrier mobility dependency on diameter in Back-Gated CNT-FET. *Mater. Today: Proc.* (2020)
10. Rahman, A., Guo, J., Datta, S., Lundstrom, M.S.: Theory of ballistic nanotransistors. *IEEE Trans. Electron Devices* **50**(9), 1853–1864 (2003)
11. Cheng, B., Cao, M., Rao, R., Inani, A., Vande Voorde, P., Greene, W.M., Stork, J.M.C., Yu, Z., Zeizoff, P.M., Woo, J.C.S.: The impact of high- $\kappa$ /gate dielectrics and metal gate electrodes on sub-100 nm MOSFETs. *IEEE Trans. Electron Devices* **46**(7), 1537–1544 (1999)
12. Farhana, S., Alam, A.Z., Khan, S.: DIBL and subthreshold swing effect on carbon nanotube field effect transistor. *Proc. World Congr. Eng.* 4–7 (2015)
13. Javey, A., Guo, J., Wang, Q., Lundstrom, M., Dai, H.: Ballistic carbon nanotube field-effect transistors. *Nature* **424**(6949), 654–657 (2003)
14. Djamil, R., Salima, B., Kheireddine, L.: Performance enhancement of CNTFETs with high-K dielectric. In: *Advanced Materials Research*, vol. 685, pp. 340–344. Trans Tech Publications (2013)
15. Sarkar, A., Maity, S., Chakraborty, P., Chakraborty, S.K.: Characterization of carbon nanotubes and its application in biomedical sensor for prostate cancer detection. *Sens. Lett.* **17** (1), 17–24 (2019)

# Comparative Study on Heat Transfer of Plastic Injection Molding Process for Quality Enhancement



Rupesh Kumar Khutey and Chhabi Ram Matawale

**Abstract** From the decades, injection molding is one of the favored manufacturing methods used in manufacturing industries. In this method, the granular plastic is fed through hopper, and the presence of pressure the melted plastic material is injected into the cavity and acquired final products. It is very useful for mass production processes with variety of applications such as automobile, toy, bottle, chair, computer part, etc. There are some inappropriate functions where injection molding process may fail such as injector stroke is not enough, material packing is high, cooling is not enough, and white mark appears on surface of product. Therefore, the molded part may classify into four categories—part design, mold design, machine performance and method conditions. With optimum design of these categories, the performance of injection molding process may increase. The main aim of this paper is to compare the mode of heat transfer, cooling time, product quality of different plastic materials used in injection molding process as well as the design parameters are summarized for optimal design of injection molding process for product quality and performance enhancement.

**Keywords** Injection molding · Mold flow · Heat transfer · Cooling time · Cooling channels

## 1 Introduction

Today's world, plastic material has become an essential material for all kind of daily-life household application. That makes plastic material more preference and focused material in various manufacturing industries. It is having several advantages such as lightweight, easily transportable, corrosion resistance, low cost, high durability as well as their application in the mobile industry, automobile industry, toy, bottle, electric industry, etc. In this context, the injection molding process is one of the methods which manufacture the plastic product and fulfill the human

---

R. K. Khutey (✉) · C. R. Matawale  
Department of Mechanical Engineering, Shri Rawatpura Sarkar University, Raipur, India

requirement. Injection molding process is one of the mass basis production processes with minimum production time and cost. In this process, generally the polymer materials such as polystyrene (PS), acrylonitrile butadiene styrene (ABS), polypropylene (PP), polyamide (PA), polyethylene (PE), polyvinylchloride (PVC) are used as raw material. Plastic injection process is similar to casting process.

### 1.1 Injection Molding Working Principle

In this process first, raw materials (pellets or granules form) send to hopper, here present of drive unit (electrical power) heat is generated and raw material melted in the plastic injection molding machine and then injected into a mold or chamber under high pressure. There, the material is cooled, solidified and afterward released by opening the two halves of the mold. This technique results in a plastic product with a predetermined, fixed form as shown in Fig. 1a To facilitate production, the parts that play a role in the plastic injection molding process must be carefully designed.

### 1.2 Heat Distribution

The thermal behavior within the injection chamber can be illustrated as shown in Fig. 1b. Melt temperature is an effective parameter which effects to the quality of product and process an injection molding process. It is very difficult to scaling and controlling because of thermal dynamic condition in injection molding process. In heating process, other parameter affected to the melt temperature such as screw rotational speed, back pressure, injection velocity, material parameters, etc. Melt temperature is not directly controlled; it is controlled by barrel and nozzle heater temperature. It results that heat distribution control is very much important for the better performance and good-quality product.

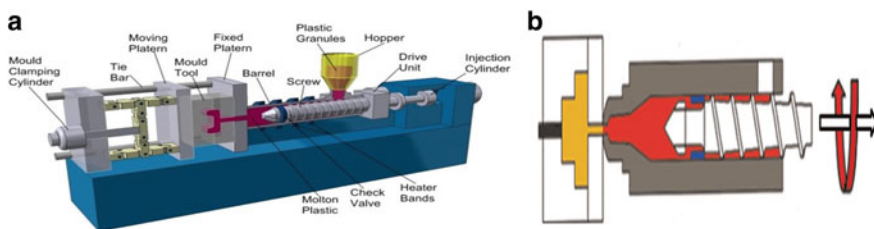


**Fig. 1** a Typical injection molding machine with different parts. b Melt preparation phase

## 2 State of Art of Literature

Injection molding is one of the effective processes for the production of plastic part. In this regard, many of researchers looked in the field of numerical simulation and validated with experimental result and some of involved in analytical analysis. Simulation process reduces the analysis time, cost, etc. Chao-Tsai Huang et al. [1] represented the deviation between experimental and numerical simulation in injection molding to find the shrinkage behavior of design part with different dimension on the basis of these parameters (cooling time, filling time, mold temperature, packing pressure, and melt temperature). The shrinkage is approximately equal for both numerical simulation and experiment and calibrated reduced by 56%. Huszar et al. [2] used thermoplastic (polypropylene, polystyrene and fiber-filled) material and investigated selection of gate location for minimizing warpage and injection pressure. Hnatkova et al. [3] used irregular shape of ceramic powder (aluminum oxide) for evaluation of critical solid load (CSL). Stearic acid (SA) is used as a binder, which increases the CSL and also affected the pseudoplastic flow that is reducing the viscosities and increases the shear rate. CSL affected the torque and shear stress in injection molding. Daver and Demirel [4] investigated thermal and structural analysis in a bottle made of polyethylene terephthalate material by injection stretch blow molding. It is represented based on different thermal condition and finds high burst strength and high top-load strength. Jahan et al. [5] investigated the thermal performance and optimum design parameter of cooling channel in injection molding, and result indicates channel cooling time and maximum von Mises stress minimized. Jahan et al. [6] investigated mathematical simulation and topology optimization techniques for reducing the cycle time an injection process; they investigate the stainless steel (15-5 PH1) power on circular channel with different diameter, pitch and channel centerline to mold wall distance. Result has shown that channel diameter increases than cycle time reduces.

Masses et al. [7] presented the effect the heat transfer in mold–polymer interface of an injection molding and find the increase the cycle time than air gap present between mold and polymer. Acrylonitrile–butadiene–styrene (ABS) mostly used as a polymer in the industry, instrumentation and other application, it has high strength, hardness, rigidity, toughness and impact strength, viscosity grade, structural and mechanical properties [8–10]. It also improves the shrinkage phenomena [11]. The PA polymer is directed to improve properties such as fracture mechanism and tensile strength [12] surface quality and flexural strength [13], chemical and thermo-morphological [14], cooling rate and conductivity [15]. Among all type of plastic, polyethylene is one of the crucial plastic material which is mostly used in injection molding process and shown good tensile strength, surface hardness, wear resistance [16], resistance to stress relaxation [17], various crystalline structures in injection mold [18], thermal behavior [19], dynamic packing factor in injection molding [20], the molecular interactions between components [21], the environmental influence in injection molding [22]. Polypropylene (PP) plays an extremely important role in polymer. Research has been studied on PP properties, optimum

parameter for warpage and shrinkage [8] implements energy consumption [9]. In injection molding process, the mechanical properties determine that is tensile strength and modulus [10] fiber length and fiber orientation [23] improved fiber–matrix interface [24] improved thermal insulation performance [25] are the new approach to product quality and environmentally friendly technique [26]. In injection molding process, polymer used polystyrene and different type of method developed for investigate the pure and blended solvent on the hydrophobic plasma-treated polystyrene [27] rearrangement of particles size by the gating arrangement [28], effect of melt temperature in thin-walled injection molding [29], importance role of the adhesion of polymer–mold interface [30]. Control approach on thin skin, small-uniform cell size to better surface quality [31], interactions of cell behavior with nanotopography without biochemical [32]. Polymer is one of the materials which not only used in injection molding process but also used as coating material such as titanium diboride ( $TiB_2$ ), diamond-like carbon (DLC) titanium nitride (TiN), titanium oxide (NiO), titanium aluminum nitride (TiAlN), chrome carbon nitride (CrCN), and perfluorooctyltriethoxysilane (PFOS/Ni) [33].

### 3 Comparative Study

Here we have compiled that the work has been done so far that represented in Table 1. The comparative study of process parameters and their responses.

### 4 Result and Discussion

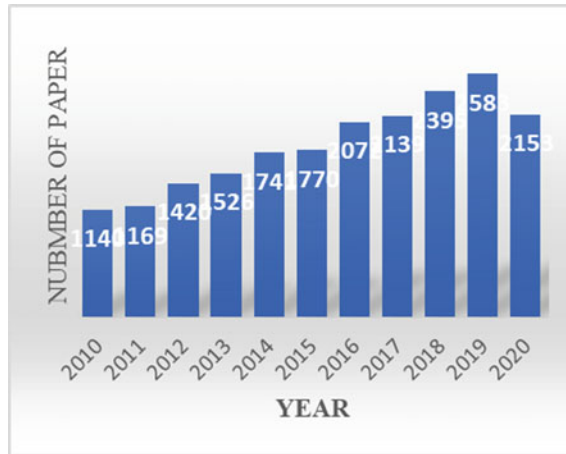
From the exclusive state of art and comparative study, we found that there is plenty of literature available on injection molding process considering different materials, analysis methods, experimental and numerical simulation. The parameter which affects the quality and molding efficiency as reported by researcher are cooling system design, cooling rate and time, surface roughness, shrinkage and warpage. These parameters could improved with some of the materials such as polypropylene, polystyrene (PS), and acrylonitrile butadiene styrene (ABS).

Figure 2 represents the number of research article published year by year from 2010 to 2020. On an average, 1800 research articles are published in a year, and day by day it is increasing that shows the interest of researchers, scientists as well as industry demands. Figure 3a represents the different types of plastic materials used for injection molding process. The most preferred plastic materials are polymers which are acrylonitrile butadiene styrene (ABS), ethylene vinyl acetate (EVA), paraffin wax (PW), stearic acid (SA), polyamide (PA), Nylon 6, polypropylene (PP), polystyrene (PS), polyvinyl chloride (PVC), polyethylene(PE), polyether ether

**Table 1** Comparative study of injection molding process parameters

S. No.	Parameters	Responses	Type of analysis	Material used	Outcomes	References
1	Cooling system	Improved	Numerical	Polymer (938 kg/m <sup>3</sup> , 1800 J/kg K, 0.25 W/m K)	Desirable affect given by using cooling channels	2018 [34], 2019 [35],
		Improved conformal channels	Analytic and CAE simulation	Polystyrene	Cooling time is reduced to 23%	
2	Surface roughness	Improvement	Experimental	Stainless steel powder	Heating rate, weight losses	2018 [20], 2012 [19]
		Increased quality	Simulation	Polypropylene copolymer	Amplitude, functional, hybrid and spatial, surface characteristics	
3	Shrinkage	Reduced	Experimental	Polybutylene terephthalate (PBT)	Conventional, microcellular, glass and wollastonite fiber filled	2019 [1], 2017 [28],
		Minimized	Simulation	Acrylonitrile–butadiene styrene/ polypropylene	Different parameter affected the packing pressure, mold temperature	
4	Bond quality	Improved	Experimental	Polyamide 12 (PA12)	Bond quality, media-tightness	2016 [29] 1996 [18]
		Optimum	Experimental	Methyl methacrylate (PMMA)	Nanoparticles enhance the quality of product	

ketone (PEEK) and stainless steel powder. Figure 3a shows that the polypropylene (PP), polyamide (PA), and polyethylene(PE) are the largely used material in injection molding. Figure3b represents the types of analysis adopted by the researchers. Mainly, the researcher and academician have concentrated on material analysis, design analysis and thermal behavior of the molding system as well as material used. In this three analysis, materials analysis are very effective and most preferred.



**Fig. 2** Number of research article published year-wise [Source sciencedirect.com (till date 02-08-2020)]

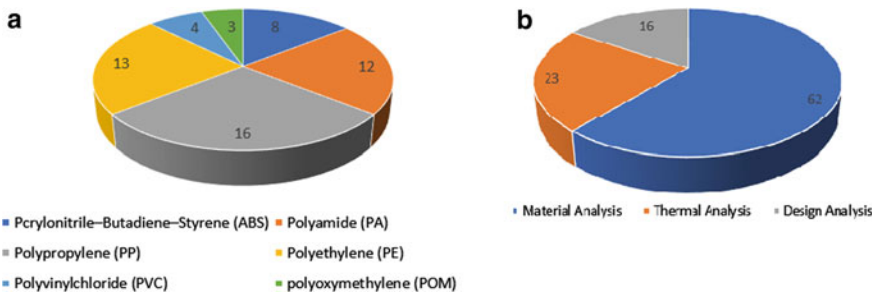


**Fig. 3** a Polymer used. b Analysis performed

## 5 Conclusions

The principal aim of this paper is to compare the different materials and there design parameters which affected by the heat transfer in injection molding process. The reported experimental and analytical result indicates various parameters like shearing action, surface roughness, cooling rate, shrinkage, etc. These parameters are improved in some of the materials such as polypropylene, polystyrene (PS), and acrylonitrile butadiene styrene (ABS). The most preferred polymer materials such as polypropylene (PP), polyamide (PA), and polyethylene (PE) are used by researchers. Based on the literature, materials analysis is very effective and most preferred analysis method. However, to improve the heat transfer cooling channel system is also used having different geometrical dimensions in many fields. Many researchers and academician have paid attention on the design of confirming

cooling channel and method of heat transfer. These factors are very much important for improvement of final product quality and efficiency.

## References

1. Huang, C.T., Hsu, Y.H., Chen, B.S.: Investigation on the internal mechanism of the deviation between numerical simulation and experiments in injection molding product development. *Polym. Testing* **75**, 327–336 (2019)
2. Huszar, M., Belblidia, F., Davies, H.M., Arnold, C., Bould, D., Sienz, J.: The impact of materials selection and gate location on part warpage and injection pressure. *Sustain. Mater. Technol.* **5**, 1–8 (2015)
3. Hnatkova, E., Hausnerova, B., Filip, P.: Evaluation of powder loading and flow properties of Al<sub>2</sub>O<sub>3</sub> ceramic injection molding feedstocks treated with stearic acid. *Ceramics Int.* **45**, 20084–20090 (2019)
4. Daver, F., Demirel, B.: A simulation study of the effect of preform cooling time in injection stretch blow molding. *J. Mater. Process. Technol.* **212**, 2400–2405 (2012)
5. Jahan, S. A., Wu, T., Zhang, J., Tover, A., El-Mounayri, H.: Thermo-mechanical design optimization of conform cooling channel using design of experimental approach. *Procedia Manuf.* **10**, 898–911 (2017)
6. Jahan, S.A., Wu, T., Zhang, Y., El-Mounayri, H., Tover, A., Zhang, Z., Acheson, D., Nalim, R., Gua, X., Lee, W.H.: Implementation of conformal cooling and topology optimization of 3D printed stainless steel porous structure injection molds. *Procedia Manuf.* **5**, 901–915 (2016)
7. Masse, H., Arquis, E., Delaunay, D., Quilliet, S., Le Bot, P.H.: Heat transfer with mechanically driven thermal contact resistance at the polymer–mold interface in injection molding of polymers. *Int. J. Heat Mass Transfer* **47**, 2015–2027 (2004)
8. Vielma, P.T., Cervera, A., Levenfeld, B., Varez, A.: Production of alumina parts by powder injection molding with a binder system based on high density polyethylene. *J. Eur. Ceramic Soc.* **28**, 763–771 (2008)
9. Zhang, K., Liu, Z., Yang, B., Yang, W., Lu, Y., Wang, L., Sun, N., Yang, M.: Cylindritic structures of high-density polyethylene molded by multi-melt multi-injection molding. *Polymer* **52**, 3871–3878 (2011)
10. Rex, I., Graham, B.A., Thompson, M.R.: Studying single-pass degradation of a high-density polyethylene in an injection molding process. *Polym. Degrad. Stab.* **90**, 136–146 (2005)
11. Boronat, T., Segui, V.J., Peydro, M.A., Reig, M.J.: Influence of temperature and shear rate on the rheology and processability of reprocessed ABS in injection molding process. *J. Mater. Process. Technol.* **209**, 2735–2745 (2009)
12. Rahimi, M., Esfahanian, M., Moradi, M.: Effect of reprocessing on shrinkage and mechanical properties of ABS and investigating the proper blend of virgin and recycled ABS in injection molding. *J. Mater. Process. Technol.* **214**, 2359–2365 (2014)
13. Arochaa, P.U., Mehler, C., Puskas, J.E., Altstadt, V.: Effect of sample thickness on the mechanical properties of injection molded polyamide-6 and polyamide-6 clay nanocomposites. *Polymer* **44**, 2441–2446 (2003)
14. Carrillo, L.Q., Boronat, T., Montanes, N., Balart, R., Torres-Ginerb, S.: Injection-molded parts of fully bio-based polyamide 1010 strengthened with waste derived slate fibers pretreated with glycidyl- and amino-silane coupling agents. *Polym. Testing* **77**, 105875 (2019)
15. Murray, J.J., Robert, C., Gleich, K., McCarthy, E.D., Brádaigh, C.M.Ó.: Manufacturing of unidirectional stitched glass fabric reinforced polyamide 6 by thermoplastic resin transfer moulding. *Mater. Des.* **189**, 108512 (2020)



16. Huang, H.X., Wang, B., Zhou, W.W.: Polymorphism in polyamide 6 and polyamide 6/clay nanocomposites molded via water-assisted injection molding. *Composites: Part B* **43**, 972–977 (2012)
17. Kuo, H.C., Chang Jeng, M.: The influence of injection molding on tribological characteristics of ultra-high molecular weight polyethylene under dry sliding. *Wear* **268**, 803–810 (2010)
18. Je Cha, K., Lim, J., He Na, M., Dong, S.K.: Physically microstriped-nanoengineered polystyrene surface (PMS-NPS) for regulating cell attachment and alignment fabricated by nano-injection molding. *Microelectron. Eng.* PII: S0167-9317(2016)30077-6
19. Chen, S.C., Liao, W.H., Yeh, J.P., Chien, R.D.: Rheological behaviour of PS polymer melt under ultra high speed injection molding. *Polym. Testing* **31**, 864–869 (2012)
20. Lu, Y., Yang, W., Zhang, K.: Ming-bo Yang, Stress relaxation behavior of high density polyethylene (HDPE) articlesmolded by gas-assisted injection molding. *Polym. Testing* **29**, 866–871 (2010)
21. Yang, B., Xia, R., Miao, J.B., Qian, J.S., Yang, M.B., Chen, P.: Probing solidification kinetics of high-density polyethylene during injection molding using an in-situ measurement technique. *Polym. Testing* **32**, 202–208 (2013)
22. Yu, F., Deng, H., Zhang, Q., Wang, K., Zhang, C., Chen, F., Fu, Q.: Anisotropic multilayer conductive networks in carbon nanotubes filled polyethylene/polypropylene blends obtained through high speed thin wall injection molding. *Polymer* **54**, 6425–6436 (2013)
23. Cao, W., Wang, K., Zhang, Q., Du, R., Fu, Q.: The hierarchy structure and orientation of high density polyethylene obtained via dynamic packing injection molding. *Polymer* **47**, 6857–6867 (2006)
24. Li, S.N., Li, B., Li, Z.M., Fu, Q., Shen, KZ.: Morphological manipulation of carbon nanotube/polycarbonate/ polyethylene composites by dynamic injection packing molding. *Polymer* **47**, 4497–4500 (2006)
25. Bleyan, D., Svoboda, P., Hausnerova, B.: Specific interactions of low molecular weight analogues of carnauba wax and polyethylene glycol binders of ceramic injection moulding feedstocks. *Ceramics Int.* (2016)
26. Elduque, A., Elduque, D., Javierre, C., Fernandez, A., Santolaria, J.: Environmental impact analysis of the injection molding process: analysis of the processing of high-density polyethylene parts. *J. Cleaner Prod.* 1–10 (2015)
27. Othman, M.H., Hasan, S., Khamis, S.Z., Ibrahim, M.H.I., Amin, S.Y.M.: Optimisation of injection moulding parameter towards shrinkage and warpage for polypropylene-nanoclay-Gigantochloa Scortechinii nanocomposites. *Procedia Eng.* **184**, 673–680 (2017)
28. Gou, G., Xie, P., Yang, W., Ding, Y.: Online measurement of rheological properties of polypropylene based on an injection molding machine to simulate the injection-molding process. *Polym. Testing* **30**, 826–832 (2011)
29. Zhao, J., Wanga, G., Zhang, L., Li, B., Wang, C., Zhao, G., Park, C.B.: Lightweight and strong fibrillary PTFE reinforced polypropylene composite foams fabricated by foam injection molding. *Eur. Polym. J.* **119**, 22–31 (2019)
30. Jiang, J., Liu, X., Lian, M., Pan, Y., Chen, Q., Liu, H.: Self-reinforcing and toughening isotactic polypropylene via melt sequential injection molding. *Polym. Testing* PII: S0142-9418(18)30168-5
31. Crema, L., Sorgato, M., Zanini, F., Carmignato, S., Lucchetta, G.: Experimental analysis of mechanical properties and microstructure of long glass fiber reinforced polypropylene processed by rapid heat cycle injection molding. *Composites: Part A* (2018) PII: S1359-835X(18)30019-8
32. Zhao, J., Zhao, Q., Wang, C., Guo, B., Park, C.B., Wang, G.: High thermal insulation and compressive strength polypropylene foams fabricated by high-pressure foam injection molding and mold opening of nano-fibrillar composites. *Mater. Des.* **131**, 1–11 (2017)
33. Yam, R.C.M., Mak, D.M.T.: A cleaner production of rice husk-blended polypropylene ecocomposite by gas-assisted injection moulding. *J. Clean. Prod.* **67**, 277–284 (2014)

34. Ogorodnyk, O., Lyngstad, O.V., Larsen, M., Martinsen, K.: Application of feature selection methods for defining critical parameters in thermoplastics injection molding. *Procedia CIRP* **81**, 110–114 (2019)
35. Tosello, G., Costa, F.S.: High precision validation of micro injection molding process simulations. *J. Manuf. Processes* **48**, 236–248 (2019)

# Corrosion Behaviour of Aluminium 6061/MWCNT Composite Prepared by Double Stir Casting Method



T. Arunkumar, K Aditya Sreevatsa, Dinesh R. Krishnan,  
and Ram Subbiah

**Abstract** In the last two decades, carbon nanotubes (CNTs) have been attracted the interest of material researchers owing to their extremely desirable mechanical, thermal and electrical properties. However, the main challenge is to control the cluster formation and homogeneous distribution within molten alloy due to strong surface attraction between CNT particles, and it has a high aspect ratio. Herein, aluminium 6061 alloy with various weight percentages of pre-synthesized MWCNT (0, 0.5, 1 and 1.5%) is prepared by double stir casting techniques. The corrosion rate of the prepared samples was studied by both salt spray and electrochemical methods in 3.5% NaCl solutions. Besides, the surface morphology of tested samples was analysed by scanning electron microscope (SEM). The corrosion rate of the samples has significantly reduced with the addition of MWCNT. However, the higher amount of CNT (1.5%) is slightly increasing the corrosion rate than 1% of CNT contain composites due to cluster formation and improper mixing.

**Keywords** Aluminium 6061 · Multi-Walled carbon nanotubes · Stir casting · Corrosion

## 1 Introduction

As technology is flourishing at a rapid pace in the engineering field, the requirements of customers are met by more durable and economical engineering materials. Currently, metal matrix composites (MMCs) have high demand in automobile, aircraft, marine and defence applications due to its greater properties [1]. Owing to modest mechanical properties, medium strength to weight ratio, facile heat treat-

---

T. Arunkumar (✉) · K. A. Sreevatsa · D. R. Krishnan  
Department of Mechanical Engineering, CMR Institute of Technology,  
Bengaluru 560037, India

R. Subbiah  
Department of Mechanical Engineering, Gokaraju Rangaraju Institute of Engineering  
and Technology, Hyderabad 500090, India

ment process and corrosion resistance, usage of aluminium 6061 alloys is propitious materials for structural and functional applications [2]. Although it has quite a good lineup of properties, the passive oxide surface layer dissolves and accelerates the corrosion rate when exposed to highly acidic or alkaline conditions [3]. To avoid this, the aluminium metal matrix composites (AMMCs) are introduced in order to increase the corrosion resistance in high-temperature atmospheres without losing the material properties [4]. Nowadays, researchers are concentrating the aluminium material to improve the whole properties for multipurpose applications so that aluminium is reinforced with superior nanoparticles like CNT, SiC, B<sub>4</sub>C and Al<sub>2</sub>O<sub>3</sub>. [5]. Generally, nano-ceramic materials like Al<sub>2</sub>O<sub>3</sub>, SiC and B<sub>4</sub>C were used as reinforcement with aluminium to improve the mechanical and tribological properties; conversely, these nanomaterials have higher density and lower strength to weight ratio than CNT [6]. In recent years, the aluminium/CNT composites have been extensively studied by researchers all over the world. Numerous previous studies have shown that CNT material has a major influence on mechanical properties. Srivastava et al. [7] reported that microhardness increased with the accumulation of CNT; on the other hand, Perez-Bustamante et al. and Liao et al. recorded that the accumulation of CNT is significantly decreased the mechanical properties when reinforcement is above 2% of CNT [8, 9]. It is due to attractive Van der Waals interactions between CNT and aluminium and forms the clusters [10]. In addition, the strengthening effect of the composite is increasing with the reduction of CNT diameter which is up to 1.5 weight % accumulation of CNT content; however, it is overturned when the accumulation of CNT range between 2 and 5 weight % [11]. There are various methods to fabricate the aluminium/CNT composites such as sintering, infiltration, casting. Among these, stir casting (SC) is commonly used in aluminium metal matrix manufacturing industries because of its simplicity and its economic consideration [12].

Altogether, until now, not many researchers performed corrosion investigations on aluminium/CNTs composites. Therefore, in this work, aluminium 6061 is reinforced with various weight percentages of pre-synthesized MWCNT (0, 0.5, 1 and 1.5%) by stir casting method. Further, corrosion behaviour of this composite is investigated by salt spray and electrochemical analysis. Finally, the precise amount of MWCNT is explored by comparing the corrosion rate of these samples.

## 2 Materials and Methods

Aluminium 6061 has been selected as base metal, and pre-synthesized MWCNT used as reinforcement material for these studies [13]. Besides, magnesium and hexachloroethane (C<sub>2</sub>Cl<sub>6</sub>) are used as wetting agents and degasser, respectively. The nanocomposite is fabricated from stir casting equipment with the following procedure. Initially, aluminium 6061 is heated at 650 °C, then C<sub>2</sub>Cl<sub>6</sub> is added in molten liquid to degases from alloy. At the same time, MWCNT nanoparticles are preheated at 100 °C to avoid oxidation. Then, this preheated MWCNT nanoparticle

is mixed with molten aluminium liquid and stirred at 300 rpm constant speed for 10 min. Later, it is allowed to cool down to semi-solid state around 450 °C. Then, again reheated above the melting point around 750 °C and stirred at 300 rpm constant speed for 10 min. This double stir casting procedure may improve the homogeneous distribution of MWCNT nanoparticles in molten aluminium alloy. Finally, this molten composite was then poured into a preheated mould box and solidified naturally. Then, these solidified composites have been extracted and machined as per ASTM standards for corrosion studies. To find the issue of the long period of corrosion evaluation, a salt spray test was carried out as per the standard ASTM B117-09. For this test cased composite was machined 10 mm  $\times$  10 mm  $\times$  6 mm and kept in a salt spray chamber at  $35 \pm 2$  °C, in 3.5% NaCl solution for 30 days. Electrochemical corrosion equipment (Biologic—model SP300) where Ag/AgCl electrodes (saturated KCl) were taken as the reference electrode, platinum (Pt) wire as counter electrode and the prepared samples as the working electrode was used to carry out the potentiodynamic polarization measurements as per ASTM G102-89. Before commencing the experiment, the well-polished specimen is allowed to stabilize in the electrolyte for 15 min. The measurement range was between  $-0.25$  V and  $+0.25$  V from the OCP at a scan rate of  $0.001 \text{Vs}^{-1}$  [14]. The surface topographies of the salt spray tested samples were obtained using the SEM method (ZEISS SUPRA 55) as per ASTM D4541 [15]. To assure the accuracy of the results, all the measurements were repeated at least thrice.

### 3 Results and Discussion

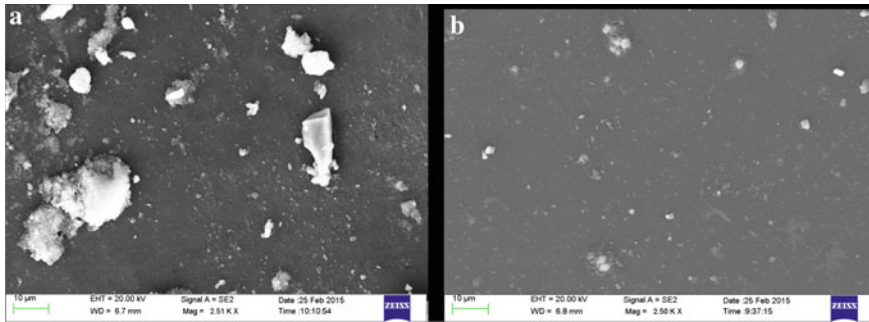
The long-period corrosion evaluation of the samples was explored using Eq. 1, after 30 days in a salt spray environment, where  $W$  = weight loss in milligrams;  $D$  = metal density in  $\text{g/cm}^3$ ;  $A$  = area of the sample in  $\text{cm}^2$ ;  $T$  = time of exposure of the metal sample in hours. The corrosion rate is significantly reduced with the addition of MWCNT with aluminium alloy as shown in Table 1.

$$\text{Rate of corrosion in millimeter per year} = \frac{87.6 \times W}{D \times A \times T} \quad (1)$$

The corrosion rate of stir casted base alloy is  $8.232 \mu\text{m/year}$ , and when MWCNT is reinforced with base alloy, the corrosion rate is decreased up to  $2.139 \mu\text{m/year}$ . It is revealed that 1% of MWCNT has improved the corrosion resistance by 74.02% from base alloy. On the other hand, 1.5% of the MWCNT reinforced sample has protected the base alloy by 56.80%; this reduction may due to inhomogeneous distribution or cluster formation of extensive MWCNT content into molten liquid. Besides, the surface morphology of the salt spray tested base alloy and 1% of MWCNT reinforced samples as shown in Fig. 1. It is clearly enlightened that the base alloy has higher oxide formation than AL +1% MWCNT samples because MWCNT is restricted to the oxide layer formation. Figure 2 shows

**Table 1** Corrosion rate of the samples in a 3.5% NaCl solution

Description of the sample	Salt spray		Polarization			
	Rate of corrosion ( $\mu\text{m}/\text{year}$ )	Protected efficiency (%)	$I_{\text{corr}}$ ( $\mu\text{A cm}^{-2}$ )	$E_{\text{corr}}$ (V)	Rate of corrosion ( $\mu\text{m}/\text{year}$ )	Protected efficiency (%)
Base alloy	8.232	–	7.50E-01	–1.072	7.98	–
Al + 0.5% MWCNT	4.252	48.34	3.07E-01	–1.118	3.27	59.02
Al + 1% MWCNT	2.138	74.02	1.11E-01	–1.088	1.19	85.13
Al + 1.5% MWCNT	3.556	56.80	2.50 E-01	–1.052	2.67	66.59

**Fig. 1** SEM images of the salt spray tested samples **a** base alloy **b** Al + 1% MWCNT

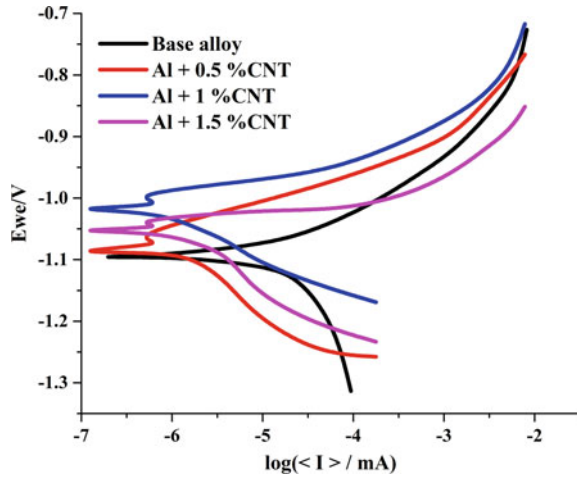
superimposed polarization curves of Al 6061, i.e. base metal alloy and its MWCNT reinforced composite in 3.5% NaCl electrolytes. It is observed that there is a linear region on both the anodic and cathodic legs in the Tafel extrapolation near the  $E_{\text{corr}}$ . The positive movement of  $E_{\text{corr}}$  confirms that MWCNT has protected the base alloy and provides superior corrosion resistance.

Likewise, the current density of the corrosion ( $I_{\text{corr}}$ ) shifted leftwards, i.e. decreases, which reduces the corrosion rate. It is observed from the Tafel curves that accumulation MWCNT samples have lower corrosion rates, i.e. higher corrosion resistance than base alloy. Also, anodic, cathodic and  $I_{\text{corr}}$  currents display their lowest values in the polarization curve of MWCNT reinforced samples causing the corrosion resistance to spike up. The electrochemical corrosion evaluation of the samples in 3.5% NaCl electrolytes was explored using Eq. 2.

$$\text{Rate of corrosion}(\text{mm}/\text{year}) = \frac{0.00327 \times \text{Equivalent weight} \times I_{\text{corr}}}{\text{Aluminium Density}} \quad (2)$$

The corrosion rate of 1% MWCNT reinforced composite is 1.9  $\mu\text{m}/\text{year}$  (Table 1), and it is protected the material by 85.13% from a base alloy (7.98  $\mu\text{m}/\text{year}$ ). It is due to

**Fig. 2** Tafel plots of the samples in 3.5% NaCl solution



MWCNT has restricted the oxide layer formation by separating oxides from the alloy and reduced the rate of corrosion [16]. Nevertheless, a higher amount of MWCNT (1.5%) having less corrosion resistance than 0.5% and 1% of MWCNT reinforced samples. In this case,  $I_{corr}$  and  $E_{corr}$  moves towards the base alloy due to chloride ions,  $Al_2O_3$  formations, attractive Van der Waals interactions between MWCNT and aluminium, clusters formations and improper mixing.

Impedance spectrum shows (Fig. 3) large capacitive and inductive loop at high and low frequencies. The constant phase element (CPE) is depicted by the high-frequency capacitive arc, whereas the inductive loop relates to the roughness of the solid surface and due to unbalanced mixing of particles. The 1% of MWCNT reinforced sample has a larger diameter of the semicircle than other samples, which

**Fig. 3** Impedance spectrum of the samples in 3.5% NaCl solution

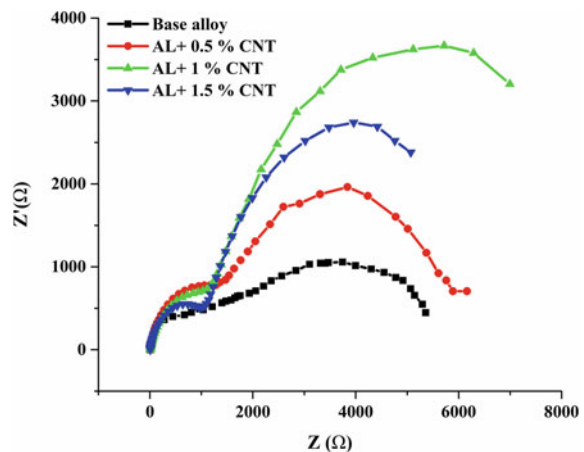
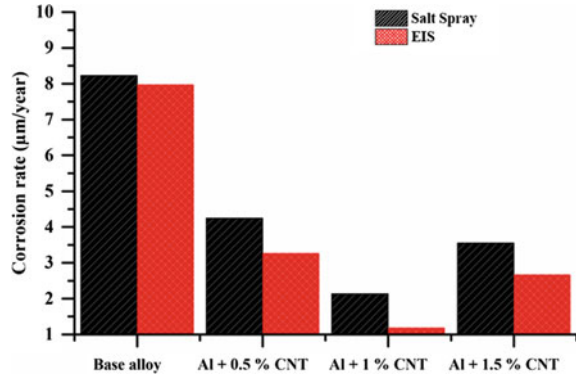


**Fig. 4** Corrosion rate of the samples by salt spray and EIS test



confirm that it has higher corrosion resistance. The corrosion rate of the samples by both salt spray test and electrochemical test values gives a similar result as shown in Fig. 4. Altogether, 1% of MWCNT reinforced samples have higher corrosion resistance than other samples.

## 4 Conclusion

Aluminium 6061 with various percentages of MWCNT is successfully fabricated by a double stir casting method. The effect of MWCNT reinforced composite is investigated by both salt spray and electrochemical method in 3.5% NaCl solution. The test results revealed that the MWCNT is a very good candidate to restrict the oxide layer formation and safeguard the material from corrosion. Besides, the precise amount of MWCNT reinforcement (1%) with aluminium alloy significantly controls the corrosion rate of up to 85.13%. Furthermore, the higher amount of MWCNT (1.5%) with aluminium by double stir casting method decreases the corrosion resistance due to improper mixing and cluster formation.

## References

1. Kannan, C., Ramanujam, R.: Comparative study on the mechanical and microstructural characterisation of AA 7075 nano and hybrid nanocomposites produced by stir and squeeze casting. *J. Adv. Res.* **8**(4), 309–319 (2017)
2. Gopinath, S., Prince, M., Raghav, G.R.: Enhancing the mechanical, wear and corrosion behaviour of stir casted aluminium 6061 hybrid composites through the incorporation of boron nitride and aluminium oxide particles. *Mater. Res. Express* **7**(1), 016582 (2020)
3. Ratna Kumar, P.S.S., Jyothi, S., Alexis, S.J.: Corrosion behavior of aluminium alloy reinforced with MWCNTs. *Corrosion Protection at the Nanoscale*, 47–61(2020)
4. Baradeswaran, A., Elaya, P.A.: Influence of B<sub>4</sub>C on the tribological and mechanical properties of Al 7075–B<sub>4</sub>C composites. *Compos. B Eng.* **54**, 146–152 (2013)



5. Mazahery, A., Abdizadeh, H., Baharvandi, H.R.: Development of high-performance A356/nano-Al<sub>2</sub>O<sub>3</sub> composites. *Mater. Sci. Eng., A* **518**(1–2), 61–64 (2009)
6. Woodhead Publishing Series in Composites Science and Engineering. Lightweight Ballistic Composites, xv–xviii (2016). Available from: <http://dx.doi.org/10.1016/b978-0-08-100406-7.09002-4>
7. Srivastava, A.K., Xu, C.L., Wei, B.Q., Kishore, R., Sood, K.N.: Microstructural features and mechanical properties of carbon nanotube reinforced aluminum—based metal matrix composites. *Sciences*, 247–255 (2008)
8. Pérez-Bustamante, R., Gómez-Esparza, C.D., Estrada-Guel, I., Miki-Yoshida, M., Licea-Jiménez, L., Pérez-García, S.A.: Microstructural and mechanical characterization of Al–MWCNT composites produced by mechanical milling. *Mater. Sci. Eng., A* **502**(1–2), 159–163 (2009)
9. Liao, J.Z., Tan, M.J.: Improved Tensile Strength of Carbon Nanotube Reinforced Aluminum Composites Processed by Powder Metallurgy. *Adv. Mater. Res.* **500**, 651–656 (2012)
10. Pérez-Bustamante, R., Estrada-Guel, I., Antúnez-Flores, W., Miki-Yoshida, M., Ferreira, P.J., Martínez-Sánchez, R.: Novel Al-matrix nanocomposites reinforced with multi-walled carbon nanotubes. *J. Alloy. Compd.* **450**(1–2), 323–326 (2008)
11. Esawi, A.M.K., Morsi, K., Sayed, A., Taher, M., Lanka, S.: The influence of carbon nanotube (CNT) morphology and diameter on the processing and properties of CNT-reinforced aluminium composites. *Compos. A Appl. Sci. Manuf.* **42**(3), 234–243 (2011)
12. Zhang, W.Y., Du, Y.H., Zhang, P.: Vortex-free stir casting of Al-1.5 wt% Si-SiC composite. *J. Alloy. Compd.* **787**, 206–215 (2019)
13. Arunkumar, T., Karthikeyan, R., Ram Subramani, R., Viswanathan, K., Anish, M.: Synthesis and characterisation of multi-walled carbon nanotubes (MWCNTs). *Int. J. Ambient Energy* **41**(4), 452–456 (2018)
14. Arunkumar, T., Sunitha, S., Theerthagiri, J., Jeevagan, J., Anish, M., Tatarchuk, T.: Effect of Polyurea Coating on Corrosion Resistance Over Mild Steel and Aluminium Substrates for Liquid Storage Applications. *Mol. Cryst. Liq. Cryst.* **670**(1), 60–73 (2018)
15. Arunkumar, T., Ramachandran, S.: Surface coating and characterisation of polyurea for liquid storage. *Int. J. Ambient Energy* **38**(8), 781–787 (2016)
16. Samuel Ratna Kumar, P.S., Robinson Smart, D.S., John Alexis, S.: Corrosion behaviour of Aluminium Metal Matrix reinforced with Multi-wall Carbon Nanotube **5**(1), 71–75 (2017)

# A Review on Recent Developments in Kenaf, Sisal, Pineapple, Bamboo and Banana Fiber-Reinforced Composites



Rittin Abraham Kurien, Ashwin Santhosh, Daniel Paul, Gowrisankar B. Kurup, and Greshma Susan Reji

**Abstract** Fibers that are produced from various geological processes, plants and animals are natural fibers. These fibers affect the polymer property, when they are used as reinforcement for composite materials. The increased awareness on devastating effect of synthetically developed materials toward nature has resulted in the development of eco-friendly and sustainable materials. Natural fibers are weak on its own; so, they are used as reinforcement in polymers. Here, we have discussed about natural fibers like kenaf, sisal, pineapple, bamboo and banana. Also, the sources and properties of each of these natural fibers have been widely considered. We have studied these natural fibers as reinforcement for some types of composites. Likewise, the mechanical properties of these five natural fibers and their applications are also discussed. The differences in reported mechanical properties and dispersed information are the issues concerned with natural fibers. Selection process of natural fibers becomes even more complex due to lack of standardized methods by consumers and producers to analyze, extract, treat and post-process the natural fibers. In fact, these are major issues that hinder the general utilization of natural fibers in various application. To mark this gap, this paper addresses the various mechanical properties and latest potential applications of the natural fibers in different commercial industries for the advancement of eco-friendly products with an intention to replace the synthetic fibers with efficient and economically effective products.

**Keywords** Natural fibers · Composite materials · Polymers · Reinforcement

---

R. A. Kurien (✉) · A. Santhosh · D. Paul · G. B. Kurup · G. S. Reji  
Department of Mechanical Engineering, Saintgits College of Engineering,  
Kottayam, Kerala 686532, India  
e-mail: [rittuak@gmail.com](mailto:rittuak@gmail.com)

© The Author(s), under exclusive license to Springer Nature Singapore Pte Ltd. 2021  
A. Patnaik et al. (eds.), *Advances in Materials Processing and Manufacturing Applications*, Lecture Notes in Mechanical Engineering,  
[https://doi.org/10.1007/978-981-16-0909-1\\_30](https://doi.org/10.1007/978-981-16-0909-1_30)

301

# 1 Introduction

Over the past few years, there has been an increase in demand for sustainable products. Innovative techniques to recycle, social impact and sustainable marketing methods have prompted society to use sustainable and degradable products [1]. Composite materials consist of natural fibers, and their arrangement influences the properties of materials. For reinforced composites, different fibers such as carbon fiber, glass fiber and natural fibers are used and as polymer matrices, namely plastic, metal, resin or rubber [2]. Natural fiber consists of plants fiber which includes leaf fiber (sisal, pineapple and abaca), main components (hemp, jute and kenaf), reed and grass fibers (corn, wheat and rice), seed fibers (coir, kapok and cotton), bast fibers (kenaf, jute, ramie, hemp and flax) and each and every other sort (roots and wood) [3]. In contrast to synthetic fibers, after its purpose, natural fibers can be burned without any CO<sub>2</sub> emission and improved recovery of energy which results in positive carbon credits and reduction in global warming [4]. For this research, we have considered kenaf, sisal, pineapple, bamboo and banana fibers. The sources and mechanical properties of all these fibers have been discussed. These fibers are used as reinforcement for different composites which is studied here. Also, the applications of all these fibers have been concentrated. Figure 1 shows the basic constituents of natural fiber-reinforced composites.

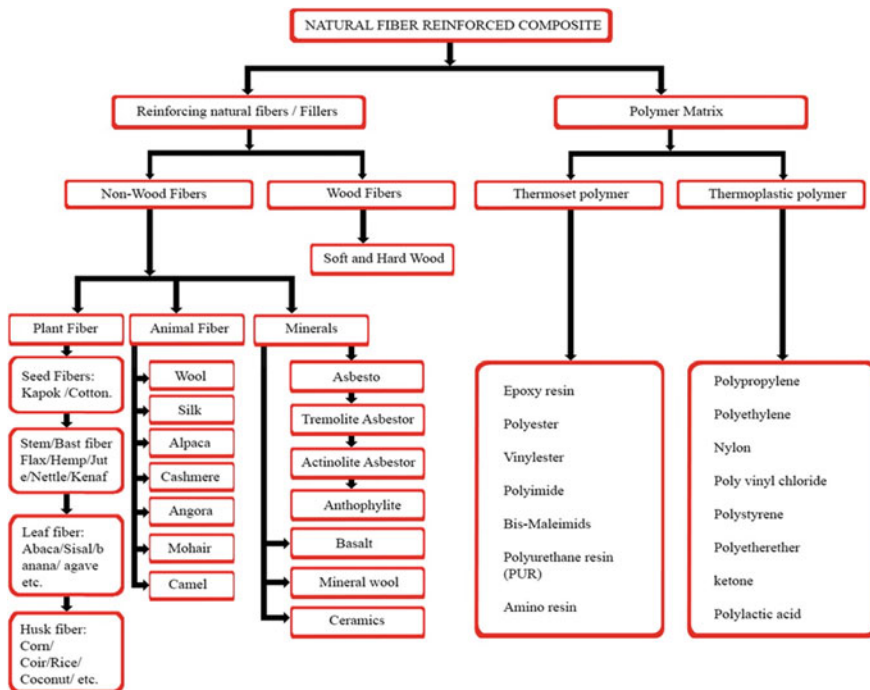


Fig. 1 Basic constituents of natural fiber-reinforced composites [1]

## 2 Source and Properties of Fibers

### 2.1 *Kenaf*

The main source of kenaf fiber is hibiscus [5]. The scientific name is *Hibiscus cannabinus* L. The fiber length in mm is 6. The fiber diameter is about 20–30  $\mu\text{m}$ . The density of kenaf fiber is 1.2  $\text{g/cm}^3$ . The main properties of kenaf are its excellent durability [6]. The main kenaf production countries of the world are India (45%), China, Malaysia and USA [7, 8]. For the production of rope and paper, the primary fiber used was kenaf, and it is considered as one of the substantial fiber in bast type [6]. Kenaf plants are rugged. They are really tough and stiff. They are highly immune to the effects of bug sprays. The kenaf plant has its origins from Asia, Africa, America and a few regions in Europe. They are present here on Earth for over a period of 4000 years. The inner and outer core and flowers are used to extract the fiber. The majority of the dry weight of the stalk is constituted by the inner core (60%), and the rest of the dry weight is from the bast (40%), also known as external fiber [9]. After harvest the plants are sent to a fiber separator, the tail section is entirely used in the pulping process. To isolate the extracted fibers from the influence of external substances like pectin or wax, they are treated using bacterial or synthetic method. These fiber strands are converted to finely woven textures. These fibers are completely biodegradable and hence are nature friendly. In ancient times, the Egyptians used these fibers to make vessels, Nowadays, they are used for manufacturing sacks, strings and ropes [6].

### 2.2 *Sisal*

Agave (*Agave sisalana*) is the source of sisal. This fiber has length up to 1000 mm, and fiber diameter lies between 200 and 400  $\mu\text{m}$ . The density of fiber is 1.2  $\text{g/cm}^3$ . The characteristic features of the sisal fibers are its hardness, high strength, stretchability, coarse nature, durability, its resistance toward moisture absorption, saltwater deterioration and its surface, which readily accepts variety of dyes. Due to these abilities, the sisal fiber is considered as one of the top reinforcement fibers. Sisal fiber, which is mainly produced in Brazil, is one of among the most used natural fiber. Native to Mexico, the mother plant is a rosette and can grow up to 2 m height. In its 6–7 years of life, it gives about 210–260 leaves for industrial use [5].

### 2.3 *Pineapple*

The source of pineapple leaf is *ananas magdalenae*. The fiber length of pineapple fiber is up to 200 mm, and fiber diameter is 106  $\mu\text{m}$  [9]. The density of fiber is

1.5 g/cm<sup>3</sup>. The main properties of pineapple fiber are its saltwater resistance and wear resistance. Philippines is one of the main pineapple producer of the world [10]. The source plant of pineapple leaf fiber is an easily accessible one and is also one of the most developed. The pineapple fiber is a waste by-product of pineapple processing. The plant which can reach up to 2 m height grows mainly in the tropical region and has a group of 20–30 leaves each about 6 cm wide [9]. Almost 90–100 tons pineapple leaves can be produced from a hectare. Comparing all natural fibers, very good mechanical properties are shown by pineapple leaf fibers [10]. These fibers are multicellular, and they are extracted from the pineapple leaf strands through scrapers.

## 2.4 *Bamboo*

Bambusoideae is the scientific name of grass pulp, which is the source of bamboo. Fiber length is up to 90 mm, and fiber diameter is about 10–20 μm. The density of the fiber is 0.85 g/cm<sup>3</sup>. The countries that vastly produce bamboo include Japan, Ecuador, China, India and Chile. Bamboo possesses some excellent properties like high durability and stability, excellent flexibility. They show great resistance to UV radiation. Bamboo fiber is otherwise called common glass fiber because of the arrangement of strands in the longitudinal ways. Bamboo is abundantly found in China; around 400 species are discovered [7]. Because of its better quality, hardness, low weightiness and easy availability, bamboo fibers are used as a major reinforcement for different polymeric materials. The extracted bamboo fibers are used for manufacturing various composites in a wide variety of businesses [11]. Bamboo has been customarily utilized for making houses, spans, customary vessels and so on.

## 2.5 *Banana*

Plantain or *Musa acuminata* is the source of banana fiber. The fiber Length of banana is 5000 mm and diameter is 10 μm. The density of the fiber is 1.35 g/cm<sup>3</sup>. The main properties are better fineness and spinnability, very strong, less elastic, shiny in appearance, light and less absorption. The main producer of banana are Thailand, South East Asia, India and Bangladesh [12–14]. Banana fiber is a waste by-product of banana cultivation at the present time. For industrial usage, banana fibers can be extracted without any extra cost. The fiber length strongly influences the properties of the fiber. As banana fibers have good potential, it can be developed into strong biocomposite materials [7, 8, 11]. Due to its durability, ability to stretch, affinity for certain dyestuff and resistance against saltwater, banana has been the forerunning material traditionally for making twines. Banana is also used as an

eco-friendly strengthening agent that has properties which can replace fiber glass and asbestos in composites in many industrial uses.

### 3 Mechanical Characteristics of Natural Fibers

While choosing the composite, whether it should be used for structural applications or else for mechanical properties play an important role. Natural fibers are generally used as reinforcement in composites because they are lighter. It has better Young's modulus and tensile strength compared to the polymer matrix, so there is no need for additional treatment of reinforced composites. Table 1 shows the mechanical properties of natural plant fibers. Graphical analysis of mechanical properties is shown in Fig. 2a–c. Mechanical properties including tensile strength, Young's modulus and elongation at break are considered here.

## 4 Natural Fiber as Reinforcement for Composites Materials

### 4.1 Kenaf Fiber Composite

Kenaf fiber could be used as reinforcement in a variety of composites, due its superior properties. Epoxy-based FRP (fiber strengthened polymer) composites have generally high thermal steadiness. Be that as it may, it shows helpless split development obstruction that limits its mechanical applications. Organoclay is an organically modified phyllosilicate, derived from a naturally occurring clay mineral. As organoclay is incorporated in the composite, it displays improved flexible properties by allowing a higher limit for fiber stacking [19]. Delamination, formation of voids and air bubbles and fiber pull out are the major failure mechanisms in reinforced composites. Highly stable polymeric structure and a lower damping factor are shown by kenaf reinforced epoxy composites [20].

**Table 1** Mechanical properties of natural fibers [15–18]

Fiber	Tensile strength (MPa)	Young's modulus (GPa)	Elongation at break (%)	References
Kenaf	612.5	41	2	[16]
Sisal	681	15.5	2.45	[17, 18]
Pineapple	898.5	71	2	[17, 18]
Bamboo	566	53	4.65	[19]
Banana	721.5	29.5	5.5	[17, 18]

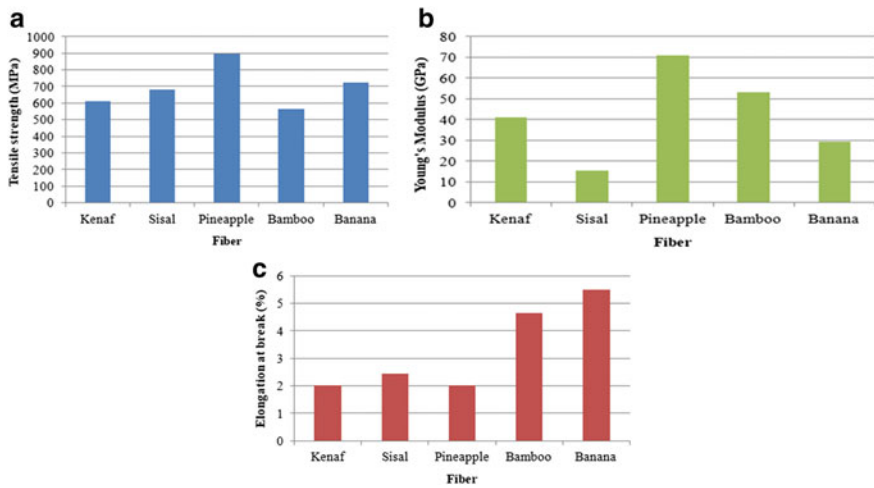


**Fig. 2** a Tensile strength of natural plant fibers [15–18] b Young's modulus of natural plant fibers [15–18]. c Elongation at break of natural plant fibers [15–18]

## 4.2 Sisal Fiber Composite

The various properties of polystyrene composites reinforced using sisal fibers are observed on basis of the fibers length and content. It has been represented that benzoylation on the fiber improves the fiber arrange connection and thusly extended the quality amazingly [5, 9]. The properties were seen to be essentially self-ruling of fiber length regardless of the way that the extraordinary unbending nature exhibits fringe change at 10 mm fiber length [20, 21].

## 4.3 Pineapple Fiber Composite

Pineapple leaf fiber (PALF)/polypropylene (PP) composite, PALF/PP fiber shows unrivaled elasticity than other normal fiber strengthened composites. Thusly, PALF/PP fiber can be a potential regular fiber fortified composite for different applications. PALF might be utilized in manufacture of eco-friendly composite items for diversified applications furthermore, and henceforth, manufactured strands can undoubtedly be supplanted with PALF [22]. The usage of pineapple leaf fiber in composite material is another wellspring of materials which can be monetary, eco-friendly and furthermore recyclable. Treatment using alkali can be done to improve various properties. The mechanical properties of the composite can be further improved by incrementing the fiber stacking [20].

#### **4.4 *Bamboo Fiber Composite***

These composites have a potential for building applications [23]. When contrasted with slick epoxy, the flexural modulus for bamboo fiber composites was consistently higher and monotonically increments with fiber length and substance. Nearness of bamboo filaments could give critical protection from break development, subsequently changing the general disappointment mode from absolutely fragile to malleable. Bamboo strands demonstrated solid holding with the epoxy lattice in the composite [20]. Fiber breakage, network splitting, debonding and fiber pull out are significant deformation types.

#### **4.5 *Banana Fiber Composite***

Banana fiber is discovered to be a decent support in polyester resin. Excellent flexural strength and flexural modulus are exhibited by banana fiber-reinforced polyester composites. Composites have most extreme mechanical quality, and it tends to be utilized as a substitute material for customary fiber strengthened polymer composites. Banana fiber can be utilized as strengthened specialist effectively in the composite business as an economical structure material. Crossover epoxy composites displayed predominant mechanical properties [20, 24].

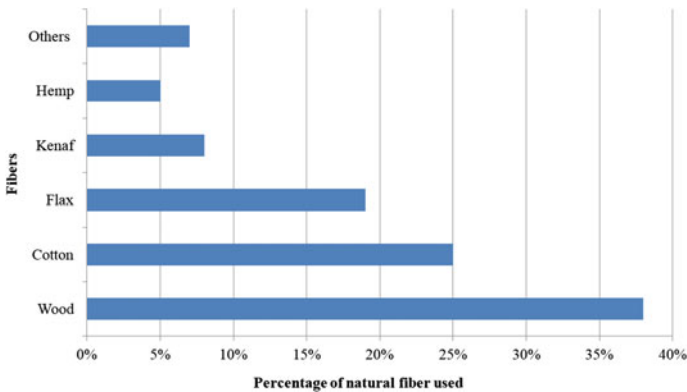
### **5 Applications**

Natural fibers find application in almost every day-to-day activities. It finds uses from household activities to even automobile, aerospace and marine industries [25]. Kenaf fibers are utilized in automotive development, bundling, furniture, materials, mats, paper mash, material for packing, carry baggage and cases for mobiles [5, 26]. Sisal fibers can be used in various industrial sectors like transportation, construction and automobile. It also finds many uses in our day-to-day life like reinforcement in steel wire links, used for making ropes [27]. It is used to manufacture paper. It also finds application in the manufacturing of roofing sheet, panels, doors and shutting plates [9, 26, 28]. Pineapple fibers of treated and surface-adjusted strands are utilized for making transport line rope, air pack and progressed composites [7, 29]. Other application includes textile, sports item, baggage, automobiles, cabinets, mats and furniture. Fibers of bamboo are used in the production of seats, other furniture and panels. Banana fibers are utilized in low-cost production of paper [30]. They are also used in carpets and mattresses, cloth, ropes, twines, panel and handicraft production. They are also be very useful in sound proofing and insulation [13, 31, 32]. Table 2 and Fig. 3 show the usage of natural fibers and wood for composites in automotive industries in Europe 2012 (total fiber volume of 80,000 tons).



**Table 2** Usage of natural fibers for composites in Europe 2012 (total fiber volume of 80,000 tons) [27]

Fiber	Percentage of natural fiber used (%)
Wood	38
Cotton	25
Flax	19
Kenaf	8
Hemp	5
Others (mainly banana, jute, coir, sisal, pineapple, bamboo and abaca)	7

**Fig. 3** Natural fiber composite usage in Europe 2012 [27]

## 6 Conclusion

The increased concern and awareness of the society toward environmental conservation has turned out to be one of the main reasons for the selection of natural fibers as the reinforcement in polymer composites. When these fibers are physically and chemically treated, they can be effectively used as a supplement for the existing materials. The results shows that the mechanical properties are increased by various chemical treatments. The adhesion between the fiber and the matrix are also improved by the same. Usage of natural fibers results in cheap composite manufacturing costs. The impact of chemical processes on natural fiber properties is also considered. The kenaf fiber shows low-density and high-specific mechanical properties. The fibers of sisal have high tensile intensity, resistance toward salt-water, alkali and acid deteriorations and toward abrasion. It also shows high tenacity. Pineapple fiber shows very good mechanical, physical and thermal properties. It is known that bamboo fiber is light, stiffer and stronger when compared to glass fiber thus making it a very good substitute. Studies showed that

banana fiber has very good durability, ability to stretch, affinity for certain dyestuff and resistance against saltwater; banana has been largely used in manufacturing even from early times and is used even now. It was found that among the mentioned fibers, pineapple showed highest tensile strength and Young's modulus. Also, it was observed that banana fiber had the highest elongation at break. With these results, it is understood that in the coming years, natural fibers will be extensively used for the making of composites as they are the non-polluting, harmless, renewable as well as sustainable source of fiber.

## References

1. Peças, P., Carvalho, H., Salman, H., Leite, M.: Natural fibre composites and their applications: a review. *J. Compos. Sci.* **2**(4), 66 (2018)
2. Harle, S.M.: The performance of natural fiber reinforced polymer composites. *Int. J. Civ. Eng. Res.* **5**(3), 285–288 (2014)
3. Kumar, K.A., Sudhanan, S.M., Kumar, K.M., Kumar, G.R.: A Study on properties of natural fibre-A Review (2017)
4. Kurien, R.A., Selvaraj, D.P., Sekar, M., Koshy, C.P.: Green composite materials for green technology in the automotive industry. In: *IOP Conference Series: Materials Science and Engineering* (Vol. 872, No. 1, p. 012064). IOP Publishing (2020)
5. Mohammed, L., Ansari, M.N., Pua, G., Jawaid, M., Islam, M.S.A.: review on natural fiber reinforced polymer composite and its applications. *Int. J. Polym. Sci.*(2015)
6. Kumar, P.S.S., Allamraju, K.V.: A Review Of Natural Fiber Composites [Jute, Sisal, Kenaf]. *Mater. Today: Proc.* **18**, 2556–2562 (2019)
7. Rohit, K., Dixit, S.: A review-future aspect of natural fiber reinforced composite. *Polym. Renew. Resour.* **7**(2), 43–59 (2016)
8. Gholampour, A., Ozbakkaloglu, T.: A review of natural fiber composites: Properties, modification and processing techniques, characterization, applications. *J. Mater. Sci.*, 1–64 (2020)
9. Senthilkumar, K., Saba, N., Rajini, N., Chandrasekar, M., Jawaid, M., Siengchin, S., Alotman, O.Y.: Mechanical properties evaluation of sisal fibre reinforced polymer composites: a review. *Constr. Build. Mater.* **174**, 713–729 (2018)
10. Todkar, S.S., Patil, S.: A Review on mechanical properties evaluation of pineapple leaf fibre (PALF) reinforced polymer composites. *Compos. B Eng.* **174**, 106927 (2019)
11. Lokesh, P., Kumari, T.S., Gopi, R., Loganathan, G.B.: A study on mechanical properties of bamboo fiber reinforced polymer composite. *Mater. Today: Proc.* **22**, 897–903 (2020)
12. Chandramohan, D., Marimuthu, K.: A review on natural fibers. *Int. J. Res. Rev. Appl. Sci.* **8** (2), 194–206 (2011)
13. Venkateshwaran, N., Elayaperumal, A.: Banana fiber reinforced polymer composites-review. *J. Reinf. Plast. Compos.* **29**(15), 2387–2396 (2020)
14. Srinivasan, T., Suresh, G., Santhoshpriya, K., Chidambaram, C.T., Vijayakumar, K.R., Munaf, A.A.: Experimental analysis on mechanical properties of banana fibre/epoxy (particulate) reinforced composite. *Mater. Today: Proc.* (2020)
15. Fiore, V., Bella, G.D., Valenza, A.: The effect of alkaline treatment on mechanical properties of kenaf fibers and their epoxy composites. *Composites: Part B* **68**,14–21 (2015)
16. Gurunathan, T., Mohanty, S., Nayak, S.K.: A review of the recent developments in biocomposites based on natural fibres and their application perspectives. *Compos. Part A Appl. Sci. Manuf.* **77**, 1–25 (2015)

17. Bhardwaj, S.: Natural Fibre Composites—An Opportunity for Farmers. *Int. J. Pure Appl. Biosci* (2017)
18. Yu, Y., Huang, X., Yu, W.: A novel process to improve yield and mechanical performance of bamboo fiber reinforced composite via mechanical treatments. *Composites: Part B* **56**, 48–53 (2017); **5**, 509–514 (2014)
19. Haniffah, W.H., Sapuan, S.M., Abdan, K., Khalid, M., Hasan, M., Hoque, M.E.: Kenaffibre reinforced polypropylene composites: effect of cyclic immersion on tensile properties. *Int. J. Polym. Sci.* (2015)
20. Chandrasekar, M., Ishak, M.R., Sapuan, S.M., Leman, Z., Jawaid, M.: A review on the characterisation of natural fibres and their composites after alkali treatment and water absorption. *Plast., Rubber Compos.* **46**(3), 119–136 (2017)
21. Rao, P.D., Rao, D.V., Naidu, A.L., Bahubalendruni, M.R.: Mechanical properties of banana fiber reinforced composites and manufacturing techniques: a review. *Int. J. Res. Develop. Technol.* **8**(7), 2349–3585 (2017)
22. Arib, R.M.N., Sapuan, S.M., Ahmad, M.M.H.M., Paridah, M.T., Zaman, H.K.: Mechanical properties of pineapple leaf fiber reinforced polypropylene composites. *Mater. Des.* **27**(5), 391–396 (2016)
23. Chokshi, S., Gohil, P., Patel, D.: Experimental investigations of bamboo, cotton and viscose rayon fiber reinforced Unidirectional composites. *Mat. Today: Proc.* (2020)
24. Santhanam, V., Dhanaraj, R., Chandrasekaran, M., Venkateshwaran, N., Baskar, S: Experimental investigation on the mechanical properties of woven hybrid fiber reinforced epoxy composite. *Mat. Today: Proc.* (2020)
25. Chen, S., Cheng, L., Huang, H., Zou, F., Zhao, H.P.: Fabrication and properties of poly (butylene succinate) biocomposites reinforced by waste silkworm silk fabric. *Compos. A Appl. Sci. Manuf.* **95**, 125–131 (2020)
26. Alhilfi, T., Chambon, P., Rannard, S.P.: Architectural control of polystyrene physical properties using branched anionic polymerization initiated at ambient temperature. *J. Polym. Sci.* **58**(10), 1426–1438 (2020)
27. Carus, M., Eder, A., Dammer, L., Korte, H., Scholz, L., Essel, R., Breitmayer, E., Barth, M.: *Wood-Plastic Composites (WPC) and Natural Fibre Composites (NFC): European and Global Markets 2012 and Future Trends in Automotive and Construction.* Nova-Institute, Hürth, Germany (2015)
28. Thyavihalli Girijappa, Y.G., Mavinkere Rangappa, S., Siengchin, S.: Natural fibers as sustainable and renewable resource for development of eco-friendly composites: a comprehensive review. *Front. Mater.* **6**, 226 (2019)
29. Yusof, Y., bin Mat Nawi, N., Alias, M.B.: Pineapple leaf fiber and pineapple peduncle fiber analyzing and characterization for yarn production. *ARPJ. J. Eng. Appl. Sci.* **11**, 4197–4202 (2020)
30. Chaudhary, V., Ahmad, F.: A review on plant fiber reinforced thermoset polymers for structural and frictional composites. *Polymer Testing*, 106792 (2020)
31. Balaji, A., Purushothaman, R., Udhayasankar, R., Vijayaraj, S., Karthikeyan, B.: Study on Mechanical, Thermal and Morphological Properties of Banana Fiber-Reinforced Epoxy Composites. *J. Bio-And Tribo-Corros.* **6**, 1–10 (2010)
32. Srinivasan, T., Suresh, G., Santhoshpriya, K., Chidambaram, C. T., Vijayakumar, K.R., Munaf, A.A.: Experimental analysis on mechanical properties of banana fibre/epoxy (particulate) reinforced composite. *Mater. Today: Proc.* (2020)

# Studies on Erosion and Oxidation Behaviour of Cobalt-Based Coatings



Prashant Kumar Singh and Pallvita Yadav

**Abstract** This work aims to investigate the performance of different cobalt-based coatings such as Stellite 6 (St6), WC-Co (W1) and Stellite 21 (St21) on the different grades of boiler steel. The different grades of boiler steel chosen for this purpose are SAE213-T91(BS1), SAE213-T12 (BS2) and SAE 208 (BS3). Coating powders were deposited on the selected substrate materials under different impact angles (30° and 90°) using the detonation gun spray method. The properties of the coatings were assessed using an optical microscope, microhardness tester and surface roughness tester. In addition, an erosion and oxidation study of the coating was also carried out for quality check of the coatings. The erosion test was performed at room temperature as well as an elevated temperature of 400 °C. The cyclic oxidation of different coated samples was carried out in air at 900 °C for 50 cycles of 1 h duration. The result shows that at room temperature, the erosion resistance of W1 coated boiler steel substrate is higher than that of steel substrate coated with St6 and St21 powder. But, at an elevated temperature of 400 °C, their resistance to erosion resistance decreases significantly which may be due to the phase softening. St6 and St21 coatings are found to be successful in lowering the oxidation rate of SAE 213-T91 boiler steel. This may happen due to the formation of a protective Cr<sub>2</sub>O<sub>3</sub> phase along with CoCr<sub>2</sub>O<sub>4</sub> phase in the oxide scale.

**Keywords** Erosion wear • Oxidation • Cobalt-based coating • Boiler steels

---

P. K. Singh

Department of Mechanical Engineering, G H Raisoni University Amravati,  
Amravati 444701, India

P. Yadav (✉)

Department of Mechanical Engineering, SVNIT Surat, Surat 395007, India

## 1 Introduction

In India, the primary sources of electric power generation are coal-based power plants. Among the plant's various divisions, the boiler is the most crucial and critical part [1]. The boiler parts are mainly manufactured by boiler tube steels such as SAE213-T2, SAE213-T9, SAE213-T12, SAE213-T22, SAE213-T91, SAE213-T122 steel, SAE 208 steel. The main constituents of these steels are Cr, Mo and C, and thus, they offer superior mechanical properties required in boiler application. The particles of fly ash impact on the boiler tubes surface. The boiler tube components are affected by erosion wear, oxidation and hot corrosion due to these ash particles [2], which reduces the service life of the boiler component, and hence, the power station unit must then be shut down to repair the damaged components or parts [3]. Therefore, it is desirable to combat the erosion wear and oxidation of the coal-fired boiler components to avoid forced outages [4].

Coating technology is the rapidly growing technology; in this work, the proper material was selected and developed on steels for coatings to improve the resistance against environmental degradation [5] such as erosion wear, oxidation and hot corrosion. Among the various coating deposition methods, detonation gun spraying is the most promising thermal spraying method of coating deposition. This method of coating is cost effective, versatile and well-established method of coating deposition [6]. It also offers better bond strength, hardness and density due to lower porosity in the coating. This happens because of its low-flame temperature (less than 4000 K) and high velocity of coating particles (around 1000 m/s) [7–11]. In order to produce coatings, several type of coating powders has been used by various researchers for improving erosion, corrosion and oxidation resistance of boiler tube materials. Ceramic-based coatings offer high hardness and superior temperature resistance and thus applicable for those components which requires wear resistance combined with oxidation and hot corrosion resistances [7–9]. Cobalt-based coatings are commonly used to enhance the material's erosion resistance because of their greater hardness and toughness as compared to steels [12, 13] and thus require more systematic study. According to Rateick et al. [14], WC-Co cermet coating has shown better erosion performance and concluded the combined effect of ductile–brittle fracture erosion mechanism. Prakash et al. [15] and Singh et al. [16, 17] investigated the high-temperature oxidation behavior of Stellite 6 coated Ni superalloy and observed the development of  $\text{CoCr}_2\text{O}_4$  oxide scale in all the environments that act as a barrier against oxidation environment.

The present study aims to assess the comparative performance of different cobalt-based coatings (St6, W1 and St 21) on the various grades of boiler steels (BS1, BS2 and BS3). The coatings were deposited on the substrate material under different impact angles ( $30^\circ$  and  $90^\circ$ ) using detonation gun spraying. The coated steel substrate's erosion resistance was checked at an elevated temperature of  $400^\circ$  and room temperature. The oxidation test of the coated sample was performed at  $900^\circ\text{C}$  for 50 cycles of 1 h duration. Based on the result, the better combination of

boiler tube steel and best suited co-based coating is recommended, which can counter the erosion and oxidation problems in a boiler environment.

## 2 Materials and Methods

In the present experimental work, different grade of boiler steel, namely BS1, BS2 and BS3 low alloy steel, was used as the substrate material. These steels were procured in the form of tube having 10 mm wall thickness. Optical emission spectroscopy (OES) was used to obtain the elemental composition (wt%) of various grades of boiler steel where Cr is major alloying element in BS1 and BS2 steel. The total alloying elements in BS3 steel are less than 1%. Using the detonation gun spray method, the St6 (Si-1, C-0.25, Fe-1, Ni-3, Mo-5.5, Cr-29, Co-60.25), W1 (C-1, Si-1, W-4, Cr-28, Co-66) and St21(C-5.5, Co-12, W-82.5) coating powders were sprayed on boiler steel substrates. The average particle size of St21 and St6 coating powder is  $53 \pm 20 \mu\text{m}$ , whereas WC-Co powder is  $45 \pm 20 \mu\text{m}$ .

Microhardness measurement of as sprayed coating sample was performed using recommended microhardness tester (HMV-2000, Shimadzu, Japan). The microhardness reading was taken at 10 different locations across the cross section for each coating, and their average value is reported.

The surface roughness measurement of each coated specimen was performed using stylus-type surface roughness tester (Taylor Hobson, Surtronic, UK). In the surface roughness measurement, a cut-off length of 4.0 mm and a traverse length of 0.8 mm were used. Each measurement was replicated five times to improve the accuracy of the result.

Air jet erosion test rig was employed for solid particle erosion test of uncoated as well as coated steel samples. Every sample was cleaned before the start of each cycle by using an ultrasonic bath. The process parameters were chosen as per ASTM standard [18] and reported in Table 1. The erosion test was continuously conducted until a steady-state erosion rate was reached [19]. As per ASTM standard, the erosion rate was calculated [20].

**Table 1** Parameters for conducting the erosion test of different samples

Sample size	25 mm × 25 mm × 5 mm (90° impact angle) and 25 mm × 20 mm × 5 mm (30° impact angle)
Erodent material	Alumina sand (50 μm)
Particle velocity	40 ± 3 m/s
Air pressure	0.3 bar
Erodent discharge rate	10 g/min
Test duration	Cycles of 5 min
Impact angle	30° and 90°
Test temperature	Room temperature (32–35 °C) and 400 °C
Nozzle diameter	1.5 mm

The study on the cyclic oxidation behavior of the coated and uncoated steel samples was carried out in a thermal cyclic furnace at an elevated temperature of 900 °C. Every oxidation test cycle consists of maintaining the specimen in the furnace for 1 h at a constant temperature of 900 °C, followed by 20 min of cooling at atmospheric temperature. The total weight of the boat along with the specimen was measured with precise limit of  $10^{-5}$  g using an electronic weighing balance. The completion of whole process is said to be one cycle of oxidation test, and the same procedure was repeated for 50 cycles.

### 3 Results and Discussion

#### 3.1 Measurement of Microhardness, Surface Roughness and Porosity of D-Gun Sprayed Coatings

The microhardness, average surface roughness and porosity of various coated sample are reported in Table 2. It can be observed that among the various coatings, W1 coated BS1 boiler steel shows the highest hardness ( $998 \pm 20$  HV), whereas St21 coating on BS3 boiler steel substrate shows the lowest value of microhardness ( $503 \pm 16$  HV). The higher hardness of W1 coated steel is due to the presence of large amount of WC hard phase in the coating. The average porosity measured along the cross section of the sample was found to be highest in St21 coated BS2 boiler steel substrate ( $1.8 \pm 0.35\%$ ), and lowest porosity ( $1.2 \pm 0.43\%$ ) is observed in BS1 boiler steel substrate coated with St6 powder. The lower values of porosity in case of later might be attributed to lower particle size and melting behavior of the powder particles. The measured value of average surface roughness was found to be highest in case of W1 coated BS2 boiler steel substrate ( $6.9 \pm 0.71 \mu\text{m}$ ), and the lowest value of surface roughness ( $5.3 \pm 0.45 \mu\text{m}$ ) is observed in St6 coated BS1 boiler steel sample.

**Table 2** Average microhardness, average surface roughness and porosity of different coated samples

Powder/ substrate	Average microhardness (HV)	Average surface roughness ( $\mu\text{m}$ )	Porosity (%)
W1/BS1	$998 \pm 20$	$5.9 \pm 0.86$	$1.4 \pm 0.13$
W1/BS2	$635 \pm 10$	$6.9 \pm 0.71$	$1.7 \pm 0.08$
W1/BS3	$528 \pm 17$	$6.7 \pm 0.75$	$1.6 \pm 0.10$
St6/BS1	$974 \pm 25$	$5.3 \pm 0.45$	$1.2 \pm 0.43$
St6/BS2	$615 \pm 11$	$6.3 \pm 0.62$	$1.5 \pm 0.27$
St6/BS3	$538 \pm 18$	$6.4 \pm 0.25$	$1.5 \pm 0.85$
St21/BS1	$918 \pm 28$	$5.5 \pm 0.18$	$1.3 \pm 0.38$
St21/BS2	$620 \pm 20$	$6.4 \pm 0.89$	$1.8 \pm 0.35$
St21/BS3	$503 \pm 16$	$6.5 \pm 0.41$	$1.6 \pm 0.55$

### 3.2 Steady-State Erosion Behavior of Coated Substrate

Steady-state erosion rate of different coated substrate for different impact angle (30° and 90°) at room temperature and at higher temperature (400 °C) is depicted in Fig. 1. It can be observed that the steady-state erosion rate of W1 coated substrate is smaller for 30° impact angle as that of 90° impact angle. The higher erosion rate is due to the presence of a higher proportion of brittle and hard phase of WC in the coating at a 90° impact angle. The similar results were observed by Wentzel and Allen [21]. They explained that the overall wear rate is moved toward higher impact angles with an increase in the amount of WC phase in the WC-Co alloy. Further, the erosion rate of W1 coated substrate at elevated temperature (400 °C) is found to be higher in comparison to room temperature irrespective of impact angle. But, the increase in erosion rate at elevated temperature in comparison with room temperature erosion rate is found to be smaller in coating performed at 90° impact angle as compared to 30° impact angle. According to Milman et al. [22], the higher erosion rate at elevated temperature is because of softening occurs in WC and Co binder phases. At room temperature, W1 coated boiler steel substrate encounters lower erosion rate than boiler steel substrate coated with St6 and St21 powder. But, at higher temperature, the erosion rate of W1 coated substrate is found to be higher in comparison to St6 and St21 coated boiler steel substrate.

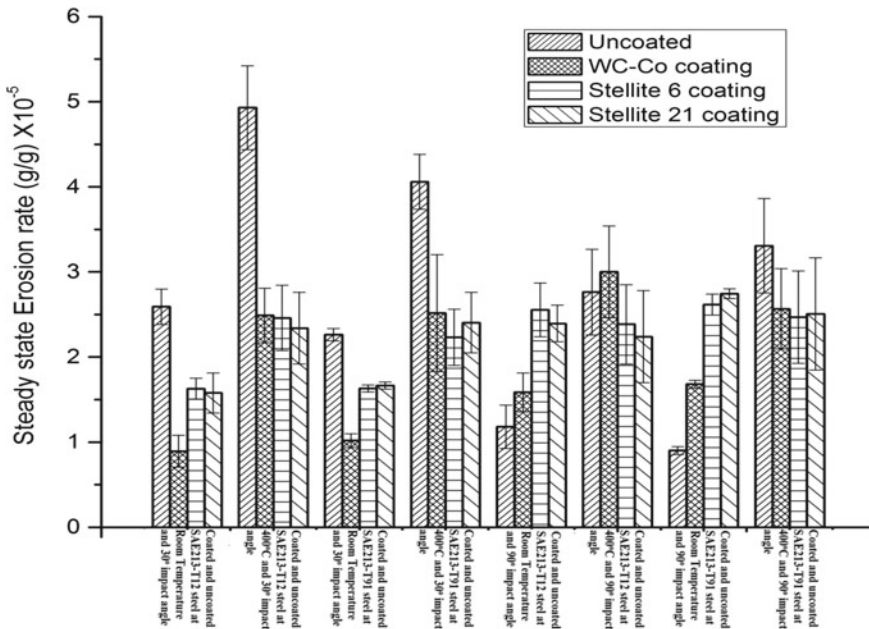


**Fig. 1** A histogram demonstrating the steady-state erosion rates of various BS1 and BS2 boiler steel coatings sprayed by D-Gun method at room temperature and 400 °C



Similar to the W1 coated substrate, the erosion rate of St6 and St21 coatings are observed to be higher at 90° impact angle than at 30° impact angle under room temperature condition. But, at elevated temperature of 400 °C, the erosion rates are found to be higher at 30° impact angle than at 90° impact angle. This is due to transition of erosion mechanism from brittle to ductile mode at elevated temperature of 400 °C.

### 3.3 Oxidation Behavior of Coated Boiler Steel Substrate

The histogram shown in Fig. 2 represents the overall weight gain of the uncoated and coated boiler steel substrate after subjecting to oxidation in air at 900 °C for 50 cycles of 1 h heating and 20 min cooling. It can be observed from the figure that W1 coated BS1 and BS2 boiler steel substrate shows the highest overall weight gain among the other coated steel substrate. This is because of formation of non-protective layer or scale of  $\text{CoWO}_4$  in the W1 coating. However, BS1 and BS2 boiler steel substrate coated with St6 shows the significant resistance against oxidation at 900 °C in comparison with other coated sample. The reason for the higher resistance to oxidation of the St6 coated steel substrate is due to the formation at 900 °C of protective oxides of chromium and cobalt.

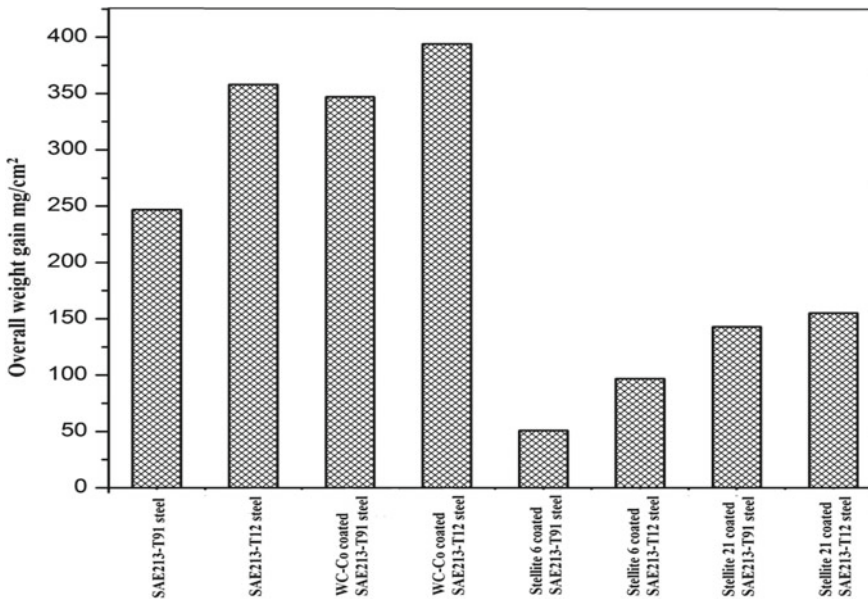


**Fig. 2** A histogram illustrating the overall weight gain of different uncoated and coated boiler steel substrate

## 4 Conclusions

W1, St6 and St21 coatings were deposited on BS1, BS2 and BS3 boiler steel substrate by detonation gun spraying method. The erosion behavior of the coated and uncoated steels is evaluated at room temperature and 400 °C. The high-temperature oxidation behavior of all these coated steels was also analyzed. Based on the result obtained, following conclusion was derived from the present experimental study.

- BS1 boiler steel substrate shows better erosion resistance as compared to other boiler steel substrate irrespective of impact angle under room temperature as well as at elevated temperature of 400 °C.
- The erosion rate at 400 °C compared to that at room temperature of the W1 coated steel substrate is found to be significantly higher. This is due to the presence of high proportions of brittle and hard WC phase in the coating at higher temperatures.
- St6 and St21 coated BS1 and BS2 boiler steels samples show lower oxidation rate as compared to other coated steel. This is because of formation of protective Cr<sub>2</sub>O<sub>3</sub> phase along with the spinel of CoCr<sub>2</sub>O<sub>4</sub> in the oxide scale.
- The St6 and St21 coatings have shown better performance under erosion tests at 400 °C as well as under oxidation test at 900 °C. These coatings may not be very effective at room temperature, but may be very useful in the boiler environment at temperature exceeding 500 °C as they will provide the requisite protection against erosion–oxidation.

**Acknowledgements** The authors want to acknowledge SVX Powder M Surface Engineering Pvt. Ltd., Greater Noida, India, for providing the facility of the Detonation Gun Spray coating. The authors would like to thank Industrial and Engine Tribology Lab, MNNIT Allahabad, India for providing testing facilities.

## References

1. Das, S.K., Godiwalla, K.M., Mehrotra, S.P., Sastry, K.K.M., Dey, P.K.: Analytical model for erosion behaviour of impacted fly-ash particles on coal-fired boiler components. *Sadhana* **31** (5), 583–595 (2006)
2. Mbabazi, J.G., Sheer, T.J., Shandu, R.: A model to predict erosion on mild steel surfaces impacted by boiler fly ash particles. *Wear* **257**(5–6), 612–624 (2004)
3. Dhamangaonkar, P.R., Kajale, S.R., Nandgaonkar, M.R., Deshmukh, A., Deshmukh, A., Thakur, S.: Use of Cold Air Velocity Test (CAVT) to locate erosion prone zones in pulverized coal fired utility boiler. In: *Proceedings of the World Congress on Engineering*, **3** (2011)
4. Levy, A.V.: *Solid particle erosion and erosion-corrosion of materials*. Asm International, Materials Park, OH (1995)
5. Stringer, J.: Role of coatings in energy-producing systems: An overview. *Mater. Sci. Eng.* **87**, 1–10 (1987)

6. Li, C., Li, S., Zeng, M., Sun, S., Wang, F., Wang, Y.: Effect of high-frequency micro-vibration on microstructure and properties of laser cladding aluminum coatings. *The International Journal of Advanced Manufacturing Technology*, 1–10(2019)
7. Du, H., Sun, C., Hua, W.G., Zhang, Y.S., Han, Z., Wang, T.G., Gong, J., Lee, S.W.: Fabrication and evaluation of D-gun sprayed WC–Co coating with self-lubricating property. *Tribol. Lett.* **23**(3), 261–266 (2006)
8. Singh, L., Chawla, V., Grewal, J.S.: A review on detonation gun sprayed coatings. *J. Miner. Mater. Charact. Eng.* **11**(3), 243 (2012)
9. Pawlowski, L.: *The science and engineering of thermal spray coatings*. Wiley, 2nd edn. (2008)
10. Shibe, V., Chawla, V.: Solid particle erosion studies of D-gun sprayed cermet coatings on ASTM A36 steel. *Int. J. Surf. Sci. Eng.* **12**(4), 317–335 (2018)
11. Gao, J.G., Tang, Z.H., Wang, C.L., Guo, M.Q., Cui, Y.J.: Microstructure, mechanical and oxidation characteristics of detonation gun and HVOF sprayed MCrAlYX coatings. *Trans. Nonferrous Metals Soc. China* **25**(3), 817–823 (2015)
12. Antony, K.C.: Wear-resistant cobalt-base alloys. *JOM* **35**(2), 52–60 (1983)
13. Crook, P., Asphahani, A.I., Matthews, S.J.: Haynes International Inc, Corrosion-and-wear-resistant cobalt-base alloy. U.S. Patent **5**(2),731(1991)
14. Rateick Jr., R.G., Karasek, K.R., Cunningham, A.J., Goretta, K.C., Routbort, J.L.: Solid-particle erosion of tungsten carbide/cobalt cermet and hardened 440C stainless steel —A comparison. *Wear* **261**(7–8), 773–778 (2006)
15. Prakash, S., Puri, D., Singh, H.: Hot corrosion behaviour of plasma sprayed coatings on a Ni-based superalloy in Na<sub>2</sub>SO<sub>4</sub>-60% V<sub>2</sub>O<sub>5</sub> environment. *ISIJ Int.* **45**(6), 886–895 (2005)
16. Singh, H., Puri, D., Prakash, S.: Studies of plasma spray coatings on a Fe-base superalloy, their structure and high temperature oxidation behaviour. *Anti-Corros. Methods Mater.* **52**(2), 84–95 (2005)
17. Singh, H., Puri, D., Prakash, S.: Corrosion behavior of plasma-sprayed coatings on a Ni-base superalloy in Na<sub>2</sub>SO<sub>4</sub>-60% V<sub>2</sub>O<sub>5</sub> environment at 900 °C. *Metall. Mater. Trans. A* **36**(4), 1007–1015 (2005)
18. ASTM standard, Designation: G76–95, Standard Test Method for Conducting Erosion Tests by Solid Particle Impingement Using Gas Jets, 100 Bar Harbor Drive, West Conshohocken, PA 19428-2959, United States, 1–5 (2000)
19. ASTM G76–04 Standard test method for conducting erosion tests by solid particle impingement using gas jets. ASTM International (2004)
20. Standard Test Method for Conducting Erosion Tests by Solid Particle Impingement Using Gas Jets, ASTM G76-02. ASTM International (2002)
21. Wentzel, E.J., Allen, C.: Erosion-corrosion resistance of tungsten carbide hard metals with different binder compositions. *Wear* **181**, 63–69 (1995)
22. Milman, Y.V., Luyckx, S., Northrop, I.T.: Influence of temperature, grain size and cobalt content on the hardness of WC–Co alloys. *Int. J. Refract Metal Hard Mater.* **17**(1–3), 39–44 (1999)

# Free Vibration Analysis of Laminated Curved Beams Using Fifth-Order Shear and Normal Deformation Theory



P. V. Avhad  and A. S. Sayyad 

**Abstract** In the present study, a fifth-order shear and normal deformation theory is applied for the free vibration analysis of laminated composite straight and curved beams. The present theory considers the effects of transverse shear and normal deformations, i.e., thickness stretching. Hamilton's principle is used to obtain the equations of motions, and Navier's solution technique is used to obtain natural frequencies of simply supported laminated curved beams. Non-dimensional fundamental frequencies of laminated straight and curved beams are obtained for different aspect ratios, radius of curvature, and modular ratios. The present results are compared with other theories wherever possible and found in good agreement.

**Keywords** Laminated · Curved beam · Fifth order · Free vibration

## 1 Introduction

Analysis of laminated composite beams is becoming a popular area of research because of its attractive properties such as stiffness-to-weight ratio and high strength. It is widely used in the different areas like aerospace, civil, automotive, mechanical, and shipbuilding industries. Khdeir and Reddy [1] have investigated the free vibration of the laminated beams with various aspect ratios and boundary conditions. Wu and Chiang [2] have developed the finite element model of uniform circular arches. Ye et al. [3] have developed the spectral sampling surface method for the vibration analysis of laminated curved and sandwich beam. Luu et al. [4] have studied the free vibration analysis of circular curved arches by considering all the effects of the axis extensibility, shear deformation, and rotary inertia. Sayyad and Ghugal [5] have used trigonometric shear and normal deformation theory to

---

P. V. Avhad (✉) · A. S. Sayyad  
Department of Civil Engineering, SRES's Sanjivani College of Engineering,  
Savitribai Phule Pune University, Kopergaon 423603, Maharashtra, India

© The Author(s), under exclusive license to Springer Nature Singapore Pte Ltd. 2021  
A. Patnaik et al. (eds.), *Advances in Materials Processing and Manufacturing Applications*, Lecture Notes in Mechanical Engineering,  
[https://doi.org/10.1007/978-981-16-0909-1\\_32](https://doi.org/10.1007/978-981-16-0909-1_32)

319

investigate the bending, buckling, and vibration of the laminated composite and sandwich beam. Qin et al. [6] have studied the higher-order shear deformation theory for the analysis of free vibration of laminated composite curved beams with various curvature and boundary condition. Sayyad and Avhad [7] have presented the static analysis of curved FGM and sandwich beams.

The objective of the present study is to develop a new higher-order beam theory considering the effects of transverse normal deformation which is neglected by many researchers in their studies. It is also observed that many researchers have used third-order polynomial in the displacement field of theory. Whereas, for the accurate description of laminated beam, it is necessary to expand the displacements up to fifth-order polynomial. Therefore, in the present study, a fifth-order shear and normal deformation theory are applied for the free vibration analysis of laminated composite straight and curved beams. Hamilton's principle is used to obtain the equations of motions, and Navier's solution technique is used to obtain natural frequencies of simply supported laminated curved beams. Non-dimensional fundamental frequencies of laminated straight and curved beams are obtained.

## 2 Modeling of Laminated Curved Beams

The laminated beam has length  $L$ , and rectangular cross section  $b \times h$  where  $b$  is the width ( $b = 1$ ),  $h$  is the total thickness (Cartesian coordinates:  $0 \leq x \leq L$ ;  $-b/2 \leq y \leq b/2$ ;  $-h/2 \leq z \leq h/2$ ), and  $R$  is the radius of curvature. The laminated beams are compiled with  $N$  numbers of layers (Fig. 1).

## 3 Displacement Field

Displacement field of the present theory is as follows [7].

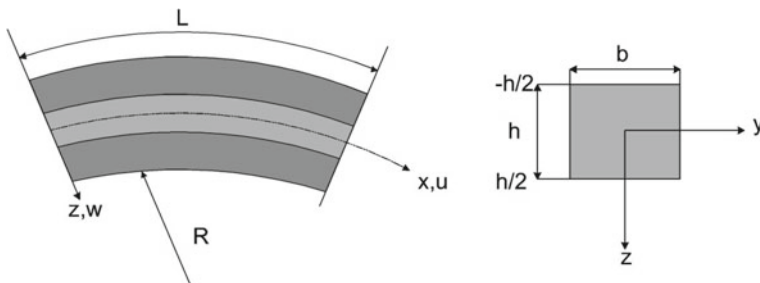


Fig. 1 Laminated curved beam

$$\begin{aligned}
 u(x, z) &= \left(1 + \frac{z}{R}\right)u_0(x) - z\frac{\partial w_0}{\partial x} + \left(z - \frac{4z^3}{3h^2}\right)\phi_x(x) + \left(z - \frac{16z^5}{5h^4}\right)\psi_x(x) \\
 w(x, z) &= w_0(x) + \left(1 - \frac{4z^2}{h^2}\right)\phi_z(x) + \left(1 - \frac{16z^4}{h^4}\right)\psi_z(x)
 \end{aligned}
 \tag{1}$$

where  $u$  and  $w$  are the displacements of any point of the beam domain in  $x$ - and  $z$ -directions, respectively;  $u_0$  and  $w_0$  are the  $x$ - and  $z$ -directional displacements of a point on the neutral axis of the beam. The strains associated with the present theory are as follows

$$\begin{aligned}
 \begin{Bmatrix} \varepsilon_x \\ \varepsilon_z \\ \gamma_{xz} \end{Bmatrix} &= \begin{Bmatrix} \frac{\partial u}{\partial x} + \frac{w}{R} \\ \frac{\partial w}{\partial z} \\ \frac{\partial u}{\partial z} + \frac{\partial w}{\partial x} - \frac{u_0}{R} \end{Bmatrix} \\
 &= \begin{Bmatrix} \frac{\partial u_0}{\partial x} - z\frac{\partial^2 w_0}{\partial x^2} + f_1(z)\frac{\partial \phi_x}{\partial x} + f_2(z)\frac{\partial \psi_x}{\partial x} + \frac{w_0}{R} + f'_1(z)\frac{\phi_z}{R} + f'_2(z)\frac{\psi_z}{R} \\ f''_1(z)\phi_z + f''_2(z)\psi_z \\ f'_1(z)\phi_x + f'_2(z)\psi_x + f'_1(z)\frac{\partial \phi_z}{\partial x} + f'_2(z)\frac{\partial \psi_z}{\partial x} \end{Bmatrix}
 \end{aligned}
 \tag{2}$$

where

$$\begin{aligned}
 f_1(z) &= \left(z - \frac{4z^3}{3h^2}\right), & f_2(z) &= \left(z - \frac{16z^5}{5h^4}\right), & f'_1(z) &= \left(1 - \frac{4z^2}{h^2}\right), \\
 f'_2(z) &= \left(1 - \frac{16z^4}{h^4}\right)
 \end{aligned}
 \tag{3}$$

### 4 Equations of Motion

Equations of motion are derived using Hamilton’s principle [8].

$$\delta \int_{t_1}^{t_2} (U + K - V) dt = 0
 \tag{4}$$

where  $U$ ,  $V$ , and  $K$  denote the strain energy, potential energy, and kinetic energy.  $t_1$  and  $t_2$  are the initial and end time, respectively.

$$\int_0^L \int_{-h/2}^{h/2} (\sigma_x \delta \varepsilon_x + \tau_{xz} \delta \gamma_{xz}) dz dx + \int_0^L \int_{-h/2}^{h/2} \rho(z) \ddot{u} \delta u + \ddot{w} \delta w dz dx$$

$$- \int_0^L q \delta w dx = 0 \tag{5}$$

where  $\delta$  denotes the variation operator and  $\rho$  is mass density. The dot-superscript convention indicates the differentiation with respect to the time variable. By collecting the coefficients of six unknown variables ( $\delta u_0, \delta w_0, \delta \phi_x, \delta \psi_x, \delta \phi_z, \delta \psi_z$ ), the governing equations of motion are obtained as follows

$$\delta u_0 : \frac{\partial N_x}{\partial x} + \left[ I_1 + 2 \frac{I_2}{R} + \frac{I_3}{R^2} \right] \frac{\partial^2 u_0}{\partial t^2} - \left[ I_2 + \frac{I_3}{R} \right] \frac{\partial^3 w_0}{\partial t^2 \partial x} + \left[ I_4 + \frac{I_5}{R} \right] \frac{\partial^2 \phi_x}{\partial t^2}$$

$$+ \left[ I_6 + \frac{I_7}{R} \right] \frac{\partial^2 \psi_x}{\partial t^2} = 0 \tag{6}$$

$$\delta w_0 : \frac{\partial^2 M_x^b}{\partial x^2} - \frac{N_x}{R} + q + \left[ I_2 + \frac{I_3}{R} \right] \frac{\partial^3 u_0}{\partial t^2 \partial x} - I_3 \frac{\partial^4 w_0}{\partial t^2 \partial x^2} + I_5 \frac{\partial^3 \phi_x}{\partial t^2 \partial x} + I_7 \frac{\partial^3 \psi_x}{\partial t^2 \partial x}$$

$$+ I_1 \frac{\partial^2 w_0}{\partial t^2} + I_{11} \frac{\partial^2 \phi_z}{\partial t^2} + I_{12} \frac{\partial^2 \psi_z}{\partial t^2} = 0 \tag{7}$$

$$\delta \phi_x : \frac{\partial M_x^{s1}}{\partial x} - Q_{xz}^1 + \left[ I_4 + \frac{I_5}{R} \right] \frac{\partial^2 u_0}{\partial t^2} - I_5 \frac{\partial^3 w_0}{\partial t^2 \partial x} + I_8 \frac{\partial^2 \phi_x}{\partial t^2} + I_9 \frac{\partial^2 \psi_x}{\partial t^2} = 0 \tag{8}$$

$$\delta \psi_x : \frac{\partial M_x^{s2}}{\partial x} - Q_{xz}^2 + \left[ I_6 + \frac{I_7}{R} \right] \frac{\partial^2 u_0}{\partial t^2} - I_7 \frac{\partial^3 w_0}{\partial t^2 \partial x} + I_9 \frac{\partial^2 \phi_x}{\partial t^2} + I_{10} \frac{\partial^2 \psi_x}{\partial t^2} = 0 \tag{9}$$

$$\delta \phi_z : \frac{\partial Q_{xz}^1}{\partial x} - \frac{V_x^1}{R} - Q_z^1 + qf'_1(z) + I_{11} \frac{\partial^2 w_0}{\partial t^2} + I_{13} \frac{\partial^2 \phi_z}{\partial t^2} + I_{14} \frac{\partial^2 \psi_z}{\partial t^2} = 0 \tag{10}$$

$$\delta \psi_z : \frac{\partial Q_{xz}^2}{\partial x} - \frac{V_x^2}{R} - Q_z^2 + qf'_2(z) + I_{12} \frac{\partial^2 w_0}{\partial t^2} + I_{14} \frac{\partial^2 \phi_z}{\partial t^2} + I_{15} \frac{\partial^2 \psi_z}{\partial t^2} = 0 \tag{11}$$

where  $N_x, M_x^b, M_x^{s1}, M_x^{s2}, V_x^1, V_x^2, Q_z^1, Q_z^2, Q_{xz}^1, Q_{xz}^2$  are stress resultants. By solving the stress resultant rigidity coefficients are obtained and  $I_{(i=1to15)}$  are inertia coefficients.

### 5 Navier’s Solution

Natural frequencies of simply supported laminated beams are obtained by using Navier’s solution technique [8].

$$\begin{aligned}
 u_0 &= \sum_{m=1}^{\infty} u_m \cos \frac{m\pi x}{L} \sin(\omega t), & w_0 &= w_m \sum_{m=1}^{\infty} w_m \sin \frac{m\pi x}{L} \sin(\omega t) \\
 \phi_x &= \sum_{m=1}^{\infty} \phi_{xm} \cos \frac{m\pi x}{L} \sin(\omega t), & \phi_z &= \sum_{m=1}^{\infty} \phi_{zm} \sin \frac{m\pi x}{L} \sin(\omega t) \\
 \psi_x &= \sum_{m=1}^{\infty} \psi_{xm} \cos \frac{m\pi x}{L} \sin(\omega t), & \psi_z &= \sum_{m=1}^{\infty} \psi_{zm} \sin \frac{m\pi x}{L} \sin(\omega t)
 \end{aligned}
 \tag{12}$$

where  $u_m, w_m, \phi_{xm}, \psi_{xm}, \phi_{zm}$  and  $\psi_{zm}$  are the unknown coefficients to be determined and  $\omega$  is the natural frequency. Substitution of Eq. (12) into the equations of motion (6) through (11) leads to the following eigenvalue problem.

$$\{[K] - \omega^2[M]\}\{\Delta\} = 0
 \tag{13}$$

where  $K$  is the stiffness matrix,  $M$  is the mass matrix, and  $\Delta$  is the amplitude vector. Nontrivial solution of Eq. (13) gives the natural frequencies of simply supported laminated curved beams.

### 6 Numerical Results

In this section, numerical examples are presented and accuracy of present theory in free vibration of simply supported functionally graded curved beam. Material properties for  $[0^\circ/90^\circ]$  and  $[0^\circ/90^\circ/0^\circ]$  are  $E_1/E_3 = \text{Open}, G_{13} = 1.378, G_{23} = 0.5, \mu_{13} = 0.25, \mu_{31} = 0.01,$  and  $\rho = \text{constant}.$  For simplicity, numerical results are presented in the following non-dimensional form.

$$\bar{\omega} = \frac{\omega L}{h} \sqrt{\frac{\rho}{E_3}}
 \tag{14}$$

Table 1 shows non-dimensional free vibrations of the straight laminated composite beams. Its shows that present results have good agreement with previously published results. Table 2 shows non-dimensional free vibrations of the laminated curved beams with various aspect ratios and radius of curvature. As the aspect ratio increases ( $L/h$ ), the non-dimensional natural frequency increases Figs. 2 and 3.



**Table 1** Non-dimensional fundamental frequency of S-S laminated straight beams

Lamination Scheme	$E_1/E_3$	Source	$L/h$				
			5	10	20	50	100
0°/90°	10	Present	4.1481	4.6041	4.7481	4.7913	4.7976
	40	Present	5.6638	6.7936	7.2175	7.3536	7.3738
		Sayyad and Ghugal [5]	6.185	6.999	7.275	7.377	7.413
		Khdeir and Reddy [1]	6.128	6.945	–	–	–
0°/90°/0°	10	Present	5.9131	7.7141	8.5226	8.8018	8.8441
		Sayyad and Ghugal [5]	6.787	8.165	8.682	8.861	8.876
		Khdeir and Reddy [1]	6.789	8.176	8.690	8.853	8.876
	40	Present	7.4545	11.846	15.438	17.259	17.577
		Sayyad and Ghugal [5]	9.245	13.675	16.450	17.638	17.647
		Khdeir and Reddy [1]	9.208	13.614	–	–	–

**Table 2** Non-dimensional fundamental frequency of [0°/90°] and [0°/90°/0°] laminated curved beams

	$E_1/E_3$	$R/h$	Theory	$L/h$				
				5	10	20	50	100
[0°/90°]	10	5	Present	4.1649	4.6124	4.7481	4.7856	4.7899
		10	Present	4.1585	4.6105	4.7505	4.7909	4.7962
		20	Present	4.1538	4.6079	4.7499	4.7917	4.7975
		50	Present	4.1505	4.6058	4.7490	4.7916	4.7977
		100	Present	4.1493	4.6050	4.7486	4.7915	4.7977
	40	5	Present	5.6826	6.8074	7.2195	7.3458	7.3625
		10	Present	5.6760	6.8039	7.2222	7.3534	7.3719
		20	Present	5.6706	6.7996	7.2208	7.3545	7.3738
		50	Present	5.6667	6.7962	7.2190	7.3542	7.3740
		100	Present	5.6653	6.7950	7.2183	7.3540	7.3740
[0°/90°/0°]	10	5	Present	5.9013	7.6986	8.5054	8.7840	8.8262
		10	Present	5.9101	7.7102	8.5183	8.7973	8.8396
		20	Present	5.9123	7.7131	8.5215	8.8007	8.8430
		50	Present	5.9129	7.7139	8.5224	8.8016	8.8439

(continued)

**Table 2** (continued)

	$E_1/E_3$	$R/h$	Theory	$L/h$				
				5	10	20	50	100
		100	Present	5.9130	7.7140	8.5225	8.8017	8.8440
	40	5	Present	7.4396	11.8230	15.4071	17.2242	17.5421
		10	Present	7.4508	11.8408	15.4304	17.2503	17.5687
		20	Present	7.4536	11.8453	15.4363	17.2569	17.5753
		50	Present	7.4544	11.8466	15.4379	17.2587	17.5772
		100	Present	7.4545	11.8468	15.4382	17.2590	17.5775

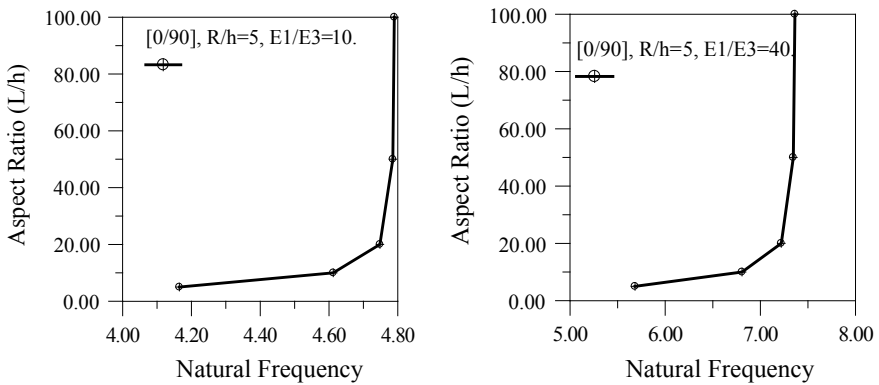


**Fig. 2** Natural frequencies of  $[0^\circ/90^\circ]$  laminated curved beam with different aspect ratios and material properties

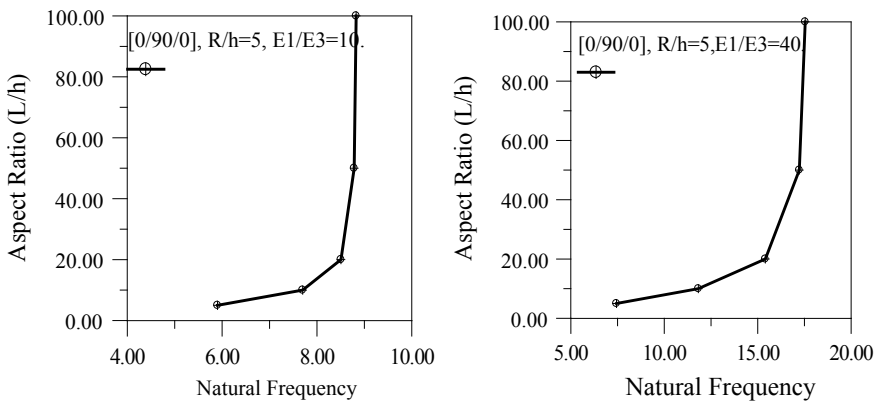


**Fig. 3** Natural frequencies of  $[0^\circ/90^\circ/0^\circ]$  laminated curved beam with different aspect ratios and material properties

## 7 Conclusions

This study highlights the application of a fifth-order shear and normal deformation theory for the free vibration analysis of laminated composite curved beams. The present theory considers the effects of transverse shear and normal deformations. Hamilton's principle is used to obtain the equations of motions, and the eigenvalue solution is obtained using Navier's solution technique. Non-dimensional fundamental frequencies of laminated straight and curved beams are obtained and compared with other theories wherever possible and found in good agreement.

## References

1. Khdeir, A.A., Reddy, J.N.: Free vibration of cross-ply laminated beams with arbitrary boundary conditions. *Int. J. Eng. Sci.* **32**(12), 1971–1980 (1994)
2. Wu, J.S., Chiang, L.K.: Free vibration analysis of arches using curved beam elements. *Int. J. Numer. Methods. Eng.* **58**, 1907–1936 (2003)
3. Ye, T., Jin, G., Su, Z.: A spectral-sampling surface method for the vibration of 2-D laminated curved beams with variable curvatures and general restraints. *Int. J. Mech. Sci.* **89**, 110–170 (2016)
4. Luu, A.T., Kim, J., Lee, N.: 2D vibration analysis of circular arches with constant double symmetric cross-sections using iso-geometric approach. *KSCE J. Civil Eng.* **21**(7), 2751–2763 (2017)
5. Sayyad, A.S., Ghugal, Y.M.: Effect of thickness stretching on the static deformations, natural frequencies, and critical buckling loads of laminated composite and sandwich beams. *J. Braz. Soc. Mech. Sci. Eng.* **40**(6), 296 (2018)
6. Qin B., Zhao X., Liu H., Yu Y., Wang Q.: Free vibration analysis of curved laminated composite beams with different shapes, lamination schemes, and boundary conditions. *Materials*, **13**(4), (2020)
7. Avhad, P.V., Sayyad, A.S.: On the static deformation of FG sandwich beams curved in elevation using a new higher order beam theory. *Sadhana* **45**, 188 (2020)
8. Reddy J.N.: *Mechanics of Laminated Composite Plates and Shells: Theory and Analysis*. 2nd edn. Boca Raton, (2003)

# Luminous Concrete as Green Building Material



Manisha Sharma, Tanpreet Singh, and Sahibdeep Singh Setia

**Abstract** People are moving from rural to urban area for better livelihood. Skyscrapers are built in metropolitan cities due to economic development and demand of space has been increased than the land available, especially in those countries with peak population. This unprecedented growth of concrete jungle leads to increase in the vertical progression of space and reducing the spacing between buildings causing the obstruction in the white light in interior space of the building. Natural lighting design building is a way of sustainable development. Luminous concrete is an emerging and environmental-friendly material that has light transmissive property. It is fibre-reinforced concrete with optical fibres infused uniformly distributed inside its body. In this review paper, brilliant properties of light guiding optical fibres arranged in concrete are developed and various tests of concrete are discussed altogether. The cost analysis and payback time of luminous concrete are also justified for its usefulness as a constructional energy efficient, aesthetical beautiful on sustainable ground. This paper finally inferred that the optimum percentage of optical fibre was 4% to be successfully used as a structural member, for architectural aesthetic purpose and as an eco-friendly sustainable material to use in green building.

**Keywords** Luminous concrete · Sustainable development · Green concrete · Optical fibre · Compressive strength · Cost analysis

## 1 Introduction

Concrete is the wonderful material which is consumed for this growing world. It is used by Romans anciently and is progressing aesthetically and structural point of view. It is a revolutionary material for the civil engineers and researchers. Initially, concrete members are used as structural member but now the tradition is changed, concrete members are also used for decorative purpose. Luminous concrete is a

---

M. Sharma (✉) · T. Singh · S. S. Setia  
Civil Engineering Department, GNDEC, Ludhiana, Punjab, India

novel material which changes the image of concrete in terms of creativity and sustainability. It is similar to traditional concrete but with light crossing capacity.

Rapidly growing industrial and economic growth is a threat to sustainable development. Today, more efforts have been done to make building sustainable and less energy consuming. Advancement in structural engineering has increased the height and complexity of the structure, and the new concept of high rise building which is labelled as ‘pigeon holes’ or ‘vertical castle’ results in closely packed building and reduces the spacing between them [1]. This leads to a major problem of natural light into the interior place of the building and increases the power consumption. According to US Energy Information Administration (EIA) in 2014, 15% of consumption of electricity was contributed by the residential and commercial sector [2]. So, luminous concrete is a material that can reduce the demand of artificial light in the building and give a better living environment. Luminous concrete is first seen in 1935 in Canada. Then after, around 1998 architect Bill Price dig into the concept of luminous concrete and conducted some strength test on few samples while working at Rem Koolhaas’s OMA. In 2001, Hungarian architect Aron Losonzi is the first one who led the concept of luminous concrete and patented with name called LitraCon and made it commercial.

Translucent is often misunderstood that it is translucent by its own. According to oxford dictionary, ‘translucent’ means something which allows light to cross throughout but not completely clear. Translucent concrete is combination of two materials, one from construction area, i.e. concrete, and second one is from sensing field, i.e. optical fibres (Fig. 1a). By combination of their advantages, the luminous concrete is prepared. Strands of optical wires are cast in the design mix concrete to transmit light. Optical fibres are a flexible material which is slightly broader than hair. Optical fibre works on total internal reflection (TIR) principle by which light signal can be transmitted from one end to another end with almost zero loss of energy, as can be seen in Fig. 1(b). Optical fibre is made up of inner cylinder having glass or plastic usually known as core of high refractive index, cladding which is having little lower refractive index and then coating. In luminous concrete, optical fibre is used without cladding as the concrete around the fibre acts as cladding for it.

## 2 Method of Manufacturing

The procedure of production of luminous concrete is very much alike normal concrete but only optical fibres are spread inside the concrete mix. Optical fibres are added by some percentage and batched by the volume. Thickness of optical fibres varies from 2 to 3 mm. Separate mould is prepared from tin or wood in which two sides are fixed and other two parallel sides are drilled at a suitable uniform distance (Fig. 2a). Optical fibres are placed in that holes in a single direction before pouring concrete mix in the mould. Pouring of concrete is most delicate step of manufacturing of luminous concrete as shown in Fig. 2(b). It is demoulded carefully after

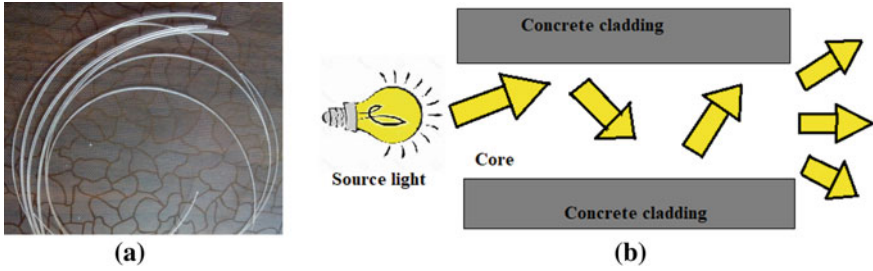


Fig. 1 Working of optical fibre; 1(a) Optical fibre 1(b) Total internal reflection



Fig. 2 Preparation of luminous concrete; 2(a) Mould and optical fibre 2(b) Mould with optical fibres and concrete mix

28 h and extra edges of fibres are cut out. After that finishing of surface is done. Then it undergoes for curing process.

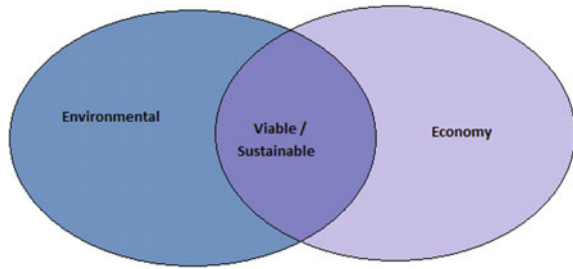
### 3 Effect of Optical Fibre on Concrete Properties

#### 3.1 Compressive and Flexural Strength

The compressive test is another property of luminous concrete which makes it prominent to use effectively. To study the effect of plastic optical fibre of 1 mm diameter on the compression strength of concrete, 0, 0.25, 0.75, 1.25% of plastic optical fibre (POF) was used. The results were compared in Fig. 3 showing the increasing pattern of compressive strength due to presence of optical fibre which behave as prestressed component [3].

Loss of compressive strength was observed with infusion of optical fibre at 0–4%. For M20 and M25 grade of concrete, 15.2% and 7% have reduced with 4% of

**Fig. 3** Factors of sustainability



POF. The target strength was achieved at 2% for M20 and 1.25–2.50% for M25 [4]. Another study was carried out with 0.06–1.59% POF ratio and with different diameter and spacing of POF. The study observed that compressive strength increases with increase in percentage of POF. Although with increasing pattern of strength 1.59% mix shows lower strength than 1.43% mix due to closely spaced fibres which might weaker the sample by lesser interconnecting distance at the time of macrocrack propagation under compressive load [2], 10% reduction in compressive strength was found when 4% POF was added in concrete [5]. The compressive strength increases with increase in spacing between the fibres and the flexural strength of translucent concrete is more than normal concrete as the POF enhances the tensile property of the concrete [6]. When the POF is incorporated in concrete at 1–5%, the target strength was achieved till 4% whereas strength at 5% was 3% less than the target strength [7].

Researcher investigated the pattern of compressive strength of conventional translucent concrete with optical fibres and compare with translucent concrete with additional material such as rice husk ash (RHA) and steel fibre (SF). For conventional as well as RHA and SF translucent concrete, the compressive strength goes down with increase of optical fibre ratio. Despite of decreasing pattern of compressive strength in both cases, at 1.5% and 2% of optical fibre there was a sudden increase in compressive strength and it was more than the compressive strength of normal concrete. They also observed the values of compressive strength of RHA and SF translucent concrete is much more than conventional concrete translucent concrete [8]. The physical properties of luminous concrete incorporating POF of 2 mm and 3 mm diameter as 2%, 4% and 6%. The bulk density of hardened translucent self-compacting concrete (TSCC) mix incorporated limestone powder and recycled glass aggregates as 30% and 20% of cement and fine aggregates (FA), respectively, with controlled concrete mix and observed declined pattern from 0.22 to 3.39% with increasing POF volume regardless its diameter. Compressive strength and flexure strength test results showed the same declined pattern as 8–24% and 9–24% decrease in translucent concrete strength as compared to controlled concrete at 28 days cured specimens [9]. Compressive strength of luminous concrete increases with POF ratio till a certain limit and the flexural strength of luminous concrete is greater than normal concrete [10]. The incorporation of 3 mm POF in translucent concrete with 36 (OFRC-36) and 49 (OFRC-49) number of fibre

strand was studied. Compression and rebound hammer strength of translucent concrete with OFRC-36 is higher than other but OFRC-49 had strength less than conventional concrete [11].

### ***3.2 Light Transmissibility***

Light transmissibility is one of the key functional properties of luminous concrete which determines the amount of light passes through it. Light transmittance can be measured with the help of light dependent resistor, lux meter, etc. Light transmissibility increases with increase in percentage of POF. 74.24% of increase has been observed with increase of POF ratio from 0.06 to 1.43%. At 1.59%, the amount of light passed by the luminous concrete decreases with respect to 1.43% of POF [2]. It was found that light transmittance is proportional to the number of fibres, i.e. volume of optical fibres. It also get effected by many other factors such as natural environment, arrangement and spacing of POF, optical fibre failure. These factors can influence the results despite of equal volume of optical fibre [3]. Optical fibre of 1 mm when infused in the concrete at ratio of 1–4% of volume of concrete showed 3.3–13.1% of light transmitted through the sample [12]. Lesser spacing raise the intensity of light passed through the translucent concrete as the numbers of fibres are more with same percentage when optical fibre of lesser diameter is used [6]. Studies have been done on light transmissibility of luminous concrete for different surface area of wall. Concrete with 36 strands of optical fibre shows indoor light intensity of 40% and 31.7% for 0.450 sqm and 0.36 sqm, respectively, with respect to outdoor light intensity. Similarly, concrete with 49 strands shows 43.29% and 34% for 0.450 sqm and 0.36 sqm of wall [11]. The intensity and distance of source light also affect the light transmitted through luminous concrete. Transmittance is checked at varied distance 100, 200, 300 and 400 mm for different dia of POF 2 and 3 mm. The position of light source and light-dependent resistor influences the amount transmission of light. As the distance increases, the light transmission decreases. More transmittance of light is observed by 2 mm dia samples than 3 mm dia. This showed that lesser diameter of fibre results in more number of optical fibre causing more amount of light transmitted through the concrete [13]. It was also found that when the luminous concrete was checked under external radiation of sunlight, maximum intensity of light was observed at afternoon session than morning and evening [7]. Comparison of glass rod and optical fibre was studied at different spacing of fibres. It was concluded that the optical fibre allows more light to pass through it as compared to the glass rod due to its principle of total internal reflection. The amount of light transmissibility decreases with the spacing of the fibres [14].



### **3.3 Ultrasonic Pulse Velocity Test**

The study showed that the luminous concrete with 0.06–1.59% of POF shows homogeneous concrete. For 7 days curing period, results were below 4 km/s which mean that the quality of concrete was good to very good but slight porosity is there but after 7 days curing period, i.e. for 14 days, 21 days and 28 days, the quality of concrete seems excellent as the results were above 4 km/s [2]. The quality of translucent concrete and normal concrete was compared and it was found that the quality of both concrete is fairly good and translucent concrete exhibit same properties as traditional concrete [15]. Uniformity and homogeneity of concrete were checked at 2.5% and 4% of POF. Experimental results show that for conventional concrete, ultrasonic pulse velocity was 4.75 km/s whereas for 2.5% and 4% of POF, it was 4.56 km/s and 4.52 km/s which indicates very good quality of concrete [16].

### **3.4 Cost and Packback**

The initial manufacturing cost of luminous concrete is high but the whole life cost of structure is reduced by the use of luminous concrete [17]. Experiment conducted shows that the payback time for a wall of 20 blocks (0.45 m<sup>2</sup> areas) for residential use was 4.3 years and for commercial use was 2.7 years. This payback period is much less than the benefits of the luminous concrete [7]. A study also found that the cost of translucent concrete is 5 times more than conventional concrete. Payback period of translucent concrete is 1.1 years for residential building and 1.7 for commercial building [11].

## **4 Advantage and Disadvantage**

The advantages of translucent concrete are that it can transmit light which makes it a green material by utilizing the natural light, saving energy by using fewer lights to meet the lighting demand and environment friendly [18]. Large-scale use of translucent concrete makes the pattern visible from distance. It gives a good aesthetic view to the structure. As optical fibre is used in translucent concrete for light transmission, it is heat insulator and becomes more effective in colder region [19]. Despite of many advantages, it has some disadvantages as it is novel material and requires a lot of research to grow. The main disadvantages are that the production cost of translucent concrete is high due to presence of optical fibre. The manufacturing process requires skilled labour, proper supervision, and maintaining quality control throughout the process. It is very important to ensure the integrity of optical fibres that the damage or breakage in the fibre would be obstacle in light transmittance.

## 5 Future Expectation

Luminous concrete is one of the green materials which uses sunlight as the source of illumination. Sustainability consists of two factors; one is environmental and second is economy (Fig. 3). Translucent concrete is a novel material which is costly. Lots of researches have been going to reduce its manufacturing cost and make it affordable product [20]. To give better life for generations to come, sustainable development plays a key role. Luminous concrete needs to be designed by keeping environmental as well as economical concern in mind, which makes it viable and true green material.

## 6 Conclusion

Luminous concrete is a new technique with light carrying capacity without changing its insulation capacity. It is energy saving material with artistic finish. It is fabricated for structural and non-structural component with different designs. It is a combination of two versatile materials (optical fibres and concrete) which gives new prospective and creative possibilities to multitudes of people. The compressive strength of luminous concrete is almost similar or greater than the normal concrete which makes it advantageous to use as a construction material. The huge increase in ratio of optical fibre influences the compressive strength of luminous concrete. Therefore, light transmitting property cannot be increased incessantly. Manufacturing of luminous concrete is a tedious process, needs skilled labour and a costly process. Furthermore, studies are requiring to enhance the strength parameter and to lower its production cost by addition of some other recycled or waste material, etc. It is a magnificent material which can be used for decoration, construction and architecture purpose. The probability of luminous concrete to emerge as a good eco-friendly material is multitudinous and it reflects the idea of energy saving material with light transmitting property. The light transmittance was increased by using plastic optical fibres (POF) in concrete. This light transmittance can be further be increased by inserting more percentage of optical fibre in concrete elements and can be used efficiently in green buildings. It can ensure natural light inside the buildings throughout the day.

Inviting optical fibre in mix concrete the initial production cost of luminous concrete is high as compared to nominal mix concrete during its preparation but the recovery period of luminous concrete is less as compared to its advantages, as various types of glowing pattern can be prepared with this concrete. Addition of other (waste and recycled) material can strengthen the properties like compressive stress of luminous concrete and reduces its overall cost of production. This makes it environmentally and economically viable and a true sustainable material.

**Acknowledgements** The special gratitude goes to Er. Tanpreet Singh and Er. Sahibdeep Singh Setia for his motivational and infrastructural support for providing essential information to carry out this research topic.

## References

1. Milana G., Gkoumas K., Bontempi F.: Sustainability Concepts in the Design of High-Rise buildings: the case of Diagrid Systems, Third International Workshop on Design in Civil and Environmental Engineering, 1–10 (2014)
2. Altomate, A., Alatshan, F., Mashiri, F., Mohamed, J.: Experimental study of light-transmitting concrete. *Int. Journal Sustain. Build. Technol. Urban Development.* **7**, 133–139 (2016)
3. Huong, W.G., Kassim, U.: Translucent Concrete by Plastics Fibre Optics as A Sustainable Material That Benefit to Residential Building. *J. Adv. Res. Eng. Knowledge.* **6**(1), 1–6 (2019)
4. Kumar, A., Ahlwat, R.: Experimental study on light transmitting concrete. *Int. J. Innov. Sci., Eng. Technol.* **4**(6), 201–210 (2017)
5. Sahoo A.K., Sahu S., Singhal A.S., Talom T., Tripathy S.S., Das S.: Experimental Study on Light Transmitting Concrete Experimental Study of Light Transmitting Concrete Using Optical Fiber, <https://www.researchgate.net/publication/321624358>. (2017)
6. Nikhil, K., Farook, U., Ahmed, S., Juraige, M.K., Saleem, R., Omar, S.: Experimental Analysis of Translucent Concrete by using Optical Fibers. *SSRG Int. J. Civ. Engineering.* **3**(3), 69–74 (2016)
7. Sawant, A.B., Jugdar, R.V., Sawant, S.G.: Light Transmitting Concrete by using Optical Fiber. *Int. J. Inven. Engineering Sci.* **3**(1), 23–28 (2014)
8. Abhishek, T., Parmod, S.: Study of Behaviour of Translucent Concrete using Rice Husk and Steel Fibre. *SSRG Int. J. Civ. Engineering.* **3**(7), 24–28 (2016)
9. Tuum A., Shitote S., Oyawa W., Biedebrhan M.: Structural Performance of Translucent Concrete Façade Panels. *Advance in Civil Engineering*, 1–10 (2019)
10. Nirmal, Y., Nehemiya, K., Prasad, G.G.: Study on Mechanical Properties of Light Transmitting Concrete. *Int. Res. J. Eng. Technol.* **4**(7), 1049–1055 (2017)
11. Shakeel, N., Mehta, S., Singh, K.: Experimental investigation on light transmission and structural performance of translucent concrete using 3 mm diameter plastic optical fibers. *Int J. Innov. Technol. Explor. Eng.* **8**(8), 426–429 (2019)
12. Ravikumar, N., Dharsika, S.: Experimental Study on Light Transparency of Concrete by Using Optical Fiber. *Int. J. Sci. Eng. Sci.* **2**(2), 1–4 (2018)
13. Tuum, A., Shitote, S., Oyowa, W.O.: Experimental Evaluation on Light Transmittance Performance of Translucent Concrete. *Int. J. Appl. Eng. Res.* **13**(2), 1209–1218 (2018)
14. Momin A.A., Kadiranaikar R.B., Jagirdar V.S., Inamdar A.A.: Study on Light Transmittance of Concrete using Optical Fibers and Glass Rods. *IOSR Journal of Mechanical and Civil Engineering*, 67–72 (2014)
15. Sasidharan, J., Teja, N.S., Sakthivel, K., Manickavel, D., Kumar, M.: Translucent Concrete. *Int. J. Eng. Res. & Technol.* **6**(4), 782–786 (2017)
16. Raghavi, D., Rajasekar, K.: Experimental studies on Strength and Durability properties of Transparent concrete. *Int. J. Res. Eng. Appl. & Manag.* **4**(7), 33–41 (2019)
17. Shamr, N.G., Tantary, M.A.: A Review on Green Building using Translucent Concrete as Energy Efficient Source. *IRE J.* **2**(7), 94–96 (2019)
18. Paul, S., Dutta, A.: Translucent Concrete. *Int. J. Sci. Res. Publ.* **3**(10), 1–10 (2013)
19. Kamdi, A.B.: Transparent Concrete as a Green Material for Building. *Int. J. Struct. & Civ. Eng. Res.* **2**(3), 172–175 (2013)
20. Gahrana, S., Raj, V., Chouhan, S., Krishnia, S.: Application of Transparent Concrete in Green Construction. *Int. J. Sci. & Technol. Res.* **7**(4), 119–122 (2018)

# Removal of Lead Using Isolated Microorganisms from Contaminated Soil



Neethu Jayan and M. Laxmi Deepak Bhatlu

**Abstract** Discharge of heavy metals even at low concentrations from different sources cause hazardous effects in humans, animals and plants. Technical as well as economic constraints encountered in the application of traditional methods for the removal of low concentration of heavy metals from effluents have directed attention to new technologies. Bioremediation using living microbes is a promising technology for treating effluents at lower concentrations. In this work lead, resistant microorganisms were isolated from the contaminated soil. By means of various staining, morphological and biochemical test the isolated lead resistant microorganism was identified as **Bacillus cereus**. The growth optimums of the isolated microorganisms were observed at 40 °C and pH of 6 when shaken in Rotech shaker of 200 rpm for 50 min. It was observed that 95.5 percentage of lead removal (10 ppm) took place when the inoculated broth solution containing lead solution was shaken in Rotech shaker at 40 °C, pH of 6 and 200 rpm for 80 min of contact time. The microbes showed resistance to lead up to 1000 ppm. The isolated microorganism also showed multiple metal resistances in addition to lead. The isolate showed resistance to zinc, arsenic and mercury. FTIR results showed that alkenes, nitro compounds and amino groups are the predominant contributors in lead uptake by microorganisms

**Keywords** Bioremediation · Bioaccumulation · Heavy metals · Microorganisms · Environmental contamination

---

N. Jayan (✉) · M. L. D. Bhatlu  
Department of Chemical Engineering, Faculty of Engineering, Karpagam Academy of Higher Education, Coimbatore 641021, India  
e-mail: [neethu.jayan@kahedu.edu.in](mailto:neethu.jayan@kahedu.edu.in)

© The Author(s), under exclusive license to Springer Nature Singapore Pte Ltd. 2021  
A. Patnaik et al. (eds.), *Advances in Materials Processing and Manufacturing Applications*, Lecture Notes in Mechanical Engineering,  
[https://doi.org/10.1007/978-981-16-0909-1\\_34](https://doi.org/10.1007/978-981-16-0909-1_34)

335

## 1 Introduction

Heavy metal is any metalloid or dense metal with high toxicity even in smaller concentrations. Heavy metals cannot be degraded normally as organic contaminants [1]. Deposition of these metals became the cardinal one now the world is facing with as well as its toxicity even at very low concentration. Ten chemicals which are included in the World Health Organization's public concern list [2] are arsenic, zinc, chromium, cadmium, mercury, copper and lead. The stable states of these metals are the most toxic forms of them, e.g., Cd (II), Pb (II), Hg (II), Ag (II) and As (III+) which form stable biotoxic compounds after reacting with the biomolecules of the body harmful effects to the entire environment, which cause threat not only to human health but also to fauna and flora made heavy metals and its contamination a primary global concern. Human beings require some toxic heavy in small quantities [3]. Lead is one of the treacherous metals which requires the existence of living species in very small concentrations. In contrast, its presence above some specified concentration makes it hazardous to health [4, 5]. This essentiate finding the toxic results of Pb (II) and eliminating from water and the environment [6]. Along with the toxicity, the mobility of heavy metals in natural water makes contamination issues in surface water and groundwater. Conventional methods which are using to eliminate heavy metals from wastewater effective obliterating heavy metals from solution at moderate to high concentrations in bulk [7]. While to eliminate the heavy metal presence from dilute metal waste, these techniques produce poor results and economically unviable. Now researchers are focusing their research on finding out a most efficient biotechnological eco-friendly process and have developed an approach called bioremediation [8]. Bioremediation can be defined as a process which makes use of microorganisms and their enzymes to revive the contaminated environment to its original condition. Since some fungal can withstand lead ion at high concentration can make use of this advantage as a biological tool. The current work was carried out to isolate and characterize lead resistant microorganism from contaminated soil. Influence of initial metal concentration was studied. Minimum inhibitory concentration, multiple resistance and FTIR analysis of isolated microorganism were also determined.

## 2 Materials and Methods

### 2.1 *Sample Collection and Isolation of Microorganism*

Soil samples required for this project were collected from industry. The collected samples were kept in a sterile plastic container. Transported to the laboratory and kept at 4 °C. Serial dilution is the technique used to reduce the concentration of microorganism in the soil sample. The soil sample was diluted from  $10^{-1}$  to  $10^{-5}$  dilutions, and the dilute soil samples were spread on sterile nutrient agar plates,

10 ppm of the lead solution also spread on it. The inoculated plates were incubated at room temperature for 24–48 h. Stored this pure culture in the refrigerator for further experiments.

## ***2.2 Determination of Optimal Microbial Growth Conditions***

The bacterial isolates were inoculated into 20 ml of sterilized nutrient broths and used for experiments. Optimum microbial growth temperature tested at different temperatures such as 25, 30, 35, 37, 40, 45 and 50 °C. Incubated the flasks according to corresponding incubation temperature for 24 h. After 24 h of incubation, the growth at different temperature was determined by measuring absorbance using ultraviolet visible spectrophotometer. Same experiment setup is done to determine the optimum growth pH and nutrient broths altered to different pH levels such as 2, 4, 6, 8, 10. After 24 h the growth, at different pH was determined by measuring absorbance using a visible ultraviolet spectrophotometer. Bacterial isolates were inoculated into 25 ml of sterilized nutrient broths in 250 ml conical flask. These inoculated flasks were shaken for one hour at optimum temperature and at optimum pH at different rpm from 100, 150, 200 and 250 in Rotech shaker. The optimum rpm was determined by measuring absorbance using visible ultraviolet spectrophotometer after one hour of shaking. For the determination of optimum growth contact time, 25 ml of culture medium was inoculated with isolated microorganisms in 250 ml conical flask. After shaking in Rotech shaker at optimum rpm and at optimum temperature and pH absorbance, reading of this inoculated culture medium was taken at regular intervals of time using UV-visible spectrophotometer.

## ***2.3 Determination of Optimal Lead Removal Conditions***

Temperature, pH, metal concentration and contact time are the sundry factors which alter the rate of removal [8]. Optimum lead removal temperature was done by adding 1 ml of 10 ppm lead solution into 20 ml of nutrient broth solution containing isolated microorganisms and incubated it at different temperatures for 24 h. Same setup was done at different pH. Optimum pH was determined by recording the lead concentration in the broth culture using atomic absorption spectroscopy. Inoculated the bacterial isolated into 25 ml of sterilized nutrient broths in 250 ml conical flask. Add 1 ml of 10 ppm lead solution into the broth. These inoculated flasks were shaken at optimum temperature and at optimum pH for one hour in Rotech shaker to determine the optimum lead removal rpm. The optimization of contact time was done by same setup. These inoculated flasks were shaken at optimum temperature, pH and optimum rpm in Rotech shaker. Lead concentration in the broth solution after a different interval of time was identified using atomic absorption spectroscopy.

## 2.4 *Resistance of Isolate*

Isolates may show multiple metal resistances: Used arsenic and mercury along with lead to determine the multiple resistance isolated microorganisms. Mercury and arsenic were poured to the Petri plate along with lead and soil sample and above these poured agar solutions. Incubated these Petri plates for 24 h.

## 2.5 *Fourier Transform Infrared Spectral Analysis (FTIR)*

Infrared spectra were recorded on PerkinElmer (Spectrum Version 10.4.00) FTIR spectrometer. For FTIR analysis, microorganisms inoculated nutrient broth solution without loading lead used as the blank and microorganism inoculated nutrient broth with lead solution was taken as sample solution.

# 3 Results and Discussions

## 3.1 *Isolation of Lead Resistant Microorganism*

The lead resistant microorganism was isolated from collected soil sample under the stress of 10 ppm of lead solution. Revamped to the environment which is contaminated by heavy metal the strain adapted inherent cellular mechanisms to restrain Pb toxicity which made them sustain its cellular functions even under high Pb(II) concentration. By means of various staining, morphological and biochemical test, the isolated lead resistant microorganism was identified as **Bacillus cereus**.

## 3.2 *Optimum Growth Temperature*

When the microbial growth is high turbidity of a solution also increases [9]. UV reading of broth solutions inoculated with microorganism incubated at different temperatures was taken. From the absorbance reading, it was found that the growth of microorganisms increased with increase in temperature. After 40 °C reading, decreased with increase in temperature. Maximum absorbance reading obtained at 40 °C. The graphical representation of data obtained by UV analysis is shown in Fig. 1a.

## 3.3 *Optimum Growth pH*

Microbial cells utilize the nutrient from the medium and produce acidic compounds to the media. This will result in the reduction of pH in the media [10].

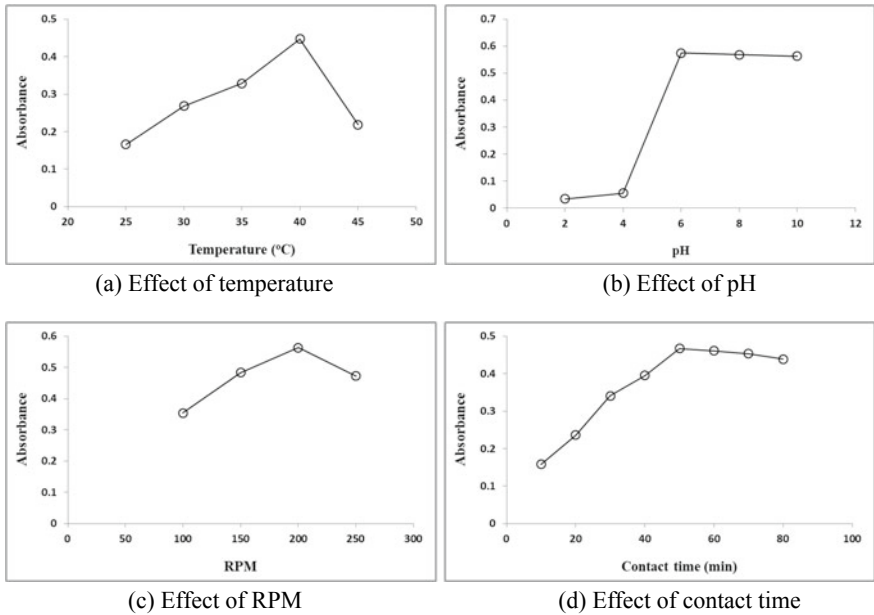


Fig. 1 Effect of parameters on optimum growth

Spectrophotometer reading was taken for broth solutions inoculated with microorganism at different pH incubated at 40 °C. From the figure showed, absorbance reading increases with increase in pH and more absorbance reading obtained at pH 6. Microbial growth increases with increase in pH and decreases after pH 6. The graphical representation of data obtained by UV analysis is shown in Fig. 1b.

### 3.4 Optimum Growth rpm

To stop the inflow of oxygen in the growing medium, the bacterial cultures are allowed to grow in cotton plugged sealed flasks. In order to enhance combining of oxygen already inside the flask with growing medium, the flasks have shaken well, which also helps to increase the surviving rate by distributing the growing medium equally to the bacterial population [10]. So, it is important to not increase the agitation rate too much by determining optimum rpm because excess agitation can create shear, which damages bacterial cells. Figure 1c shows microbial growth increases when rpm increases from 100 up to 200 rpm, and there occurred a decrease in microbial growth at optimum temperature 40 °C and at a pH of 6. This may occur due to at high rpm cause shear, which may damage the bacterial cells. The graphical representation of values obtained is shown in Fig. 1c.



### **3.5 Optimum Contact Time**

The inoculated broth solutions were shaken in Rotech shaker at 200 rpm under optimum conditions of 40 °C and pH of 6. Figure 1d shows reading obtained at regular intervals of time from 10 to 80 min. The microbial growth increases with increase in contact time, and after 50 min, there was a decline in the absorbance reading, which indicated the reduction in microbial growth [11]. This may due to microorganism attained maximum growth under these conditions. The graphical representation of the data is shown in Fig. 1d.

### **3.6 Optimum Removal Temperature**

Since removing metals is an energy dependent mechanism, the temperature of the adsorption medium is one of the main factors [12]. The lead removal percentage increased with increasing temperature. Obtained maximum lead removal at 40 °C, and there was a decrease in removal percentage after that temperature [13]. The cell wall stability, ionization and its configuration of chemical moieties are affected by the temperature. The binding sites on isolated fungal and bacterial species may be affected by all these factors resulting in the reduction in heavy metal removal [14]. The values obtained are represented graphically as shown in Fig. 2a.

### **3.7 Optimum Removal pH**

The metal speciation, as well as surface properties of cells of bacteria will get affected by pH change in the case of metal removal [15]. Figure 2b shows that the lead removal percentage augmented along with the rise of pH of the solution and maximal lead removal percentage obtained at pH 6 [13]. Accumulation of Pb (II) ions was enhanced with an increase in pH up to 6, and then it reduced with a rise in pH. The consumption of high hydroxyl ion resulted in precipitation of lead ions at pH values greater than pH = 6 in the medium. The competition of cations and protons for the same site is the reason for the reduction of metal uptake at low pH levels.

### **3.8 Optimum Removal rpm**

Metal intake is also affected by metal ions got adsorbed in active sites of the biomass resulted by the agitation or shaking diffusion of metal through a hydrodynamic boundary layer around the biosorbent surface. The shaken conditions of

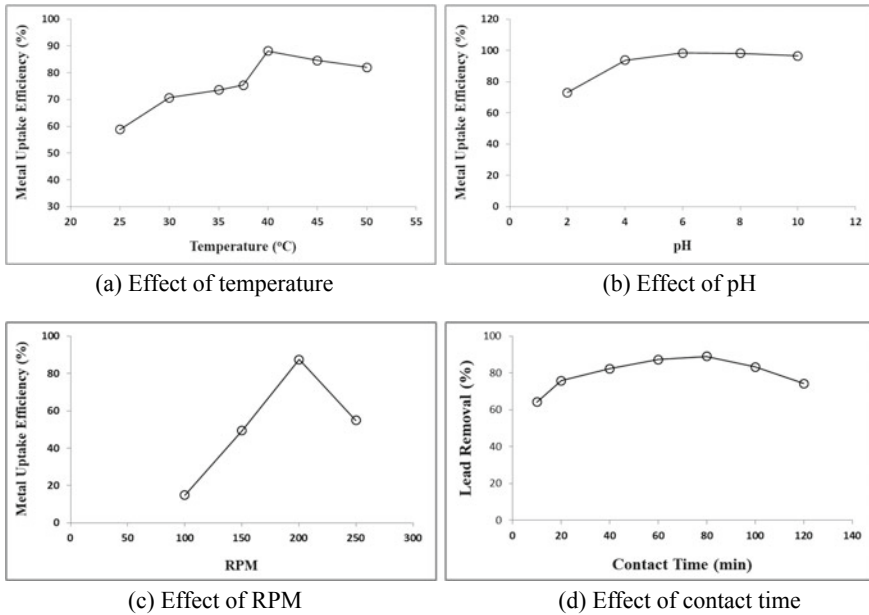


Fig. 2 Effect of parameters on removal of lead

solutes and biomass by mixing of solutes and biomass in the system subdue limitation of bulk transport of metal ions [8]. One of the vital factors in creating toxic pressure resistance to harmful metals in microorganism is contact time [16]. Figure 2c shows that the lead removal percentage ameliorating with a rise in rpm and reduces after 200 rpm. Maximum lead uptake percentage was observed at 200 rpm.

### 3.9 Optimum Contact Time

The data is shown in Fig. 2d. The experimental results showed that the percentage survival of organisms reduced with the increased presence of lead as well as with the increase of contact time [10]. Data acquired from the contact time effect on the lead uptake at various lead concentrations for the isolated strain revealed that there is an augmentation in metal uptake with raise in contact time and maximum lead uptake was observed after 80 min of exposure. This showed that with the duration of exposure, the isolate was not only resistant to lead toxicity but also had the capacity of accumulating lead. After 80 min, observed a decrease in the lead removal percentage [17]. This decrease in uptake might be due to with an increase in time, under this optimum condition's microorganism may reach saturated state, and microbial mechanism may fail to withstand the toxic action of the lead.

### 3.10 Multiple Resistance of Isolate

A potential source for the heavy metal resistant microorganisms is sampling environments which contain high concentrations of harmful metals [17]. Researchers reported that organisms isolated from heavy metal contaminated sites had resistivity to the toxicity of such metals. The lead resistant microorganism isolated from the contaminated site showed resistance to other heavy metals such as arsenic and mercury.

### 3.11 FTIR Analysis

Infrared spectra give valuable information about the chemical groups acquired by the biosorbents [18]. The main effective binding sites have been identified by FTIR by spectral comparison between native and lead adsorbed organism [11]. FTIR analysis of the sample is shown in Fig. 3. FTIR spectra display various vibrational bands representing the complex nature of the native organism. FTIR spectra of sample loaded with Pb ion showed that the peaks at 3370.83, 1558.71 and 1634.68  $\text{cm}^{-1}$ , respectively, shifted to 3371.18, 1554.67, 1634.97  $\text{cm}^{-1}$ . Alkenes, nitro compounds and amino groups are the leading contributors found after spectral analysis in microorganisms due to lead uptake. These shifts in chemical groups may be accredited to the changes in counter ions associated with amino groups, nitro compounds and alkenes groups in lead ion uptake.

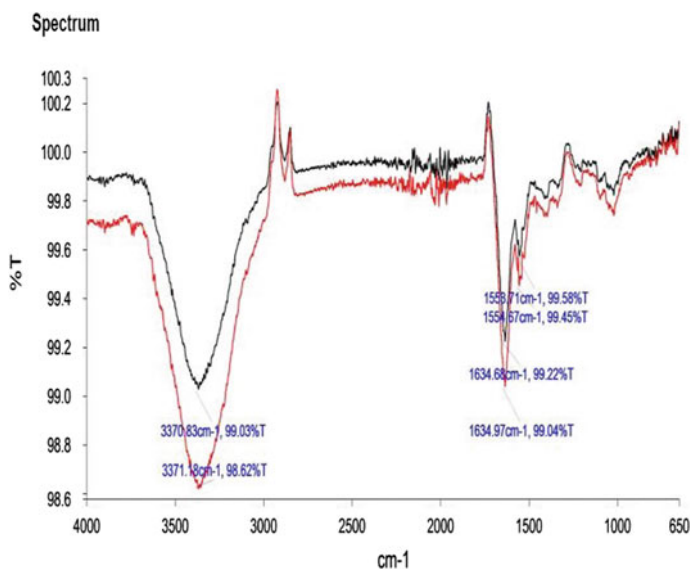


Fig. 3 FTIR analysis of the sample

## 4 Conclusion

Biological treatment is very innovative eco-friendly technology that can be used to remove harmful heavy metal from the polluted site. Lead resistant microorganisms were isolated and tested for metal tolerance with a wide range of lead concentrations. Optimization studies were conducted for growth and removal efficiency. By means of various staining, morphological and biochemical test, the isolated lead resistant microorganism was identified as **Bacillus cereus**. Growth optimums obtained for the isolated microorganism were pH of 6, at 40 °C, at 200 rpm and at a contact time of 50 min. Maximum lead removals by this microorganism were obtained at 40 °C, at pH of 6, at 200 rpm and at a contact time of 80 min. Obtained 95.58% lead removal for 10 ppm lead under optimum conditions using the isolated microorganisms. Minimum inhibitory concentration obtained was 1000 ppm. The isolated microorganism showed multiple metal resistances in addition to lead. The isolate showed resistance to zinc, arsenic and mercury. FTIR analysis of the microorganism loaded with lead and without lead carried out. The difference in the spectral analysis in the presence and absence of Pb ion binding showed that nitro compounds, amino groups and alkenes are the main contributors for the lead intake in microorganisms.

## References

1. Sharma, B., Shukla, P.: Lead bioaccumulation mediated by *Bacillus cereus* BPS-9 from an industrial waste contaminated site encoding heavy metal resistant genes and their transporters. *J. Hazard. Mater.* **401**, 123285 (2020)
2. Needs, N.P.: Protecting Children from Exposure to Lead. *Soc. Policy Rep.* **24**(1), 1 (2010)
3. Chakraborty, S., Mukherjee, A., Das, T. K., Chakraborty, S., Mukherjee, Das, A.: Biochemical characterization of a lead-tolerant strain of *Aspergillus foetidus*: an implication of bioremediation of lead from liquid media. *Int. Biodeterior* **84**,134–142 (2013)
4. Timkova, I., Sedlakova-Kadukova, J., Pristas, P.: Biosorption and bioaccumulation abilities of actinomycetes/streptomycetes isolated from metal contaminated sites. *Separations* **5**(4), 54 (2018)
5. Aslam, F., Yasmin, A., Sohail, S.: Bioaccumulation of lead, chromium, and nickel by bacteria from three different genera isolated from industrial effluent. *Int. Microbiol.*, 1–9 (2019)
6. Cao, D.J., Shi, X.D., H, Li., Xie, P.P., Zhang, H.M., Deng, J.W., Liang, Y.G.: Effects of lead on tolerance, bioaccumulation, and antioxidative defense system of green algae, *Cladophora*. *Ecotoxicol. Environ. Saf.* **112**, 231–237 (2015)
7. Abdelkrim, S., Jebara, S.H., Saadani, O., Chiboub, M., Abid, G., Jebara, M.: Effect of Pb-resistant plant growth-promoting rhizobacteria inoculation on growth and lead uptake by *Lathyrus sativus*. *J. Basic Microbiol.* **58**, 579–589 (2018)
8. Odokuma, L.O., Akponah, E.: Effect of concentration and contact time on heavy metal uptake by three bacterial isolates. *J. Environ. Chem. Ecotoxicol.* **2**, 84–97 (2010)
9. Leong, Y.K., Chang, J.S.: Bioremediation of heavy metals using microalgae: Recent advances and mechanisms. *Biores. Technol.* **303**, 122886 (2020)

10. Saranya, K., Sundaramanickam, A., Shekhar, S., Swaminathan, S.: Biosorption of mercury by *Bacillus thuringiensis* (CASKS3) isolated from mangrove sediments of southeast coast India. *Indian J. Geo-Mar. Sci.* **48**, 143–150 (2019)
11. Mahmoud, M.S., Mostafa, M.K., Mohamed, S.A., Sobhy, N.A., Nasr, M.: Bioremediation of red azo dye from aqueous solutions by *Aspergillus niger* strain isolated from textile wastewater. *J. Environ. Chem. Eng.* **5**(1), 547–554 (2017)
12. Tarekegn, M.M., Salilih, F.Z., Ishetu, A.I.: Microbes used as a tool for bioremediation of heavy metal from the environment. *Cogent Food & Agric.* **6**(1), 1783174 (2020)
13. Ameen, F.A., Hamdan, A.M., El-Naggar, M.Y.: Assessment of the heavy metal bioremediation efficiency of the novel marine lactic acid bacterium, *Lactobacillus plantarum* MF042018. *Scientific Reports* **10**(1), 1–11 (2020)
14. Congeevaram, S., Dhanarani, S., Park, J., Dexilin, M., Thmaraiselvi, K.: Biosorption of chromium and nickel by heavy metal resistant fungal and bacterial isolates. *J. Hazard. Mater.* **146**, 270–277 (2007)
15. Mane, P.C., Bhosle, A.B.: Bioremoval of Some Metals by Living Algae *Spirogyra* sp. and *Spirulina* sp. from aqueous solution. *Int. J. Environ.* **6**, 571–576 (2012)
16. Murugavelh, S.: Removal of heavy metals from waste water using different biosorbents. *Current World Environ.* **5**, 299 (2010)
17. Naik, M.M., Dubey, S.K.: Lead resistant bacteria: lead resistance mechanisms, their applications in lead bioremediation and biomonitoring. *Ecotoxicol. Environ. Saf.* **98**, 1–7 (2013)
18. Kumar, R., Sharma, A.K., Singh, P., Dhir, B., Mehta, D.: Potential of some fungal and bacterial species in bioremediation of heavy metals. *J. Nucl. Phy. Mat. Sci. Rad. A.*, 213–223 (2014)

# Overview of Physical Properties and Applications: Ferroelectric Lithium Niobate (LiNbO<sub>3</sub>)



Madhu, Muskaan Jain, and Prashant Povel Dwivedi

**Abstract** Ferroelectric lithium niobate (LiNbO<sub>3</sub>) is widely utilized in integrated and guided wave optics due to its promising optical, piezoelectric, electro-optic, elastic, photoelastic and photorefractive properties. In this paper, we studied the physical properties, synthesis of lithium niobate (LiNbO<sub>3</sub>), and therefore, the advantages and disadvantages of the synthesis techniques.

**Keywords** LiNbO<sub>3</sub> properties · Optics · Techniques

## 1 Introduction

Lithium niobate (LiNbO<sub>3</sub> or LN) is halfway significant in coordinated and guided wave optics. It is a human-made dielectric material that does not exist in nature. It was first found to be ferroelectric in 1949 [1]. Lithium niobate was blended in single crystal form and explored in detail at Bell Laboratories. Lithium niobate is a colorless solid, and it is insoluble in water. It has a three-sided crystal system, which lacks inversion symmetry and showcases ferroelectricity.

*Crystal structure:* Trigonal

*Chemical formula:* LiNbO<sub>3</sub>

*Density:* 4.65 g/cm<sup>3</sup>

*Solubility in water:* None

Lithium niobate is one of the most technologically explored crystalline ferroelectric materials due to some interesting combination of properties and characteristics exhibited by it. Based on the lithium niobate crystal, those properties lead to very promising device applications.

---

Madhu · M. Jain · P. P. Dwivedi (✉)

Department of Electronics and Communication Engineering, Manipal University Jaipur, Jaipur, Rajasthan 303007, India

e-mail: [prashant.dwivedi@jaipur.manipal.edu](mailto:prashant.dwivedi@jaipur.manipal.edu)

Lithium niobate is a transparent, electro-optic crystal, and it is known for its high Pockel's coefficients, which make lithium niobate a widely used material for experiments in nonlinear optics and also for the fabrication of Mach–Zehnder Interferometers for high-speed data transfer. Devices on lithium niobate are fabricated by diffusion-based techniques, like proton exchange and titanium diffusion [2].

The richness of large magnitude physical effects has caused lithium niobate to become widely utilized in various applications [3].

Although lithium niobate is important in several wide areas of technological significance, the details of its physical properties and its applications are not readily available in textbooks. In its place, a large number of research papers must be studied in considerable detail to gain a definitive insight into its properties and applications. It is the purpose of this paper together, basic information about the physical properties and applications of lithium niobate in one place.

## 2 Physical Properties of Lithium Niobate

Lithium niobate is available as large, transparent, single crystals with excellent electro-optical and acousto-optical properties. Therefore, it constitutes a good material substrate for several active-integrated optoelectronic devices. In fact, many devices formed on lithium niobate such as modulators, switches, polarization controllers and ring resonators have been demonstrated in the last few years [4]. Some of the important properties of the crystal are discussed, which are essential for understanding the performance of different devices that are formed utilizing lithium niobate crystal.

### 2.1 *Permittivity*

For lithium niobate crystal, the relationship between the electric flux density and electric field is represented as  $D = \epsilon E$ , where  $\epsilon$  is a second-rank permittivity tensor.

### 2.2 *Electro-Optic Effect*

The electro-optic effect describes the changes in the optical properties of a material with the application of an electric field. The electro-optic effect is always associated with those crystals which are lacking a center of symmetry. Lithium niobate's electro-optic coefficients are the largest that are available in crystalline optical materials.

### 2.3 Piezoelectric Effect of LN

The lithium niobate crystal is also a piezoelectric solid. An induced polarization and surface charge appear under the applied mechanical stress. The relationship between induced polarization and applied stress is denoted as  $P = d\sigma$ , where  $P$  is the induced polarization,  $d$  is the third-rank piezoelectric tensor, and  $\sigma$  is the stress applied.

### 2.4 Pyroelectric Effect

Pyroelectric effect is related to the change of the spontaneous polarization as a result of the change in its temperature.

The pyroelectric effect is very common for those crystals lacking inversion symmetry in their structure. It is a straightforward effect relative to other stress related effects such as the piezoelectric and the elasto-optic effects and has a single non-vanishing coefficient related to a unique axis, that is, the  $z$ -axis for lithium niobate crystal. Hence, the pyroelectric effect is not observed in the  $x$ - or  $y$ -directions of the lithium niobate crystal. The two factors contributed to this effect: The first one being the pyroelectric effect itself due to a temperature-dependent electric polarization variation and the second one being associated with the change of shape of the crystal due to temperature variation, and subsequently by reverse piezoelectric effect, electric polarization of the crystal is modified.

### 2.5 Linear Electro-Optic Effect (Pockels Effect)

The linear electro-optic effect (Pockels effect) is shown in a solid by a change within the index of refraction as a function of applied electric field.

### 2.6 Photovoltaic Effects

The dark conductivity of congruent lithium niobate crystal at room temperature is  $<10^{-18} \Omega^{-1} \text{ cm}^{-1}$ . However, for light incidence with photon energy larger than the band gap of lithium niobate, free electron hole pairs are generated and transferred to the surface due to the built-in electric field in the crystal. The photovoltaic current density is proportional to the illumination intensity and absorption coefficient  $\alpha$ .



## 2.7 Photoelastic Effects

The volumetric change of the crystal lattice, due to the strain, creates modification of the optical properties of the crystal which is usually known as the photoelastic effect. Generally, it is defined as a change in the refractive index due to the mechanical strain in the material.

## 2.8 Nonlinear Optical Effects

Nonlinear optical effect is associated with the fact that the relation between the induced polarization ( $P$ ) to the external electric field ( $E$ ), applied across the lithium niobate crystal, is nonlinear.

# 3 Applications of Lithium Niobate

Applications that use the large electro-optic coefficients of lithium niobate are optical modulation and Q-switching of infrared wavelengths and applications that utilize the large nonlinear  $d_{33}$  coefficient of  $\text{LiNbO}_3$  include optical parametric oscillation (OPO), difference frequency mixing to generate tunable infrared wavelengths and second harmonic generation (SHG). Lithium niobate is mainly effective for the second harmonic generation of low-power laser diodes in the 1.3–1.55  $\mu\text{m}$  range. Due to various extraordinary properties of lithium niobate, it finds a lots of device applications. Till now numerous papers were published, and many device schemes and applications were patented based on LN crystals. Here we are going to discuss some specific device applications of lithium niobate.

## 3.1 Basic Waveguide Elements

Waveguides formed by in-diffusion of transition elements, mainly titanium, in  $\text{LiNbO}_3$  are the most widely used technique for waveguide formation in lithium niobate and have several important applications. Basic waveguide elements such as linear polarizer, lens and Bragg grating can be fabricated with simple technical steps. For example, lenses of desired types are formed on proton exchanged planar waveguides. The proton exchange method includes large refractive index variations over the processed regions which can produce short focal length and hence acts as lens. Proton exchange technique is also useful for fabricating linear polarizers using the anisotropic refractive index modifications of TE and TM polarizations.

### 3.2 *Basic Electro-Optic Devices*

Some basic widely used electro-optic devices fabricated on channel waveguides are modulators, directional couplers, switches, interferometers, etc. In general, the abovementioned electro-optic devices use single mode fibers, and the control voltage is 2–10 V with the control frequency limitation of  $\approx 20$  GHz or 10 Gbps for digital applications. Also these devices show very stable and predictable characteristics in different environments with huge lifetimes.

### 3.3 *Basic Acousto-Optic Devices*

Acousto-optic devices are based on the acousto-optic property of the lithium niobate crystal. Generally, surface acoustic waves (SAW), produced by interdigital electrode transducers over the surface of the crystal, are utilized as the modulating signal in these devices. Usually, these devices are used as input/output sections in optical fiber systems.

### 3.4 *Nonlinear Optical Devices*

The great advancement in the quasi-phase matching technique with lithium niobate crystal paved its dominance for fabricating nonlinear optical devices. In lithium niobate crystal, the value of the nonlinear coefficient  $d_{33}$  is the highest compared to other competing nonlinear optical crystals, and hence, it is most preferred in comparison with other nonlinear crystals.

Nowadays, quasi-phase matching (QPM) in periodically structured crystals has become significant importance in nonlinear optics. Meanwhile, QPM crystals find numerous of applications such as second harmonic generation, optical parametric oscillators and difference frequency generation [5]. Quasi-phase matching devices based on ferroelectric crystals are extensively used as highly efficient optical frequency conversion devices.

Almost all nonlinear optical devices are based on periodically poled lithium niobate (PPLN) bulk materials and planar waveguides. Nonlinear optical devices formed by waveguides in periodic structures have the advantages of fetching the high optical power density inside the waveguides. This is of great importance as efficient nonlinear effects give rise to the associated periodic modulation of nonlinear coefficients which finally leads to the quasi-phase matching conditions. Hence, it is expected that high efficiency frequency conversion can be achieved. Here we are going to discuss some of the specific nonlinear devices.

Second harmonic generator (SHG) is most important among all nonlinear optical devices as it can be useful for producing blue and green laser radiations. These laser

light beams from small dimensions sources are of great interest for applications such as optical data storage, displays and medicine. The second harmonic generation tuning curve is usually measured to judge the final quality of a QPM device, as it provides direct estimation of overall performance of the device [6].

All-optical quasi-phase matched wavelength converters based on second-order nonlinearity in periodically poled lithium niobate have attracted increasing attention. Over the past few years, research on cascaded second-order nonlinear interactions in QPM-PPLN has been growing fast to satisfy the needs of high-speed and large capacity optical networks [7].

Optical parametric oscillator is a device in which an incident laser beam of frequency  $\omega_p$  generates two waves, the signal of frequency  $\omega_s$  and the idler of frequency  $\omega_i$ . Periodically poled lithium niobate acts as the nonlinear material and is placed inside the optical cavity of the device so that resonance of the longitudinal modes of the signal and idler wave can take place. When the power of the incident wave is equal to or greater than the threshold power, which is equal to the losses of the signal and idler waves, the parametric oscillation is obtained. The main benefit of the periodically poled lithium niobate (PPLN)-based device is the possibility to produce efficient laser radiation of various frequencies from the original input frequency and also the possibility of tuning these frequencies by controlling the phase matching conditions.

Difference frequency generation finds applications in producing mid-infrared laser radiations, which is needed for high resolution molecular spectroscopy and also for detection of impurity molecules. Emission in the range of 2000–5000 nm can be generated by the difference of frequencies of two lasers.

### ***3.5 Holographic Applications Based on Photorefraction***

Lithium niobate exhibited the photorefractive effect, although unwanted in most of the photonic applications has been utilized in applications like holographic recording, optical data storage, etc. The holographic recording is done by placing the LN crystal at the position where fringe pattern is formed by interference of two coherent light waves.

These holograms have significant features as discussed in the following. First of all, these holograms can have 100% diffraction efficiency, which is essential for some applications where the transformed wave should have sufficiently high intensity. Secondly to reconstruct the image from the hologram with the same recording wavelength, the incidence angle must be the same as during recording, which is known as Bragg selectivity condition. Moreover, several holograms can be recorded in a single bulk of the crystal, sometimes which is defined as hologram multiplexing. These all holograms are characterized by their own fundamental grating vectors. Two holograms stored with different recording angle or with a different wavelength will have different grating vectors, hence which means they

will not be mixed. So each hologram can be read separately. Clearly, these specific characteristics make them suitable for applications in optical applications.

Based on the abovementioned hologram recording technique, holographic digital memory can be found which is very promising. These memories are based on the recording of large number of holographic pages, containing bits, in the majority of the crystal. During the process of recording, the signal beam is first modulated according to the data bits. The modulated signal and a reference beam are made to interfere over some desired region of the crystal bulk, and the hologram is recorded. Interference with different reference beams for all the holograms gives the key for encoding each hologram data page during the reading of the data. The Bragg selectivity allows independent readout of each page corresponding to the reference beam for recording. Readout of the desired hologram page is performed only once, when the required reference beam is incident on the medium. The part of this beam diffracted by the hologram is detected finally in a CCD device. Digital memories based on  $\text{LiNbO}_3$  with smaller sizes are possible with the advancement of technology.

The associated photorefraction can partially erase the hologram. This can be avoided by considering lithium niobate crystal that are doubly doped with Fe and Mn. Recording of the hologram is achieved by a red (633 nm) beam after exciting the doubly doped lithium niobate crystal by an ultraviolet (365 nm) radiation, which finally produces a stable digital holographic memory.

## 4 Conclusion

In this paper, the discussion is focused on lithium niobate. In this paper, an overview of the basic physical properties of lithium niobate is given. Further, some important applications are illustrated.

## References

1. Matthias, B.T., Remeika, J.P.: *Phys. Rev.* **76**, 1886–1887 (1949)
2. Saha, S., Yohanes, S.S., Jun, D., Danner, A., Tsang, M.: *Fabrication and Characterization of Optical Devices on Lithium Niobate on Insulator Chips @ 2015 ICMAT* (2015)
3. Weis, R.S., Gaylord, T.K.: *Lithium Niobate: Summary of Physical Properties and Crystal Structure. Appl. Phys. A* **37**, 191–203 (1985)
4. Armenise, M.N.: *Fabrication techniques of lithium niobate waveguides. IEE proceedings*, **135** (2), April (1988)
5. Ridderbusch, H., Klein, M.E., Gross, P., Lee, D., Meyn, J., Wallenstein, R.: *Electro-optic modification of second-harmonic phase-matching spectra in segmented periodically poled  $\text{LiNbO}_3$ . J. Opt. Soc. Am. B* **19**(2), February (2002)

6. Pandiyan, K., Sook Kang, Y., Lim, H.H., Kim, B.J., Cha, M.: Nondestructive quality evaluation of periodically poled lithium niobate crystals by diffraction. **17**(20), published 21 September 2009
7. Ahlawat, M., Tehranchi, A., Pandiyan, K., Cha, M., Kashyap, R.: Tunable all-optical wavelength broadcasting in a PPLN with multiple QPM peaks. **20**(24), 19 November 2012

# A Study on Austenitic Stainless-Steel Machining by Wire EDM



Shatarupa Biswas, Yogesh Singh, and Manidipto Mukherjee

**Abstract** Austenitic stainless steel (ASS) is a special type of stainless steel (SS). Among the five types of SS (such as austenitic SS, martensitic SS, ferritic SS, duplex SS, and precipitation hardening SS), ASS has been majorly used in the chemical industry, food industry, aircraft industry, building nuclear reprocessing plants, etc. due to its excellent properties (such as high ductility and durability, excellent corrosion resistance). ASS contains 16–30% chromium (Cr), 2–20% nickel (Ni) and sometimes in addition of manganese (Mn), nitrogen (N<sub>2</sub>), etc. This steel is difficult-to-cut by the conventional process (such as lathe, drill, etc.) as compared to the other types of SS. Because it has low heat conductivity and high built-up edge (BUE) formation. Whereas it can be machined easily by wire electrical discharge machining (wire EDM) which is a contact (between wire and work piece)-free process. During the machining time, electrical energy creates a plasma channel between anode and cathode. That converts electrical energy into thermal energy which generates a high temperature between the wire and work piece, and the temperature range is 8000–12,000 °C. For this reason, metal is eroded from the work piece. This review has been carried out on ASS machining by wire EDM and improvement of response parameters (such as material removal rate, surface roughness, Kerf width). Also, the review shows the previous works of researchers in this field. Furthermore, this review paper concludes with a discussion and give an insight about some upcoming research scopes.

**Keywords** Austenitic stainless steel · Wire EDM · Input variables · Response parameters

---

S. Biswas (✉) · Y. Singh  
NIT Silchar, Silchar, Assam 788010, India

M. Mukherjee  
CAMM, CSIR-CMERI, Durgapur, West Bengal 713209, India

## 1 Introduction

Austenitic stainless steel (ASS) is basically non-magnetic allotrope iron. When alpha ( $\alpha$ ) iron's (ferrite) temperature is increased from 912 to 1394 °C, then the phase changes from body-centered cubic (bcc) to the face-centered cubic (fcc) formation; this formation is known as gamma ( $\gamma$ ) iron or ASS [1]. It is an alloying component which contains 16–30% chromium (Cr), 2–20% nickel (Ni) and also sometimes in addition manganese (Mn), nitrogen (N<sub>2</sub>). ASS properties include such as good formability, weldability, ductility, and excellent toughness even at cryogenic temperature (−150 to −273 °C) to red hot temperatures (above 460 °C). Basically, this steel is corrosion resistant among all grades of stainless steel (SS). Because ASS has a high % of Cr and Ni content compared to other SS grades. For this reason, today ASS is most favored and majorly used (such as in chemical industry, food industry, aircraft industry, building nuclear-reprocessing plants) compared to other steel grades. Generally, ASS is categorized into 200 and 300 series, and it is very difficult-to-cut in the conventional processes (such as lathe, milling, drill) due to their high work hardening, low heat conductivity and high built-up edge (BUE) formation. So for machining of ASS, wire electrical discharge machine (Wire EDM) may be an option. It is a non-traditional machining process, i.e., where the tool and the work piece do not make any direct contact [2, 3]. Wire EDM mostly used to cut difficult profiles of materials. This cutting process is based on electro-thermal mechanism. The first commercially manufactured WEDM was made by USSR in the year 1967 [4]. In WEDM, the tool is attached to the negative (−ve) terminal, and the workpiece is attached to the positive (+ve) terminal. Deionized water is used as a dielectric fluid because it offers a good cooling rate and low viscosity [2, 5]. Due to the electrical flow, the work piece liberates metal ion and wire liberates +ve ions. At this stage, deionized water also breaks into +ve and −ve ions. These ions are combined together and create a spark between the wire and work piece [6]. A micro-level gap (0.025 mm to 0.05 mm) is maintained between the wire and the work piece [7]. The gap is used to generate the spark which tends to erode or melt the work piece on the tool's forward approach due to the generation of a high temperature of 8000 to 11,700 °C [8]. The moving wire is controlled by two pulleys (driven and take up), and normally the wire is made of zinc or brass or molybdenum, etc. Generally, the wire diameter's range varies from 0.05 mm to 0.30 mm [9–11]. Figure 1a shows the metallic structure (fcc) of ASS, and Fig. 1b shows the cutting mechanism of wire EDM.

Though many studies have been reported on wire EDM with steels, limited studies have been observed about ASS machining. The objective of this study is to provide an overall view of ASS machining on wire EDM and improvement of response parameters (such as material removal rate, surface roughness, Kerf width) with respect to input variables (such as current, voltage, pulse time).

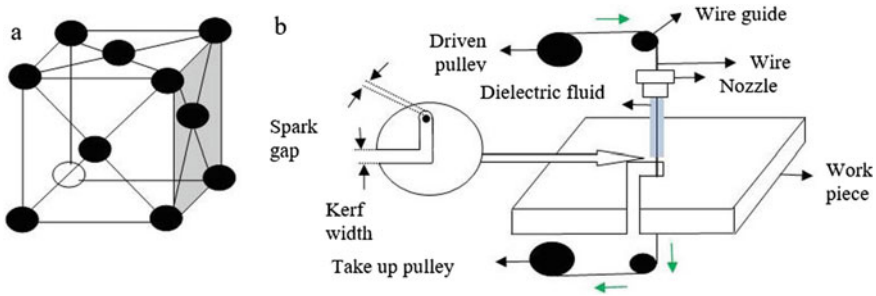


**Fig. 1** a Metallic structure of ASS (fcc); b cutting mechanism of wire EDM

## 2 Austenitic Stainless Steel (ASS)

The most common industrial SS grade is ASS, and it is non-magnetic steel [12]. When extra Ni is added to SS, then metallurgical structure changes from bcc to fcc. This steel is mostly used for producing industrial equipment, surgical equipment, nuclear vessel, etc. [13]. In industries, 200 series (such as AISI 201, AISI 202, AISI 205) and 300 series (such as SS 301, SS 302, SS 303, SS 304, SS 304L, SS 316, SS 316L) grades are mainly used [14]. The 'L' grade has extra corrosion resistance. Because it has a high % of Cr and Ni and low C% (<0.03) [1]. ASS has some excellent mechanical properties such as good corrosion and oxidation resistance, and it offers low creep-resistant properties as well [15]. That's why ASS is very popular and extensively used compared to other SS grades. Some ASS's chemical composition and properties are shown in Table 1.

## 3 Parameters of Wire EDM

Generally, parameters are two types, i.e., input variables and response parameters. For WEDM, response parameters are dependent on input variables. Different types of parameters (input and response) are described below.

### 3.1 Input Variables

For machining, several types of input variables are used to control the response parameters. Some input variables are listed below.

**Pulse on time ( $T_{on}$ ):** It is described as when the voltage is applied between the gap of work piece and the wire, then the discharge occurs (with the help of deionized water). The measuring unit of  $T_{on}$  is microsecond ( $\mu s$ ).



**Table 1** Grades, composition, and properties of some ASS

AISI number	UNS number	EN number	Chemical composition (% wt.)	Mechanical properties	Physical properties
301	S30100	1.4310	Cr 16.00–18.00, Ni 6.00–8.00, Mn 2.00, C 0.15, S 0.03, P 0.045, Si 1.00 (according to AZO materials)	Ultimate tensile strength 758 Mpa, yield strength 276 MPa, Poisson's ratio 0.27–0.28, hardness Rockwell B86 (according to AZO materials)	Density 7.88 g/cm <sup>3</sup> , Elastic modulus 193 Gpa, melting point temp. 1399–1421 °C (according to united performance metals)
302	S30200	1.4310	Cr 17.00–19.00, Ni 8.00–10.00, Mn 2.00, C 0.15, S 0.03, P 0.045, Si 1.00 (according to AZO materials)	Ultimate tensile strength 620 Mpa, yield strength 275 MPa, Poisson's ratio 0.27–0.3, Hardness Rockwell B85 (according to AZO materials)	Density 7.90 g/cm <sup>3</sup> , elastic modulus 19 Gpa melting point temp. 1399–1421 °C (according to American Metals co.)
303	S30300	1.43050	Cr 17.00–19.00, Ni 8.00–10.00, Mn 2.00, C 0.10, S 0.35, Si 1.00 (according to Matmatch)	Ultimate tensile strength 690 Mpa, yield strength 415 Mpa, Poisson's ratio 0.25, hardness Rockwell B96 (according to Matweb)	Density 7.80 g/cm <sup>3</sup> , modulus of elasticity 193 Gpa, melting point temp. 1400–1420 °C (according to Matweb)
304L	S30403	1.4307	Cr 18.00, Ni 8.00, Mn 2.00, N 0.10, C 0.03, S 0.03, Si 0.75, P 0.045 (according to Lenntch)	Ultimate tensile strength 485 Mpa, yield strength 170 Mpa, Poisson's ratio 0.28, hardness Rockwell B92 (according to JSL)	Density 8.03 g/cm <sup>3</sup> , modulus of elasticity 195 Gpa, melting point temp. 1400–1450 °C (according to Matweb)
316	S31600	1.4401	Cr 16.00–18.50, Ni 10.00–14.00, Mn 2.00, Mo 2.00–3.00, Si 1.00, N 0.10, C 0.08, P 0.05, S 0.03 (according to Matmatch)	Ultimate tensile strength 515 Mpa, yield strength 205 Mpa, Poisson's ratio 0.27–0.28, hardness Rockwell B95 (according to JSL)	Density 7.99 g/cm <sup>3</sup> , modulus of elasticity 193 Gpa, melting point temp. 1371–1399 °C (according to AK steel)

(continued)

**Table 1** (continued)

AISI number	UNS number	EN number	Chemical composition (% wt.)	Mechanical properties	Physical properties
316L	S31603	1.4404	Cr 16.00–19.00, Ni 10.00–15.00, Mn 2.00, Mo 2.00–3.00, Si 1.00, C 0.03, S 0.03, P 0.05 (according to Matmatch)	Ultimate tensile strength 485 Mpa, yield strength 170 Mpa, Poisson’s ratio 0.27–0.3, hardness Rockwell B95 (according to JSL)	Density 7.99 g/cm <sup>3</sup> , modulus of elasticity 193 Gpa, melting point temp. 1390–1440 °C (according to American Metals co.)

Notes AISI—American Iron and Steel Institute, UNS—Unified Numbering System, EN—European Norms

**Pulse off time (T<sub>off</sub>):** It is described as the total duration of non-discharge time, i.e., when no voltage is applied between the wire and the work piece. Its measuring unit is microsecond (μs).

**Wire feed (WF):** It is expressed as a unit of wire length passing through a point per unit time, and it’s measuring unit is millimeter/minute.

**Wire tension (WT):** It is expressed as the tensile force of wire in between the upper nozzle and the lower nozzle. WT is controlled by the help of different pulleys. It’s measuring unit is either gram (gm) or Newton (N).

**Servo voltage (SV):** The working voltage is known as SV. It’s measuring unit is volt (v).

**Water pressure (WP):** It is expressed as an amount of perpendicular force, applied on an object per unit area and it’s measuring unit is Pascal (Pa).

### 3.2 Response Parameters

Various types of response parameters are presented below.

**Material removal rate (MRR):** It can be described as the volume of material eroded per time. It is an important output response. Because it gives the cutting rate (either slow or fast) which is very important to control productivity. Its measuring unit is millimeter<sup>3</sup>/minute. MRR is calculated by using this Eq. (1) [16, 17].

$$MRR = \text{cutting velocity} \times \text{kerf width} \times \text{thickness of job} \quad (1)$$

**Surface roughness (SR):** It gives the quality of the product, and it is important to assemble the product. SR is calculated by the deflection of the normal vector (direction of a vector) to a real surface. If the measured deflection is huge, then the surface quality is described as rough, and if the measured deflection is little, then

the surface quality is described as smooth. Its measuring unit is micrometer ( $\mu\text{m}$ ), and it is measured by the surface roughness tester [18].

**Kerf width (KW):** After machining, the cutting width of material is known as KW and it controls the dimensional correctness of the machining part [19]. Its measuring unit is micrometer ( $\mu\text{m}$ ), and it is measured by optical microscope [17]. KW can be calculated by using following Eq. (2) [20].

$$\text{KW} = \text{wire diameter} + (2 \times \text{Spark gap}) \quad (2)$$

**Wire wear rate (WWR):** It is described as the wire weight loss (WWL) to the wire initial weight (IWW). The WWR can be calculated by using the following Eq. (3) [21].

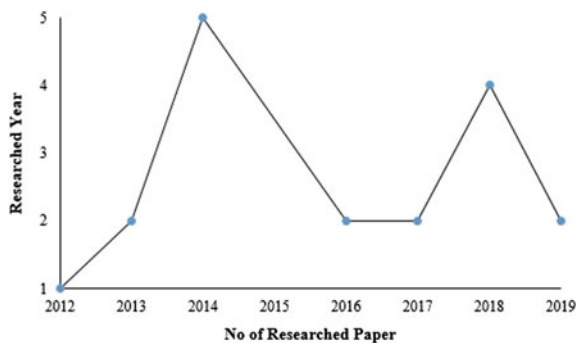
$$\text{WWR} = \frac{\text{WWL}}{\text{IWW}} \quad (3)$$

**Over cut (OC):** After cutting, the slot width becomes higher than the wire diameter because of the spark. If wire diameter is subtracted from KW, then the portion is called OC. Its measuring unit is millimetre (mm). OC can be calculated by using the following Eq. (4) [22].

$$\text{OC} = \frac{\text{KW} - \text{wire diameter}}{2} \quad (4)$$

This paper reviews some previous ASS machining on WEDM and shows the parametric optimization. Figure 2 shows a graphical representation of the previous researched year with number of previous research paper published on ASS machining by WEDM.

**Fig. 2** Previous research year with number of the previous research paper plots on ASS machining



## 4 A Comprehensive Summary of Earlier Research

See Table 2.

**Table 2** Summary of earlier research on ASS machining on WEDM

Year	Author	Work piece	Wire	Input variables	Responses	Remarks
2012	Lingadurai et al. [13]	SS 304	Brass	$T_{on}$ , $T_{off}$ , WF, GV	MRR, SR, KW	It is shown that the gap voltage (GV) is the most effective process parameter to get maximum MRR (0.0511 g/min). For finding minimum SR (1.5 $\mu$ m) and minimum KW (0.333 mm), WF and $T_{on}$ are the important input variables
2013	Durairaj et al. [23]	SS 304	Brass	GV, $T_{on}$ , $T_{off}$ , WF	SR, KW	It is discovered that when used Taguchi technique then minimum SR value is 2.02 $\mu$ m and minimum KW value is 0.289 mm. For using grey relational analysis, minimum SR value is 0.7088 $\mu$ m and minimum KW value is 0.9175 mm
2013	Geetha et al. [24]	SS 304	Brass	$T_{on}$ , $T_{off}$ , WT, WP	SR	It is shown that when $T_{on}$ (114 $\mu$ s), $T_{off}$ (60 $\mu$ s), WT (7gm), WP (8 kg/cm <sup>2</sup> ) then SR is minimum (1.42 $\mu$ m)
2014	Khan et al. [25]	SS 304	–	$T_{on}$ , $T_{off}$ , C	KW, SR	It is shown that when $T_{on}$ (15 $\mu$ s), $T_{off}$ (3 $\mu$ s), current, i.e., C (2 amp) then SR is minimum (2.88 $\mu$ m) for TT and when $T_{on}$ (15 $\mu$ s), $T_{off}$ (5 $\mu$ s), C (3 amp) then KW is minimum

(continued)

**Table 2** (continued)

Year	Author	Work piece	Wire	Input variables	Responses	Remarks
						(0.210 mm) for TT. But for GRA technique, SR (0.371 mm) and KW (0.333 mm) are minimum when $T_{on}$ (25 $\mu$ s), $T_{off}$ (3 $\mu$ s), C (4 amp)
2014	Paliwal et al. [26]	SS 302	Molybdenum	$T_{on}$ , $T_{off}$ , C	KW, SR	It is found that when C (3 amp), $T_{on}$ (15 $\mu$ s), $T_{off}$ (4 $\mu$ s), then KW is minimum (0.236 mm). When C (3 amp), $T_{on}$ (20 $\mu$ s), $T_{off}$ (5 $\mu$ s), then SR is minimum (3.25 $\mu$ m)
2014	Raju et al. [27]	SS 316L	Brass	$T_{on}$ , C, SV, WT	SR	In this study, it is found that $T_{on}$ is the most significant factor for finding minimum SR (1.54 $\mu$ m) when $T_{on}$ (15 $\mu$ s), C (9 amp), SV (5 v), WT (12 m/min)
2014	Nayak and Mahapatra [28]	SS 304	Broncocut-W	PT, TA, $T_{on}$ , C, WF, WT	AE, SR, CS	It is shown that taper cutting is a difficult operation for cutting deep slots with multiple angle. When $T_{on}$ (14 $\mu$ s), C (32 amp), WF (120 mm/s), WT (16 N) are set as the input variables then shows minimum SR (2.15 $\mu$ m) and maximum CS shows for $T_{on}$ (18 $\mu$ s), C (24amp), WF (150 mm/s), WT (16 N)
2014	Mathew et al. [29]	SS 304	Brass	$T_{on}$ , $T_{off}$ , WF,	MRR, SR	It is found that $T_{on}$ is a most significant parameter for finding

(continued)

**Table 2** (continued)

Year	Author	Work piece	Wire	Input variables	Responses	Remarks
				GV, WT, WP		maximum MRR (15.423 mm <sup>3</sup> /min) and minimum SR (1.71 μm)
2016	Kumar et al. [30]	SS 304	Brass, Diffused wire	T <sub>on</sub> , T <sub>off</sub> , SV	MRR	It is discovered that when used diffused wire then shows maximum MRR (11.18 mm <sup>3</sup> /min). But when used brass wire then MRR is 10.97 mm <sup>3</sup> /min. For both cases T <sub>on</sub> (125 μs), T <sub>off</sub> (45 μs), and SV (35 v), respectively
2016	Bharathi et al. [31]	SS 304	Brass	T <sub>on</sub> , T <sub>off</sub> , WF, SV	MRR, SR, KW	It is found that when SV (60 v), T <sub>on</sub> (4 μs), T <sub>off</sub> (4 μs), WF (5 m/min) then SR is minimum (1.5 μm). When SV (50 v), Ton (4 μs), T <sub>off</sub> (6 μs), WF (5 m/min), then KW is minimum (0.333 mm). But when SV (50 v), T <sub>on</sub> (6 μs), T <sub>off</sub> (4 μs), WF (7 m/min), then MRR is maximum (0.0511 g/min)
2017	Suresh et al. [32]	SS 304	Brass, Zinc coated brass	T <sub>on</sub> , T <sub>off</sub> , WT, WF	MRR	It is found that for finding maximum MRR, Zn-coated brass wire (MRR value is 98.08 mm <sup>3</sup> /min) is better than brass wire (MRR value is 61.83 mm <sup>3</sup> /min)
2017	Nayak and Mahapatra [33]	SS 304	Broncocut-W	PT, TA, T <sub>on</sub> , C, WF, WT	AE, SR, CS	It is found that for finding minimum SR (2.145 μm) and maximum CS (1.66 mm/min) T <sub>on</sub> and C are the most significant parameters

(continued)

**Table 2** (continued)

Year	Author	Work piece	Wire	Input variables	Responses	Remarks
2018	Babu and Subbaratnam [34]	SS 304	Molybdenum	$T_{on}$ , $T_{off}$ , C, WF	MRR	It is invented that when $T_{on}$ (35 $\mu$ s), $T_{off}$ (10 $\mu$ s), C (3amp), WF (2 m/min), then MRR is maximum (25.23 mm <sup>3</sup> /min)
2018	Ugrasen et al. [35]	SS 304	Molybdenum	$T_{on}$ , $T_{off}$ , C, BS	MRR, SR	In this study, it is observed that $T_{on}$ has more effect than other parameters for finding minimum SR (1.76 $\mu$ m) and for finding maximum MRR (17.15 mm <sup>2</sup> /min), C and BS have a significant effects
2018	Choudhuri et al. [36]	SS 304	Brass	$T_{on}$ , $T_{off}$ , C, SV, WT	SR, RLT	It is discovered that $T_{on}$ (0.35 $\mu$ s), $T_{off}$ (15 $\mu$ s), C (160 amp), V (30 v) and WT (0.6 kg) are the optimal parameters for finding minimum SR (1.851 $\mu$ m) and $T_{on}$ (0.35 $\mu$ s), $T_{off}$ (30 $\mu$ s), C (220 amp), V (60 v), WT (1.2 kg) are the optimal parameters for finding minimum RLT (5.26 $\mu$ m)
2018	Padmavathi et al. [37]	SS 316	–	$T_{on}$ , $T_{off}$ , WF, WT, C	MRR, SR	It is observed that C, $T_{on}$ both are the most effective input variables for finding maximum MRR (25.5 mm <sup>2</sup> /min) and minimum SR (3.20 $\mu$ m)
2019	Ishfaq et al. [38]	SS 304	Molybdenum	SV, DS, C, NOD	SR, CS, KW	It is invented that maximum CS (2.62 mm/min), minimum SR (4.47 $\mu$ m) and KW (0.32 mm) shows for C (3 amp) and SV

(continued)

**Table 2** (continued)

Year	Author	Work piece	Wire	Input variables	Responses	Remarks
						(50 v) which are effective parameters for finding the above responses
2019	Bhatt and Goyal [12]	SS 304	Copper	$T_{on}$ , $T_{off}$ , WT, SG, WF, GV	MRR, SR	It is discovered that when $T_{on}$ (118 $\mu$ s), $T_{off}$ (50 $\mu$ s), WT (10 kg), WF (5 mm/sec) and GV (60 v) then shows maximum MRR (3.705 mm <sup>3</sup> /min) and when WT (15 kg) and GV (40 v), $T_{on}$ (106 $\mu$ s), $T_{off}$ (60 $\mu$ s), WF (2 mm/sec) then shows minimum SR (0.177 $\mu$ m)

## 5 Conclusions

From the entire study, it is found that most of the previous work has been done with ASS 300 series on WEDM. The following conclusions are observed after study:

- $T_{on}$ ,  $T_{off}$ , WF, WT, and C are the commonly used input variables in WEDM for ASS machining. MRR, SR, and KW are the major measured parameters.
- Among the 300 series of ASS, 304 grade is mainly used as a work piece, and maximum researchers used brass wire as a cutting tool.
- Zn-coated brass wire is used: It is observed that SS 304 shows maximum MRR (98.08 mm<sup>3</sup>/min).
- Molybdenum wire as a cutting tool: It is observed that SS 304 shows minimum KW (0.32 mm), and the input variables are C (3 amp) and SV (50 v), respectively.
- Copper wire as a cutting tool: It is observed that SS 304 shows minimum SR (0.177  $\mu$ m) when is used as a cutting tool then input variables are  $T_{on}$  (106  $\mu$ s),  $T_{off}$  (60  $\mu$ s), WF (2 mm/sec), WT (15 kg), and GV (40 v), respectively.
- SS 302 and SS 316L both are rarely used material in previous work. When molybdenum wire is used as a tool, then SS 302 shows minimum KW (0.236 mm) then C (3 amp),  $T_{on}$  (15  $\mu$ s),  $T_{off}$  (4  $\mu$ s) respectively, and SR (3.25  $\mu$ m) shows minimum then C (3 amp),  $T_{on}$  (20  $\mu$ s),  $T_{off}$  (5  $\mu$ s), respectively.
- SS 316L shows minimum SR (1.54  $\mu$ m) when  $T_{on}$  (15  $\mu$ s), C (9 amp), SV (5 v), WT (12 m/min), respectively.



**Acknowledgements** The authors would like to recognize the support of the Department of Mechanical Engineering, NIT Silchar, India, and CSIR-CMERI, Durgapur, India.

## References

1. Kaladhar, M., Venkata Subbaiah, M.K., Srinivasa Rao, C.H.: Machining of austenitic stainless steels—a review. *Int. J. Mach. Mach. Mater.* **12**, 178–192 (2012)
2. Gowthaman, P.S., Gowthaman, J., Nagasundaram, N.: A study of machining characteristics of AISI 4340 alloy steel by wire electrical discharge machining process *Mater. Today Proc.*, 1–6 (2019)
3. Prakash, J.U., Juliya, S.J., Pallavi, P., Moorthy, T.V.: Optimization of Wire EDM Process Parameters for Machining Hybrid Composites (356/B 4 C/Fly Ash) using Taguchi Technique *Mater. Today Proc.*, **5**, 7275–7283 (2018)
4. Shanmuga Prakash, R., Sivakumar, M., Jeevaraja, M., Saravanan, G.: Review on wire electrical discharge machining of die and tool grade steels. *Int. J. Appl. Eng. Res.* **10**, 521–527 (2015)
5. Raju, P., Sarcar, M.M.M., Satyanarayana, B.: Optimization of Wire Electric Discharge Machining Parameters for Surface Roughness on 316 L Stainless Steel Using Full Factorial Experimental Design. *Procedia Mater. Sci.* **5**, 1670–1676 (2014)
6. Dhobe, M.M., Chopde, I.K., Gogte, C.L.: Investigations on surface characteristics of heat treated tool steel after wire electro-discharge machining. *Mater. Manuf. Process.* **28**, 1143–1146 (2013)
7. Kumar, A., Kumar, V., Kumar, J.: Experimental investigation on material transfer mechanism in WEDM of pure titanium (Grade-2), *Adv. Mater. Sci. Eng.* 1–21 (2013)
8. Asgar, M.E., Singholi, A.K.S.: Parameter study and optimization of WEDM process: A Review. *Mater. Sci. Eng.* **404**, 1–6 (2018)
9. Sharma, N., Khanna, R., Gupta, R.: Multi Quality Characteristics Of WEDM Process Parameters With RSM, *Procedia Eng.* **64**, 710–719 (2013)
10. Kumar, A., Kumar, V., Kumar, J.: Investigation of machining characterization for wire wear ratio & MRR on pure titanium in WEDM process through response surface methodology, *J. Process Mech. Eng.* **232**, 108–126 (2018)
11. Chaudhary, T., Siddiquee, A.N., Chanda, A.K.: Effect of wire tension on different output responses during wire electric discharge machining on AISI 304 stainless steel. *Def. Technol.* **15**, 514–544 (2019)
12. Bhatt, D., Goyal, A.: Multi-objective optimization of machining parameters in wire EDM for AISI-304, *Mater. Today Proc.* **18**, 4227–4242 (2019)
13. Lingadurai, K., Nagasivamuni, B., Muthu Kamatchi, M., Palavesam, J.: Selection of Wire Electrical Discharge Machining Process Parameters on Stainless Steel AISI Grade-304 using Design of Experiments Approach, *J. Inst. Eng. Ser. C* **93**, 163–170 (2012)
14. Kalpakjian, S., Schmid, S.R.: *Manufacturing Processes for Engineering Materials—Solution Manual* (2008)
15. Behera, A., Masanta, M.: Effect of Pulse-on-time on Machining Performance during WEDM of nano-TiO<sub>2</sub> Dispersed Austenite Steel, *Mater. Today Proc.* **5**, 20560–20566 (2018)
16. Soundararajan, R., Ramesh, A., Mohanraj, N., Parthasarathi, N.: An investigation of material removal rate and surface roughness of squeeze casted A413 alloy on WEDM by multi response optimization using RSM. *J. Alloys Compd.* **685**, 533–545 (2016)
17. Choudhuri, B., Sen, R., Ghosh, S.K., Saha, S.C.: Comparative machinability characterization of wire electrical discharge machining on different specialized AISI steels, *Bull. Mater. Sci.* 1–12 (2020)

18. Venkatarao, K., Anup Kumar, T.: An experimental parametric analysis on performance characteristics in wire electric discharge machining of Inconel 718. *J. Mech. Eng. Sci.* 1–14 (2019)
19. Banu, A., Abu, M., Bakar, M., Ali, Y., Adesta, E.Y.T.: Analysis of WEDM Process Parameters on Surface Roughness and Kerf using Taguchi Method, *Int. J. Eng. Mater. Manuf.* **2**, 103–109 (2017)
20. Sivanaga Malleswara Rao, S., Venkata Rao, K., Hemachandra Reddy, K., Parameswara Rao, C.V.S.: Prediction and optimization of process parameters in wire cut electric discharge machining for high-speed steel (HSS), *Int. J. Comput. Appl.* **39**, 1–9 (2017)
21. Pitayachaval, P., Jittamai, P., Baothong, T.: A review of machining parameters that effect to wire electrode wear. In: 4th International Conference on Industrial Engineering and Applications 1–4 (2017)
22. Debnath, T., Patowari, P.K.: Fabrication of an array of micro-fins using Wire-EDM and its parametric analysis. *Mater. Manuf. Process.* 1–10 (2018)
23. Durairaj, M., Sudharsun, D., Swamynathan, N.: Analysis of process parameters in wire EDM with stainless steel using single objective Taguchi method and multi objective grey relational grade, *Procedia Eng.* **64**, 868–877 (2013)
24. Geetha, M., Sreenivasulu, B., Gowd, G.H.: Modeling & Analysis of performance characteristics of Wire EDM of SS304, *Int. J. Innov. Technol. Explor. Eng.* **3**, 122–125 (2013)
25. Khan, Z.A., Siddiquee, A.N., Zaman, N., Khan, U., Quadir, G.A.: Multi response optimization of Wire electrical discharge machining process parameters using Taguchi based Grey Relational Analysis. *Procedia Mat. Sci.* **6**, 168/36–1695 (2014)
26. Paliwal, S., Solanki, P., Soni, M., Chanda, A.K.: Parameter Optimization of Wire Electrical Discharge Machining for Minimum Surface Roughness and Kerf Width using Taguchi Method, *Int. J. Ind. Electron. Electr. Eng.* **2**, 36–39 (2014)
27. Raju, B.S.P., Sarcar, M.M.M.: Optimization of Wire Electric Discharge Machining Parameters For Surface Roughness On 316L Stainless Steel Using Full Factorial Experimental Design. *Procedia Mat. Sci.* **5**, 1670–1676 (2014)
28. Nayak, B.B., Mahapatra, S.S.: A Utility Concept Approach for Multi-objective optimization of Taper Cutting Operation using WEDM. *Procedia Engineering* **97**, 469–478 (2014)
29. Mathew, B., Babu, J.: Multiple Process parameter Optimization of WEDM on AISI304 Using Taguchi Gray Relational Analysis. *Procedia Mat. Sci.* **5**, 1613–1622 (2014)
30. Kumar, S., Garg, S.K., Chawla, G.: Experimental Investigation of Effect of Process Parameters on Material Removal Rate during WEDM, *Int. J. Curr. Eng. Technol.* **6**, 40–45 (2016)
31. Bharathi, P., Gouri, T., Priyanka, L., Rao, G.S., Rao, B.N.: Optimum WEDM Process Parameters of SS304 Using Taguchi Method, *Int. J. Ind. Manuf. Syst. Eng.* **1**, 69–72 (2016)
32. Suresh, T., Aruneash, P., Gunasekar, S., Janakiraman, B.: Comparison of Brass and Zinc Coated Wire Electrode Using Wire Cut EDM Concerning MRR of Machining SS304, *Int. J. Innov. Res. Sci. Eng. Technol.* **6**, 4970–4976 (2017)
33. Nayak, B.B., Sankar Mahapatra, S.S.: An intelligent approach for multi-response optimisation of WEDM parameteres, *Int.J. Ind. Syst. Eng.* **25**, 197–227 (2017)
34. Babu, T.V., Subbaratnam, B.: Experimental investigation of Wire Electrical Discharge Machining (WEDM) Process Parameters on SS304 using Taguchi method, *Int. J. Curr. Eng. Technol.* **8**, 0–3 (2018)
35. Ugrasen, G., Bhagawan Singh, M.R., Ravindra, H.V.: Optimization of Process Parameters for SS304 in Wire Electrical Discharge Machining using Taguchi's Technique. *Mater. Today Proc.* **5**, 2877–2883 (2018)
36. Choudhuri, B., Sen, R., Ghosh, S.K., Saha, S.C.: Study of surface integrity and recast surface machined by Wire electrical discharge machining, *Materials Today: Proceedings* **5**, 7515–7525 (2018)

37. Padmavathi, K.R., Devaraj, S., John Solomon, I., Premkumar, A.: Influence of Process Parameters on Wire EDM Process for AISI 316 Stainless Steel, *Int. J. Eng. Res. Technol.* **6**, 1–6 (2018)
38. Ishfaq, K., Ahmad, N., Jawad, M., Ali, M.A., Al-Ahmari, A.M.: Evaluating material's interaction in wire electrical discharge machining of stainless steel (304) for simultaneous optimization of conflicting responses, *Materials (Basel)*. **12**, 1–15 (2019)

# Design Optimization and Analytical Study of a Modified Hydrous Aluminium Phyllosilicate Pantile



Anantha Krishna Somayaji , Narasimha Marakala ,  
K. Raghavendra Pai , and Ajit M. Hebbale 

**Abstract** Pantiles had overall notoriety. However, presently, these are in conclusion situation attributable to a few causes. One of the causes might be shortage of raw material, for example, hydrous aluminium phyllosilicates. The arrival of aesthetic pantiles is gradually becoming a due piece of pie. The functional territory of hydrous aluminium phyllosilicates material pantiles is extended; currently, pantiles could be utilized to cover the RCC rooftops to keep structure from warming. These pantiles are good systems to defy the water channelling and seepage issue of RCC working during monsoon season. In this examination, an endeavor is made to consider and break down the pantile material utilizing solid works software and followed with validation through ANSYS. The pantile model was developed through solid works followed with mesh, load and boundary conditions were applied as per desire. The conceivable result of the task is to find stress distribution over the tile.

**Keyword** RCC · Pantile · Aluminium · Phyllosilicates

## 1 Introduction

Pantiles are of level example and are furnished with appropriate protrusions, so they intertwine with one another, when set in location. The pantiles are in red shade, and they are of two folded structures. The cut section of pantiles is accessible for hip, edge and valley bit of rooftop. It was reported that approximately 15 pantiles are required to cover one square metre of the rooftop territory [1]. Pantiles are produced on vast extent for huge scope in southern India particularly at coastal regions. These industries were built up in the mid-nineteenth century by German Missionaries. The designed pantiles are getting into mainstream in villages and semi-urban regions [2]. These pantiles are widely utilized by all class of people of society, for example,

---

A. K. Somayaji · N. Marakala · K. Raghavendra Pai · A. M. Hebbale (✉)  
Department of Mechanical Engineering, N.M.A.M. Institute of Technology,  
Nitte, Udupi District, Karnataka 574110, India

compositional impact, shortage and rising costs of different substitutes, development of populace, and so forth, the existence of these pantiles is around 25 years with substitution of 6% every year. Be that as it may, presently, a day such a large number of these businesses are in a closure state inferable from the few reasons [3–5]. Shortage of expendable crude material, for example, hydrous aluminium phyllosilicates are one of the obvious causes. The introduce of beautifying pantiles is becoming the due pieces of the pie. Indeed, even these pantiles can be used to cover the RCC structure to keep this from overheating, and furthermore, these pantiles are best methodologies to counter water channelling and leakage issue of RCC working in stormy periods [6–9]. This examination an endeavour is done to contemplate and dissect plan of rooftop pantiles thinking about affecting boundaries. Pantiles might be characterized as dainty pieces of block. These are scorched in furnace. They are more slender compared to block, and consequently, they ought to be deliberately dealt with to stay away from any harm to them. The pantiles can be ordered in the accompanying classifications as: (1) frequent pantiles these with uneven shape and sizes whose main application is for flooring and roofing purpose; (2) encaustic pantiles are specifically designed and fabricated for aesthetic purposes.

### ***1.1 Objectives***

- The general pantile design configuration is done by modelling as per the required measurement, and to break down the design utilizing Ansys software, loads followed up on pantile and ensured the chance of sparing expendable raw material of hydrous aluminium phyllosilicates through re-structuring the tile model.
- Gathering different information identified with pantile material tile for programming model of pantile material tile utilizing solid works and breaking down utilizing Ansys software, taking all possible conditions.
- To ensure the well-being of current structure.

### ***1.2 Methodology***

The basic procedure that is being planned to be employed is discussed as follows: Modelling of pantile roofing element using solid works software. Finding the possible loads, i.e. load due to wind, rain, self-weight, importing. IGS model of solid works to Ansys workbench. Analysis of the various process parameters using analysis software. Determining stress, strains and deformation and inferring the conclusion. Iterative process to be continued to obtain optimized design.

### 1.3 Modelling

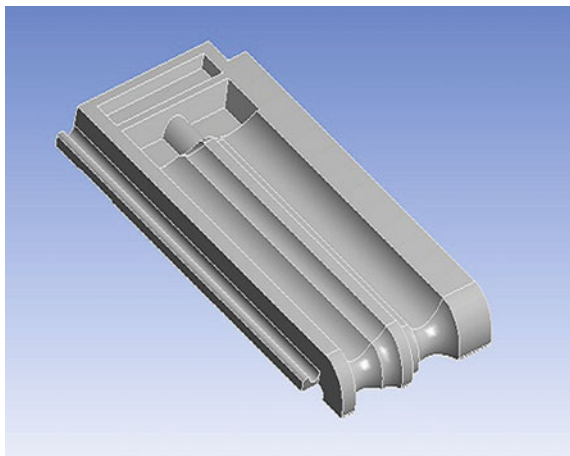
Creating programming model for hydrous aluminium phyllosilicates tile utilizing solid works programming, it is exceptionally useful programming in displaying perspective; instruments are helpful to show any sort of plan. Considering the component hydrous aluminium phyllosilicates of tile, breaking down the tile model considering loads, for example, wind load, load due to water and load due to dead weights, yet wind load is considered. Significant design characteristics of the element of this model are  $420 \times 250$  mm , depth is around 8 mm at bends, and by and larger depth is 15 mm. The developed product is demonstrated as follows. Figure 1 shows the solid work model of pantile.

### 1.4 FE Model

The desired load and boundary conditions were applied in the Ansys software. The type of the element that was used in the meshing is three noded constant strain triangular elements which had a total of 7976 nodes. The total number of elements was accounted to 4127, with consideration of stress concentration factor near the discontinuity. For further increase in accuracy, hyper mesh software can be used (Fig. 2; Table 1).

Material properties: Hydrous aluminium phyllosilicates are used for production of pantile. The characteristics of pantile are listed in Table 2. Static examination accomplished for pantile material tile considering three significant loading conditions wind load (pressure), downpour loading condition and self-weight. The initial cycle was finished with self-weight as it is finished. Second cycle depends on self-load, wind pressure, and the third case depends on all above cases. Final case is overhauled and tried with similar loads.

**Fig. 1** Solid works model of pantile



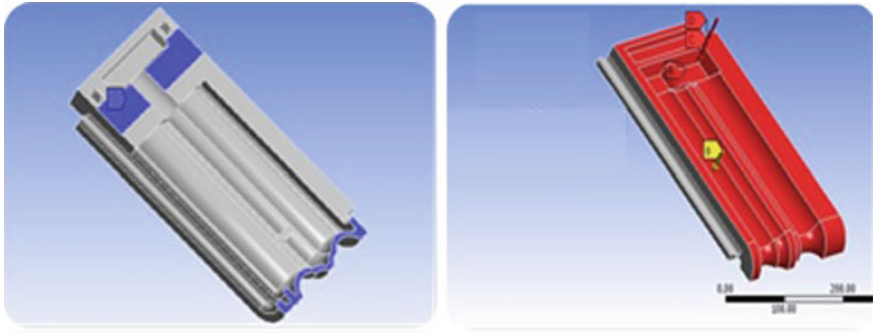


**Fig. 2** Boundary conditions and loads considered on pantiles

**Table 1** Boundary conditions of FE model of pantiles

S. no.	Parameter	Remarks
1	Dimensions	420 × 250 mm
2	Thickness	8 mm
3	Type of element	3-N-CST
4	No.of elements	4127
5	No. of nodes	7976
6	Boundary condition	Fixed support (represented in blue colour of Fig. 3) in back side of tile
7	Load	On top portion (red) with concentration at key points
8	Dead load	22,54 N IS code book 875 (parts 1–3)
9	Wind pressure	0.002079 MPa
10	Load due to rain	60.015 N

**Table 2** Properties of raw material

Material	Properties	Values
Hydrous aluminium phyllosilicates (clay)	Density	0.0000017 kg/mm <sup>3</sup>
	Young’s modulus	13789.514 MPa
	Poisson’s ratio	0.19
	Compressive ultimate strength	7.79 MPa

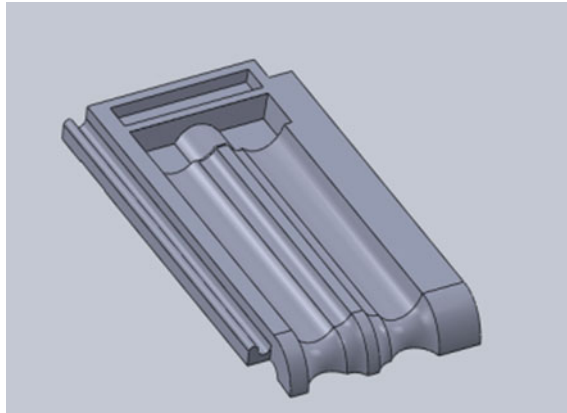


**Fig. 3** Redesigned model of pantiles

### 1.5 Software Redesign of Current Model

For final design, considering the assistance of solid works programming and decreasing the depth of pantile by 75% of the first depth and investigated utilizing Ansys software. Figure 3 is final planned model of pantile.

## 2 Results and Discussion

### 2.1 First Case

The principal case is wind weight and self-weight, which is considered as wind pressure (0.002079 MPa) and self-weight (2.3 kg). Figure 4a presenting the stress plot of pantile design material tile. Greatest stress acquired in examination is 0.68391 MPa, and least pressure is 0.00030583 Mpa. Deformation plot of pantile material tile is given below, and greatest twisting observed was 0.009947 mm (Table 3).

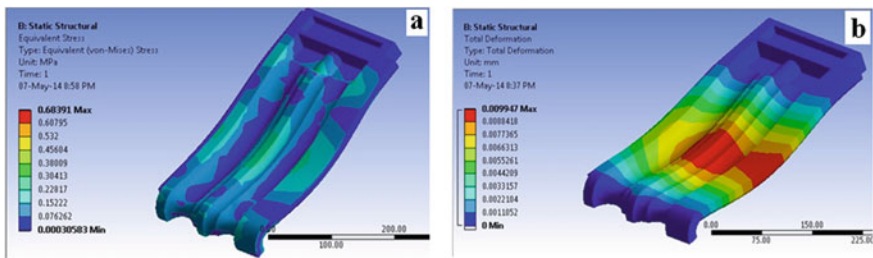


**Fig. 4** a Stress plot obtain of first case and b deformation plot of first case



**Table 3** Stress and deformation results in first case

Stress and deformation results obtained from Ansys		
Max.	0.68391 MPa	0.009947 mm
Min.	0.00030583 MPa	0

Most extreme stress (0.68391 MPa) was found in fixed spot of pantile that bits are less unsafe area of pantile. Dim blue shading parcels are most secure area that we can find in the above figures. Maximum disfigurement happens at the centre bit of the tile and that is 0.009947 mm which is low. This is weak material, even less distortion likewise influences the nature of pantile. In Fig. 4b, least stress is 0.0003058 MPa and the greater part of the area shows the dim blue shading those locales which are most secure districts.

## 2.2 Second Case

Three major loads considered viz rain load, wind pressure and self-weight, and obtained results are summarized as follows. For this situation, additional weight is considered, for example, rain load, wind weights and self-weights. The rain load does not make enormous variety in the outcomes; it is little considering breeze load. Wind load is the overwhelming weights following up on the pantile so the help of the pantiles ought to be a decent quality. Deformation plot is demonstrated as follows (Fig. 5; Table 4).

For the previous case, there is variety in stress and deformation results greatest pressure that was seen was 0.85576 Mpa, and most extreme dimension change that was obtained is 0.01264 mm. On account of a tile, it ought to be extraordinary variation of results; however, stress and deformation plots are not significantly more distinction (Fig. 6).

## 2.3 Third Case

For this situation, there just a single distinction from the past case, for example, most extreme wind pressure is considered for remaining two weights as past. The obtained results acquired in this case were demonstrated as follows. In the past case, there is high variety of stress and deformation results, most extreme stress attained is 1.4744 Mpa, and greatest deformation acquired was 0.02180 mm. On account of a pantile, it ought to incredible variation of results yet stress and deformation plots does not have substantially more distinction. In this condition, most extreme weight is utilized the greatest outcomes acquired for this situation. Be that as it may, the most extreme weight not continually acting over pantile, second one is typical (Fig. 7; Table 4).

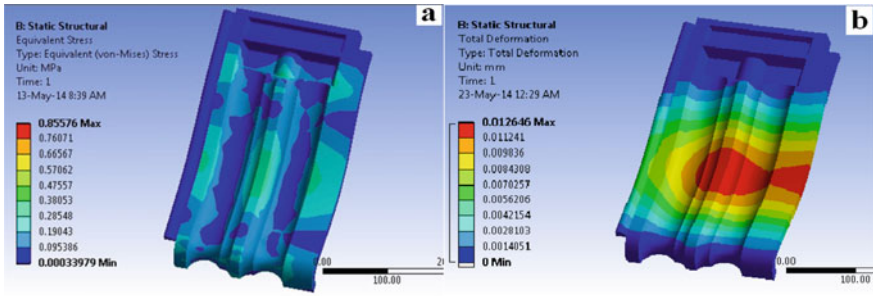


Fig. 5 a Stress plot obtains of second case and b deformation plot of second case

Table 4 Stress and deformation plot in second case

Stress and deformation results obtained from Ansys		
Max.	0.85576 MPa	0.01264 mm
Min.	0.00033979 MPa	0

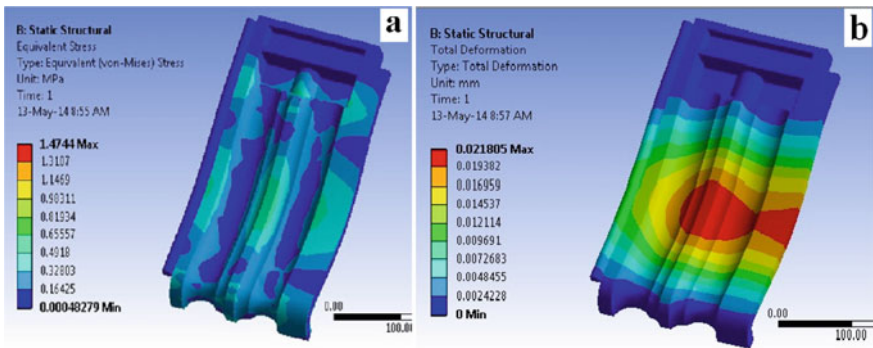


Fig. 6 a Stress plot obtains of third case and b deformation plot of third case

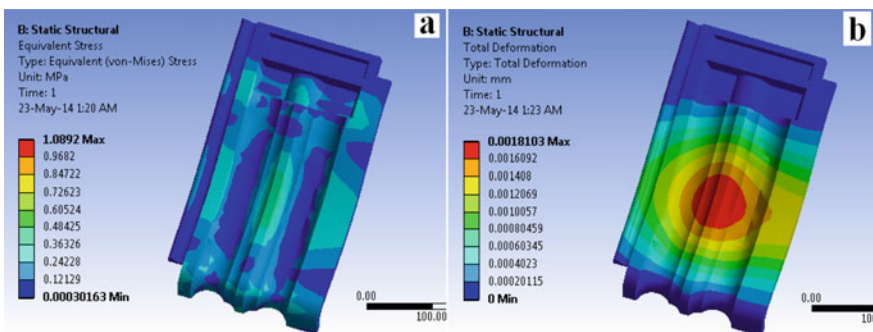


Fig. 7 a Stress plot obtains of fourth case and b deformation plot of fourth case

**Table 5** Stress and deformation results in third case

Stress and deformation results obtained from Ansys		
Max.	1.4744 MPa	0.02180 mm
Min.	0.0004827 MPa	0

### 3 Conclusions

From the examination accomplished for the first pantile material tile model  $420 \times 250$  mm. It is clear that material pantile is for the conceivable load circumstance. The deformation and load plots additionally given a similar state, yet it is an over structure. The measure of hydrous aluminium phyllosilicates per pantile for first assembling model is 2.29 kg. Since hydrous aluminium phyllosilicates is expendable crude material; we attempted another model with less depth 75% of the first depth, and the measure of earth required for the model is 1.99 kg. From the investigation, it is discovered that the new design is safe with adequate quality. It saves about 26% of complete weight crude material than first developed model. Other than this, the time need to dry was additionally less which improve the manufacturing rate. Temperature required to burn for these pantiles additionally less which spares the consumption of consumption. But strength in wet condition after a long time is questionable. However, strength of such pantiles can be enhanced with some other types of reinforced as in composite material technology.

### References

1. Rangwala, S.C., Rangwala, K.S., Rangwala, P.S.: Engg Materials [Material Science], 38th edition. Charotar Publishing House Pvt. Ltd. (2011)
2. IS 3978:1993 Manufacture of burnt clay Pantile pattern roofing pantiles—Code of practice (first revision), December 2011
3. IS 654: Clay roofing pantiles, Pantile pattern—Specification (third revision) (1992)
4. Duggal, S.K.: Building Materials, 3rd edition. New Age International (2008)
5. Mirmiran, A., Chowdhury, A.G., Gu, M., Huang, P.: Fem Analysis of Tile Roofs under Simulated Typhoon Impact, The Seventh Asia-Pacific Conference on Wind Engineering, November 8–12, 2009, Taipei, Taiwan
6. Rajapakse, J.P., Madabhushi, G., Fenner, R., Gallage, C.: Properties of hand-made clay balls used as a novel filter media. *Geomechanics and Engineering*, 4(4), 281–294
7. IS 875(Part 1): Dead loads-unit weights of building materials and stored materials, Code of Practice for Design Loads (other than earthquake) for Buildings and Structures, 2nd rev., 1987
8. IS 875(Part 2): Imposed Loads-Code of Practice for Design Loads (other than earthquake) for Buildings and Structures, 2nd rev., 1987
9. IS 875(Part 3): Wind Loads-Code of Practice for Design Loads (other than earthquake) for Buildings and Structures, 2nd rev., 1987

# A Study on Recent Developments in Jute, Cotton, Coir, Silk and Abaca Fiber-reinforced Composites



Rittin Abraham Kurien, Ashwin Santhosh, Daniel Paul,  
Gowrisankar B. Kurup, Greshma Susan Reji, and D. Philip Selvaraj

**Abstract** The high cost and environmental hazard caused by the artificial fibers like kevlar and carbon have created an urge toward the development of natural fiber-reinforced polymer composites. Using natural fibers as reinforcement has decreased the risk toward the nature. By changing the resin structures or the natural fiber framework, bio-composites can be prepared for various applications. Here, we have discussed about the natural fibers like jute, cotton, coir, silk and abaca. Also, the sources and properties of each of these natural fibers have been widely considered. We have studied these natural fiber as reinforcement for some types of composites. Likewise, the mechanical properties of these natural fibers and their applications are also discussed. From the study, it is clear that abaca has the highest tensile strength, jute has the highest Young's modulus, and silk has the highest elongation at break. This shows that in the coming years, natural fibers will be extensively used for the making of composites as they are the non-polluting, harmless, renewable as well as sustainable source of fiber.

**Keywords** Natural fibers · Polymer composites · Reinforcement · Degradability

## 1 Introduction

Over the most recent couple of years, there has been a great urge toward new items from sustainable sources. Natural fibers are widely utilized as a part of composite materials, where the direction of natural fibers impacts the properties [1]. Fiber-reinforced composites utilizes various kinds of strands for reinforcement [2]. Plant fibers comprise of leaf strands, for example, pineapple, sisal and abaca,

---

R. A. Kurien (✉) · D. P. Selvaraj  
Department of Mechanical Engineering, Karunya Institute of Technology and Sciences,  
Coimbatore 641114, India

A. Santhosh · D. Paul · G. B. Kurup · G. S. Reji  
Department of Mechanical Engineering, Saintgits College of Engineering, Kottayam 686532,  
Kerala, India

whereas coir and cotton are the examples of seed fibers. The example of grass fiber includes rice and wheat. Bast fibers include flax, jute and ramie [3]. Composite materials are significant designing materials due to their remarkable mechanical properties. They are materials in which the attractive properties of isolated materials are consolidated by precisely or metallurgic binding, restricting them together. Every parts hold its structure and characteristic; however, the composite has better properties. For this research, we have considered jute, cotton, coir, silk and abaca fiber. The sources and mechanical properties of all these fibers have been discussed. These fibers are used as reinforcement for different composites which is studied here. Also, the applications of all these fibers have been concentrated. The differences in reported mechanical properties and dispersed information are the issues concerned with natural fibers. Selection process of natural fibers becomes even more complex due to lack of standardized methods by consumers and producers to analyze, extract, treat and post-process the natural fibers. In fact, these are major issues that hinder the general utilization of natural fibers in various application. To mark this gap, this paper addresses the various mechanical properties and latest potential applications of the natural fibers in different commercial industries for the advancement of eco-friendly products with an intention to replace the synthetic fibers with efficient and economically effective products. Figure 1 shows the basic constituents of natural fiber-reinforced composites.

## 2 Source and Properties of Fibers

### 2.1 Jute

The source of jute is vegetable plant which belong to the linden family, whose scientific name is *corchoruscapsularis* (white jute), *corchorusolitorius* (tossa jute). The fiber length in mm is up to 4000. Fiber diameter is 17–20  $\mu\text{m}$ . The density of fiber is 1.23  $\text{g}/\text{cm}^3$ . Jute fiber, growing mostly in the tropical regions, where the humidity is high (60–70%), is characterized by low thermal conductivity, high insulation, moderate absorption of moisture and high-anti-static properties [4–6]. The main producers of jute in the world are India (60%), Bangladesh and Myanmar [7, 8].

### 2.2 Cotton

The source of cotton is a shrub called *gossypium*, whose fiber length varies between 100 and 650 mm, and diameter is about 11–22  $\mu\text{m}$ . The density of fiber is 1.21  $\text{g}/\text{cm}^3$ . Rapid moisture absorption and high tensile strength are some of the main properties of cotton fiber. The countries which produce cotton fiber are China, Brazil, India and Pakistan.

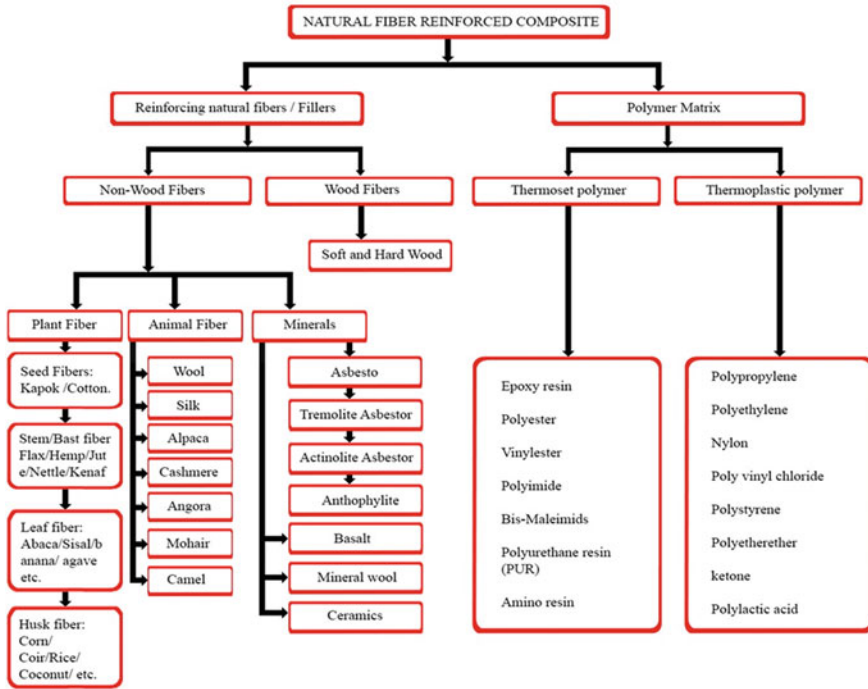


Fig. 1 Basic constituents of natural fiber-reinforced composites [1]

### 2.3 Coir

The source of coir is coconut, whose scientific name is *cocos nucifera*. Fiber length of coir is about 350 mm, and fiber diameter lies between 12 and 15  $\mu\text{m}$  [6, 9]. The density of fiber is 1.2  $\text{g}/\text{cm}^3$ . High strength, better resistance toward salt water damage, microbial action and better rigidity than cotton are the properties provided by coir fiber. The coir fiber has high concentration of lignin and is unsuitable for dye treatments. India, Sri Lanka, Thailand and Philippines are the main coconut producers of the world [8, 10].

### 2.4 Silk

Chinese mulberry silkworm is the source of silk fiber. The length of silk fiber is up to 1500 mm and diameter is about 10–13  $\mu\text{m}$ . The main properties of silk fiber are its good absorbency, low conductivity and easy dye finish. China, India and Thailand are the main silk producers of the world [11–14].

## 2.5 *Abaca*

Musa textiles is the scientific name of abaca fiber, which is the source. The fiber is having a length of 3000 mm, and the diameter is 151  $\mu\text{m}$  [15]. The density of fiber is 1.5  $\text{g}/\text{cm}^3$ . Resistance toward deterioration caused by saltwater, buoyancy and great mechanical strength are the properties presented by the abaca fiber [16, 17]. These properties make them one of the finest fiber. Philippines (85%) and Ecuador are the main producers of abaca [8].

## 3 Mechanical Characteristics of Natural Fibers

Reinforcement materials which were used traditionally can be replaced by natural fibers which have better mechanical properties. The different tensile strength and Young's modulus allow various natural fibers to be used as reinforcement in composites owing to numerous structural and non-structural applications. Table 1 displays plant fibers mechanical properties. Graphical representation of these properties is displayed in Fig. 2a–c. Mechanical properties including tensile strength, Young's modulus and elongation at break are considered here.

## 4 Natural Fiber as Reinforcement for Composites Materials

### 4.1 *Jute Fiber Composite*

The fabrication of jute fiber-reinforced polypropylene composite along with the addition of glass fibers shows that maximum impact strength and tensile strength are attained when 10% jute fiber is used as reinforcement in the polypropylene matrix. This composition has the maximum hardness. By using 15% jute fiber in the PP matrix along with 15% glass fiber, maximum flexural strength is attained [23]. Maleic anhydride is used to improve the bonding of jute fiber and polypropylene.

**Table 1** Mechanical properties of natural fibers [18–22]

Fiber	Tensile strength (MPa)	Young's modulus (GPa)	Elongation at break (%)	References
Jute	480	37.5	2.3	[18, 19]
Cotton	442	8	6	[20, 21]
Coir	175	6	20	[18, 19]
Silk	390	9.26	22.5	[20, 21]
Abaca	621.5	32.35	2.9	[22]

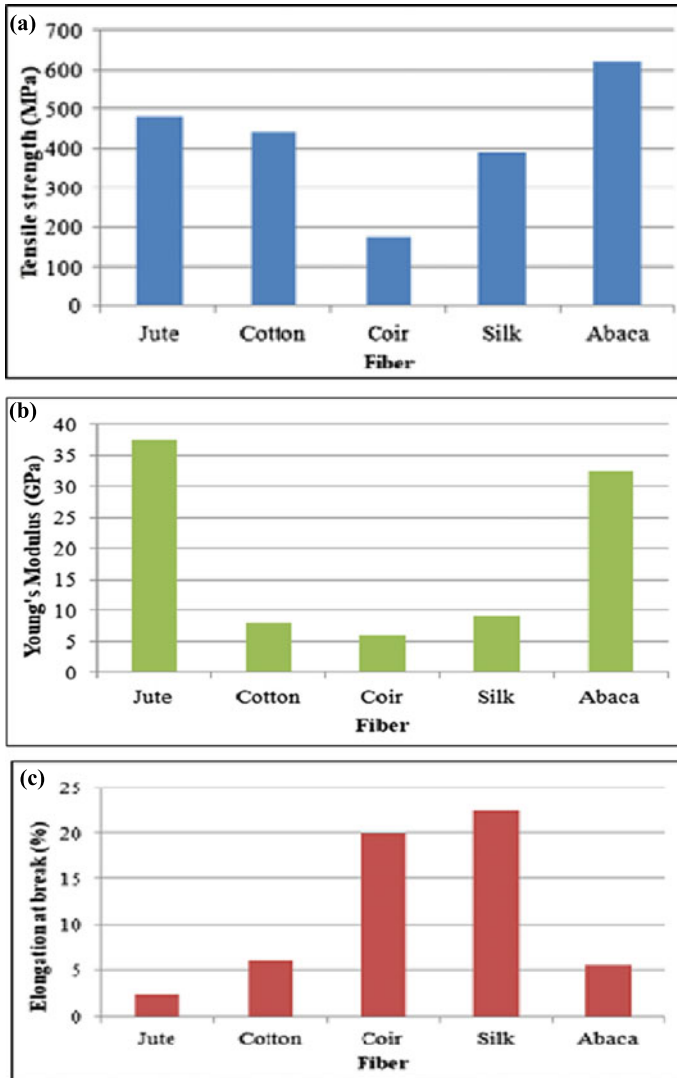


**Fig. 2** a Tensile strength of natural plant fibers [18–22]. b Young’s modulus of natural plant fibers [18–22]. c Elongation at break of natural plant fibers [18–22]

Jute fiber-reinforced epoxy composites are fabricated using matrix modification method. The composite with most attractive properties is the jute fiber-reinforced composite with alkaline treated fibers which has higher mechanical properties compared to untreated fiber composites [24, 25].



## **4.2 Cotton Fiber Composite**

Cotton fiber can be used to reinforce geopolymer (the inorganic polymer which is formed by alkaline treatment of aluminosilicates are called geopolymers) composites. The composite can be manufactured effectively with a fiber loading of 4.5–8.3 wt%. As the fiber content in the composite is increased, the flexural modulus and strength, hardness and impact and fracture strengths also increase when the fiber content is expanded which leads to an increase in dissemination coefficient and better water absorbing ability. Due to the absorption of water, properties like fracture strength, flexural quality and modulus, hardness and strength on impact becomes reduced. When the fiber has low dampness and surface vitality, the composite tends toward a hydrophobic character. The composites turn harder, when the composites have higher mechanical properties. At room temperature, increment in quantity of fibers results in the increase in the water retaining capacity of the cotton fiber-reinforced composites. As compared to the cotton fiber, the crystallinity and thermal stability of the composite are higher. The composite became more stable, and there is an improvement in its thermal stability. For the composite, its mechanical properties became almost double that of the fiber [26, 27].

## **4.3 Coir Fiber Composite**

Tensile strength and resistance against impact improve for coir fibers when they are silanated after treatment with alkali. In comparison with other natural fibers, better elongation and specific strength are showed by modified/treated coir fibers. Although the density of the natural fiber increases after treatment with alkali, a decrease in the thermal stability is shown by the fiber. The content of fiber in the composite and the matrix used affects the mechanical properties of the composites of coir. The quantity of voids that forms due to fiber pullout in coir composites is deducted by fiber treatment. As the degradation temperature of coir fibers is low, increasing the content of fiber in the composite reduces the thermal stability of the coir polymer composite.

## **4.4 Silk Fiber Composite**

Silk fiber is fused inside the lattice of thermoplastic polymer as reinforcement to produce a composite. Silk fiber can be found abundantly and hence can be easily accessed. It can be used as a reinforced material because it is economical and nature friendly. Silk fiber is introduced in the epoxy lattice as a reinforcement. This fiber has got great deformability and superior quality which contributes to the properties of the fundamental structure of the composite. Poly butylene succinate (PBS) can be

reinforced with short silk fibers by utilizing the method of pressure forming. This bio-composite shows better thermal stability along with flexural and mechanical properties [11]. Thus, silk fibers have a major role in composite materials as they can vastly improve mechanical properties when used as reinforcement [12]. To improve the bonding between the polymer matrix and fiber, surface treatments can be performed on the silk fiber [13].

#### ***4.5 Abaca Fiber Composite***

Abaca fiber be considered as a suitable substitute to replace synthetic materials as the help to improve mechanical properties much better [28]. The orientation of the fibers, the amount of fiber used inside the lattice, fiber dimension and the interface between the lattice and the fiber all affect the mechanical properties of the composite material. The distribution and orientation of fibers are based on the condition of processing of polymer lattice. Abaca fibers are difficult to work with due to their strong polarization characteristic [16]. The polymeric matrix is hydrophobic, and the polarization reduces adhesiveness at the interface. To increase the affinity toward matrix, treatments like esterification and usage of coupling agents can be used [29]. The nature of the polymer lattice or matrix has a direct effect on the surface bonding. Hence, surface interface is greatly dependent on the matrix. Thermoset and thermoplastic polymers can both utilize abaca fiber as a reinforcement in their matrix which makes it very versatile. The mechanical properties of polypropylene can be improved using abaca fiber reinforcements. As a reinforcement for polypropylene abaca fiber exhibits better damping properties than jute fiber, abaca fiber can also be incorporated in thermosetting matrices like epoxy. When compared to original polymer matrix, this composite has better flexural and impact strength [30]. Urea formaldehyde when reinforced using abaca fiber shows a great deal of improvement in impact strength, flexural and tensile strengths.

### **5 Applications**

Natural fibers find application in almost every day today activities. It finds uses from household activities to even automobile, aerospace and marine industries [31]. Door shutters and frames, packaging, panels and sheets for construction, textiles and clothing are some of the common applications of the jute fibers. Goods, ropes, textile and furniture industries use the cotton fiber. Construction of panels, roofing sheets, post boxes, casings, covers, brushes, brooms, seats and its components, ropes and yarns, nets, bags and mats, storage tanks, weights and helmets are the major areas where coir fiber find its application [32]. Silk fibers are utilized in furniture industry and in textile industries to produce yarns and sewing threads. They find applications in medical field such as suture for surgical purposes. It can be found in daily use

items such as ropes, twins, fishing lines [33]. Abaca fibers find application in automobile industry such as fabrication of floor and body panels. In construction, they are used to manufacture insulated panels, windows and door frames.

## 6 Conclusion

Compared to their polymeric rivals, natural fiber-reinforced polymer composites show better properties, and due to this, they are widely used as reinforcement material. We can alter the properties of the composites accordingly by controlling the amount of natural fiber used and the type of natural fiber used inside the matrix. Moreover, considering the rising environmental hazards caused by production and utilisation of synthetic material, there is a need to reduce their use. Very good strength to weight ratio and insulating properties are shown by jute fiber. A good absorbency rate is shown by cotton fibers. Among both synthetic and natural fibers, cotton is one of the most used fiber. Coir is considered as an important fiber as it has better durability than majority of natural fibers. Also it does not need chemical treatment, it has strong resistance to salt water and is easily available. Unlike plant fibers, silk fibers are obtained from animals. They have some great highlights like high elongation, low density and resistance to flame which prolongs even at low temperature. Studies and researches on silk fiber-reinforced composites are comparatively less, and they are restricted either to continuous silk fiber-reinforced thermosetting composites or discontinuous silk fiber-reinforced thermoplastic composite. For reinforced injection-molded thermoplastics, especially polypropylene, discontinuous natural fibers are used mainly due to their property of recyclability. Abaca fiber-reinforced polypropylene composite is a significant natural fiber composite, has outstanding properties like high tensile strength, high flexural strength, good acoustic resistance and good abrasion. They have a very good resistance to UV light rays and better resistance to mold and rot. Due to their ease of availability, this fiber is widely used in automotive industries. From the above study, it is clear that abaca has the highest tensile strength, jute has the highest Young's modulus, and silk has the highest elongation at break. This shows that in the coming years, natural fibers will be extensively used for the making of composites as they are the non-polluting, harmless, renewable as well as sustainable source of fiber.

## References

1. Peças, P., Carvalho, H., Salman, H., Leite, M.: Natural fibre composites and their applications: a review. *J. Compos. Sci.* 2(4), 66 (2018)
2. Harle, S.M.: The performance of natural fiber reinforced polymer composites. *Int. J. Civ. Eng. Res.* 5(3), 285–288 (2014)

3. Kumar, K.A., Sudhanan, S.M., Kumar, K.M., Kumar, G. R.: A Study on properties of natural fibre-A Review (2017)
4. Kumar, P.S.S., Allamraju, K.V.: A Review Of Natural Fiber Composites [Jute, Sisal, Kenaf]. *Mater. Today: Proc.* **18**, 2556–2562 (2019)
5. Alhilfi, T., Chambon, P., Rannard, S.P.: Architectural control of polystyrene physical properties using branched anionic polymerization initiated at ambient temperature. *J. Polym. Sci.* **58**(10), 1426–1438 (2020)
6. Rohit, K., Dixit, S.: A review-future aspect of natural fiber reinforced composite. *Polym. Renew. Resour.* **7**(2), 43–59 (2016)
7. Gogna, E., Kumar, R., Sahoo, A.K., Panda, A.: A comprehensive review on jute fiber reinforced composites. In *Advances in industrial and production engineering*, pp. 459–467. Springer, Singapore (2019)
8. Gholampour, A., Ozbakkaloglu, T.: A review of natural fiber composites: Properties, modification and processing techniques, characterization, applications. *J. Mater. Sci.*, 1–64 (2020)
9. Widnyana, A., Rian, I.G., Surata, I.W., Nindhia, T.G.T.: Tensile Properties of coconut Coir single fiber with alkali treatment and reinforcement effect on unsaturated polyester polymer. *Mater. Today: Proc.* **22**, 300–305 (2020)
10. Walte, A.B., Bhole, K., Gholave, J.: Mechanical Characterization of Coir Fiber Reinforced Composite. *Mater. Today: Proc.* **24**, 557–566 (2020)
11. Babu, G.D., Krishnan, V.G., Gopi, G.: Mechanical Behaviour of silk fabric reinforced ecofriendly polymer matrix composite. *Carbon* **1**(4000), 235
12. Hamidi, Y.K., Yalcinkaya, M.A., Guloglu, G.E., Pishvar, M., Amirhosravi, M., Altan, M.C.: Silk as a natural reinforcement: processing and properties of silk/epoxy composite laminates. *Materials* **11**(11), 2135 (2018)
13. Akash, S., Avinash, S., Ramachandra, M.: A Study on Mechanical Properties of Silk Fiber Reinforced Epoxy Resin Bio-Composite with SiC as Filler Addition. *Mater. Today: Proc.* **5** (1), 3219–3228 (2018)
14. Gholampour, A., Ozbakkaloglu, T. A review of natural fiber composites: Properties, modification and processing techniques, characterization, applications. *J. Mater. Sci.*, 1–64 (2020)
15. Elanchezian, C., Ramnath, B.V., Ramakrishnan, G., Rajendrakumar, M., Naveenkumar, V., Saravanakumar, M.K.: Review on mechanical properties of natural fiber composites. *Mater. Today: Proc.* **5**(1), 1785–1790 (2018)
16. Kurien, R.A., Selvaraj, D.P., Sekar, M., Koshy, C.P. Green composite materials for green technology in the automotive industry. In *IOP Conference Series: Materials Science and Engineering* (Vol. 872, No. 1, p. 012064). IOP Publishing (2020)
17. Sinha, A.K., Narang, H.K., Bhattacharya, S.: Evaluation of bending strength of abaca reinforced polymer composites. *Mater. Today: Proc.* **5**(2), 7284–7288 (2018)
18. Averous, L., Digabel, F.L.: Properties of biocomposites based on lignocellulosic fillers. *Carbohydr. Polym.* **66**, 480–493 (2006)
19. Chand, N., Fahim, M.: *Tribology of natural fiber polymer composites*. Woodhead Publishing Limited, Cambridge, UK, 1–58 (2008)
20. Gurunathan, T., Mohanty, S., Nayak, S.K.: A review of the recent developments in biocomposites based on natural fibres and their application perspectives. *Compos. Part A Appl. Sci. Manuf.* **77**, 1–25 (2015)
21. Bhardwaj, S.: *Natural Fibre Composites—An Opportunity for Farmers*. *Int. J. Pure Appl. Biosci* (2017)
22. Jeyapragash, R., Srinivasan, V., Sathiyamurthy, S.: Mechanical properties of natural fiber/particulate reinforced epoxy composites—A review of the literature. *Mater. Today: Proc.* **22**, 1223–1227 (2020)
23. Ray, K., Patra, H., Swain, A.K., Parida, B., Mahapatra, S., Sahu, A., Rana, S.: Glass/jute/sisal fiber reinforced hybrid polypropylene polymer composites: Fabrication and analysis of mechanical and water absorption properties. *Mater. Today: Proc.* (2020)

24. Shivamurthy, B., Naik, N., Thimappa, B.H.S., Bhat, R.: Mechanical property evaluation of alkali-treated jute fiber reinforced bio-epoxy composite materials. *Mater. Today: Proc.* (2020)
25. Chandrasekar, M., Ishak, M.R., Sapuan, S.M., Leman, Z., Jawaid, M.: A review on the characterisation of natural fibres and their composites after alkali treatment and water absorption. *Plast., Rubber Compos.* **46**(3), 119–136 (2017)
26. Sharma, K., Khilari, V., Chaudhary, B.U., Jogi, A.B., Pandit, A.B., Kale, R.D.: Cotton based composite fabric reinforced with waste polyester fibers for improved mechanical properties. *Waste Manag.* **107**, 227–234 (2020)
27. da Silva, C.C., de Faria Lima, A., Moreto, J.A., Dantas, S., Henrique, M.A., Pasquini, D., Gelamo, R.V.: Influence of plasma treatment on the physical and chemical properties of sisal fibers and environmental application in adsorption of methylene blue. *Materials Today Communications*, 101140 (2020)
28. Pothan, L.A., Thomas, S.: Polarity parameters and dynamic mechanical behaviour of chemically modified banana fiber reinforced polyester composites. *Compos. Sci. Technol.* **63**, 1231–1240 (2003)
29. Ramadevi, P., Dhanalakshmi, S., Ranganagowda, R.P., Basavaraju, B., Pramod, V.B., Srinivasa, C.V.: Surface modification of abaca fiber by benzenediazonium chloride treatment and its influence on tensile properties of abaca fiber reinforced polypropylene composites. *Cie`nc. Tecnol. dos Materiais* **26**(2), 142–149 (2014)
30. Xue, L., Tabil, L.G.: Chemical treatments of natural fiber for use in natural fiber reinforced composites: a review. *J. Polym. Environ.* **15**(1), 25–33 (2007)
31. Chen, S., Cheng, L., Huang, H., Zou, F., Zhao, H.P.: Fabrication and properties of poly (butylene succinate) biocomposites reinforced by waste silkworm silk fabric. *Compos. A Appl. Sci. Manuf.* **95**, 125–131 (2020)
32. Chaudhary, V., Ahmad, F.: A review on plant fiber reinforced thermoset polymers for structural and frictional composites. *Polymer Testing*, 106792 (2020)
33. Tg, Y.G., Mr, S., Siengchin, S.: Natural fibers as sustainable and renewable resource for development of eco-friendly composites: a comprehensive review. *Front. Mater.* **6**, 226 (2019)

# A Computational Methodology for the Synthesis of Assur Groups



H. Manikandan, Vijayananda Kaup, and Harish Babu

**Abstract** Assur group is an open kinematic chain, which when added to any kinematic chain but not to the same link does not alter the degree of freedom of the chain. Assur group finds its application in synthesizing mechanisms, complex structures and robotics, wherein serial or parallel kinematic chains are required. The present work aims at synthesizing Assur group from  $N$ -link zero degree of freedom simple jointed kinematic chains and thus to present a complete collection of Assur groups. It is done by removing a link from the given kinematic chain and checking for its definition as Assur group. Also, identically disposed links are determined and removed so as to address the isomorphic Assur group during synthesis. In other words, isomorphism test is also adopted in the present work while reporting the complete collection.

**Keywords** Assur group · Simple jointed kinematic chain · Isomorphism test

## 1 Introduction

Synthesis of Assur group is of much important area of research for the past decades. Assur groups find vast applications in the field of synthesis of mechanisms as well as the synthesis of kinematic chains. Also, in the field of robotics, Assur group finds its own place wherever parallel or serial kinematic links have to be generated. Generally, Assur group is an open kinematic chain which when added to a given

---

H. Manikandan (✉) · V. Kaup · H. Babu  
Department of Mechanical Engineering (VTU-RC), CMR Institute of Technology,  
Bengaluru 560037, Karnataka, India  
e-mail: [manikandan.h@cmrit.ac.in](mailto:manikandan.h@cmrit.ac.in)

V. Kaup  
e-mail: [vijayananda.k@cmrit.ac.in](mailto:vijayananda.k@cmrit.ac.in)

H. Babu  
e-mail: [harish.b@cmrit.ac.in](mailto:harish.b@cmrit.ac.in)

kinematic chain (but not to the same link) does not alter the degree of freedom of the latter.

Manolescu [1] in his work to synthesize planar mechanisms from Baranov trusses used Assur groups. Position analysis of planar mechanisms was done by Martins et al. [2], in which Assur groups were used to synthesize kinematic fractionated chains up to 6 degree of freedom (*DOF*). A methodology for designing robot hand fingers based on Assur groups was proposed by Tischler et al. [3]. Similarly, Campos et al. [4] synthesized hybrid mechanisms using Assur groups.

Assur groups with two, four and six links were reported by Dobrovosky [5]. Krokhmal and Krokhmal [6] did structural synthesis of Assur groups based on topology. Furthermore, Han et al. [7], in his work, proposed a methodology to synthesize 13 Assur groups with two, four and six links from simple jointed kinematic chains up to eight links. Tartakovsky [8] restored Baranov's synthesis and reported 173 eight-link Assur groups. By integrating Assur groups, Li. et al. [9] developed a methodology for structural synthesis and reported a list of mechanisms and included the Assur group in the adjacency matrix. Shai [10], synthesized all two-dimensional mechanisms using the Assur groups. Huang and Ding [11] synthesized Assur groups up to 12 links and reported as a database. Campos et al. [4] used the Assur groups for type synthesis to build kinematic chains for hybrid robot structures. Peisak [12] gave an algorithm for structural synthesis of Assur groups and reported an atlas of Assur groups with given number of links. Many people have done work towards Baranov truss synthesis (see [13–15]), which is basically a zero *DOF* closed kinematic chain with no rigid sub-chain.

With the above literatures, it is very much evident the importance of Assur groups. The present work aims at developing a methodology to synthesize Assur groups up to 14 links from  $N$ -link, zero *DOF* simple jointed kinematic chains (Baranov Truss).

## 2 Methodology

A Baranov truss is a planar zero *DOF* kinematic chain. Removing any one of its links results an Assur group. Assur groups are open chains which when added to an existing kinematic chain, the degree of freedom of the latter remains unchanged. Thus, it can be understood that, upon the removal of any one link at a time from a Baranov truss, results in an open chain which is an Assur group.

### Example 1

Consider a three-link Baranov truss possessing zero *DOF* as per Grubler's criterion (Fig. 1). Now, removing either of the three links (link-1 or link-2 or link-3) results in a two-link open chain which is an Assur group by definition. Also, links 1, 2 and 3 are identically disposed, and hence, removing either of the links results in Assur groups which are isomorphic to each other. Thus, the number of Assur group possible from a three-link Baranov truss is only one.

**Example**

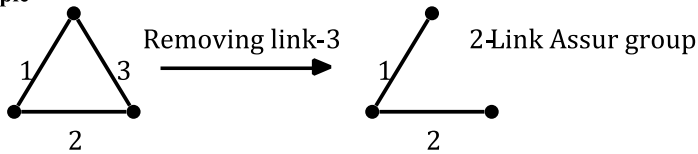


**Fig. 1** Synthesis of two-link Assur group

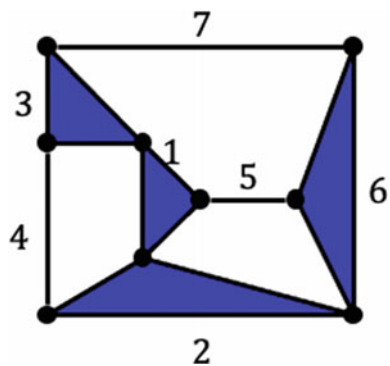
**Example 2**

Consider a seven-link Baranov truss as shown below (Fig. 2).

It can be noted that the links {1, 2}, {4, 5}, {7}, {3, 6} are identically disposed, i.e., removing link-1 results in an Assur group which is identical to the one which is resulted by removing link-2. Hence from {1, 2}, removing either of the one ternary link results in one unique Assur group. Similar case with links {4, 5}, in which, the removal of either link-4 or link-5 results in identical Assur groups, and hence, the number of unique Assur group from {4, 5} is one. Again, from the identically disposed links {3, 6}, removal of either link-3 or link-6 will result in an Assur group. Hence from the links {3, 6}, the number of unique Assur group synthesized is one. Finally, the removal of link-7 results in one unique Assur group. Thus, the total number of distinct Assur groups possible from a seven-link Baranov truss shown in Fig. 2 is four. This is explained in Figs. 3, 4 and 5 respectively.

Thus, it can be seen that the identically disposed links have to be determined to prevent isomorphism in the synthesis of Assur groups. The authors have used the methodology which is proposed in [16] for detecting the isomorphism index from which the identically disposed links can be found out. The advantage out of this proposed methodology is that, since the methodology itself contains the synthesis from identically disposed links, it keeps out a separate isomorphism test for the synthesized Assur groups because, by the virtue of the synthesis methodology itself, the Assur groups synthesized are distinct. In the present work, Assur groups

**Fig. 2** Seven-link Baranov truss





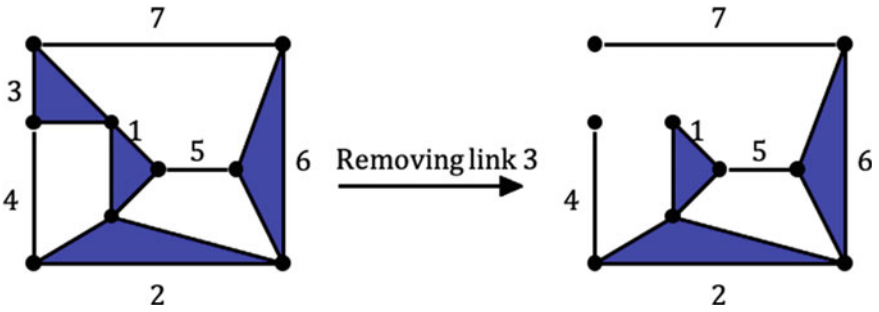


Fig. 3 Synthesis of Assur group by removing link-3

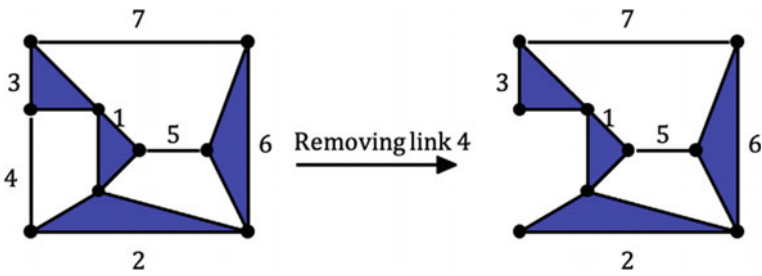


Fig. 4 Synthesis of Assur group by removing link-4

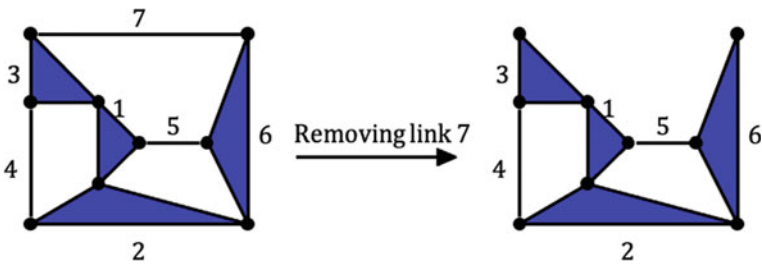


Fig. 5 Synthesis of Assur group by removing link-7

up to 14 links are synthesized, and the results are compared against those reported earlier and found valid. Also, 14-link Assur group is synthesized for the first time in this work. The results are given in Table 1.

**Table 1** Synthesis of Assur group results

Number of Links	Number of Assur Groups (Present Work)	Results reported in [11]
6	10	10
8	173	173
10	5,438	5,438
12	251,637	251,811
14	15,082,693	Not Reported

### 3 Conclusion

In the present work, Assur groups up to 14-links are synthesized. The methodology is very simple, i.e., by removing one link from a given Baranov truss resulted in an Assur group. Also the determination of identically disposed links helps in synthesizing distinct Assur groups. The results are compared against the literatures and found correct. Fourteen-link Assur group is synthesized using this methodology and is reported in this paper. Computation is done using Python programming for obtaining the synthesis results. The number of six-link Assur group synthesized is 10 chains, similarly, eight-link Assur groups synthesized are 173 chains. Under ten links, the number of Assur groups synthesized is 5,438 chains and 251,637 Assur groups of 12 links were synthesized. Also, 14-link Assur group is synthesized which gave 15,082,693 chains. In short, an atlas of Assur groups is created which can be used for the synthesis non-fractionated kinematic chains, parallel mechanisms and series mechanisms of links for robotics and complex structures involving more number of links or members.

### References

1. Manolescu, N.I.: A method based on Baranov trusses, and using graph theory to find the set of planar jointed kinematic chains and mechanisms. *Mech. Mach. Theory* **8**(1), 3–22. Elsevier (1973)
2. Martins, D., Simoni, R., Carboni, A.P.: Fractionation in planar kinematic chains: Reconciling enumeration contradictions. *Mech. Mach. Theory* **45**(11), 1628–1641. Elsevier (2010)
3. Tischler, C.R., Samuel, A.E., Hunt, K.H.: Kinematic chains for robot hands—II. Kinematic constraints, classification, connectivity, and actuation. *Mech. Mach. Theory* **30**(8), 1217–1239 (1995)
4. Campos, A., Budde, C., Hesselbach, J.: A type synthesis method for hybrid robot structures. *Mech. Mach. Theory* **43**(8), 984–995 (2008)
5. Dobrovolsky, V.V.: Osnovnye principy racional'noj klassifikatsii mekhanizmov [Basic principles of rational classification of mechanisms]. V kn.: Dobrovol'skii VV (1939)
6. Krokmal, N., Krokmal, O.: Structural analysis and synthesis of Assur groups based on their topological properties. In *Proceedings of 13th World Congress of IFToMM, Mexico* (2011)
7. Han, J., Yuan, Y., Lv, X., Zhang, Q., Lu, T.: Methodology for the automatic generation of assur groups from planar multi-bar linkages. *J. Mech. Eng.* **51**(19), 1–10 (2015)

8. Tartakovsky, I.I.: Indecomposable statically determinate trusses and groups of stratifying of mechanisms. *Appl. Mech.* XIX **11**, 105–110 (1983)
9. Li, S., Wang, H., Dai, J.S.: Assur-Group inferred structural synthesis for planar mechanisms. *J. Mech. Robot.* **7**(4) (2015)
10. Shai, O.: Topological synthesis of all 2D mechanisms through Assur graphs. In: *International Design Engineering Technical Conferences and Computers and Information in Engineering Conference*, vol. 44106, pp. 1727–1738 (2010)
11. Huang, P., Ding, H.: Structural synthesis of Assur groups with up to 12 links and creation of their classified databases. *Mech. Mach. Theory* **145**, 103668 (2020)
12. Peisakh, E.E.: An algorithmic description of the structural synthesis of planar Assur groups. *J. Mach. Manuf. Reliab.* **36**(6), 505–514 (2007)
13. Shai, O., Pennock, G.R.: A study of the duality between planar kinematics and statics. *J. Mech. Des.* **128**(3), 587–598 (2006)
14. Lee, C.C. Lo, C.Y.: Movable Focal-Type 7-Bar Baranov-Truss Linkages. In: *International Design Engineering Technical Conferences and Computers and Information in Engineering Conference*, vol. 55942, p. V06BT07A071. American Society of Mechanical Engineers (2013)
15. Huang, P., Ding, H.: Structural synthesis of Baranov trusses with up to 13 links. *J. Mech. Des.* **141**(7) (2019)
16. Manikandan, H., Kaup, V., Harish, B.: In quest of a reliable and efficient isomorphism index for simple jointed kinematic chains. In: *AIP Conference Proceedings*, vol. 2134, no. 1 (2019) <https://aip.scitation.org/doi/abs/10.1063/1.5120238>

# A Methodology for Derivation of Isomorphism Index for Epicyclic Gear Transmission Systems



H. Manikandan, Vijayananda Kaup, and Harish Babu

**Abstract** Suitable graph representation of epicyclic gear transmission systems (EGTs) and identification of such systems by means of a reliable isomorphism index are important area of research interests in the emerging field of structural enumeration of epicyclic transmission systems. A methodology to represent the EGTs based on rooted tree structure is proposed in the present work. EGTs can be represented as a kinematic chain. This work aims at deriving an isomorphism index for this kinematic chain which will be a robust identification of the underlying EGT structure. The first invariant of the link, which is the degree of the link itself, is used to express the kinematic chain of EGT in the present work.

**Keywords** Epicyclic gear transmission · Graph representation · Rooted tree structure · Link invariants · Isomorphism index

## 1 Introduction

Multi-speed epicyclic gear transmissions (EGTs) are systems that consist of several interconnected planetary gear trains (PGTs). They have, for many years, been the subject of study due to their wide-ranging applications in automobile gear boxes, steering mechanisms, in machine tools, etc. A suitable representation of EGTs is an important step not only in the synthesis phase but also in the process of identifying isomorphic EGT layouts. Graph theory concepts are found to be very useful in this regard. By using graph theory, an EGT is converted into an equivalent graph, and

---

H. Manikandan (✉) · V. Kaup · H. Babu  
Department of Mechanical Engineering (VTU-RC), CMR Institute of Technology,  
Bengaluru 560037, Karnataka, India  
e-mail: [manikandan.h@cmrit.ac.in](mailto:manikandan.h@cmrit.ac.in)

V. Kaup  
e-mail: [vijayananda.k@cmrit.ac.in](mailto:vijayananda.k@cmrit.ac.in)

H. Babu  
e-mail: [harish.b@cmrit.ac.in](mailto:harish.b@cmrit.ac.in)

various methods can be adopted to address the isomorphism of geared trains. Freudenstein [1] presented a method based on Boolean algebra for the structural topology of epicyclic gear trains. Castillo [2] developed a procedure for the analysis of graphs of epicyclic gear trains possessing one degree of freedom based on functional aspects and constraints. Chen and Yao [3] synthesized fractional geared kinematic mechanisms which was found to be efficient. Random number technique was used by Tsai [4, 5] for designing manipulators for robot using gears. A study of kinematics of epicyclic spur gear trains was done by Hsu. et al. [6] and developed a model using graph theory applications. Manikandan et al. [7, 8] used graph theory and rooted tree structure and developed an isomorphism test for simple jointed kinematic chains, and the same methods were found to be effective for multiple jointed kinematic chains too. Ding et al. [9] used the adjacency matrices and characteristic number string-based isomorphism index while synthesizing geared mechanisms. TSai [10] and Xue et al. [11], in their work, had a brief discussion of the application of graph theory for isomorphism identification in epicyclic gear trains. Kamesh et al. [12] used graph theory and vertex-incidence polynomial for generating epicyclic gear trains up to six links and thereby eliminated all the isomorphic trains during synthesis phase itself. Also, graphical representation with bold and thin lines was used for representing EGTs. Yang et al. [13], in their work, presented an atlas of PGTs up to six links using perimeter loop-based method and found it to be reliable and efficient. The method was checked with seven, eight and ten links PGTs also. Rai et al. [14] developed a unique maximum binary code as the invariant for the kinematic chain using an algorithm of labeling the links and performed a binary search to find out the sequence in which the links are disposed, and finally a maximum binary code was generated which in turn provided the chain invariant. The algorithm was tested for simple and multiple jointed KCs and also EGTs with four, five and six links and found to be reliable. Mustafa et al. [15], used a path matrix method which is derived from link connectivity matrix to address the isomorphism of EGTs. It was verified with five link, six link and eight link EGTs.

Thus, from the literatures, it is evident that the isomorphism index for epicyclic gear trains is an important research area for decades. The present work aims at a generalized representation of epicyclic gear transmission systems with multiple planetary gear trains (PGTs) with elements of constraints such as brakes, clutches and permanent connections between the shafts.

## 2 Graph Representation of an EGT

In the view of the above-discussed facts, it is proposed to model a PGT as a graph consisting of three vertices. Each vertex in the graph denotes a shaft in PGT. The fact that three shafts of a PGT are considered to be identical and that they are interconnected to each other is expressed by means of a graph complete graph of three vertices. Similarly, EGT consisting of multiple PGTs (say three PGTs) uncoupled from each other can be represented as by means of a nine-vertex

disconnected graph. Here, the first three elements (1, 2, 3) are considered to belong to PGT-1 unit, the next set of three elements (4, 5, 6) to PGT-2 unit and the last set of three elements (7, 8, 9) to PGT-3 unit.

A simple PGT unit is an unconstrained two degrees of freedom (*d.o.f*) system. The mobility of gear box has to be reduced to unity if it has to provide positive transmission ratio. This requires imposition of constraints on the system *d.o.f* until the mobility of the system becomes unity. Constraints are imposed on the system by (i) directly and permanently interconnecting certain element of the PGTs; (ii) temporarily interconnecting certain elements of PGTs elements by engaging pre-installed clutches based on the need and (iii) temporarily arresting the motion of some members of the PGT by applying brake on the elements. Thus, these constraining or freedom-reducing elements also have to be appropriately addressed while representing EGT systems. Determination of the number of aforementioned constraining elements necessitates definition of port elements. Port elements of an EGT system represent those PGT elements (or shafts) which serve as an input or an output or brake element. Thus, port elements identify those shaft elements which directly interact with the outside world by way of connection with the engine shaft (input); external transmission element (output of the gear box) and the brake drum (which again is part of the machine/engine frame. An EGT system with four PGTs (numbered in roman numeral) and five permanent connections, namely

- between element-2 of PGT-I and element-5 of PGT-II; (one permanent connection)
- between element-3 of PGT-I, element-9 of PGT-III, element-12 of PGT-IV; (two permanent connections)
- between element-4 of PGT-II, element-7 of PGT-III, element-10 of PGT-IV; (two permanent connections)

is shown in Fig. 3a along with its equivalent graph representation shown in Fig. 3b.

Since it is required that the EGT system delivers positive transmission ratio, the constraining elements also have to be represented in the equivalent graph. Figure 1a shows the schematic of EGT possessing four PGTs coupled to each other through permanent connections and clutches. The five port elements identified are labeled as P1, P2, P3, P4 and P5 as shown in Fig. 3a and as filled circles in Fig. 1b

Also, clutch-C1 is placed between the port P1 of PGT-1 and the shaft-4 of PGT-2. Similarly, another clutch-C2 is placed between the port P3 of the PGT-2 and shaft-9 of PGT-3 as shown in Fig. 1a. These constraining elements which when accommodated in the equivalent graph (Fig. 1b) are shown in Fig. 4. By incorporating all the above permanent connections, the number of vertices reduces from 12 to 7, since some of the vertices merge due to the introduction of permanent connections inside the system. Thus, even though Fig. 3a shows 12 elements, after incorporating the permanent connections, the graph representation (Fig. 1b) has seven vertices. It has to be noted that all the clutch and brakes cannot be applied or engaged simultaneously as it makes the EGT a rigid structure, as evident from Molian–Salamoun equation which is given by

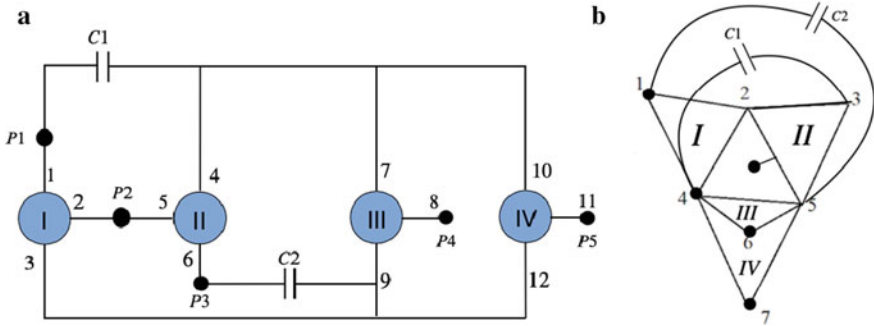


Fig. 1 EGT and its graph representation

$$L + C + B = 2N - M \tag{1}$$

where

- L* Number of permanent connections
- C* Number of clutches
- b* Number of brakes
- N* Number of PGTs
- M* Mobility (Degrees of freedom).

In the present case, if  $L = 5$ ,  $C = 2$ ,  $B = 3$  and  $N = 4$ , then  $M = -2$  (Negative mobility).

Thus, for the mobility of EGT to be unity ( $M = 1$ ), the number of clutches that should be engaged must be 1 and the number of brakes that should be engaged must be 1. Hence, the proposed isomorphism index contains information of only those constraining elements (brakes and clutches) which are engaged when EGT is in constrained motion (i.e., mobility = 1). The graph representation for EGT after adopting Molian–Salamoun equation is shown in Fig. 2.

### 3 Rooted Tree Structure

Now, for the EGT with C1 engaged (graph representation as shown in Fig. 2), adopting the rooted tree structure (RTS)-based representation of kinematic chain as reported earlier by the authors [7, 8], by assigning all the links as the root, the RTS for Fig. 2 is as shown in Fig. 3a.

The next step is to introduce the link invariants. The invariants of a link in the kinematic chain denote those features which are native to the link and are independent of the way the kinematic chain is represented. Here, the first link invariant is used which is the degree of the link itself. In other words, binary link is represented as ‘b’, ternary link as ‘c’ and quaternary link as ‘d’ and so on. Also the port

**Fig. 2** Graph representation of EGT with clutch C1 engaged

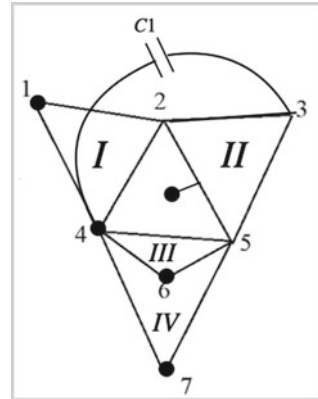
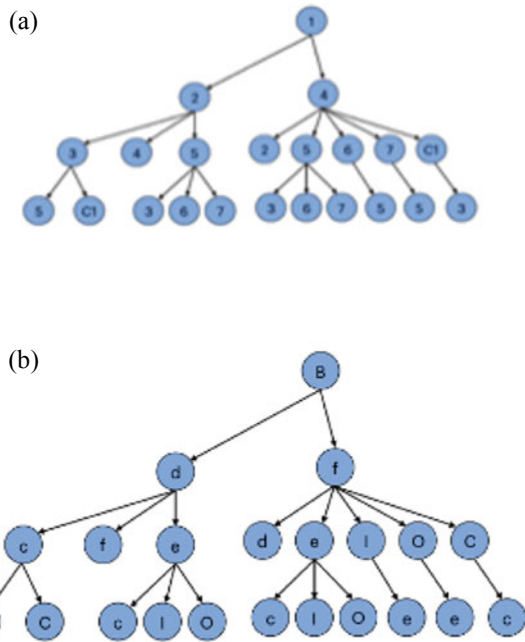


**Fig. 3** Rooted tree structure (root node—1) for EGT with clutch C1 engaged. **a** RTS with Link number. **b** RTS with Link Invariant



elements, viz. input is represented as ‘*I*’, output as ‘*O*’ and brake as ‘*B*’. For the clutch, ‘*C*’ is used as the invariant. It is to be noted that while deriving the isomorphism index based on rooted tree structure, either of the two clutches will be present in the EGT system and its equivalent graph. Also out of five ports, two are



assigned input and output elements each and the remaining ports are for brakes, out of which, only one brake will be engaged at a time. In the present case, we assume engagement of clutch C1 and port element 1 (vertex 1 of the graph) as the brake.

Figure 3b shows the rooted tree structure with link numbers replaced by link invariants.

### 4 Isomorphism Index

The isomorphism index is derived from the rooted tree structures by converting each level of nodes into a string and merging with the previous level strings, till the root link is reached. Consider the rooted tree generated by choosing link-1 as the root (see Fig. 3a). Substituting, say, the first link invariants in place of the link labels in Fig. 3a will produce the tree shown in Fig. 3b. The first invariant has been deliberately used here in order to verify the effectiveness of the description scheme adopted in the isomorphism test despite the use relatively weak link invariant, i.e., first invariant rather than the second.

To begin with, the two leaf nodes d and c in level-3 (see Fig. 3b) are merged with their parent nodes in level-2 to generate strings c(e), c(C), e(c), e(I), e(O), e(c), e(I), e(O), I(e), O(e) and C(c) in level-3. This is indicated in Fig. 4a. The resulting tree, upon removal of level-3, is shown in Fig. 4b. Next, merging the eight leaf nodes c(e),c(C), f, e(c),e(I),e(O), d, e(c),e(I),e(O), I(e), O(e) and C(c) in level-2 with their parent in level-1 will produce the tree as shown in Fig. 4c. Whenever a parent node has multiple leaf nodes, the string of each leaf node is sorted in the order of increasing string value and arranged in a line with a comma separator before merging with the parent node. Upon removal of level-2, the tree is shown in Fig. 4c. Proceeding along similar lines, the tree is shown in Fig. 4d. The rooted tree obtained taking link-1 as the root will be B(d(c(C,e),e(I,O,c),f),f(C(c),I(e),O(e),d,e(I,O,c)))

The string represents the disposition of link-1 with respect to all other links in the given kinematic chain. Procedure is repeated keeping all the links as root nodes. And the strings are sorted in some order which finally represents the isomorphism index for the EGT.

The final string representation for the EGT is shown below.

Link number	RTS_string
1	B(d(c(C,e),e(I,O,c),f),f(C(c),I(e),O(e),d,e(I,O,c)))
2	d(B(f),c(C,e),e(I,O,c),f),f(B,C,I,O,e))
3	c(C(f(B,I,O)),d(B(f),e,f(B,I,O)),e(I(f),O(f),d,f(B,I,O)))
4	f(B(d),C(c),I(e),O(e),d(B,c,e),e(I,O,c,d))
5	e(I(f),O(f),c(C,d),d(B,c,f),f(B,C,I,O,d))
6	I(e(O,c(C,d),d(B,c),f),f(B(d),C(c),O,d(B,c),e))
7	O(e(I,c(C,d),d(B,c),f),f(B(d),C(c),I,d(B,c),e))
8	C(c(d(B,e),e(I,O,d)),f(B(d),I(e),O(e),d(B,e),e(I,O,d))

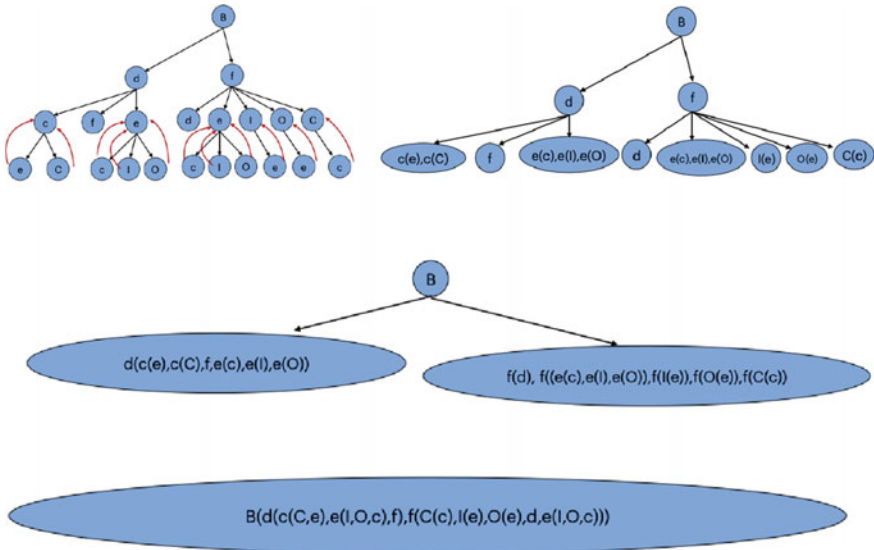


Fig. 4 Stages of conversion of rooted tree structure into string

KC\_string\_representation

$B(d(c(C,e),e(l,O,c),f),f(C(c),l(e),O(e),d,e(l,O,c)))\_C(c(d(B,e),e(l,O,d)),f(B(d),l(e),O(e),d(B,e),e(l,O,d)))\_I(e(O,c(C,d),d(B,c),f),f(B(d),C(c),O,d(B,c),e))\_O(e(l,c(C,d),d(B,c),f),f(B(d),C(c),l,d(B,c),e))\_c(C(f(B,I,O)),d(B(f),e,f(B,I,O)),e(l(f),O(f),d,f(B,I,O)))\_d(B(f),c(C,e),e(l,O,c),f),f(B,C,I,O,e))\_e(l(f),O(f),c(C,d),d(B,c,f),f(B,C,I,O,d))\_f(B(d),C(c),l(e),O(e),d(B,c,e),e(l,O,c,d))$

### 5 Conclusion

The present work addresses the problem of isomorphism in EGTs. The fact that such systems have features like permanent connections between different constituent PGTs; that certain elements in a PGT are identified as points of input and output of an EGT; that some elements act as brakes and that there may exist clutch connections across different elements of PGT, demonstrate wide variety of possibilities that may occur in the structure of EGTs. A new representation scheme to accommodate these features and variations is successfully attempted in this study. The method uses a robust way of describing the graph taking the form of a tree. One tree is constructed from each vertex. This is followed by the definition of vertex invariants which uniquely identify the type of element present in the graph. Replacement of vertex labels appearing in the tree with their invariants will make the trees independent of original labels of the vertices. The trees are then reduced to a unique string through a contraction procedure so as to ensure one-to-one

correspondence with each other. It has been found that the method offers flexibility in terms of changing the status of a particular vertex to a brake or an input or an output element without the effort of rebuilding the trees. The effort required to handle such redefinitions of EGT elements is simple string manipulations, done with ease using modern computer languages. Using a computer program, an isomorphism index is derived by considering a typical EGT consisting of all possible elements that such a system may possess.

## References

1. Freudenstein, F.: An application of Boolean algebra to the motion of epicyclic drives. *ASME J. Eng. Ind. Ser. B* **93**, 176–182 (1971)
2. Castillo, J.M.D.: Enumeration of 1-dof planetary gear train graphs based on functional constraints. *ASME J. Mech. Des.* **124**(4), 723–732 (2002)
3. Chen, D.Z., Yao, K.L.: Topological synthesis of fractionated geared differential mechanisms. *ASME J. Mech. Des.* **122**(4), 472–478 (2000)
4. Tsai, L.W.: An application of the linkage characteristic polynomial to the topological synthesis of epicyclic gear trains. *ASME J. Mech. Transm. Autom. Des.* **109**(3), 329–336 (1987)
5. Tsai, L.W., Lin, C.C.: The creation of non-fractionated two-degree-of-freedom epicyclic gear trains. *ASME J. Mech. Transm. Autom. Des.* **111**(4), 524–529 (1989)
6. Hsu, C.H., Lam, K.T.: A new graph representation for the automatic kinematic analysis of planetary spur-gear trains. *ASME J. Mech. Des.* **114**(1), 196–200 (1992)
7. Manikandan, H., Kaup, V., Babu, H.: In quest of a reliable and efficient isomorphism index for simple jointed kinematic chains. In: International Conference on Applied Mechanics and Optimisation (ICAMeO-2019) AIP Conf. Proc. 2134, 070004-1–070004-9
8. Manikandan, H., Kaup, V., Babu, V.: In quest of a reliable and efficient isomorphism index for multiple jointed kinematic chains. In: International Conference on Applied Mechanics and Optimisation (ICAMeO-2019) AIP Conf. Proc. 2134, 070005-1–070005-11
9. Ding, H., Liu, S., Huang, P., Cai, C., Huang, Z.: Automatic structural synthesis of epicyclic gear trains with one main shaft. In: Proceedings of ASME IDETC/CIE, (Boston, Massachusetts, USA, 2015), pp. 1–10
10. Tsai, L.W.: *Mechanism Design: Enumeration of Kinematic Structures According to Function*. CRC Press, Boca Raton (2001)
11. Xue, H.L., Liu, G., Yang, X.H.: A review of graph theory application research in gears. *Proc. Inst. Mech. Eng. Part C J. Mech. Eng. Sci.* **230**(10), 1697–1714 (2016)
12. Kamesh, V.V., Mallikarjuna Rao, K., Srinivasa Rao, A.B.: A novel method to detect isomorphism in epicyclic gear trains. *i-Manag. J. Future Eng. Technol.* **12**(1), 28 (2016)
13. Yang, W., Ding, H.: The perimeter loop-based method for the automatic isomorphism detection in planetary gear trains. *J. Mech. Des.* **140**(12) (2018)
14. Rai, R.K., Punjabi, S.: A new algorithm of links labelling for the isomorphism detection of various kinematic chains using binary code. *Mech. Mach. Theory* **131**, 1–32 (2019)
15. Mustafa, J., Hasan, A., Khan, R.A.: An application of modified path matrix approach for detection of isomorphism among epicyclic gear trains. *J. Inst. Eng. (India) Ser C* 1–10 (2020)

# Study and Review of Quality 4.0 in the Industry



**Gaurav Gohane, Atul Bulkunde, Anish Parate, Prabhat Nagdeve,  
Vikas Mendhe, Shivam Pandey, and Hrithik Yadav**

**Abstract** Quality is a common term but has a different impact in different sectors of various organizations. The old history to the current era of quality depicts the rise of quality. The main objective of the paper is to analyze the history of quality to industry-related problems in terms of quality. In this, we have told you about the significance of quality and quality-related terms to the current quality term, i.e., Quality 4.0.

**Keywords** Six sigma · Ecosystem of Quality 4.0 · 11 axes of Quality 4.0 · Industries-related problem · Systematic literature review

## 1 Introduction

History of quality began at late thirteenth century since period of craftsmanship where craftsmen sold their product in local market. To make lot of customer, they started to inspect their own product before sell. After that factory system came in which craftsmen started working in big factories. During the World War II, the inspection of equipment became the most important prospective for safety of arm force. Still, many lower companies are facing the problem related to quality, cost, etc. To support and educate these types of organizations, “American Society for Quality Control” (ASQC) is formed and now it has changed to “American Society for Quality” (ASQ). To improve further quality, Japan has bought the idea of management system, quality circle, seven quality tools, 5S, etc. After observing the Japanese management system, USA bought the new idea of “total quality management” (TQM) in twentieth century.

Finally, Fourth Industrial Revolution came in twenty-first century. In this current era, technology, computer programming, and better management system help the quality go beyond the concept of TQM. Quality has moved beyond the manufac-

---

G. Gohane · A. Bulkunde (✉) · A. Parate · P. Nagdeve · V. Mendhe · S. Pandey · H. Yadav  
JDCOEM, Nagpur 441501, India

turing sector in further areas such as health care, education, and government. It is the concept of six sigma, ecosystem of Quality 4.0 tool and 11 axes of Quality 4.0.

## **2 Six Sigma**

### **2.1 DMAIC**

Define, measure, analyze, improve, and control should be used when a product is in existence at your company but is not meeting customer satisfaction is not performing adequately [1].

### **2.2 DMADV**

Define, measure, analyze, design, and verify should be used when product or process is not in existence at your company and needs to be developed [1].

## **3 The Ecosystem of Quality 4.0 Tools**

### **3.1 Artificial Intelligence**

Computer vision, language processing, chatbots, personal assistance, navigation, robotics, and making complex decision this is all are the feature of AI. Artificial intelligence is simply any code technique or algorithm that enable machine to mimic develop and demonstrate human cognition or behavior. AI are used in four technologies such as data technology (DT), analytic technology (AT), perform technology (PT), and operation technology (OT) are enablers for achieving success in connection, conversion, cyber, cognition, and configuration, or 5C.

### **3.2 Machine Learning**

Machine learning has a feature of text analysis, filter the email spam and also detect the fraud in data. Visual quality inspection of ML helps in detect defect in product. ML is categorized into a statistical and deep learning for the pattern recognition process. It can use in industries such as retail, manufacturing, airport baggage, food industry, and medicine. Prediction, classification, pattern identification, data reduction, anomaly detection, and pathfinding are some task of machine learning.

### ***3.3 Deep Learning***

Deep learning is type of machine learning inspired by human brain work in artificial neural network. It can tell the difference in object or images and this feature is taken out by neuro network. Deep learning is applied in customer support, medical care, and self-driving cars such as Apple, Tesla, and Nissan. Auto text generation and creating new fictitious video base on real video with the help of deep learning.

### ***3.4 Blockchain***

Blockchain is a collection of records, strongly resistant to alteration and protected using cryptography. One's the data as recorded inside the blockchain, it becomes very difficult to change it. Each block contains some data, the hash of the block, and the hash of the previous block. It makes it very hard to temper with the block. It is used in creation of new contracts, storing medical records, creating a digital notary, or even collecting taxes. Blockchain of a product, assembly, or component identifying information help in quantifying and managing quality problems with a higher level of specificity [2].

### ***3.5 Big Data***

Infrastructure, easier access to data sources, tools for managing and analyzing large data sets without having to use supercomputers. Classification of data as big data is possible by concept of 5V's known by volume, velocity, variety, veracity, and value. To store the large amount of data, various frameworks are available such as Cassandra, Hadoop, and Spark.

### ***3.6 Enabling Technologies***

An enabling technology is associate invention or innovation which is able to be applied to drive radical modification inside the capabilities of a user or culture. It is an area unit defined by quick development of later spinoff technologies, sometimes, in varied fields. It has affordable sensors and actuators, cloud computing, open-source software, augmented reality (AR), mixed reality, virtual reality (VR), data streaming (such as Kafka and Storm), 5G networks, IPv6, and IoT [3].

### **3.7 *Statistics and Data Science***

Business problems will be able to help with what needs to be done and what needs to be tackled. With the help of data acquisition, we can gather and scrape data from multiple sources like Web servers, logs, databases, API's and online repositories. After gathering data comes data preparations, this step includes data cleaning and data transformation. Now with the help of exploratory data analysis (EDA), we can define and refine the selection that will be used in the model development [4].

## **4 Axes of Quality 4.0**

### **4.1 *Analytics***

Principle of analytics: Business should develop on analytics strategy after or concurrently with a data strategy. 37% of organizations identify poor metrics as the main roadblock to achieve quality objectives. Analytics can be categorized in forms in 11 axes of Quality 4.0.-Big data; traditional data. The companies which are building toward Quality 4.0 should build their analytics strategy. Analytics helps us to identify the insights within data.

### **4.2 *Data***

Principles of data: Companies must use data to drive decision making and to find ways to combine data from various systems to ensure accuracy and transparency. Data can be categorized in two forms in 11 axes of Quality 4.0.-Big data; Traditional data. Traditional data comes under the element volume (low to high). Big data can be used in infrastructure (such as high) MapReduce, Hadoop, Hive, and MySQL, and other databases can have easier access to date elements sources, the tools for managing and analyzing data sets without having use of supercomputers.

### **4.3 *App Development***

It is powered by advanced digital technologies such as artificial intelligence, augmented reality, virtual reality, IoT, and other various technologies. To achieve this goal of mobile manufacturing via mobile devices and smartphones, we have used some specific applications to work and finish the job or task. The application in industry will reduce the manpower, time, and cost while increasing the overall performance of the industry.

#### ***4.4 Connectivity***

Connectivity is defined as the ability to establish communication between two or more electronic devices such as mobile, computers, smartwatches, and sensors through software's and Internet. Connectivity is the pillar of Quality 4.0 and it is going to have a major role in industry to make factories and offices wireless. A proper connectivity will lead to smart manufacturing, smart warehousing, mining operations, etc., providing a safe working environment. Connectivity will help to improve communication between business information technology and operational technology.

#### ***4.5 Scalability***

Scalability can be defined as the ability to support processes, data volume, analytics, users, devices, and platforms on global level. With the help of big data and cloud computing, we can keep an eye on how scalability is and how we can increase it. The leaders must adapt these methods on a global level to increase their production and productivity and to remove the fragmented systems and sources. Traditional and Quality 4.0 are nearly as ineffective without global scale and the company will be not able to harmonize the knowledge which is learned in the corporate world. Scalability is very important in Quality 4.0, in general, scalability is the pillar of Quality 4.0.

#### ***4.6 Collaboration***

Collaboration is essential for quality management. Collaboration has transformed in recent years, within worldwide across various companies and with customer. Collaboration is an essential word from the 11 axes of Quality 4.0 for innovation and the betterment of quality and has been altered by connectivity, data, and analytics. Employees and employers of an organization should team up and build a safe and secure data sharing strategy that meets collaboration goals such as better competency, more streamlined oversight, improved security, and audit-ability.

#### ***4.7 Competency***

Competency is a set of skill, ability, knowledge, attribute, and motivation on individual needs to scope with job-related tasks and challenge efficiency. Technical, methodologist, social, and personal to create a competency model tools to assess



specific competencies of individual employees by customizing it to specific department or job profile and to identify the competence gap.

#### ***4.8 Leadership***

Leadership is one of the most important pillars of 11 axes of Quality 4.0 which decide how you compete in this automated environment to get success in your organization. Leader should possess a quality of brainstorming, quality circle which admire leader to provide a platform to his team that they freely express their thoughts and ideas without any barrier and hesitation in front of leader so they adjust themselves to reach their goals or objectives, and all the efforts of both leader and his team lead toward company success.

#### ***4.9 Culture***

Many organizations have an initiative to build a culture of quality. If top organizations maintain a culture to produce top-quality products so they can compete in this era of automated world. As you not all but few companies have moved toward automation and to enhance this automation, there exists a concept of Quality 4.0 by the collaboration of these Quality 4.0 top organizations moved toward innovation and improvement of quality products.

#### ***4.10 Compliance***

Compliance can be a top priority in quality management. Automation and digitalizing compliance processes and further reducing the total cost of quality can be done through Quality 4.0. Compliance plays a huge role in various activities such as conforming to regulatory, industry, customer, and internal requirements. The combination of business information technology (IT) and operation technology (OT) helps in the automated compliance-related tasks and data collection. Quality 4.0 allows organizations to observe current compliance strategies and seek the opportunities for improvement.

#### ***4.11 Management System***

The enterprise quality management system had only been adopted by 21% of the organizations. Management systems or EQMS can be called as the vital cog within

quality management because it provides a suitable solution to automate workflows, connect quality processes, improve data veracity, provide centralized analytics, ensure compliance, and foster collaboration. Management system defines a way in which an organization manages the related or connected parts of its business in order to achieve its objectives.

## **5 Industries-Related Problem**

As we know quality is the most important parameter in an industry, but at the same time, some organizations are not looking at quality-related issues seriously. So, as we need to add culture in industry to go seriously for quality-related issue. Various companies or organizations belongs to different sectors like management, manufacturing and service sectors so accordingly different the problems are occurred or seen, and that is why every problem having different solutions. In the development of any service or product, first, we need to reduce problems which are occurring in an organization. Depends upon that the accuracy and lenient nature of any organization will help it to have qualified service or product.

As we observed in MMS industry as it works on powdered metallurgy method, so we think accordingly to that aspect only. We have observed many issues in the industry, some are technical and other are non-technical. The non-technical issue includes some ergonomic issues with respect to machinery and equipment in the industry. It also includes some man-to-man errors which directly affects the quality, even here some communication gap due to notice in working field, so according to it, we are looking toward it.

### ***5.1 Benefit of Quality 4.0***

In Quality 4.0, the quality inspection is done during the processes. So, if the product does not satisfy one condition, either it is re-treated or rejected and not treated further. In Quality 4.0, a software named UTS is used which gives not only real-time data but also the theoretical analysis necessary for the material which is been treated. It tells whether there is a problem which can lead to degrade the quality of final product. As the quality inspection is done after every process, so the product which does not satisfy quality inspection is rejected immediately, therefore, saving time, energy, and much more. Some factories/companies have already adapted Quality 4.0, but others have not because of various reasons like they think that they are doing well with their technique. They think why should we adapt different techniques and invest money on that. They are afraid that they could go on loss by adapting Quality 4.0. They are not willing to take the risk. It will still take some time for industries to realize that Quality 4.0 is beneficial for them [5].

## 6 Literature Review

The literature review is presented in Table 1.

**Table 1** Literature review

Paper	Author	Date	Conclusion
Quality 4.0 is reshaping product development [3]	Scott Reddy	December 2019	As development is getting more and more complicated in Quality 4.0, the modern manufacturers are relying on distributed teams and supply chains, including design partners, contract manufacturers, and tiered component suppliers to speed product development. As Quality 4.0 is a part of Industrial Revolution, it has greater impact on digital data, analytics, connectivity, scalability, and collaboration
Quality 4.0—how to handle quality in the Industry 4.0 revolution master’s thesis in quality and operations management [1]	Daniel Forero, Raoul sisodia	January 2020	It can be concluded that as Quality 4.0 is the part of Industrial Revolution, it has transformed itself in a proper managerial system. Several case studies are done by Swedish and international organizations, focusing on understanding how the organization had undergone changes or are changing in Quality 4.0. It has given a brief explanation on how Quality 4.0 is presented and a general plan for changes of Q4.0 is proposed, which includes six sequential phases and is applicable to different organizations that plan to undergo change in Quality 4.0

(continued)

**Table 1** (continued)



Paper	Author	Date	Conclusion
Have you transitioned to Quality 4.0? [5]	Assurx	September 2019	The modern technology integrates into production quality system through Quality 4.0. Several examples are given in the paper such as cloud computing, big data, virtual reality, blockchain, artificial intelligence, machine learning, and Internet of things. It has given us a structured method for completing quality throughout each step of the manufacturing process and thus Quality 4.0 is resulting us in an adaptable approach which reduces product risk
Quality 4.0—the challenging future of quality engineering [6]	Avigdor Zonnenshain and Ron S. Kenett Icon	February 27, 2020	As quality is a data driven, it has various applications of modeling and simulation for evidence-based quality engineering, health monitoring and prediction for quality, coordinated quality management, maturity levels with respect to the Fourth Industrial Revolution, coordinated innovation with quality and managing for innovation, Quality 4.0 and data science, coordinated reliability engineering with quality engineering, and finally, information quality

**References**

1. Forero, D., Sisodia, R.: Quality 4.0—how to handle quality in the Industry 4.0 revolution master’s thesis in quality and operations management (2020)
2. Kupper, D., Knizek, C., Ryeson, D., Noecker, J.: Quality 4.0 takes more than technology (2019)
3. Reddy, S.: Quality 4.0 is Reshaping Product Development (2019)
4. Radziwill, N.: Quality and Innovation (2018)
5. Assurx: Have you transitioned to quality 4.0? (2019)
6. Kenett Icon, R.S., Zonnenshain, A.: Quality 4.0—The Challenging Future of Quality Engineering (2020)

# Experimental Investigation of Tool Wear Rate (TWR) During the EDM of Hybrid Aluminum Metal Matrix Composite Reinforced with SiCp and Grp



Mandeep Singh , Pardeep Kumar Mishra,  
Pragyan Parimita Mohaty, and Rasmeet Singh 

**Abstract** The EDM is the suitable and effective machining process for machining the hybrid aluminum metal matrix composites. This paper investigates the significant effect of machining parameters (pulse-on time, pulse-off time, voltage, and current) on the response variable tool wear rate (TWR). In this experimental work, three different aluminum metal matrix composite (Al MMC) samples were fabricated with distinct compositions of reinforcements by the stir casting process. The SiCp and Grp were used as reinforcements. Machining was done through EDM, with three different electrodes materials (steel-304, brass, and copper) with Ø12 mm each. The design matrix and mathematical models were developed by RSM using the Design-Expert 9.0.6 software. To check the signification of model, the ANOVA technique was used. The SEM and EDS were used to study the surface characteristics and elements analysis, respectively, of the machined electrodes. It was inspected that the cracks and craters are produced in all the fabricated samples. In this study, it was also examined that the Al MMC-1 (10% SiCp and 3% Grp) is the best fabricated composite as compared to the other two composites in terms of wear resistance and hardness.

**Keywords** Al MMC · EDM · Stir casting · RSM · SEM · EDS

---

M. Singh (✉)

School of Mechanical and Mechatronic Engineering, University of Technology Sydney,  
Ultimo 2007, NSW, Australia

e-mail: [Mandeep.Singh@uts.edu.au](mailto:Mandeep.Singh@uts.edu.au)

P. K. Mishra

Department of Mechanical Engineering, College of Engineering and Technology,  
Tiruchirappalli, India

P. P. Mohaty

Department of Mechanical Engineering, VSSUT, Burla, India

R. Singh

Dr. S.S. Bhatnagar University Institute of Chemical Engineering & Technology,  
Panjab University, Sector 14, Chandigarh 160014, India

## 1 Introduction

Metal matrix composite (MMC) is one of the most advance man-made materials. A MMC has very light in weight, low coefficient of thermal expansion and thermal resistance, and good damping capacity [1]. By adding the reinforcement into various forms and configurations, the strength and stiffness of prepared MMC sample are directly affected. When at least two different reinforcements (materials) are added into the metallic matrix phase to fabricate an MMC, then that composite material is called as hybrid metal matrix composite [1]. In this research work, three different hybrid MMC materials were fabricated. To fabricate these three hybrid MMC materials, the Al 6061 is used as the matrix phase, where the SiCp and Grp are reinforced into three different compositions with same configurations. To develop these three hybrid MMC samples, the stir casting method is used [2]. The SiCp and Grp are used as reinforcements due to their unique sets of properties and applications [3]. In this experimental study, the electric discharge machine (EDM) was used to machine the three developed samples. Three different material rods of copper, brass, and steel 304 (each have 12 mm  $\varnothing$ ) are used as electrodes in this experimental work to machine the fabricated samples (Al MMC). To perform the EDM operations, a design matrix/sheet is developed in "Design-Expert 9.0.6" software by using "response surface methodology," in which 52 experiments are attained [4]. By taking four machining parameters (pulse-on time ' $T_{on}$ ', pulse-off time ' $T_{off}$ ', voltage ' $V$ ', and current ' $I$ ') and also fluctuating their values (up to 3 levels), the desire response (TWR) was calculated. To optimize the EDM process parameters, the mathematical models made by response surface methodology (RSM) were studied.

## 2 Materials and Methods

It was a big challenge to prepare a metal matrix composite with uniform distribution of the reinforcement phase and without any microstructure defects. To prepare three different composites samples, the Aluminum 6061 is used as a matrix phase for each one, where the silicon carbide particles and graphite particles are utilized as reinforcements. The SiCp and Grp are reinforced into three different compositions. The Al MMC-1, Al MMC-2, and Al MMC-3 for Grp are 3, 5, and 8%, respectively. And for SiCp, it is 10, 15, and 20%, respectively. The configuration of both SiCp and Grp is the same; they both reinforced via 200 mesh size with an average size of 75  $\mu\text{m}$ . The homogeneous distribution of reinforcement particles was achieved in order to get the best results.

The properties of Al 6061 (matrix phase), Sic, and Gr (reinforcements) are shown in Table 1. In the stir casting process, the Al 6061 alloy (matrix phase) is kept in graphite crucible inside the electric vertical muffle furnace. The high temperature (850  $^{\circ}\text{C}$ ) of the muffle furnace is quickly melted the aluminum alloy.

The SiCp and Grp were preheated at 800 °C temperature into another electric muffle furnace to improve the wet-ability of reinforcements [5]. After melting the Al 6061, it is cooled down to come into a semi-solid state where the preheated particles of Sic and Gr are reinforced into three different compositions. A graphite stirrer is used for carrying the mechanical stirring during the mixing of reinforcements. After the proper mixing, the molten metal was poured into the preheated cast-iron mold, and then the mold was left at environmental temperature for cooled down; after the solidification, the required cast composites achieved. The pictorial views of three developed AL MMC samples and three different electrodes are shown in Fig. 1i and ii, respectively.

### 3 Experimental Work

The experimental work has been done through three-level and four process parameters. Further, the final design matrix established through Design-Expert 9.0.6 version software [6, 7]. The selected machining parameters and their levels are shown in Table 2. The designed experiments were performed on the Oscar Max Die-Sinking EDM machine (Taiwan made).

The specifications of the Oscar Max machine are shown in Table 3. Three different tools are made of copper, brass, and steel-304 with Ø 12 mm; each was used as an electrode. During the EDM process, both *W/p* and electrodes are immersed in the dielectric fluid. A commercial-grade EDM oil (density = 0.76) was utilized as dielectric fluid. An EDM machine has a various number of process parameters such as (pulse-on time, pulse-off time, applied voltage, peak current, flushing pressure, etc.). Here, in this experimental work, we choose four process parameters (pulse-on time, pulse-off time, voltage, and current) and fluctuate their levels to design a sheet of 52 experiments by response surface methodology in Design-Expert 9.0.6 software as earlier discussed. These 52 experiments were performed on the EDM machine to calculate our desire response-TWR and investigate the significant parameters which mostly affected TWR. A hole cavity of 1 mm depth is crated during each machining process, and the machining time of each specimen is noted. To determine the TWR, we calculated the weight difference of tool electrodes (before and after the machining) and over the machining time. Equation (1) is used to calculate the TWR.

**Table 1** Properties of matrix and reinforcements

	<i>P</i> (g/cm <sup>3</sup> )	<i>M</i> (°C)	<i>G<sub>T</sub></i> (µm/m °C)	<i>A</i> (W/mk)	<i>E</i> (Gpa)
Al 6061	2.7	650	166	23.4	70
Sic	3.23	2913	126	4	410
Gr	2.23	3915	85	2-6	10

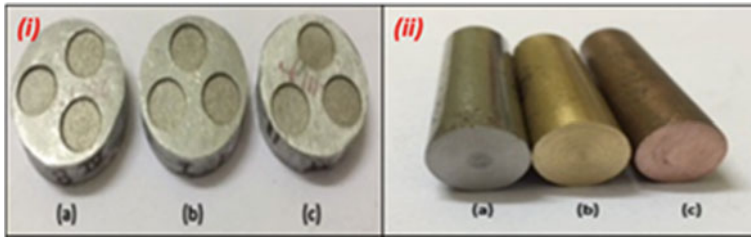


**Fig. 1 i** Three developed samples (a) Al MMC-1 (SiCp10% and Grp3%), (b) Al MMC-2 (SiCp15% and Grp5%), and (c) Al MMC-3 (SiCp20% and Grp8%). **ii** Three different electrodes (before machining), (a) steel-304, (b) brass, and (c) copper

**Table 2** Selected machining parameters and their levels

Levels	$T_{on}$ ( $\mu s$ )	$T_{off}$ ( $\mu s$ )	$V$ (V)	$I$ (I)	Tool	$W/p$
1	30	30	6	10	Steel-304 (-1)	Al MMC-1 (-1)
2	60	60	7	12	Brass (0)	Al MMC-2 (0)
3	90	90	8	14	Copper (1)	Al MMC-3 (1)

**Table 3** EDM machine specifications

Model/machine name	S645 CMAX/Oscar Max
Work tank	1500 mm (L), 940 mm (W), 520 mm (H)
Max. workpiece weight	2000 kg
Max. current	180 A
Max. MRR	1500 mm <sup>3</sup> /min
Weight	3600 kg
Table travel (X)/(Y)	600 mm/450 mm

$$TWR(g/s) = \frac{(T_{bm} - T_{am})}{MT} \tag{1}$$

To quantify the weight of the tool/electrode, a weighing machine (model PGB 200) with a maximum capacity of 200 gm and readability of 0.001 gm are used.

### 4 Response Surface Methodology (RSM)

The RSM has applied here to get the experimental design matrix by means of optimization of parameters of EDM, thereby changing the value of TWR. The concept of central composite design (CCD) is applied to carry out the experiments with the evaluation parameters, which can show the impacts [8]. The principles of



RSM with the combination of mathematical and statistical capabilities and can be used to enhancing, developing, and study the practices. Moreover, the RSM method generally executes with four phases; in phase I, the experiments can be designed; in phase-II, the analysis can be done through mathematical models, the optimization of the parameter can find in phase-III, and finally, in phase-IV, prediction analysis will be performed. The machining parameters with the levels are presented in Table 4.

The nonlinear assessment is a traditional fit technique that exhibits the correlation between the dependent variable and independent variables [9]. The regression model can be stated in Eq. (2).

$$Y = f(X1, X2, X3, X4) \tag{2}$$

In Eq. (2), the “Y” is referred to as dependent variables, and whereas f is the function of independent variables [10]. In order to examine the approximation of “Y,” a polynomial regression model is developed, which is called a quadratic model. The quadratic model of “Y” can be written as follows in Eq. (3).

$$Y = \beta_0 + \sum_{i=1}^k \beta_i x_i + \sum_{i=1}^k \beta_{ii} x_i^2 + \sum_{i < j} \beta_{ij} x_i x_j + \epsilon \tag{3}$$

The developed matrix through RSM techniques, along with the response parameters, is presented in Table 5.

### 5 Mathematical Model

The developed mathematical model for the response (TWR) with process parameters in the coded form is expressed in Eq (4). The mathematical model proved that the two parameters ( $T_{on}$  and  $I$ ) are directly affected our desire response (TWR), whereas, on the other side, it examined that the voltage has no significant effects on TWR. By increasing the  $T_{on}$  and  $I$ , the TWR rate, increases. The maximum tool wear is considered on the brass electrode as compare to steel-304 and copper tools.

**Table 4** Machining parameters and their level

	Machining parameters	$T_{on}$ (μs)	$T_{off}$ (μs)	V (V)	I (A)
Levels	-1.56	15	15	5	9
	1	30	30	6	10
	2	60	60	7	12
	3	90	90	8	14
	1.56	120	120	9	16

**Table 5** Design matrix

Exp. No	$T_{on}$ ( $\mu$ s)	$T_{off}$ ( $\mu$ s)	V (V)	I (A)	Tool	W/p	TWR (g/s)
1	2	2	2	2	0	0	0.000661
2	2	2	2	2	0	0	0.000661
3	2		2	2	0	0	0.000661
4	2	2	2	2	0	-1	0.0007943
5	2	2	-1.56	2	0	0	0.0007147
6	3	1	1	1	1	-1	4.301E-05
7	3	3	1	1	-1	-1	7.514E-05
8	2	2	2	-1.56	0	0	0.0007396
9	1	3	3	1	-1	-1	0.0000561
10	2	-1.5	2	2	0	0	0.0014054
11	3	1	3	1	1	1	2.142E-05
12	2	2	2	2	0	0	0.000661
13	1	1	1	3	1	-1	0.0001567
14	3	1	3	3	1	-1	6.185E-05
15	2	2	2	2	0	0	0.000661
16	3	3	1	3	-1	1	0.0001428
17	1	3	1	3	1	1	0.0000872
18	2	2	2	2	1	0	0.0000573
19	2	2	1.56	2	0	0	0.0006944
20	1	3	3	3	1	-1	5.835E-05
21	2	2	2	2	0	0	0.000661
22	1	3	3	1	1	1	0.00004
23	2	2	2	1.56	0	0	0.001039
24	1	3	1	1	-1	1	8.474E-05
25	3	3	3	1	1	-1	0.000034
26	1	3	3	3	-1	1	0.0000946
27	3	1	1	3	-1	-1	0.000288
28	3	1	3	1	-1	-1	0.0001168
29	3	1	1	1	-1	1	0.0001605
30	2	2	2	2	0	0	0.000661
31	3	3	1	3	1	-1	5.759E-05
32	1	1	3	3	-1	-1	0.0001898
33	1	1	3	1	1	-1	0.0000514
34	-1.56	2	2	2	0	0	0.0003127
35	2	2	2	2	-1	0	0.0000645
36	3	3	3	1	-1	1	0.0000996
37	2	2	2	2	0	1	0.0006517
38	1	3	1	1	1	-1	2.935E-05
39	2	2	2	2	0	0	0.000661
40	1	1	3	3	1	1	0.0001208

(continued)

**Table 5** (continued)

Exp. No	$T_{on}$ ( $\mu s$ )	$T_{off}$ ( $\mu s$ )	$V$ (V)	$I$ (A)	Tool	W/p	TWR (g/s)
41	3	3	1	1	1	1	2.342E-05
42	1	3	1	3	-1	-1	0.0000853
43	3	3	3	3	-1	-1	0.0001063
44	1.56	2	2	2	0	0	0.0009508
45	3	1	3	3	-1	1	0.0001896
46	1	1	1	1	-1	-1	0.0001046
47	3	3	3	3	1	1	2.502E-05
48	1	1	1	3	-1	1	0.0001507
49	1	1	3	1	-1	1	0.0001111
50	1	1	1	1	1	1	0.0000463
51	3	1	1	3	1	1	9.375E-05
52	2	1.56	2	2	0	0	0.0004941

It is also determined that the tool wear is mainly lower when the pulse-off time is increasing.

$$\begin{aligned}
 \text{TWR (g/s)} = & + 7.898E-004 + 2.901E-005 * A - 6.052E-005 * B \\
 & - 7.700E-006 * C + 3.467E-005 * D - 3.027E-005 * E \\
 & - 6.665E-006 * F - 4.781E-007 * AB - 6.465E-006 * AC \\
 & - 9.012E-007 * AD - 1.662E-005 * AE - 9.506E-007 * AF \\
 & + 3.413E-006 * BC - 1.191E-005 * BD + 1.019E-005 * BE \\
 & + 6.664E-006 * BF - 5.596E-006 * CD + 1.063E-007 * CE \\
 & + 2.432E-006 * CF - 2.067E-006 * DE - 5.503E-006 * DF \\
 & - 1.436E-006 * EF - 1.238E-004 * A^2 + 6.067E-006 * B^2 \\
 & - 9.404E-005 * C^2 - 1.861E-005 * D^2 - 3.568E-004 * E^2 \\
 & - 8.650E-005 * F^2
 \end{aligned}$$

$$R2 = 84.06 \tag{4}$$

By increasing the pulse-on time and current, the thermal heat energy and the strike rate of charged particles are increased, respectively, causes to increase the volume of molten metal of electrodes and leads to a higher TWR. The ANOVA is employed to check out the second-order mathematical model of above Eq. (4), and the result is shown in Table 6. In this model, the value of “Prob > F” is less than 0.0500, which indicates that the model is “Significant.”

**Table 6** ANOVA for TWR

ANOVA for response surface quadratic model					
Analysis of variance table (partial sum of squares – Type III)					
Source model	Sum of squares 4.82E-06	df 27	Mean square 1.79E-07	F Value 4.687183	p-value Prob > F 0.000141 (significant)
A-on time	3.11E-08	1	3.11E-08	0.814993	0.37562
B-off time	1.35E-07	1	1.35E-07	3.546813	0.071834
C-voltage	2.19E-09	1	2.19E-09	0.057421	0.812655
D-current	4.44E-08	1	4.44E-08	1.164359	0.291289
E-tool	3.38E-08	1	3.38E-08	0.887097	0.35565
F-w/p	1.64E-09	1	1.64E-09	0.043015	0.837447
AB	7.32E-12	1	7.32E-12	0.000192	0.989059
AC	1.34E-09	1	1.34E-09	0.035102	0.852957
AD	2.6E-11	1	2.6E-11	0.000682	0.979379
AE	8.84E-09	1	8.84E-09	0.231983	0.63442
AF	2.89E-11	1	2.89E-11	0.000759	0.97825
BC	3.73E-10	1	3.73E-10	0.009784	0.92203
BD	4.54E-09	1	4.54E-09	0.119216	0.732894
BE	3.33E-09	1	3.33E-09	0.08728	0.770205
BF	1.42E-09	1	1.42E-09	0.037293	0.848494
CD	1E-09	1	1E-09	0.026302	0.872523
CE	3.61E-13	1	3.61E-13	9.48E-06	0.997569
CF	1.89E-10	1	1.89E-10	0.004967	0.944399
DE	1.37E-10	1	1.37E-10	0.00359	0.952719
DF	9.69E-10	1	9.69E-10	0.025434	0.874625
EF	6.6E-11	1	6.6E-11	0.001731	0.967158
A <sup>2</sup>	2.1E-07	1	2.1E-07	5.506394	0.027536
B <sup>2</sup>	5.04E-10	1	5.04E-10	0.013232	0.909379
C <sup>2</sup>	1.21E-07	1	1.21E-07	3.179213	0.087235
D <sup>2</sup>	4.75E-09	1	4.75E-09	0.124544	0.727239
E <sup>2</sup>	1.74E-06	1	1.74E-06	45.77133	5.36E-07
F <sup>2</sup>	1.03E-07	1	1.03E-07	2.690307	0.114003
Residual	9.14E-07	24	3.81E-08		
Lack of fit	9.14E-07	17	5.38E-08		
Pure error	0	7	0		
Cor total	5.74E-06	51			
Std. Dev.		0.000195	R-square		0.840589
Mean		0.000312	Adj R-squared		0.661251
C.V. %		62.60888	Pred R-squared		0.325798

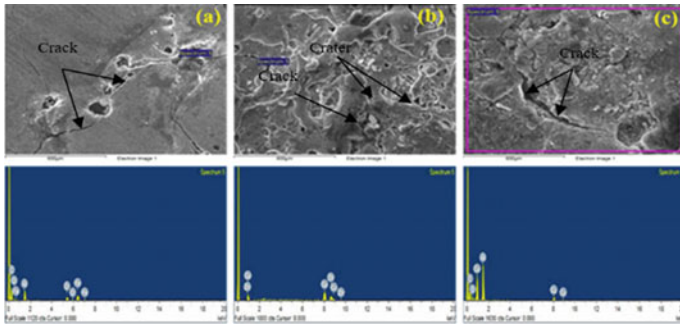


Fig. 2 SEM images of electrodes after EDM, a steel-304, b brass, and c copper

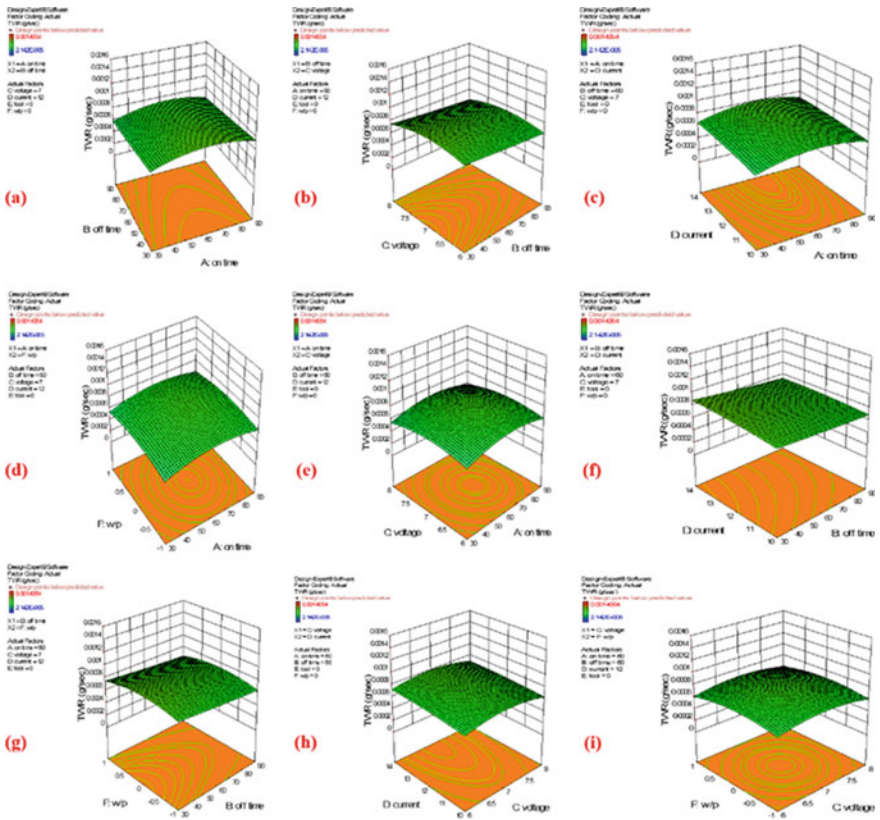


Fig. 3 3D response surface diagrams demonstrate the effect of TWR by means

## 6 Result and Discussion

EDM devices have emerged as one of the breakthrough technologies to making the fine materials through non-tradition methods. The non-destructive analysis was carried out by using SEM equipped with an EDS, as shown in Fig. 2. From SEM images of used electrodes, it was investigated that the cracks and craters are formed in all of three electrodes after the EDM operations.

It was examined that the brass material electrode has a high tool wear rate as compared to other electrodes. To examine the effects of machining parameters on a response variable, the 3D response surface diagrams were examined by selected software. From the SEM images (Fig. 2a–c) of used workpieces, it was analyzed that the cracks and craters are produced in all of them.

In this experimental study, it was also examined that the Al MMC-1 (10% SiCp and 3% Grp) is the best fabricated composite as compared to the other two composites in terms of wear resistance and hardness. Figure 3 demonstrates the concurrent effect of TWR by means of process parameters. Further, it is evident that with the increase in ' $T_{on}$ ' and ' $I$ ', the level of TWR is also increasing. This is because when the pulse-off time is increasing the supply of heat thermal energy between the tool and W/p is increase which leads a high TWR. Other side, the ' $T_{off}$ ' does not have a remarkable effect to increases the TWR.

## 7 Conclusion

The selected approach has been found effective for evaluating the optimum parameter setting. Furthermore, the 3D graphs were generated for analyzing the effect of process parameters using the Design-Expert, which were efficient enough to solve the approach. The ' $T_{on}$ ' and ' $I$ ' were the key parameters considered that directly increase the TWR of all the three material electrodes. The TWR was found minimum at a high level of ' $T_{on}$ ', however, changing the ' $V$ ' has a constant effect on TWR. The confirmatory test has validated the parametric setting determined by the desirability approach. The supposed approach can be recommended for the improvement of a process.

## References

1. Chawla, N., Williams, J., Saha, R.: Mechanical behavior and microstructure characterization of sinter-forged SiC particle reinforced aluminum matrix composites. *J. Light Met.* **2**(4), 215–227 (2002)
2. Hutchings. I.: Tribological properties of metal matrix composites. *Mater. Sci. Technol.* **10**(6), 513–517 (1994)

3. Tan, A., Teng, J., Zeng, X., Fu, D., Zhang, H.: Fabrication of aluminium matrix hybrid composites reinforced with SiC microparticles and TiB<sub>2</sub> nanoparticles by powder metallurgy. *Powder Metall.* **60**(1), 66–72 (2017)
4. Mitrović, S., Babić, M., Stojanović, B., Miloradović, N., Pantić, M., Džunić, D.: Tribological potential of hybrid composites based on zinc and aluminium alloys reinforced with SiC and graphite particles. *Tribol. Ind.* **34**(4), 177–185
5. Mahdavi, S., Akhlaghi, F.: Effect of SiC content on the processing, compaction behavior, and properties of Al6061/SiC/Gr hybrid composites. *J. Mater. Sci.* **46**(5), 1502–1511 (2011)
6. Velmurugan, Subramanian C.R., Thirugnanam, S., Ananadavel, B.: Experimental investigations on machining characteristics of Al 6061 hybrid metal matrix composites processed by electrical discharge machining. *Int. J. Eng., Sci. Technol.* **3**(8), 87–101 (2011)
7. Chomsamutr, K., Jongprasithporn, S.: Optimization parameters of tool life model using the Taguchi approach and response surface methodology. *Int. J. Comput. Sci. Issues (IJCSI)* **9**(1), 120 (2012)
8. Bhandare, R.G., Sonawane, P.M.: Preparation of aluminium matrix composite by using stir casting method. *Int. J. Eng. Adv. Technol. (IJEAT)* **3**(3), 61–65 (2013)
9. Radhika, N., Subramanian, R., Prasat, S.V.: Tribological behaviour of aluminium/alumina/graphite hybrid metal matrix composite using Taguchi's techniques. *J. Miner. Mater. Charact. Eng.* **10**(5), 427 (2011)
10. Barenji, R.V., Pourasl, H.H., Khojastehnezhad, V.M.: Electrical discharge machining of the AISI D6 tool steel: Prediction and modeling of the material removal rate and tool wear ratio. *Precis. Eng.* **45**, 435–444 (2016)

# Effect of Process Parameter on Plastic Parts Using ANOVA with Moldflow Simulation



Kalpit Jain, Devendra Somwanshi, and Akshay Jain

**Abstract** This research work has been conducted on polypropylene (PP) material using Moldflow Adviser (MFA). Moldflow Adviser (MFA) has been used to contemplate and confirm the impact of procedure boundaries and advance the volumetric shrinkage and fill time. Streamlining of procedure boundaries is finished using L27 design of experiments (DOE). Further, analysis of variance (ANOVA) has been conducted. Ideal blend of procedure boundaries is represented by ANOVA. Two unique combinations of sprue and sprinker framework are utilized for simulation. Analysis of variance shows that packing pressure is most huge variable for volumetric shrinkage in both of the cases. Regression model conditions for volumetric shrinkage and fill time are likewise created in this investigation. It will assist little with micro industry in improving nature of an injection molded plastic parts.

**Keywords** Volumetric shrinkage · Regression model equations · ANOVA

## 1 Introduction

For building up the thermoplastic materials on higher production rate, plastic injection molding (PIM) is most significant method which has gigantic dimensional control [1]. PIM is most critical methodologies for assembling the plastic items due to top part surfaces, short product cycles, and lightweight [2]. In PIM, a framework is a client intelligent framework giving a well-disposed condition to the end-client for providing essential data from the framework [3]. The location of the gate for filling of the mold cavity is very significant effects on warpage. The effect of melt temperature, injection time, and packing pressure is more significant as compared to mold temperature and packing time on fill time [4]. Timon-3D v.6.11 CAE programming was utilized to complete the simulation. The runner, sprue, and gate are

---

K. Jain (✉) · D. Somwanshi · A. Jain  
Poornima College of Engineering, Jaipur, India  
e-mail: [kalpit.jain@poornima.org](mailto:kalpit.jain@poornima.org)



the segments of the conveyance framework [5]. The metering size, melt temperature, injection rate, and injection pressure influence the thickness of the article [6]. Natural fiber composite material is one of the suitable materials to manufacture window frame [7]. To examine the warpage, the melt temperature and packing pressure are most significant boundaries [8]. The intensity of packing pressures influences the volumetric shrinkage which occurs near the gate at the end of fill location. Lower shrinkage is indicated by higher packing pressure, and high volumetric shrinkage is a result of low packing pressure [9]. Conformal cooling channel is the most appropriate cooling framework for the plastic part among other cooling channels. Flow simulation for various gate size and locations was broke down. Air traps can be limited by giving air vents in center and hole embeds [7]. Holding pressure was the fundamental factor impacting all injection molding procedures and creating varieties of the TR up to 9% for IM, 3.5% for ICM, and 5.5% for VIM. Injection speed was additionally the second most significant factor [8]. PIM is most commonly used method for developing thermoplastic materials [9]. Plastic injection molding machine can be a used to obtain molded product by melted plastic material by heat into a mold. Parametric optimization of machining input parameter is required to get the desired optimized results [10–14].

## 2 Research Methodology

First step is the planning of simulation-based design of experiments. In the second step, apply Autodesk Moldflow Adviser (MFA) software to conduct MFA simulations based on the planned DOE. To identify most or least significant factors, ANOVA is used as third step.

In the fourth step, regression analysis has been done to find out the statistical relationship between input and output parameters. Once the regression has been done, modeling equations for output parameters have been generated using residual analysis.

In this investigation, a typical material was chosen for item making and determination depended on absolutely writing audit and statistical surveying, and material name was polypropylene (PP). L27 orthogonal array has been used for data analysis on two different sprue and runner locations. In this investigation, five input parameters with three levels have been used. L27 OA has been used for design of experiment. Primary reactions from all tests were volumetric shrinkage, and fill time of item chose. Two designs of sprue and runner were utilized in this investigation, which are shown in Fig. 1a and b.

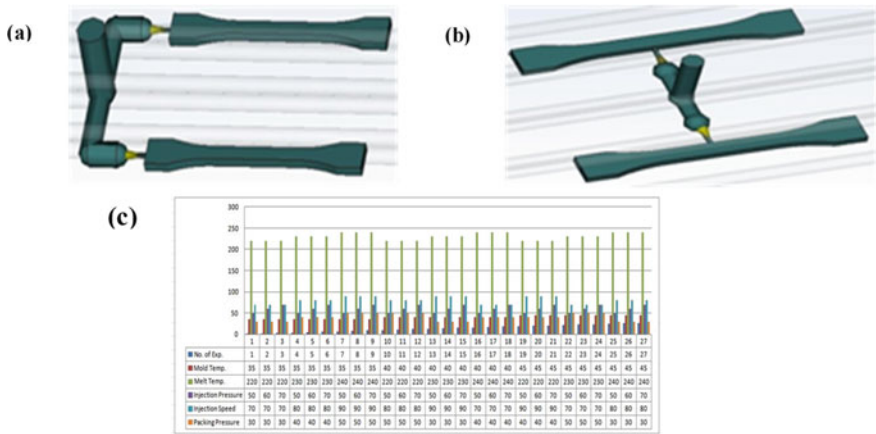


Fig. 1 a Sprue location at side for Case 1, b sprue location at center for Case 2, c orthogonal array for Case 1 and Case 2

### 2.1 Factors and Levels Along with Orthogonal Array

Design of experiments table was just conceivable by determination of proper factors and their levels. In this research work, five input parameters with three levels have been used which have been shown in Table 1.

Response parameters for this investigation are volumetric shrinkage (%) and fill time (s). Here, L27 has been used for five parameters and their three levels for each parameter.

## 3 Experimental Result and Analysis

The simulated values of fill time and volumetric shrinkages have been shown in Fig. 2a and b for both cases 1 and 2, respectively.

Table 1 Factor and level for case 1 and Case 2

Levels	Mold temp.	Melt temp.	Injection pressure	Injection speed	Packing pressure
1	35	220	50	70	30
2	40	230	60	80	40
3	45	240	70	90	50

Units: temperature in °C, pressure in Mpa, injection speed in %

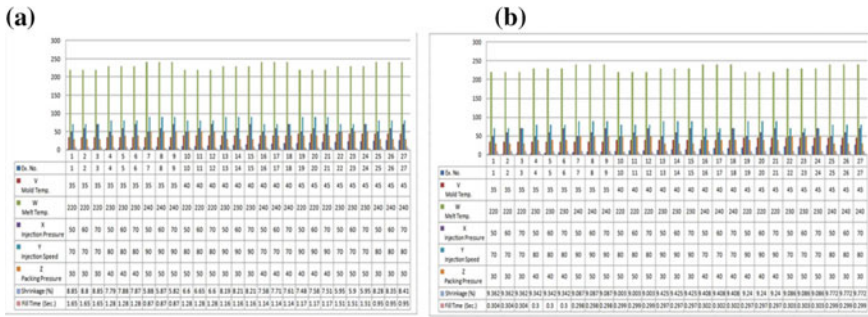


Fig. 2 a Shrinkage and fill time values for Case 1, b shrinkage and fill time values for Case 2

### 3.1 Analysis of Variance (ANOVA)

The analysis of variance (ANOVA) was determined for the two cases, and results were appeared in Tables 2 and 3. F-test was directed for contrasting a model variance and a residual variance in ANOVA examination. *F* esteem was determined by isolating a model mean square by residual mean square value. On the off chance that *f* esteem was drawing closer to one method, the two differences were same, concurring *F* esteem most noteworthy was ideal to discover basic input parameter.

From literature review, it has been found that *P* esteem has exceptionally little (under 0.05) at that point the terms in the regression model have a huge impact to the reactions.

Table 2a and b has shown one important result that F-value for regression models is very high (Table 2 *F*-value was 73.20 for Case 1, and like Table 3, *F*-value was 358.92 for Case 2) than *P*-value is very less (approx. 0.0000) suggested that all parameters are significant.

### 3.2 Regression Equation

In this study, regression equations were also obtained from Minitab for both cases, for both responses volumetric shrinkage and fill time.

Regression equation for shrinkage for Case 1

$$\begin{aligned} \text{Shrinkage} = & 18.45 - 0.0245 * V - 0.01905 * W + 0.00118 * X \\ & - 0.01358 * Y - 0.11627 * Z \end{aligned} \tag{1}$$

**Table 2** Comparison analysis of ANOVA results of shrinkage for Case 1 and Case 2

	Case 1	Case 2	Case 1	Case 2	Case 1	Case 2	Case 1	Case 2	Case 1	Case 2
Source	DF	Adj. SS	Adj. MS	F-value	P-value	F-value	P-value	F-value	P-value	F-value
Regression	5	25.5921	5.1184	0.2456	0.9877	73.2	0	58.77	0	0
V	1	0.2699	0.2699	0.04712	0.831	3.86	0.063	11.28	0.003	0.003
W	1	0.6532	0.6532	0.21912	0.632	9.34	0.006	52.43	0	0
X	1	0.0025	0.0025	0	1	0.04	0.851	0	1	1
Y	1	0.3318	0.3318	0.0054	0.931	4.75	0.041	1.29	0.268	0.268
Z	1	24.3346	24.3346	0.95634	0.334	348	0	228.85	0	0
Error	21	1.4685	0.0699	0.08776	0.912					
Total	26	27.0605		1.31576						

**Table 3** Comparison analysis of ANOVA results of fill time for Case 1 and Case 2

	Case 1	Case 2	Case 1	Case 2	Case 1	Case 2	Case 1	Case 2	Case 1	Case 2
Source	DF	Adj. SS	Adj. MS	Case 1	Case 2	F-value	P-value	Case 1	Case 2	P-value
Regression	5	1.27532	0.255064	0.000163	0.000033	29.9	0	358.92	0	0
V	1	0.01491	0.01491	0.00004	0.00004	1.75	0.2	46.35	0	0
W	1	0.65677	0.656773	0	0	77	0	1.38	0	0.254
X	1	0	0	0	0	0	1	0	0	1
Y	1	0.59809	0.59809	0.000158	0.000158	70.12	0	1746.36	0	0
Z	1	0.00554	0.005544	0	0	0.65	0.429	0.5	0.429	0.489
Error	21	0.17912	0.00853	0.00002	0					
Total	21	1.45444	0.000165	0.000165						

Regression equation for shrinkage for Case 2

$$\text{Shrinkage} = 7.416 + 0.01023 * V + 0.01103 * W - 0.000 * X - 0.00173 * Y - 0.02305 * Z \tag{2}$$

Regression equation for fill time for Case 1

$$\text{Fill time} = 7.376 - 0.00576 * V - 0.01910 * W + 0.00 * X - 0.01823 * Y - 0.00176 * Z \tag{3}$$

Regression equation for fill time for Case 2

$$\text{Fill time} = 0.32902 - 0.000097 * V - 0.000008 * W + 0.0 * X - 0.000297 * Y + 0.000005 * Z \tag{4}$$

Residual results for regression equations have been shown in Fig. 3a and b, respectively. The residual result shows the differences between simulation and predicted results.

Figure 4 shows that the normal probability plot is near to the straight line, so it is residual.

### 4 Conclusion

The point of this investigation is to advance MFA simulation results for mold flow plastic injection process. This investigation uses L27 orthogonal array for informative investigation on two distinctive sprue and location of runner. In this investigation, analysis of variance (ANOVA) and regression analysis were principle input strategies to explain reaction and factor relations emphatically.

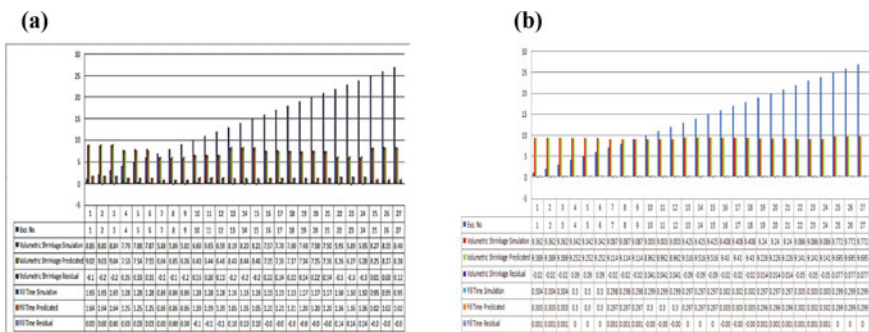
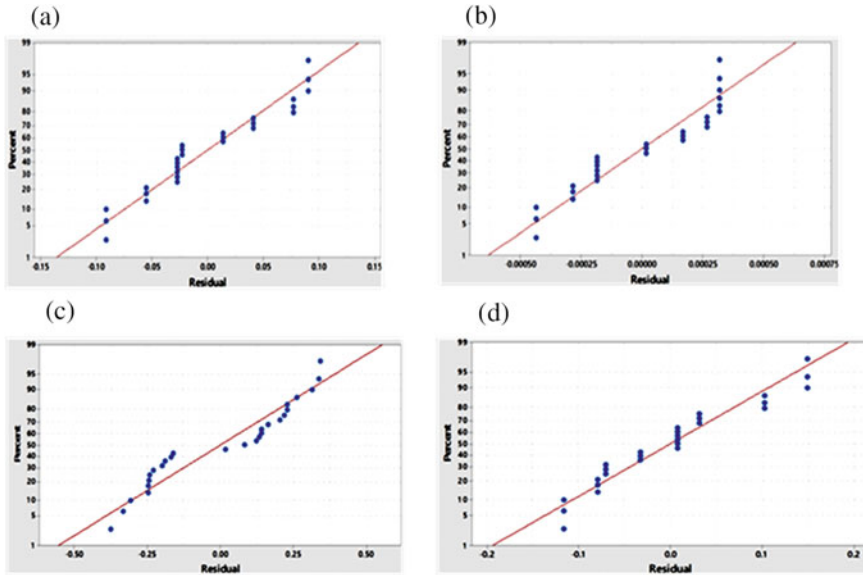


Fig. 3 a Residual results for Case 1, b residual results for Case 2



**Fig. 4** **a** Case 1 shrinkage normal probability plot, **b** Case 1 fill time normal probability plot, **c** Case 2 shrinkage normal probability plot, **d** Case 2 fill time normal probability plot

ANOVA outcomes demonstrate that the packing pressure is major noteworthy factor for volumetric shrinkage for Case 1 and packing pressure with melt temperature was most critical element for volumetric shrinkage for Case 2. Like that for fill time, melt temperature and injection speed were most critical variables for Case 1, and for Case 2, mold temperature and injection speed were most noteworthy elements.

Model conditions related to fill time and shrinkage were anticipated precisely with Minitab programming and show 90% great forecast for reactions and can be utilized by any plastic injection molding procedure producer.

## 5 Future Scope

In this investigation, two cases were examined utilizing symmetrical cluster idea, structure change depended on sprue, and location of runner, yet in this investigation, sprue and runner were fixed for all reproduction cases for both cases. For future work, it will be a great way to deal with study factor change dependent on geometrical difference in sprue and runner framework.

ANT colony and response surface optimization can be used for prospect investigation to get the better consequences of process related to plastic injection molding.

## References

1. Oktem, H., Erzurumlu, T., Uzman, I.: Application of Taguchi optimization technique in determining plastic injection molding process parameters for a thin-shell part. *Mater. Des.* **28**, 1271–1278 (2007)
2. Song, M., Liu, Z., Wang, M., Yu, T., Zhao, D.: Research on effects of injection process parameters on the molding process for ultra-thin wall plastic parts. *J. Mater. Process. Technol.* **187**, 668–671 (2007)
3. Rahman, W.A.W.A., Sin, L.T., Rahmat, A.R.: Injection moulding simulation analysis of natural fiber composite window frame. *J. Mater. Process. Technol.* **197**, 22–30 (2008)
4. Chen, C.-P., Chuang, M.-T., Hsiao, Y.-H., Yang, Y.-K., Tsai, C.-H.: Simulation and experimental study in determining injection molding process parameters for thin-shell plastic parts via design of experiments analysis. *Expert Syst. Appl.* **36**, 10752–10759 (2009)
5. Azaman, M., Sapuan, S., Sulaiman, S., Zainudin, E., Khalina, A.: Shrinkages and warpage in the processability of wood-filled polypropylene composite thin-walled parts formed by injection molding. *Mater. Des.* **1980–2015**(52), 1018–1026 (2013)
6. Mohamed, O.A., Masood, S., Saifullah, A.: A simulation study of conformal cooling channels in plastic injection molding. *Int. J. Eng. Res.* **2**, 344–348 (2013)
7. Vikas, B., Chandra Kumar, R.: Influence of feeding system in injection molding for lower washer of a bearing. *Int. J. Res. Eng. Technol.* **2**, 396–399 (2013)
8. Sortino, M., Totis, G., Kuljanic, E.: Comparison of injection molding technologies for the production of micro-optical devices. *Procedia Eng.* **69**, 1296–1305 (2014)
9. Jain, K., Kumar, D., Kumawat, S.: Plastic injection molding with taguchi approach-a review. *Int. J. Sci. Res.* **2**, 147–149 (2013)
10. Jain, A., Singh, B.: Parametric analysis during laser cutting of basalt-glass hybrid composite. *Lasers Manuf. Mater. Process.* **7**, 111–139 (2020)
11. Jain, A., Singh, B., Shrivastava, Y.: Reducing the heat-affected zone during the laser beam drilling of basalt-glass hybrid composite. *Compos. B Eng.* **176**, 107294 (2019)
12. Jain, A., Singh, B., Shrivastava, Y.: Investigation of kerf deviations and process parameters during laser machining of basalt-glass hybrid composite. *J. Laser Appl.* **31**, 032017 (2019)
13. Jain, A., Singh, B., Shrivastava, Y.: Heat-affected zone investigation during the laser beam drilling of hybrid composite using statistical approach. *Arab. J. Sci. Eng.* **45**, 833–848 (2020)
14. Jain, A., Singh, B., Shrivastava, Y.: Analysis of heat affected zone (HAZ) during micro-drilling of a new hybrid composite. *Proc. Inst. Mech. Eng. Part C J. Mech. Eng. Sci.* **234**, 620–634 (2020)



# Study of Tool Wear in Friction Stir Processing of Metal Matrix Composites—A Review



Pratap Singh and K. Hans Raj

**Abstract** The tool wear is an important issue in the fabrication of the metal matrix composites (MMCs). Friction stir processing (FSP) is a technique utilized to manufacture MMCs. It refines microstructure and enhances mechanical properties and also removes casting defects. Mostly, FSP has been carried out in non-ferrous alloys like aluminum, magnesium, copper, etc., to improve their strength and hardness. Now, this process is implemented for metals like steel and titanium also. During the rotation and traverse action, the FSP tool comes in contact with the ceramic powder which is much harder and sharper resulting in tool wear. The tool wear depends on the interaction between the tool and the workpiece materials. The tool geometry, FSP parameters, and the reinforcement material also play an important role in tool wear. The selection of the tool type, tool material, and tool geometry is important to produce a good quality workpiece. This selection depends on the stir zone temperature, wear resistance, material toughness, etc. This study aims to investigate the rate of tool wear, tool types, tool material, and tool dimensions in FSP of surface composites and metal matrix composites. FSP of hard materials is still a challenging task. More studies of tool design, tool wear, and selection of tool material are still required to be conducted to make this process more useful in future.

**Keywords** Friction stir processing (FSP) · Tool wear · Metal matrix composites

## 1 Introduction

Metal matrix composites (MMCs) are widely used in industries as compared to other composites such as polymer matrix composite (PMC) and ceramic matrix composite (CMC). MMC is composed of metal matrix and reinforced particles.

---

P. Singh (✉) · K. Hans Raj  
Faculty of Engineering, Dayalbagh Educational Institute (Deemed University),  
Dayalbagh, Agra 282005, India  
e-mail: [pratapsingh@dei.ac.in](mailto:pratapsingh@dei.ac.in)

© The Author(s), under exclusive license to Springer Nature Singapore Pte Ltd. 2021  
A. Patnaik et al. (eds.), *Advances in Materials Processing and Manufacturing Applications*, Lecture Notes in Mechanical Engineering,  
[https://doi.org/10.1007/978-981-16-0909-1\\_44](https://doi.org/10.1007/978-981-16-0909-1_44)

These particles may be in the form of ceramic powder or fibrous material. The addition of reinforcement particles of micro- or nano-size makes the composites stronger and harder. The composites reinforced with nano-size particles exhibit better mechanical and surface properties. There are various methods used for reinforcing such particles into composites such as direct pasting [1–3], spray technique [4–6], groove method [7–9], blind holes method [10–12], etc. FSP is nowadays adopted for grain refinement, surface modification, and enhancing mechanical properties. This technique is implemented for making PMC also [13–16]. In FSP, a rotating tool traverses along a specified path as shown in Fig. 1. Due to severe plastic deformation of metal around the rotating pin in the stir zone, high temperature is generated (below the melting point), and the grain refinement takes place.

## 2 Tool Wear in FSP

Tool wear is an important issue for an industry as it directly affects the cost of the production. The high strength, high hardness, and sharpness of ceramic reinforcement causes wear in tool. The tool wear is the result of friction between the metal matrix and the hard and sharp ceramic particles. Excessive tool wear results in poor surface quality. The tool wear also causes intermetallic phases which may result in the deterioration of mechanical properties. The important FSP parameters that influence the tool wear include rotational speed, number of FSP passes, traverse speed, axial force, etc. By increasing the rotational speed, more heat will be generated. Homogeneous distribution of reinforcing particles takes place at higher

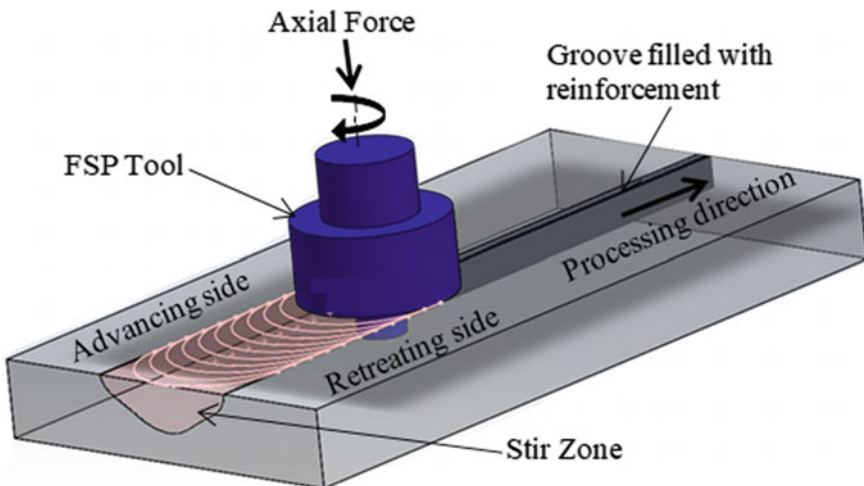


**Fig. 1** Schematic illustration of FSP

rotational speeds of the tool. Molla Ramezani et al. [17] reported that the tool wear decreased with an increase in rotational speed. Their statistical analysis showed that the rotational speed has 52.9% and pass numbers have a 13.1% impact on tool wear. The higher rotational speed causes higher strain rate and greater elongation of the materials which results in a reduction in grain size. The product with the smaller grain size is found to be stronger and harder. There is a temperature limit, up to which, the strength increases and then decreases. Ma et al. [18] suggested the temperature range of 450 to 500 °C gives better grain refinement for the aluminum composites. The tool geometry plays an important role in the microstructural evolution and is considered as a critical parameter in the tool wear [19]. The threaded pin of the tool generates more heat and helps in the flow of material. Grain refinement and better mechanical properties are attained with threaded pin as compared to the pin having no thread. However, more tool wear is noticed in the threaded pin [17]. Few studies on tool wear are given in Table 1.

### 3 Tool Types

The tools used in FSP may be categorized into four types depending on the pin (fixed pin, adjustable pin, self-reacting tool, and hollow pin-less tool) and end-use requirement. The fixed pin tool is most commonly used in FSP (Fig. 2a). This tool relates to a single piece containing both the shoulder and pin. The use of this tool is limited because of its fixed pin length. This issue is resolved in adjustable tools (Fig. 2b) [23], where the pin is adjusted according to the thickness of the specimen. The shoulder and pin are two independent parts. The independent pin is allowed to

**Table 1** Effect of process parameters on tool wear [17, 20–22]

Process parameters	Workpiece/ tool material	Effect on tool wear
Rotational speed	Al7075/H-13 tool steel	Tool wear decreased with increasing rotational speed. Rotational effect has 52.9% impact on tool wear
	Ti-6Al-4V/PCBN	At rotational speed of 400 rpm, maximum tool wear occurred at a location 7 mm from the tool plunge point. At higher rotational speed of 800 and 1200 rpm, the tool wear occurred at the tool plunge point
	Steel/PCBN	Increasing rotational speed results better heat generation, homogeneous distribution of reinforcement particles (RPs) with lesser tool wear
Traverse speed	Al7075/H-13 tool steel	Tool wear is almost constant with respect to traverse speed
Number of passes	Al7075/H-13 tool steel	Tool wear increases up to three passes and then it remains constant. Number of passes has 13.1% impact on tool wear
Travel distance	Al6061/H13 steel	Tool wear is found in three distinct phases, tool wear is rapid in phase 1, gradual in phase 2, and constant in phase 3

adjust in the shoulder, so the pin length is easily altered based on thickness of the specimen. The third one is self-reacting tools [24] (Fig. 2c). It is made up of three parts: top shoulder, pin, and bottom shoulder. The length of the pin is adjusted between these two shoulders. The last one is hollow and pin-less tool as shown in Fig. 2d. Huang et al. [25] used this type of tool for the induction of RPs in friction stir processing of surface composites.

If the tool is made in a single piece, the whole tool is to be getting replaced with a new one, which ultimately increases the manufacturing cost. To reduce such costs, two parts or even three-part tools might be beneficial. Most of the researchers observed more tool wear in the threaded portion of the tool pin. The threaded pin after wear out can be easier to replace as compared to replacing the whole tool. Another type of tool in which the shoulder is stationary is studied by Impero et al. [26], where effect of stationary shoulder FSP (SSFSP) on tool wear is investigated. The SSFSP is quite similar to conventional FSP except that the tool shoulder is fixed and traverses along the specified path. Only the tool pin rotates inside this stationary shoulder. It is found that the processed specimen through SSFSP exhibits a smoother surface without shoulder marks. Tool wear with this method was found to be negligible, and less flash is observed on the workpiece.

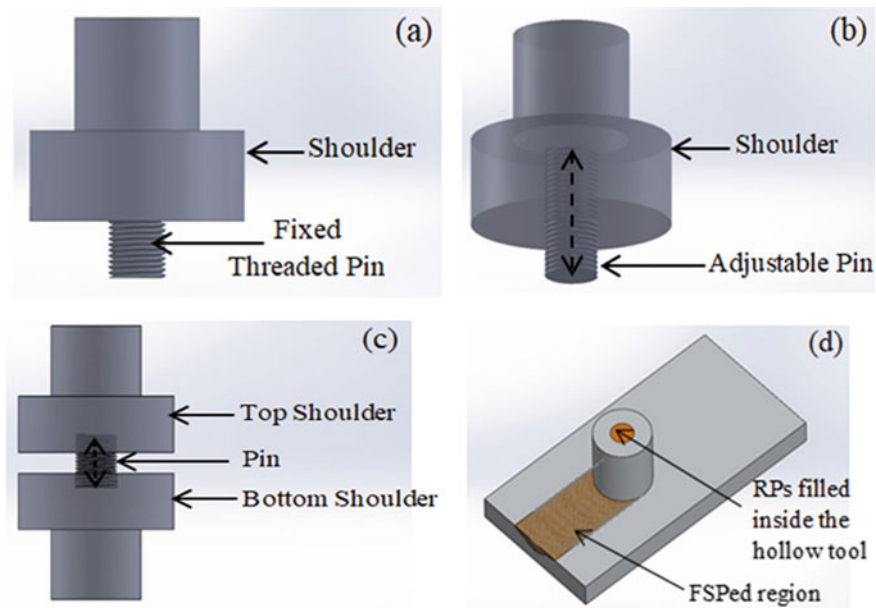


**Fig. 2** Types of tools: **a** Fixed pin; **b** Adjustable pin; **c** Self-reacting type tool; **d** Hollow and pin-less tool filled with (RPs)

## 4 Tool Materials

Tool material selection is one of the important considerations in FSP. An excellent review was done by Zhang et al. [19] that identified various properties which should be available in the tool materials. These are: higher compressive yield strength; creep resistance; good thermal fatigue strength; good fracture toughness; low thermal expansion coefficient; good machinability, and low or affordable cost. Chiteka [27] studied the influence of tool materials considering various tool materials (tool steels, metal carbides and ceramics, nickel alloys and cobalt base alloys, refractory metals, etc.) that have been used in the friction stir welding/processing (FSW/P) process. Table 2 exhibits the tool materials selected by researchers for FSP of various alloys and composites. In general, both the soft and hard materials of the specimen can be processed with very hard tool materials with ease.

**Table 2** Tool materials used in FSP

Tool materials		Materials processed by FSP
Tool steels	H13	Al2024 [4], A356 [5], AA1050 [28, 29], Al5083 [10, 30], AA6063 [31], AA6061 [32], AA7075 [33], AA8011 [34], Al6061/SiO <sub>2</sub> [35]
	High-carbon high-chromium steel (HCHCr)	AA6061 [12, 36, 37]
	High carbon steel (HCS)	AA1050 [38]
	D2 steel	Al7075 [8], Pure Al [39],
	D3 tool steel	AA7075 [9]
	Mild steel (MS)	Al6061 [40]
	High-speed steel (HSS)	[41]
Ceramic-based material	Tungsten carbide—cobalt materials (WC-Co)	High-strength low-alloy steel [42]
	Tungsten carbide (WC)	Steel/TiC [43], steel [44], Ti [45]
Polycrystalline cubic boron nitride (PCBN)		Tool steel [46], AA7075 [47], Ti-6Al-4V [20], AA 7075 [22]

## 5 Tool Dimensions

Tool dimensions and shape are also responsible for tool wear during FSP. The heat developed during FSP causes tool wear. During FSP, the rubbing of the tool against workpiece is considered as a heating source. The heat input Eq. (1) proposed by Frigaard et al. [48] is used for calculating the heat developed during FSP.

$$q_0 = \frac{4}{3} \pi^2 \mu P N R^3 \text{ (watt/m}^2\text{)} \quad (1)$$

where  $\mu$  is the effective friction coefficient between the tool and the workpiece,  $P$  is the pressure distribution (MPa),  $N$  is the rotation speed (rpm), and  $R$  is the surface radius (mm).

It is clear from Eq. (1) that the heat input in FSP is strongly dependent on the shoulder size. Zhang et al. [19] found a relationship between shoulder diameter and workpiece thickness. They summarized the shoulder diameters and probe diameters as a function of the thickness of sheet. They considered 53 sets of studies including Al, Cu, Mg, Ti, Ni, and steel as a base material and found a trend using a least-square approximation method as mentioned in Eqs. (2), (3), and (4).

$$\text{Shoulder diameter(mm)} = 2.22 \times \text{specimen thickness} + 7.3 \quad (2)$$

$$\text{Probe diameter(mm)} = 0.8 \times \text{sample thicknes} + 2.2 \quad (3)$$

$$\text{Shoulder diameter(mm)} = 2.1 \times \text{probe diameter} + 4.8 \quad (4)$$

## 6 Tool Wear Measurement

The percentage of tool wear calculation was carried out using Eq. (5) [49, 50].

$$\% \text{Tool Wear} = \frac{m_i - \Delta m}{m_i} \quad (5)$$

where  $m_i$  is the initial mass of the probe and  $\Delta m$  is the change in mass of the probe.

Prater et al. [49] studied the behavior of the wear resistance of various tool materials. The tool materials are: steel, tungsten carbide with micro-grain and sub micro-grain cobalt binders (WC-Co), and diamond-coated WC. They concluded that the wear of tool can be minimized by selecting the harder tool materials. The harder materials prolong tool life.

## 7 Conclusion

It is evident from literature that the tool wear is an important parameter in fabrication of surface composites and metal matrix composites. From Table 2, it is concluded that most of the studies of FSP are performed using Al alloys as base metal with tool steels (H13, HCHCr, HCS, D2 steel, D3 steel, MS, HSS, etc.) as a tool materials. Tools made up of tungsten carbide with cobalt and polycrystalline cubic boron nitride are generally used for FSP of steel and titanium. The tool wear not only increases the production cost but also affects the quality of the workpiece. Selection of tool material and tool types can be important consideration to reduce the tool wear. Tool wear estimation with empirical relation is also briefly reviewed in this work. To overcome such problems, more studies on optimization of tool design and process parameters are required.

**Acknowledgements** The authors wish to acknowledge Most Revered Professor P. S. Satsangi Sahab, Chairman, Advisory Committee on Education, Dayalbagh Educational Institute for his inspiration and motivation.

## References

1. Mishra, R.S., Ma, Z.Y., Charit, I.: Friction stir processing: a novel technique for fabrication of surface composite. *Mater. Sci. Eng., A* **341**, 307–310 (2003)
2. Miranda, R.M., Santos, T.G., Gandra, J., Lopes, N., Silva, R.J.C.: Reinforcement strategies for producing functionally graded materials by friction stir processing in aluminium alloys. *J. Mater. Process. Technol.* **213**, 1609–1615 (2013)
3. Kurt, A., Uygur, I., Cete, E.: Surface modification of aluminium by friction stir processing. *J. Mater. Process. Technol.* **211**, 313–317 (2011)
4. Zahmatkesh, B., Enayati, M.H.: A novel approach for development of surface nanocomposite by friction stir processing. *Mater. Sci. Eng., A* **527**, 6734–6740 (2010)
5. Mazaheri, Y., Karimzadeh, F., Enayati, M.H.: A novel technique for development of A356/Al<sub>2</sub>O<sub>3</sub> surface nanocomposite by friction stir processing. *J. Mater. Process. Technol.* **211**, 1614–1619 (2011)
6. Li, C., Feng, X., Shen, Y., Chen, W.: Preparation of Al<sub>2</sub>O<sub>3</sub>/TiO<sub>2</sub> particle-reinforced copper through plasma spraying and friction stir processing. *Mater. Des.* **90**, 922–930 (2016)
7. Tang, J., Shen, Y., Li, J.: Influences of friction stir processing parameters on microstructure and mechanical properties of SiC/Al composites fabricated by multi-pin tool. *J. Manuf. Process.* **38**, 279–289 (2019)
8. Roy, P., Singh, S., Pal, K.: Enhancement of mechanical and tribological properties of SiC- and CB-reinforced aluminium 7075 hybrid composites through friction stir processing. *Adv. Compos. Mater* **28**, 1–18 (2019)
9. Tonelli, L., Morri, A., Toschi, S., Shaaban, M., Ammar, H.R., Ahmed, M.M.Z., Ramadan, R. M., El-Mahallawi, I., Ceschini, L.: Effect of FSP parameters and tool geometry on microstructure, hardness, and wear properties of AA7075 with and without reinforcing B4C ceramic particles. *Int. J. Adv. Manuf. Technol.* **102**, 3945–3961 (2019)
10. Singh Yadav, R.K., Sharma, V., Venkata Manoj Kumar, B.: On the role of sliding load and heat input conditions in friction stir processing on tribology of aluminium alloy–alumina surface composites. *Tribol. Mater. Surf. Interfaces.* **13**, 88–101 (2019)

11. Jain, V.K.S., Yazar, K.U., Muthukumaran, S.: Development and characterization of Al5083-CNTs/SiC composites via friction stir processing. *J. Alloys Compd.* **798**, 82–92 (2019)
12. Balakrishnan, M., Dinaharan, I., Palanivel, R., Sathiskumar, R.: Influence of friction stir processing on microstructure and tensile behavior of AA6061/Al 3 Zr cast aluminum matrix composites. *J. Manuf. Process.* **38**, 148–157 (2019)
13. Azarsa, E., Mostafapour, A.: On the feasibility of producing polymer-metal composites via novel variant of friction stir processing. *J. Manuf. Process.* **15**, 682–688 (2013)
14. Gao, J., Shen, Y., Li, C.: Fabrication of high-density polyethylene/multiwalled carbon nanotube composites via submerged friction stir processing. *J. Thermoplast. Compos. Mater.* **30**, 241–254 (2017)
15. Rostamiyan, Y., Zaferani, M.: Fabrication of polyethylene-based surface composite reinforced by carbon nano-tube and nano-clay through friction stir processing. *Proc. Inst. Mech. Eng. Part L J. Mater. Des. Appl.* **233**, 580–587 (2019)
16. Huang, Y., Meng, X., Xie, Y., Wan, L., Lv, Z., Cao, J., Feng, J.: Friction stir welding/processing of polymers and polymer matrix composites. *Compos. Part A Appl. Sci. Manuf.* **105**, 235–257 (2018)
17. Molla Ramezani, N., Davoodi, B., Aberoumand, M., Rezaee Hajideh, M.: Assessment of tool wear and mechanical properties of Al 7075 nanocomposite in friction stir processing (FSP). *J. Brazilian Soc. Mech. Sci. Eng.* **41**, 1–14 (2019)
18. Ma, Z.Y., Mishra, R.S., Mahoney, M.W.: Superplastic deformation behaviour of friction stir processed 7075 Al alloy. *Acta Mater.* **50**, 4419–4430 (2002)
19. Zhang, Y.N., Cao, X., Larose, S., Wanjara, P.: Review of tools for friction stir welding and processing. *Can. Metall. Q.* **51**, 250–261 (2012)
20. Wu, L.H., Wang, D., Xiao, B.L., Ma, Z.Y.: Tool wear and its effect on microstructure and properties of friction stir processed Ti-6Al-4 V. *Mater. Chem. Phys.* **146**, 512–522 (2014)
21. Netto, N., Tiryakio, M., Eason, P.: Characterization of Anomalous Tool Degradation During Friction Stir Processing of 6061-T6 Aluminum Alloy Extrusions : A Failure Analysis Study, vol. 99, pp. 1–6 (2019)
22. Kumar, S.P., Raveendra, A.: Practical Investigation of Tool Wear Mechanism of PCBN Material by Using FSP.pdf (2019)
23. Ding: United States Patent (19) (1998)
24. Skinner, M., Edwards, R.L.: Improvements to the FSW process using the self-reacting technology. *Mater. Sci. Forum* **426–432**, 2849–2854 (2003)
25. Huang, Y., Wang, T., Guo, W., Wan, L., Lv, S.: Microstructure and surface mechanical property of AZ31 Mg/SiCp surface composite fabricated by Direct Friction Stir Processing. *Mater. Des.* **59**, 274–278 (2014)
26. Impero, F., Scherillo, F., Silvestri, A.T., Casarin, R., Astarita, A., Squillace, A.: Stationary shoulder friction stir processing: Influence of tool wear on surface properties. *Key Eng. Mater.* **813 KEM**, 393–398 (2019)
27. Chiteka, K.: Friction stir welding/processing tool materials and selection. *Int. J. Eng. Res. Technol.* **2**, 8–18 (2013)
28. Bourkhani, R.D., Eivani, A.R., Nateghi, H.R.: Through-thickness inhomogeneity in microstructure and tensile properties and tribological performance of friction stir processed AA1050-Al<sub>2</sub>O<sub>3</sub> nanocomposite. *Compos. Part B Eng.* **174**, 107061 (2019)
29. Sanusi, K.O., Akinlabi, E.T.: Friction-stir processing of a composite aluminium alloy (AA 1050) reinforced with titanium carbide powder. *Mater. Tehnol.* **51**, 427–435 (2017)
30. Huang, G., Wu, J., Hou, W., Shen, Y., Gao, J.: Producing of Al-WC surface composite by additive friction stir processing. *Mater. Manuf. Process.* **34**, 147–158 (2019)
31. Rathee, S., Maheshwari, S., Siddiquee, A.N., Srivastava, M.: Distribution of reinforcement particles in surface composite fabrication via friction stir processing: Suitable strategy. *Mater. Manuf. Process.* **33**, 262–269 (2018)



32. Rathee, S., Maheshwari, S., Siddiquee, A.N., Srivastava, M.: Effect of tool plunge depth on reinforcement particles distribution in surface composite fabrication via friction stir processing. *Def. Technol.* **13**, 86–91 (2017)
33. Girish, G., Anandkrishnan, V.: Tribological behaviour of recursive friction stir processed AA7075. *Ind. Lubr., Tribol* (2020)
34. Ranganathan, S., Ramachandran, S.V., Palanivelu, R., Ramasamy, S.: Critical wear assessment of AA8011/hybrid metal matrix composites with surface amendment using friction stir process. *SAE Tech., Pap* (2019)
35. Mazaheri, Y., Heidarpour, A., Jalilvand, M.M., Roknian, M.: Effect of Friction stir processing on the microhardness, wear and corrosion behavior of Al6061 and Al6061/SiO<sub>2</sub> nanocomposites. *J. Mater. Eng. Perform.* **28**, 4826–4837 (2019)
36. Dinaharan, I., Balakrishnan, M., David Raja Selvam, J., Akinlabi, E.T.: Microstructural characterization and tensile behavior of friction stir processed AA6061/Al<sub>2</sub>Cu cast aluminum matrix composites. *J. Alloys Compd.* **781**, 270–279 (2019)
37. Thangarasu, A., Murugan, N., Dinaharan, I., Vijay, S.J.: Synthesis and characterization of titanium carbide particulate reinforced AA6082 aluminium alloy composites via friction stir processing. *Arch. Civ. Mech. Eng.* **15**, 324–334 (2015)
38. Fotoohi, H., Lotfi, B., Sadeghian, Z., Byeon, J.W.: Microstructural characterization and properties of in situ Al-Al<sub>3</sub>Ni/TiC hybrid composite fabricated by friction stir processing using reactive powder. *Mater. Charact.* **149**, 124–132 (2019)
39. Singh, S., Pal, K.: Effect of texture evolution on mechanical and damping properties of SiC/ZnAl<sub>2</sub>O<sub>4</sub>/Al composite through friction stir processing. *J. Mater. Res. Technol.* **8**, 222–232 (2019)
40. Raj, K.H., Sharma, R.S., Singh, P., Dayal, A.: Study of friction stir processing (FSP) and High Pressure Torsion (HPT) and their effect on mechanical properties. *Procedia Eng.* **10**, 2904–2910 (2011)
41. Vijayan, S., Gnanavel, J.P.L., Selvakumar, G., Rao, S.R.K.: Study on surface characteristics of friction stir processed az91 with titanium carbide micro particles. *Indian J. Eng. Mater. Sci.* **26**, 205–210 (2019)
42. Yamamoto, H., Danno, Y., Ito, K., Mikami, Y., Fujii, H.: Weld toe modification using spherical-tip WC tool FSP in fatigue strength improvement of high-strength low-alloy steel joints. *Mater. Des.* **160**, 1019–1028 (2018)
43. Yuvaraj, N.: Tribological characteristics of steel/TiC surface composite fabricated by friction stir processing **6**, 86–89 (2018)
44. Aktarer, S.M., Küçükömeroğlu, T.: The microstructure and mechanical properties of FSPed HSLA steel. *J. Achiev. Mater. Manuf. Eng.* **75**, 55–60 (2016)
45. Farias, A., Batalha, G.F., Prados, E.F., Magnabosco, R., Delijaicov, S.: Tool wear evaluations in friction stir processing of commercial titanium Ti-6Al-4 V. *Wear* **302**, 1327–1333 (2013)
46. Chen, Y., Nakata, K.: Friction stir processing of skd61 tool steel. *Int. J. Mod. Phys. B* **23**, 1116–1121 (2009)
47. Tambe, K., Krishna Mohan, G., Sarath Kumar, A., Jayanendrababu, K.: Effect of process parameters on pcbn tool wear rate in friction stir process of aluminium 7075 Sic. *Int. J. Recent Technol. Eng.* **7**, 546–549 (2019)
48. Frigaard, O., Grong, O., Midling, O.T.: A process model for friction stir welding of age hardening aluminum alloys. *Metall. Mater. Trans. A Phys. Metall. Mater. Sci.* **32**, 1189–1200 (2001)
49. Prater, T., Strauss, A., Cook, G., Gibson, B., Cox, C.: A comparative evaluation of the wear resistance of various tool materials in friction stir welding of metal matrix composites. *J. Mater. Eng. Perform.* **22**, 1807–1813 (2013)
50. Kraiklang, R., Onwong, J., Santhaweesuk, C.: Multi-performance characteristics of AA5052 + 10% SiC surface composite by friction stir processing. *J. Compos. Sci.* **4**, 36 (2020)

# Graphene–Alumina Composite: The Advanced Coating Material for Developing Harder Surface of Steel Strip Substrate



Tapan Dash, Gaurab Kumar Sahoo, Binod Bihari Palei,  
and Tapan Kumar Rout

**Abstract** We successfully coated composite of alumina–graphene (0.5 and 1.5 wt%) on steel strip substrate in this work. The coating was carried out by the transferred plasma torch method. Better adhesion with good microstructural of alumina–graphene (1.5 wt%) was observed on steel substrate. XRD shows peaks of alumina and carbon related to graphene. Micro-Raman spectroscopy shows graphene present on coating is in bilayer structure. Adhesion quality and formation of coating with no defect and porous-free nature were confirmed from the FESEM study. While bare steel exhibits hardness and Young’s modulus values of 168 VHN and 190 GPa, respectively, alumina–graphene coated (1.5 wt%) on steel exhibits hardness and Young’s modulus values of 250 VHN and 270 GPa, respectively. Improved microstructure with mechanical property attributed to optimized coating condition and absence of coating defect. The as-prepared coating with improved properties will inspire industries to focus and use this material for advanced critical applications, especially for developing wear-resistant components.

**Keywords** Graphene · Steel · Coating · Hardness

## 1 Introduction

Generally, the steel industry’s development is considered an indicator of economic progress because of its potential application in various infrastructural and engineering fields. It is a widely used material for its excellent mechanical behavior. But it has great disadvantages because of its corrosion, low surface hardness, and poor wear resistance compared to other ceramics [1–5]. Different methods have been

---

T. Dash (✉) · G. K. Sahoo  
Centurion University of Technology and Management, Bhubaneswar, Odisha, India

B. B. Palei  
CSIR-Institute of Minerals and Materials Technology, Bhubaneswar, Odisha, India

T. K. Rout  
Research and Development Department, Tata Steel Ltd, Jamshedpur, India

continuously addressing to improve these limitations [5–7] and to improve the quality of steel. Scientists have been working on different alloying methods, different compositions, coating, etc., to improve steel [8–10]. Referring to the literature, it can be addressed that a suitable coating is less cost-effective to develop the behavior of working surface contact of steel to be used at different critical conditions of mechanical and thermal load and corrosion resistance environment [10]. Today, graphene is considered a disruptive technology that invites new markets and replacing existing materials and technologies. Graphene-based materials (GBMs) have been used for producing various nanocomposite coatings to develop surface and mechanical properties, including strength, corrosion resistance, and stability, etc. Particularly, it has high “mechanical properties (strength  $\sim 130$  GPa, Young modulus  $\sim 1$  TPa)” [11–23]. Ni/GO–Al<sub>2</sub>O<sub>3</sub> (mass ratio of GO and Al<sub>2</sub>O<sub>3</sub> of 1:1) coated on steel shows microhardness of 500 HV [19]. Steel coated with Al<sub>2</sub>O<sub>3</sub> and CNT shows decrease trend of Young’s modulus with increased content of carbon (from 41 GPa for Al<sub>2</sub>O<sub>3</sub> to 9 GPa for containing 25% C) [24]. Alumina (Al<sub>2</sub>O<sub>3</sub>) is essentially used in the materials industry. It has been employed in various critical applications such as cutting tools working under high-speed, parts of wear resistant, and multifunctional coatings, because of having excellent hardness and excellent adhesion with metals [25–28]. It is considered that by exploring the properties of Al<sub>2</sub>O<sub>3</sub> and graphene composite, a protecting material expected to be developed for improving next generation coatings for industrial applications useful for enhancing hardness and the anti-corrosion applications.

First of all, in this work, successfully Al<sub>2</sub>O<sub>3</sub>-graphene composite (0.5 and 1.5 wt%) by 8 h of dry planetary balling milling was prepared. This work explores the coating of Al<sub>2</sub>O<sub>3</sub>-graphene composite on the steel substrate using plasma torch technique (non-transferred type). “The microstructural, spectroscopic, and mechanical properties of steel with a coating of Al<sub>2</sub>O<sub>3</sub>-graphene composites were investigated by employing various techniques such as X-ray diffraction (XRD), field emission scanning electron microscopy (FESEM), micro-Raman spectroscopy, microhardness, and Young’s modulus by nanoindentation.” It was found that the coating of alumina-graphene (1.5 wt%) improves the mechanical properties of steel.

## 2 Experimental

At first, alumina-graphene (0.5 and 1.5 wt%) was synthesized from graphite of high purity. It was prepared via “a horizontal high energy dry planetary ball milling technique.” For 8 h, milling of samples was carried out. Milling was carried out at the charge to ball ratio of 1:7. The rotation speed of milling was 350 rpm. After successfully composites are prepared, samples are taken to carry out coating experiment on steel (using a non-transferred plasma torch). An “APS plasma system (metallization) consists of PS50M plasma gun” is used to spray alumina-graphene (0.5 and 1.5 wt%) coating carried out on substrate of steel at an energy

level of 20 KWh. Before coating on steel, blasting of the substrate was carried out by  $\text{Al}_2\text{O}_3$  grit to achieve  $\approx 14 \mu\text{m}$  for developing adhesion for coating. NiCrAlY was used as bond coat on the substrate for decreasing the thermal expansion of it. By burning of electric arc between the cathode and anode, plasma state is generated. Argon (Ar) was used for the generation of plasma. The carrier gas flow rate of 3 L per minute (LPM) was maintained in the experiment. The composite powder at molten state coated on the substrate of mild steel ( $5 \text{ cm} \times 5 \text{ cm} \times 2 \text{ cm}$ ). In substrate holder, the substrate was kept at a distance of 120 mm from the plasma gun. Plasma coating was carried out with to and fro motion of torch. After coating over, the coated products are left for a rapid solidification process. The cooling was maintained with  $120 \text{ }^\circ\text{K/s}$  cooling rate. The properties of the coated samples of steel were carried out by employing various techniques. “XRD was carried out by PANalytical X’Pert Pro diffractometer equipped with  $\text{CoK}\alpha$  radiation. Micro-Raman spectra were taken by employing a dispersive type Renishaw inVia Reflex (UK) spectrometer. The microstructures of samples were carried out by FESEM (model: ZEISS SUPRA 55). Energy dispersive spectra (EDS) were taken using the Oxford, X-Max system. The constituents of different phases grown in the sample were confirmed by EDS analysis. Nano-indenter-UMIS system (Fisher-Cripps, Australia) with diamond Berkovich indenter (tip diameter: 400 nm) at a maximum applied load of 50 mN was used for hardness and Young’s modulus calculation.”

### 3 Results and Discussion

To know the crystal structure and phases of the substrate (steel) and coating surface (coating of alumina–graphene (0.5 and 1.5 wt%) composite) XRD analysis was carried out (Figs. 1 and 2). XRD analysis of Fe substrate shows peaks due to Fe only. Major peaks of Fe are found as Fe(110) at around two theta of  $52^\circ$ . The phases and planes are identified in this work by comparing the determined “ $d$ -values (experimentally determined) with the  $d$ -values of standard powder diffraction data file, C: 00-041-1487,  $\text{Al}_2\text{O}_3$ : 01-075-1862, and Fe: 00-045-1488 supplied in JCPDS-ICDD PDF-2 (2004).” The XRD analysis of samples was taken in 2 theta range of  $50\text{--}80^\circ$ . XRD analysis confirms the purity of the substrate. XRD analysis of alumina–graphene coated Fe shows the peaks of  $\text{Al}_2\text{O}_3$  and the peak of C (graphene).  $d$ -spacing value of C confirms the presence of graphene on coating. The different phases with different planes with their position and FWHM of were studied. The results were made comparison with their standard values, which indicate the regular-ordered and crystalline nature of the samples. No other impurity phase is detected in the coating.

Microstructural behavior of typical coating material like alumina–graphene (1.5 wt%) coated on steel substrate is observed from FESEM (Fig. 3a). An almost uniform distribution of composite on steel substrate is observed. For various advanced applications, it is understood that the uniform distribution of composite

**Fig. 1** XRD study of steel substrate

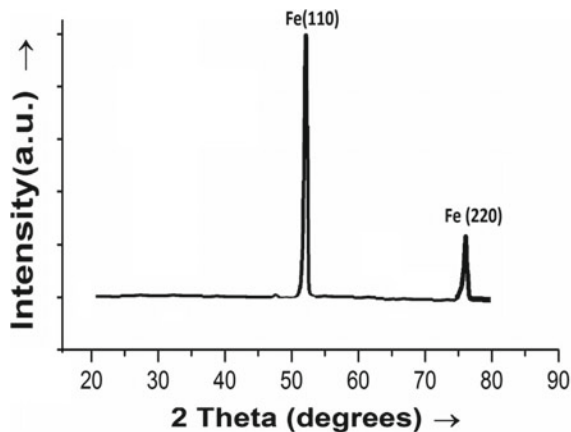
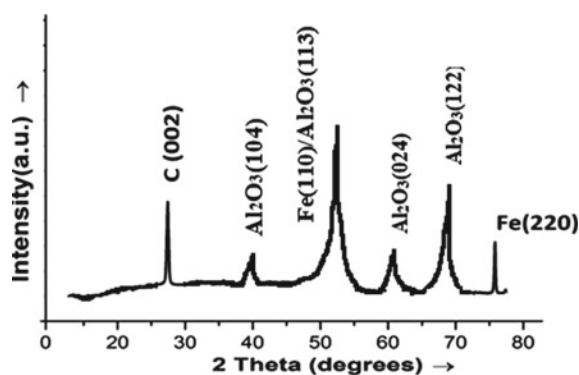


**Fig. 2** XRD study of  $\text{Al}_2\text{O}_3$ -graphene (1.5 wt%) coated steel substrate



on steel substrate is crucial to prepare the superior quality coating. The coating is also found to free from microporosity and any surface defects. EDS result (Fig. 3b) carried out on FESEM shows Al as major peak along with low intense peaks for O and C. Micro-Raman spectroscopy characterization of alumina-graphene (1.5 wt%) coated is shown in Fig. 4. Micro-Raman spectra show different peaks of carbon, i.e., G, D, 2D. Being Fe metal, no peak related to iron is observed. In the Raman spectra, it is observed that 2D to G intensity ratio is nearly one that indicates graphene's bilayer nature. Micro-Raman shows the presence of  $\text{Al}_2\text{O}_3$  in the spectrum. The result confirms the successful coating formed on the steel substrate.

Microhardness and Young's modulus of bare steel and coating surface of steel (composites of  $\text{Al}_2\text{O}_3$ -graphene (0.5 and 1.5 wt%) coated on steel) were determined by nanoindentation method are presented in Table 1. On the samples' surface, 15 indentations were taken, and their average values for materials are reported here. The microhardness and Young's modulus of bare steel were determined to be 168 VHN and 190 GPa, respectively. In this work,  $\text{Al}_2\text{O}_3$ -graphene (1.5 wt%) composite coated on steel shows relatively higher hardness and Young's modulus

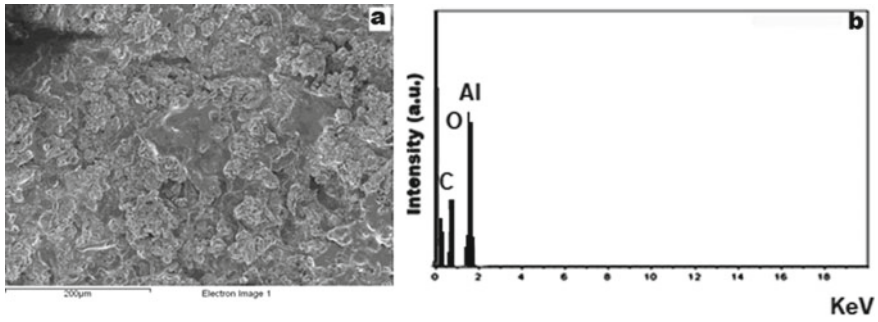
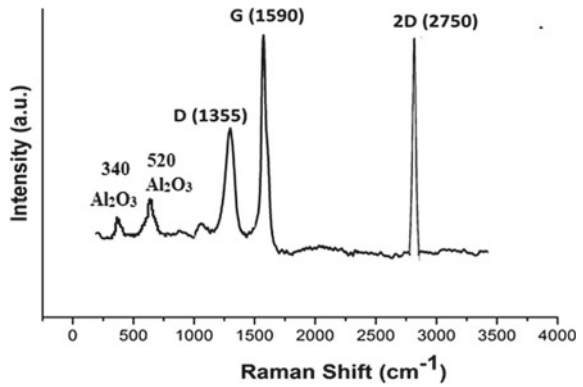


**Fig. 3** FESEM and EDS studies of Al<sub>2</sub>O<sub>3</sub>–graphene (1.5 wt%) coated on substrate of steel: **a** FESEM image carried out on the steel coating (the top surface), **b** EDS carried out on FESEM

**Fig. 4** Micro-Raman analysis of Al<sub>2</sub>O<sub>3</sub>–graphene (1.5 wt%) coated steel substrate



of 250 VHN and 270 GPa, respectively. The above improved mechanical properties of steel coated with Al<sub>2</sub>O<sub>3</sub>–graphene composite may be attributed to the improved dispersion of graphene in the composite and good adhesion of composite on the substrate.

**Table 1** Microhardness and Young’s modulus values of bare and coated steel

Sample ID	Microhardness in VHN	Young’s modulus in GPa
Steel	168 ± 12	190 ± 11
Alumina–graphene coated (0.5 wt%) steel	188 ± 06	202 ± 06
Alumina–graphene coated (1.5 wt%) steel	250 ± 10	270 ± 14

## 4 Conclusion

In this work, it has been possible to prepare the coating of alumina–graphene (0.5 and 1.5 wt%) on the steel substrate. The successful coating is confirmed from various advanced characterizations like XRD, micro-Raman, and FESEM. Graphene present on coating is found in bilayer form. XRD of composite coated on steel shows peaks of  $\text{Al}_2\text{O}_3$  along with peaks of graphene. Raman shows peaks of  $\text{Al}_2\text{O}_3$ , G, D, and 2D. Adhesion quality and formation of coating are confirmed from the FESEM study. No surface defect and porous nature are detected in the FESEM study. In the Raman spectra, it is observed that the intensity ratio of 2D to G is nearly one, which indicates the bilayer nature of graphene. Bare steel shows hardness and Young's modulus values of 168 VHN and 190 GPa, respectively. Whereas alumina–graphene coated (1.5 wt%) on steel exhibits hardness and Young's modulus values of 250 VHN and 270 GPa, respectively.

## References

1. Singh, T.B., Singh, M.N., Basu, D.K., Narang, S.K.: Corrosion behaviour of electro deposited zinc–iron alloy coatings on mild steel. *J. Metall. Mater. Sci.* **45**, 199–203 (2003)
2. Yanjerappa, A.N., Thimmappa, V.V., Perdur, V.N.: Electrodeposition of zinc from chloride solution. *Turk. J. Chem.* **26**, 725–734 (2002)
3. Yogesha, S., Hegde, A.C.: Optimization of deposition conditions for development of high corrosion resistant Zn–Fe multilayer coatings. *J. Mater. Process. Technol.* **211**, 1409–1415 (2011)
4. Shivakumara, S., Manohar, U., Naik, Y.A., Venkatesha, T.V.: Influence of additives on electrodeposition of bright Zn–Ni alloy on mild steel from acid sulphate bath. *Bull. Mater. Sci.* **30**, 455–462 (2007)
5. Daniyan, A.A., Umore, L.E., Popoola, P., Fayomi, O.S.I.F.: Comparative studies of microstructural, tribological and corrosion properties of Zn– $\text{TiO}_2$  and Zn– $\text{TiO}_2$ – $\text{WO}_3$  nano-composite coatings. *Results Phys.* **7**, 3222–3229 (2017)
6. Aramaki, K.: The inhibition effects of cation inhibitors on corrosion of zinc in aerated 0.5 M NaCl. *Corros. Sci.* **43**, 1573–1588 (2001)
7. Chen, W.X., Tu, J.P., Wang, L.Y., Gan, H.Y., Xu, Z.D., Zhang, X.B.: Tribological application of carbon nanotubes in a metal-based composite coating and composites. *Carbon* **41**, 215–222 (2003)
8. Balani, B., Harimkar, S.P., Keshri, A., Chen, Y., Dahotre, N.B., Agarwal, A.: Multiscale wear of plasma-sprayed carbon-nanotube-reinforced aluminum oxide nanocomposite coating. *Acta Mater.* **56**, 5984–5994 (2008)
9. Keshri, A.K., Agarwal, A.: Wear behavior of plasma-sprayed carbon nanotube-reinforced aluminum oxide coating in marine and high-temperature environments. *J. Therm. Spray Technol.* **20**, 1217–1230 (2012)
10. Dash, T., Rout, T.K., Palei, B.B., Bajpai, S., Kundu, S., Bhagat, A.N., Satpathy, B.K., Biswal, S.K., Rajput, A., Sahu, A.K., Biswal, S.K.: Synthesis of  $\alpha$   $\text{Al}_2\text{O}_3$ –graphene composite: a novel product to provide multi functionalities on steel strip surface. *SN Appl. Sci.* **2**, 1–9 (2020)
11. Geim, A.K., Novoselov, K.S.: The rise of graphene. *Nat. Mater.* **6**, 183–191 (2007)

12. Dash, P., Dash, T., Rout, T.K., Sahu, A.K., Das, S., Biswal, S.K., Mishra, B.K.: Preparation of graphene oxide by dry planetary ball milling process from natural graphite. *RSC Adv.* **6**, 12657–12668 (2016)
13. Gunasekaran, R.K., Jayasankar, K., Dash, T., Dash, A., Jena, B.K., Mishra, B.K.: Shear-force-dominated dual-drive planetary ball milling for scalable production of graphene and its electrocatalytic application with Pd nanostructures. *RSC Adv.* **6**, 20067–20073 (2016)
14. Böhm, S.: Graphene against corrosion. *Nat. Nanotechnol.* **9**, 741–742 (2014)
15. Allen, M.J., Tung, V.C., Kaner, R.B.: Honeycomb carbon: a review of graphene. *Chem. Rev.* **110**, 132–145 (2010)
16. Aneja, K.S., Bohm, S. Khannaa, A.S., Mallika Bohmc, H.L.: Graphene based anticorrosive coatings for Cr(vi) replacement. *Nanoscale* **7**, 17879–17888 (2015)
17. Sun, Y., Wu, Q., Shi, G.: Graphene based new energy materials. *Energy Environ. Sci.* **4**, 1113–1132 (2011)
18. Ovidko, I.A.: Metal-graphene nanocomposites with enhanced mechanical properties: a review. *Rev. Adv. Mater. Sci.* **38**, 190–200 (2014)
19. Yina, H., Daia, Q., Haob, X., Huang, W., Wang, X.: Preparation and tribological properties of graphene oxide doped alumina composite coatings. *Surf. Coat. Technol.* **352**, 411–419 (2018)
20. Dash, S., Dash, T., Rout, T.K.: Preparation of graphene oxide by dry planetary ball milling technique under oxygen atmosphere. *IOP Conf. Ser.: Mater. Sci. Eng.* **872**(012180), 1–6 (2020)
21. Palei, B.B., Dash, T., Biswal, S.K.: Reduced graphene oxide synthesis by dry planetary ball milling technique under hydrogen atmosphere. *IOP Conf. Ser.: Mater. Sci. Eng.* **872**(012158), 1–6 (2020)
22. Palei, B.B., Dash, T., Biswal, S.K.: Successful synthesis of graphene-aluminum composite with improved microhardness. *Int. J. Eng. Adv. Technol.* **9**, 2218–2221 (2020)
23. Dhar, S., Dash, T., Palei, B.B., Rout, T.K., Biswal, S.K., Mitra, A., Sahu, A.K.: Silicon-graphene composite synthesis: Microstructural, spectroscopic and electrical conductivity characterizations. *Mater. Today Proc.* (2020). Accepted article, <https://doi.org/10.1016/j.matpr.2020.02.858>
24. Hentour, K., Marsal, A., Turq, V., Weibel, A., Ansart, F., Sobrino, J.M., Chen, Y.M., Garcia, J., Franc, P., Cardey, O., Laurent, C.: Carbon nanotube/alumina and graphite/alumina composite coatings on stainless steel for tribological applications. *Mater. Today* **8**, 118–126 (2016)
25. Ahmad, I., Cao, H.Z., Chen, H.H., Zhao, H., Kennedy, A., Zhu, Y.Q.: Carbon toughened aluminium oxide nanocomposite. *J. Eur. Ceram. Soc.* **30**, 865–873 (2010)
26. Choudhary, R.K., Kain, V., Hubli, R.C.: Formation of alumina aluminate coatings on ferritic-martensitic T91 steel. *J. Min. Metall. Sect. B.* **50**, 165–170 (2014)
27. Stolyarov, V.V., Misochenko, A.A., Zholnin, A.G., Grigiriev, E.G., Klyatskina, E.A.: Structure and properties of Al<sub>2</sub>O<sub>3</sub>/Graphene nanocomposite processed by spark plasma sintering. *IOP Conf. Ser.: Mater. Sci. Eng.* **218**, 1–4 (2017)
28. Gheorghies, C., Condurache-bota, S., Dinescu, M., Constantinescu, C., Cazacu, N.: New reinforcing technique of alumina coatings on steel substrates. *Optoelectron. Adv. Mater.* **2**, 569–577 (2008)



# Recent Advances of Reinforced Natural Polymers: A Review



Sartaj Singh, Saurabh Kango, Nitin Sharma, and Sumit Sharma

**Abstract** In recent years, the growth of the composites of natural polymers has made a noticeable impact on the research of the polymer composites. Inspired by the superhydrophobicity, researchers are in consistent pursuit on creating these advanced wax materials and surfaces. As these materials have huge applications in the diverse modern engineering sectors, researchers are driving themselves to work on the improvements of performance parameters of these surfaces. The present review aims to highlight the important trends and advances in the research and development of these natural polymers and their different properties. A summary on the recent advancements of natural reinforced polymers (NRP), waxes and sponges is provided for their effective use in oil–water separation applications. The review also covers current research and strives on the fabrication of these ‘special’ materials, their important mechanical, tribological and thermal properties, anti-wetting behavior and biodegradability along with challenges in the field. In the end, the critical conclusions of the present review and scopes for future work have been discussed.

**Keywords** Biomaterials · Polymers · Wax · Tribology · Superhydrophobicity · Oil–water separation

## 1 Introduction

### 1.1 *Natural Reinforced Polymers (NRP)*

The trend of fiber composites began when researchers discovered plastics and other composites which have been widely used now as a sticking/gluing material. In 1930, the manufactured plastics like vinyl, polyester, phenolic and polystyrene were

---

S. Singh · S. Kango (✉) · N. Sharma · S. Sharma  
Department of Mechanical Engineering, Dr. B. R. Ambedkar National Institute  
of Technology, Jalandhar, Punjab, India  
e-mail: [kangos@nitj.ac.in](mailto:kangos@nitj.ac.in)

discovered and found to be valuable. However, due to their bad plastic qualities, they could not meet to fit in certain applications which includes moving components of automobile and aircraft, load-carrying components of machines, wind turbine blades and sports equipment. So to increase the important properties of these materials, some special reinforced polymers were introduced. In 1935, the first ever reinforced fiber composite was created. Despite significant development of fiber composites, the need for light and strong material still felt during World War II. By the end of 1970, various engineered fibers had been found which completely changed the utilization of materials [1, 2]. Carbon fiber, glass fiber and aramid fiber strands are the most widely recognized reinforced materials due to their availability in certain mechanical applications [3]. Despite their attractive mechanical properties, these fibers, however, are non-biodegradable which create ecological and environmental issues [4]. Hence, the use of natural fiber is more preferable on conserving ecology and environment. They possess the property of low weight and density and are also cheap. Thus, the ecological, economic and organic properties of these materials can improve the composites and their utilization in various present-day applications. The degradation of these polymers would support the recyclability and empowers researchers to develop NRP [5]. The density of natural reinforced fiber ( $1.16\text{--}1.7\text{ g/cm}^3$ ) is usually lower than that of glass fiber ( $2.4\text{ g/cm}^3$ ), which make them to be used as lightweight composites in various industrial applications [6].

## 1.2 Waxes

Nature gave us waxes, one of the most hydrophobic substances [7]. The superhydrophobicity (SHPY) in plants is due to the presence of the epicuticular wax layer and the level of micro/nanostructure on the plant surface [8, 9]. The waxy bump crystals present on the lotus leaf have the water contact angle (WCA) of about  $161 \pm 2.7^\circ$ . The individual length and diameter of these special pillars (nonacosanol wax tubules) are  $0.3\text{--}2\ \mu\text{m}$  and  $100\text{--}200\ \text{nm}$ , respectively [10]. Waxes are of two types: natural waxes and synthetic waxes. The natural waxes can be renewable or non-renewable. Examples of renewable waxes are plant and animal waxes. Some plant waxes include soy wax, carnauba wax, candelilla wax, rice grain wax, wax from sunflower, etc. Animal waxes include wool wax and beeswax. On the other hand, mineral waxes can be categorized as non-renewable. Petroleum is an example of mineral waxes. Montain is also considered as mineral wax. Paraffin and microcrystalline are types of petroleum waxes [11–13]. Waxes are characterized by their long chain which includes 10–60 carbon atoms, hydrocarbons, unsaturated fats, alcohols, aldehydes, esters, etc. [14–17]. Paraffin which is a derivative of petroleum wax has a wide range of applications in coatings on paper and light candle making. Microcrystalline waxes are another type of petroleum waxes which are primarily utilized in the rubber and cosmetics industry. More details of various kinds of waxes can be found in other research articles [18–21].

## 2 Anti-wetting Behavior of Different Polymers

### 2.1 Reinforced Polymers

The hydrophilic property of the NRP fiber is an important factor for its poor behavior to absorb moisture. The moisture present in the fiber may lead to the development of cracks in the construction of the matrix which affect the strength and consequently reduce the life cycle of these composites [22]. The mechanism of moisture absorption of these composites is categorized into three types. In the first type, the diffusion of water molecules takes place due to the presence of micro-voids in the polymer matrix. In the second type, the capillary is transferred through the gaps at the interface of fiber matrix. In the third type, the presence of micropores in the composite surface allows water to diffuse through the gaps which results in the increase of moisture in these polymers [23]. Figure 1 shows the effect of moisture in the de-bonding of the fiber matrix.

Haameem et al. [24] examined Napier grass fiber reinforced polyester composite for their water absorption characteristics. The investigation revealed that the treatment of fiber is powerful in enhancing the water resistance qualities of the composites. The untreated short composites absorbed 13% of water, whereas long composite absorbed 20% of water. After treatment, both short and long fiber composites absorbed only 5% and 7% water, respectively. IAnother study by Munirah Abdullah and Ahmad [25] showed that the treatment of fiber is helpful in upgrading the water resistance behavior of the coconut fiber polyester composites. Wu et al. [26] studied the effect of water absorption behavior of fabricated hemp fiber composites covered with a film of polyethylene. Their result showed a reduction in water absorption behavior which is more along the edges of the composites. Akil et al. [27] investigated water absorption behavior of jute polyester composite using distilled water, seawater and acidic solution. Their result showed that with the increase of immersion time, the water absorption rate was found to be increasing.

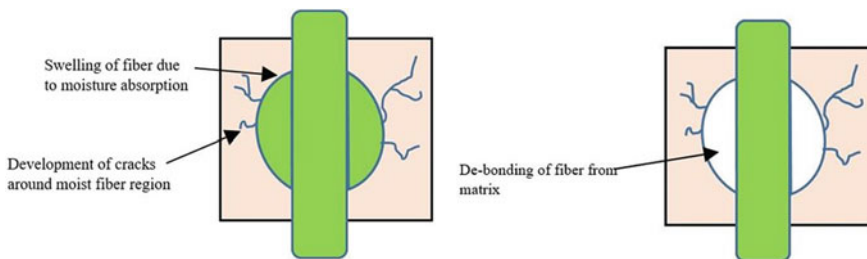


**Fig. 1** Swelling and de-bonding of fiber from the matrix after moisture absorption

## 2.2 Waxes

Separation of oil–water is a worldwide challenge ‘inferable’ from the frequent oil spill accidents and in other modern-day industrial wastage. As of late, superoleophilic surfaces were proven to be important surfaces in the separation of oil–water applications. Many reports [28–30] were published on porous materials having properties of superoleophilicity and superhydrophilicity–superoleophobicity, where waxes are used along with ceramic nanoparticles and polymers. Using the electrospinning process, the superhydrophobic and superoleophilic nanofibers of polycaprolactone (PCL) and beeswax (BW) have been investigated.

Through electrospinning, a solution of PCL/BW (10% weight to volume) was prepared. In the procedure, BW was first dissolved in dichloromethane and then stirred. The weight percentage of beeswax was in the range from 0 to 25. Then PCL was added in the solution. The collected nanofibers were then heated in vacuum at 40 °C to eliminate any leftover contents. Beeswax membrane of 25 wt% (PCL-25BW) showed superhydrophobicity with WCA of 153°. The corresponding surface roughness for PCL and PCL-25BW was found to be increasing from 2.1 nm to 19.1 nm, respectively. With increase in the wax concentration, WCA gradually increased. The sliding angle (SA) for PCL and PCL-25BW was also found to be significantly reduced from 46° to 8°, respectively. Samples also showed good corrosion resistance in various acidic solutions [31].

## 2.3 Sponges

Sponges/wipes (PDMS, melamine, polyurethane, CNT wipes) have received specific attention in oil separation. The oil absorbed by these sponges can be collected through mechanical squeezing. Though, these sponges are normally non-renewable and non-biodegradable. An eco-friendly natural sponge was reported by Wang et al. [32]. The wettability was modified by dip coating the sponge in an emulsion of bran–candelilla wax. The natural sponge was kept in the emulsion at 60 °C and then squeezed, taken out, squeezed and cooled. The pore diameter was 20 µm, and the size was in the range of 20–200 µm. The initial WCA of the sponge was 123°, which increased to 153.8° after three cycles of dip coatings treatment. Sliding angles were found to be 7.9°. In the following work, researchers fabricated loofah sponge with properties of superhydrophobic and superoleophilic using similar methods [33]. Yin et al. [34] fabricated a melamine magnetic sponge by synthesizing with Fe<sub>3</sub>O<sub>4</sub> and coating with candelilla wax. Firstly, the sponge was precipitated by Fe<sub>3</sub>O<sub>4</sub> and then squeezed at 70 °C in a candelilla wax–ethanol solution. The sponge was then taken out of the solution and dried at a temperature of 60 °C. The treated sponge showed excellent absorption capacity of 55–104 g/g<sup>-1</sup> with high WCA (158.8°). Hunag et al. [35] showed similar results by using polyethylene polytetrafluoroethylene mixture spray coatings on microfiber reinforced

with polyphenylene sulfide. Wang et al. [36] dispersed TiO<sub>2</sub> nanoparticles in a molten carnauba wax to get a composite coating on a filter paper. The treated filter paper was capable of expelling water from a water/diesel solution and showed WCA of about 140°. Gupta et al. [37] added nano-alumina particles in beeswax and paraffin. Their result showed increased WCA of 156° and extremely low hysteresis of less than 5° with improved mechanical and thermal stability.

### 3 Other Desirable Properties

#### 3.1 Tribological Properties of NRP

Materials go through rubbing, friction and wear when in relative motion with different materials. This results in the tribological wear of the material, and due to prolonged wear, the material surface starts to deteriorate. This wear damage influences the degradation of reliability, durability and strength of the material and consequently results in high maintenance or repairable cost. Matejka et al. [38] revealed that by selecting the appropriate reinforcements in the polymer, one could increase the tribological performance of the components. Composites with an ideal weight percentage of fiber reinforcements offer better wear resistance [39, 40]. Dwivedi and Chand [41] studied the effect of increasing load on the reinforced fiber composites. Their result showed that with the increase in the load the wear rate of selected sisal fiber polypropylene composite reduces. Narish et al. [42] examined wear and frictional qualities of kenaf fiber polyurethane composite. The treated reinforced fiber showed improvements in the wear rate of the composites to about 78%. Similar results were found by Chin and Yousif [43] using kenaf reinforced fiber with epoxy composite. The treated fiber increased the tribological performance of the composite to about 85%. It has been seen that fiber length also influences tribological wear. Singh et al. [44] and Boopathi [45] used epoxy composite reinforced with fruit fiber to see the effect of different length of fiber in the tribological wear characteristics. Their result showed that the use of short fiber reinforcements improves the wear performance of the material.

#### 3.2 Adsorption Capacity of Sponges

In this section, the adsorption capacity of special hydrophobic sponges has been discussed. Sponges with high porosity possess high adsorption value. The porosity of untreated polyurethane sponge is nearly 97% [46, 47]. After modifying, the porosity decreased slightly as compared to the untreated sponge. This is due to the effect of surface loading. The modified sponges have the adsorption capacity of 18–50 g/g for different types of oils and solutions [48]. The retainability of high

porosity also helps in increasing the adsorption capacity. An enormous number of reports showed that the addition of graphene changes the amphiphilic property of sponges to hydrophilicity or oleophilicity. Besides the property of graphene to absorb a wide range of oils and organic liquids, the graphene-modified sponge also has increased adsorption capacity [49, 50].

## 4 Conclusions

On reviewing the important considerations for natural reinforced polymers and wax-type polymers, the following keynotes have been concluded:

- Natural fibers and waxes are essential materials of intrigue when considering superhydrophobic surfaces and coatings. Modifications on the eco-friendly fibers and waxes lead to the advantages of being more economical, easy to fabricate more in scope for large-scale production. Waxes which exhibit superhydrophobic property experience the problem of mechanical durability and low thermal stability which can be reasonably reduced to an extent by using additives of suitable nanoparticles like  $\text{Al}_2\text{O}_3$ ,  $\text{SiO}_2$ ,  $\text{TiO}_2$ ,  $\text{CuO}_2$ , etc. Similarly, surface energy can also be modified by using surface energy agents which can increase the wettability of these waxes. Wax based also exhibits the property of atmospheric corrosion protection.
- Modified sponges are also a prominent area of research as oil absorbents in oil–water separation applications. Considerable work has been reported on changing anti-wetting properties of these specially modified sponges. Depending upon the application, small sponges can also be used to extract oil from water as they could float easily in the sea. Thus, this could reduce environmental and health hazards by eliminating harmful oil contents from water. Sponges are also shown to have a high absorption rate with high porosity, thus holds much suitability to be used as oil–water separation applications.

## 5 Future Scope

This article covered the in-depth review of natural reinforced polymers, waxes and sponges, their various properties like mechanical, tribological, water resistance and biodegradability which are important to consider when using these natural polymers in industrial and practical applications. Researchers have added different types of reinforced composites to the existing polymers to increase their performance parameters. Further, research can be improved on developing these natural existing polymers with additives and coupling agents from numerous renewable biodegradable resources. On wax-based polymers, several works have been reported till date using wax-based anti-wetting surfaces but only a few works have

been reported on wax-based materials for oil–water separation applications in biomedical marine and other applications. The case of sponges absorbing of high viscosity oils and organic liquids is a problem as these sponges do not let these high viscosity liquids to pass through them. Also, these sponges face difficulties in recycling after use which could result in waste environmental pollution. So many challenges still exist toward the fabrication of these sponges, and the prominent task still needs to be done toward the better fabrication, better absorption, better usability and recyclability of these ideal absorbents.

## References

1. Tsai, S.W., Hahn, H.T.: *Introduction to Composite Materials*. Technomic Publishing Co., Westport (1980)
2. Vinson, J.R., Chou, T.W.: *Composite Materials and Their Use in Structures* (1975)
3. Buckley, J.D., Edie, D.D.: *Carbon-Carbon Materials and Composites*. William Andrew (1993)
4. Harish, S., Michael, D.P., Bensely, A., Lal, D.M., Rajadurai, A.: Mechanical property evaluation of natural fiber coir composite. *Mater. Charact.* **60**(1), 44–49 (2009)
5. Al-Oqla, F.M., Sapuan, S.M.: *Materials Selection for Natural Fiber Composites*. Woodhead Publishing (2017)
6. Tg, Y.G., Mr, S., Siengchin, S.: Natural fibers as sustainable and renewable resource for development of eco-friendly composites: a comprehensive review. *Front. Mater.* **6**, 226 (2019)
7. Basson, I., Reynhardt, E.C.: An investigation of the structures and molecular dynamics of natural waxes. I. Beeswax. *J. Phys. D: Appl. Phys.* **21**(9), 1429 (1988)
8. Barthlott, W., Neinhuis, C.: Purity of the sacred lotus, or escape from contamination in biological surfaces. *Planta* **202**(1), 1–8 (1997)
9. Feng, L., Li, S., Li, Y., Li, H., Zhang, L., Zhai, J., Zhu, D.: Super-hydrophobic surfaces: from natural to artificial. *Adv. Mater.* **14**(24), 1857–1860 (2002)
10. Koch, K., Bhushan, B., Jung, Y.C., Barthlott, W.: Fabrication of artificial Lotus leaves and significance of hierarchical structure for superhydrophobicity and low adhesion. *Soft Matter* **5**(7), 1386–1393 (2009)
11. Tinto, W.F., Elufioye, T.O., Roach, J.: *Waxes in Pharmacognosy: Fundamentals, Applications and Strategy*, pp. 443 – 455 (2016)
12. Saji, V.S.: Wax-based Artificial superhydrophobic surfaces and coatings. *Coll. Surf. A: Physicochem. Eng. Aspects* 125132 (2020)
13. Bennett, H.: *Industrial Waxes—Compound Waxes and Technology*, vol. 2. Chemical Publishing Company, New York (1963)
14. Barthlott, W., Mail, M., Bhushan, B., Koch, K.: Plant surfaces: structures and functions for biomimetic innovations. *Nano-Micro Lett.* **9**(2), 23 (2017)
15. Bennett, H.: *Industrial Waxes—Natural and Synthetic Waxes*, vol. 1. Chemical Publishing Company, New York (1963)
16. Riederer, M., Markstädter, C.: Cuticular waxes: a critical assessment of current knowledge. *Plant Cuticles* 189–200 (1996)
17. Cottom, W.P.: Waxes. In: Kirk-Othmer (ed.) *Encyclopedia of Chemical Technology*. John Wiley & Sons (2001)
18. Bower, J.D.: *Waxes in Coatings Technology Handbook*, 3rd edn. CRC Press, Boca Rayton (2006)

19. de Freitas, C.A.S., de Sousa, P.H.M., Soares, D.J., da Silva, J.Y.G., Benjamin, S.R., Guedes, M.I.F.: Carnauba wax uses in food—a review. *Food Chem.* **291**, 38–48 (2019)
20. Fei, T., Wang, T.: A review of recent development of sustainable waxes derived from vegetable oils. *Curr. Opin. Food Sci.* **16**, 7–14 (2017)
21. Veale, K., Adali, S., Pitot, J., Brooks, M.: A review of the performance and structural considerations of paraffin wax hybrid rocket fuels with additives. *Acta Astronaut.* **141**, 196–208 (2017)
22. Mohanty, A.K., Misra, M., Drzal, L.T.: *Natural Fibers, Biopolymers, and Biocomposites*. CRC Press (2005)
23. Dhakal, H.N., Zhang, Z.Y., Richardson, M.O.W.: Effect of water absorption on the mechanical properties of hemp fibre reinforced unsaturated polyester composites. *Compos. Sci. Technol.* **67**(7–8), 1674–1683 (2007)
24. JA, M.H., Majid, M.A., Afendi, M., Marzuki, H.F.A., Hilmi, E.A., Fahmi, I., Gibson, A.G.: Effects of water absorption on Napier grass fibre/polyester composites. *Compos. Struct.* **144**, 138–146 (2016)
25. Munirah Abdullah, N., Ahmad, I.: Effect of chemical treatment on mechanical and water-sorption properties coconut fiber-unsaturated polyester from recycled PET. *ISRN Mater. Sci.* 1–8 (2012)
26. Wu, Y., Xia, C., Cai, L., Shi, S.Q., Cheng, J.: Water-resistant hemp fiber-reinforced composites: in-situ surface protection by polyethylene film. *Ind. Crops Prod.* **112**, 210–216 (2018)
27. Akil, H.M., Cheng, L.W., Ishak, Z.M., Bakar, A.A., Abd Rahman, M.A.: Water absorption study on pultruded jute fibre reinforced unsaturated polyester composites. *Compos. Sci. Technol.* **69**(11–12), 1942–1948 (2009)
28. Wang, S., Liu, K., Yao, X., Jiang, L.: Bioinspired surfaces with superwettability: new insight on theory, design, and applications. *Chem. Rev.* **115**(16), 8230–8293 (2015)
29. Zhang, S., Huang, J., Chen, Z., Yang, S., Lai, Y.: Liquid mobility on superwetttable surfaces for applications in energy and the environment. *J. Mater. Chem. A* **7**(1), 38–63 (2019)
30. Parvate, S., Dixit, P., Chattopadhyay, S.: Superhydrophobic surfaces: insights from theory and experiment. *J. Phys. Chem. B* **124**(8), 1323–1360 (2020)
31. Reshmi, C.R., Sundaran, S.P., Juraij, A., Athiyanthil, S.: Fabrication of superhydrophobic polycaprolactone/beeswax electrospun membranes for high-efficiency oil/water separation. *RSC Adv.* **7**(4), 2092–2102 (2017)
32. Wang, F., Lei, S., Ou, J., Li, C., Li, W.: Novel all-natural material for oil/water separation. *Ind. Eng. Chem. Res.* **58**(5), 1924–1931 (2019)
33. Wang, F., Xie, T., Zhong, W., Ou, J., Xue, M., Li, W.: A renewable and biodegradable all-biomass material for the separation of oil from water surface. *Surf. Coat. Technol.* **372**, 84–92 (2019)
34. Yin, Z., Li, Y., Song, T., Bao, M., Li, Y., Lu, J., Li, Y.: An environmentally benign approach to prepare superhydrophobic magnetic melamine sponge for effective oil/water separation. *Sep. Purif. Technol.* **236**, 116308 (2020)
35. Huang, H., Liu, M., Li, Y., Yu, Y., Yin, X., Wu, J., Wang, H.: Polyphenylene sulfide microfiber membrane with superhydrophobicity and superoleophilicity for oil/water separation. *J. Mater. Sci.* **53**(18), 13243–13252 (2018)
36. Wang, Y., He, B., Zhao, L.: Fabrication of hydrophobic coating on filter paper from self-emulsifying carnauba wax-alcohol emulsions with nano-TiO<sub>2</sub> particles for water/diesel separation. *BioResources* **12**(4), 7774–7783 (2017)
37. Gupta, S., Babu, A., Arora, H.S., Grewal, H.S.: High durability of non-fluorinated superhydrophobic nanocomposite coatings. *Mater. Lett.* 127717 (2020)
38. Matějka, V., Fu, Z., Kukutschová, J., Qi, S., Jiang, S., Zhang, X., Lu, Y.: Jute fibers and powdered hazelnut shells as natural fillers in non-asbestos organic non-metallic friction composites. *Mater. Des.* **51**, 847–853 (2013)



39. Liu, Y., Ma, Y., Yu, J., Zhuang, J., Wu, S., Tong, J.: Development and characterization of alkali treated abaca fiber reinforced friction composites. *Compos. Interfaces* **26**(1), 67–82 (2019)
40. Zhong, L.X., Fu, S.Y., Zhou, X.S., Zhan, H.Y.: Effect of surface microfibrillation of sisal fibre on the mechanical properties of sisal/aramid fibre hybrid composites. *Compos. A Appl. Sci. Manuf.* **42**(3), 244–252 (2011)
41. Dwivedi, U.K., Chand, N.: Influence of MA-g-PP on abrasive wear behaviour of chopped sisal fibre reinforced polypropylene composites. *J. Mater. Process. Technol.* **209**(12–13), 5371–5375 (2009)
42. Narish, S., Yousif, B.F., Rilling, D.: Adhesive wear of thermoplastic composite based on kenaf fibres. *Proc. Inst. Mech. Eng., Part J: J. Eng. Tribol.* **225**(2), 101–109 (2011)
43. Chin, C.W., Yousif, B.F.: Potential of kenaf fibres as reinforcement for tribological applications. *Wear* **267**(9–10), 1550–1557 (2009)
44. Singh, T., Kumar, N., Grewal, J.S., Patnaik, A., Fekete, G.: Natural fiber reinforced non-asbestos brake friction composites: Influence of ramie fiber on physico-mechanical and tribological properties. *Mater. Res. Express.* **6**(11), 115701 (2019)
45. Boopathi, L., Sampath, P.S., Mylsamy, K.: Influence of fiber length in the wear behaviour of borassus fruit fiber reinforced epoxy composites. *Int J Eng Sci Technol.* **4**, 4119–4129 (2012)
46. Pham, V.H., Dickerson, J.H.: Superhydrophobic silanized melamine sponges as high efficiency oil absorbent materials. *ACS Appl. Mater. Interfaces* **6**(16), 14181–14188 (2014)
47. Zhou, X., Zhang, Z., Xu, X., Men, X., Zhu, X.: Facile fabrication of superhydrophobic sponge with selective absorption and collection of oil from water. *Ind. Eng. Chem. Res.* **52**(27), 9411–9416 (2013)
48. Lei, Z., Deng, Y., Wang, C.: Ambient-temperature fabrication of melamine-based sponges coated with hydrophobic lignin shells by surface dip adsorbing for oil/water separation. *RSC Adv.* **6**(108), 106928–106934 (2016)
49. Zhou, S., Hao, G., Zhou, X., Jiang, W., Wang, T., Zhang, N., Yu, L.: One-pot synthesis of robust superhydrophobic, functionalized graphene/polyurethane sponge for effective continuous oil–water separation. *Chem. Eng. J.* **302**, 155–162 (2016)
50. Zhou, C., Lai, C., Zhang, C., Zeng, G., Huang, D., Cheng, M., Yang, Y.: Semiconductor/boron nitride composites: synthesis, properties, and photocatalysis applications. *Appl. Catal. B* **238**, 6–18 (2018)

# Analysis on Different Types of Viscometers, Design, Materials, and Technology: A Review



Priyanka S. Bankar and M. B. S. Sreekara Reddy

**Abstract** Viscosity as a sensitive measure of liquids changes is a potential quality-control parameter for simple and rapid assessment of fluid. Measuring viscosity is important for the quality assurance of liquid products, as well as for monitoring the viscosity of clinical fluids as a potential hemodynamic biomarker. However, conventional viscometers and their micro-fluidic counterparts typically rely on bulky and expensive equipment and lack the ability for rapid and field-deployable viscosity analysis. Viscometers are broadly employed in a wide range of sensing and monitoring applications, such as biochemical optimization, biomedical diagnostics, pharmaceuticals, and various adulteration detections. When realizing them in a micro-fluidic environment, the viscometers can potentially be used in an automated and robust point-of-care setting. Even after so much evolution, one of the constant challenges faced in the development of micro-fluidic devices is to choose the best fabrication scheme, particularly, in terms of a simplified process, cost, and time. Here, we present a 3D printed electro-micro-fluidic viscometer (EMV). The EMV measures the reference fluid viscosity, under laminar flow, by automatically evaluating the travel time of the sample fluid vis-à-vis to that of a reference fluid. In this paper, we discuss about different types of viscometers, design, materials, and technology.

**Keywords** Materials · 3D printing · Technologies · Viscometer

## 1 Introduction

The development of science and technology nowadays is increasing rapidly and getting more sophisticated. The needs of researchers begin to increase along with the increasing of accuracy, precision, efficiency, and eco-friendly of the measurements that will be measured to get the characteristics of an object. These measurements

---

P. S. Bankar (✉) · M. B. S. S. Reddy  
Mechanical Engineering Department, Koneru Lakshmaiah Educational Foundation,  
Vaddeswaram, Guntur 522502, India

© The Author(s), under exclusive license to Springer Nature Singapore Pte Ltd. 2021  
A. Patnaik et al. (eds.), *Advances in Materials Processing and Manufacturing Applications*, Lecture Notes in Mechanical Engineering,  
[https://doi.org/10.1007/978-981-16-0909-1\\_47](https://doi.org/10.1007/978-981-16-0909-1_47)

could be in the form of macro-scale research and micro-scale research. One measurement that plays a role in micro-scale measurements is Brownian motion, which is a phenomenon of the random movement of some particles that can be observed under the objective lens of a microscope caused by the collisions between particles and the molecules of the surrounding liquid [1].

Brownian motion has been used in general in several studies such as biology, medical sciences, and physics. This method is especially useful for microrheology, where micron-sized dielectric balls or namely microbeads are mixed into a fluid and then the movements of microbeads are observed by using the assembly of a high-resolution video camera and microscope optical systems making it possible to obtain the viscosity values of the fluid. The Brownian motion-based system is made to create a method for measuring the viscosity of a liquid with equipment that is easier and simpler than conventional methods by utilizing the minimum quantity of liquid (in microliters). Several studies on the analysis of Brownian motion-based system have been carried out as in that observed Brownian motion at short-time scales, with a focus on the measurement of the instantaneous velocity of a Brownian particle in a gas and the observation of the transition from ballistic to delusive Brownian motion in a liquid. Moreover, the article examines the capability of mean square displacement (MSD) analysis to extract reliable values of the diffusion coefficient  $D$  of a single particle undergoing Brownian motion in an isotropic medium in the presence of localization uncertainty. In the article [1, 3], liquid viscosity measurement was observed by using optical tweezers.

Not all liquids are the same; some are thin and flow fast, while some are thick or goeey and flow slowly. The property that accounts for these differences in properties of flow is known as viscosity. Viscosity is defined as the measure of its resistance to deformation at a given rate which corresponds to the informal concept of thickness for liquids. The international systems of units (SI) measures the unit of viscosity in Newton seconds per meter squared ( $\text{Ns/m}^2$ ) which is synonymous to a Pascal second (Pa s). The imperial units measure viscosity in pounds-force second per foot squared  $\text{ibfs/ft}^2$  [3]. The study of this property of substances is known as rheology. This property is measured with a viscometer which provides data that are useful in quality-control applications in the production of a wide variety of products including inks, paints, motor oils, food, and cosmetic [3]. Dharmiah et al. [4] discussed the effect of viscous dissipation on free convective heat and mass transfer characteristics. Sivaiah et al. [5] performed numerical study on MHD boundary layer flow of a visco-elastic fluid over a porous plate in the presence of thermal radiation.

Viscosity measurement is very important in the world of science. Some of these areas where viscosity measurements are important are hydraulics, lubrication, construction, refrigeration, and fabrication. In lubrication, lubricating oils are of different grades, and these grades are determined greatly by their viscosity. Hence, accordingly [6], viscosity is considered as a major property of lubricating oil. In the construction industry, viscosity measurement is important in paint industries for quality control; production of adhesives, and in concreting, viscosity determines self-leveling and pumping behavior of a mix. Viscometers are used to measure

viscosity, and there are of seven different classes. These are capillary viscometers, orifice viscometers, high-temperature high-shear-rate viscometers, rotational viscometers, falling ball viscometers, vibrational viscometers, and ultrasonic viscometers [7–9]. Asserted that the commonly used viscometers are the capillary flow type, the orifice type, and the rotational viscometers. Currently most commonly used viscosity measurements techniques require that the liquid comes in contact with a solid material. This method is in most cases impracticable for very thin liquids. The falling sphere viscometer is one of these commonly used techniques for measuring viscosity [10]. Gudala et al. [5] investigated the effect of bio-additive on the viscosity and flow of heavy crude oil water. Nagasantoshi et al. [11] observed the heat and mass transfer of nano-fluid with variable viscosity.

Micro-viscometer where two immiscible fluids were made to flow in a solitary Y-shaped micro-channel under laminar flow, where one was reference fluid, while the other being a test fluid. Based on the viscosities of both the fluids, the width occupied by both the fluids was found to vary [12]. This was proven by modeling, simulations, and experimentally by different fabrication approaches for diverse applications, such as to monitor biodiesel blending, milk adulteration, and automobile fuel adulteration [10]. Microscopic images were taken and processed to measure the width of the fluid. The limitation of this approach was a bulky system due to the requirement of image capturing. Elsewhere, this approach was slightly modified and extended with the help of a smart phone and an extra accessory of 4X lens [13, 7].

Still, the requirement of image capturing and analysis persists. Furthermore, the viscosity values were found to change with the variation of the inclination of the camera during image capturing. The aim of this approach is to develop a micro-fluidic viscometer avoiding the requirement of image acquisition, leading to have an integrated, miniaturized, robust, and automated micro-fluidic device capable of calculating viscosity with the help of microelectronics with the aid of a simple and inexpensive 3DP.

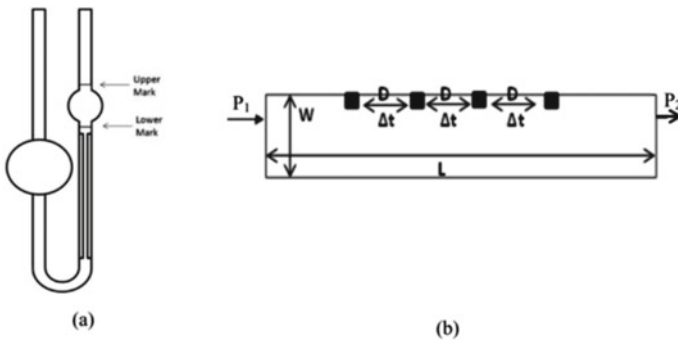


**Fig. 1** a Schematic of a typical Ostwald viscometer. b Schematic of the proposed micro-fluidic [12]

## 2 Literature Review

### 2.1 General Study

Viscosity measurement is very important in the world of science. Some of these areas where viscosity measurements are important are hydraulics, lubrication, construction, refrigeration, and fabrication. In lubrication, lubricating oils are of different grades, and these grades are determined greatly by their viscosity. Hence, according viscosity is considered as a major property of lubricating oil. In the construction industry, viscosity measurement is important in paint industries for quality control, production of adhesives and in concreting, viscosity determines self-levelling, and pumping behavior of a mix. Viscometers are used to measure viscosity, and there are of seven different classes. These are capillary viscometers, orifice viscometers, high-temperature high-shear-rate viscometers, rotational viscometers, falling ball viscometers, vibration viscometers, and ultrasonic viscometers.

### 2.2 Designing of Viscometer

Mr. Derrick [1]: Current laboratory equipment used for undergraduate engineering courses can be enriched inexpensively by adding acquisition boards and requiring students to write code to enable to obtain data from these devices. Programming can be completed prior to the laboratory session, and then the code will be tested. This paper presents one laboratory experiment developed at Indiana-University Purdue University Indianapolis (IUPUI). The primary objectives of the project were to develop a viscometer apparatus prototype (1) with a significantly lower acquisition cost compared to current model and (2) that enhances students' understanding of viscosity and drag principles. The apparatus is implemented for use in the IUPUI Mechanical and Energy Engineering Department's fluid mechanics laboratory. Current acquisition cost is shown to be expensive and can produce inaccurate data due to the method of testing. Increasing accuracy of the results will allow students to feel more confident in learning the fundamental theory they are being taught. A prototype was developed that met sponsor requirements, engineering requirements, and abided by ASTM viscometer measurement standards. The fully built and assembled prototype provides a cost-effective way for students to accurately and precisely determine the viscosity of different oils. Compared to the older model, the newer model showed 30–40% reduction in error. An assessment study is a work in progress to identify the overall impact the redesign and programming add to student learning.

Augustine [3]: Viscosity plays an important role in sciences and engineering world. Knowledge of viscosity and flow parameters are essential in liquids for their production, quality control, and development. The construction industry makes use

of different liquids for different applications. Plasters, sealers bond breakers, liquid floor hardeners, coatings, and more are liquids used in the construction industry. Conclusions about their processing characteristics, pumpability, sprayability shelf life, as well as flow ability and application characteristics can be retrieved from successful measurements. It is therefore important that related measurements should be carried out with equipment that is accurate and less expensive.

Kondrashov [2]: In this paper, the problem of determining the viscosity coefficient of a Newtonian liquid for the development of a rotary viscometer is considered. The least squares method is proposed to be used for processing the measurement results. Conversion factors of electric sensor readings are proposed. The calibration instrument is designed to calculate the conversion coefficient of the torsional moment to current of the sensor. The proposed formulas are useful for developing an algorithm for calculating a rotary viscometer with more accurate processing of measurement results.

Zulfahmi [14]: As the development of science and technology is increasing rapidly, there is one research method that plays an important role in micro-scale measurements, namely Brownian motion. Brownian motion is a phenomenon of the random movement of several particles that can be observed under the objective lens of a microscope due to collisions between particles and surrounding liquid molecules. In this study, the author will observe how the Brownian motion method can be used to determine the liquid viscosity value through the relation between the displacement of polymer particles in various concentration of the solutions and the size of polymer particles that will be used in the observation.

### ***2.3 Material Required for Viscometer***

Anjorin [15]: This paper presents the design and testing of a locally fabricated viscometer. The need for a locally fabricated viscometer to measure the viscosity of lubricants is underpinned by the prohibitive cost of imported laboratory equipment such as the viscometers. The kinematic viscosities of SAE 40, palm oil, and soybean oil were measured using the fabricated viscometer. Experimental results showed that the viscosity of palm oil and soybean oil at 40 °C was 40.87 mm<sup>2</sup>/s and 32.01 mm<sup>2</sup>/s, respectively. The viscosity of SAE 40 (engine oil) was 13.65 ± 0.013 mm<sup>2</sup>/s (90% confidence level) at 100 °C.

Sariyerli [16]: The present study was realized for measuring viscosities of reference liquids using capillary viscometers and Stabinger viscometer SVM 3001 with viscosity interval between 1 and 5000 mm<sup>2</sup>/s with temperatures from 20 to 80 °C. Based on our measurement with various liquids, we determine the viscosity values and compare both of the results. The aim of this study is to evaluate the results of the primary level viscosity measurement system and Stabinger viscometer and to compare the measurement results due to the providing traceability of Stabinger viscometer by TUBITAK UME. An increasing number of national metrology institutes and accredited laboratories provide viscometer calibration with

reference liquids in a wide viscosity range. It is a common practice to use the viscosity of water as the metrological basic of viscometry.

Stephen [3]: Viscosity plays an important role in sciences and engineering world. Knowledge of viscosity and flow parameters are essential in liquids for their production, quality control, and development. The construction industry makes use of different liquids for different applications. Plasters, sealers bond breakers, liquid floor hardeners, coatings, and more are liquids used in the construction industry. Conclusions about their processing characteristics pumpability, sprayability, shelf life, as well as flow ability and application characteristics can be retrieved from successful measurements.

## ***2.4 Analysis on Types of Viscometers***

Basumatary [6]: In this work, he reports a fiber-optic sensor to measure the viscosity of Newtonian liquids. The sensor is made of a rectangular channel and two separate multimode optical fibers, which are properly inserted via through-holes provided at the extremities of the rectangular channel. Both the optical fibers do have a decladded zone for each to allow leakage of optical power from the zones when light is coupled into the fibers. When suitable liquid type flows inside the channel, liquid comes into contact with decladded zones thereby reducing leakage of optical power from the decladded zones. Under this condition, optical power levels available at output ends of the fibers undergo step change one after another with a time delay. And, the time delay is found to be proportional to viscosity of liquid and inclination of the channel through which liquid flows.

Digilov [7]: We describe an unsteady pressure-driven capillary viscometer, in which the liquid under test is forced through a capillary tube by compressed air pressure. The principle of operation involves measurement of the driving pressure versus time that decays progressively as the fluid flows and covers continuously a broad shear rate range in a single measurement. The viscosity is determined by curve fitting of the experimental data to the explicit expression for the transient pressure as a function of time. A laboratory bench test shows the validity of the theoretical approach for viscosity determination of both Newtonian and non-Newtonian liquids.

Kawatra [9]: A viscometry system involving a vibrating sphere viscometer and a rotational viscometer has been developed for online measurement of viscosity and for rheological characterization of mineral slurries into either Newtonian or non-Newtonian flows. Special precautions were taken to allow measurements of viscosity of rapidly settling mineral suspensions.

## 2.5 *Designing Technologies*

Oh [10]: Viscosity as a sensitive measure of material changes is a potential quality-control parameter for simple and rapid assessment of frying oil quality. However, conventional viscometers require improvements in throughput, portability, cost-effectiveness, and usability to be widely adopted for quality-control applications. Here, we present a 3D printed multichannel viscometer for simple, inexpensive, and multiplexed viscosity measurement. The multichannel viscometer enables both parallel actuation of multiple fluid flows by pressing the plunger of the viscometer by hand and direct measurement of their relative volumes dispensed with naked eye, during deep frying of potato strips and the recovery of used frying oil after treatment with an adsorbent agent to remove frying by-products.

Puneeth [12]: Viscometers are broadly employed in a wide range of sensing and monitoring applications, such as biochemical optimization, biomedical diagnostics, pharmaceuticals, and various adulteration detections. When realizing them in a micro-fluidic environment, the viscometers can potentially be used in an automated and robust point-of-care setting. Even after so much evolution, one of the constant challenges faced in the development of micro-fluidic devices is to choose the best fabrication scheme, particularly, in terms of a simplified process, cost, and time.

Choi [17]: Measuring viscosity is important for the quality assurance of liquid products, as well as for monitoring the viscosity of clinical fluids as a potential hemodynamic biomarker. However, conventional viscometers and their micro-fluidic counterparts typically rely on bulky and expensive equipment and lack the ability for rapid and field-deployable viscosity analysis.

Ngo [18]: Freedom of design, mass customization, waste minimization, and the ability to manufacture complex structures, as well as fast prototyping, are the main benefits of additive manufacturing (AM) or 3D printing. A comprehensive review of the main 3D printing methods, materials, and their development in trending applications was carried out. In particular, the revolutionary applications of AM in biomedical, aerospace, buildings, and protective structures were discussed.

Suresh et al. [19] presented various 3D printing technologies that find applications in automobile, aerospace, and medical field. Overall, this paper gives an overview of different types of viscometers, their design, and material aspects with a main focus on 3D printing including a survey on its benefits and drawbacks as a benchmark for future research and development.

## 3 **Conclusion**

In this review, we discuss about different types of viscometers, design, materials, and technology and also the 3D printed multichannel viscometer for high-throughput viscosity measurement, by comparing multiple fluid flows without inter-channel interference. The proposed 3D printed multichannel viscometer



enables inexpensive, accurate, high-throughput, and field-deployable measurement of fluid viscosity. The micro-fluidic device, with micro-channel and embedded electrode junctions, was fabricated in a single step using a simple and inexpensive desktop 3DP. The EMV platform, consisting of micro-fluidic device, microcontroller, and pumping mechanism, mimics the conventional Ostwald viscometer enabling to measure the fluid viscosity within a minute. The platform was harnessed to measure the viscosities of three different fluids, which is comparable to the bench top systems. Viscometers are broadly employed in a wide range of sensing and monitoring applications, such as biochemical optimization, biomedical diagnostics, pharmaceuticals, and various adulteration detections. When realizing them in a micro-fluidic environment, the viscometers can potentially be used in an automated and robust point-of-care setting. Even after so much evolution, one of the constant challenges faced in the development of micro-fluidic devices is to choose the best fabrication scheme, particularly in terms of a simplified process, cost, and time.

## References

1. Shin, S.: Continuous viscosity measurement of non-newtonian fluids over a range of shear rates using a mass-detecting capillary viscometer (2002)
2. Derrick, J.M.: A low-cost affordable viscometer design for experimental fluid viscosity verification and drag coefficient calculation (2018)
3. Augustine, E.O.: Design fabrication and testing of a viscometer for testing viscosity of liquids (2019)
4. Zulfahmi: Design of liquid viscosity measurement system using brownian motion (2019)
5. Nagasantoshi, P., Ramana Reddy, G.V., Gnaneswara, M., Padma, P.: Heat and mass transfer of non-newtonian nanofluid flow over a stretching sheet with non-uniform heat source and variable viscosity. *J. Nanofluids*, 821–832 (2018)
6. Oh, S., Choi, S.: 3D-printed capillary circuits for calibration-free viscosity measurement of newtonian and non-newtonian fluids (2018)
7. Suresh, G., Reddy, M.H., Gurram, N.: Summarization of 3D-printing technology in processing and development of medical implants. *J. Mech. Continua Math. Sci.* 176–191 (2019)
8. Dharmiah, G., Chamkha, A.J., Vedavathi, N., Balamurugan, K.S.: Viscous dissipation effect on transient aligned magnetic free convective flow past an inclined moving plate. *Front. Heat Mass Transf.* (2019)
9. Sivaiah, G., Reddy, K.J., Reddy, P.C., Chandra Raju, M.C.: Numerical study of mhd boundary layer flow of a viscoelastic and dissipative fluid past a porous plate in the presence of thermal radiation. *Int. J. Fluid Mech. Res.* 27–38 (2019)
10. Kim, B.: A 3D-printed multichannel viscometer for high-throughput analysis of frying oil quality (2018)
11. Gudala, M.K., Banerjee, S., Rao, T.R.M., Naiya, T.K., Mandal, A.: The effect of a bio additive on the viscosity and the energy requirement on heavy crude oil flow. *Pet. Sci. Technol.* 99–107(2018)
12. Stephen, O.E.: Design fabrication and testing of a viscometer for testing viscosity of liquids (2020)
13. Ngo, T.D.: Additive manufacturing (3D printing): a review of materials, methods, applications and challenges (2018)

14. Sariyerli, G.S.: Comparison tests for the determination of the viscosity values of reference liquids by capillary viscometers and stabinger viscometer SVM 3001 (2018)
15. Anjorin, S.A.: Design, construction and testing of a viscometer (2019)
16. Basumatary, T.: Fibre optic sensor based viscometer to measure viscosity of newtonian fluids (2017)
17. Kawatra, S.K.: On-line measurement of viscosity and determination of flow types for mineral suspensions (1996)
18. Digilov, R.M.: Pressure-driven capillary viscometer: fundamental challenges in transient flow viscometry (2011)
19. Kondrashov, I.P.: Determination of Newtonian fluid viscosity and design constants of a rotary viscometer (2020)
20. Puneeth, S.B.: 3-D printed integrated and automated electro-microfluidic viscometer for biochemical applications (2018)

# Approach Toward Design for Manufacturing Assembly of Fiber Reinforced Plastics Fan Blade for Cooling Tower



**Ankush Sharma, Vikas Kukshal, Pankaj Agarwal,  
and Aniruddha V. Kapre**

**Abstract** Design (DFM) and design for assembly (DFA) are now known as a single process, and in other words, it is called DFMA. The most common methods of DFMA are then studied in the production assembly concept with the features of each block. DFA is a tool used to select the most expensive items and product selection for a variety of product types. The aim of the case study was to arrive to the conclusion or generalized design aspects for the fan design in today's industrial requirement such as cooling tower where the steel blade fans are being converted to fiber reinforced plastics where we can choose the glass material of varied density and difference combinations can be altered. Also approach of the design for failure mode calculates the priority or necessity of the design aspects and stages of the product design which depicts the time saving, material saving, and cost-effective approach.

**Keywords** DFM · DFA systems · Functionality of DFM · Evaluation · Sub-assemblies

---

A. Sharma

Department of Mechanical Engineering, Malaviya National Institute of Technology, Jaipur, Rajasthan 302017, India

V. Kukshal

Department of Mechanical Engineering, National Institute of Technology Uttarakhand, Srinagar (Garhwal), Uttarakhand 246174, India

P. Agarwal

Department of Mechanical Engineering, Amity University, Jaipur, Rajasthan 302006, India

A. V. Kapre (✉)

Customizing and Logistics, Belimo Actuators India Pvt. Ltd., Mumbai, India

© The Author(s), under exclusive license to Springer Nature Singapore Pte Ltd. 2021

469

A. Patnaik et al. (eds.), *Advances in Materials Processing and Manufacturing*

*Applications*, Lecture Notes in Mechanical Engineering,

[https://doi.org/10.1007/978-981-16-0909-1\\_48](https://doi.org/10.1007/978-981-16-0909-1_48)

## 1 Introduction

A detailed description of the design, manufacturing, and assembly (DFMA) strategies is generally used to diminish the cost of manufacturing by designing and improving the process. Currently, the fan assembly for cooling towers has various components such as hub, fan stack, and fan blades. The integration of these sub-components becomes more critical over time. Flexible fan bush drivers are with shaft box outlet assembly box. The short-term collapse caused by Lean's efforts will be required to be curtailed through the proper implementation of the concurrent engineering and DFMA principles [1]. It is worthwhile to point out that the financial benefits of sound and organized meetings are equally important. Unfortunately, many managers see mergers as a "necessary evil" and fail to see that significant contributions can be made available to improved productivity. The differences and similarities between DFM and DFA as well as how the design of the product has an impact on product knowledge [2, 3]. It includes an analysis of the quantity of design efficiency. It is highly recommended to involve product engineers, product managers, and product manufacturers in this analysis. Facilitate production construction by working with a team from concept via prototype to production. Whether you are using an existing design or developing a new product design using DFMA techniques, you will benefit from improved quality, increased reliable components, and at the same time reduced complexity and cost [4]. The end result is your design that allows repetitive components that meet your purpose and product needs. By designing the first production, the DFMA helps customers reduce the amount of design updates required and reduce the time and cost of model duplication [5]. As a result, DFMA helps companies bring products to market faster. Based on the literature review, it was observed that in the construction and integration of complex fan segments, the application of DFMA still required the proper understanding. In order to achieve the specified performance in the manufacturing sector, based on well-prepared meeting techniques, this study therefore analyzed the implementation of DFMA in the current meetings in the construction and other industries. Well now the significance of the DFMA is to be understood first before we move forward. As the name depicts design for manufacturing assembly, it states that the design of the product or any process should be designed in such a way that the overall efficiency of the product after being manufactured is to be of optimal value and so as the manufacturing process [6]. So, to get the optimized solution, these are bifurcated into two distinct methodologies mainly DFA and DFM. The latter comes first, so we can alter the design in the process so called in process inspections, and once the product is ready, we can set the processes for the assembly, which is one of the important techniques to get the maximum production with high efficiency [7].

## 2 Problem Statement

Each stage of product production has its own distinctive features that lead to a different level of impact throughout the life project. Here, we limit our study to major challenges in production and assembly operations and how the production process can be simplified by increasing the tools available. The backbone to achieve an effective production rate is by providing a variety of processes and changing the process where necessary.

## 3 Objectives and Research Methods

The success of the stated performance means not only a reduction in costs and/or expiration, but also a process such as a reduction in problems like human effort, traffic interruption, and other costs. Flexible and quick assembly techniques should be met with the goal of encouraging this productivity in a fan meeting, as this can allow them to turn store locations through high-tech regions with clean workplaces, quiet, and healthy environments.

In this paper, the engineering solutions and production and design methods used for axial flow fans in cooling towers are researched, well-known, modernized, and rated for their possible use in the cooling tower whether for compulsory refurbishment/counter-flow/cross-flow cooling towers.

The scope of this work is described in

- Implementation of DFMA principles for bridge integration
- Introduce tested technical concepts and integration techniques used in their industries
- Review of meeting methods in terms of a comprehensive view of DFMA principles that will be divided into multiple projects. The test will not be performed in the form of a test procedure, where the conditions are continuously rearranged and re-evaluated
- Introduction of new industrial information on DFMA at the intersection of bridges and submission of ongoing design work recommendations in accordance with the criteria set for testing
- The entire DFMA project cycle encompasses a large part of the project, from layout to organization, and when working with DFMA, it is hard to concentrate on only one phase of the project.

Design for manufacturing and assembly (DFMA) is an integrated process from building blocks born of a variety of ethical engineering processes and a product life production system. DFM and DFA are the parameters that determine the improved percentage of time spent in the intangible product development project phase. The basic principle of DFM was formulated in 1780s; the development of 'simple production guidelines' had begun in the early 1960s. Figure 1 shows the process flowchart for DFMA [7].

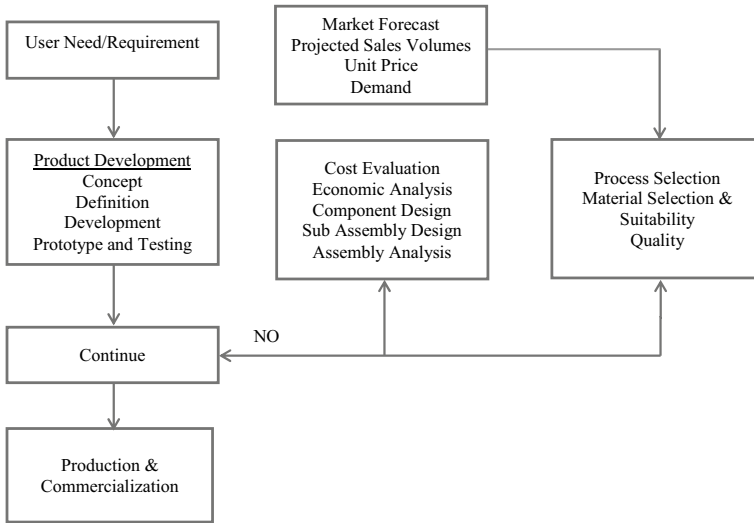


Fig. 1 DFMA process flowchart [6]

The concept of DFA is to prepare a design and simplifies the component structure that verifies the cost beneficial assembly operations by validating assembly processes and associated design process into the project. DFA is related with the process and terminologies planned in DFM block. DFM is a very complex process and if not grabbed properly does not give the precise results.

### 4 DFMA Procedure

It is quite relevant at this stage to analyze how other industries have respected the DFMA concepts and the result obtained. In the early stages of growth, contrary to conventional work ethics in some industries, project engineers are excessively concerned with functional needs and not differentiated from the productivity in previous decisions [8]. Due to its over-the-top performance feature, the traditional building culture can, however, cause teams to miss out on their customer costs. Whether the design cycle or product life cycle should be reviewed and verified in order to improve the process. Construction activities including product costs allow industries to get more product performance at a lower cost. In this paper, different production strategies allow to compare product costs, which improve the differentiation of the costs of competitive products. The DFMA procedure adapted in the present study is shown in Fig. 2a.

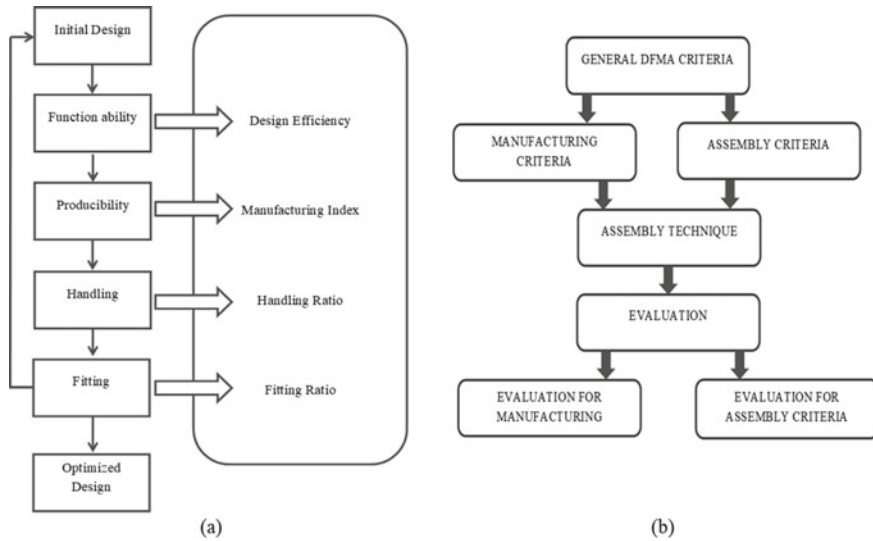


Fig. 2 a DFMA procedure b flowchart used to test assembly methods and technical concepts [8]

## 5 DFMA Performance

Some rules need to be followed to facilitate product design, for example, product costs and production costs ignored at the beginning of a project. Many design features considered cost-effectiveness which later becomes the bottle of other works.

In 1990, a global survey was carried out of car manufacturers. Japan then had some of the biggest car makers in the world. Research has tried to understand the product variability and the level of automation used in various plants. Research findings show that only one third of the product variations between plants can be recorded through automation. Japan has become one of the world's most productive plants, accounting for 32% of its spontaneous compaction volume. However, this plant had only a part of human effort compared with the European equivalent plant. While not a self-supporting plant with an automation organization of 48%, a greater man-held assembly has been found in this European plant than an automated unit. This indicates that performance in a meeting determines the meeting process extremely strongly. In addition, the study concludes that regardless of how it performs in production, a plant cannot compete if it has defects in design as product design failure cannot be compensated for by the type of production system produced for creation of the product [9]. This makes it equally necessary for high-quality goods such as efficient production to be made. DFMA or other tools to help design decisions aim to create a comprehensive and faultless product that produces a product that is inefficient. DFMA is used nowadays to reduce the overall product cost of the product, work-in-progress, assembly time, ease of production, and repeated geometry of the parts features that are avoided [8].

### **Few design difficulties observed by designers**

Guessing the product cycle of different products and similar operating conditions was the point of discussion. Design ideas need to be submitted early, so that other production activities can be started in the same way. The next challenge is to share information with the department's internal departments.

At this stage, it is very promising to decide what new DFMA innovations are being developed that other organizations have achieved. According to the latest operating practice in some industries, during design and growth, design engineers are preoccupied with production requirements only and do not incur product costs. Cost-targeted customers completely miss out on this acquisition period. In this paper, advanced production technologies are introduced that allow for the achievement of defined objectives and operational costs. Another significant part of this stage is the study of the usage of DFMA resources in many industries to understand the implementation of concepts in the construction context. DFMA can be considered as an instrument for promoting the introduction of the advanced manufacturing technology (AMT), including modern production techniques and advanced manufacturing techniques.

### **Testing Methods**

Occasional estimates (precise assembly method) require the use of proven construction measures that are considered during the calculation. As the calculation is completed, an important measure follows the design process, design testing, and verification of the design of the specified product [8]. The evaluation includes points covered during the process such as safety, ease of handling, environmentally friendly, and last but not strictly according to the required design standards.

Once the construction is completed and further confirmation is accepted, various conditions are considered where the product can be tested at different levels of complexity. The verification team has full rights to modify or propose any modifications to be made in order to smooth out operations and product placement in various site conditions, for example, a fan blade shank can be made to a smaller size and the structure can be made to accommodate a smaller space in the assembly.

### **Execution of the design aspects**

In order to measure fan satisfaction methods and technological models effectively, the specifications for the fan assembly process must be understood when requested. The mass compliance of mass-produced reinforced concrete, along with the management of large and heavy concrete components, is an example. This can be pointed to as one of the problems in the fan meeting process. On the other hand, the weight of the fiber reinforced polymer fan blade can be managed heavily based on modern molding techniques, such as vacuum infusion molding, although major design issues can occur in reinforcement of fiber glass fittings and reliability on other hardware. Because of the obvious discrepancies in the working environment between the two, the problems related with various building works often vary in nature. For the purpose of establishing a common playing field, so that assembly



methods can be tested without reducing the scope of the study, and consideration is only given to site assembly or installation of bridge sections.

Depending on today's installation techniques, one can use a variety of methods such as size or quality. Measurement testing includes evaluating the performance of a product or system. From the perspective of the meeting, the evaluation test does not provide specific recommendations and procedures and objectives for constructing components of an effective assembly program. Obviously the DFMA tool provides a guide or quality information on how difficult the product is, from a meeting point, to make it easier and therefore make it less expensive. Just the price results from the price test not provided the clear details regarding the preferred solution of the meeting process.

The one proposed by Boothroyd and Dewhurst [10] is a typical representation of a quantitative test process. The process, in this example, uses the DFA indicator given by the equation, to evaluate project and product output from a meeting perspective.

$$\varphi_i = \left( \frac{Z_m \times T_m}{T_a} \right) \times 100$$

Here:  $\varphi_i$ ,  $Z_m$ ,  $T_m$ , and  $T_a$  represents the DFA index, small number of parts, minimum meeting time appropriate for each segment, and estimated total meeting time, respectively.

It meets at least one, two, or all three falling into your system, depending on the equation, while a high index value is indicative of the correct composition of the assembly product. This decrease can involve a large number of products, additional times for each part, and more time for product integration overall. The results of the DFA index are used to classify circumstances which require attention and make initial decisions for the completion or reconstruction of an undesired part of a meeting requiring additional time and additional costs. The measurement process, as seen in the example above, involves price data and measuring variables, and the output gives calculated time and cost. The findings should be interpreted by their influence on output or composition.

The quality ranking, on the other side, is based on a number of processes or requirements that a product needs to follow in order to satisfy its organizational function. It can include additional steps to measure how far a product has come from the right solution. The ideal solution for this thesis task refers to a meeting process that completes all the DFMA elements translated into the indicators for each session. The process of the meeting incorporates the conclusions placed on quality assessment that improves the lessons and research aimed at providing clear information about the solutions selected in the conference process [10]. Obviously, not all DFMA policies can be achieved through a specific meeting process, making it difficult to make consistent decisions between different strategies. Therefore, when quality measures are taken, performance comparisons will be made to the extent that the implementation of the DFMA in each meeting indicator is met

through assembly methods. Therefore, in this work, the same concepts of quality assessment, which are quality assessments, are based on a set of procedures used to determine whether the meeting method satisfies the DFMA methods used to interpret the indicators for each meeting. The process and flowchart used to test assembly methods and technical concepts are shown in Fig. 2b.

## 6 Inputs from Market

The tasks covered here are interconnected, leaving no connections with others to explain the different sections of hard work. The following section demonstrates the significance of this study, the challenges faced during the analysis, and the results achieved. The goal of this creative concept is to create and explore a method of exploring strategies to incorporate fan designs that engage in the sustainability of the urban environment. During the job, many obstacles hamper at the desired level in the achievement of the goals. Among the various challenges, the key difficulties involved were the construction of the structural analysis of FRP, the production of other industrial designs and the transmission of knowledge in the hub spool, the quest for realistic and improved assembly methods, and the necessary testing methods. There are a variety of previous works or pre-established knowledge in this principal doctrine which can be connected with many of the functions. In the construction industry, for example, improvements and implementations of the DFMA as a design and testing tool have been recently created. This work should also be performed with due consideration. Moreover, the findings of such studies should be available for debate in order to use more components in practices aimed at enhancing outcomes. Any of the main problems can be posed and addressed in conjunction with the above activities.

To define the principles of development and integration for the construction sector, it is important to transfer awareness of design techniques and priorities to other industries. The method to design based on this core principle is a methodology to help design decisions that have been used and has demonstrated its participation to reduced values, waste reduction, and system performance. The actual content of the DFMA applications is ambiguous; however, its cost analysis does not provide a good image of the costs of the application which are below their benefits. This, in turn, leaves tool users and methods used in case studies a potential danger. Moreover, this definition has mostly been written by developers in the literature studied in the DFMA field and explicitly enables the use of compatible resources, regardless of how different the sector is. The principles and guidelines used in other industries when implementing DFM, DFA, and DFMA methods are to be used in a varying production environment and represent a different set that is appropriate in construction. The selection of design processes and goals is therefore focused on their implementation and purpose. The selection is based on data collected from the fan selected on the Web site. A selection role takes a lot of experience and expertise in the subject, as there are many things to think about and many decisions to take.

As a result, the DFMA principles can be implemented in several various ways based on how each doctor involved in creating such construction methods perceives them. In addition, the principles and guidelines are not so relevant that they can be taken into account when designing and installing bridge pieces. For example, where the additional testing needed for the performance of the elements does not substantially affect the actual site meeting and lessens the effect on other assembly metrics directly relevant to construction plans relative to the types of materials and components or the number of elements used in assembly.

The complexity in focusing on a project process when designing such a construction program as DFMA spans the project execution cycle (from construction to convergence) is another barrier to implementing DFMA programs. It is a difficult task to harmonize construction processes with DFMA programs, although this construction process includes often physically separated tasks that impede the normal replication of the execution of DFMA programs. Reconsideration of processes only seems feasible between building projects when carrying out particular learning activities. Better and cheaper methods between development and incorporation of building materials can be difficult within the same project [10]. With respect to the use of construction methods in the construction industry, many considerations do need to be addressed. Problems like procurement processes that affect the degree of participation of the professionals and the ability of customers/projects may be one of the primary sectors where attention is required. Nevertheless, we should speak briefly in which they pose important issues which require existing procurement systems.

## 7 Conclusion

The emphasis on direct cost savings and timeliness has become popular in the construction industry, through rigorous assessment of conference activities. Different approaches to resolving these needs should be taken when contemplating other sustainable problems, e.g., minimizing human activity, FRP design, and structural analysis of the glass fiber. In this report, another aspect of resource utilization and cost reduction in the use of DFMA methods was explored. While considerable initial investment is needed, the DFMA significantly facilitates the implementation of the predetermined goals of organizations and companies operating according to sustainability objectives.

It is clear that such industrial thought and advanced design techniques as assembly methods and the principle of DFMA play a role in representing new priorities and concepts in a range of building activities. We may also assume that the DFMA definition guides designers to do something right rather than right, since the system-supported method makes it easier for stakeholders to understand, so problems of all product development levels can be taken into consideration in the reconstruction process. For this reason, employees in the industry will be able to enjoy opportunities to explore, select, and develop best practices in all available “practical” ways.

## References

1. Andreason, M.M., Kähler, S., Lund, T.: Design For Assembly, 2nd edn. Springer-Verlag (1988)
2. Bardasz, T., Zeid, I.: Cognitive model of memory for mechanical-design problems. *Comput. Aided Des.* **24**(6), 327–342 (1992)
3. Favi, C., Germani, M., Mandolini, M.: Design for manufacturing and assembly vs. design to cost: toward a multi-objective approach for decision-making strategies during conceptual design of complex products. *Procedia CIRP* **50**(1), 275–280 (2016)
4. Boothroyd, G., Dewhurst, P., Knight, W.: *Product Design for Manufacture and Assembly*, 2nd edn. Marcel Dekker, New York (2002)
5. Nitesh-Prakash, W., Sridhar V.G., Annamalai, K.: New product development by DFMA and rapid prototyping. *J. Eng. Appl. Sci.* **9**(3), 274–279 (2014)
6. Edwards, K.L.: Towards more strategic product design for manufacture and assembly: priorities for concurrent engineering. *Mater. Des.* **23**(7), 651–656 (2002)
7. Annamalai, K., Naiju, C.D., Karthik, S., Mohan-Prashanth, M.: Early cost estimate of product during design stage using design for manufacturing and assembly (DFMA) principles. *Adv. Mater. Res.* **622–623**, 540–544 (2013)
8. Todić, V., Lukić, D., Milošević, M., Jovičić, G., Vukman, J.: Manufacturability of product design regarding suitability for manufacturing and assembly (DfMA). *J. Prod. Eng.* **16**(1) (2012)
9. Bayoumi, A.M.E.: Design for manufacture and assembly (DFMA): Concepts, benefits and applications. In: *Current Advances in Mechanical Design and Production VII*, Pergamon, pp. 501–509 (2000)
10. Boothroyd, G., Dewhurst, P.: *Design for Assembly: Selecting the Right Method*. Penton/IPC, Inc. (1983)

# Synthesis, Structural and Magnetic Properties of Gadolinium-Doped Ni–Zn Ferrites Synthesized by Sol–Gel Auto-Combustion Route



D. L. Chaudhari, A. M. Shahare, A. K. Nandanwar, D. S. Choudhary, and K. G. Rewatkar

## 1 Introduction

Nickel–zinc ferrites are technologically important class of soft magnetic materials for their widespread industrial applications, ranging from microwave to radio frequencies such as microwave devices, computer memories and magnetic recording [1]. Spinel ferrites including Ni–Zn compositions are of great interest due to their potential applications in microelectronics, magneto-optics and as microwave device components [2, 3]. The properties of ferrite materials are known to be strongly influenced by their composition and microstructure that in turn are sensitive to the processing methods used to synthesize them. In an attempt to prepare high-performance ferrites with reproducible stoichiometric compositions and desired microstructure, the present work aimed at preparing Ni–Zn ferrites using the sol–gel combustion method. The sol–gel combustion techniques for ferrite synthesis have been proved to be more convenient, since the ferrite powders with nano-sized particles can be formed directly from combustion of dried in air [4]. In the present study, we prepared  $\text{Ni}_{0.65}\text{Zn}_{0.35}\text{Gd}_x\text{Fe}_{2-x}\text{O}_4$  ( $x = 0.0, 0.05, 0.10, 0.15, 0.20$  and  $0.25$ ) nanoferrites using sol–gel technique. XRD, FE-SEM and VSM were employed to study the structure, microstructure and magnetic behaviours of the Gd-doped Ni–Zn samples. The detailed investigation of the  $\text{Gd}^{3+}$  effects on the structural and magnetic properties was studied from theoretical and experimental point of view.

---

D. L. Chaudhari (✉)

Department of Physics, S. S. Jaiswal College, Arjuni/Mor, Gondia 441701, India

A. M. Shahare · D. S. Choudhary

Department of Physics, D. B. Science College, Gondia 441601, India

A. K. Nandanwar · K. G. Rewatkar

Department of Physics, Dr. Ambedkar College, Deeksha Bhoomi, Nagpur 440010, India

© The Author(s), under exclusive license to Springer Nature Singapore Pte Ltd. 2021

479

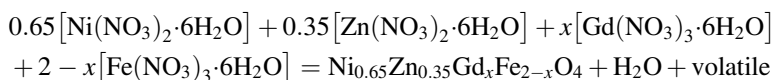
A. Patnaik et al. (eds.), *Advances in Materials Processing and Manufacturing*

*Applications*, Lecture Notes in Mechanical Engineering,

[https://doi.org/10.1007/978-981-16-0909-1\\_49](https://doi.org/10.1007/978-981-16-0909-1_49)

## 2 Experimental Procedure

Gadolinium-doped Ni–Zn ferrite powders with compositions of  $\text{Ni}_{0.65}\text{Zn}_{0.35}\text{Gd}_x\text{Fe}_{2-x}\text{O}_4$  ( $x = 0.0, 0.05, 0.10, 0.15, 0.20$  and  $0.25$ ) were synthesized by sol–gel auto-combustion method. The analytical grade  $\text{Fe}(\text{NO}_3)_3 \cdot 9\text{H}_2\text{O}$ ,  $\text{Zn}(\text{NO}_3)_2 \cdot 6\text{H}_2\text{O}$ ,  $\text{Ni}(\text{NO}_3)_2 \cdot 6\text{H}_2\text{O}$ ,  $\text{Gd}(\text{NO}_3)_3 \cdot 6\text{H}_2\text{O}$  and citric acid ( $\text{C}_6\text{H}_8\text{O}_7 \cdot \text{H}_2\text{O}$ ) were used as raw materials. The appropriate amount of nitrates and citric acid is first dissolved into de-ionized water to form a mixed solution with molar ratio of nitrates to citric acid 1:1. The pH value of solution was adjusted to about 7 using ammonia. Then, the mixed solution was poured into a beaker and heated at  $80^\circ\text{C}$  under constant stirring to transform into a dried gel. Being ignited, the dried gel was burnt in a self-propagating combustion way to form loose powder. The solutions were evaporated by continuous heating at  $100^\circ\text{C}$  with agitation until the formation of viscous gel [5]. The samples were dried, and the dried powders were annealed in air furnace at  $700^\circ\text{C}$  for 7 h., then slowly cooled to the room temperature. Finally, the annealed powder was grounded using the mortar and pestle. The equation used for calculating the stoichiometric values of the metal nitrates is as follows:



The microstructure and the chemical composition of the samples were investigated by X-ray diffraction using  $\text{Cu-K}\alpha$  ( $\lambda = 1.5406 \text{ \AA}$ ), scanning electron microscopy and transmission electron microscopy. The values of the coercive fields, saturation and remanent magnetizations were obtained from the hysteresis loops obtained from a vibrating sample magnetometer (VSM).

## 3 Result and Discussion

### 3.1 XRD Analysis

The XRD pattern of the samples under investigation is shown in Fig. 1a. Higher intensity peaks in pattern show the peaks which were indexed corresponding to (220), (311), (222), (400), (422), (511) and (440). All XRD patterns show the single-phase structure of the Ni–Zn–Gd spinel nanoferrites. These spectra were confirmed from ICDD standard JCPDS card no.'s 008-0234. Table 1 show the different parameter calculated from the XRD patterns of  $\text{Ni}_{0.65}\text{Zn}_{0.35}\text{Gd}_x\text{Fe}_{2-x}\text{O}_4$  ( $x = 0.0, 0.05, 0.10, 0.15, 0.20$  and  $0.25$ ) nanoferrites. The broadness of the maximum intensity peak shows the nano-sized Ni–Zn–Gd ferrites [6]. The crystallite size was calculated using the Debye's Scherrer formula [7–9].

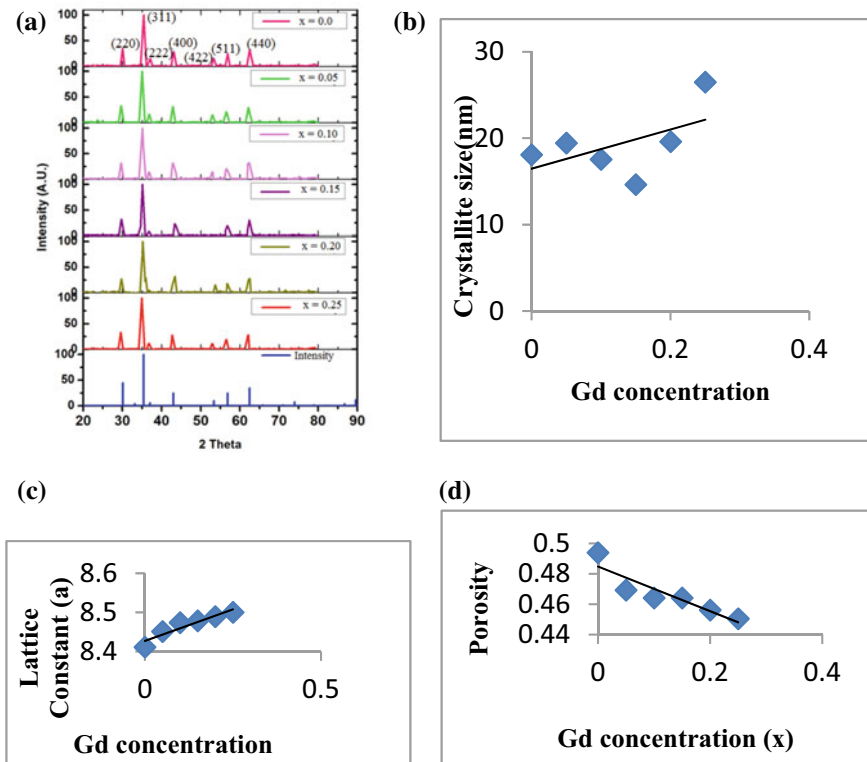


**Fig. 1** a XRD pattern of  $\text{Ni}_{0.65}\text{Zn}_{0.35}\text{Gd}_x\text{Fe}_{2-x}\text{O}_4$ . b Variation of crystallite size with Gd. c Variation of lattice constant with Gd concentration. d Variation of porosity with Gd concentration

**Table 1** Effect of  $\text{Gd}^{3+}$  ion concentration on structural parameters

$x$	$a$ (Å)	Crystallite size (nm)	Grain size (nm)	$\rho_x$ (gm/cm <sup>3</sup> )	Porosity
0.0	8.410	18.09	31.40	5.20	0.4940
0.05	8.451	19.44	42.36	5.64	0.4692
0.10	8.474	17.55	51.33	5.94	0.4641
0.15	8.478	14.64	58.80	6.45	0.4641
0.20	8.489	19.61	63.78	6.85	0.4562
0.25	8.50	26.50	71.88	7.25	0.4504

The X-ray density of the samples was calculated by relation

$$\rho_x = \frac{8M}{Na^3} \quad (1)$$

where  $M$  is the molecular weight of the sample,  $N$  is the Avogadro's number and  $a^3$  the volume of the cubic unit cell.

The bulk density was calculated by using relation,

$$\rho_m = \frac{M}{\pi r^2 t} \quad (2)$$

where  $M$  is the mass,  $r$  is the radius and  $t$  be the thickness of the pellet.

Porosity ( $P$ ) of the ferrite samples was determined by using the following relation

$$P = \frac{\rho_x - \rho_m}{\rho_x} \times 100 \quad (3)$$

where  $\rho_x$  is the X-ray density and  $\rho_m$  be the bulk density in ( $\text{gm}/\text{cm}^3$ ).

Induced strain in the Ni–Zn–Gd ferrites for different concentrations of Gd was calculated from Williamson–Hall method [10].

$$\beta \cos \theta = 4 \epsilon \sin \theta + \lambda/D \quad (4)$$

where  $D$  is crystallite size,  $\lambda$  is wavelength of X-ray,  $\beta$  is FWHM measure in radian,  $\epsilon$  is the induced strain and  $\theta$  is Bragg angle. A strain occurs due to negative pressure imposed due to replacement of  $\text{Fe}^{3+}$  ions by  $\text{Gd}^{3+}$  ions [10]. It was found that induced lattice strain increases systematically with increase of Gd doping in Ni–Zn Spinel ferrites. Table 1 shows the values of the crystallite size ranging from 14.64 to 26.5 nm. Figure 1b, c and d shows the variations of crystallite size, lattice parameter and porosity of  $\text{Ni}_{0.65}\text{Zn}_{0.35}\text{Gd}_x\text{Fe}_{2-x}\text{O}_4$  ( $x = 0.0, 0.05, 0.10, 0.15, 0.20$  and  $0.25$ ) nanoferrites. It is clear from Table 1 that the crystallite size increases with the concentration of the Gd. The lattice parameter of the nanoferrites increases with increasing Gd contents. This behaviour of lattice parameter with Gd contents is described on the basis of difference in ionic radii of  $\text{Fe}^{3+}$  (0.6459 Å) and  $\text{Gd}^{3+}$  (0.938 Å) ions. The values of the lattice parameter demonstrated an almost linear dependence; therefore, it obeys Vegard's law [9, 11]. Similar results of the lattice parameter of the spinel ferrite were reported by other researchers [12]. Porosity of the ferrite slightly decreases with increase in Gd concentration which shows that resistivity may be decreased with increase in concentration of Gd and conductivity may be increased as observed by the researchers [11, 12]. In nickel–zinc ferrite,



the site occupancy of the Ni, Zn and Fe ions has certain preferences in the spinel structure. Ni ions might prefer to occupy B site, and Zn ions occupy A site, whereas Fe ions are equally distributed among A and B sites [13].

### 3.2 FE-SEM Analysis

The microstructure of the studied ferrite samples was analysed using SEM micrographs as shown in Fig. 2a. The micrographs show the agglomerated grainy structure [14] and observed that the grain size increases with increase in Gd content. The grain size derived from SEM micrographs is found to be larger than that estimated from XRD data. This indicates that every grain is formed by aggregation of a large number of crystallites or particles. This result is consistent with other studies about Gd nanoparticles [15]. Also, SEM images revealed that the grains have an almost regular shape and homogeneous distribution in the range 31.4–71.88 nm as shown by histogram plot in Fig. 2b and c.

The elemental composition of the samples with varying Gd dopant was confirmed through the EDX technique. Thus, the present research reveals the extent of purity of the nanoparticles prepared via the sol–gel route. Also, the EDX analysis of gadolinium substituted Ni–Zn sample clearly shows that the stoichiometric  $\text{Fe}^{3+}$  ion content decreases with growing concentration of  $\text{Gd}^{3+}$  ions as shown in Fig. 2d and e.

### 3.3 HR-TEM

It is evident from Fig. 3a that the particles are single crystalline in nature, with clear lattice fringes that can be observed on the entire region. Majority of particles were found to be dominantly faceted into crystallites. Atomic planes for the lattice system are clearly visible with ‘ $d$ ’ spacing of about 0.25–0.29 nm. This ‘ $d$ ’ value has good agreement with XRD data.

Also, the crystallographic interpretations of the prepared sample were done in the reciprocal space by recording the selected area electron diffraction patterns (SAED) of the Ni–Zn–Gd ferrite. Figure 3b shows a SAED pattern of gadolinium-doped Ni–Zn ferrite from an aggregate of nanoparticles. A set of important Debye rings corresponding to (h k l) planes (2 2 0)  $d = 0.3178 \text{ \AA}$ , (3 1 1)  $d = 0.2636 \text{ \AA}$ , (4 0 0)  $d = 0.2086 \text{ \AA}$ , (4 2 2)  $d = 0.1857 \text{ \AA}$ , (5 1 1)  $d = 0.1681 \text{ \AA}$  and (4 4 0)  $d = 0.1432 \text{ \AA}$  of the basic Ni–Zn ferrite cubic crystal structure (Space Group  $\text{Fd}\bar{3}m$ ,  $a = 8.41 \text{ \AA}$ ) are marked. These Debye rings appeared to be continuous and are diffused. No other rings except for the preferred plane are found in the pattern. The observed crystallographic interplanar spacing ‘ $d$ ’ values agree well with those obtained from XRD analysis.

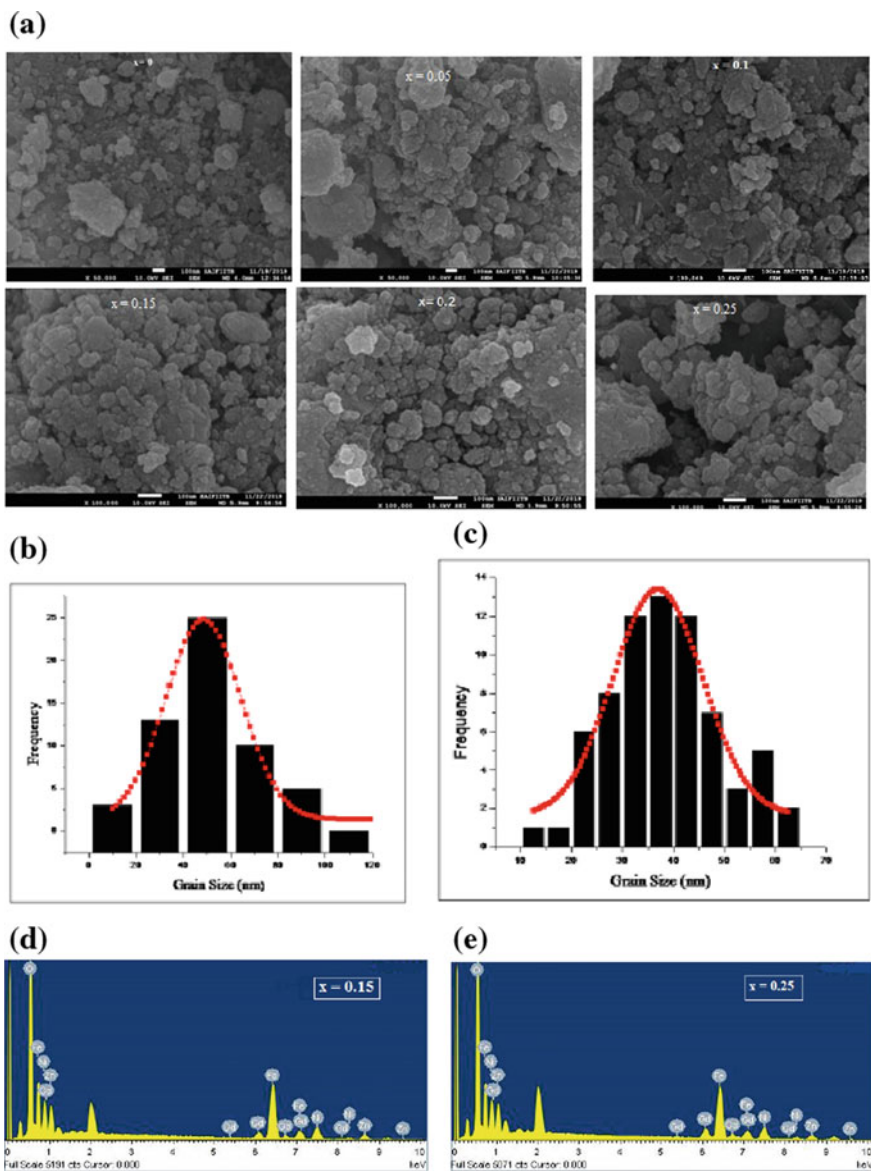


**Fig. 2** **a** SEM micrograph of the samples with  $x = 0.0, 0.05, 0.01, 0.15, 0.20, 0.25$ . **b** Histogram plot of  $\text{Ni}_{0.65}\text{Zn}_{0.35}\text{Gd}_{0.15}\text{Fe}_{0.85}\text{O}_4$ . **c** Histogram plot of  $\text{Ni}_{0.65}\text{Zn}_{0.35}\text{Gd}_{0.25}\text{Fe}_{1.75}\text{O}_4$ . **d** EDX Spectra of  $\text{Ni}_{0.65}\text{Zn}_{0.35}\text{Gd}_{0.15}\text{Fe}_{0.85}\text{O}_4$ . **e** EDX Spectra of  $\text{Ni}_{0.65}\text{Zn}_{0.35}\text{Gd}_{0.25}\text{Fe}_{1.75}\text{O}_4$

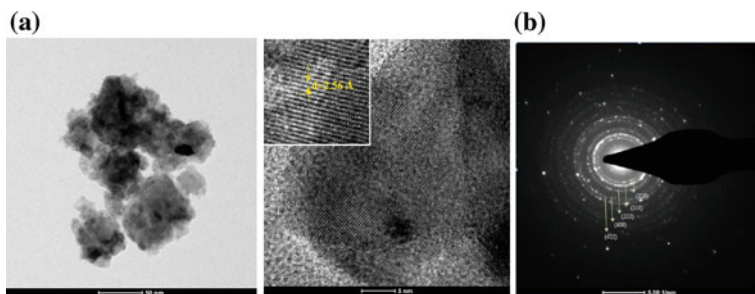


Fig. 3 a TEM image of  $\text{Ni}_{0.65}\text{Zn}_{0.35}\text{Gd}_{0.25}\text{Fe}_{1.75}\text{O}_4$ . b SAED Pattern

### 3.4 Magnetic Properties

Room temperature hysteresis loops of  $\text{Ni}_{0.65}\text{Zn}_{0.35}\text{Gd}_x\text{Fe}_{2-x}\text{O}_4$  nanoferrites at ( $x = 0.0, 0.05, 0.10, 0.15, 0.20$  and  $0.25$ ) were recorded under the maximum applied field of 1500 Gauss. The magnetic loops are shown in Fig. 4a. Table 2 depicts the magnetic parameters which were calculated from M-H loops. The saturation magnetization and magnetic remanence decrease with the Gd substitution, and also, the coercivity decreased accordingly [15]. It is noticed that the magnetic parameters were influenced by the extrinsic factors such as porosity, homogeneity, morphology, density and distribution of cations at lattice sites [11, 16, 17]. Figure 4b and c shows the variation of magnetic saturation ( $M_s$ ) and remanence ( $M_r$ ) and coercivity ( $H_c$ ) and their ratio with Gd concentration. The Bohr magneton, magneto-crystalline anisotropy constant ( $K$ ) and initial permeability were calculated using the following relations [18].

$$\text{Anisotropy constant } (K) = \frac{H_c \times M_s}{0.96} \quad (5)$$

$$\text{Initial Permeability } (\mu_i) = M_s^2 \times \frac{D}{K} \quad (6)$$

$$\text{Bohr magneton } (\mu_B) = \frac{M \times M_s}{5585} \quad (7)$$

where  $M_s$  is the saturation magnetization,  $M$  is the molecular weight of the samples,  $D$  is the grain size and  $H_c$  is the coercivity. From Eq. 5, it is clear that anisotropy constant is directly proportional to saturation magnetization and coercivity. The decrease in saturation magnetization and Bohr magneton is noticed with increasing  $\text{Gd}^{3+}$  ion concentration. The observed variations can be understood on the basis of super exchange interactions among the tetrahedral (A) and octahedral (B) site ions in the spinel lattice [19]. Saturation magnetization depends on the type and the number of ions located at the tetrahedral (A) and octahedral (B) sites in the spinel

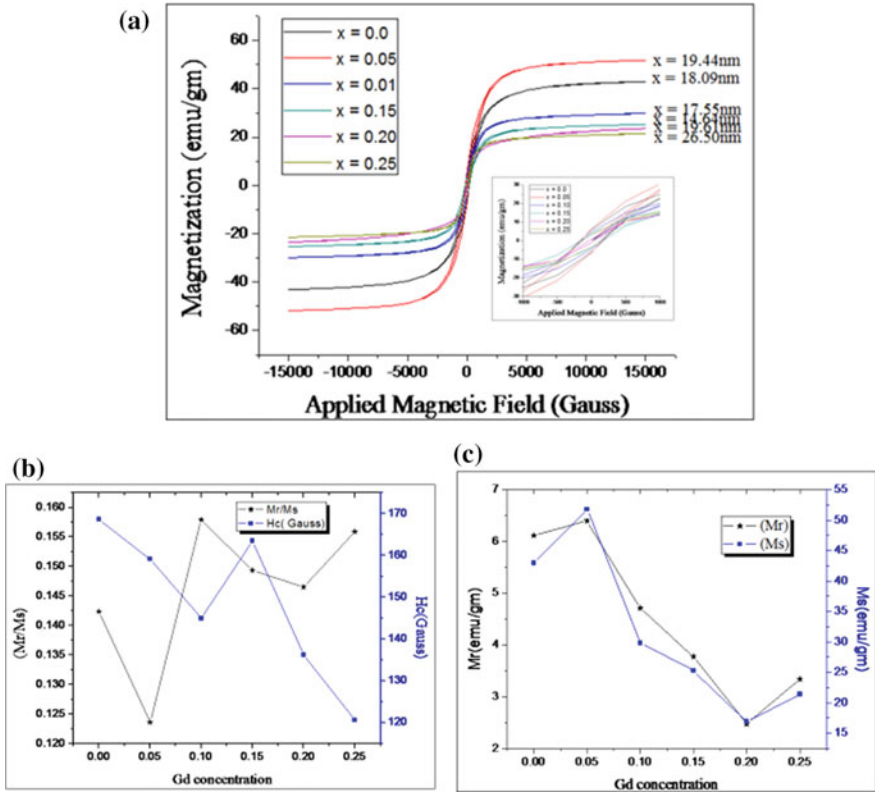


**Fig. 4** a Compositional variation of saturation magnetization of  $Ni_{0.65}Zn_{0.35}Gd_xFe_{2-x}O_4$ . b Variation of squareness ratio (SQR) and coercivity with Gd. c Variation of saturation magnetization and remanence with Gd

**Table 2** Magnetic parameters of  $Ni_{0.65}Zn_{0.35}Gd_xFe_{2-x}O_4$  ferrites

$x$	$M_r$ (emu/g)	$M_s$ (emu/g)	$M_r/M_s$	Bohr Magneton ( $\mu_B$ )	$H_c$ (Oe)	Anisotropy constant (erg/Oe)	Initial Permeability ( $\mu_i$ )
0.0	6.119	42.98	0.1423	1.821	168.62	7549.25	4.426
0.05	6.397	51.75	0.1236	2.376	159.16	8579.71	6.067
0.10	4.711	29.83	0.1579	1.468	144.94	4503.70	3.467
0.15	3.776	25.29	0.1493	1.340	163.48	4306.67	2.174
0.20	2.475	16.89	0.1465	0.955	136.19	2396.94	2.335
0.25	3.336	21.40	0.1559	1.286	120.67	2690.43	4.512

structure because this distribution affects the magnetizations,  $M_A$  and  $M_B$  of the A and B sublattices, respectively.

The saturation magnetization initially falls rapidly at lower doping of gadolinium and decreases slightly at higher concentrations. Figure 4a can be understood on the basis of the Neel model [19] in which A–B exchange interaction in ferrites is stronger and more effective than B–B and A–A super-exchange interactions. The net magnetic moment of the ferrite lattice as a whole is equal to the difference between the magnetic moments of A and B sublattices, i.e.  $M = M_B - M_A$  [20].

Ferromagnetic gadolinium ( $7 \mu_B$ ) has its preference for A sites only, and an improvement in A site magnetic moment is expected as it replaces tetrahedral iron ion having less magnetic moment ( $5 \mu_B$ ). Thus, the difference in the net magnetization decreases with increasing gadolinium concentration and is reflected in magnetization measurements [21, 22]. If ferromagnetic gadolinium prefers to occupy only B-sublattices, increase in saturation magnetization is expected with the replacement of octahedral  $Fe^{3+}$  ion [22]. The gadolinium at B-sites at lower concentrations may be expected as the available octahedral site radius in the order of the substituent ion, and the observed decrease in magnetization might be attributed to some factors other than the magnetic moments of the ions and the super-exchange interactions among them. Continuous increase of gadolinium content might be a responsible factor for the observed decrease in the saturation magnetization [23] which have been reported similar observations with rare-earth ion substitution in Ni–Zn ferrites.

## 4 Conclusions

$Ni_{0.65}Zn_{0.35}Gd_xFe_{2-x}O_4$  nanoferrite samples were prepared using sol–gel method. XRD, FE-SEM, TEM and VSM measure the structure, morphology and magnetic properties of NiGdZn nanoferrites, respectively. XRD, SEM and TEM micrographs confirmed that the incorporation of Gd in the crystal lattice results in higher crystallinity, crystallite size, lattice constant and the lower porosity. The entry of gadolinium into B-sites has affected Fe-RE interactions by distorting the ferrite lattice and is evident from the large reduction in magnetization. Magnetic saturation, coercivity, remanence, Bohr magneton, magneto-crystalline anisotropy constant ( $K$ ) and initial permeability values revealed the use of these NiGdZn nanoferrites for magnetic storage and microwave absorption applications.

**Acknowledgements** This work is acknowledge to SAIF IIT Mumbai and SAIF IIT Madras for their valuable analyses.

## References

1. Snelling, E.C.: Soft ferrites; properties and their application. Butterworth, London (1988)
2. Soka, M., Usakova, M., Usak, E., Dosoudil, R., Lokaj, J.: Magnetic properties analysis of rare-earth substituted nickel zinc ferrites. *IEEE Trans. Magn.* **50**(4), 2–5 (2014)
3. Ahmed, T.T., Rahman, I.Z., Rahman, M.A.: Study on the properties of the copper substituted NiZn ferrites. *J. Mater. Process. Technol.* **153–154**, 797–803 (2004)
4. Sakka, S.: Sol gel process and applications, 883–910 (2013)
5. Majid, N.A., Muhammad, A.K.: *J. Magn. Magn. Mater.* (2018)
6. Venkateswarlu, K., Sandhyarani, M., Nellaippan, T.A., Rameshbabu, N.: Estimation of crystallite size, lattice strain and dislocation density of nanocrystalline carbonate substituted hydroxyl apatite by X-ray peak variance analysis. *Procedia Mater. Sci.* **5**, 212–221 (2014)
7. Chaudhari, D.L., Choudhary, D.S., Rewatkar, K.G.: Spinel ferrite nanoparticles: synthesis, characterization and applications. *IJTSRD* **4**(3), 973–978 (2020)
8. Rahman, S., Nadeem, K., Anis-Ur-Rehman, M., Mumtaz, M., Naeem, S., Letofsky-Papst, I.: Structural and magnetic properties of ZnMg-ferrite nanoparticles prepared using the co-precipitation method. *Ceram. Int.* **39**(5), 5235–5239 (2013)
9. Gabal, M.A., Ata-Allah, S.S.: Effect of diamagnetic substitution on the structural, electrical and magnetic properties of  $\text{CoFe}_2\text{O}_4$ . *Mater. Chem. Phys.* **85**(1), 104–112 (2004)
10. Kaur, B., Arora, M., Shankar, A., Srivastava, A.K., Pant, R.P.: Induced size effects of  $\text{Gd}^{3+}$  ions doping on structural and magnetic properties of Ni-Zn ferrite nanoparticles. *Adv. Mater. Lett.* **3**(5), 399–405 (2012)
11. Mangalaraja, R.V., Ananthakumar, S., Manohar, P., Gnanam, F.D.: Magnetic, electrical and dielectric behaviour of  $\text{Ni}_{0.8}\text{Zn}_{0.2}\text{Fe}_2\text{O}_4$  prepared through flash combustion technique. *J. Magn. Magn. Mater.* **253**, 56–64 (2002)
12. El-Shabasy, M.: DC electrical properties of Zn-Ni ferrites. *J. Magn. Magn. Mater.* **172**, 188–192 (1997)
13. Souilah, Z., Mansor, H., Daud, A.R.: Synthesis, magnetic properties and microstructure of Ni-Zn ferrite by sol-gel technique. *J. Magn. Magn. Mater.* **308**, 177–182 (2007)
14. Shirsath, S.E., Toksha, B.G., Jadhav, K.M.: Structural and magnetic properties of  $\text{In}^{3+}$  substituted  $\text{NiFe}_2\text{O}_4$ . *Mater. Chem. Phys.* **117**, 163–168 (2009)
15. Eltabey, M.M., El-Shokrofy, K.M., Gharbia, S.A.: Enhancement of the magnetic properties of Ni-Cu-Zn ferrites by the non-magnetic  $\text{Al}^{3+}$  ions substitution. *J. Alloys Compd.* **509**(5), 2473–2477 (2011)
16. Goldman, A.: Modern ferrite technology (2nd ed), pp. 117 (1990)
17. Smit, J., Wijn, H.P.J.: Ferrites, pp. 245 (1959)
18. Akhtar, M.N., Rahman, A., Sulong, A.B., Khan, M.A.: Structural, spectral, dielectric and magnetic properties of  $\text{Ni}_{0.5}\text{Mg}_x\text{Zn}_{0.5-x}\text{Fe}_2\text{O}_4$  nanosized ferrites for microwave absorption and high frequency applications. *Ceram. Int.* **43**(5), 4357–4365 (2017)
19. Néel, L., Pauthenet, R., Dreyfus, B.: Chapter VII the rare earth garnets. *Prog. Low Temp. Phys.* **4**(C), 344–383 (1964)
20. Kumar, A.M., Varma, M.C., Dube, C.L., Rao, K.H., Kashyap, S.C.: Development of Ni-Zn nanoferrite core material with improved saturation magnetization and DC resistivity. *J. Magn. Magn. Mater.* **320**(14), 1995–2000 (2008)
21. Han, D.H., Wang, J.P., Luo, H.L.: Crystallite size effect in saturation magnetization of fine ferrimagnetic particles. *J. Magn. Magn. Mater.* **136**, 176–182 (1994)
22. Mahesh Kumar, A., Chaitanya Varma, M., Choudary, G.S.V.R.K., Prameela, P., Rao, K.H.: Influence of gadolinium on magnetization and DC resistivity of NiZn nanoferrites. *J. Magn. Magn. Mater.* **324**, 68–71 (2012)
23. Rezlescu, N., Rezlescu, E., Pasnicu, C., Craus, M.L.: Effects of the rare-earth ions on some properties of a nickel-zinc ferrite. *J. Phys.: Condens. Matter.* **6**(29), 5707–5716 (1994)

# Numerical Investigation on the Friction Factor Estimation for Laminar and Turbulent Flow in Smooth Pipe



S. A. Mashalkar and S. P. Nagdewe

**Abstract** Fluid flow through pipes is a commonly used application in industries. The fluid is enforced by a fan or pump to flow through the pipe. The pressure loss or head loss during the flow is related to friction between fluid and pipe wall. Pumping power required to transport the fluid in pipe is calculated from the pressure loss. Hence, the friction factor plays an essential role in the transport of fluid in industries. Loss in pressure through steady pipe flow is calculated by using the Darcy–Weisbach equation, which includes Darcy friction factor ( $f$ ). In the current work, numerically calculated friction factor for the laminar and turbulent pipe flow is compared with the Blasius equation, Swamee–Jain equation and experiment data for different Reynolds numbers. A pipe can say to be smooth when the flow relies only on the Reynolds number ( $Re$ ) and not on the roughness (roughness is minimal). In the present study, a 2D smooth pipe is considered. Commonly used turbulence models, such as  $k$ -omega SST and  $k$ -eps realizable models, are considered to evaluate the friction factor. Steady-state Navier–Stokes equations are determined with the second-order accuracy. Friction factors are calculated from the numerical simulation for different  $Re$  numbers and compared well with the theoretical data and experiment data of Oregon and Princeton for the laminar and turbulent flow. CFD modeling results are verified by comparing them with available data in the literature. The model results show the best correlation.

**Keywords** Turbulent flow • Computational fluid dynamics (CFD) • Friction factor

---

S. A. Mashalkar (✉)

Marathwada Mitra Mandal's College of Engineering, Karvenagar, Pune 411052, India

S. P. Nagdewe

3DPLM Software Solutions Ltd, Pune 411057, India

© The Author(s), under exclusive license to Springer Nature Singapore Pte Ltd. 2021

A. Patnaik et al. (eds.), *Advances in Materials Processing and Manufacturing*

*Applications*, Lecture Notes in Mechanical Engineering,

[https://doi.org/10.1007/978-981-16-0909-1\\_50](https://doi.org/10.1007/978-981-16-0909-1_50)

## 1 Introduction

In the field of heat transfer and fluid dynamics, turbulent flow with rough surfaces has been an interesting topic. This flow notices in various engineering applications like wind tunnel, heat exchangers, fluid catalytic cracking, nuclear reactor, air foil, and turbine blade. A study in pipe flow observes the sound outcome of Reynolds number on velocity distribution, and friction factor has been performed by Bradshaw [1].

Understanding the fluid mechanics of turbulent flow in rough pipes is controversy because mathematically demanding approaches are not recognized and theoretical concepts must rest on the clarifications of the data. The problem considered in this paper is linked to how flows in rough pipes link to flows which are virtually smooth in the same rough pipe.

### 1.1 K-Omega Model

The  $k$ -omega ( $k - \omega$ ) turbulence model [2] is frequently used models. It fits into the Reynolds-averaged Navier–Stokes (RANS) family of turbulence models.

It is a 2D model, along with the conservation equations. It explains two transport equations, which consider for the antiquity effects as diffusion and convection of turbulent energy.  $\omega$  is also mentioned as the measure of turbulence.

The standard  $k - \omega$  model applied with small Reynolds number and the boundary layer has comparatively dense and viscous sublayer. Thus, the standard  $k - \omega$  model is best for near-wall treatment. It includes a composite boundary layer flow with superior performance beneath separations and contrary pressure gradients. On the other hand, this model also shows to expect extreme and primary separations.

In  $k$ -omega SST model, SST views as Shear Stress Transport. The  $k - \omega$  SST model offers an improved assessment of flow parting than RANS model and considers its good behavior in contrary pressure gradients. It accounts for the transportation of the major shear stress in boundary layers with contrary pressure gradient. It gives high accuracy to expenditure ratio, so most regularly used in the industry.

### 1.2 K-Epsilon Model

It is the standard turbulence model [3], while it does not execute well in case of big contrary pressure gradients. It is a 2D model, which includes two different transport equations to signify the turbulence characteristics of the flow. It permits a two-equation model to consider for the past effects like diffusion and convection of turbulence energy.



The *k*-epsilon model [4] is advantageous for free-shear level flows with small pressure gradients. For internal flows and wall-bounded, this model provides good outcomes only where average pressure gradient is small. In the realizable *k*-epsilon model, realizable implies the model which satisfies certain mathematical restraints on the normal stresses, reliable with the behavior of turbulent flows.

Turbulent data appropriate for correlations is found from the book of Barenblatt (2003) [5]. The correlation for friction factors in turbulent liquid flow is investigated by Garcia (2003, 2005) [6].

This study aims to frame a model of computational fluid dynamics that can demonstrate the entirely turbulent flow in the pipe by a higher Reynolds number. Moreover, an extreme Reynolds number predicts a fully developed flow for the existing pipe length at the outlet and has 20 mm pipe diameter and zero relative roughness. This paper demonstrates inlet velocity and the sound effects of Reynolds number on a friction factor. The predicted friction factor is compared with the experimental values to authenticate the results. Figure 1 shows the schematic pipe applied in this study.

## 2 Mathematical Modeling

### 2.1 Blasius Equation

The Blasius equation [7] is used for solving Darcy friction factor, and it is effective only for smooth pipes. However, the Blasius equation is occasionally applicable in rough pipes for its easiness. The Blasius equation is useful up to Reynolds number  $10^5$ . The Blasius equation is

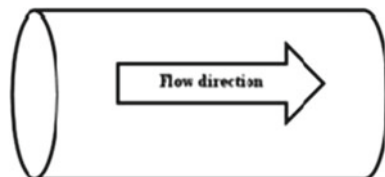
$$f = \frac{0.316}{Re^{0.25}}$$

where *f* = Darcy friction factor; *Re* = Reynolds number.

### 2.2 Swamee–Jain Equation

Swamee and Jain [8] have advanced the Blasius equation, and they customized the following equation for Darcy friction factor. This equation can be used both for

**Fig. 1** Schematic layout of fluid flow



smooth and rough pipes because he has commenced the roughness factor, which indicates the rough pipe, and for smooth pipe, the value of  $e$  may be zero or very small.

$$f = 0.25 \left[ \log \left( \frac{e}{3.7D} + \frac{5.74}{Re^{0.9}} \right) \right]^{-2}$$

$f$  = Darcy friction factor;  $e$  = roughness for the pipe;  $D$  = inner dia. of the pipe,  $e/D$  is named as the relative roughness and the equation calculates the Reynolds number;

$$Re = \frac{U * D}{\nu}$$

### 3 Simulation Setup and Numerical Discretization

One of the intentions of this paper is to evaluate the performance of two-equation models ( $k - \epsilon$  and  $k - \omega$ ) as implemented in the Finite Element Package ANSYS FLUENT™ [9].

The computational domain consists of a short segment of the pipe, bounded by the wall. Since we are investigating a fully developed flow, we are not interested in any temporal behavior, so that the steady Navier–Stokes equations are used.

Figure 2 displays the configuration of the pipe. Total pipe length is 1 m with a diameter of 0.02 m. The water enters a pipe with a particular velocity. ANSYS FLUENT™ software is used to create the 2D pipe and makes use of hexahedral grids throughout (nodes are 17,280 and elements are 13,717) as shown in Fig. 2. The water density is 1000 kg/m<sup>3</sup> and viscosity about 1.8e-5 kg/ms. The water velocity at the inlet varies from 2, 5, 14, 20, 25, 30, 35 m/s. Incompressible Navier–Stokes steady state is considered in this analysis.

In steady-state results, several Reynolds numbers have been united by 1000 iterations.

$$Re = \frac{\text{density} * \text{velocity} * \text{diameter}}{\text{Viscosity}}$$

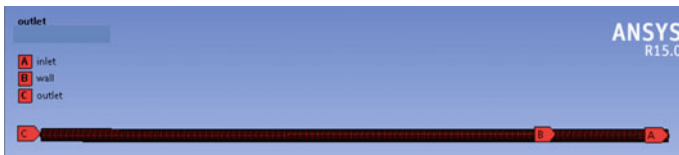


Fig. 2 Computational framework of 2D pipe

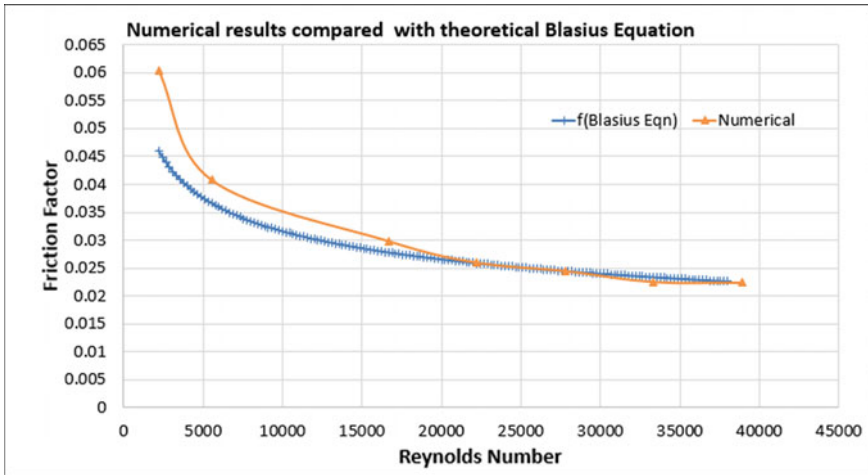


Fig. 3 Numerical results compared with the theoretical data

The Darcy–Weisbach equation [10] narrates the head loss, or pressure loss by friction beside a given pipe length to the mean velocity since an incompressible fluid flow.

$$\frac{\Delta p}{L} = f \frac{0.5 * \rho * V^2}{2 * D}$$

The loss per length ( $\Delta p/L$ ) and fluid density ( $\rho$ ), length of the pipe ( $L$ ), the hydraulic pipe diameter ( $D$ ), mean flow velocity ( $V$ ), and the dimensional friction factor ( $f$ ) indicate in the above equation.

## 4 Results

In this case study, simulation is performed and compared the Reynolds numbers effect on turbulence intensity and friction factor [11]. Moreover, the extreme Reynolds number is determined also to achieve a fully established turbulent flow.

Table 1 shows the friction factor by the Blasius equation and numerical simulation for different readings of the Reynolds number. In this, we have provided only some values for friction factor and  $Re$ . Figure 3 depicts that the friction factor by Blasius equation for greater than  $20 \times 10^3$   $Re$  values is precisely coincident with the numerical friction factor values. So, the correlation is nearby one.

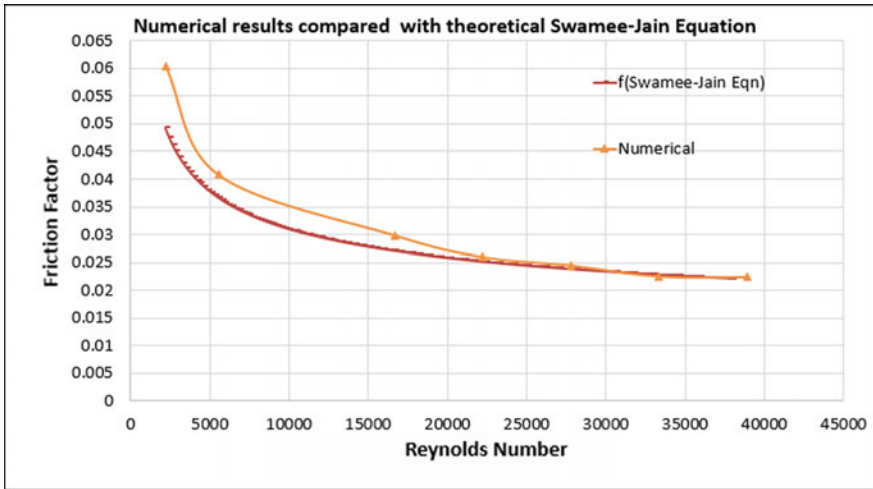


Fig. 4 Numerical results compared with the theoretical data

Table 2 shows the friction factor by the Swamee–Jain equation and numerical simulation for different readings of the Reynolds number. In this, we have provided only some values for friction factor and *Re*. So, Fig. 4 concludes that the friction factor from the theoretical equation is closely matching with the numerical friction factor values.

Table 3 shows the numerical friction factor calculated from simulation for the laminar and turbulent pipe flow experiment data (McKeon) [12] of Oregon and Princeton for different Reynolds numbers. And Fig. 5 depicts that the experimental and numerical values of friction factor give the correlation nearly coinciding.

The above graph shows Reynolds number versus friction factor numerical results compared well with the experimental and theoretical data for laminar and turbulent stream. The above graphs illustrate the effect of different Reynolds numbers on the friction factor. The Reynolds number rises as the friction factor decreases, which is companionable by the friction factor calculated from co-relation stated in the literature [13].

Table 1 Friction factor values for Blasius equation and numerical data

Dia. of pipe	Velocity	<i>Re</i>	<i>f</i> (Blasius equation)	<i>Re</i>	<i>f</i> (Numerical)
0.02	2	2222.222	0.04602462	2222.22	0.0605
0.02	2.2	2444.444	0.044940928	5555.56	0.0408
0.02	2.4	2666.667	0.043973891	16,666.67	0.0299

**Table 2** Friction factor values for Swamee–Jain equation and numerical data

Dia. of pipe	Velocity	$Re$	$f$ (Swamee–Jain equation)	$Re$	$f$ (Numerical)
0.02	2	2222.222	0.049242687	2222.22	0.0605
0.02	2.2	2444.444	0.047653881	5555.56	0.0408
0.02	2.4	2666.667	0.046269613	16,666.67	0.0299

**Table 3** Friction factor values for experimental (Oregon, Princeton) and numerical data

$Re$	Oregon data	$Re$	Princeton data	$Re$	$f$ (Numerical)
3264	0.0426	31,310	0.02364	2222.22	0.0605
8162	0.03364	41,440	0.02216	5555.56	0.0408
10,900	0.03088	56,360	0.02061	16,666.67	0.0299

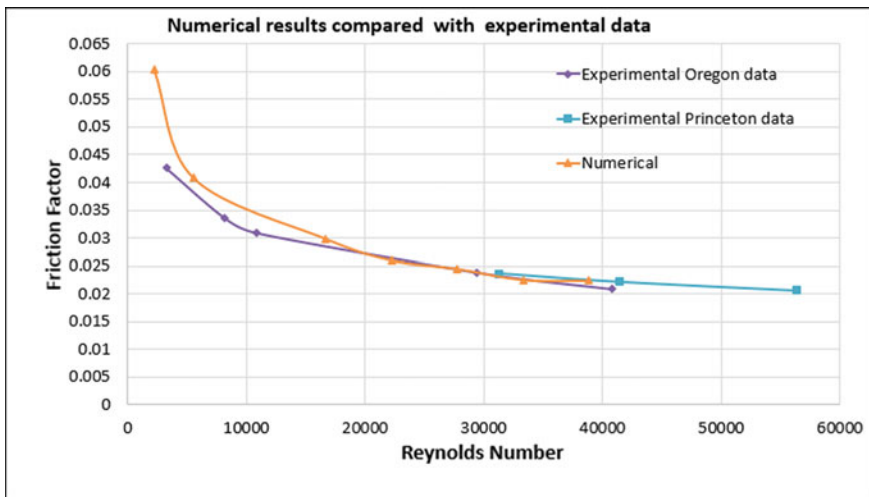


**Fig. 5** Numerical results compared with the experimental data

## 5 Conclusions

The difference in the co-relation values and numerical results is minor. We can operate the numerical results obtained from the CFD model to regulate the other fluid characteristics efficiently. To summarize, we get that as friction factor is decreasing, Reynolds number increases gradually, and finally, the values smooth out at a stable value in case of more Reynolds number. CFD investigation is embedded to study the hydrodynamics of a problem precisely at more Reynolds number.

Two most noticeable representatives of turbulence models to be used: the  $k - \epsilon$  and the  $k - \omega$  models. These simulations represent that twain models perform soundly acceptable in the case of pipe flow, with a small advantage of the  $k - \epsilon$  model over the  $k - \omega$  model at low Reynolds numbers ( $10^4 < Re < 10^5$ ). Also, it represents that the theoretical, experimental and simulation results are closely produced.

## References

1. Bradshaw, P.: A note on “critical roughness height” and “transitional roughness”. *Phys. Fluids*, **12**, 1611 (2000)
2. Menter, F.R.: Two-equation eddy-viscosity turbulence models for engineering applications. *AIAA J.* **32**(8), 1598–1605 (1994)
3. Wilcox, D.C.: *Turbulence modeling for CFD* (2nd edn). DCW Industries, Anaheim, pp. 174 (1998)
4. Bardina, J.E., Huang, P.G., Coakley, T.J.: *Turbulence modeling validation, testing, and development*. NASA Technical Memorandum 110446 (1997)
5. Barenblatt, G.I., Chorin, A.J., Prostokishin, V.M.: Scaling laws for fully developed flows in pipes: discussion of experimental data. *Proc. Natl. Acad. Sci.* **94**(3), 773–776 (1997)
6. Garcia, F., Garcia, R., Padrino, J.C., Matta, C., Trallero, J., Joseph, D.D.: Power law and composite power-law friction factor correlations for laminar and turbulent gas-liquid flow in horizontal pipelines. *Int. J. Multiphase Flow* **29**, 1605–1624 (2003)
7. Fox, W., Pritchard, P., McDonald, A.: *Introduction to fluid mechanics* (7th edn). Wiley, Netherlands, p. 754 (2010)
8. Swamee, P., Jain, A.: Explicit equations for pipe-flow problems. *J. Hydraul. Div. (ASCE)* **102** (5), 657–664 (1976)
9. Fluent, A.: *ANSYS FLUENT user guide manual* (2013)
10. Jukka Kijja’rvi Darcy Friction Factor Formulae in Turbulent Pipe Flow: Lunowa Fluid Mechanics Paper 110727
11. Daniel, D.J., Bobby, H.Y.: Friction factor correlations for laminar, transition and turbulent flow in smooth pipes. *Physica D: Nonlinear Phenomena*
12. Moody, L.F.: Friction factors for pipe flow. *Trans. ASME* **66**(8), 671–684 (1944)
13. McKeon, B.J., Swanson, C.J., Zagarola, M.V., Donnelly, R.J., Smits, A.J.: Friction factors for smooth pipe flow. *Fluid Mech.* **511**, 41–44 (2004)

# Performance of SoilTech MK III Polymer and Fly Ash on Problematic Soil



Taranpreet Kaur, Pardeep Singh, and Heena Malhotra

**Abstract** Roads are considered the best mode of transportation, and after USA, Indian road network is the world's second largest road network in the world. According to the Ministry of Road Transport and Highways, March 2019, India had about 142,126 km (88,313 mi) of national highway and expressways and 176,166 km (109,464 mi) of state highways (Rajput and Yadav in Int. J. Innov. Res. Sci. Technol. 2(3):9–13, 2015). Road's thickness depends upon its geotechnical properties and the load applied to it. Good pavement should follow some guidelines like it should be safe, economical, and comfortable. This research describes the impact of SoilTech MK III Polymer and Fly Ash as stabilizer on black cotton soil and on clay and the positive impact on the pavement as well as on the cost of the pavement. For this research, 20% Fly Ash and 0.2, 0.4, 0.6, and 0.8% SoilTech MK III Polymer were used. With the addition of Fly Ash and SoilTech MK III Polymer, the OMC value increases and the value of MDD decreases. CBR value also increases with the combination of these two materials. The optimum mix obtained to improve the construction of pavements with poor strength was 79.2:20:0.8 (Sample: Fly Ash: SoilTech MK III Polymer). Because of these stabilizers, the cost of pavement reduces up to 20–30%.

**Keywords** Black cotton soil (BCS) · Clay · SoilTech MK III Polymer · Fly Ash · California bearing ratio (CBR)

## 1 Introduction

It is always a challenge for highway engineer to improve the geotechnical properties of the problematic soil at that time. Stabilization is one of the best methods adopted by the engineers. Chemical stabilization [1], mechanical stabilization, and biological [2] are such methods which are implemented on weak soil to improve its properties so that the service life of the pavement can be increased [3, 4]. Various

---

T. Kaur (✉) · P. Singh · H. Malhotra  
Department of Civil Engineering, GNDEC, Ludhiana, Punjab, India

© The Author(s), under exclusive license to Springer Nature Singapore Pte Ltd. 2021  
A. Patnaik et al. (eds.), *Advances in Materials Processing and Manufacturing Applications*, Lecture Notes in Mechanical Engineering,  
[https://doi.org/10.1007/978-981-16-0909-1\\_51](https://doi.org/10.1007/978-981-16-0909-1_51)

497

types of the stabilizer are being used by different researchers where they use waste, or any chemical [5]. However, the selection of any stabilizer depends upon the soil and the availability of stabilizers and funds. Like BCS, clay is considered problematic soil because of its shrinkage and swelling effects on the pavements. These soils provide strength until it is dry but when it is wet, it loses strength. Many studies have been done in past using marble powder [6, 7], crushed glass and coconut coir fiber [8, 9], and Fly Ash [5, 10], RBI 81 stabilizer in BCS [11]. The result of all these studies concludes that the engineering properties of soil improve and soil gains its strength. BCS for this research was collected from Jamnagar M. P. and clay from Pamal village near Ludhiana, Punjab.

## 2 Material Properties and Methodology

### 2.1 *SoilTech MK III Polymers*

MK III Polymer which is a third-generation polymer is used by the US Military in Afghanistan, South Africa, Australia, Middle East, and Indian Projects. India Polyroads Private Limited (IPPL) (2010) [12] explains that polymers are materials made up of a long shapeless chain of repeated molecules units which provides a plastic atmospheric structure that provides good strength and toughness. With mechanical compaction, it provides the best results as the strength increases, the life cycle, and load taking capacity of the pavements increases at a very high level. This polymer uses water as a carrier that moisturizes the fine particles at the molecular level that interconnect after compaction. After providing more compaction, the stabilization becomes stronger because the water present inside the soil vaporizes out and leaves a thin layer or film on the soil which prevents water admittance. CBR increases with repelling water, and production of carbon also reduces. As per reports, 1 km of cement stabilized road which is 7 m wide produces 50,449 tons of carbon in the air, whereas roads with SoilTech MK III Polymer produce 1217 tons of carbon [12]. SoilTech MK III Polymer reduces the construction cost of roads by 20–30% as well as construction time reduces up to 30%. Properties of MK III Polymer are displayed in Table 1.

#### 2.1.1 Preparation of MK III Polymer Sample

For this research, 0.2, 0.4, 0.6, and 0.8% percentages are used for compaction tests. For example, to prepare the sample 0.2%, 2 ml of the SoilTech MK III Polymer is mixed into 1 L of water and then mixed thoroughly [13] and then this solution is added in the soil to perform different tests.



**Table 1** Properties of SoilTech MK III Polymer

Property	Description
Color	Black/gray liquid
Odor	Pungent smell
pH	8.0–9.0
Boiling point	Approx 100 °C
Specific gravity	>1.0
Vapor pressure	As per water
Flammability	N/A

## 2.2 Fly Ash

Pulverized fuel is another name for Fly Ash. It is obtained when coal explodes into flames and the particles discharged out from the boiler with the fuel gases and the ash which settled down to the base of the boiler is known as bottom ash. According to the Environmental Protection Agency (EPA), Fly Ash is considered the most toxic waste for the environment as it contains acidic, toxic, radioactive matter, lead, arsenic, mercury, cadmium, and uranium [14–16]. For this research, I collected Fly Ash from Ludhiana in a fine form.

## 3 Method of Testing

### 3.1 Experimental Methodology

Different tests were performed on the plain BCS and clay included: Atterberg's limit, Proctor, and CBR [4]. To determine the effect of the stabilizer on BCS and clay with percentages of Polymer and 20% Fly Ash, respectively, used and mixed with the soil (Fig. 1 and Table 2).

## 4 Results and Discussions

### 4.1 OMC Value

With the addition of 0.2, 0.4, 0.6, and 0.8% of SoilTech MK III Polymer to the clay, OMC changes from 16% to 16.2, 16.4, 16.6, and 18% and for BCS, OMC changes from 27.5% to 28.2, 28.5, 28.9, and 29.5%, respectively. When 20% of the Fly Ash and 0.2, 0.4, 0.6, and 0.8% of SoilTech MK III Polymer combination mixed to the clay OMC changes to 16.3, 16.7, 17.1, and 18.3% and in the case of BCS, OMC

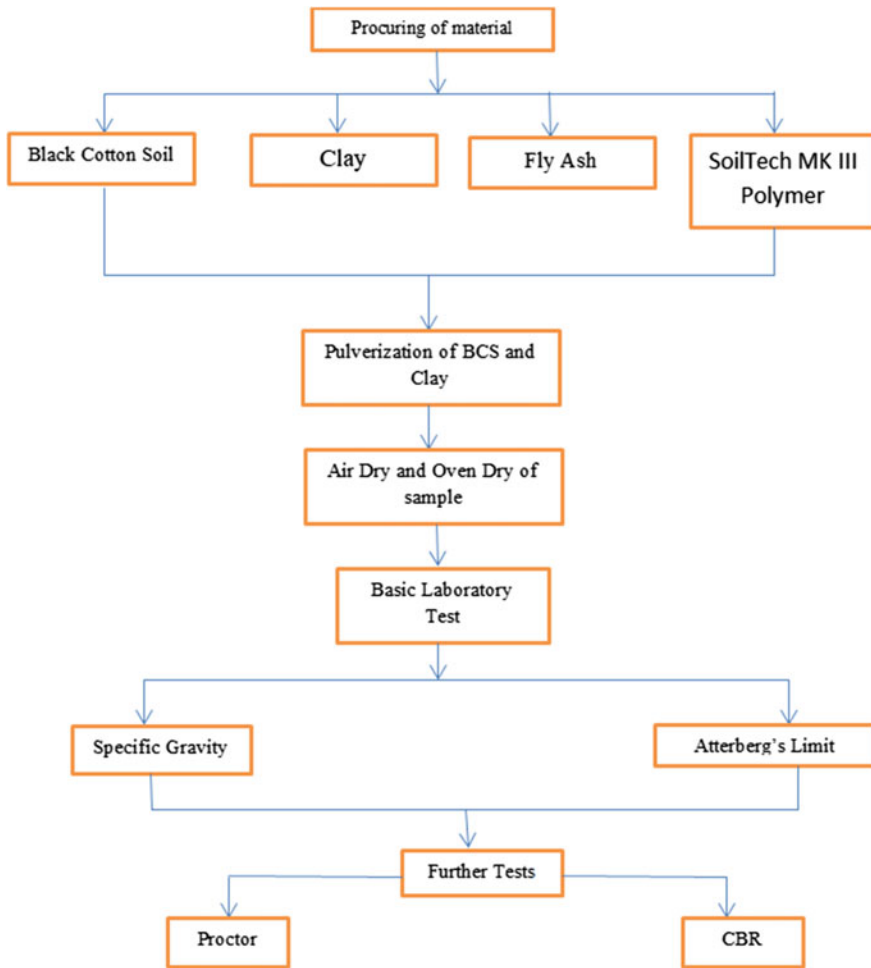


Fig. 1 Plan of the experimental work to be carried out

Table 2 Geotechnical properties of BCS, clay, and Fly Ash

Characteristics	BCS	Clay	F.A.
SG	2.5	2.6	1.6
LL (%)	59.8	43.5	33.2
PL (%)	29.5	18	–
PI (%)	30.3	25.5	–
MDD (g/cc)	1.76	1.55	1.032
OMC (%)	27.5	16	28.6
CBR (%)	1.48	1.52	–

increases to 27.9, 28.4, 28.7, and 29.3%, respectively. The combination of Fly Ash and SoilTech MK III Polymer changes the OMC, as the particles of Fly Ash have got more surface area, which requires more water hence, OMC increases (Figs. 2 and 3).

### 4.2 MDD Value

The MDD value of raw clay was 1.55 g/cc which reduced to 1.57, 1.56, 1.55, and 1.54 g/cc and BCS was 1.76 g/cc which reduces to 1.78, 1.77, 1.76, and 1.75 g/cc with the addition of 0.2, 0.4, 0.6, and 0.8% of SoilTech MK III Polymer. The MDD value of raw clay reduces to 1.56 g/cc and BCS reduce to 1.71 g/cc with the

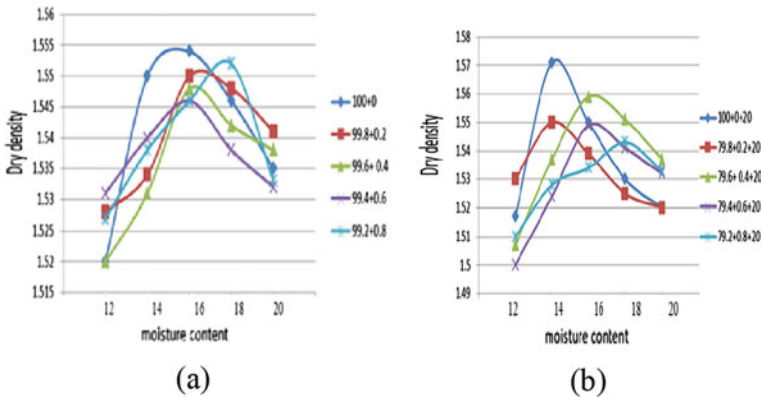


Fig. 2 OMC of Clay; **a** OMC of Clay + MK III Polymer, **b** OMC of Clay + MK III Polymer + F.A.

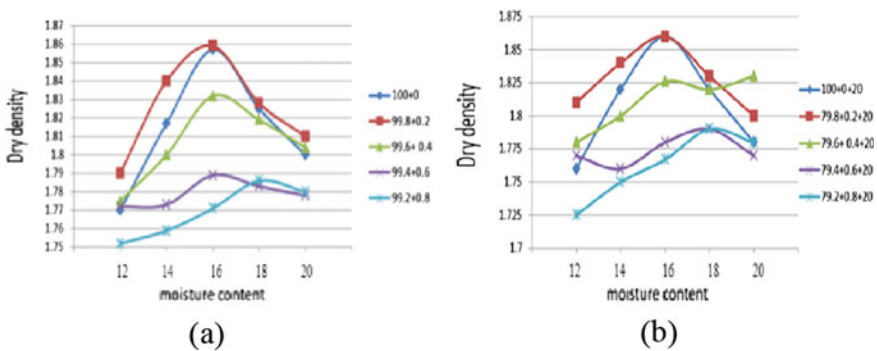
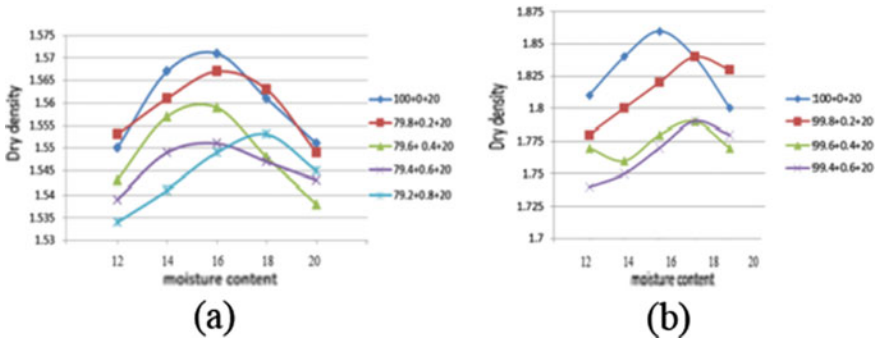


Fig. 3 OMC of BCS; **a** OMC of BCS + MK III Polymer, **b** OMC of BCS + MK III Polymer + F.A.



**Fig. 4** a MDD of Clay + MK III Polymer + F.A., b MDD of BCS + MK III Polymer + F.A.

addition of Fly Ash at 20%. This reduction of MDD occurs due to negative charge particle of soil combine with the charges of cations resulting in [17] a fluctuating structure which is light in weight and having a high [17] amount of voids ratio. As Fly Ash and SoilTech MK III Polymer consist of less amount of specific gravity than the raw soil, the MDD decreases (Fig. 4).

### 4.3 California Bearing Ratio Test

The design for a pavement depends upon the CBR value of subgrade soil. The CBR value of raw clay increased from 1.52% to 3.92, 5.55, 6.44, and 9.62% corresponding to the addition of 0.2, 0.4, 0.6, and 0.8% of SoilTech MK III Polymer. After the addition of 20% of Fly Ash to the clay with 0.2, 0.4, 0.6, and 0.8% of polymer, the CBR changes to 4.66, 5.92, 7.03, and 9.62%. Similarly, the CBR value after adding polymer into the BCS changes from 1.52% to 3.33, 5.18, 5.92, and 9.25% and after the addition of Fly Ash at 20% with different percentages of polymer, CBR changes to 3.703, 4.81, 6.29, and 8.14%. This change in CBR represents that the strength of the sample increases and a strong bond occurs with the combination of Fly Ash and SoilTech MK III Polymer as a stabilizers. An optimum mix of BCS: Fly Ash: SoilTech MK III Polymer and Clay: Fly Ash: SoilTech MK III Polymer was obtained at 79.2:20:0.8 (Fig. 5).

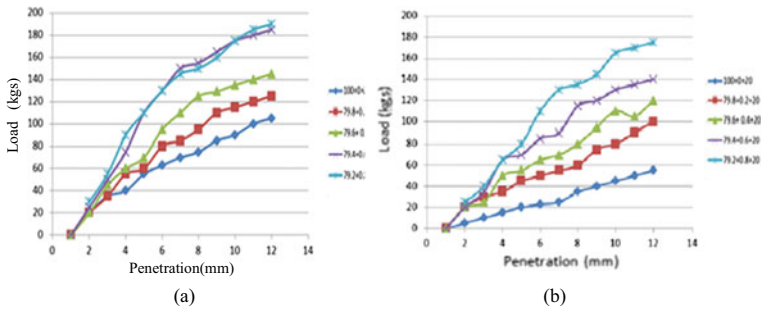


Fig. 5 a CBR of Clay + MK III Polymer + F.A., b CBR of BCS + MK III Polymer + F.A.

### 5 Conclusions

1. After the addition of 20% of Fly Ash and SoilTech MK III Polymer at different percentages, the OMC value was observed on increasing whereas the value of MDD decreases after this addition.
2. With 20% of Fly Ash and 0.8% of SoilTech MK III Polymer, an optimum mix is obtained after the addition of this in BCS, and clay CBR value increases. After performing laboratory tests, with a ratio of 79.2:20:0.8 (Sample: Fly Ash: SoilTech MK III Polymer), the optimum mix can be used for the construction of pavements with poor strength.
3. SoilTech MKIII polymer is a chemical stabilizer, which is used as a potential stabilizer for expansive soils or weak soils.
4. The CBR values of BCS and clay increases with SoilTech MK III Polymer as compared to the untreated BCS and clay.
5. SoilTech MK III polymer is an ecofriendly stabilizer and reduces 92% of CO<sub>2</sub>; hence it is an effective soil stabilizer as compared to others.
6. It is a cost-effective stabilizer. And if Fly Ash is also used as stabilization then this stabilizer will not become only effective and reduce the cost but the waste Fly Ash is also being used without harming the environment.

**Acknowledgements** The special gratefulness to Er. Pardeep Singh, Dr. Heena Malhotra, and Dr. Prashant Garg for their motivation, counseling, and support for this research topic.

### References

1. Dubey, Jain, R.: Effect of common salt (NaCl) on engineering properties of black cotton soil. *Int. J. Sci. Tech. Eng.* 2(01), 64–68 (2015)
2. Mhlongo, S.M., Ndambuki, J.M., Kupolati, W.K., Abiola, O.S.: Laboratory evaluation of recycled pavement materials stabilized with nano polymer. *ACE* (2014)

3. Patidar, Mahiyar: An experimental study on stabilization of black cotton soil using HDPE wastage fibres, stone dust and lime. *Int. J. Adv. Sci. Tech. Res.* **6**(04), 90–98 (2014)
4. Soil mechanics and foundation engineering by “Dr. K.R. Arora”
5. Radhakrishnan, G., Anjan, K., Prasada, G.V.R.: Swelling properties of expansive soils treated with chemicals and flyash. *Am. J. Eng. Res.* **03**(4), 245–250 (2014)
6. Bhavsar, Joshi, B.H., Shrof, K.P., Patel, A.J.: Impact of marble powder on engineering properties of black cotton soil. *Int. J. Sci. Res. Develop.* **2**(02), 136–139 (2014)
7. Chayan, G., Ravi, K.S.: Black cotton soil modification by the application of waste materials. *Period. Polytech. Civ. Eng.* **60**(4), 479–490 (2016)
8. Verma, V., Abhishek: *Stabilization of clayey soils using fly ash and RBI grade 81*. Springer, Berlin, pp. 95–102 (2019)
9. Dalal, Patel, R., Dalal, D.P.: Effect on engineering properties of black cotton soil treated with agricultural and industrial waste. In: *International conference on recent trends in engineering and material science* (2016)
10. Bidula, B.: Geo-engineering properties of expansive soil stabilized with fly ash. *EJGE* **17** (2012)
11. Lekha, Shankar, A.U.R.: Laboratory performance of RBI 81 stabilize soil for pavements. *Int. J. Civ. Eng. Res.* **5**(02), 105–110 (2014)
12. Shumba, S., Kusosa, C., Vassileva, L.D.: *Stabilisation of a road pavement using polymeric stabilisers: case study of Christian Road, Shamva District, Zimbabwe* (2015)
13. Ranjitha, J., Supritha, D.K., Kumar, P.: Experimental study on black cotton soil stabilized using soiltech MK III polymer. *Int. J. Res. Eng. Tech.* ISSN 2321–7308 (2016)
14. Anil, K.S., Sudhanshu, S.S.: Laboratory study on soil stabilization using fly ash and rice husk ash. *Int. J. Res. Eng. Tech.* (2014)
15. Gyanen, T., Savitha, A.L., Krishna, G.: Laboratory study on soil stabilization using fly ash mixtures. *Int. J. Eng. Sci. Innov. Tech.* **2**(1) (2013)
16. Rajput, Yadav, R.K.: Effect of fly ash on geotechnical characteristics of black cotton soil. *Int. J. Innov. Res. Sci. Technol.* **2**(3), 9–13 (2015)
17. Tiwari, Mahiyar, H.K.: Experimental study on stabilization of black cotton soil by fly ash, coconut coir fibre & crushed glass. *Int. J. Emerg. Technol. Adv. Eng.* **4**(2), 330–333 (2014)
18. Google. [https://en.wikipedia.org/wiki/Roads\\_in\\_India#:~:text=According%20to%20Ministry%20of%20Road,109%2C464%20mi\)%20of%20state%20highways](https://en.wikipedia.org/wiki/Roads_in_India#:~:text=According%20to%20Ministry%20of%20Road,109%2C464%20mi)%20of%20state%20highways)
19. Gobinath, Ganapathy, P.G., Akinwumi, I.I., Hena, S., Thangaraj, M.: *Plasticity, strength, permeability and compressibility characteristics of black cotton soil stabilized with precipitated silica*. Springer, Berlin (2016)
20. Miller, Azad, S.: Influence of soil type on stabilization with Cement Kiln Dust. *Const. Build. Mater.* 89–97 (2000)

# Equal Channel Angular Pressing (ECAP) with Al Alloy—A Review



Nani Gopal Roy, Debayan Mondal, Partha Pratim Dey,  
and Manojit Ghosh

**Abstract** Modern days are driven by advanced technology which put forward the challenges of invention related to advanced engineering materials and advanced manufacturing process in order to cope up with burning global demand for new item or alternative product in more complicated and competitive atmosphere. While choosing an engineering material or any manufacturing process, researcher has to consider not only utility, application, feasibility, effectiveness but also bio-compatibility with a rational chronological priority, based on their immediate as well as long-term impact and sustainability. The rigorous study and research is needed for development of an alternative manufacturing process or material or both for commercialization. ECAP is commonly employed for severe plastic deformation (SPD) techniques to form ultra-fine-grained (UFG) microstructure. Excellent past research work on rolled Al alloy Al7075 with ECAP confirmed high strength associated with maximum value of elongation at failure of 322% at 300 °C with rate of strain as  $10^{-3} \text{ s}^{-1}$ . Mechanical properties with precipitation kinetics of Al7000 series alloy through ECAP have been already studied in the previous research. ECAP with Al7075 at different temperature in one of the researches is carried at recent past. The objective of present researcher is to find out the future scope of work among existing researches. The introduction of suitable back pressure which may improve the workability of the specimen by removing dead zones through filling outer corner needs to be studied. The future attempt may be made in finding the optimum process parameters or complex combination of all parameters for best mechanical properties and through achieving maximum strengthening effect.

**Keywords** SPD · ECAP · Ultra-fine-grain · High-pressure torsion

---

N. G. Roy (✉) · P. P. Dey

Department of Mechanical Engineering, IIST, Shibpur, Howrah 711103, India

D. Mondal

Technology Campus, University of Calcutta, Kolkata 700106, India

M. Ghosh

Department of Metallurgy and Materials Engineering, IIST, Shibpur, Howrah 711103, India

© The Author(s), under exclusive license to Springer Nature Singapore Pte Ltd. 2021

505

A. Patnaik et al. (eds.), *Advances in Materials Processing and Manufacturing*

*Applications*, Lecture Notes in Mechanical Engineering,

[https://doi.org/10.1007/978-981-16-0909-1\\_52](https://doi.org/10.1007/978-981-16-0909-1_52)

## 1 Introduction

The present technology advancing toward micro- and nanolevels, lightweight but high strength domestic and industrial application of metal and alloys is increasing drastically. Manufacturing professional concentrated upon strengthening processes of the existing engineering materials. ECAP is found to be the most effective method of producing nanocrystalline (NC) and ultra-fine-grain (UFG) materials among various strengthening mechanisms. From past decade, equal channel angular pressing (ECAP) became familiar with an effective process to produce ultra-fine-grained and nanocrystalline (NC) material. Many researches have been carried out on these particular field with various metal and alloys to prove ECAP as commercially one of the best methods for superior mechanical properties. Process of SPD was introduced first in the USA by extensive work of Bridgman. Present concentration of the research on the plastic behavior of the materials rather than its elastic zones developed various strengthening mechanisms through the process of SPD. The objective of the process is to improve the mechanical properties of the metal and alloys through deformability by introducing high pressure (up to 0.2 Gpa) through the concept of high-pressure torsion (HPT) [1, 2], directional forging [1], cyclic extrusion compression [1], constrained groove pressing (CGP) [1], accumulative roll bonding (ARB) [1], and submerged friction stir processing (SFSP) [1], considering crystal structure, geometry along with the process of microstructures having grain size ranging from 70 to 50 nm approx.

Out of various procedures, ECAP [1, 3, 4] is found to be unique because of several reasons. Primarily, ECAP can be implemented preferably to large billets so that there is a possibility for converting substances, that possibly further utilized in a broad spectrum of structural applications and can be executed on a wide range of metal and alloys. Observation has been pointed toward advancement of new and various approaches that may be utilized to produce ultra-fine-grained materials of grain sizes in the sub-micrometer and nanometer level. In order to understand above-mentioned review, it is required to define a formal definition of UFG [1, 3]. The characteristics of polycrystalline UFG materials are known as polycrystals with appreciably small grains of average grain size in order of less than 1  $\mu\text{m}$ . For bulk UFG materials, there are secondary requirement of fairly homogeneous along with sufficiently equiaxed microstructures and with a majority of grain boundaries with high angles of misorientation. Among the different procedures in use for the production of nanostructured materials, only SPD technique implemented for producing large samples, suitable for industrial utility. In order to create nano- or ultra-fine-grained structure at low homologous temperature (typically below 0.3 of the melting temperature) SPD is the best process. In order to obtain the smallest microstructure, plastic strains of more than 600–800% are necessary. Such high degrees of plastic deformation are possible because one sample can be subjected several times to SPD in order to accumulate the total amount of plastic strain.



## 2 Principle Involved in ECAP

The basic principle involved in ECAP process is based on the Hall–Petch equation which provides the correlation between the strength, more specifically the yield point strength ( $\sigma_y$ ) and the size of grain of the particle as per relation furnished as follows.

$$\sigma_y = \sigma_0 + k_y d^{-1/2} \quad (1)$$

where  $\sigma_0$  is the friction stress, “ $d$ ” is the grain size, and  $k_y$  is a constant of yielding. The strength maybe drastically improved by reducing grain size.

## 3 Literature Review

Valiev’s et al. [1] investigation and detailed study tell us very significant information related to equal channel angular pressing (ECAP) process.

Zhao et al. [3] investigated combine effect of ECAP processed UFG along with precipitation hardening for 7000 series Al alloy with key objective for investigation on the effect ECAP processing for the study of precipitation kinetics with associated mechanical properties of the Al–Zn–Mg–Cu 7075 alloy. The ECAP processed alloy was further immediately treated with solution treatment to form UFG structure, and naturally aged at ambient temperature for one month. During non-isothermal annealing the microstructure, mechanical properties of aged UFG 7075 Al were investigated. He concluded that ECAP processing can enhance the precipitation kinetics and addition of significant strengthening effect to the precipitation hardening in the 7075 Al alloy. He has pointed out that, the strength of Al 7000 alloys can be improved significantly, by making them more useful and effective in high strength structural applications. The microstructure and mechanical properties have been investigated for coarse-grained (CG) and ultra-fine-grained (UFG) 7075 Al alloys during annealing. Zhao et al. [3] further established that after the same natural aging, the tensile yield strength, ultimate strength (UTS), and microhardness of the UFG samples were 103, 35, and 48% higher, respective than those of the CG samples due to high density of Guinier–Preston (G–P) zones.

Mohammad Mahdih and Ramzan Mahdavejad investigated EDM on UFG Al 2017 alloy sample and hence measure the stored energy before and after the EDM process, which contribute remarkably in recent past research work.

Extensive work of Cepeda-Jimenez on rolled Al7075 with ECAP is able to provide high strength at maximum elongation to failure approximately 322% at 300 °C along with a high strength rate of  $10^{-3} \text{ s}^{-1}$ , which has remarkable application in aeronautical field. However, Al7075 alloy has only limited form-ability by conventional forging process at elevated temperature.

Investigation reveals that the enhancement of ductility is highly depended upon no. of passes (ECAP process parameter). However, super-plastic behavior is lost above 350 °C due to abnormal grain growth and deformation mechanism change. The preliminary objective is to examine the intermediate high temperature and hence to study the conditions for super-plastic behavior.

Sabbaghianrad and Terence Langedon investigated combine effect of ECAP followed by HPT on Al 7075 alloy converting into super-plastic deformation at elevated temperature. They concluded that HPT is more efficient than ECAP in producing material with small grain size. Sabbaghianrad reported that HPT processing after ECAP produces additional grain size refinement and hence increases hardness with saturated grain size. The combine effect of ECAP and HPT able to manage superplasticity with elongation approximately 800% and grain size was refined to 310 nm approx in the center of the sample.

Shaeri investigated the effect of ECAP at different temperature (ambient temperature, 120, 150, and 180 °C) on Al7075 alloy and concluded that ECAP process with Al 7075 at 120° is optimum process parameter [1, 5] for achieving better mechanical properties due to grain refinement strengthening, [5] precipitation strengthening [5], and dislocation strengthening [5]. The dislocation density of ECAP specimen decreases drastically by increasing ECAP temperature, and the maximum dislocation density of ECAP specimen at room temperature is about 2 times greater than that of ECAP specimen at 180 °C.

Dileep et al. have done excellent experimental research work on the study of microstructure [6] along with associated mechanical properties [6] of Al 7075 with nickel-reinforced composites through ECAP [1, 3, 4, 6] and without ECAP [1, 3, 4, 6] sample and the effects were studied and enumerated through measuring the hardness (BHN) and energy dispersive X-ray spectroscopy (EDS) method and scanning elector microscope (SEM). Curve was plotted considering percentage reinforcement (Ni) versus porosity levels and percentage reinforcement of (Ni) versus hardness (BHN).

Hussein Naser Radhi has reviewed the current trends of research on ECAP process at different conditions and influence of tribological and mechanical properties of Al and Brass alloys. Researcher reported that the mechanical properties of fully annealed Al alloy (like 1100, 6061, 7075) may be enhanced in the first pass of ECAP 0.80–90% of their yield strength (may be attained after one pass of ECAP). It is further added that the dislocation density through (ECAP) plays a vital role in improving the strengthening effect, while the rate of precipitation did play the same role in subsequent aging process .

**Table 1** Highlight of the different research work in present days

Sl. no.	Investigation	Year of publication	Relevant future scope of work	References
1	The effect of strengthening for 7000 series Al alloy under combined effect of ECAP along with precipitation hardening	2004	Commercial 7075 Al alloy CG sample and ECAPed sample immediately after solution treatment with varying die angle $\varphi$ and corner angle $\psi$ combination need to be experimented	[3]
2	ECAP process detail along with effect of process parameters	2006	Scaling up mechanical properties microstructure and hot work ability on Al7075 alloy	[1]
3	Study of mechanical properties and precipitation kinetics of Al7000 series alloys due to ECAP process	2006	Thermal analysis Al7075 alloys	[3]
4	Enhancement of ductility depends on influence of number of pass (ECAP process parameter)	2011	Introduction of back pressure on ECAP process	[7]
5	Exceptionally small grain sizes are produced efficiently by HPT	2014	Calculation of stored energy with Al7075 ECAP followed by HPT sample	[2]
6	Al 2017 alloys ECAP and followed by EDM process	2016	The investigation of ECAP with Al7075, application of with back pressure and without the application of back pressure followed by EDM need to be investigated	[4]
7	The effect of ECAP at various temperature	2016	Investigation of ECAP on Al7075 with $\varphi$ and $\psi$ values of $135^\circ$ and $20^\circ$ , respectively, with different temperature (like room temperature, 120, 150, 180 °C) needs to be studied. ECAP at different temperature and combination with thermomechanical treatment of Al7075 alloy may be taken as new research challenges	[5]
8	The coefficient of friction and specific wear rate of AA7075 alloy	2017	Fracture, toughness and wear resistance may be investigated	[8]

(continued)

**Table 1** (continued)

Sl. no.	Investigation	Year of publication	Relevant future scope of work	References
9	Investigation of microstructure with associated mechanical properties of Al 7075 alloy, reinforced with nickel through ECAP process by liquid metallurgy technique	2018	Corrosion and wear may be investigated while changing various weight percentage of nickel	[6]
10	Tribological along with associated mechanical properties of Al and Brass alloy with the variation of different ECAP process conditions	2020	Corrosion and wear resistance properties of ECAPed Al7075 alloy need to be studied	[9]

## 4 Conclusion

Recent trends of research are not limited to a particular field of study. Most of the research work needs specialized knowledge and desired skills as well as knowledge of interdisciplinary as a prerequisite. Owing to the fact that present work of the researcher is to find out the future scope of work on ECAP with Al alloy. Among various engineering materials, the reason for choosing Al alloy is due to high value of strength-to-weight ratio, low specific weight, associated minimum cost, fatigue performance, low elastic modulus, high specific strength, and excellent corrosion resistance properties. Chosen field of research is excellent for application point of view because of aerospace and automobile application as concern. Though number of researches has already done in this field, still there is wide scope of work in this particular field.

Extensive and rigorous research work can only establish the alternative manufacturing process to commercialize it for the betterment of mankind.

Conclusion is made in finding the optimum process parameters or complex combinations of all process parameters where all four types of strengthening (namely solid solution, precipitation, grain refinement, and dislocation) will be in a additive mode and a compromising state so that the net effect of strengthening has reached the maximum value and obtain best mechanical properties [10, 11].

## 5 Future Scope of Work

The study of scaling up of mechanical properties, microstructure, and hot workability on Al7075 alloy with 100 mm diameter may be investigated [1].

The study on mechanics of metal flow and its behavior along with microstructural evaluation may be used as key tool for further development [1].

The following area may be considered as future scope of work on ECAP with Al7000 series alloy relevant or extended research work of Zhao et al. [3] in his journal titled “Micro structure and mechanical properties of ultra-fine-grained 7075 Al alloy processed by ECAP and their evaluations during annealing” [3]. In thermal analysis, Zhao et al. [3] investigated the precipitation kinematics of Al7075 alloy with two distinct values of heating rates 5 and 10 °C per minute. Thermal analysis may be performed altering holding time other than 5 h with different heating rate, hence microstructure and mechanical properties may be investigated [3].

The impact of holding temperature on UFG as well as coarse grain (CG) sample more than 480 °C during annealing process may be studied with different cooling rate other than as mentioned in his work [3]. The ECAP process parameters, such as number of passes, may be increased along with different process routes and the impact of different values of channel angles and corner angles combination ( $\varphi$  and  $\Psi$ ) may be investigated [3]. The influence of furnace cooling need to be studied, ensuring different cooling rates [3]. Investigation of combine effect of ECAP and electrical discharge machining (EDM) [4] of Al7075 may be carried out with the application of back pressure and without the application of same [4]. The effect of back pressure and presence of a viscous-ductile medium at the exit point of channel may be investigated [7]. The same ECAP process may be investigated attaining ECAP pressing at slow speed (less than 5 mm per minute) [7]. Introduction of microchannel within the die geometry for rapid cooling rate of die may be investigated [7]. Introducing a secondary punch with a pressure (P2) and the effect of material flow pattern during the process may be investigated [2]. The combine ECAP and high-pressure torsion sample may be future processed with EDM and the change in the mechanics of material removal may be studied and investigated [2]. In Al 7075 ECAP + HPT sample, stored energy [4] may be calculated from the experimental data [2]. The variation of dislocation density [5] with the variation of sample size may be investigated. Study of stored energy [4] in ultra-fine-grained [1–3, 5] aluminum alloy Al7075 at 120 °C with processing speed of 0.5 mm s<sup>-1</sup> through  $B_c$  process route and sample size of  $7 \times 7 \times 50$  mm<sup>3</sup> [5] with  $\varphi = 90^\circ$  and  $\psi = 20^\circ$ , respectively, may be investigated .

**Table 2** Proposed application areas with future manufacturing challenges

Sr. no.	Proposed application areas
1	Aviation, aerospace, and aircraft industries
2	Connecting rod and crank shaft of automobiles
3	Marine propulsion system
4	Production of chemical plant and process plant equipment
5	Parts of reciprocating compressor
6	Parts of radial engines

(continued)

**Table 2** (continued)

Sr. no.	Proposed application areas
7	Parts of tower cranes
8	Roof sheeting applications
9	Silencer/outlet manifold of IC engines
10	Food and drinks packaging industries
11	Sporting goods and accessories
12	Printing and plotting devices and machines

## 6 Difficulty Level to Carry Out Tensile, Bending, and Impact Testing with Microsamples

As there is no sufficient infrastructural facilities to carry out tensile, bending, and impact testing with microsamples in the Eastern Part of India, the researcher from this area needs to face difficulties in testing of microsample as the provision for destructive test of microsample is very limited. Unwanted delay is unavoidable in the research on this particular area.

## References

1. Valiev, R.Z., Langdon, T.G.: Principles of equal channel angular pressing as a processing tool for grain refinement. *Prog. Mater. Sci.* **51**, 881–981 (2006)
2. Sabbaghianrad, S., Terence Langdon, G.: A critical evaluation of the processing of an aluminum 7075 alloy using a combination of ECAP and HPT. *Mater. Sci. Eng. A* **596**, 52–58 (2014)
3. Zhao, Y.H., Liaon, X.Z., Jin, Z., Valiev, R.Z., Zhu, Y.T.: Microstructures and mechanical properties of ultra-fine grained 7075 Al alloy processed by ECAP and their evolutions during annealing. *Acta Mater. Sci.* **52**, 4589–4599 (2004)
4. Mohammad Mahdieh, S., Ramezan Mahdavejad, A.: A study of stored energy in ultra-fine grained aluminum machined by electrical discharge machining. *IMEchE2016*, pp. 1–9
5. Shaeri, M.H., Shaeri, M., Ebrahimi, M., Salei, M.T., Seyyedein, S.H.: Effect of ECAP temperature on microstructure and mechanical properties of Al-Zn-Cu alloy. *Prog. Nat. Sci. Mater. Int.* **26**, 182–191 (2016)
6. Dileep, B.P., Vitata, H.R., Ravi Kumar, V., Suraj, M.M.: Effect of ECAP on mechanical and micro-structural properties of Al7075-Ni alloy. *Mater. Today Proc.* **5**, 25382–25388 (2018)
7. Cepeda-Jimenez, C.M., Garcia-Infanta, J.M., Ruano, O.A., Carreno, F.: High strain rate super-plasticity at intermediate temperature of the Al 7075 alloy severely processed by equal channel angular pressing. *J. Alloys Compd.* **509**, 9589–9597 (2011)
8. Avcu, E.: The influences of ECAP on the dry sliding wear behavior of AA7075 aluminum alloy. *Tribol. Int.* **110**, 173–184 (2017)
9. Vishnu, P., Raj Mohan, R., Krishna Sangeetha, E., Raghuraman, S., Venkatraman, R.: A review on processing aluminium and its alloy through equal channel angular pressing die. *Mater. Today Proc.* **21**, 212–222 (2020)

10. Shaeri, M.H., Salehi, M.T., Seyyedin, S.H., Abutalebi, M.R., Park, J.K.: Microstructure and mechanical properties of Al-7075 alloy processed by equal channel angular pressing combined with aging treatment. *Mater. Des.* **57**, 250–257 (2014)
11. Naseri, R., Kadkhodayan, M., Shariati, M.: Static mechanical properties and ductility of bio medical ultra-fine-grained commercially pure titanium produced by ECAP process. *Trans. Nonferrous Met. Soc. China* **27**, 964–975 (2017)

# Comparative Analysis of the Payback Period for Different Types of Solar Energy Systems Used in India



Abhishek Dhiman and Gulshan Sachdeva

**Abstract** Due to the geographical location of India, solar energy is sufficient to fulfill the continuously rising energy demand. Under different operating conditions (solar intensity, ambient temperature, energy demand), solar energy systems could be more economically efficient as compared to conventional systems (LPG stove, induction cooker, electric geyser, gas geyser, etc.). But it is necessary to know the economic feasibility of the solar energy systems before use. In this study, the payback period (PBP) of different solar energy systems is calculated in terms of energy saving over conventional systems. For SK14 solar cooker, PBP in terms of years is shorter when the substituted conventional system is an induction cooker and PBP is higher when the substituted conventional system is an LPG stove. Similarly, the PBP of the solar water heater (SWH) is about 2.5 years when the substituted conventional system is an electric geyser and about 6.5 years when the substituted conventional system is a gas geyser. PBP of the photovoltaic solar system is about 5.5 years. The findings of the present study would motivate the end user for the use of solar energy systems for different applications.

**Keywords** Payback period · Solar energy systems · Solar cooker · Solar water heater

## 1 Introduction

To fulfill the rapid increase in energy demand has become a crucial concern in the last few decades. And the use of conventional sources causes climate change and global warming. According to WHO, 1.6 lakh people die due to the direct and indirect effect of climate change [1]. Moreover, natural disasters such as floods and drought are the consequences of climate change. Hence, to minimize the negative effect on the environment, the conventional sources must be replaced with environment-friendly substitutes.

---

A. Dhiman (✉) · G. Sachdeva  
National Institute of Technology Kurukshetra, Kurukshetra, India



There are many substitutes such as solar energy, wind energy, tidal energy, and geothermal energy. Solar energy is one of the best substitutes as it is free, clean, and available in abundance at most of the places. The deficiency of fossil fuel has increased the demand of solar energy [2]. Although solar energy covers a very small portion of energy demand, it has great future potential.

Solar energy is divided into radiant energy and heat energy. Radiant energy easily converts into electricity with the help of a PV panel. Heat energy is utilized by using a different type of concentrators and collectors. For cooking applications box-type collectors, Scheffler reflectors, and parabolic dish collectors are mainly used [3]. Steam generation for industrial and domestic applications is done with the help of concentrators having a high concentration ratio [4]. Evacuated tube solar heat collector has also been utilized for the regeneration process of the LDAC system by various researchers [5–7].

Solar systems become more popular if they are economically feasible. To evaluate the economic feasibility of the system, the payback period of that system is calculated. The payback period is the number of years to return the fund invested.

$$\text{Payback period (PBP)} = \text{Initial investment} / \text{saving per year} \quad (1)$$

## 2 Solar Cookers

Food is the basic need of all human beings. Different types of cookers, stoves, and chulhas are used to cook food. Most of the population in urban areas use the LPG gas stove and the population in villages uses traditional chulhas. Cow dung cake or dry wood is used in chulhas which causes a lot of pollution and many diseases like Asthma. A solar cooker is the best alternate of these stoves and chulhas as it is free of cost and available in abundance.

A wide range of solar cookers is available in the market. These solar cookers are classified as the non-concentrating-type and concentrating-type solar cookers based on the concentration ratio. Further solar cookers can be classified as direct- and indirect-type solar cookers according to the position of the cooking pot. If the cooking pot is directly placed at the focus of the concentrator, then the cooker is a direct type solar cooker. In indirect-type solar cooker, first steam is generated and which is used for cooking inside the kitchen. Evacuated tube collectors have also been used for cooking purposes [8]. Box-type solar cooker and SK14 solar cooker are suitable for domestic cooking. SK14 solar cooker can be used for both low temperature and medium temperature cooking, whereas a box-type solar cooker can be used only for low-temperature cooking. Therefore, cost analysis of SK14 solar cooker is done because it is a medium-temperature solar cooker (Fig. 1 and Table 1).

The approximate cost of the LPG stove, induction cooker, and SK14 solar cooker is taken. To calculate cost per MJ of energy, the price of a subsidized LPG cylinder is taken and the cost of 1 kWh energy is assumed to be 5 Indian rupees

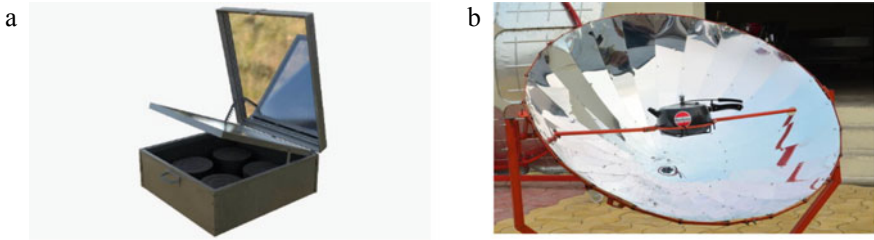


**Fig. 1** **a** Represents the pictorial view of the box-type solar cooker; **b** represents the pictorial view of SK14 solar cooker

**Table 1** Initial cost and running cost of different types of cookers

S. no.	Type of cooker	Price (INR)	Cost per MJ of energy (INR)
1	LPG stove	5000	1.15
2	Induction cooker	2500 [9]	1.54
3	SK14 solar cooker	9500 [10]	Negligible

(INR). Also, the overall efficiency of the LPG stove and induction cooker is about 68 and 90%, respectively [11, 12]. The calorific value of LPG is about 46 MJ per kg [13]. Per day energy required for cooking food in a family of 4 persons is approximately 14.5 MJ [14]. Solar energy is only available in the daytime so it is impossible to completely depend on solar energy. So, it is assumed that 5 MJ of energy is taken from SK14 solar cooker and the remaining energy is taken from the LPG stove (Fig. 2).

From the graph, it is observed that the PBP of SK14 solar cooker is about 2 years. Hence, it is very helpful to reduce monthly expenditure on LPG or electricity bills. But the use of SK14 solar cooker is not convenient for the user because it has to be tracked with time.

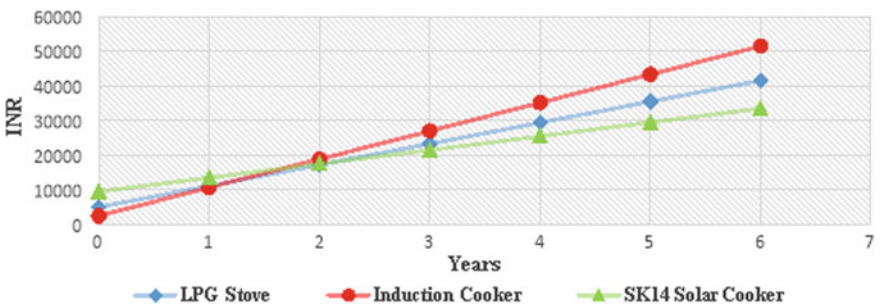


**Fig. 2** Cost analysis of different cooking appliances

### 3 Solar Water Heater (SWH)

Hot water is required in the daily activities of every household and many industrial processes, especially in low-temperature regions. In household, hot water is mainly required for bath and to maintain the hygiene standards of the kitchen. Many industries like food, chemical, leather, clothes, laundry, etc., use hot water for different processes.

There are different equipment available for heating water like LPG geyser, electric geyser, SWH, kerosene stove, traditional chulha. Two types of SWH are available in the market. The first one is a flat plate-type water heater (FWH) and the second is an evacuated tube-type water heater (EWH). In FWH, copper tube is mounted in different patterns inside a flat plate collector. A collector consists of a metal box that is painted black from inside to absorb maximum radiation and a glass cover to prevent the escape of long-wavelength radiation from the box. In EWH, evacuated tubes are used for heating water. Evacuated tube consists of two concentric glass tube and vacuum is created between these tubes (Fig. 3).

The approximate price and cost of heating 1 L of water for the different water heater is listed in Table 2. The cost of heating 1 L of water is 0.075 INR for subsidized LPG gas cylinder, whereas 0.141 INR for unsubsidized LPG gas cylinder. The approximate cost of 100 L capacity EWH is taken in Table 2.

To calculate the PBP of SWH, the graph is plotted between the yearly expenditure of different water collector and time. The approximate cost of different water heaters is taken to calculate yearly expenditure. The charge of 1 kWh unit electricity is taken 5 INR. It is assumed that a small family requires 80 L of hot water per day. Also, there are 280 clear sky days per year where the SWH is installed and an LPG gas geyser is used in the rest of the days for heating water. A subsidized LPG gas cylinder is used in gas geyser for heating water (Fig. 4).

SWF is economically feasible for domestic as well as industrial applications. It is observed that the PBP of SWH is approximately 2.5 years when used instead of an electric geyser and 6.5 years when used instead of a gas geyser.

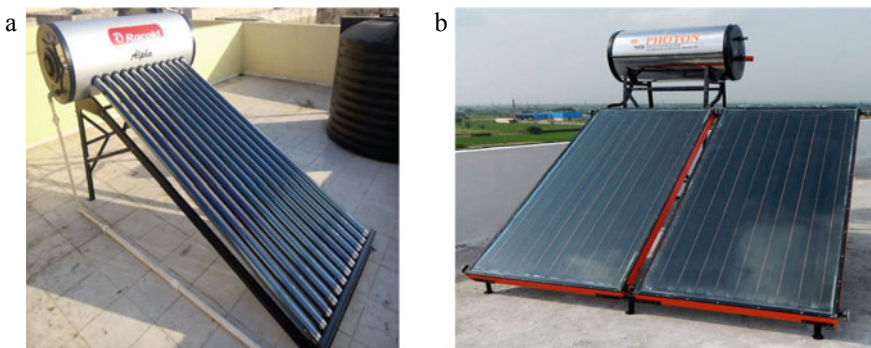


**Fig. 3** a Represents the pictorial view of EWH; b represents the pictorial view of FWH

**Table 2** Initial cost and running cost of different types of water heating systems

S. No.	Equipment	Initial cost (INR)	Cost of heating 1 L of water (INR)
1	LPG Geyser	4500 [15]	0.075–0.141 [16]
2	Electric Geyser	7000 [17]	0.145 [16]
3	SWH	15,000 [18]	Negligible

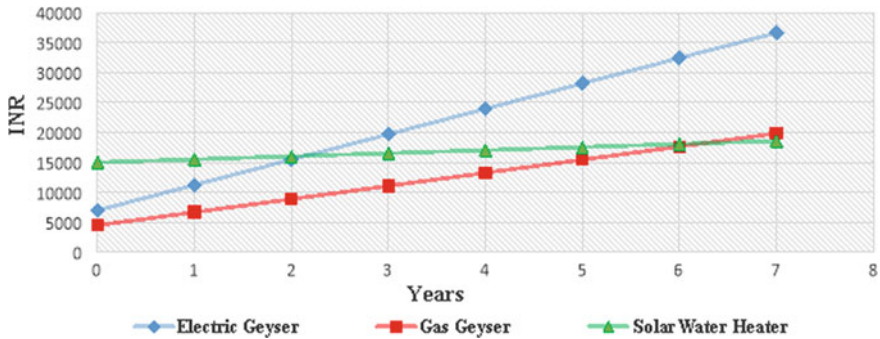


**Fig. 4** Cost analysis of the different types of water heating systems

### 4 Solar Photovoltaic System

Electric energy is the most useful form of energy because it is high-grade energy and easily transformable. Most of the domestic and industrial machines are working with the help of electric energy. Electric energy is produced in power plants like hydropower plants, thermal power plants, and nuclear power plants. The installation of PV panels is an alternate method to produce electricity. PV panels work on the principle of photovoltaic effect and it converts directly solar energy into electric energy.

The initial installation cost for a large solar PV power plant is quite high but its running cost is negligible. If we do not store energy for off sunshine hours, the electricity generation cost with the help of solar PV panels is almost zero. The cost of batteries will be added if we store energy for an off sunshine hour (Table 3).

The installation cost of the PV panel is about 40,000 INR per kW for the on-grid system and 60,000 INR per kW for the off-grid system. The charges for 1 kWh energy vary from Rs 2.75 to Rs 6.25 depending upon the amount of electricity used (Fig. 5).

From the graph, it is observed that the PBP of the on-grid PV system is less than one year if it is used in the remote area where the diesel generator is used to fulfill electricity demand. The PBP of this system is about 5.5 years with respect to the conventional power supply.

**Table 3** Initial cost and cost per kWh for different sources of electricity

S. no.	Sources of electricity	Initial cost (INR) per (kW)	Cost of one kWh energy (INR)
1	Conventional power supply	2000–10,000	2.75–6.25
2	Generator	5000–20,000 [19]	20
3	Solar photovoltaic system	50,000 [20]	Negligible

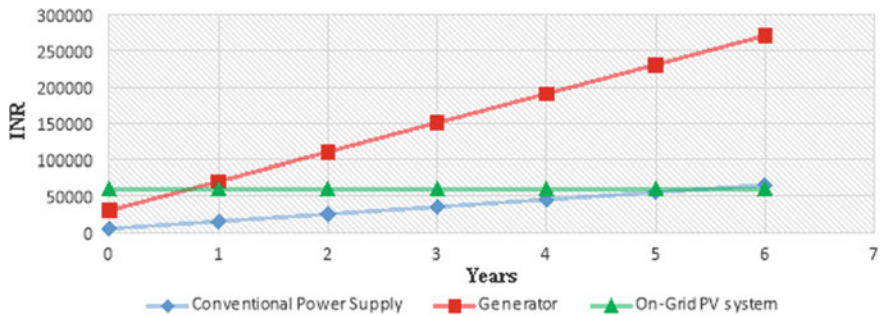


**Fig. 5** Cost analysis of different sources of electricity

## 5 Conclusions

In this study, the payback period of different solar systems is observed. The study gives the payback period of different solar systems under specific conditions. The conditions like the price of solar systems, electricity, LPG are different for different places. Also, the solar intensity and atmospheric temperature depend upon the geographical location which greatly affects the performance of the system. Specific findings obtained in the cost analysis of the solar system:

- The use of SK14 solar cooker is very economical as its PBP is less than 2 years. Also, its maintenance is negligible. But still, its use is very limited because of difficult tracking. SK14 solar cooker is a very useful product in villages where people use traditional chulhas as it does not produce any smoke.
- It is observed that the PBP of SWH is 2.5 years and 6 years for electric geyser and gas geyser, respectively. SWH is very easy to use as it does not require any kind of tracking.
- PBP is depended on the solar intensity and the number of clear sky days in the year at that location where the solar system has been installed. PBP is higher for the location having a higher number of clear sky days and vice versa.
- PBP of the on-grid PV system is about 5.5 years for conventional power supply and less than one year for a diesel generator. PBP of the on-grid PV system mainly depends upon the cost of one kWh of energy at that location.

**Acknowledgements** The authors would like to thank for the support and equipment provided by NIT-Kurukshetra.

**Conflict of Interest** The authors reported no conflicts with other studies and researches.

## References

1. Mekhilef, S., Saidur, R., Safari, A.: A review on solar energy use in industries. *Renew. Sustain. Energy Rev.* **15**(4), 1777–1790 (2011)
2. Garg, H., Kandpal, T.: Renewable energy education: challenges and problems in developing countries. *Renew. Energy* **9**(1–4), 1188–1193 (1996)
3. Cuce, E., Cuce, P.M.: A comprehensive review on solar cookers. *Appl. Energy* **102**, 1399–1421 (2013)
4. Kamboj, V., et al.: Thermal performance of the steam boiler based on Scheffler solar concentrator for domestic application: experimental investigation. *Aust. J. Mech. Eng.* 1–11 (2019)
5. Sharma, A., Kaushal, R.: Experimental investigation of a novel multi-channel flat plate liquid desiccant dehumidification system. *Energy Sources, Part A: Recovery, Utilization, and Environmental Effects*, pp. 1–19 (2020)
6. Kaushal, R., Sharma, A.: Parameter optimization of flat plate liquid desiccant dehumidification system using Taguchi method. *Int. J. Eng. Adv. Technol.* **8**(6), 5026–5029 (2019)
7. Sharma, A., Kaushal, R.: Experimental investigation of the dehumidification performance of a novel flat plate liquid desiccant dehumidification system. *Int. J. Emerg. Technol.* **11**(3), 257–266 (2020)
8. Chaudhary, R., Yadav, A.: Experimental investigation of a solar cooking system inhibiting closed airtight cooking pot and evacuated tube collector for the preparation of Indian cuisine items. *Environ. Dev. Sustain.* **1**(1), 1–23 (2020)
9. Amazon. [https://www.amazon.in/s?k=induction&ref=nb\\_sb\\_noss\\_1](https://www.amazon.in/s?k=induction&ref=nb_sb_noss_1)
10. Indiamart. <https://dir.indiamart.com/search.mp?ss=SK14&prdsrsc=1>
11. Khan, M., Saxena, A.: Performance of LPG cooking stove using different design of burner heads (2013)
12. Sadhu, P.K., et al.: Review of induction cooking-a health hazards free tool to improve energy efficiency as compared to microwave oven. In: 2010 the 2nd international conference on computer and automation engineering (ICCAE). IEEE (2010)
13. Wikipedia Homepage. <https://www.wikipedia.org/>
14. De, D.K., et al.: Minimizing energy usage in cooking to protect environments and health. *Int. J. Energy Environ. Res.* **2**(3), 20–44 (2014)
15. Amazon. [https://www.amazon.in/s?k=gas+gyeser&i=kitchen&ref=nb\\_sb\\_noss\\_2](https://www.amazon.in/s?k=gas+gyeser&i=kitchen&ref=nb_sb_noss_2)
16. Bijlibachao Homepage. <https://www.bijlibachao.com/>
17. Amazon. [https://www.amazon.in/s?k=electric+geyser&ref=nb\\_sb\\_noss](https://www.amazon.in/s?k=electric+geyser&ref=nb_sb_noss)
18. Indiamart. <https://dir.indiamart.com/search.mp?ss=solar+water+heater&prdsrsc=1>
19. Indiamart. <https://dir.indiamart.com/impcat/generator.html>
20. Indiamart. <https://dir.indiamart.com/search.mp?ss=pv+price&prdsrsc=1&mcatid=69789&catid=87>

# Three-Wheeler (Loading Auto-Rickshaw) Suspension by FEA



Rajat Yadav and Kamal Sharma

**Abstract** The paper manages pressure test of helical spiral spring, placed in three-wheel automatic rickshaws on medium intersection of an Indian car display. The elastic properties and fatigue resistance in the plan of this form of spring must both be viewed as important aspects. This paper contains a helical bow spring that supports load and determines shear stress. Nonetheless, the investigative work needed to minimize the weight of an element running the production facility allows these springs to face high work stress. The structural integrity of helical spiral must be ensured. In order to determine exact stress distribution of spring, a static stress analysis with the finite element method was performed.

**Keywords** Fatigue strength · Finite element analysis · Helical coil compression spring

## 1 Introduction

Three-wheeled auto-rickshaws (TWA) are a key accessible vehicle for India's working class urban population. TWA are still utilized in open cars and in freight transport worldwide, with the exception of India [1]. The suspension system is bad for three wheels, since it is concerned with the driving consolation of the driver. The lack of a rear pit differential was labelled roll-over and pitching supporters, which moderately increased the amount of gravity. This improves comfort of traveller. Few distributions test the daily show of TWA for mass transportation [2, 3]. The company pattern is now decreasing weight in each portion and more springs are not depleted. The tension feeling in the springs is increasing through the wide open streets, where these TWA usually transport freight. The helical coil pressure springs are a fundamental part of this suspension system and are therefore extremely important for full spring pressure study. When such sources encounter government fluctuations, the weariness of the counterpart should be identified to the

---

R. Yadav (✉) · K. Sharma  
Department of Mechanical Engineering, IET, GLA University, Mathura, India



greatest degree possible [4]. The mechanical spring is a versatile body, which is essential to diversify and twist under loads when the heap is expelled. First stage of spring scheme is to define heaps and avoidances suitable on the basis of stacking for a specific spring application [5]. The material must nevertheless be calculated temporarily. With a broadest helical spring planning technique, the spring wire may be the most concerned with direct shear and torsional shear pressure [6]. There is a very easy technology designed to structure hypothesis of eBB's direct shear and flow for hydration of spinning water for tiny spikes [7]. The theory that helical spiral component is pivotal functions as direct bar in turn. If  $p$  is spring edge,  $d$  is gap between spring wires,  $d$  averages width of belt and then power in spiral is provided, with direct pivot power  $P$ . The power supply is supplied with  $P$ . The power supply is supplied with part. Anxieties induced by bending of latter are first considered and then are superimposed on concerns by immediate shear [8]. On inner side of the spindle, however, highest shear pressure occurs and can exceed a rudimentary assumption of a number depending on list of springs. The goal is as illustrated in Fig. 1a and b shows that elemental section of helical coil compression spring, to have a small fibre within this roll. This allows the inner fibre to experience considerably greater pressure and shear stress than the outer muscle of the fibre if the band and spiral areas swing around the spring centre via one edge. In the same way, the shear problem on the inner side of the belt was caused by direct pivotal load  $P$ . Then the pressure within the belt is typically much higher than elsewhere and in this place,

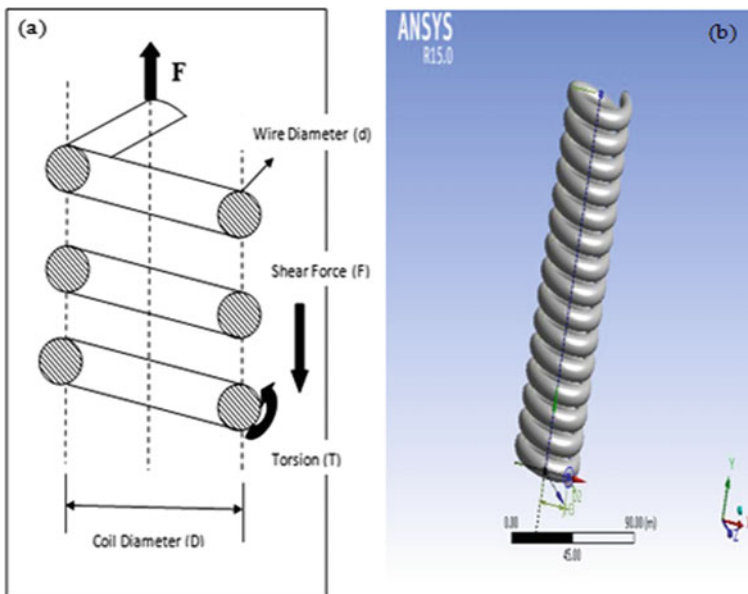


**Fig. 1** a and b Elemental section of helical coil compression spring



therefore, disappointment of fatigue often begins. This is why the spiral's shear is most intense.

$$\tau_{\max} = \frac{8PD}{\pi d^3} K \quad (1)$$

where

$$K = \left[ \frac{(4C - 1)}{(4C + 1)} + \frac{0.615}{C} \right] \quad (2)$$

$$C = D/d$$

The unmistakably spring file's composition directly influences the pressure circulation.  $K$  is Wahl's factor as ebb and flow effect product and  $C$  is recognized for consideration of pressure remedy as a spring record. These formulas can be checked with the limited part technique to better understand pressure propagation. A formula is used to measure deflection.

$$\delta = \frac{Gd^4}{8D^3N} \quad (3)$$

where  $G$  is material shear module and  $N$  is a number of active turns of helical spring [1].

## 2 ANSYS Analysis of Helical Spring

### 2.1 Finite Element Analysis

An significant incentive to be included FEA in configuration of coil spring is their willingness to minimize mistakes improving conditions, in particular regarding the timing edge. A FEA-based software begins by determining type of component, nature of model, the reliability and pace of running of the model. The most precise FEA outcomes can be achieved by making a 3D spinner section and the seats tracked by cross section with a powerful 3D portion.

A stronger cross-area with higher demand components produces more consistent performance. In either case, a higher number of components and nonlinearity could take either time-out to inspect due to the interaction between a spindle spring and its seats or between the spindle and itself. The measurement duration for consolidating FEA into a whirling strategy must be sensitive, while precision and accuracy of outcomes are important. In order to make the measurement time in strong model, revolver and seats are always shown as 3D shaft part. A seat as an inflexible body's

material characteristic is quite defined as it is insignificant and cannot be taken into account when a seat is failing under pressure. Bending components or non-bending components are described by the interaction between spindle or seat or spindle.

## 2.2 Geometry and Material Properties

Table 1 is indicated by viable spring point by point. This spring is used in three-wheeler front suspension. Spring is composed of ASTM A227 material, square and placed on floor. Table 2 displays the characteristics of the material. In this spring, the process of extinction of oil was improved and pressures of 395  $\mu\text{C}$  were mitigated over 25 min. After a while, a decent finish on the surface took with ball size of 2 mm.

In this study, the effects of residual stresses were ignored. Pro-E Wildfire 4 was programmed, as shown in Fig. 2a generates simple models of strong spring. This research does not model spring seats and is regarded as a rigid body for interaction of the seats with the spring surface.

## 2.3 Criteria by ANSYS on Mesh Convergence and Element Type

ANSYS 15.0 is product before and after preparation. This spring is compatible with various helical spring factors and cross sections, along with relative controls to detect assembly laws. From the beginning, the source had been fitted with SOLID197. This feature is a 10-hub part of a higher request that is three-dimensional. This is an ideal for showing periodic cross sections (like the ones supplied by many cad/cam structures). SOLID197 has quadratic de rooting behaviour. This segment consists of 10 hubs, each of which gives a three grad chance:  $x$ ,  $y$  and  $z$  nodal perceptions. It uses the segment Tet-Meshing. The second

**Table 1** Helical spring specifications

Spring parameter	Value	Unit
Wire diameter, $d$	8.5	mm
Outer diameter, $D_o$	53.0	mm
Inner diameter, $D_i$	36.5	mm
Mean diameter, $D_m$ or $D$	45.0	mm
No. of active turns, $N_a$	9.0	
No. of total turns, $N_t$	11.0	
Free length, $l_0$	192.0	mm
Solid length, $l_s$	95.0	mm
Spring index, $C$	5.75	

**Table 2** Material specifications of ASTM A227 steel spring

Material properties	Value	Unit
Modulus of elasticity, $E$	192.575	GPa
Poisson’s ratio, $\mu$	0.250	
Shear modulus, $G$	75.45	GPa

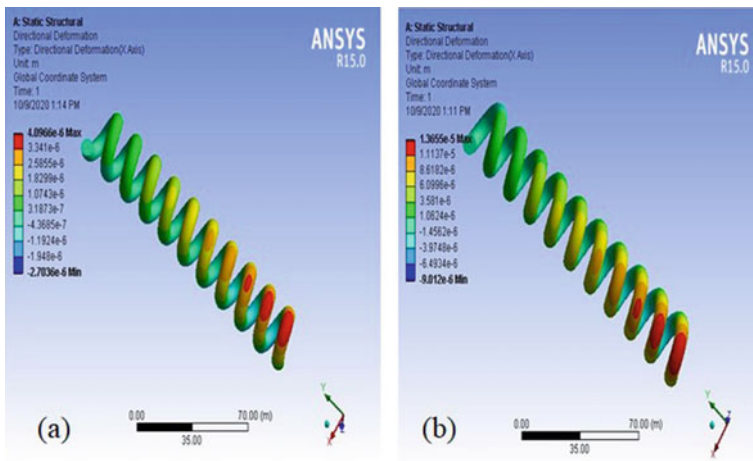


**Fig. 2** Solid model (a) and finite element analysis by ANSYS (b) with Tet-Mesh (SOLID 197)

case shows the SOLID95/SOLID196 portion. For 3D displays in powerful designs, twenty jackets are used. Without loss of accuracy, it can withstand irregular shapes. The components of SOLID196 are well-shaped and bendable. There are three degrees of chance in any hub perception in eight hubs of  $x$ ,  $y$  and  $z$  nodal headings. This section is used for hex cross section. Working testing in the FE model is conducted with the goal of making sure that the precision of the measured result (CPU time) is assured by sufficiently fine steps. The shear pressure is chosen and its assembly is simultaneously checked and evaluated as the preset variable in the field. Depending on estimate, model geography, investigational objectives, portion of best are crossing methods. Tetrahedral coincidence allows high-quality designs for solids display models from most CAD frames to be imported. Following individual measurements of different component sizes using the specifications SOLID197 and SOLID196, the smaller work size was shown to enhance pressure estimate. SOLID197 segment with test mesh is shown in Fig. 2b. However, the littler component size less than 2 mm for two types of components has not been achieved because component produces a large number of hubs and needs almost unnecessary computational capacities of PC. Consider the exact layout and time required at that time for different grid alternatives for the equivalent. In comparing the hypothetical

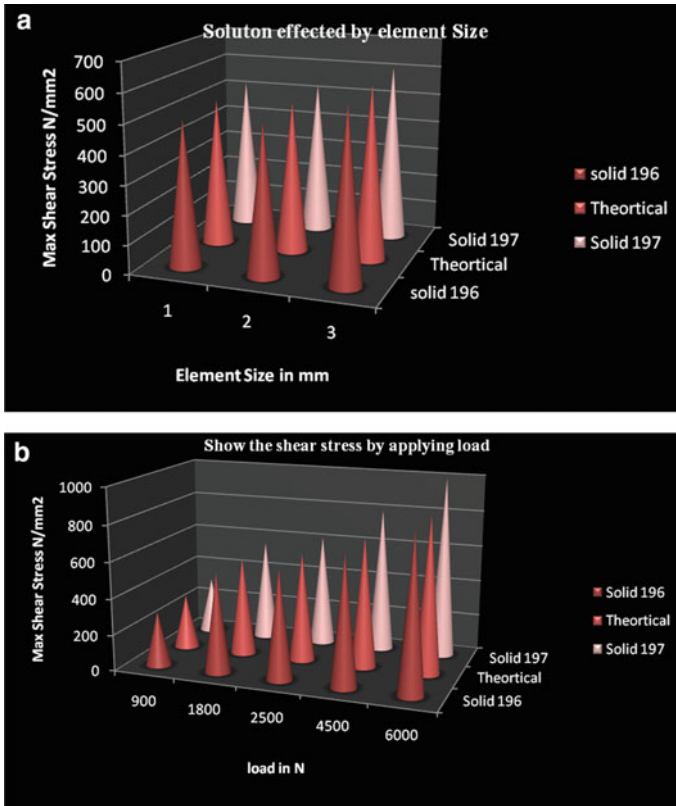


Fig. 3 a Various meshing-type material. b Graph between load versus shear stress

measurement of the highest shear pressure contest and using Wahl’s equation, the best FEM model was obtained. In relation to heap of approx.  $474.08 \text{ N/mm}^2$  and the distinct pieces are seen at Fig. 3a hypothetical loan pressure counter of approximately 167 kg or 1637.27 N shows. The most combined model of hypothetical accuracy is Tet-Mesh (SOLID197). Part size 2 mm and refined at level one within the spiral.

### 3 Results

#### 3.1 Applied Weight on Helical Spring

For exploration in both static conditions and strong conditions heap followed by spring in real development is essential since hubs are used in front suspension. The vehicle normally weighs around. The COG gathers 405 kg with one passenger and

500 kg on a safer side on a motorcycle. It is expected that this weight will be split into two rear springs and an early spring. On the front suspension spring, there is around 167 kg of load. This heap is seen in the analysis using the mass variable. Consequently, unbending bodily touch conditions will be applied between this part and the spring's upper surface components.

### 3.2 Static Stress Analysis of Helical Coil Spring

The anxiety results from the model of a limited variable were calculated during the straight static test. This work uses a straight isotropic flexible material. For the direct flexible material model, the decision is fundamentally regulated. The models are stacked according to the mechanical load used to illustrate the heap control and load control. The study indicates the biggest problems on the inner side of helical spool spring. Spring's maximum shear pressures. The result is that  $467.664 \text{ N/mm}^2$  has the most serious shear worries. In  $xy$ -plane hubs were held on the inside of each mm spin. Figure 3b shows the effects of burden on FEM shear strain.

### 3.3 Fatigue Analysis of Helical Spring

Helical spring exhaustion is ANSYS measured and spring life is calculated. This method can calculate total and lateral deformation. At this point, the broken colour shows the spring and the fixed point brake unexpectedly. The fatigue life of the spring is illustrated by Fig. 4.

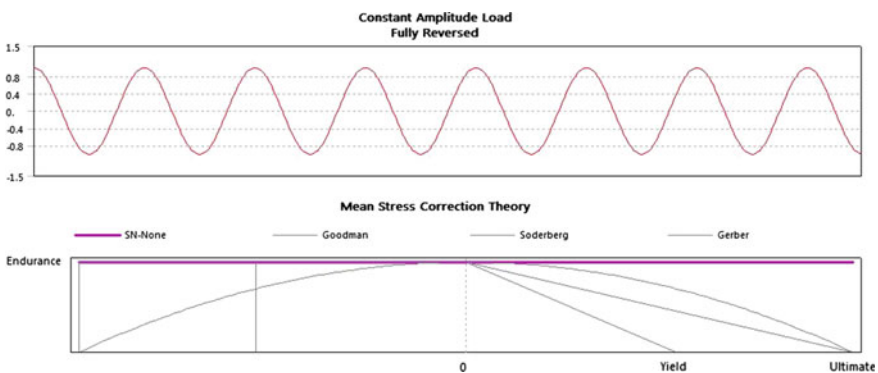


Fig. 4 Graph of fatigue inspection

## 4 Conclusions

The flexibility tests of the springs used for the three front suspension wheelers are introduced and discussed in this article. The findings of a complete 3D FEM analysis also illustrate the hindrance of the old spring model when measuring these springs. In relation to applied weight on helical spring and values obtained from using the basic scientific model in the reading material, relative error at the majority of shear pressure varies from 1.5 to 4%. The pressure circulation shows unmistakably that shear pressure on inside side of each spin is most soothing. Each spindle has a comparative pressure transmittance. Therefore, except for sweeps at the top, there is the same risk of spring deception in every spindle. There may be major problems in each spindle in this scenario which affect disappointment.

## References

1. Shigley, J.E., Mischke, C.R.: Mechanical engineering design (5th edn.). McGraw Hill Inc. (1989)
2. Prawoto, Y., Ikeda, M., Manville, S.K., Nishikawa, A.: Failure analysis of automotive suspension coil springs. In: Association for iron & steel technology proceedings, pp. 35–48 (2008)
3. Dojoong, K.: Development of a finite element program for dynamic analysis of helical springs. Mechanics, Korus, pp. 309–314 (1999)
4. Forrester Merville, K.: Stiffness model of die spring. M.S. Thesis, Virginia University (2001)
5. Berger, C., Kaiser, B.: Result of very high cycle fatigue tests on helical compression springs. Int. J. Fatigue **28**, 1658–1663 (2006)
6. Al-Mahasne, M., Abu ShreehahTareq, A.: Experimental investigation of polymeric compound cross section spring. Am. J. Appl. Sci. **4**(1), 33–36 (2007)
7. Mulla, T., Kadam, S., Kengar, V.: Finite element analysis of helical coil compression spring for three wheeler automotive front suspension (2012)
8. Jiang, W.J, Henshall, J.L.: A novel finite element model for helical spring. In: Finite elements in analysis and design, vol. 35, pp. 363–377 (2000)

# 3D-Printed Orthosis: A Review on Design Process and Material Selection for Fused Deposition Modeling Process



Ravi Kumar and Saroj Kumar Sarangi

**Abstract** Physical impairments and functional limitations have become a serious concern for people in under-developed countries affecting their socio, physio, and financial life. The high-cost orthosis is the major barrier to access assistive devices for rehabilitation. The conventional orthosis casts are bulky and poorly ventilated causing uneasiness and various skin problems. 3D-printed orthosis give better alternatives to replace this conventional cast. Customized product, design flexibility, controls over porosity make it more popular over conventional orthosis. For diabetes patients with a risk of foot ulcers, custom-made 3D-printed insoles result in better for offloading their foot pressure as compared with prefabricated insoles made by the conventional method. The current review paper focuses on discussing design processes for fabrication orthosis insoles and also highlights the technologies barrier in the fabrication of conventional insole. Advancement in materials available for FDM technology such as polymer and their composites is also reviewed in detail. In the concluding remarks, future strategies for the betterment are suggested.

**Keywords** 3D-printing · Orthosis · FDM · Polymers · Composite

## 1 Introduction

The number of persons with physical or functional disabilities is increasing rapidly in recent years due to an increase in population, change in lifestyle, and aging peoples. There are rapidly increasing cases of accidents, muscular, and skeletal conditions [1], non-communicable diseases like diabetes [2–4], and stroke [5, 6]

---

R. Kumar  
Department of Mechanical Engineering,  
Motihari College of Engineering, Motihari, Bihar, India

S. K. Sarangi (✉)  
Department of Mechanical Engineering, National Institute of Technology, Patna, India

causing disabilities like a fracture, misalignment, foot ulcer, etc., which need to be rehabilitated. It is estimated that an average of 0.5% of the world population would require prosthetics and orthotics devices globally of which more people will need orthosis for rehabilitation [7].

An orthosis is an externally wearable mechanism developed for supporting or correcting the weakened muscles of the spine, arms, foot, and legs. Orthosis enables people with disabilities to live healthily and independently. Each orthosis has specific purposes, such as maintaining or correcting the positioning of a body segment, improving its mobility, and relieving pain. The orthosis is classified according to the joint and the limb into three categories, i.e., upper limb orthosis, spinal orthosis, and lower-limb orthosis. The classification for most commonly used orthosis aids is explained in Table 1 [8].

The orthosis can be fabricated either by using the traditional method or custom-made using additive manufacturing methods. The traditional method uses plaster casts for orthotic treatment which are bulky, breathless, and fixed. Many times, the casts create problems that may include different skin diseases, joint, and ligament problems [9]. For patients having diabetes and at risk for foot ulcers, custom-made insoles result in better for offloading their foot pressure as compared with prefabricated insoles made by the traditional method [10]. The use of 3D printing technology for optimization and stress analysis on the materials showed that the device effectively decreases the production cost and also fulfills the requirements to modify the patient's gait [11].

The current review paper focuses on discussing design processes for fabrication orthosis insoles and also highlights the technologies barrier in the fabrication of conventional insole. Advancement in materials available for FDM technology such as polymer and their composites is also reviewed in detail. In the concluding remarks, future strategies for the betterment are suggested.

## 2 Design Methods

The traditional method of insole fabrication is costly and time consuming. They do not fulfill functional requirements. The important advantage of the design process is the possibility of design insole based on the foot scans, without requiring preparation of individual mold for every consumer. Caravaggi et al. [12] compared the

**Table 1** Orthosis nomenclature [8]

Upper-limb orthosis		Lower-limb orthosis		Spinal orthosis	
WO	Wrist orthosis	AFO	Ankle-foot orthosis	CO	Cervical orthosis
				LO	Lumbar orthosis
WHO	Wrist Hand orthosis	FO	Foot orthosis	TO	Thoracic orthosis
EO	Elbow orthosis	IO	Insole orthosis	SIO	Sacroiliac orthosis



custom made insoles with traditional pre-fabricated and off-the-shelf insoles. In his case study, seventeen workers were selected and their feet were 3D scanned, concerning their plantar view, and these images were used to design 34 insoles. The study suggested that customized insoles are an effective solution for decreasing overloading and redistributing plantar pressure in workers' feet for different working activities. Khodaei et al. [13] selected 19 flatfoot persons between 18 and 45 for their case study. CAD-CAM foot orthoses and conventional prefabricated foot orthosis were made. Plantar pressure, force, and contact area of both types of insoles were measured using pedar®-x in-shoe system. Repeated measures ANOVA model with posthoc, Bonferroni comparison were used to test differences. They found increased forces at hallux and lateral toes in prefabricated foot orthoses as compare to CAD-CAM foot orthoses [13]. CAD modeling overcomes these limitations with freedom of design and customized insole. Surmen et al. (n.d.) created the 3D model of foot insole by taking multiple pictures from various angles and uploading these data to photogrammetry software technology. He next, transferred the 3D scan data to a CAD package and the model was altered for representing the geometric parameters of the subject's foot appropriately ready to 3D print [14]. Algar and Guldberg [15] proposed a system in which the 3D scanning of the foot was performed using Microsoft Kinect 3D sensors using three different views. The Kinect 3D range data were taken to a general reference mechanism taking marker data and aligned with RGB images. These data are then converted to a polygon mesh representation using Delaunay triangulation. The last foot model was generated by merging meshes as well as coloring mesh faces with RGB image colors [15]. The paper of Davia et al. [16] designed the framework for the implementation of the CAD-based platform for customized shoe design. The proposed system framework (KB system, foot pressure viewer, last designer, and foot-last validation tool) worked as a single tool combining the foot acquired geometrical data and the plantar foot pressure map having advantages over the traditional method [16]. Wang et al. developed turnkey-based User Interface (UI) to detect the dimensions as well as the plantar pressure distribution of the foot pair instantly which consume less time as compared to the traditional method [17]. Ranganathan et al. developed the design method of manually masking the plantar pressure region into various anatomical zones with one outer zone. They split into zones for assigning different material parameters for printing customized split insole using 3D printing [18]. Anggoro et al. [19] used the Handy SCANN 700TM scanner for capturing digital data image and communication of medicine (DICOM) images of the patient's foot. The DICOM images available are then modified into stereolithography (STL) file format. STL data file was edited and corrected using the color map developed by VX Element and Geomagic package and prepared for 3D print the insole. Hale et al. scanned the patient's head using the 'Artec EVA', a handheld scanner, with the software Artec Studio 12 Professional. The scan data was imported into the Houdini software to keep simple geometry over interesting areas and feedback given regarding geometry placement relating to the 3D scan. This geometry is fitted and relaxed from the 3D scan surface for improving patient

comfort. Energy of deformation is mapped to surface through design optimization to generate a porous pattern. Finally, orthosis is 3D printed using Stratasys Fortus 380 mc [20].

### 3 Fused Deposition Modeling (FDM)

The 3D printing technologies commonly used for orthosis fabrication are SLS, SLA, and FDM.

In SLA (stereolithography), high-intensity light beam, i.e., laser is used to harden a soft resin in the desired dimension. The materials used in SLA are photosensitive resin in a liquid form. SLA technique print product of high resolution and smooth surface finish. However, objects made are not strong enough.

Selective Laser Sintering (SLA) uses a high-powered CO<sub>2</sub> laser to sinter powdered particles together to form 3D objects without support structures need. SLS-printed parts have isotropic properties. However, grainy surface finish, high equipment cost, and high porosity between fused powder particles are some of the limitations of SLS technology.

Fused deposition modeling (FDM) is cheap and is the generally used 3D printing technique. The polymer filaments are extruded through the nozzle in a layer-by-layer manner to print the 3D objects. The layer height, wall thickness, infill density, and printing orientation of filaments are principal processing specifications affecting the mechanical properties of the object [21]. One unique advantage of this FDM technology is that the infill density of the object can be altered which greatly reduces the weight when compared to other 3D printing technologies. Low cost, low weight, and simplicity are important benefits of the FDM process over other 3D printing technologies. Anisotropic behavior, layered appearance, poor surface quality [22] high manufacturing time, and limited varieties of thermoplastics are the main limitations of FDM [23]. FDM printers are capable of making plastics objects that have good but not great resolution. The layer thickness in FDM printing can be as low as 100  $\mu$  per layer so the object will strong but not have a good surface finish.

Zheng et al. used FDM technology to produce a porous structure with varying porosity that reduces the contact stress between the foot and insole, which is a critical factor for ulcer development. Other 3D printing technologies lack this property [24]. Hale et al. performed a case study of a patient with a neurological disorder. They used fused deposition modeling (FDM) with anisotropic structural property, for more correct simulation and orientated deposited materials being optimized as per the loading directions. The porous pattern is developed for improved ventilation and reduced material cost as well as the weight of the final orthosis which is missing in other 3D printing technologies [20]. Palousek et al. conducted the pilot study of hand orthosis using FDM technology with ABS plastic and found that the orthosis was better flexible and resistant to bending stress. The connection hooks for the metal clips are not prone to cracking or breaking [25].

Abreu de Souza et al. presented a case study based on a volunteer who needs an immobilization orthosis, and found that orthosis made through FDM technology has a mass of 53 g, having a material cost having U\$2.40. This took 45 min to get printed by the basic 3D printing model Graber i3 [26].

## 4 Materials for Orthosis Fabrication

The selection of the right material for the fabrication of orthosis is very important for its success. The materials should be biocompatible, durable, and economical. Physical properties of these orthotic materials are elasticity, hardness, density, flexibility, compressibility, resilience, etc. [27].

FDM printer is compatible with most of the thermoplastic polymers. Polylactic acid (PLA), acrylonitrile butadiene styrene (ABS), polyamide (PA), thermoplastic polyurethane (TPU), and polyethylene terephthalate glycol-modified (PETG) are commonly available polymer of which ABS and PLA are the most popular and stable materials. Abreu de Souza et al. [28] used PLA-based material for the fabrication of custom-made wrist orthosis as the material is biodegradable, commercially available, and cheap. Dal Maso et al. [29] AFO-printed ankle-foot orthosis using PLA material and suggested it have high tensile strength and Young's modulus value, though the material is anisotropic having lower toughness value. Models and prototypes are generally printed using PLA materials. ABS is usually preferred over PLA because of higher temperature resistance and higher toughness value. The orthosis made of ABS is more flexible and more resistant to bending stress. As per Palousek et al. [12], ABS filaments have good tensile and bending strength and suggest that the material properties are sufficient for the fabrication of wrist orthosis. Cotoros et al. [30] used ABS material for the rapid prototyping of corrective insole. There is a certain limitation of using ABS material as orthosis fabrication. ABS is not biocompatible material and is a toxic smell that is not good for medical applications. Wang et al. [31] suggested PETG filament instead of PLA and ABS because of like moisture-bearing and more mechanical strength for customized insole fabrication. In his second experiment, Salles et al. [32] conducted the test using TPU material and suggested that the use and variability of their geometries favored the modification of shock-absorption properties of the personalized insoles. Mogan et al. [33] printed the specimens by varying infill pattern percentages in TPU materials of two different make Filaflex and Ninjaflex. Hardness, tensile, and flexure test were performed on these specimens. They observed that tensile strength and hardness for infill pattern of Filaflex are higher compared to the Ninjaflex and based on result suggested that infill percentage of material could affect the hardness, tensile as well as flexural property. TPU materials can be suggested for applications in fabrication of orthotics insoles where flexibility and shock-absorbing are the desired properties.

From the literature review of polymers, it is observed that not a single polymer fulfills the desired mechanical properties for orthosis fabrication which includes

properties like biocompatibility, flexibility, and good tensile and bending strength and there is a need to developed composite filaments by adding certain materials into a polymer matrix, as they offer desired mechanical properties. Tao et al. [34] prepared the TPU/PLA composite to compare with PLA filament. They found that the composite with 25% TPU exhibited better toughness value than PLA filament without compromising the tensile strength. The insole was printed with TPU/PLA composite with the same tensile strength and better flexibility. Tekinalp et al. [35] prepared a composite by reinforcing the 3.5 mm carbon fiber by 10, 20, 30, and 40% weight in ABS polymer matrix and observed that there is an increase in the tensile strength (up to 115%) and modulus (up to 700%) in the composite. Another experiment was carried out by Dul et al. [36] on the ABS matrix reinforced with graphene for 2, 4, and 8% weight fraction. Graphene-reinforced composites have increased the value of elastic modulus and dynamic storage modulus; however, the maximum tensile strength and elongation at break have decreased. Rimasauskas et al. [37] embedded 6.6 volume % continuous carbon fiber (CF) and 6.1 volume % jute fiber in the PLA polymer matrix and studied the reinforcement effect. PLA matrix reinforcement with 9.5 weight % continuous aramid fiber (8.6 volume %) has improved strength and modulus [38].

## 5 Important Conclusions

A comprehensive review of design methods and selection of materials for orthosis fabrication was carried out in this article. Different design methods for the 3D model of orthosis are reviewed. 3D scanning of the patient's affected part in transferring scan data to design modeler software, simulation, and optimization all are discussed in detail. However, the studies clearly showed that there is a need for single modeling software that should incorporate all designing steps starting from scanning to simulation and preparing for printing the model. Therefore, research should be carried out in this area. Materials available for the FDM technique are studied in this paper. Polymers available for fabrication of orthosis have limitations and therefore, further studies are needed to develop the polymers with desired properties suitable for an orthosis. Polymer matrix composite showed better mechanical properties. Further research should be carried out for developing environment-friendly composite filaments, such as jute fiber, pineapple extract, and animal extract which could be assessed for a sustainable future.

## References





1. Chen, R.K., Jin, Y., Wensman, J., Shih, A.: Additive manufacturing of custom orthosis and prostheses—a review. *Addit. Manuf.* **12**, 77–89 (2016)
2. Kate, J.T., Smit, G., Breedveld, P.: 3D-printed upper limb prostheses: a review. *Disabil. Rehabil. Assistive Technol.* **12**(3), 300–314 (2017)

3. Fisk, J.R., DeMuth, S., Campbell, J., DiBello, T., Esquenazi, A., Lin, R.S.: Suggested guidelines for the prescription of orthotic services, device delivery, education and follow-up care: a multidisciplinary whitepaper. *Mil. Med.* **181**, 11–17 (2016)
4. Priority assistive products list. Geneva, World Health Organization. [http://www.who.int/phi/implementation/assistive\\_technology/global\\_survey-apl/en/](http://www.who.int/phi/implementation/assistive_technology/global_survey-apl/en/). Accessed 30 Aug. 2016
5. General terms for external limb prostheses and external orthoses. Geneva, International Organization for Standardization, ISO 8549-1, Prosthetics and orthotics, Vocabulary, Part 1 (1989)
6. Terms relating to external limb prostheses and wearers of these prostheses. Geneva, International Organization for Standardization, ISO 8549-2, Prosthetics and orthotics, Vocabulary, Part 2 (1989)
7. Rietmacher, G.: Report of a consensus conference on appropriate prosthetic technology for developing countries. In: Copenhagen: international society for prosthetics and orthotics, Hanoi, Vietnam, 3–8 April (2006)
8. Shurr, D.G., Michael, J.W., Cook, T.M.: Prosthetics and orthotics. Prentice Hall (2002)
9. Kim, H., Jeong, S.: Case study: hybrid model for the customized wrist orthosis using 3D printing. *J. Mech. Sci. Technol.* **29**(12), 5151–5156 (2015)
10. Hellstrand Tang, U., Zügner, R., Lisovskaja, V., Karlsson, J., Hagberg, K., Tranberg, R.: Comparison of plantar pressure in three types of insole given to patients with diabetes at risk of developing foot ulcers—a two-year, randomized trial. *J. Clin. Transl. Endocrinol.* **1**, 121–132 (2014)
11. Meen, T.H.: Institute of Electrical and Electronics Engineers. Tainan Section. Sensors Council Chapter, International Institute of Knowledge Innovation and Invention, and Institute of Electrical and Electronics Engineers.. In: Knowledge innovation and invention: 1st IEEE international conference on knowledge innovation and invention (IEEE ICKII 2018): Jeju Island, South Korea, July 23–27 (2018)
12. Caravaggi, P., Giangrande, A., Lullini, G., Padula, G., Berti, L., Leardini, A.: In shoe pressure measurements during different motor tasks while wearing safety shoes: the effect of custom made insoles vs. prefabricated and off-the-shelf. *Gait. Posture* **50**, 232–238 (2016). <https://doi.org/10.1016/j.gaitpost.2016.09.013>
13. Khodaei, B., Saedi, H., Jalali, M., Farzadi, M., Norouzi, E.: Comparison of plantar pressure distribution in CAD–CAM and prefabricated foot orthoses in patients with flexible flatfeet. *Foot* (2017). <https://doi.org/10.1016/j.foot.2017.07.002>
14. Surmen, K., Ortes, F., Arslan, Y.Z.: Design and production of subject specific insole using reverse engineering and 3D printing technology. Available [Online] [www.ijesi.org](http://www.ijesi.org)
15. Algar, D., Guldberg, A.: Insole modeling using Kinect 3D sensors
16. Davia, M., Germani, M., Mandolini, M., Mengoni, M., Montiel, E., Raffaelli, R.: Shoes customization design tools for the ‘diabetic foot’. *Comput. Aided. Des. Appl.* **8**(5), 693–711 (2011). <https://doi.org/10.3722/cadaps.2010.693-711>
17. Peixoto, J., Flores, P., Souto, A.P.: A new approach to implement a customized anatomic insole in orthopaedic footwear of lower limb orthosis. In: IOP conference series: materials science and engineering, vol. 254, no. 23 (2017). <https://doi.org/10.1088/1757-899x/254/23/232006>
18. Ranganathan, R., Ganesan, S.: Design and development of customised split insole using additive manufacturing technique. *Int. J. Rapid Manuf.* **7**(4), 295 (2018). <https://doi.org/10.1504/ijrapidm.2018.10016859>
19. Anggoro, P.W., Tauviquirrahman, M., Jamari, J., Bayuseno, A.P., Bawono, B., Avelina, M.M.: Computer-aided reverse engineering system in the design and production of orthotic insole shoes for patients with diabetes. *Cogent Eng.* **5**(1) (2018). <https://doi.org/10.1080/23311916.2018.1470916>
20. Hale, L., Linley, E., Kalaskar, D.M.: A digital workflow for design and fabrication of bespoke orthoses using 3D scanning and 3D printing, a patient-based case study. *Sci. Rep.* **10**(1) (2020). <https://doi.org/10.1038/s41598-020-639371>

21. Mohamed, A., Masood, S.H., Bhowmik, J.L.: Optimization of fused deposition modeling process parameters: a review of current research and future prospects. *Adv. Manuf.* **3**(1), 42–53 (2015)
22. Chohan, J.S., Singh, R., Boparai, K.S., Penna, R., Fraternali, F.: Dimensional accuracy analysis of coupled fused deposition modeling and vapour smoothing operations for biomedical applications. *Compos. B* **117**, 138–149 (2017)
23. Wang, X., Jiang, M., Zhou, Z., Gou, J., Hui, D.: 3D printing of polymer matrix composites: a review and prospective. *Compos. B* **110**, 442–458 (2017)
24. Ma, Z., et al.: Design and 3D printing of adjustable modulus porous structures for customized diabetic foot insoles. *Int. J. Light. Mater. Manuf.* **2**(1), 57–63 (2019). <https://doi.org/10.1016/j.ijlmm.2018.10.003>
25. Palousek, D., Rosicky, J., Koutny, D., Stoklásek, P., Navrat, T.: Pilot study of the wrist orthosis design process. *Rapid Prototyp. J.* **20**(1), 27–32 (2014). <https://doi.org/10.1108/RPJ-03-2012-0027>
26. Abreu de Souza, M., Schmitz, C., Marega Pinhel, M., Palma Setti, J., Nohama, P.: Proposal of custom made wrist orthoses based on 3D modelling and 3D printing (2017)
27. Vaish, A., Vaish, R.: 3D printing and its applications in orthopedics. *J. Clin. Orthop. Trauma* **9**, 74–75 (2018)
28. Abreu de Souza, M., Schmitz, C., Marega Pinhel, M., Palma Setti, J., Nohama, P.: Proposal of custom made wrist orthoses based on 3D modelling and 3D printing (2017)
29. Dal Maso, A., Cosmi, F.: ScienceDirect 3D-printed ankle-foot orthosis: a design method. Available [www.sciencedirect.com](http://www.sciencedirect.com) (2019)
30. Cotoros, D., Baritz, M.: Implementing rapid prototyping technologies for corrective insoles (2012)
31. Wang, J.C., Dommati, H., Cheng, J.: A Turnkey manufacturing solution for customized insoles using material extrusion process. In: 3D printing and additive manufacturing technologies. Springer, Singapore, pp. 203–216 (2018)
32. Salles, A.S., Gyi, D.E.: Delivering personalised insoles to the high street using additive manufacturing. *Int. J. Comput. Integr. Manuf.* **26**(5), 386–400 (2013). <https://doi.org/10.1080/0951192X.2012.717721>
33. Mogan, Y., Tun, U., Onn Malaysia, H., Periyasamy, R.: Thermoplastic elastomer infill pattern impact on mechanical properties 3D printed customized orthotic insole. Development of Smart injection Molding Machine System View project Flexible filament feasibility study View project Mohd Halim Irwan Ibrahim (2016)
34. Tao, Y., Shao, J., Li, P., Shi, S.Q.: Application of a thermoplastic polyurethane/polylactic acid composite filament for 3D-printed personalized orthosis. *Materiali in Tehnologije* **53**(1), 71–76 (2019). <https://doi.org/10.17222/MIT.2018.180>
35. Tekinalp, H., Kunc, V., Velaz-Garcia, G.M., Duty, C.E., Love, L.J., Naskar, A.K., Blue, C. A., Ozcan, S.: Highly oriented carbon fiber polymer composites via additive manufacturing. *Compos. Sci. Technol.* **105**, 144–150 (2014)
36. Dul, S., Fambri, L., Pegoretti, A.: Fused deposition modelling with ABS–graphene nanocomposites. *Compos. A Appl. Sci. Manuf.* **85**, 181–191 (2016). <https://doi.org/10.1016/j.compositesa.2016.03.013>
37. Matsuzaki, R., Ueda, M., Namiki, M., Jeong, T.K., Asahara, H., Horiguchi, K., Nakamura, T., Todoroki, A., Hirano, Y.: Three-dimensional printing of continuous-fiber composites by in-nozzle impregnation. *Sci. Rep.* **6**, 1–7 (2016). <https://doi.org/10.1038/srep23058>
38. Bettini, P., Alitta, G., Sala, G., Di Landro, L.: Fused deposition technique for continuous fiber reinforced thermoplastic. *J. Mater. Eng. Perform.* **26**, 843–848 (2017). <https://doi.org/10.1007/s11665-016-2459-8>

# Experimental Investigation During Machining of P20 Tool Steel Using EDM



Manoj Kumar , Ankit D. Oza , Mehul Prajapati ,  
and Gaurang Joshi 

**Abstract** Machining hard material demands precision, which is the main reason for the EDM process suitability for such applications. The EDM process is most flexible in its operation with significant control over the machined surface that is the prime need of engineering components. This article presents the machining performance of P20 tool steel, studied by commercially available EDM machine. The hybrid Taguchi-ANOVA technique is used during planning and analyzing the experimental results. The machining characteristics like MRR and EWR are studied using changing the input factors such as discharge current, pulse-on and pulse-off time. The experiments conclude that the higher tool wear was observed at higher current and pulse-off-timings. The current is the significant parameter for the response factor contributing 65.58% and 92.12% for MRR and EWR, respectively. Moreover, an attempt was made to investigate the prospect of forecasting the MRR and EWR for machining of P20 tool steel to establish a pragmatic relationship among input factors. The optimized set of input parameters for MRR and TWR are A3B2C2 and A1B1C2, respectively.

**Keywords** EDM • Tool steel • Optimization • MRR • Machining • Current

---

M. Kumar (✉)

Department of Production and Industrial Engineering, Punjab Engineering College (Deemed to be University), Chandigarh 160012, India

A. D. Oza

Department of Engineering and Physical Sciences, The University for Innovation, Gandhinagar 382007, India

M. Prajapati

Department of Production Engineering, D. J. Sanghvi College of Engineering, Mumbai 400056, India

G. Joshi

Department of Mechanical Engineering, Marwadi University, Rajkot 360003, India



## 1 Introduction

In recent times, EDM and its variants emerge as a practical, cost-effective solution to machine hard-to-machine materials. Electric discharge machining is an advanced machining technique utilized to machine mainly electrically active material regardless of its melting point, strength, etc. It can machine almost all types of a conductive materials such as metals, alloys, superalloys and composites. Steel is one of the most common engineering materials used in industries. Higher-strength and hardened steel processing such as P20 tool steel to be useful industrial products have a significant challenge. Several techniques are available to machine P20 tool steel material [1–3].

P20 tool steel has better working properties than the conventional steel material as it has compositional elements like chromium and molybdenum. P20 tool steel material is extensively utilized in the precise die and molding applications [4, 5]. Few researchers studied various machining parameters such as discharge current ( $I_p$ ), applied voltage, pulse-on-time ( $T_{on}$ ) and pulse-off-time ( $T_{off}$ ), for machining performance. For EN31 tool steel, the machining parameters were identified with the L27 OA (as per Taguchi orthogonal array) and observed that  $I_p$  played a vital role on material removal rate (MRR) and noticed that with increases in  $I_p$  and  $T_{off}$  parameters, MRR increases [6]. The integrated approach for simulation and modeling and the FEM and artificial neural network (ANN) has been carried for P20 tool steel, reduced the crater size and tool wear rate and improved the MRR [7]. Another fruitful study for 40CrMnNiMo864 tool steel (AISI P20) through EDM was conducted and analyzed the surface quality and machining nature. With increasing  $I_p$  and  $T_{on}$ , the surface roughness increases. Further, electrode wear was observed during the process [8]. The machining stability performance analyzed for AISI P20 material. It concludes that minimum surface roughness was observed with the negative polarity of the used tool due to the dissimilar material melting performance of the anode and cathode for a particular discharge [9].

The performance of P20 steel is enhanced through boronizing by increasing the resistance to corrosion, cracks and fatigue during operations by increasing its hardness [10]. The P20 tool material is an essential clad material. Chen et al. [11] studied the residual stress in laser cladding on pre-hardened wrought P20 substrate with P20 tool steel material. The study concludes the martensite formation with retained austenite and refined dendritic structure. Vardhan et al. [12] improved the process governing factors during conventional CNC milling operation of P20 steel with response surface methodology and Taguchi methodology. For MRR response, the cutting depth has a maximum contribution among all input parameters. Zelmann et al. [13] investigated the machining performance during the drilling of AISI P20 steel using carbide tools subjected to reduce cutting fluid conditions. The problem of chip removal is observed during drilling leads to a high chip-packing factor. Mukoti et al. [14] optimized machining parameters for CNC milling of P20 steel using the NSGA-II technique. The influence of deep cryo-action considerably improves the tool (WC) life by reducing the tool wear rate.



In the literature as mentioned above, various optimization approaches are highlighted. Few investigations have been carried out for AISI P20 material, but limited work is available on MRR and tool wear rate. Therefore, in the proposed study, the Taguchi orthogonal array is used to identify the machining parameters for improving the process performance.

## 2 Materials and Method

The P20 tool steel is purchased from Purohit Steel India Pvt. Ltd. Thane, India. The P20 tool steel material is used as workpiece material owing to its carbon content. It is widely used in various engineering applications such as precision molds, dies and wears strip. The copper electrode was selected as tool material due to its better sparking capabilities under potential difference. The Ipol Spark erosion oil 350 was used as a dielectric medium during experiments. The detailed properties and composition are presented in Tables 1 and 2, respectively [11].

The experiments were conducted on the commercially available double-headed EDM as presented in Fig. 1. Before performing the experiments, the tool and fixture positioning is adjusted with a dial indicator to ensure the experiments free from any error(s). Firstly, the machinability of tool steel is checked with pilot experiments. Based on the trial experiments and machine constraints, the governing factors discharge current, pulse-on-time and pulse-off time were selected for the study. The details of the input parameters are shown in Table 3, with level values.

The experiments were conducted using an L9 orthogonal array and ANOVA tables using a MINITAB-17 software package [15–17]. The L9 OA is adopted following three input parameters selected for the study. In this method, only nine experiments have to perform instead of 27 experiments to examine the experimental data. The MRR and electrode wear rate (EWR) are selected as response parameters. The values chosen for current were 4, 5 and 6 (Amp), and based on the CNC program, the corresponding pulse-on and pulse-off durations are also selected. The reason for choosing a range of 4–6 (Amp) for current is that because it contains 6 (Amp) for roughing and 4 (Amp) for finishing, which is the ideal and most common setting. Based on these signal levels, the parameters’ values were divided into nine readings based on array arrangement.

**Table 1** Properties of P20 tool steel

Properties	Metric
Density	7861 kg/m <sup>3</sup>
Hardness, Brinell (typical)	300
Tensile strength, yield	827–862 MPa
Elastic modulus	190–210 GPa
Thermal conductivity	41.5 W/m/°K
Thermal expansion	12.8 × 10 <sup>-6</sup> /°C at 20–425 °C

**Table 2** Chemical composition of P20 tool steel

Element	C	Mn	Si	Cr	Mo	Fe
Percentage	0.28–0.40	0.60–1.00	0.20–0.80	1.40–2.00	0.30–0.55	Balance

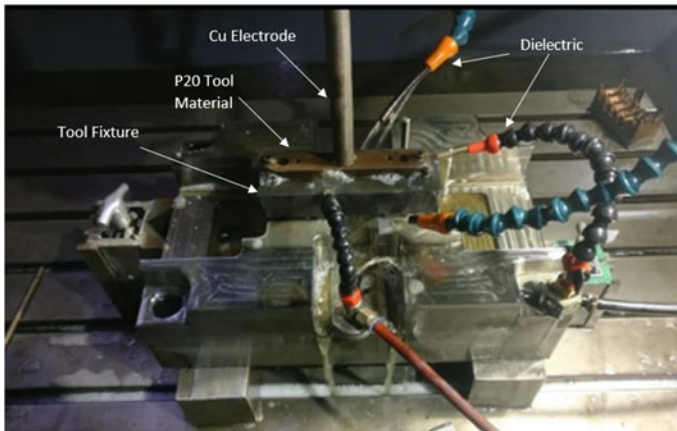


**Fig. 1** Experimental setup of EDM machine

**Table 3** Readings of each parameter based on signal values

Input parameters		Level 1	Level 2	Level 3
Discharge current ( <i>I</i> )	A	4	5	6
Pulse-on-time ( <i>T</i> -on)	B	80	100	120
Pulse-off-time ( <i>T</i> -off)	C	40	50	60

The MRR is evaluated using the weight change method, as shown in Eq. (1) [18]. The weight of samples was taken before and after machining utilizing a digital weighing instrument having the accuracy of 0.1 mg. Similarly, electrode wear rate is calculated using Eq. (2) [19].

$$MRR = \frac{W_b - W_a}{d \times t} \tag{1}$$

where  $W_b$ —P20 steel weight afore machining (g);  $W_a$ —P20 steel weight after machining (g);  $d$ —density of P20 Tool steel (g/cc);  $t$ —machining duration (mins).

$$EWR = \frac{E_b - E_a}{d \times t} \tag{2}$$

where  $E_b$ —electrode weight afore machining (g);  $E_a$ —electrode weight after machining (g);  $d$ —density of electrode (g/cc);  $t$ —machining duration (mins).

### 3 Results and Discussion

The Taguchi L9 experiments were conducted considering three input factors at three levels, as presented in Table 4. The *S/N* ratio was calculated considering different desirability criteria for both output factors. For MRR, higher is better, and for surface roughness, lower is better was selected. The *S/N* ratio is evaluated using Eq. (3). The *S/N* ratio value after calculation for the L<sub>9</sub> orthogonal array is presented in Table 4.

$$(S/N) = -10 \times \log (\text{mean square deviation}) \tag{3}$$

The ANOVA table is generated to evaluate individual input factors’ influence on output parameters, i.e., MRR and EWR using a 95% confidence interval, as shown in Tables 5 and 6. From Tables 5 and 6, it is clear that the material removal for both MRR and EWR is greatly affected by the discharge current. In contrast, *T*-off has a minimum effect on material removal rate among all input parameters.

The material removal is evaluated by Eq. (1). The material removal rate highly depends on the discharge energy transferred to workpiece material during machining. The energy transferred is directly related to the current applied across the electrode and the duration (*T*-on) to which spark occurs. Figure 2 depicts that with an increase in current, the MRR also increases as higher current and *T*-on enhances the transferred energy responsible for material removal. However, material removal is considerably inversely varying with *T*-off time, i.e., duration to which the spark is not active across the electrode, as shown in Fig. 2 [20–22].

The tool wear rate is evaluated by Eq. (2). The tool wears due to intense heat generation across the tool electrode’s tip due to the rapid flow of electrons caused by the immense potential difference across electrodes. The potential difference is influenced by current and *T*-on duration, as both increases the tool wear rate. From Fig. 3, it is evident that with an increase in current and *T*-on duration, the TWR also

**Table 4** Response values of MRR and EWR

Exp. no.	Current ( <i>I</i> )	Pulse-on time ( <i>T</i> <sub>on</sub> )	Pulse-off time ( <i>T</i> <sub>off</sub> )	MRR	<i>S/N</i> ratio	EWR	<i>S/N</i> ratio
1	4	80	40	2.11	6.4856	2.05	-6.2351
2	4	100	50	2.72	8.6914	2.64	-8.4321
3	4	120	60	3.24	10.2109	3.13	-9.9109
4	5	80	50	4.50	13.0643	4.85	-13.7148
5	5	100	60	5.18	14.2866	5.58	-14.9327
6	5	120	40	2.92	9.3077	9.13	-19.2094
7	6	80	60	3.22	10.1571	11.16	-20.9533
8	6	100	40	9.60	19.6454	8.58	-18.6697
9	6	120	50	6.66	16.4695	10.30	-20.2567

**Table 5** ANOVA table for MRR

Source	DOF	Adj SS	Adj MS	F-value	% age contribution
<i>I</i>	2	22.005	11.0024	1.81	65.58
<i>T</i> -on	2	9.963	4.9817	0.82	29.71
<i>T</i> -off	2	1.613	0.8067	0.13	4.71
Error	2	12.146	6.0728		
Total	8	45.727			100

**Table 6** ANOVA table for EWR

Source	DF	Adj SS	Adj MS	F-value	% age contribution
<i>I</i>	2	82.3763	41.1881	10.99	92.12
<i>T</i> -on	2	6.1128	3.0564	0.82	6.87
<i>T</i> -off	2	0.9133	0.4566	0.12	1.01
Error	2	7.4949	3.7474		
Total	8	96.8972			100

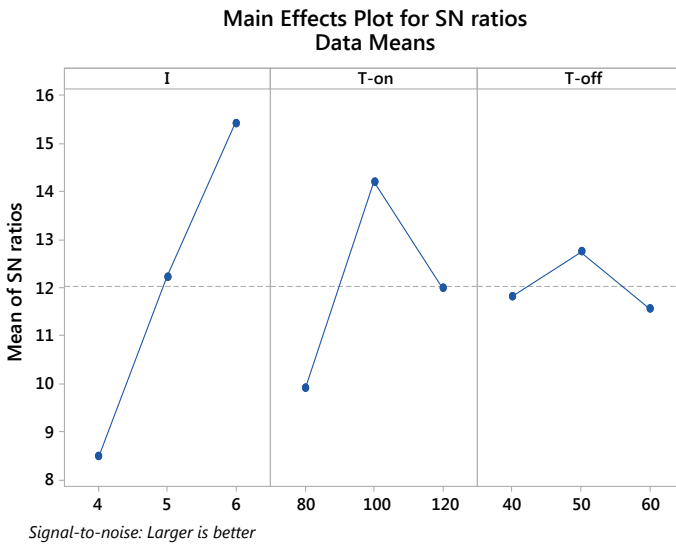


**Fig. 2** S/N ratio plot for MRR

increases. However, with an increase in *T*-off time, the EWR is first slightly decreased, after that increases as initially sufficient time is required to proper flushing, which lowers the temperature across the machining zone [23–25].

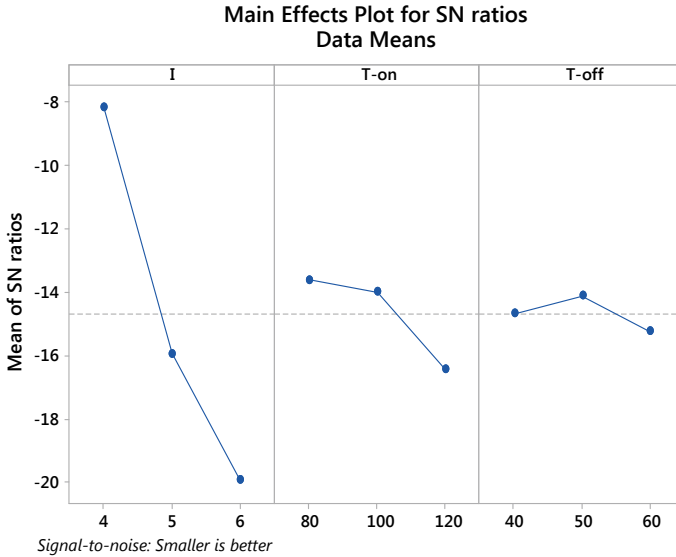


Fig. 3 S/N ratio plot for EWR

### 4 Conclusion

In the present study, the machining characteristics of P20 tool steel are studied using commercially available EDM. The discharge current, pulse-on, and pulse-off duration factors were utilized to investigate the MRR and EWR. The hybrid Taguchi-ANOVA approach is being used in designing and analyzing experimental data. The following observations were made based on experimentations.

1. The copper tool can effectively machine the P20 tool steel material.
2. High input energy available across the electrodes, mainly accountable for material removal from both the electrodes, i.e., tool and workpiece material.
3. High MRR is obtained when higher-end parameters are used for machining. The circuit current is mainly accountable for material removal from a workpiece with a 65% contribution followed by *T-on* and *T-off* time.
4. Lower tool wear rate is obtained when lower-end parameters were selected. The circuit current is mainly accountable for material removal from a workpiece with a 92% contribution followed by *T-on* and *T-off* time.
5. The optimized set of input factors for MRR and TWR are A3B2C2 and A1B1C2, respectively.
6. The hard-to-machine P20 tool steel can be machined with the EDM process by suitably selecting the combination of input parameters for lower TWR and higher MRR.

## References

1. Jain, V.K., Sidpara, A., Ravisankar, M., Das, M.: Micromanufacturing: an introduction. *Micromanuf. Process.*, 3–37 (2016)
2. Jain, V.K., Balasubramaniam, R., Mote, R.G., Das, M., Sharma, A., Kumar, A., et al.: Micromachining: an overview (part I). *J. Micromanuf. (Part I)*:251659841989582 (2020)
3. Singh, J., Vaishya, R., Kumar, M.: Fabrication of micro features on quartz glass using developed WECDM setup. *ARPN J. Eng. Appl. Sci.* **14**(3), 725–731 (2019)
4. Amorim, F.L., Weingaertner, W.L.: The behavior of graphite and copper electrodes on the finish die-sinking electrical discharge machining (EDM) of AISI P20 tool steel. *J. Brazilian Soc. Mech. Sci. Eng.* **29**(4), 366–371 (2007)
5. Kapil, S., Legesse, F., Negi, S., Karunakaran, K.P., Bag, S.: Hybrid layered manufacturing of a bimetallic injection mold of P20 tool steel and mild steel with conformal cooling channels. *Prog. Addit. Manuf.* **5**(2), 183–198 (2020)
6. Das, M.K., Kumar, K., Barman, T.K., Sahoo, P.: Optimization of material removal rate in EDM using Taguchi method. *Adv. Mater. Res.* **626**, 270–274 (2013)
7. Joshi, S.N., Pande, S.S.: Development of an intelligent process model for EDM. *Int. J. Adv. Manuf. Technol.* **45**(3–4), 300–317 (2009)
8. Kiyak, M., Çakir, O.: Examination of machining parameters on surface roughness in EDM of tool steel. *J. Mater. Process. Technol.* **191**(1–3), 141–144 (2007)
9. Amorim, F.L., Weingaertner, W.L.: The influence of generator actuation mode and process parameters on the performance of finish EDM of a tool steel **166**, 411–416 (2005)
10. Uslu, I., Comert, H., Ipek, M., Ozdemir, O., Bindal, C.: Evaluation of borides formed on AISI P20 steel. *Mater. Des.* **28**(1), 55–61 (2007)
11. Chen, J.Y., Conlon, K., Xue, L., Rogge, R.: Experimental study of residual stresses in laser clad AISI P20 tool steel on pre-hardened wrought P20 substrate. *Mater. Sci. Eng. A* **527**(27–28), 7265–7273 (2010)
12. Vishnu Vardhan, M., Sankaraiah, G., Yohan, M., Jeevan, Rao H.: Optimization of parameters in CNC milling of P20 steel using Response Surface methodology and Taguchi Method. *Mater. Today Proc.* **4**(8), 9163–9169 (2017)
13. Zeilmann, R.P., Nicola, G.L., Vacaro, T., Teixeira, C.R., Heiler, R.: Implications of the reduction of cutting fluid in drilling AISI P20 steel with carbide tools. *Int. J. Adv. Manuf. Technol.* **58**(5–8), 431–441 (2012)
14. Mukkoti, V.V., Mohanty, C.P., Gandla, S., Sarkar, P., Srinivasa Rao, P., Dhanraj, B.: Optimization of process parameters in CNC milling of P20 steel by cryo-treated tungsten carbide tools using NSGA-II. *Prod. Manuf. Res.* **8**(1), 1–22 (2020)
15. Oza, A.D., Kumar, A., Badheka, V., Arora, A.: Traveling wire electrochemical discharge machining (TW-ECDM) of quartz using zinc coated brass wire: investigations on material removal rate and kerf width characteristics. *Silicon* **11**(6), 2873–2884 (2019)
16. Kumar, M., Vaishya, R.O., Oza, A.D., Suri, N.M.: Experimental investigation of wire-electrochemical discharge machining (WECDM) performance characteristics for quartz material. *Silicon* **12**(9), 2211–2220 (2020). <https://doi.org/10.1007/s12633-019-00309-z>
17. Oza, A.D., Kumar, A., Badheka, V.: Improving quartz micro-machining performance by magnetohydrodynamic and zinc-coated assisted traveling wire-electrochemical discharge machining process. *Mater. Today Proc.* **28**, 970–976 (2020)
18. Kumar, M., Vaishya, R.O., Suri, N.M.: Machinability study of zirconia material by micro-ECDM. In: Vishal, S., Sharma, Uday, S., Dixit, Knut Sørby, Arvind Bhardwaj, R.T. (eds) *Manufacturing engineering*. Springer, Singapore, pp. 195–209 (2020)
19. Kumar, M., Vaishya, R.O., Suri, N.M., Manna, A.: An experimental investigation of surface characterization for zirconia ceramic using electrochemical discharge machining process. *Arab. J. Sci. Eng.* (2020). <https://doi.org/10.1007/s13369-020-05059-4>

20. D'Urso, G., Maccarini, G., Ravasio, C.: Process performance of micro-EDM drilling of stainless steel. *Int. J. Adv. Manuf. Technol.* **72**(9–12), 1287–1298 (2014). <https://doi.org/10.1007/s00170-014-5739-1>
21. Yilmaz, O., Okka, M.A.: Effect of single and multi-channel electrodes application on EDM fast hole drilling performance. *Int. J. Adv. Manuf. Technol.* **51**(1–4), 185–194 (2020). <https://doi.org/10.1007/s00170-010-2625-3>
22. Oza, A.D., Kumar, A., Badheka, V., Nema, A., Kumar, M.: Quartz micro-machining using wire electrochemical spark machining process. In: Dave, H.K., Nedelcu, D. (eds) *Advances in manufacturing processes. Lecture Notes in Mechanical Engineering*. Springer, Singapore (2021). [https://doi.org/10.1007/978-981-15-9117-4\\_8](https://doi.org/10.1007/978-981-15-9117-4_8)
23. Yadav, S., Verma, R.K.: Multi criteria optimization approaches in electric discharge machining. *Mater. Today Proc.* **18**, 4243–4252 (2019). <https://doi.org/10.1016/j.matpr.2019.07.382>
24. Kumar, U.A., Laxminarayana, P.: Optimization of electrode tool wear in micro holes machining by die sinker EDM using Taguchi approach. *Mater. Today Proc.* **5**(1), 1824–1831 (2018). <https://doi.org/10.1016/j.matpr.2017.11.281>
25. Singh, A.K., Patowari, P.K., Chandrasekaran, M.: Experimental study on drilling micro-hole through micro-EDM and optimization of multiple performance characteristics. *J. Brazilian Soc. Mech. Sci. Eng.* **42**, 506 (2020). <https://doi.org/10.1007/s40430-020-02595-w>

# Techno Economic and Life Cycle Assessment of 1 MW Solar Parabolic Trough System for Udaipur Zone



Neelam Rathore and Vijayendra Singh Sankhla

**Abstract** Owing to increasing energy demand and population, solar energy has become prominent solution to fulfill the future energy needs. Solar photovoltaic (SPV) technology is an efficient option to generate electricity and mitigate climate change. Building India as worldwide ambassador in generating power using solar energy is the target of national solar mission. Either solar photovoltaic (SPV) or solar thermal technology (STE) can be used for transmitting this generated power to grid. But solar thermal technologies are less studied compared to SPV, especially their designing, economic analysis, performance analysis and life cycle assessment (LCA). In spite of huge availability of solar thermal potential, STE are not much popular due to technical, market and environmental challenges. Therefore, in this study 1 MW solar parabolic trough system (SPT) is designed along with conducting economic assessment and LCA. Main aim of this study is to determine environmental impact of designed power plant especially production process, hence calculating cumulative energy demand, energy payback time and greenhouse gas emissions. For 25 years of plant life, LCOE, IRR and payback period are determined. LCOE of the solar power plant at 10% discount rate came out to be Rs 6.47/kWh. For solar parabolic trough systems, internal rate of return is 28% while the payback period is 3.91 years of the project. The use of solar energy for meeting the electricity will eliminate substantial use of fossil fuel and bring 277.16 tons of CO<sub>2</sub> emission reduction into the environment. This work on designing, economic evaluation and LCA will surely help in enhancing the development.

**Keywords** Life cycle assessment · Parabolic trough system · LCOE · Therminol VP-1

---

N. Rathore (✉)  
DREE, CTAE, Udaipur, India

V. S. Sankhla  
DME, GITS, Udaipur, India



## 1 Introduction

As it is known that government is emphasizing more on generating power using solar energy by putting up a major target of 100 GW electric power from solar installations [1]. Solar thermal energy (STE) can be implemented in India as solar resources and large wasteland areas are widely available in the country. As far as present situation is concerned, the total installed capacity for electricity generation in the country has increased to 365.96 GW as on 31.12.2019. Of total installed capacity, thermal power plants contribute about 63.40%, and renewable energy sources (small hydro projects, biomass gasifiers, biomass power, solar energy and wind energy) contribute share of about for 21.9%. The country's solar installed capacity reached 29 GW as of December 31, 2019 [2].

Solar energy has the highest potential in energy generation among all renewable technologies [3, 4–6]. Solar technologies can be classified as solar PV and solar concentrating technologies (CSP). Although SPV is commonly used technology for harnessing solar energy from both energy security and environmental point of view, at the same time CSP technologies can contribute more in reducing CO<sub>2</sub> emission at higher pace by supplying bulk electricity in coming years [1]. This CSP technology can provide vital alternatives in addressing global energy crisis within short span of time. Indian tropical location indicated India to be an ideal country for operation of concentrating solar plants (CSP). IEA reported CSP to be cost-effective technology which will reduce CO<sub>2</sub> emissions to half by 2050 and further it also concluded that CSP could produce 2200 TWh annually by 2050 [7]. From last many years, much research had been done in utilizing solar energy using concentrating solar power plants [8] emphasized on finding scope of utilizing solar energy in India, whereas potential of solar energy utilization was found by [9]. Many studies show that solar energy has enormous potential to reduce the gap between demand and supply; but further research is required related to levelized cost of electricity and life cycle assessment for solar concentrating power plants. Among all CSP technology, parabolic trough collector (PTC) is well known, cost effective and has been most developed. India lacks information on costs, environmental assessment and techno economic analysis of parabolic trough collector technology (PTC). Further research and mold are necessary for greater exploitation of this technology. One of the city Udaipur (Rajasthan) being best in India having solar radiation of 6–7 kWh/m<sup>2</sup>/day with approximately 300 sunny days per year was selected for installation [10]. Rajasthan receives DNI of 5.69 kWh/m<sup>2</sup>/day [10]. Therefore, this paper presents the technical, economic and life cycle analysis of designed 1 MW parabolic trough collector (PTC) in Rajasthan location.

## 2 Methodology and Goals

### 2.1 Designed SPT System

Parabolic trough collectors concentrate direct normal irradiation on an absorber tube positioned along their focal line. A steel structure holds parabolic mirrors and tracking system tracks the sun by rotating them around. Typically, four collector assemblies are connected to one loop. A complete collector field consists of up to hundreds of such loops. Therminol is pumped through the individual loops and is heated as it flows through loop by about 400 °C. Further REC and CDM are also calculated for assessing reduced emissions.

Designed solar parabolic trough (SPT) system for 1 MW capacity is shown in Fig. 1 and Table 1. Characteristics of designed 1 MW SPT system are shown in Table 1 in which Therminol VP-1 is used as heat transfer fluid (HTF) due to its superior thermal stability [11]. HTF is pumped to steam generator after heating it to 400 °C. This steam generator is connected to steam turbine. High-temperature tank stores the fluid heated by PTC. This heated fluid is then pumped to heat exchanger where high-temperature steam is generated. This steam is directed to steam turbine which generates electrical power. The steam exhausted from turbine is sent to condenser which is condensed there and is recirculated again for generating steam. Calculated overall efficiency of designed SPT plant is 22.22%.

Heat transfer fluid (HTF), Therminol, is circulated through linear receiver which is again returned to heat exchangers. To absorb maximum solar radiation, receiver is placed at center of reflector. Series of heat exchangers transfer this heat to fluid (water), where high-pressure superheated steam is generated. Turbine uses this superheated steam to produce electricity. Like this water is reused and regenerated in closed loop. PTC uses tracking system to track the sun from east to west. Properties of Therminol VP-1 are shown in Table 2.

Modification in simple rankine cycle is reheating and superheating rankine cycle which was employed in designing of 1 MW PTC. In simple rankine cycle, steam is

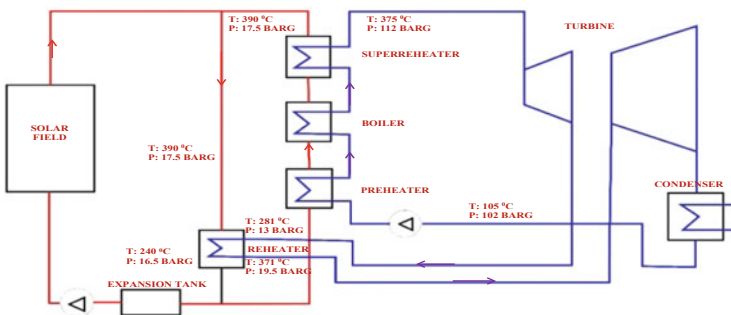


Fig. 1 Designed solar parabolic trough system

**Table 1** Characteristics of the designed solar parabolic trough (SPT) system

Technology type	Solar parabolic trough power plant
Installed capacity	1 MW
Technical lifetime	25 years
Monthly average DNI for Udaipur	5.69 kWh/m <sup>2</sup> /day
Net efficiency	22.22%
Calculated aperture area	7452 m <sup>2</sup>
Number of solar collector assembly (SCA) loops	4 loops
Number of calculated solar collector assembly	16
Number of solar collector elements	128
Number of receiver tubes	384
Minimum distance between two SCA rows	12 m
Required land for solar field	6.3 acres
Type of HTF (heat transfer fluid) used	Therminol VP-1
Steam consumption in turbine	14.15 Ton hour <sup>-1</sup>
Mass flow rate of HTF	18.13 kg/s
Type of tracking system	East–West single axis tracking
Number of actuators required in tracking system	8
Auxiliary consumption	14.10%

**Table 2** Properties of Therminol VP-1

Freezing point	13 °C
Upper operating temperature	400 °C
Density at 300 °C	815 kg m <sup>-3</sup>
Viscosity at 300 °C	0.2 cP
Heat capacity at 300 °C	2.319 kJ kg <sup>-1</sup> K
Heat capacity of Therminol VP-1	2.319 kJ kg <sup>-1</sup> K
Fluid temperature at the inlet of first SCA in each loop	290 °C
Fluid temperature at the outlet of each loop	391 °C

fed to condenser for condensation, while in reheat rankine cycle for improving efficiency, two types of turbine (high pressure and low pressure) are used. In this process, steam after getting expanded (isentropically) in high-pressure turbine is sent to boiler where it is heated again. This steam is then directed to low-pressure turbine which is now sent to condenser after attaining condenser pressure. This, in turn, increases efficiency of cycle, and deterioration of blades is also reduced as moisture content in the mixture is reduced when it flows through turbine. Technical specification of designed system is shown in Table 3.

**Table 3** Technical specifications of designed system

<b>Turbine</b>	
Overall efficiency	37.7%
Nominal pressure of output steam	1.2 (abs)
Generator efficiency	96%
Electrical power at generator terminal	1000 kW
<b>Preheater</b>	
HTF temperature at inlet of steam generator	390 °C
HTF temperature at outlet of steam generator	281 °C
<b>Reheater</b>	
HTF temperature at inlet of reheater	390 °C
HTF temperature at outlet of reheater	240 °C

## 2.2 Project Cost of SPT

Table 4 shows capital cost released by Indian Central Electricity Regulatory for 1 MW solar thermal power plant. Direct cost includes cost of solar block, power block, land and general civil and structural works, while indirect cost includes preliminary expenses, contingency, etc.

Operation and maintenance norms released by the Indian Central Electricity Regulatory Commission: 18.74 lakhs/MW.

**Table 4** Capital cost norms released by the Indian Central Electricity Regulatory Commission

S. no.	Item description	Capital Cost Norm for Solar Thermal (million INR/MW)
1	Direct cost	101.8
2	Solar block	96.0
3	Power block	
4	Land	1.8
5	General civil and structural works	4.0
6	Indirect cost	18.2
7	Preliminary and pre-operative expenses	
8	Contingency	
9	IDC (Interest during construction)	
10	Total capital cost	120.0

### 2.3 Levelized Cost of Energy

Levelized cost of energy (LCOE) equal to the common fee shoppers would have to pay to precisely repay the investor for capital, O&M and gasoline expenses with a fee of return equal to the bargain rate. Thus, LCOE is minimal fee at which strength has to be offered for an strength venture to smash even

$$\text{LCOE} = \frac{(F_R + O_f) C_o}{F_C} \frac{C_o}{P} + C_{O\&M} + \sum \frac{C_i}{\eta}$$

where

$F_R$  = Capital recovery factor (% per annum),  $O_f$  = Fixed O&M cost (% per annum),

$F_c$  = Capacity factor,  $C_o$  = Capital cost (INR),  $P$  = Installed capacity (kW),

$C_{O\&M}$  = Variable O&M cost (INR),  $\frac{C_i}{\eta}$  = Cost of inputs/conversion efficiency (INR kWh<sup>-1</sup>).

LCOE depends on discount rate, project life and installed cost and changes if any of these three parameters varies. Variations of LCOE for 25 years and 20 years life span are shown in Tables 6 and 7.

For the solar thermal power plant, LCOE is **Rs 6.47 kWh<sup>-1</sup>**, taking 25 years life of power plant @ 10% discount rate as shown in Table 5.

### 2.4 Monthly Energy Yield from Designed System

**The designed** SPT plant could generate 3.38 GWh/year in the first year of operation at 38.58% capacity factor.

Techno economic metrics like payback period and internal rate of return (IRR) were also calculated.

Monthly energy yield for designed system and for aperture area (7450 m<sup>2</sup>) is also shown in Table 6.

**Table 5** LCOE at different discount rate

Discount rate	6%	7%	8%	9%	10%	11%	12%	15%
Life of plant (years)	LCOE (Rs kWh <sup>-1</sup> )							
25	5.34	5.61	5.89	6.18	<b>6.47</b>	6.78	7.09	8.06
20	5.66	5.91	6.18	6.45	<b>6.73</b>	7.02	7.32	8.24

**Table 6** Calculation of monthly energy yield for aperture area 7450 m<sup>2</sup>

S. no.	Month	Monthly sum of DNI (kWh m <sup>-2</sup> )	Energy yield (kWh)
1	January	214	350,840.16
2	February	190.12	311,755.9
3	March	205	336,085.2
4	April	203	332,806.32
5	May	198	319,690.8
6	June	152	249,194.88
7	July	91	149,189
8	August	84	137,712.96
9	September	146	239,358.24
10	October	190	311,493.6
11	November	198.6	325,592.7
12	December	195	319,690.8
13	Annual avg	172	281,983.68
14	Annual sum	2064	3,383,804.16

### 2.5 Payback Period

The payback length in reality measures the time elapsed between the factor of preliminary funding and the factor at which amassed savings, and Internet of different amassed fees is enough to offset the preliminary funding outlay.

$$\sum_{n=0}^n (B_n - C_n) \geq 0$$

where  $B_n$  and  $C_n$ , respectively, represent the cash receipts (benefits) and cash expenses (costs) associated with the investment at the end of each period  $n$ . The payback period can be obtained by calculating the cumulative net cash flows, based on the cash flow statement of PTC project investment; that is, payback period is the time point where the cumulative net cash flows turn from negative value to positive value.

### 2.6 Internal Rate of Return

Internal rate of return (IRR) is a widely accepted discounted measure of funding well worth and is used as an index of profitability for the appraisal of project. The IRR is described as the price of hobby that equates the current fee of a sequence of money flows to zero. In different words, it is the pastime fee at which the NPV of an funding is zero. Mathematically, the internal rate of return is the interest rate that satisfies the equation

$$\text{NPV} = \sum_{t=0}^n \frac{B_n - C_n}{(1+i)^t} = 0$$

where

$B_n$  = Benefits associated with  $n$ th year

$C_n$  = Cost associated with  $n$ th year

$i$  = interest rate.

For solar parabolic trough systems, internal rate of return is 28% while the payback period is 3.91 years of the project.

### 3 Renewable Energy Certificate and Clean Development Mechanism

REC benefit and CDM were also calculated as shown below.

#### 3.1 Calculation for REC Benefit

Annual energy yield in first year = 3383 MWh/a.

1 REC = 1 MWh of renewable energy generated.

Total REC earned in first year = 3383.

1 REC worth Rs. 1000.

Total REC benefit in first year =  $3383 \times 1000 = 33,83,000 = 33.83$  lakhs.

#### 3.2 Calculation for CDM Benefit

Annual energy yield in first year = 3383 MWh  $a^{-1}$ .

For India, 1 MWh electricity generation is equivalent to 0.82 ton of CO<sub>2</sub> emission [12].

Total emission reduction in first year =  $3383 \times 0.82 = 277.16$  ton of CO<sub>2</sub> emission reduction.

1 CER = 1 ton of CO<sub>2</sub> emission reduction (certified emission reduction).

Total CER earned in first year = 277.16 CERs.

1 CER worth 7 Euro [12].

Total CER benefit =  $277.16 \times 7 \times 75.18 = \text{Rs } 145,858.22$  (1 Euro = 75.18 INR).

## 4 Life Cycle Assessment (LCA)

LCA is a general approach used for assessing environmental impacts related to renewable technologies. Impact from upstream and downstream activities over entire life cycle of any plant is included in LCA. Figure 2 shows the phases of life cycle assessment for any system.

Areas of high impact are identified by evaluating following systems:

- Heat transfer fluid (HTF) system: HTF, header piping and circulation pumps.
- Solar field system: frames, heat collecting elements (HCE), mirrors, tracking, controls, drive systems, foundations, insulation, heat exchangers.
- Power plant system: power block, turbine, generator set, etc.
- Global warming emissions (GWE): Emissions of individual GWEs from the CSP plant LC are presented as the sum of each GHG weighted by its 100-year global warming potential to obtain grams of CO<sub>2</sub> equivalents (g CO<sub>2</sub> eq/kWh).

### 4.1 Description of the Assessment

Evaluation of environmental impact and systematic analysis of any kind of power plant is known as LCA. This assessment is used to describe and assess all flows entering in system from nature along with flows from system to nature, throughout life cycle. LCA was carried out using SIMAPRO software.

LCA study consists of the following steps:

- Step first includes energy demand for extracting raw materials and manufacturing components of plant.
- Transporting components and raw materials to site.
- The construction activities cover workshop, tower and pipeline.

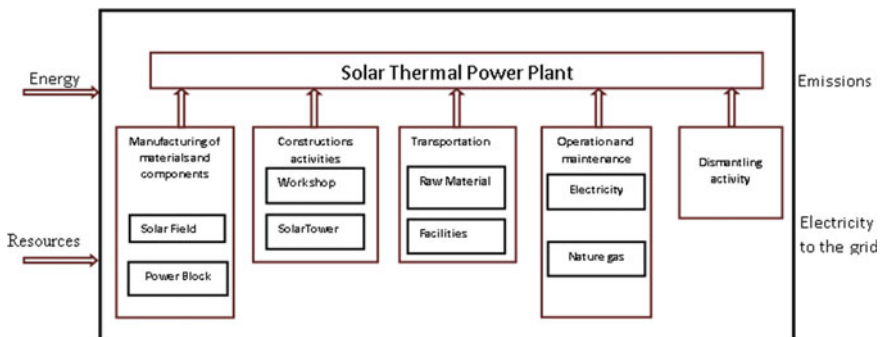


Fig. 2 Phases of life cycle assessment



- Operation stage where no fossil fuel is used for transforming solar energy into electricity. This includes calculation of energy demand for operation of plant.
- Life cycle assessment of all process is involved. LCI was performed using tool SIMA PRO.

#### **4.2 Life Cycle Inventory of Solar Parabolic Trough Power Plant: (II) Emissions (g/kWh)**

Data required for performing LCA was taken from firms working on SPT plant and literature. While considering similar materials as used in coal power plant, some assumptions were also made for carrying out LCA for SPT plant. Basically, materials whose weight is less than 5% can be neglected in this procedure. Primary input and output of LCA are shown in Table 7.

#### **4.3 Cumulative Energy Demand in the Life Cycle of Solar Parabolic Trough Power Plant**

Energy demand values for PTC are listed in Table 6. Little fossil fuel is used for starting generating set, otherwise only self-produced electricity is utilized for the operation of solar parabolic trough power plant. Table 8 shows that most of energy demand is required for operation of plant.

**Table 7** Primary input and output of LCA

	Types	Materials extraction and production of equipment	Transport	Buildings construction	Operation	Total
Input	Steel	11.55	–	0.86	–	12.41
	Glass	2.28	–	–	–	2.28
	Concrete	–	–	2.56	–	2.56
	Diesel	–	0.0160	–	–	0.0160
	Gasoline	–	0.0686	–	–	0.0686
Output	CO <sub>2</sub>	24.93	0.65	3.78	2.21	31.6
	SO <sub>2</sub>	0.0370	–	0.0032	0.0030	0.0432
	NO <sub>x</sub>	0.0051	0.0050	0.0036	0.0011	0.0148
	HC	–	0.00166	–	1.26*10 <sup>-4</sup>	0.0018
	CO	–	0.0132	–	9.91*10 <sup>-4</sup>	0.0142
	Powder and soot	0.0242	6.29*10 <sup>-4</sup>	0.0025	0.0021	0.0293

**Table 8** Cumulative energy demand in life cycle of SPT Plant

Power plants	Energy demand values (MJ/kWh)
Solar field	0.09
Power block	0.0037
Storage system	0.08
Buildings construction	0.006
Transports	0.0035
Operation	2.62
Decommissioning	-2.87 E - 04
Total	2.80

### 4.4 Energy Payback Time (EPT)

Furthermore, cumulative energy demand (CED) has been calculated and shown in Table 8. Based on CED, energy payback time (EPT) has been calculated by the following formula [4]. EPT is defined as the time it takes for a renewable energy system to save the same amount of primary energy as is consumed for its production, operation and dismantling.

$$EPT = \frac{CED}{\left(\frac{E_{net}}{g} - CED_0\right)}$$

where CED is cumulative primary energy demand required for constructing plant,  $E_{net}$  is net electricity produced annually (MJ/yr), and  $g$  is utilization grade of primary energy source to produce electricity.  $g$  is usually taken as 44.28%.  $CED_0$  is annual primary energy demand for operation and maintenance (MJ/yr). As per calculations, the life cycle inventory of solar thermal power plant on the EPT is achieved as 1.89 years.

## 5 Conclusions

Fewer studies are available regarding solar concentrating technologies; therefore useful information concerning SPT can be gathered by assessing CO<sub>2</sub> emissions, cumulative energy demand and energy payback time. After identification of literature gaps and environmental issue related to concentrating solar technologies, this study was carried out in order to provide designing and assessment of 1 MW SPT. Cumulative energy demand is lower than energy produced and EPT also came out to be 1.89 years. Self-produced electricity is used for operation of SPT which reduces CO<sub>2</sub> emissions as compared to fossil technologies. Solar field is mainly responsible for contributing much toward environmental impact. Steel has the highest impact among all construction materials of PTC followed by glass and concrete. System reduces the carbon emission as solar is clean and green source of

energy. In the existing system (diesel and coal), carbon is emitted through required power generation and steam generation, since the system is completely green and clean source of energy which has negligible carbon emission. As per life cycle assessment, PTC are best option for reducing greenhouse gases and other pollutants without creating other environmental risks or contamination. The use of solar energy for meeting the electricity will eliminate substantial use of fossil fuel and bring 277.16 tons of CO<sub>2</sub> emission reduction into the environment. Total REC benefit for first year came out to be 33.83 lakhs. For the solar parabolic trough power plant, LCOE is **Rs 6.47 kWh<sup>-1</sup>**, taking 25 years life of power plant @ 10% discount rate. For solar parabolic trough systems, internal rate of return is 28% while the payback period is 3.91 years of the project.

**Conflict of Interest** On behalf of all authors, the corresponding author states that there is no conflict of interest.

## References

1. Rathore, N., Panwar, N.L., Gama, A., et al.: Solar map of India under clear sky conditions. *Int. J. Sustain. Energy* **38**(5), 415–446 (2019)
2. Energy statistics. Ministry of statistics and programme implementation, Government of India (2019) accessed on 5/10/2020
3. Rathore, N., Panwar, N.L., Gama, A., et al.: A comprehensive review of different types of solar photovoltaic cells and their applications. *Int. J. Amb. Energy*, 1–18 (2019a)
4. More, M., Agrawal, C., Sharma, D., Rathore, N., Samar, K.: Development of pellet machine for utilization of biogas slurry. In: Rakesh, P.K., Sharma A.K., Singh, I. (eds) *Advances in engineering design. Lecture notes in mechanical engineering*. Springer, Singapore. [https://doi.org/10.1007/978-981-33-4018-3\\_48](https://doi.org/10.1007/978-981-33-4018-3_48) (2021)
5. Sharma, K., Kothari, S., Panwar, N.L., Rathore, N.: Design and development of solar energy powered maize milling machine. *Int J Ambient Energy*. <https://doi.org/10.1080/01430750.2020.1712241> (2020)
6. Sharma, K., Kothari, S., Panwar, N.L., Rathore, N., Samar, K.: Experimental investigation on farmer-friendly hybrid dryer for indoor drying of mushroom. In: Singh, S., Ramadesigan, V. (eds) *Advances in energy research*, vol. 2. Springer Proceedings in Energy. Springer, Singapore. [https://doi.org/10.1007/978-981-15-2662-6\\_8](https://doi.org/10.1007/978-981-15-2662-6_8) (2020)
7. IEA: Technology roadmap: concentrating solar power. International Energy Agency/Organization for Economic Cooperation and Development, OECD/IEA, Paris, France (2010)
8. Sanjay, G.: Scope for solar energy utilization in the Indian textile industry. *Sol. Energy* **42**(4), 311–318 (1989)
9. Abdel-Dayem Adel, M., Mohamad, M.A.: Potential of solar energy utilization in the textile industry—a case study. *Renew. Energy* **23**, 685–694 (2001)
10. Mahaver, V.K., Rao, K.V.S.: Solar energy potential of the state of Rajasthan in India. In: 2018 3rd international innovative applications of computational intelligence on power, energy and controls with their impact on humanity (CIPECH), pp. 56–61. IEEE (2018)
11. Abbas, M., Belgroun, Z., Aburidah, H., Merzouk.: Assessment of a solar parabolic trough power plant for electricity generation under Mediterranean and arid climate conditions in Algeria. *Energy Proc.* **42**, 93102 (2013)

12. Bhawan, A., Sewa, P., Puram, R.K.: CO<sub>2</sub> baseline database for the Indian power sector. Central Electricity Authority, Ministry of Power, Government of India, New Delhi, India (2017)
13. Lechon, Y., Cristina de la, R., Rosa, S.Á.: Life cycle environmental impacts of electricity production by solar thermal power plants in Spain. *J. Sol. Energy Eng.* **130**(2), 021012 (2008)
14. Zhang, M., Wang, Z., Jiang, C.: Embodied energy and energy analyses of a concentrating solar power (CSP) system. <https://www.sciencedirect.com/science/article/pii/S0301421511009785> (2012)

# Micromechanical Modeling and Simulation of Natural Fiber Polymer Composite



Love Kerni, Sarbjeet Singh, and Narinder Kumar

**Abstract** Fiber-reinforced composite are widely used materials in today's world. They have various applications in modern world viz. aircrafts, automobiles, construction industries, etc. Fiber-reinforced composites consist of matrix and fiber. The mechanical properties of composites depend upon various factors such as type of fiber, fiber length, and concentration of fiber. In this paper, micromechanical analysis of natural fiber-reinforced composite is presented. The experimental analysis of the composites is costly and time consuming. So, numerical analysis of composites is carried out. The analysis of composites is a tedious job due to the heterogeneous nature of composites. To overcome this, RVE model-based analysis is used which models the composite as homogeneous mixture of matrix and reinforcement by taking the properties of matrix and fiber as input. This analysis is carried out using DIGIMAT software and the results obtained are validated using rule of mixture model. From the results obtained, it is found out that mechanical properties enhance with the increase in weight concentration of fibers.

**Keywords** Fiber-reinforced composites · Micromechanical modeling · Rule of mixtures

## 1 Introduction

In the last few decades, the demand for composite materials has been rising. This rise in demand is due to their promising properties viz. high specific strength, good damping capacity and high specific modulus that makes them suitable for modern applications [1]. Along with this, the disposal of non-degradable waste is also a big problem as they causes the damage to environment and leads to various types of

---

L. Kerni (✉) · S. Singh  
Mechanical Engineering Department, GCET Jammu, Jammu 181122, India

L. Kerni · N. Kumar  
Mechanical Engineering Department, CT University, Ludhiana, Punjab 142024, India

pollutions. To prevent the environment from this damage, we have to limit the use of these types of material [2]. Owing to above reasons, natural fiber as reinforcement and biodegradable resins as matrix are preferred over synthetic fibers and non-biodegradable resins in composite materials [3]. Natural fibers have various advantages over synthetic fibers and lead to green technology in manufacturing of composites [4]. Among different natural fibers, sisal fiber has gained importance as the reinforcement material because of its promising mechanical properties and large amount of cellulose as compared to other natural fibers [5]. There are various applications of natural fiber-reinforced composites like aircraft interior structures, door and window panels, car bumpers, etc. [6]. These composites can grasp additional benefits of various properties of their components, microstructure, and interaction between components which in turn improve the mechanical performance of parts made from them [7]. Mechanical properties of these composites determine the application of these composites. So, it is required to understand the mechanical properties of composites. There are various factors that affect the mechanical properties of composites like content of fibers, their types and fiber orientation, etc. The effect of these factors on properties of composites can be studied experimentally, analytically, or by numerical simulation [8]. It will be a time consuming and costly task to understand the properties of composites by experimental method [9]. Therefore, analytical methods and numerical simulation have gained a lot of importance in determining the properties of composites. Rule of mixtures and the Hapsin-Tsai equation are analytical methods that provide the mathematical relationship between properties of composite and microstructural parameters [10]. Numerical simulation of composites involves various methods like finite element method, mean field homogenization, etc. There are few studies available in literature about the numerical simulation of composites for determining their properties. Patnaik et al. [11] have used finite element method for investigation of micromechanical and thermal characteristics of glass fiber-reinforced epoxy composite. Ping et al. [12] have formulated a multi-scale computational method to study the non-linearity of piezoelectric materials. They have validated their method by investigating various microstructures and found that his method is capable of predicting the accurate mechanical and nonlinear electrical responses for heterogeneous materials. Melro et al. [13] have developed different RVEs for investigating the fracture and inelastic deformation of randomly distributes unidirectional fiber-reinforced polymer composites. Nayak and Sahu [8] have presented the experimental and representative volume element based analysis of aluminum alloy nano composite. There are generally two approaches in numerical simulation of composites namely micromechanical analysis and macromechanical analysis. In micromechanical analysis, the composite is analyzed at the fiber and matrix level whereas in macromechanical analysis composite is treated as a homogeneous continuum [5]. By performing the micromechanical analysis, we find out the various mechanical properties of composites which further can be used as input for the macromechanical analysis [14]. In order to study the linear and nonlinear behavior of composites as a function of its stress-strain relation and mechanical properties, micromechanical analysis is an effective tool [15]. The correctness of determination

of mechanical properties of composites largely depends upon the precision of defining the components of composites. Microstructure of the components of composite also plays an important role in deciding the properties of composites. Representative volume element (RVE) is used to explain the properties of the complete microstructure [16]. RVE is a small element of material microstructure comprises of different phases of morphology and is similar to its bulk form [17]. RVE modeling is a powerful technique for simulating the properties of composites at microscale. RVE forms a link between microscopic and macroscopic scales.

Therefore, this paper presents the details about the constituents of natural fiber-reinforced composite. Micromechanical analysis of composite is carried out using DIGIMAT software. For carrying out micromechanical analysis, a RVE of natural fiber-reinforced composite was developed and microstructure deformation of composite was evaluated using DIGIMAT.

### ***1.1 Microscale Modeling***

Due to anisotropy and heterogeneous nature of reinforced composites, it is difficult to determine its properties and doing a reliable analysis based on macroscopic modeling. The traditional method that is used in other materials cannot give reliable results in case of composites due to its heterogeneity and complexity. So, we have to look for some other procedures. Microscale modeling is one of such procedures that can be effectively used for simulating the composites as it models the composites at microlevel. In microscale analysis, the behavior of both fiber and matrix and its effect on composite properties is taken into consideration. The results obtained from this analysis enable us to predict the behavior of composite materials which leads to design of a novel material having modern applications.

### ***1.2 Micromechanical Analysis***

Micromechanical analysis is a technique of studying the constituent materials of composites, effect of their volume fractions on properties of composites and investigation of bonding between different constituents [18]. The elastic constants of a composite material can be assessed from known mechanical properties of its constituents (fiber and matrix) through micromechanical analysis using RVE modeling approach [7]. We cannot analyze the structural problem at the microlevel. For analyzing the structural problem, we have to consider the RVE which comprises of different microstructure. The results obtained from micromechanical analysis can be used as a basis for macro-analysis and for solving the structural problem [19].

Mean-filed homogenization (MFH) and Finite element Homogenization (FEH) are the two most commonly used approaches for solving the RVE problem.

There are different semi-analytical models such as Volgt and Reuss model, Mori-Tanaka and Eshelby's model that are used in mean field homogenization approach for precise and effective prediction of various properties at macroscopic level [20, 21]. Finite element homogenization is also used for finite element formulations of composites [22, 23]. In DIGIMAT software, DIGIMAT-MF is based on mean field homogenization and DIGIMAT-FE is based on finite element homogenization and both these modules are used for solving the RVE problem [24]. DIGIMAT-FE is used to develop real RVE model of composite and developed RVE can be solved by using FEA solver. There are some limitations of DIGIMAT-FE such as difficulty in producing the mesh of a RVE and more computational time and cost. DIGIMAT-MF module is easy to model and solve the RVE. DIGIMAT-MF provides the results for constituents of composites at microscopic level. DIGIMAT-FE predicts the local properties of composites at both microscopic and macroscopic level.

## 2 Materials and Methods

DIGIMAT-MF and DIGIMAT-FE are important tools for modeling and solving the various materials [25]. In this paper, a natural fiber-reinforced composite is analyzed using DIGIMAT-MF and DIGIMAT-FE. The constituents of this natural fiber-reinforced composite are epoxy polymer as matrix and Sisal fiber as reinforcement. The properties of these constituents are given in Table 1. The constituents, matrix, and reinforcement are modeled as elastic and isotropic material. The fibers are modeled as continuous fibers which are uniformly distributed in the matrix. The composite materials can be described on the basis of volume of fraction of composites. In case of two-phase fiber-reinforced composites, we have to specify only the volume fraction of fiber ( $V_f$ ) and by using the formula  $V_m = 1 - V_f$ , we can find out the volume fraction of matrix as sum of two phases must be equal to one. In this study, the volume fraction of fiber in composite varies and effect of different volume fraction of fiber on the elastic constants of composites is studied.

After developing the RVE in the DIGIMAT, periodic boundary conditions are applied to the RVE model of composite. For applying the periodic boundary conditions to the RVE, we have to impose the continuity criteria to the RVE to ensure that all the RVEs are connected to form a continuum body. The continuum criteria are imposed in terms of displacement to ensure the non-separation of adjacent RVEs [26].

**Table 1** Mechanical Properties of constituents of composite

Material	Young's Modulus (MPa)	Poisson's ratio	Density (kg/mm <sup>3</sup> )
Sisal fiber	12,000	0.2	1.6
Epoxy matrix	3760	0.39	1.15



Then, fibers are again modeled as inclusions which are positioned at certain positions specified by orientation tensor. Also, fibers are aligned perfectly in  $X$ -direction and aligned at  $45^\circ$  in the  $X$ - $Z$ -plane. In Digimat—MF, fibers are assumed as ellipsoids of revolution. Aspect ratio of inclusion defined as the ratio of length and diameter of particle of inclusion is fixed at 25 for this analysis. Orientation of inclusions is defined by orientation tensor and two angles  $\theta$  and  $\Phi$  that determine the alignment of fibers in the composite. Orientation tensor represents the probability distribution of finding out the fibers in 3D space. 2D orientation tensors are represented by an ellipse of which the largest and smallest diameters are eigenvalues of orientation tensor and direction of these axes are the Eigen vectors. In present work, orientation angles are fixed as  $\theta = 90^\circ$  and  $\Phi = 0^\circ$  which means that fibers are aligned in  $X$  plane. In present work, Mechanical loading is applied in the  $X$  direction. Different analyses are carried out by varying the eigenvalues of orientation tensor and stress–strain curves and elastic constants have been obtained.

### 3 Numerical Results and Discussions

#### 3.1 Effect of Weight Concentration of Fiber on Elastic Constants of Composite

The elastic constants of natural fiber reinforced composites for different concentrations of natural fibers using DIGIMAT has been obtained and given in Table 2.

From Table 2, it is clear that with the increase in weight concentration of fibers in natural fiber-reinforced composite, the elastic constants of the composite also increases which is according to the results reported in literatures [19]. As elastic

**Table 2** Elastic constants of composite for different weight concentration of fibers obtained from Digimat

% Weight concentration of fiber →	5%	10%	15%	20%	25%	30%
Elastic constants ↓						
Axial Young’s Modulus (MPa)	4066.2	4380.9	4704.2	5036.6	5378.6	5730.4
In plane Young’s Modulus (MPa)	3933.6	4114.5	4304.2	4504.3	4716.3	4942.3
In plane Shear Modulus (MPa)	1405	1461.6	1522.7	1589	1661.2	1740
Transverse Shear Modulus (MPa)	1410.3	1472.5	1539.4	1611.8	1690.2	1775.5
In plane Poisson’s ratio	0.40	0.41	0.41	0.42	0.42	0.42
Transverse Poisson’s ratio	0.38	0.38	0.37	0.36	0.35	0.34
Global Density (g/cm <sup>3</sup> )	1.17	1.18	1.2	1.22	1.24	1.26

constant demonstrate the ability of composite to withstand the deformation on the application of load so, by increasing the weight concentration of fiber in composite the ability of composites to withstand the load without failure enhances. This is due to the reason that fibers act as reinforcement in composites which are main load bearing elements in composites and by increasing their concentration, load bearing capacity of composites increases.

There are various micromechanical analytical models available such as rule of mixtures (ROM), Halpin-Tsai, etc., to evaluate and validate the various properties of natural fiber-reinforced composites [27]. Out of all analytical models, rule of mixture models is most commonly used. We also use this model to validate the obtained results from DIGIMAT. Following are the equations of rule of mixtures that relates the properties of constituents of composites with the properties of composites.

For calculating the density of composite,

$$\rho_c = \frac{1}{\frac{W_m}{\rho_m} + \frac{W_f}{\rho_f}} \quad (1)$$

where,  $\rho_c$  = Density of composite.

$W_m$  = Weight fraction of matrix in composite.

$W_f$  = Weight fraction fiber in composite.

$\rho_m$  = Density of matrix.

$\rho_f$  = Density of fiber.

The Young's modulus of composite can be calculated by using the following equation,

$$E = E_m V_m + E_f V_f \quad (2)$$

where  $E$  = Young's Modulus of composite

$E_m$  = Young's Modulus of matrix

$E_f$  = Young's modulus of fiber

$V_m$  = Volume fraction of matrix =  $\frac{W_m * \rho_c}{\rho_m}$

$V_f$  = Volume fraction of fiber =  $1 - V_m$ .

Following equation is used to determine the Poisson's ratio on the basis of rule of mixture,

$$\mu = \mu_m V_m + \mu_f V_f \quad (3)$$

where  $\mu$  = Poisson's ratio of composite

$\mu_m$  = Poisson's ratio of matrix

$\mu_f$  = Poisson's ratio of fiber.

The validation of results obtained from DIGIMAT using the analytical model viz. rule of mixture is shown in Fig. 1a, b, and c. Figure 1a, b, and c shows the comparison between the densities, Poisson's ratio, and Young's Modulus respectively for different weight concentration of fibers obtained from DIGIMAT and rule of mixture. From Fig. 1, it is clear that elastic constants of composite obtained from DIGIMAT are approximately equal to that of obtained from rule of mixture which validates these results.

### ***3.2 Effect of Weight Concentration of Fiber on Stress Strain Curve of Composite***

The comparison of stress–strain curve for different weight concentrations of fibers is shown in Fig. 2. From Fig. 2, it is clear that slope of stress–strain curve increases with the increase in weight concentration of fibers which signifies that with increase in content of fiber stiffness of composite to resist the elastic strain improves.

### ***3.3 Effect of Fiber Orientation on the Elastic Constants of Composite Using Digimat***

Table 3 gives the elastic constants of composites for different orientations of fibers. In this analysis, two orientations of fibers are taken into consideration, i.e., fibers aligned in  $X$ -direction and fibers aligned at  $45^\circ$  in the 1–2 plane. From Table 3, it is clear that value of Young' Modulus for the fiber aligned in  $X$ -direction is greater than the fibers aligned at  $45^\circ$  in the  $X$ – $Z$ -plane. It is because of the reason that as load is applied in  $X$ -direction and fibers in  $X$ -direction provides more stiffness to the composite in comparison to the other orientations [28]. Density of composite for both the orientations is same which means that orientation of fibers do not have any effect on the density of composite.

## **4 Conclusions**

From the above discussion, it can be concluded that composites are potential candidates for replacing the conventional materials due to their promising properties like high specific strength, lightweight, and high stiffness. Natural fibers are

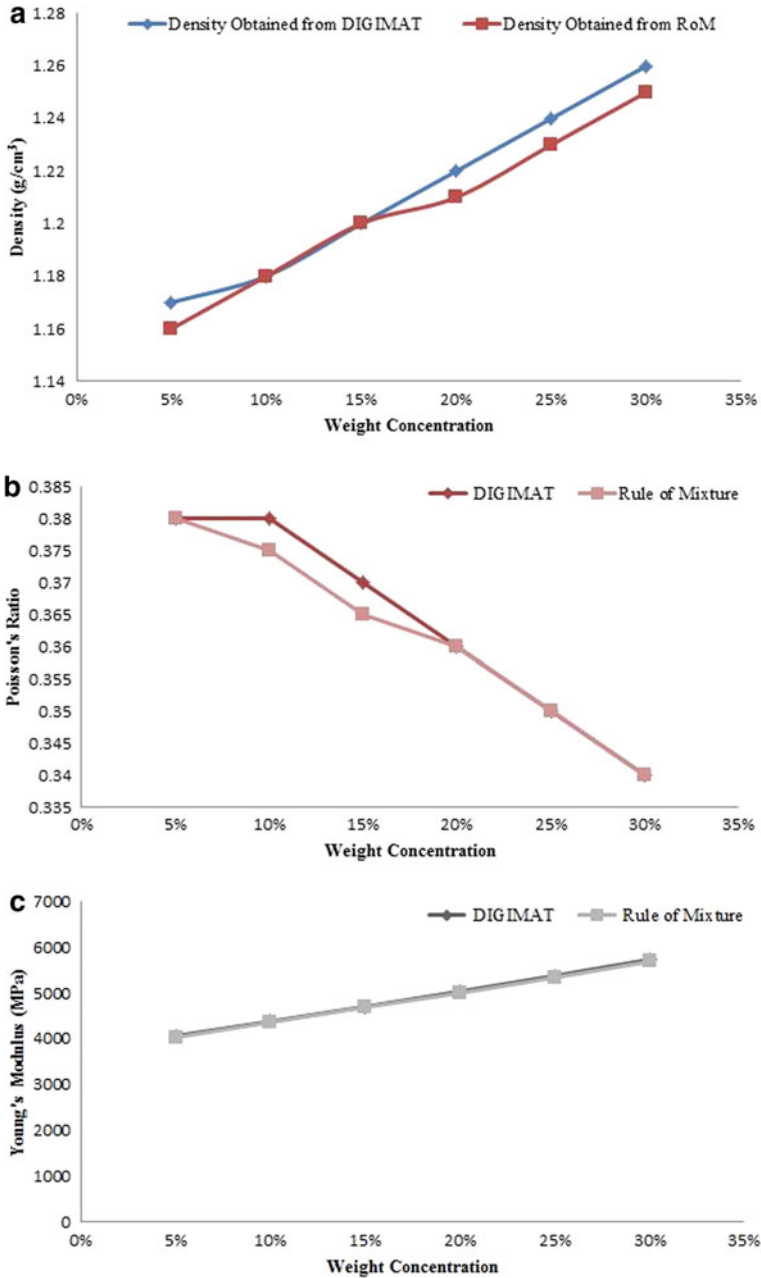


**Fig. 1** a Comparison of density for different weight concentrations of fiber. b Poisson's ratio for different weight concentrations of fiber. c Young's Modulus for different weight concentration of fibers

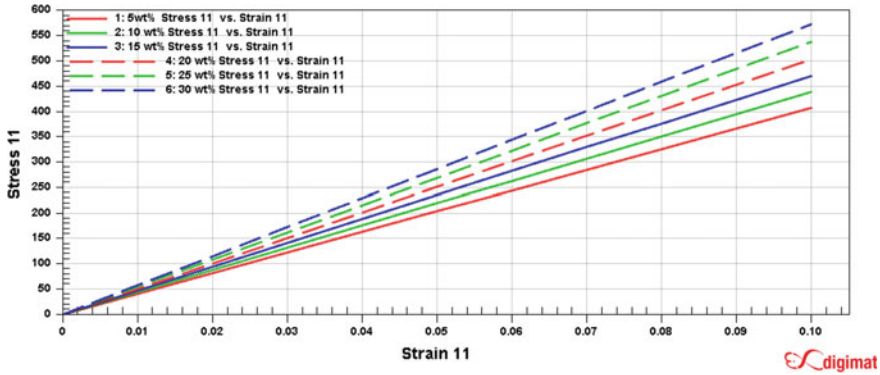


**Fig. 2** Stress–strain relation for natural fiber reinforced composite for different weight concentrations of fiber

**Table 3** Elastic constants of composite for different orientation of fibers obtained from Digimat

Fiber orientation →	Perfectly aligned in X direction	Aligned at 45° in the X–Z plane
Elastic constants ↓		
Axial Young’s Modulus (MPa)	5693.5	4899.4
In plane Young’s Modulus (MPa)	4936.8	4899.4
In plane Shear Modulus (MPa)	1740.4	1799
Transverse Shear Modulus (MPa)	1777.2	1799
In plane Poisson’s ratio	0.42	0.36171
Transverse Poisson’s ratio	0.35	0.36171
Global Density (g/cm <sup>3</sup> )	1.26	1.26

used as reinforcement in composites due to their biodegradability and recyclability. The simulation of sisal fiber-reinforced epoxy composites is carried out using DIGIMAT software for determining the mechanical properties. The composite is simulated for different concentrations of fibers and effect of fiber concentration on properties of composite is analyzed. It has been found out that mechanical properties of composites improve with the increase in concentration of fibers. The results obtained by the simulation are validated using the rule of mixtures analytical model. The effect of different orientations of fibers on the mechanical behavior of composites has also been analyzed. Elastic constants of composites have been determined for two orientations of fibers, i.e., aligned in X-direction and aligned at 45° in the X–Z-plane. From this, it is found out that orientation of fibers parallel to the direction of applied load leads to the more stiffness of composite. Then stress–strain curve has been obtained for different orientation of fibers in X-direction and found out that orientation of fiber perfectly in X-direction have the maximum slope of stress–strain curve whereas fibers oriented in Y-direction have the least slope of this curve.

## References

1. Kerni, L., Singh, S., Patnaik, A., Kumar, N.: A review on natural fiber reinforced composites. *Mater. Today Proc.* (2020). <https://doi.org/10.1016/j.matpr.2020.04.851>
2. Bharath, K.N., Basavarajappa, S.: Applications of biocomposite materials based on natural fibers from renewable resources: a review. *Sci. Eng. Compos. Mater.* **23**(2), 123–133 (2016)
3. Eloy, F.S., Costa, R.R.C., de Medeiros, R., Ribeiro, M.L., Tita, V.: Comparison between mechanical properties of bio and synthetic composites for use in aircraft interior structures. *Proc. Meet. Aeronaut. Compos. Mater. Struct.* (2015)
4. Dos Santos, D.J., Tavares, L.B., Batalha, G.F.: Mechanical and physical properties investigation of polyurethane material obtained from renewable natural source, vol. 54, issue 2. [jamme.acmsse.h2.pl](http://jamme.acmsse.h2.pl) [cited 2020 Sep 1]. Available from [http://jamme.acmsse.h2.pl/papers\\_vol54\\_2/5428.pdf](http://jamme.acmsse.h2.pl/papers_vol54_2/5428.pdf) (2012)
5. Faruk, O., Bledzki, A.K., Fink, H.P., Sain, M.: Progress report on natural fiber reinforced composites. In: *Macromolecular materials and engineering*, vol. 299, pp. 9–26 (2014)
6. Koronis, G., Silva, A., Fontul, M.: Green composites: a review of adequate materials for automotive applications. *Compos. Part B Eng.* **44**(1), 120–127 (2013). <http://dx.doi.org/10.1016/j.compositesb.2012.07.004>
7. Devireddy, S.B.R., Biswas, S.: Effect of fiber geometry and representative volume element on elastic and thermal properties of unidirectional fiber-reinforced composites. *J. Compos.* **2014**, 1–12 (2014)
8. Nayak, B., Sahu, R.K.: Experimental and digimat-FE based representative volume element analysis of exceptional graphene flakes/aluminium alloy nanocomposite characteristics. *Mater. Res. Express.* **6**(11), 0–13 (2019)
9. Lu, J., Zhu, P., Ji, Q., Feng, Q., He, J.: Identification of the mechanical properties of the carbon fiber and the interphase region based on computational micromechanics and Kriging metamodel. *Comput. Mater. Sci.* **95**, 172–180 (2014). <http://dx.doi.org/10.1016/j.commatsci.2014.07.034>
10. Hancox, N.L.: Engineering mechanics of composite materials. In: *Materials & design*, vol. 17, p. 114 (1996)
11. Patnaik, A., Kumar, P., Biswas, S., Kumar, M.: Investigations on micro-mechanical and thermal characteristics of glass fiber reinforced epoxy based binary composite structure using finite element method. *Comput. Mater. Sci.* **62**, 142–151 (2012). <http://dx.doi.org/10.1016/j.commatsci.2012.05.020>
12. Fu, P., Liu, H., Chu, X.: An efficient multiscale computational formulation for geometric nonlinear analysis of heterogeneous piezoelectric composite. *Compos. Struct.* **167**, 191–206 (2017). <http://dx.doi.org/10.1016/j.compstruct.2017.02.005>
13. Melro, A.R., Camanho, P.P., Andrade Pires, F.M., Pinho, S.T.: Micromechanical analysis of polymer composites reinforced by unidirectional fibres: part II-micromechanical analyses. *Int. J. Solids Struct.* **50**(11–12), 1906–1915 (2013). <http://dx.doi.org/10.1016/j.ijsolstr.2013.02.007>
14. Jagath Narayana, K., Burela, R.G.: Multi-scale modeling and simulation of natural fiber reinforced composites (Bio-composites). *J. Phys. Conf. Ser.* **1240**(1) (2019)
15. Hosseini, N., Javid, S., Amiri, A., Ulven, C., Webster, D.C., Karami, G.: Micromechanical viscoelastic analysis of flax fiber reinforced bio-based polyurethane composites. *J. Renew. Mater.* **3**(3), 205–215 (2015)
16. Schmidt, K., Becker, J.: Generating validated 3d models of microporous ceramics. *Adv. Eng. Mater.* **15**(1–2), 40–45 (2013)
17. Ogierman, W., Kokot, G.: Particle shape influence on elastic-plastic behaviour of particle-reinforced composites. *Arch. Mater. Sci. Eng.* **67**(2), 70–76 (2014)
18. Bert, C.W., Reddy, J.N.: Mechanics of bimodular composite structures. In: *Mechanics of composite materials: recent advances*. Pergamon Press Inc., pp. 323–337 (1983). <http://dx.doi.org/10.1016/B978-0-08-029384-4.50027-4>

19. Article, R.: A review on mechanical characterization of natural fiber reinforced polymer composites
20. Morit, T., Tanaka, K.: Average stress in matrix and average elastic energy of materials with misfitting inclusions\*. Elsevier, Netherlands. Available from <https://www.sciencedirect.com/science/article/pii/S0001616073900643/pdf?md5=06d6cc1d6ed495b42817c9d758eebcc0&pid=1-s2.0-0001616073900643-main.pdf> [cited 2020 Sep 1]
21. The elastic field outside an ellipsoidal inclusion. Proc. R. Soc. London Ser. A Math. Phys. Sci. **252**(1271), 561–569 (1959). Available from <https://royalsocietypublishing.org/doi/10.1098/rspa.1959.0173> [cited 2020 Sep 1]
22. Brassart, L., Doghri, I., Delanny, L: Homogenization of elasto-plastic composites coupled with a nonlinear finite element analysis of the equivalent inclusion problem. Elsevier, Netherlands (2010). Available from <https://www.sciencedirect.com/science/article/pii/S002076830900448X> [cited 2020 Sep 1]
23. Pierard, O., Llorca, J., Segurado, J., Doghri, I.: Micromechanics of particle-reinforced elasto-viscoplastic composites: finite element simulations versus affine homogenization. Elsevier, Netherlands (2007). Available from <https://www.sciencedirect.com/science/article/pii/S0749641906001598> [cited 2020 Sep 1]
24. Arora, G., Pathak, H.: Multi-scale fracture analysis of fibre-reinforced composites. Mater. Today Proc. **18**, 687–695 (2019). <https://doi.org/10.1016/j.matpr.2019.06.469>
25. Ghorashi, S., et al.: Orthotropic enriched element free Galerkin method for fracture analysis of composites. Elsevier, Netherlands (2011). <https://www.sciencedirect.com/science/article/pii/S0013794411001196> [cited 2020 Sep 1]
26. Hollister, S.J., Kikuchi, N.: A comparison of homogenization and standard mechanics analyses for periodic porous composites. Comput. Mech. **10**(2), 73–95 (1992)
27. Silva, L., Panzera, T., Christoforo, A., et al.: Micromechanical analysis of hybrid composites reinforced with unidirectional natural fibres, silica microparticles and maleic anhydride. SciELO Bras. (2012). Available from [https://www.scielo.br/scielo.php?pid=S1516-14392012000600026&script=sci\\_arttext](https://www.scielo.br/scielo.php?pid=S1516-14392012000600026&script=sci_arttext) [cited 2020 Sep 1]
28. Yong, C.K., Ching, Y.C., Chuah, C.H., Liou, N.S.: Effect of fiber orientation on mechanical properties of kenaf-reinforced polymer composite. BioResources **10**(2), 2597–2608 (2015)

# Author Index

## A

Abhishek, Kumar, 215  
Agarwal, Deepak, 175  
Agarwal, Pankaj, 469  
Aggarwal, Deepshikha, 37  
Ajay, V.S., 29  
Akilan, T., 113  
Arivarasu, M., 155  
Arunkumar, T., 293  
Aswini, Chinna, 275  
Athulya, S., 29  
Avhad, P. V., 319

## B

Babu, Harish, 385, 391  
Bankar, Priyanka S., 459  
Bhandari, Manish, 197  
Bhatlu, M. Laxmi Deepak, 335  
Biswas, Shatarupa, 353  
Borse, Deepak, 145  
Bulkunde, Atul, 399

## C

Chandran, Sudhin, 207  
Chaturvedi, Manish, 189  
Chaudhari, D.L., 479  
Choudhary, D.S., 479  
Choudhary, Kavita, 49

## D

Dangayach, G.S., 95  
Dash, Tapan, 441  
Das, Supriya Priyadarshini, 1  
Dev Anand, M., 207  
Dey, Partha Pratim, 505

Dhiman, Abhishek, 515  
Dinbandhu, 215  
Dwivedi, Prashant Povel, 345

## G

Gaurav, Gaurav, 95  
Ghosh, Manojit, 505  
Gohane, Gaurav, 399  
Gopalakrishnan, Balamurugan, 125  
Gupta, Aditi, 57

## H

Hans Raj, K., 431  
Hebbale, Ajit M., 367  
Hubballi, Suresh, 13

## J

Jain, Akshay, 421  
Jain, Kalpit, 421  
Jain, Muskaan, 345  
Jain, Sameer, 49  
Jayan, Neethu, 335  
Jindal, Anil, 229  
Jithesh, K., 155  
Joshi, Gaurang, 539

## K

Kango, Saurabh, 449  
Kapre, Aniruddha V., 469  
Kaup, Vijayananda, 385, 391  
Kaur, Taranpreet, 497  
Kerni, Love, 563  
Khutey, Rupesh Kumar, 283  
Krishnan, Dinesh R., 293  
Kukshal, Vikas, 469



Kumar, Anil, 241  
 Kumar, Dinesh, 21  
 Kumar, Manoj, 539  
 Kumar, Narinder, 563  
 Kumar, Parlad, 229  
 Kumar, Ravi, 531  
 Kumar, Virendra, 241  
 Kurien, Rittin Abraham, 301, 375  
 Kurup, Gowrisankar B., 301, 375

**M**

Madhu, 345  
 Mahendiran, M., 113  
 Malhotra, Heena, 497  
 Manikandan, H., 385, 391  
 Marakala, Narasimha, 367  
 Masalvad, Shrivankumar Shivappa, 13  
 Mashalkar, S.A., 489  
 Matawale, Chhabi Ram, 283  
 Meena, M.L., 95  
 Mendhe, Vikas, 399  
 Mishra, Pardeep Kumar, 409  
 Mittal, Sushil, 229  
 Mohan, Mahesh, 79  
 Mohanty, Ankita, 1  
 Mohapatra, Rupam, 1  
 Mohaty, Pragyan Parimita, 409  
 Mondal, Debayan, 505  
 Mordia, Ravikant, 261  
 Mukherjee, Manidipto, 353

**N**

Nagdeve, Prabhat, 399  
 Nagdewe, S.P., 489  
 Nagnath, Ankita, 79  
 Nancharaiah, T., 251  
 Nandanwar, A.K., 479  
 Narain, Jai, 95

**O**

Oza, Ankit D., 539

**P**

Padmavathy, N., 275  
 Palei, Binod Bihari, 441  
 Pandey, Anoop, 189  
 Pandey, Shivam, 399  
 Parate, Anish, 399  
 Pargaonkar, Prateek, 79  
 Patil, D.R., 145  
 Paul, Daniel, 301, 375  
 Philip, Reshma B., 29  
 Prajapati, Mehul, 539  
 Pugalendhi, Arivazhagan, 125

**R**

Raghavendra Pai, K., 367  
 Rajesh, R., 207  
 Ranganathan, Rajesh, 125  
 Rao, M. Nageswara, 155  
 Rathore, Neelam, 549  
 Reddy, M.B.S. Sreekara, 459  
 Reji, Amal K., 29  
 Reji, Greshma Susan, 301, 375  
 Rewatkar, K.G., 479  
 Rout, Tapan Kumar, 441  
 Roy, Nani Gopal, 505

**S**

Sachdeva, Gulshan, 515  
 Sahoo, Gaurab Kumar, 441  
 Sakare, Praveen Kumar, 13  
 Sankhla, Vijayendra Singh, 549  
 Santhosh, Ashwin, 301, 375  
 Santhosh, Asween, 29  
 Sarangi, Saroj Kumar, 531  
 Sarkar, Argha, 275  
 Satputaley, Sushant, 79  
 Saxena, Archana B., 37  
 Sayyad, A.S., 319  
 Selvaraj, D. Philip, 375  
 Sen, Rahul, 135  
 Šerić, Neven, 87  
 Setia, Sahibdeep Singh, 327  
 Shahare, A.M., 479  
 Sharma, Abhishek, 241  
 Sharma, Ankush, 469  
 Sharma, Deepti, 37  
 Sharma, D.K., 49  
 Sharma, Harshit, 69  
 Sharma, Kamal, 523  
 Sharma, Manisha, 327  
 Sharma, Nitin, 449  
 Sharma, Rahul, 135  
 Sharma, Shubhatma, 197  
 Sharma, Sumit, 449  
 Shendekar, Vikalp, 79  
 Singh, Anil Kumar, 21  
 Singh, Anurag, 175  
 Singh, L.P., 21  
 Singh, Mandeep, 409  
 Singh, Pardeep, 497  
 Singh, Prashant Kumar, 311  
 Singh, Pratap, 431  
 Singh, Rasmeeet, 165, 409  
 Singh, Sarbjeet, 563  
 Singh, Sartaj, 449  
 Singh, Tanpreet, 327  
 Singh, Yogesh, 353

Somayaji, Anantha Krishna, [367](#)  
Somwanshi, Devendra, [421](#)  
Sreevatsa, K Aditya, [293](#)  
Stojanović, Anđela Jakšić, [87](#)  
Subashini, M. Monica, [69](#)  
Subbiah, Ram, [293](#)  
Suresh, Raja, [275](#)

**T**

Tiwari, Anamika, [175](#)  
Tungikar, V.B., [145](#)

**V**

Verma, A.K., [261](#)  
Verma, Deepak, [57](#), [261](#)

**Y**

Yadav, Anamika, [13](#)  
Yadav, Anshul, [241](#)  
Yadav, Hrithik, [399](#)  
Yadav, Pallvita, [311](#)  
Yadav, Rajat, [523](#)  
Yadav, Surendra Kumar, [241](#)